University of Bath

UNIVERSITY OF BATH

PHD

Power consumption and gas dispersion in agitated vessels.

Kobbacy, Khairy A. H.

Award date:
1981

Awarding institution:
University of Bath

Link to publication

POWER CONSUMPTION AND GAS DISPERSION

IN AGITATED VESSELS

Submitted by Khairy A H Kobbacy

for the degree of PhD of the
University of Bath

1981

ProQuest Number: U322020

All rights reserved

INFORMATION TO ALL USERS
The quality of this reproduction is dependent upon the quality of the copy submitted.

In the unlikely event that the author did not send a complete manuscript
and there are missing pages, these will be noted. Also, if material had to be removed,
a note will indicate the deletion.
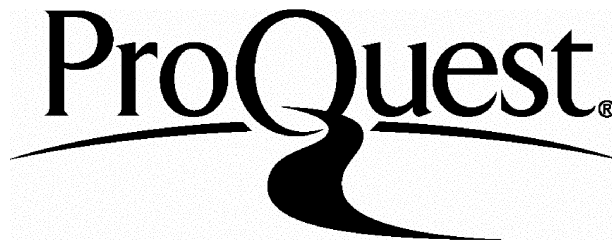
ProQuest U322020

SUMMARY

An experimental study of the steady-state and dynamic characteristics
of gas-liquid mixing in an agitated vessel has been made. The effect
of impeller speed and gassing rate on the power consumption, bubble
size, gas holdup and specific interfacial area was investigated over a
wide range of conditions, in both coalescing and 'non-coalescing'
systems. A further extension of this included the effect of
continuous liquid flow. The experiments were carried out using a
fully baffled tank of 0.2m diameter and three sizes of Rushton turbine
with D/T = 0.375 to 0.66. The bubble size in the vessel was measured
by a capillary probe technique.

In the ungassed state (no sparging of gas) and at sufficiently high
Reynolds number, surface aeration plays an important role. Sampling
of the entrained bubbles near to the liquid surface and in the impeller
region revealed that surface aeration takes place before there is any
drop in Power number and at correspondingly much lower impeller speeds.
A mechanism for surface aeration is proposed and correlations are
presented.

A new measure of gas dispersion efficiency, η, has been defined. It
can be used to identify the different regions of gas-liquid mixing as
well as providing estimates of the degree of flooding or gas
recirculation. The correlations of η obtained from the gassed power
measurements enable a more accurate prediction of Pg to be made for
any region of gas-liquid mixing. The impeller power response has
been studied using pulse and step change in gas flow rate. These
dynamical measurements have provided further insight into the cavity
formation processes occurring behind the impeller blades and the

reverse process of cavity stripping. A simple lumped parameter model has been proposed to describe the process of cavity formation. The physical implications of this model are analysed and estimates of η_R obtained are compared with the steady-state results.

Extensive measurements have been made of the bubble size produced in air-water and air-electrolyte dispersions. These are presented in the form of spatial and point distributions, gas-holdup and specific interfacial area. Averaged overall estiamtes of these dispersion properties have been analysed and compared with other results and correlations.

The position of the inlet and outlet liquid flows in a continuous-flow system have a very significant effect on the gas-liquid mixing. However, having the liquid inlet at the bottom of the tank and the outlet pipe at the side does not substantially alter the pattern of mixing from that observed in a batch vessel.

ACKNOWLEDGEMENTS

CONTENTS

CHAPTER 1

INTRODUCTION

Gas-liquid reactors constitute an important segment of chemical reactor technology. Mechanically agitated vessels have found many applications in gas-liquid contacting to promote physical and chemical absorption (or stripping) of gasses, eg, fermentation and many types of hydro-geneation, chlorination and sulphonation processes. A great deal of research has been done to investigate the behaviour of these systems, particularly concerning the impeller power requirements and dispersion properties. However, because of the very complex nature of the three-dimensional turbulent two-phase flow in a stirred vessel, theoretical analysis poses intractable and, as yet, insurmountable problems in terms of fundamental fluid mechanics and mathematical solution. To date, and perhaps for some time to come, most of the work in this field has tended to emphasise the development of useful empirical correlations. Despite the extensive studies that have been made, serious discrepancies still exist in the results and correlations obtained, although there are also a number of important aspects that have not yet been investigated. As an example, there has not been any treatment of a dynamic nature, reflecting that a gas-liquid dispersion is itself a dynamic process. Also very little attention has been directed to the study of continuous (liquid) flow mixing systems, even though they are of major industrial importance. In addition, surface aeration effects likely to be present whenever there is a free gas-liquid surface, have not been adequately quantified.

The impeller power consumption is one of the most important design parameters. In order to achieve an optimally engineered process, a reliable prediction method for this parameter is required. The input of turbulence energy through the impeller, and the way in whcih it is distributed in the vessel, determines the gas-liquid interfacial area and the rates of mass transfer. Knowledge of the mechanisms

determining the energy dissipation from the stirrer, despite being based mainly on visual observations and qualitative analysis, seems to be more advanced than the understanding of measured power effects. A dynamical study of the impeller power characteristics should complement the steady-state picture and may also aid in understanding the physical processes involved.

Gas-liquid mass transfer constitutes the rate determining step in physical absorption processes, eg, fermentation, and also in many cases of chemical reaction. A major parameter affecting the rate of mass transfer is the interfacial area which is directly dependent on the rate of energy dissipation. The important requirement here is for accurate estimation of the gas holdup and bubble size. The trend recently has been growing towards developing experimental techniques which can provide unambiguous measurements of bubble size in agitated vessels. To date, though, a technique has not emerged which combines all of the advantages required, ie, high accuracy, fast response and ease of application over a wide range of bubble size and point gas holdup. Such a technique would enable a more systematic investigation of parameter effects in terms of distribution of bubble size, gas holdup and interfacial area.

The objectives of this study can be divided into three parts. The first is to make a critical analysis of the impeller power consumption under steady-state conditions and to extend this by considering the impeller power dynamics; secondly, to develop a technique for measurement of point bubble size and gas holdup which can be used to study the gas-liquid dispersion properties. The third objective of this study is to extend the investigations of batch vessel operation to continuous-flow. These objectives also form an important precursor to any study of 3-phase aerated slurry reactors for which part of the

equipment that was used in this study was constructed.

The overall aim of this study is directed towards a deeper understanding of the processes involved in stirred gas-liquid reactors so that useful correlations and design methods can be developed for batch and continuous-flow systems. For convenience of presentation, each area of research investigated is covered in a separate chapter, starting with an introduction, and followed by literature review; results and discussion; and conclusions. Slight exceptions to this format are to be found in Chapters 5 and 8 where the review is included in the introduction section. This is because of the small amount of previous work in these areas. Whenever there has been a need to use a specific observation, conclusion, or correlation from a chapter, adequate cross-reference is given. Although the literature reviews were made as comprehensive as possible, a significant portion of the critical comment is often mainly concentrated in the results and discussion sections. This is principally because the form of empirical correlations encountered tends to make objective criticism an otherwise inherently difficult process. The equipment and measurement techniques used are described in Chapter 2. Chapter 3 deals with the ungassed power consumption. This particular research was not originally intended but was prompted by the recognition that surface aeration effects could be significant. The steady-state requirements and the dynamical characteristics of the impeller power in batch gas-liquid system are studied in Chapters 4 and 5, respectively. A description of the capillary technique developed for bubble size and point gas holdup measurements is given in Chapter 6. The distributions and correlations obtained for bubble size are also included in Chapter 6. Chapter 7 is concerned with gas holdup and specific interfacial area as

represented by local and overall values.   The impeller power consumption and gas holdup in the continuous-flow system are covered in Chapter 8.   Finally, recommendations for future work are given in Chapter 9.

CHAPTER 2

EQUIPMENT AND MEASURING TECHNIQUES

2.1   INTRODUCTION

This chapter deals with the equipment and the measuring techniques used in this study.   In Section 2.2 the general layout and some design aspects of the equipment are discussed.   The mixing vessel and impeller dimensions, and liquid media used are given in Section 2.3.   This is followed by description of some specific measuring techniques, eg, impeller power consumption and gas holdup in Section 2.4.   The capillary probe technique which has been developed for bubble size measurements is also described briefly in that section.

Finally the use of a microprocessor system for on-line real time data acquisition and analysis is explained in Section 2.5.

2.2   GENERAL DESCRIPTION OF EQUIPMENT

Few experimental studies have been done on continuous flow stirred tanks.   Two alternative designs for equipment used in single phase studies are described in the literature.   The first is using a closed vessel (1) (2).   Once the vessel is full of the incompressible liquid the rate of flow out becomes equal to the pumping rate of liquid to the vessel.   The second uses an open vessel (3) with an overflow weir fixed at the desired height from the tank bottom.

However, if a second gaseous phase is introduced, this leads to more complexity of equipment design.   By the nature of the process the liquid has to have a free surface to allow for the continuous flow of gas through the vessel.

In the present study, a closed tank design was selected.   The liquid level inside the tank was controlled to allow a free liquid surface.   This design has advantages over using an open tank.   With a closed

tank design it is easier to change the positions of the liquid intake and outflow. A high liquid flow rate could be achieved with no difficulties arising due to the size of the outflow piping. Also the flow rate of the gas leaving the liquid could be measured.

The equipment was designed to fulfil the following aims :

1. to be used in the study of batch and continuous flow multiphase mixing;   —

2. to run at pressures up to 100 psig;

3. to be used in steady state runs and transient tests;

4. to maintain high accuracy in measurements.

The equipment is described in the following four subsections. The specifications of the main components are listed in Appendix B.

2.2.1 Power System and Driving Shaft Suspension

Figure 2.1 demonstrates the assembly of the impeller shaft driving unit. A 0.25 HP DC shunt motor was used to drive the impeller shaft. The power was transmitted from the motor to the shaft through a strain gauge torque sensor. A feedback thyristor control circuit was used for the measurement and control of the motor speed.

As the equipment was designed to work at moderately high pressures, it was necessary to design a special stuffing box for the drive shaft. This is illustrated in Figure 2.2.

2.2.2 Liquid Flow Circuit

Figure 2.3 demonstrates the circuit diagram for liquid flow. A tank (Tl) of one metre diameter was used to prepare the liquid (filtered tap water in this study). The tank was fitted with propeller to obtain uniform temperature distribution throughout the tank. The
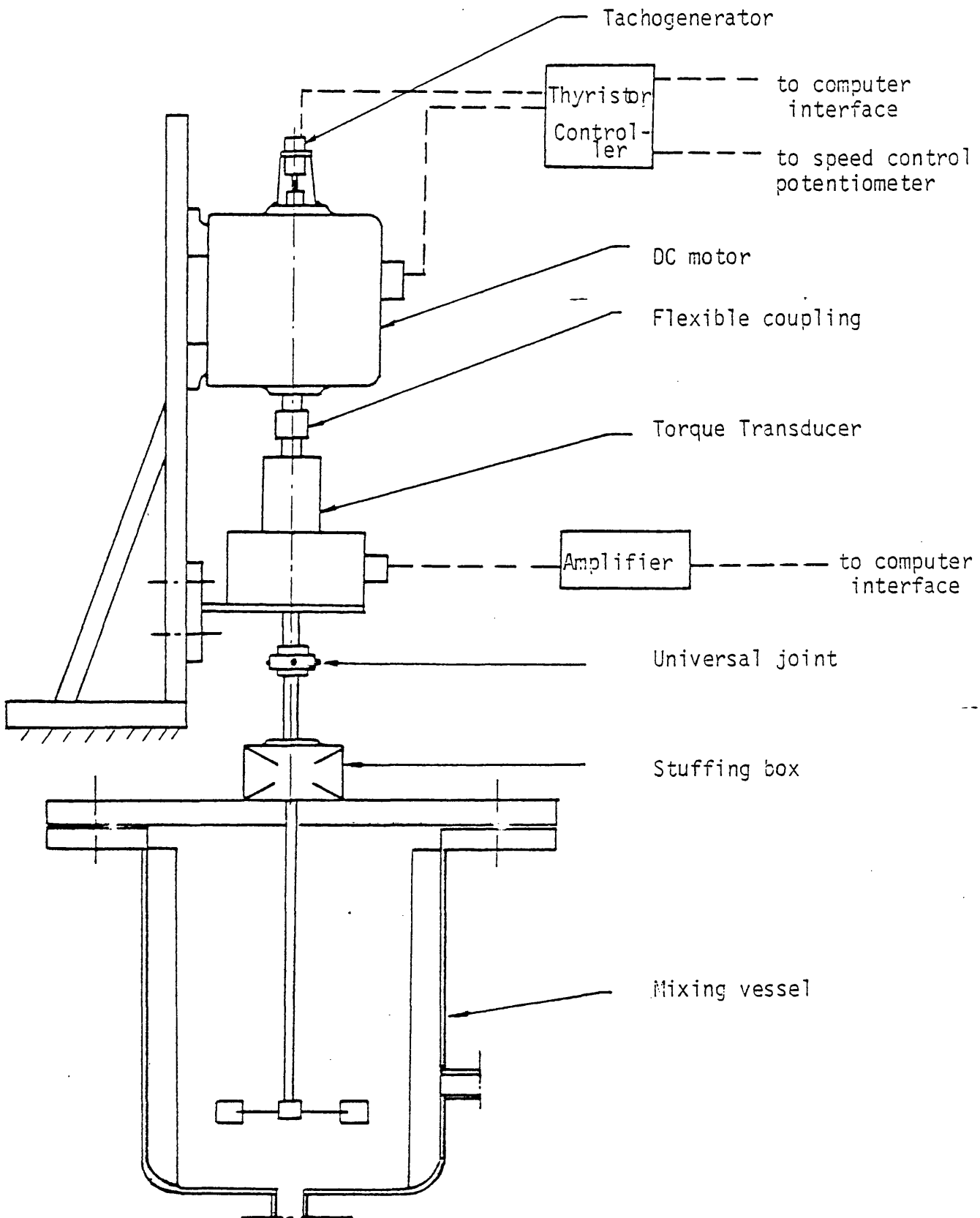
Figure 2.1 : Schematic drawing of power system

Figure 2.2 :   Impeller driving shaft stuffing box.

Housing Material :   brass.   scale 1:1

Driving shaft

Ball bearing

Thrust
ball bearing

Ball bearing

spring
rubber bellows

graphite seal
face
ceramic seal ring
rubber seat

Mechanical seal

45^ϕ

85^ϕ
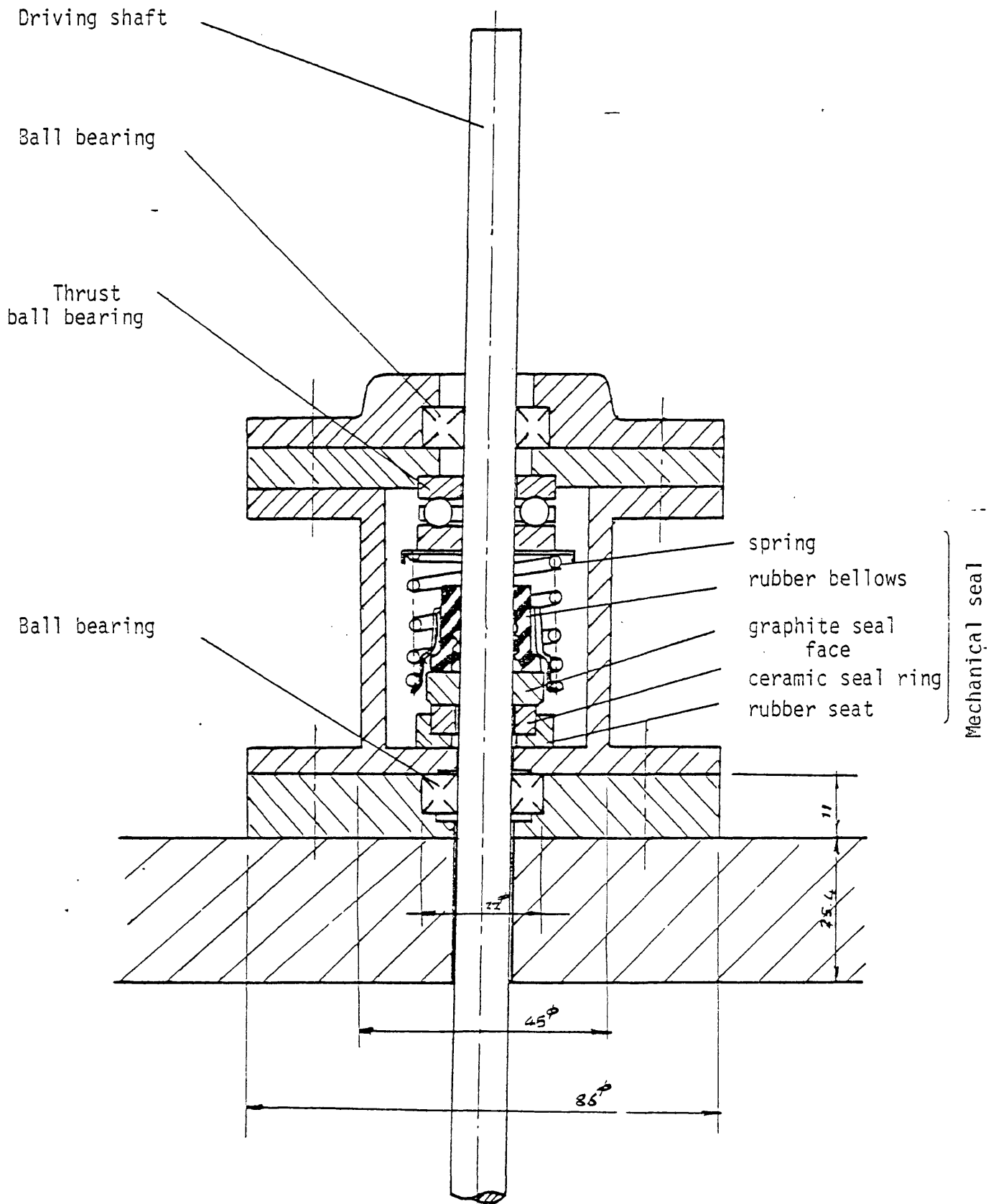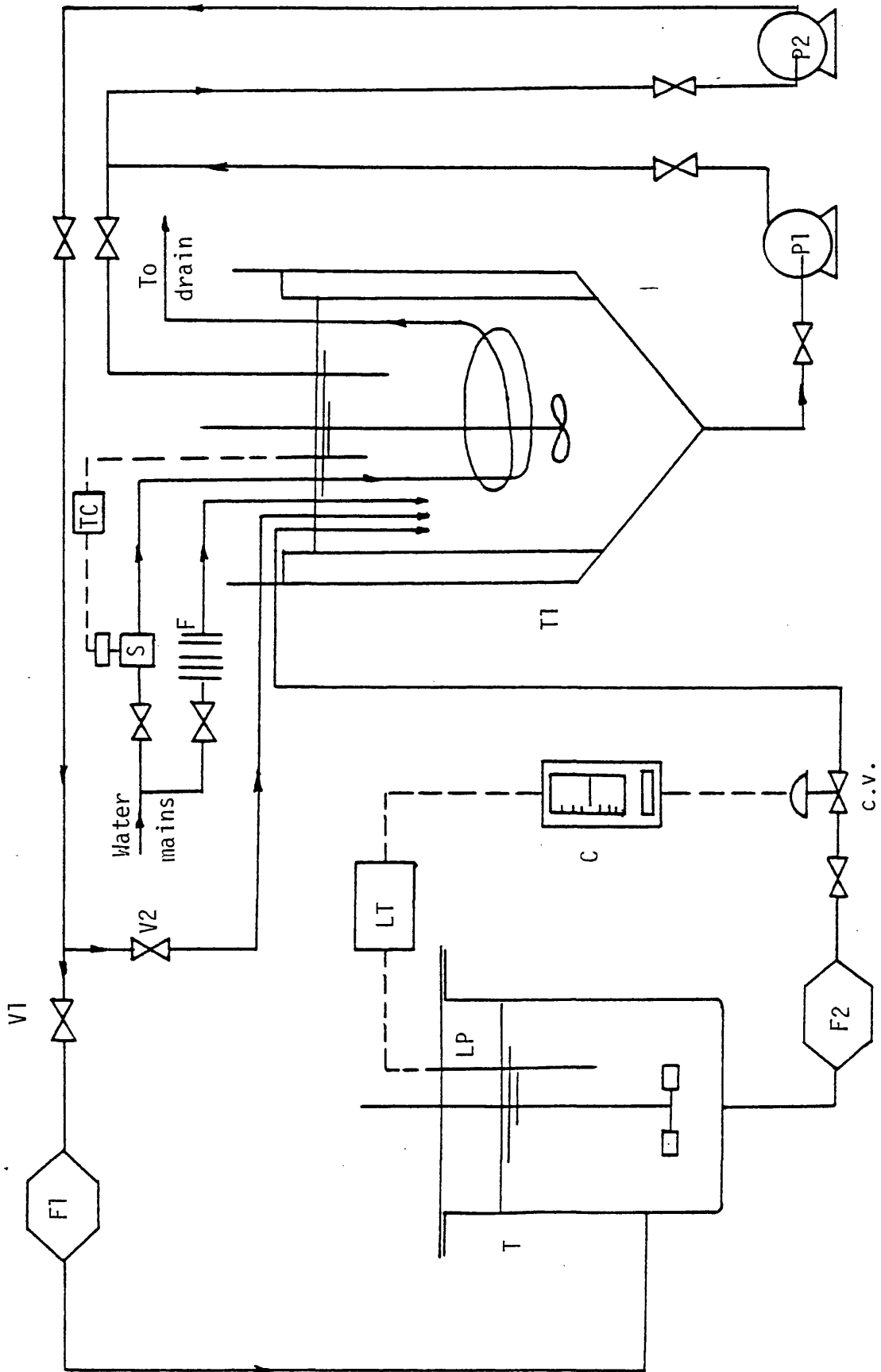
Figure 2.^ : Circuit diagram for liquid flow

water temperature in the tank was kept constant at $20^{\circ}C$ during the runs by a cooling coil equipped with a feedback control circuit. The on-off temperature control loop consisted of thermocouple immersed inside the tank, temperature controller (TC), and solenoid valve (S).

A two-stage pumping system was used to supply liquid to the mixing vessel. A centrifugal pump (P1) circulates the water back to the tank (T1), whilst a mono-pump (P2) feeds the line to the mixing vessel. The intake of the mono-pump was fitted inside the outlet pipe of the centrifugal pump.

The flow rate of water to the mixing vessel was controlled by two ball valves (V1) and (V2), by bypassing part of the water back to the conditioning tank (T1). Two magnetic flowmeters (F1) and (F2) were used to measure the flow into and out of the mixing vessel.

The liquid level inside the mixing vessel was controlled by feedback control circuit. This consisted of level probe (LP) connected to level transmitter (LT) which feeds the level signal to PID controller (C). The controller operates a pneumatic control valve (CV) fitted on the outlet pipe of the mixing vessel.

2.2.3 Gas Flow Circuit

Figure 2.4 is a schematic diagram of the gas (air) flow circuit. A pressure regulator (2) was used to control and measure the pressure of filtered air coming from mains at a pressure of approximately 80 psig. The air flow rate to the mixing vessel was measured by a venturimeter (3) and flow transducer (4). Control was effected by a needle valve(12).

After passing through the liquid, the air was allowed to flow out of the mixing vessel through a pipe fitted on the cover flange. The flow rate of the gas leaving the vessel was measured by venturimeter
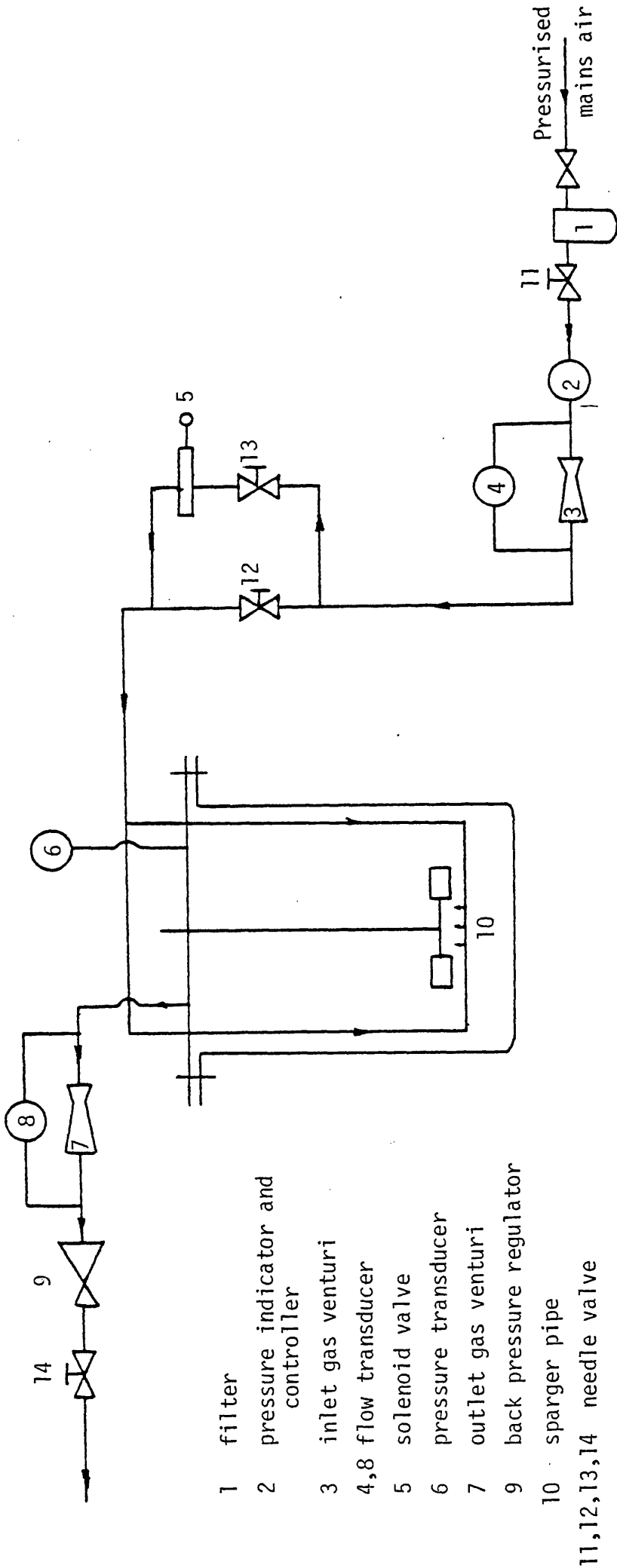
Figure 2.4 : Gas flow circuit

1   filter

2   pressure indicator and
    controller

3   inlet gas venturi

4,8 flow transducer

5   solenoid valve

6   pressure transducer

7   outlet gas venturi

9   back pressure regulator

10 sparger pipe

11,12,13,14 needle valve

and flow transducer (7,8). The back pressure regulator (9) was used to control the pressure inside the vessel, which was measured by pressure transducer (6).

A needle valve (13) and solenoid valve (5) were used to introduce pulse and step changes in the gas flow rate to the vessel. These were used in the study of impeller power dynamics and are explained in detail in Chapter 5.

2.2.4 Measurement and Data Acquisition System

Figure 2.5 illustrates schematically these circuits. The signals derived from the various measuring devices which are illustrated in Figures 2.3 and 2.4 were first conditioned in a suitable transmitter. These transmitters provided standard signals (4-20 mA, or 0-10 mA) to the main signal conditioning box. Each signal was fed through a channel of the signal conditioning box which stabilised the signals and provided standard 0-5 volts output. These signals were measured by a microprocessor.

A five digit digital panelmeter was used for digital display of the voltage signal of any channel of the signal conditioning box, while a dual-beam oscilloscope was used for displaying the signals for visual observation. the MACSYM II microprocessor (Analog Devices Ltd) which was used for measurement and data acquisition was interconnected with teletypewriter.

Photographs 2.1 and 2.2 show the control panel, the microprocessor and a general view of the equipment. The conditioning tank is shown in photograph 2.3 with the pumping unit, while photograph 2.4 shows the impeller driving unit.
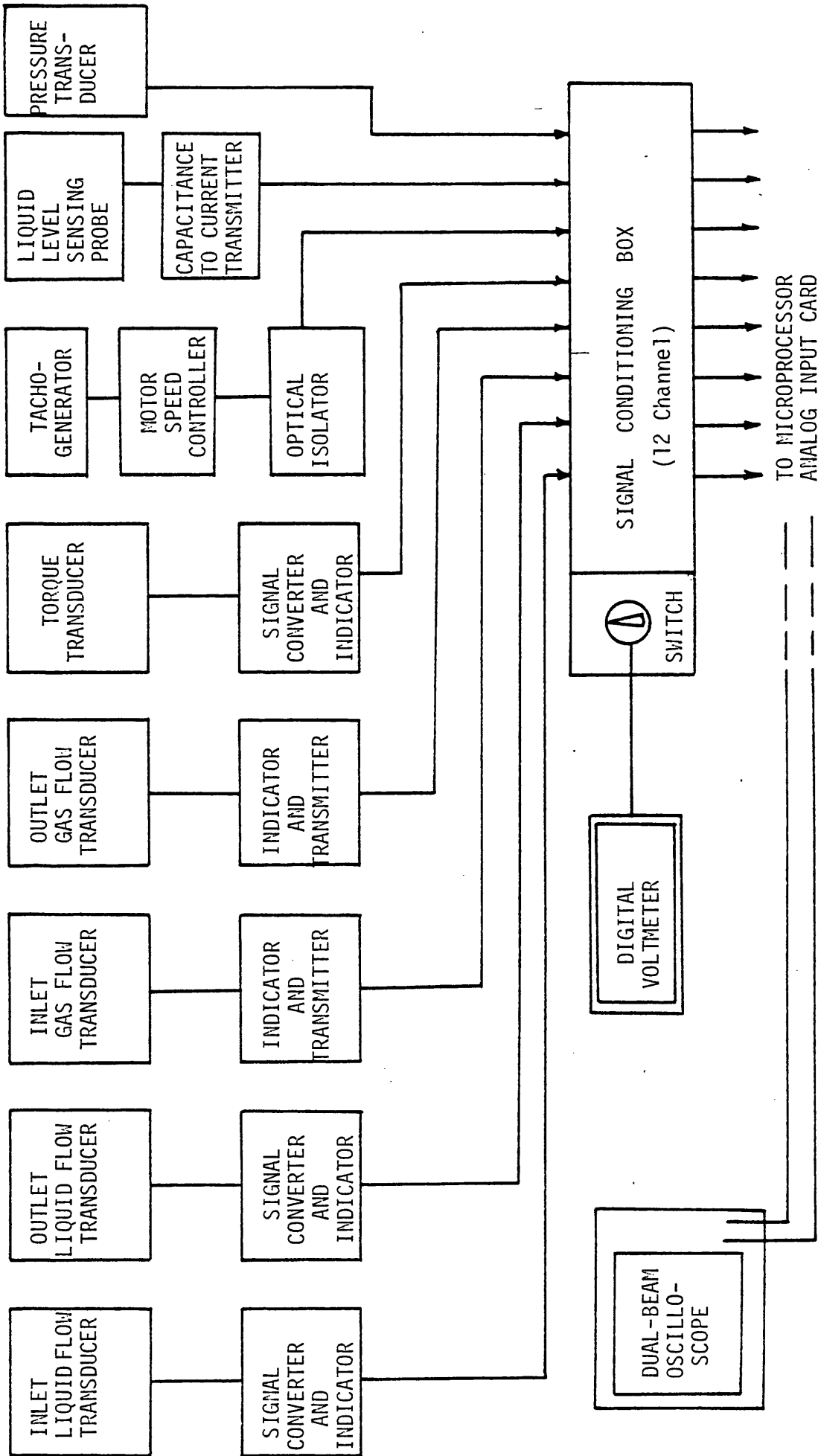
Figure 2.5 : Schematic circuit diagram for measurement and data acquisition
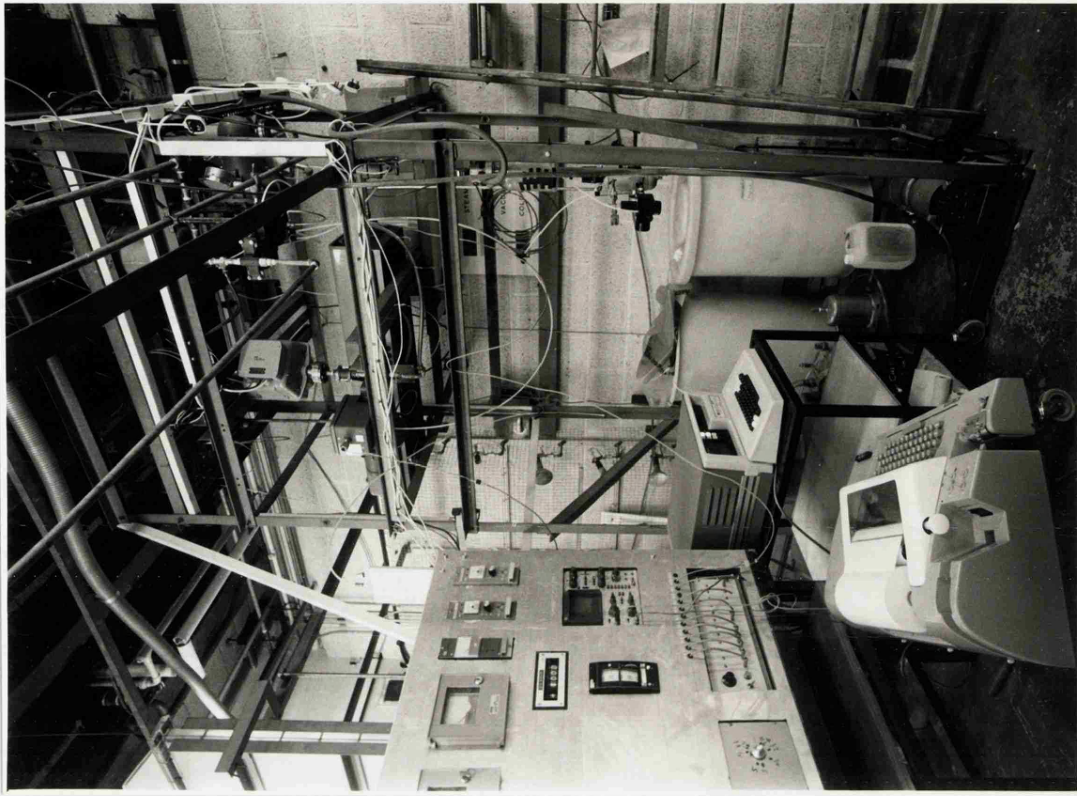
Photograph 2.2 : General view of the equipment
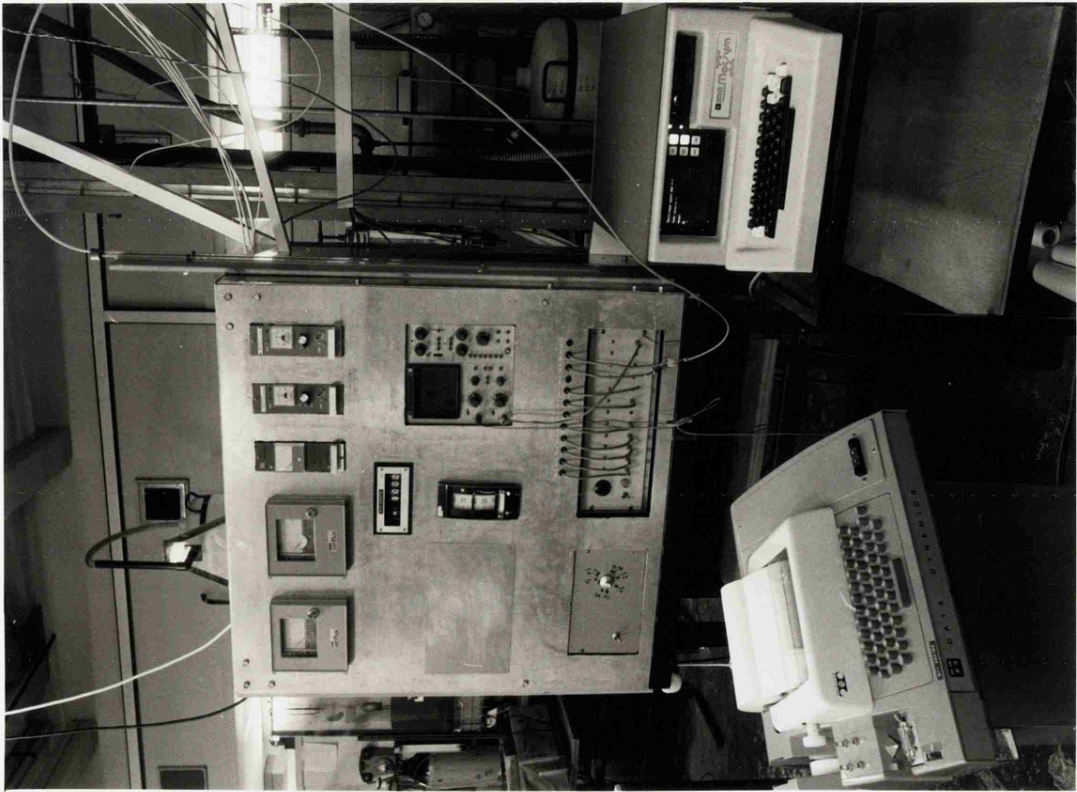
Photograph 2.1 : The control panel and microprocessor

Photograph 2.4 : Top view of mixing vessel with the power system

Photograph 2.3 : The conditioning tank with the pumping unit

2.3 MIXING VESSEL, IMPELLERS, AND LIQUID MEDIA

2.3.1 Mixing Vessel and Gas Sparging Unit

A flat-bottomed tank of 0.203m diameter and 0.267m height was used throughout the experimental program of this study. As shown in Figure 2.6, the tank was fitted with four standard wall baffles each one tenth of the tank diameter. These baffles were extended from bottom to the top of the tank. A standard ASA 150 lb rating flange was welded to the top end of the tank.

Two ½in. BSP pipes of 15mm inner diameter were fitted into holes at the wall of the tank. One of these pipes was welded at the centre of the tank bottom, and the other pipe at the side at a height equal to one third of the tank diameter. These pipes were used for the flow of water into and out of the tank.

Eight bolts were used to tighten a top cover plate to the tank flange. A PTFE gasket was used for sealing. A set of ¼in. BSP holes were drilled on the top flange for the sparger tube, level probe, pressure transducer, air exit pipe, and for the bubble analysis probe.

The sparger unit was an ⅛in. diameter horizontal tube connected between two vertical inlet pipes. The compressed air was fed from both ends of the tube. Five holes of 1.2mm diameter were drilled at equal distances of ½in. in the horizontal sparge tube beneath the impeller.

The tank, top cover plate, and the sparging tube were all made of 316 stainless steel.

2.3.2 Impellers

Standard 6 blade Rushton turbines were used for agitation. Figure

PTFE gasket

gas

$8 \times 0.75"$ ⌀

level probe

T/o

$10.5"$

$T/4$

$T/3$

gas sparger

$T = 8"$

$\frac{1}{2}"$ BSP pipe
(15mm inner diameter)
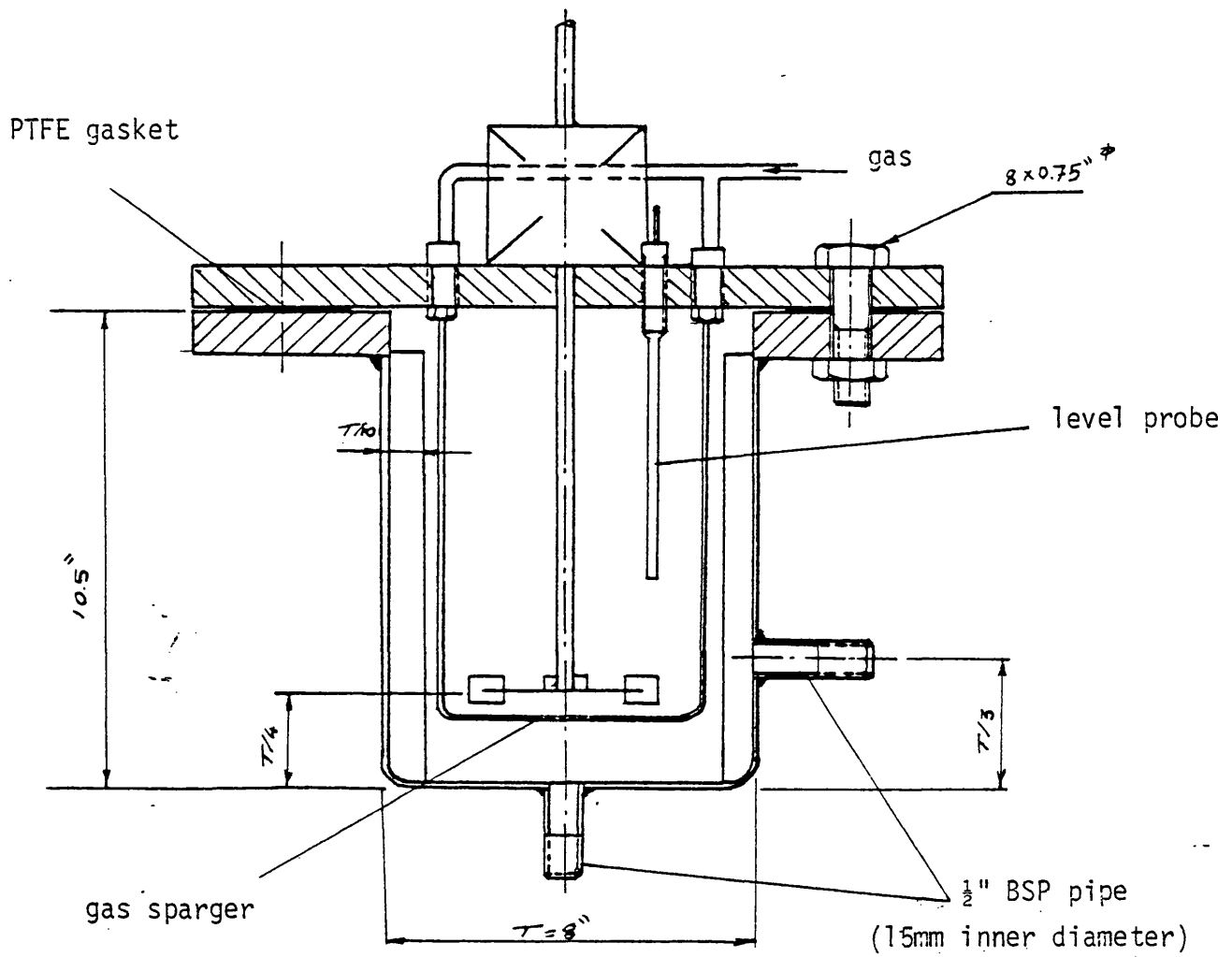
Figure 2.6 : Details of the mixing vessel

2.7 illustrated the geometry of this impeller, and Table 2.1 gives

the details of the impeller's dimensions. The impellers were made of

brass and were chromium plated. In all experimental runs the distance

from the centre of the impeller to the tank bottom was fixed at

0.05m (H/4).

Table 2.1   Dimensions of Impellers Used (x10^3 m)

Impeller *	D1	D2	D3
D	76.2	101.6	135
d'	57.15	76.2	101
a'	1.587	1.587	1.00
b'	1.587	1.587	1.587
c'	19.05	19.05	17.46
e'	7.937	7.937	7.937
f'	9.52	9.52	9.52

* see Figure 2.7

2.3.3 Liquid Media

Filtered air was used as the dispersed phase in this study. Filtered

tap water, distilled water and 0.11 M potassium sulphate solution

were used as continuous phase media. The analysis of the tap water

used is illustrated in Appendix D.

2.4   MEASURING TECHNIQUES

2.4.1 Power Measurement

The power dissipated to the liquid by the rotating impeller was

calculated by

Figure 2.7 : Disc turbine geometry
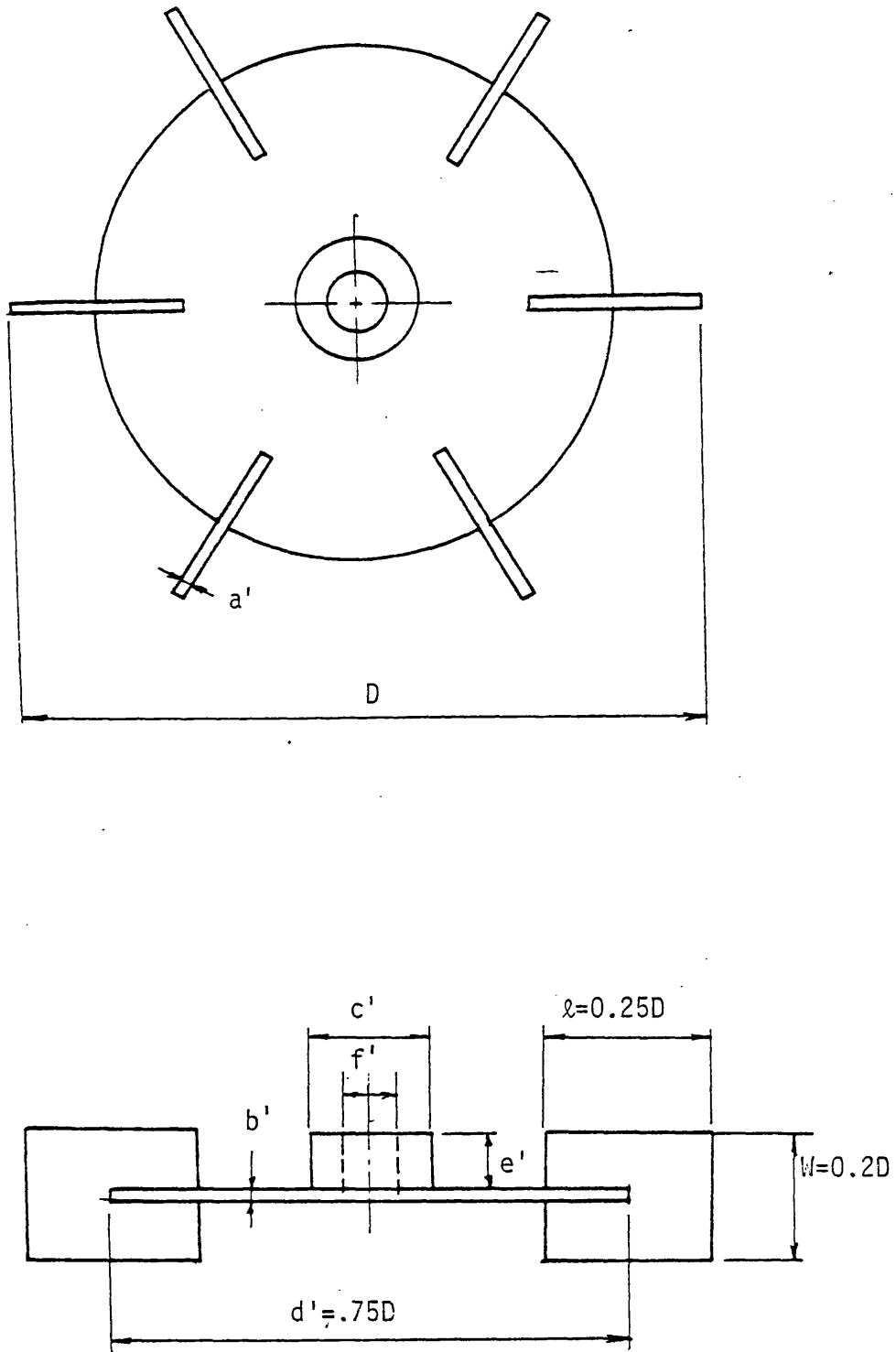
$$P = K \cdot T_i \cdot N \qquad\qquad 2.1$$

where

P	impeller power
T_i	Torque exerted on the impeller
N	Impeller speed
K	conversion constant

As described by Nienow et al (4), accurate power measurement is a much more difficult problem than it first appears. The specifications of equipment, as well as the measuring techniques have to be carefully selected if a reasonable range of impeller Reynolds number is to be covered.

2.4.1.1 Impeller speed

As illustrated in Figure 2.1, the tachogenerator was fitted to the rotor of the DC motor. When the motor rotates the tachogenerator generates a DC signal. This signal is used for the purpose of measurement and control of the impeller speed. It is first fed to the thyristor controller as the feedback signal of the speed control loop. An optical isolator was further used to isolate this signal before it was fed to the microprocessor interface for measurement. Because of nonlinearity in the isolator circuit the relation between the motor speed and the output signal of the optical isolator was slightly nonlinear. However, that relation was fitted accurately to third order polynomial such that

$$N = a + bV + cV^2 + dV^3 \qquad\qquad 2.2$$

where

N	impeller speed r.p.s.
V	output signal of optical isolator volts.
a,b,c and d	coefficients

The microprocessor measured this signal by averaging 5,000 readings in 5 seconds (see Appendix C). The measured value of this signal was then substituted in Equation 2.2 to calculate the impeller speed. The error in measurement of impeller speed was less than 0.7%.

2.4.1.2 Impeller Torque

A strain gauge torque transducer was used for measuring the torque exerted on the impeller (Figure 2.1). This torque sensor measures the transmitted torque between the motor and the impeller shaft. The measured torque is equal to the torque exerted on the impeller plus the friction torque dissipated in the mechanical seal, ie,

$$T_m = T_i + T_f \qquad\qquad 2.3$$

where

T_i the torque exerted on the impeller

T_m measured torque by the transducer

T_f friction torque

The friction torque was measured under a 'dry' run, ie, with the mixing vessel empty, at each impeller speed and vessel pressure. The impeller torque T_i was calculated from Equation 2.3.

The torque transducer had a high sensitivity and accuracy, and its specifications are listed in Appendix B. Thus the accuracy of measurement was dependent on the accuracy of measuring the friction torque, and its ratio to the total torque measured. The friction torque normally increased by about 30% when the motor speed was increased from the lowest to the highest values (2-20 r.p.s.). It was always measured within 10% or better.

At the lowest end of the speed range the impeller torque was of the same order as the friction torque. So in that speed range the

impeller torque was measured within the accuracy of measuring the
friction torque, ie, 10%. However as the impeller torque increases
in a quadratic relation with increasing the impeller speed ($T \alpha N^2$), a
substantial improvement in its measuring accuracy was achieved at
high speeds. The error in measuring the impeller torque for impeller
Reynolds number greater than 4×10^4 was always less than 5%, and for the
majority of the experiments significantly better than this.

2.4.2 Gas Holdup Measurement

The total gas holdup was calculated by observing the difference in the
height of the dispersion above the tank bottom, and the height of the
ungassed unagitated liquid.

$$h = \frac{H'-H}{H'} \hspace{3cm} 2.4$$

where

h	gas holdup
H'	height of the aerated liquid
H	height of the ungassed unagitated liquid.

This is the conventional method for estimating the gas holdup.
However, in most of the published studies it is not obvious whether
the height of the ungassed liquid was measured under stagnant or
agitated conditions.

When the impeller speed under ungassed conditions exceeds certain
limits, surface aeration phenomenon starts to take place (Chapter 3).
Gas bubbles are entrained at the liquid surface and are circulated
into the bulk of the liquid. Obviously this is accompanied by a rise
in the liquid level. Thus, if the interference of surface aeration
with gas holdup measurement is to be avoided, the ungassed liquid
height H in Equation 2.4 has to be measured without agitation.

The surface aeration phenomenon might have caused possible confusion in previous investigations. Robinson and Wilke (5) used manometric method to measure the gas holdup. They observed that in an ungassed liquid the manometer differential increased with increasing impeller speed just as it would in a gas-liquid dispersion wherein the gas holdup increases. Although their investigations were conducted at conditions under which surface aeration possibly occurred (see Section 2.3.1.2), they attributed this as being only due to a dynamic pressure difference. They have added "Some previous investigators also measured gas holdup by manometric techniques ..... No mention of a dynamic pressure contribution was made in these works, but it is difficult to see how their manometrics were free from this source of interference." Recently Sridhar and Potter (6) have reported a similar observation. Having also attributed it to a dynamic pressure effect, they measured the liquid height in clear and in gassed liquid at the same impeller speed, and used this as a correction factor. In the present study the liquid height was measured by a capacitance sensing probe and hence the dynamic pressure can have no possible effect on measurement. Nevertheless, the ungassed liquid height still increased with increasing impeller speed, a fact which emphasises the role of surface aeration and its possible interference with gas holdup measurement.

Few methods are reported in literature for measuring the ill defined liquid level in agitated gas-liquid dispersion. Foust et al (7) developed what they called a level taker to obtain a calm and average level surface. It consisted of two concentric copper tubes, with a number of nonconcentric holes drilled in the upper portion of the tubes. The level device was connected to a small hook gauge which

was used to take readings of the level in the tank. Rushton and
Bimbinet (8) used a similar device but with a loose packing of glass
wool between the inner and outer tubes to obtain a quiescent liquid
surface in the inner tube. A similar technique was employed by Lee
and Meyrick (9) but they used a cathetometer to measure the level in
a manometer connected to the level taker. A more popular method
involving manometry was developed by Calderbank (10) and was used in
other investigations (5), (6), (11), (12). A manometer was used to
measure the pressure P_x at position in the dispersion at height x from
tank bottom. This measurement was repeated for positions at different
heights. Using curve fitting or extrapolation of the data on x vs. P_x
plot, indicated the free surface height, where $P_x=0$. Hassan and
Robinson (13) used a cathetometer directed at the impeller shaft
region to obtain direct measurement of the level. They claimed that
this would avoid the fluctuations in the level that occur at the tank
wall due to the baffles.

In the present work, the liquid level was measured for both batch and
continuous flow runs using the capacitance sensing probe. This
method of measurement involves the use of an electrode which forms a
capacitance between itself and the surrounding material. A variation
in the value of the capacitance is achieved as the depth of the vessel
contents alters. The level probe was used with a capacitance to
current transmitter to produce a standard 4-20 mA DC current output
signal that is directly proportional to the input capacitance of the
probe.

The level probe was made of $\frac{1}{8}$in. diameter brass rod. An outer shell
made of PTFE and of $\frac{1}{4}$in. outer diameter was used for insulation.
The very low wettability of the electrode insulation coupled with the

fast response of the transmitter (0.1 sec) provided a fast and accurate method for measuring the level.

After the complete installation of the level probe and the associated electrical circuit, it was calibrated. A known volume of water was added to the vessel and the corresponding changes in the output signal of the level transmitter were recorded. The level of water in the vessel was determined from the obtained linear relationship (see Appendix B).

In batch gas-liquid runs the typical fluctuations in liquid level were observed. The output signal from the level transmitter was estimated by averaging 1000 measurements over 5 seconds using the Macsym processor. In essence that averaging is equivalent to the use of physical damping device, like the level taker used in previous studies (7), (8), (9).

The level probe was fitted at a radial distance of 1.8in. from impeller shaft and between two baffles. That position was selected such that it was far enough from the baffles where fluctuations in water level were visually observed. And at a distance from the impeller shaft where a limited degree of vortex motion may occur at high impeller speeds (14).

2.4.2.1 Gas Holdup Measurement in Batch Runs

The ungassed unagitated liquid level H was set at 0.203m (H=T) throughout the batch runs, and the dispersion level H' was measured by the level probe. Equation 2.4 was used to calculate the gas holdup. The measurements of gas holdup were reproducable within 5%.

2.4.2.2 Gas Holdup Measurement in Continuous Flow Runs

In the continuous flow runs the dispersion level H' was kept constant at a value equal to tank diameter (0.203m). A 'shutting-off' technique was used to measure the corresponding ungassed unagitated liquid height H.

The experimental arrangement for shutting-off the mixing vessel is shown in Figure 2.8. Two normally closed solenoid valves (S1) and (S2) were fitted in the water flow line just before and after the vessel. A third solenoid valve (S3) was used to bypass the liquid. The electrical coils of the three solenoid valves were connected with an octal electrical relay (R). When the relay was energised by closing the manual switch (SW), valves (S1) and (S2) were opened, and valve (S3) was closed.

The experimental procedure for gas holdup measurement was :

1. Set the equipment at the desired conditions, ie, impeller speed, water and gas flow rates.

2. After achieving the steady state conditions with the level properly controlled, the switch (SW) is opened. The solenoid valves (S1) and (S2) are shut simultaneously, stopping the flow of water to and from the vessel. Solenoid valve (S3) is opened to avoid any excess pressure in the water pipes.

3. The gas flow to the vessel is stopped as well as the impeller.

4. A period of time is allowed for any gas entrained in the liquid to flow out. A fast drop of level was normally observed on the indicator of the level controller.

5. Measure the liquid level in the vessel. This level is the clear liquid height H, which corresponds to the steady state
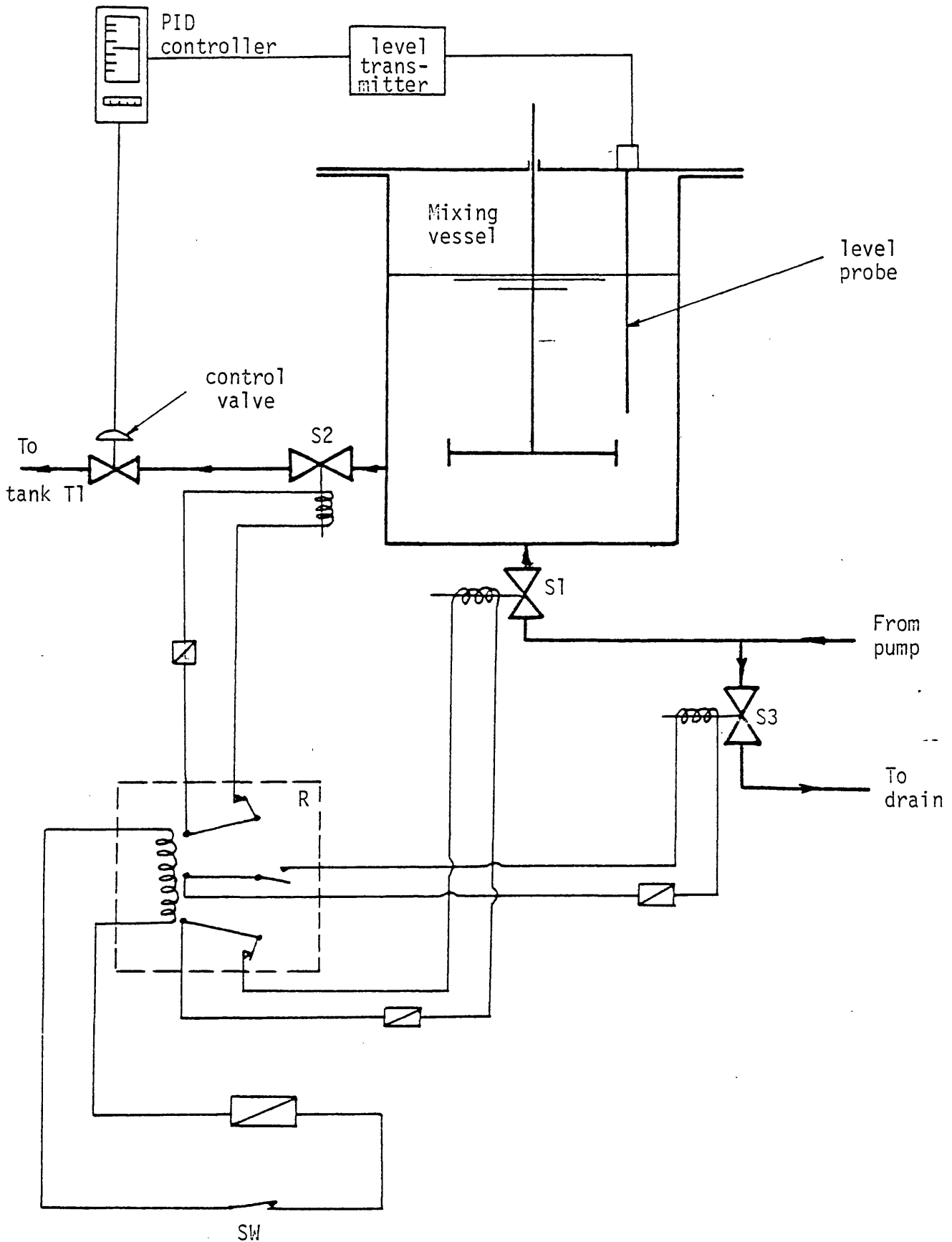
Figure 2.8 : Shut-off and electrical circuit for
measuring liquid level with continuous flow

conditions as adjusted in step 1.

6.   Equation 2.4 is used to calcualte the gas holdup.

Although this method was fairly accurate, its accuracy was
proportional to the magnitude of the measured gas holdup.   Also in
the case where the water inlet pipe was at the side of the tank, at
high impeller speeds and water flow rates, the level was difficult to
control which affected the accuracy of measurement.   Nevertheless,
the reproducability of gas holdup measurement was mainly in the region
of 10% but deteriorated to 20% in extreme cases.

2.4.3 Bubble size and Point Gas Holdup Measurement

An experimental technique for fast and accurate measurement of point
bubble size and gas holdup in agitated dispersion has been developed.
The method involves direct sampling of bubbles from the dispersion
through glass capillary tube.   The bubbles were detected by optical
switch fixed on the capillary tube.   The microprocessor was used for
on-line real time processing of the output signal of the optical
switch.

The bubble analysis technique is described in detail in Chapter 6,
and Appendix A.

2.5   EXPERIMENTAL PROCEDURE AND THE USE OF MICROPROCESSOR FOR
MEASUREMENT

A computer program was written for each specific experiment.   The
general format for such programs is :

1.   measuring the output signals of the measuring devices;

2.   using the appropriate correlations to produce the real values
      of the variables, eg, N, Q, and P, and then calculating the

relevant parameters such as N_p, F_ℓ, R_e, h and P/V;

3. printing out the results on a teletypewriter.

The calibration of the measuring devices and the computer programs are listed in Appendix B and Appendix C respectively.

Use of the microprocessor for measurement was essential. Without fast on-line measurement and analysis, it would have been practically impossible to use the bubble analysis technique. Signal sampling at a very high frequency (up to 2,000 per second) with ensuing high orders of calculations were required. For the dynamical tests, a fast data acquisition system was required to measure two signals simultaneously at a fast rate, while for the continuous flow runs the process of recording measurements would have been very time-consuming without it. Time was then freed to enable observation of the equipment operation.

CHAPTER 3

POWER CONSUMPTION AND SURFACE AERATION

IN UNGASSED SYSTEMS

3.1 INTRODUCTION

The impeller power consumption in ungassed liquids has been extensively studied, but certain discrepancies have been noted by some investigators. The value of the power number has been found to be sensitive to any minor changes in impeller geometry. Although many investigators have noticed the existence of surface aeration, an adequate description of this phenomenon has not yet been achieved. It is important therefore that its effect in ungassed systems be studied in more detail. Furthermore, it is of significance in the interpretation of results of gas-liquid and continuous-flow mixing as will be shown in subsequent chapters.

3.2 LITERATURE REVIEW

Using dimensional analysis, a correlation for the agitator power was first presented by Rushton et al (15). For geometrically similar non-swirling system, ie, fully-baffled tanks, the simplified functional relationship is :

$$N_{Po} = K \ Re^{c} \qquad\qquad 3.1$$

where N_{Po} is the Power Number and Re the impeller Reynolds Number. Equation 3.1 can also be derived directly from the equations of motion, eg, as described by Dickey and Fenic (16).

For fully-developed turbulent agitation $(Re \geqslant 10^{4})$ where inertial forces dominate over viscous forces, the value of N_{Po} becomes independent of Reynolds number. Therefore Equation 3.1 can be stated as :

$$N_{Po} = K \qquad\qquad 3.2$$

where K is a constant which depends on the impeller configuration.

Several studies reported different values for N_{P_0} for standard 6-blade disc turbines. Rushton et al (15) reported a high value of 6.4, while Bates et al (17) found the Power number to be 5.0. The study of Nienow and Miles (18) indicated an increase of the N_{P_0} when the vessel was closed, while increase of the material thickness of the turbine was shown to cause significant reduction in its value (from 5.7 to 4.4) (19).

It is widely known that in an unbaffled vessel there is a continuous reduction in N_{P_0} with increasing Re which is due to the vortexing effect. Extending this concept to baffled tanks, Clark and Vermeulen (14) claimed that an increase of the ratio $(\frac{D^2W}{T^2H})$ should bring the system into a region where the baffling effect is overcome. They identified the onset of surface aeration by a sudden drop in N_{P_0}, and suggested that the air bubbles are introduced into the liquid at a surface or region of high shear where fluids flowing in opposite directions meet (20). The following correlation was proposed for predicting the speed for onset of surface aeration

$$Fr \frac{D^2W}{T^2H} (\frac{C}{H})^{2/3} = 5\times10^{-3} \qquad\qquad 3.3$$

where

Fr	Froude number
T	tank diameter
H	liquid height
D	impeller diameter
W	impeller width
C	impeller clearance

Dierendonck et al (21) defined two impeller speeds for the onset of surface aeration. The first is the minimum stirrer speed required for bubble aspiration N*, at which the first gas bubbles are sucked

in between the stirrer shaft and baffles by vortices at the surface of the liquid. The second was called the Characteristic stirrer speed for bubble aspiration (N_0^*). This was defined as the point of intersection of their correlating line for gas holdup with the impeller speed axis. The following correlations were obtained

$$\left[\frac{\mu N^* D^2}{\sigma}\right] \left[\frac{\rho \sigma^3}{g \mu^4}\right]^{\frac{1}{4}} = 1.55 \left[\frac{H-C}{T}\right]^{\frac{1}{2}} \qquad 3.4$$

for $0.1 \leqslant (H-C)/T < 0.20 + 1.75 D/T$

and $1.4 < T/D < 7.5$

$$\left[\frac{\mu N_0^* D^2}{\sigma}\right] \left[\frac{\rho \sigma^3}{g \mu^4}\right]^{\frac{1}{4}} = 2.0 \left[\frac{H-C}{T}\right]^{\frac{1}{2}} \qquad 3.5$$

for $0.1 \leqslant (H-C)/T \leqslant 0.2 + 1.75 D/T$

where μ liquid dynamic viscosity

           σ surface tension

Wisdom [19] reported that for a 6-blade turbine, the Power number initially rises with increasing Reynolds number. After reaching a maximum value, which remains relatively constant over limited speed range, any further increase in Re then causes a reduction in N_{PO}. The initial rise in N_{PO} occurred at high values of Re ($Re > 10^4$) which is generally accepted to be well above the transition region. Nienow et al [4] attributed the increase in N_{PO} to the complexity of flow around the impeller blades. A similar effect is known to occur for flow over an aerofoil at an incidence where both drag and lift vary with velocity [22]. From velocity measurements in the trailing vortex behind the impeller blades, van't Riet [23] estimated the effect on N_{PO} to be of the order of 5% for $Re > 10^4$. However, the rise in N_{PO} in Widsom's data was much greater than this. The fall-off in N_{PO} at higher Re was attributed to surface aeration.

3.3   RESULTS

The impeller power consumption data are presented as Power number against Reynolds number as shown in Figures 3.1 to 3.7.   With the exception of the case where the small diameter tank (T=0.152m) was used (Figure 3.1), all the power curves exhibited trends similar to those reported by Wisdom (19).   That is, an initial increase of N_{Po} up to a maximum value and decreasing with any further increase in Re.

It should be mentioned that the smaller tank was used for preliminary investigations only.   The results for this case indicated that the onset of surface aeration occurred at low impeller speeds.   This, therefore, significantly reduced the speed range available for studying the system in the absence of surface aeration.   For this reason it was excluded from further investigations, and the only reported results with this tank are those included in Figure 3.1.   For the rest of the work only the 0.203m diameter tank was used.

Impeller Clearance

Increase of the impeller clearance has two effects o· the power curves as shown in Figures 3.1 and 3.2.   The first is an upward shift of the initial rising section of the curve, which also becomes less steep. The second effect is that the onset of the drop in N_{Po} occurs at a lower Re.   This means that the commencement of surface aeration therefore starts at a lower impeller speed.   For this reason the impeller clearance was fixed at H/4 throughout the rest of this study.

Impeller Diameter

The maximum Power number achieved for the three impeller sizes in the 0.203m diameter tank are relatively close, ranging from 4.6 to 5.05, as shown in Figure 3.3.   However, for impeller D2 (D/T=0.5) a steeper variation in the power number occurs.   All of the impellers were
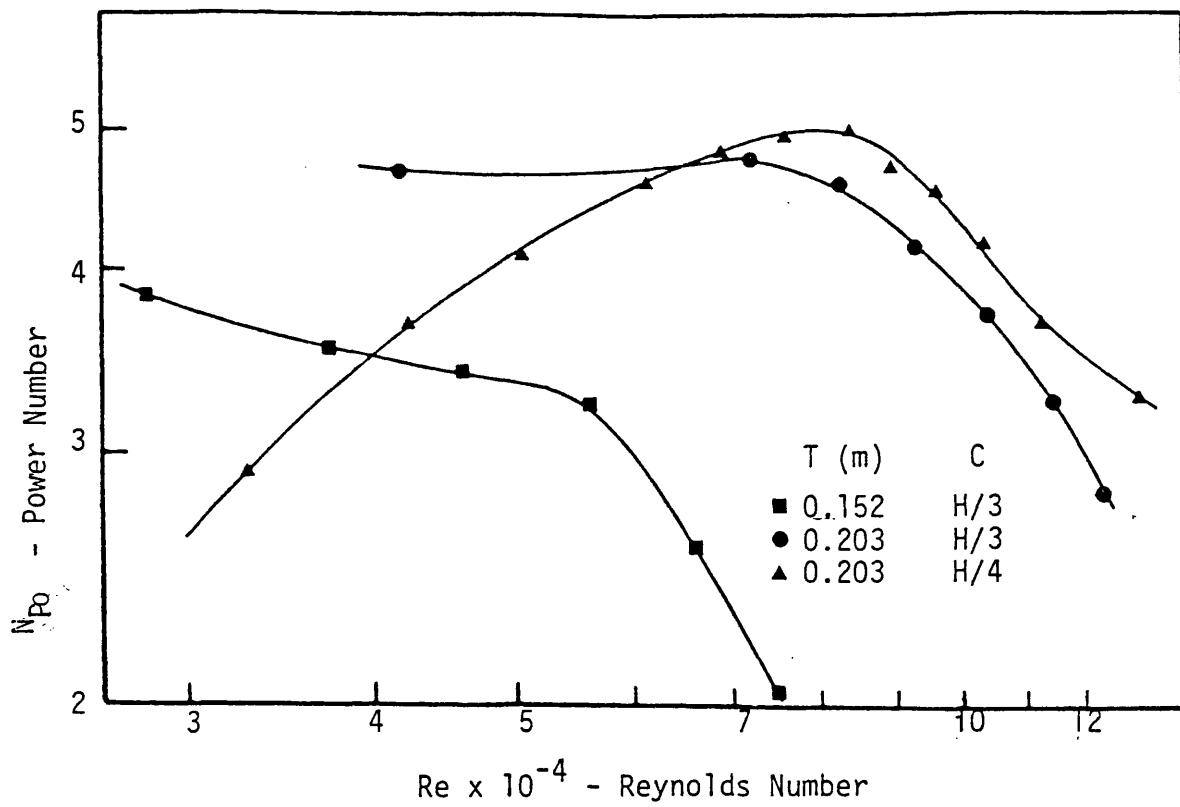
Fig.3.1 Effect of Tank Diameter and Impeller Clearance on N_{Po}
(D = 0.1016 m)
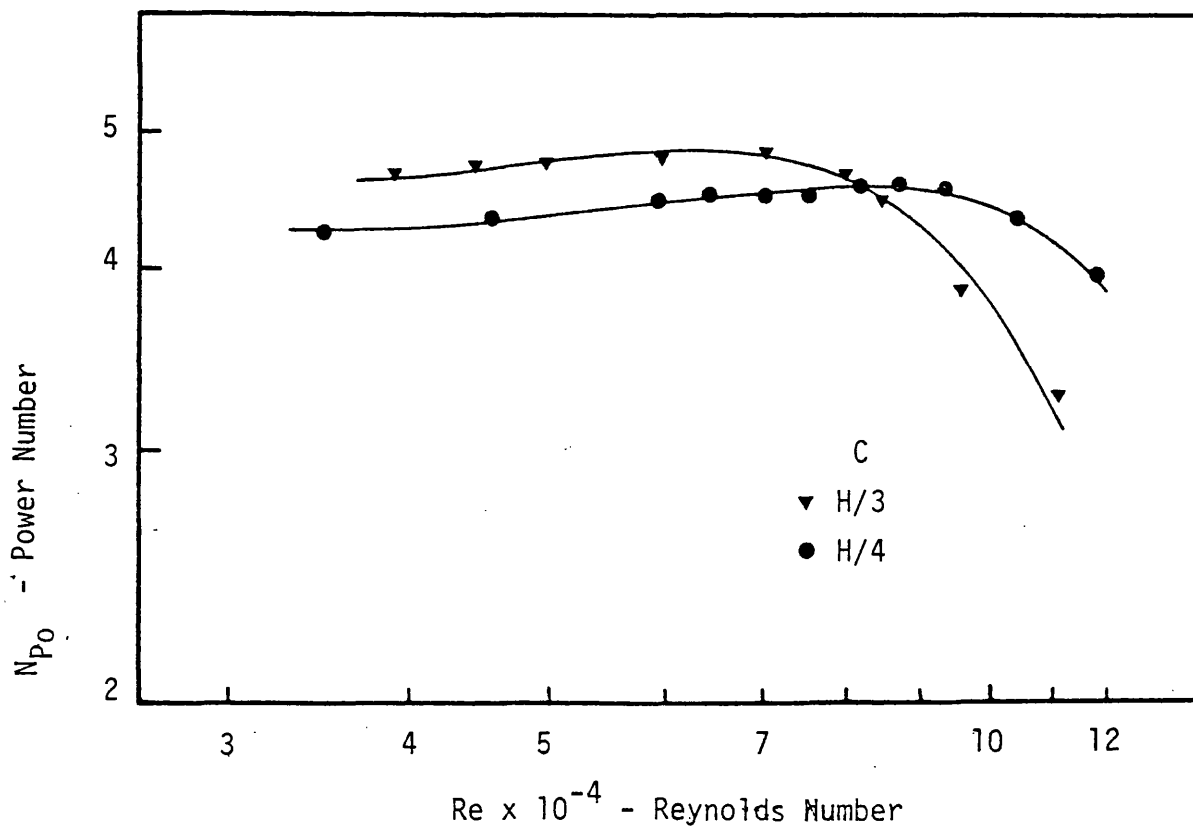
Fig.3.2 Effect of Impeller Clearance on N_{Po} (D = 0.0762m, T = 0.203m)
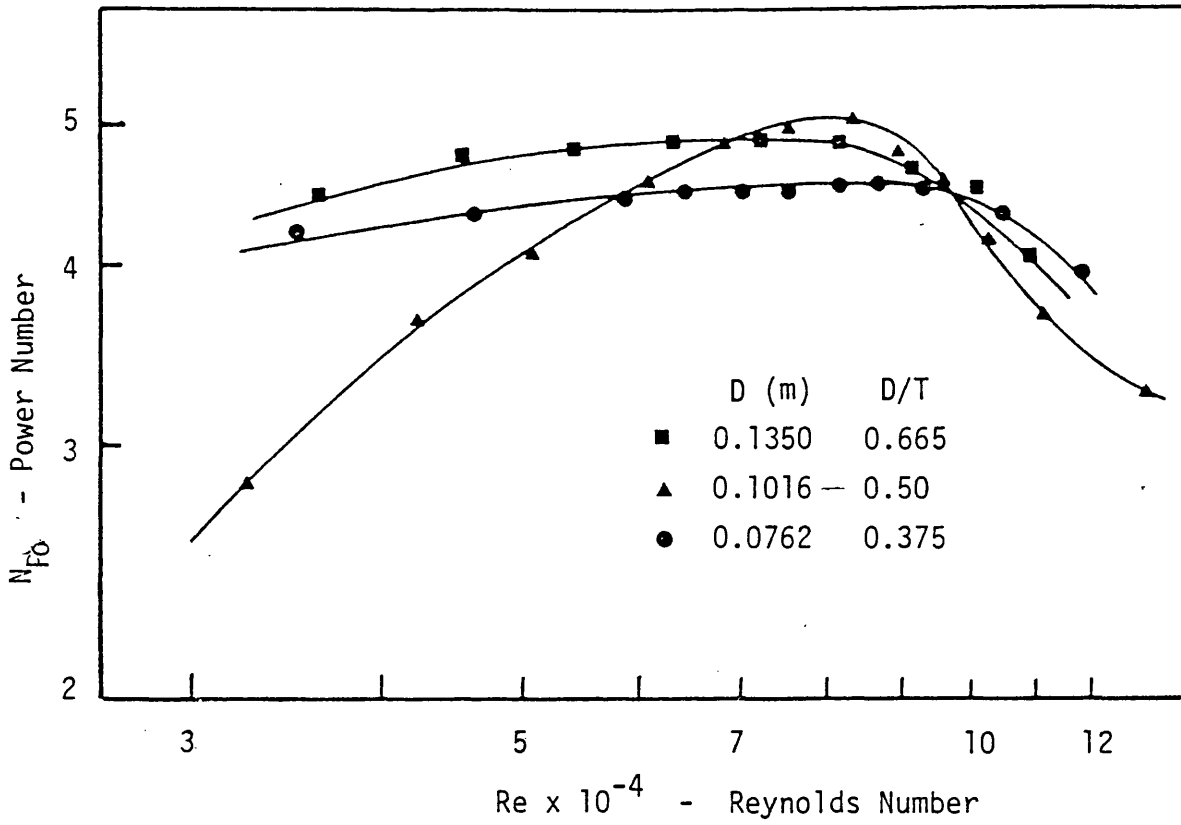
Fig.3.3 Effect of Impeller Diameter on N_{Po} (T = 0.203m, C= H/4)
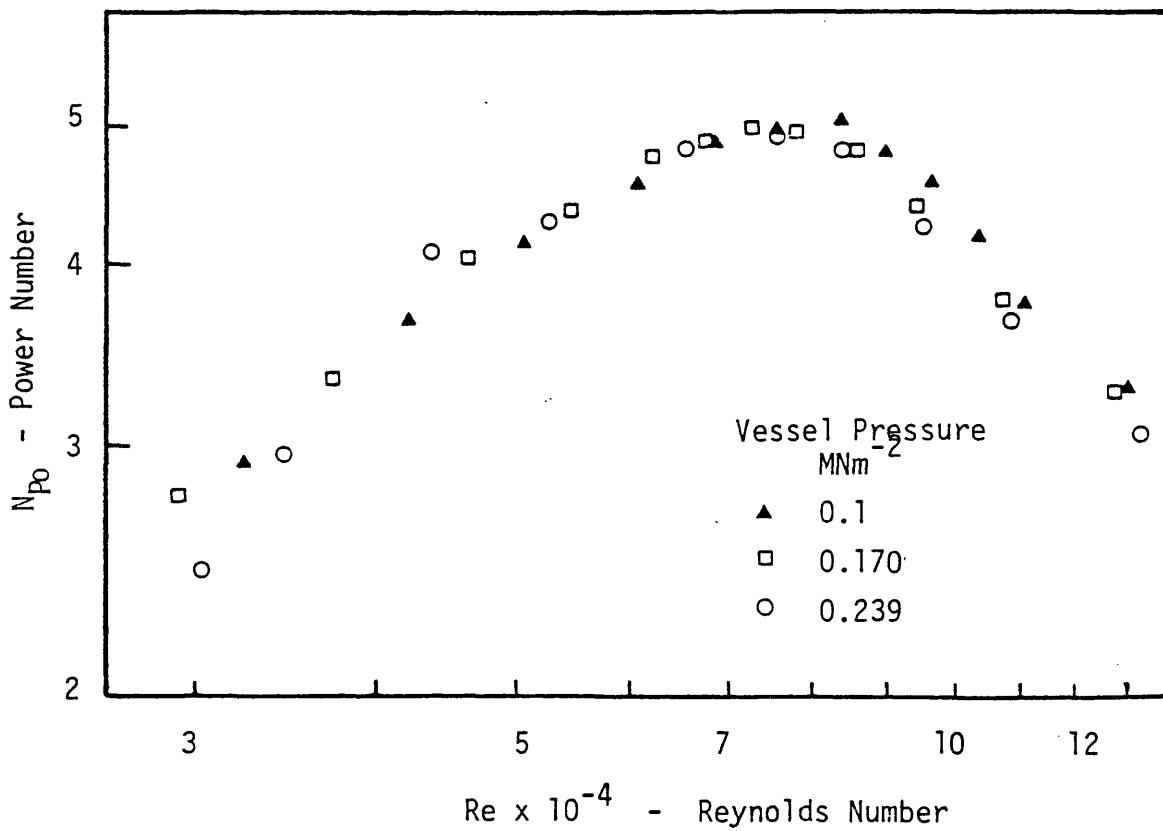
Fig.3.5 Effect of Vessel Pressure on N_{Po} (D = 0.1016m, T = 0.203m)
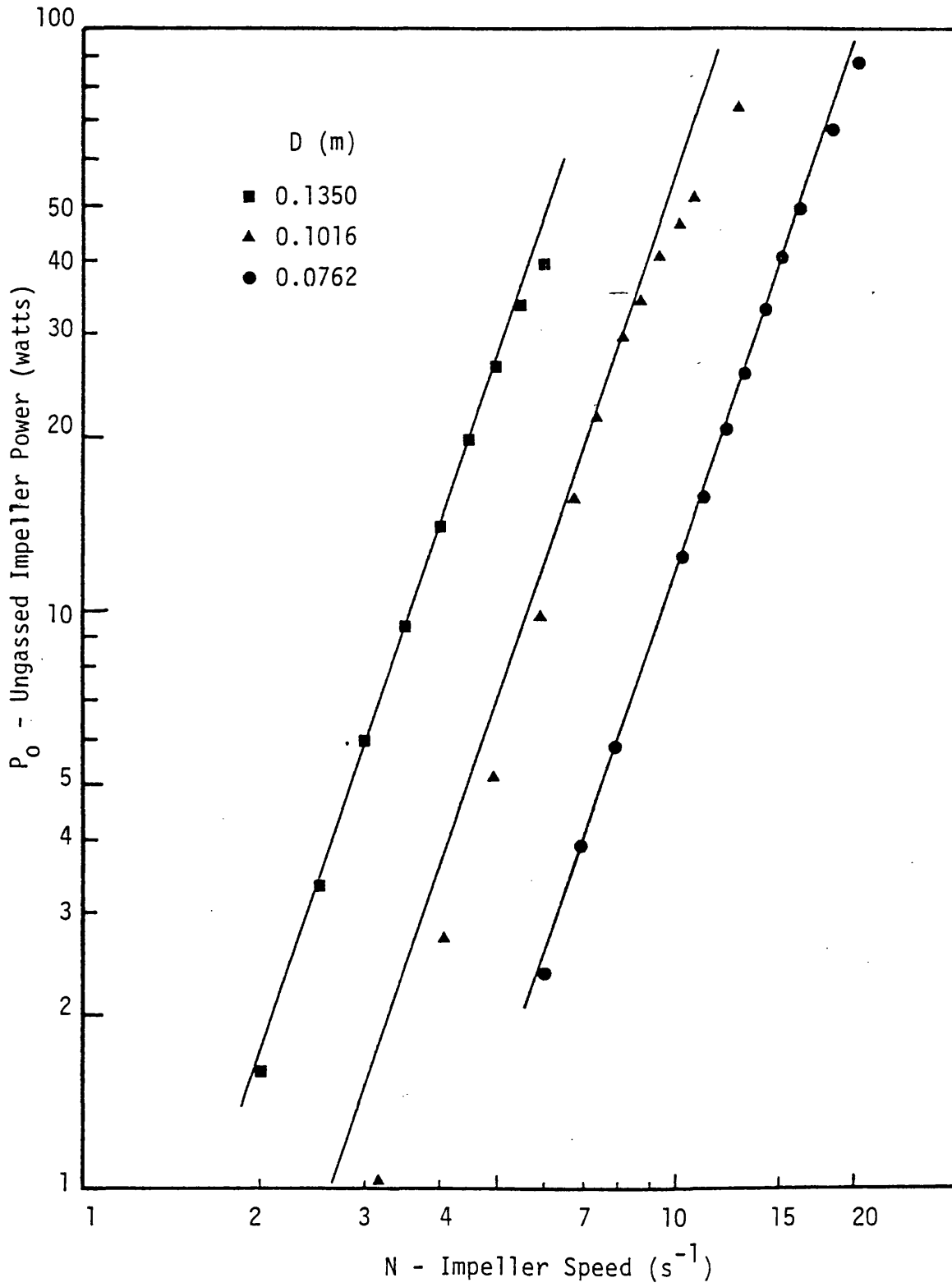
Fig.3.4 Ungassed Impeller Power Consumption against Impeller Speed
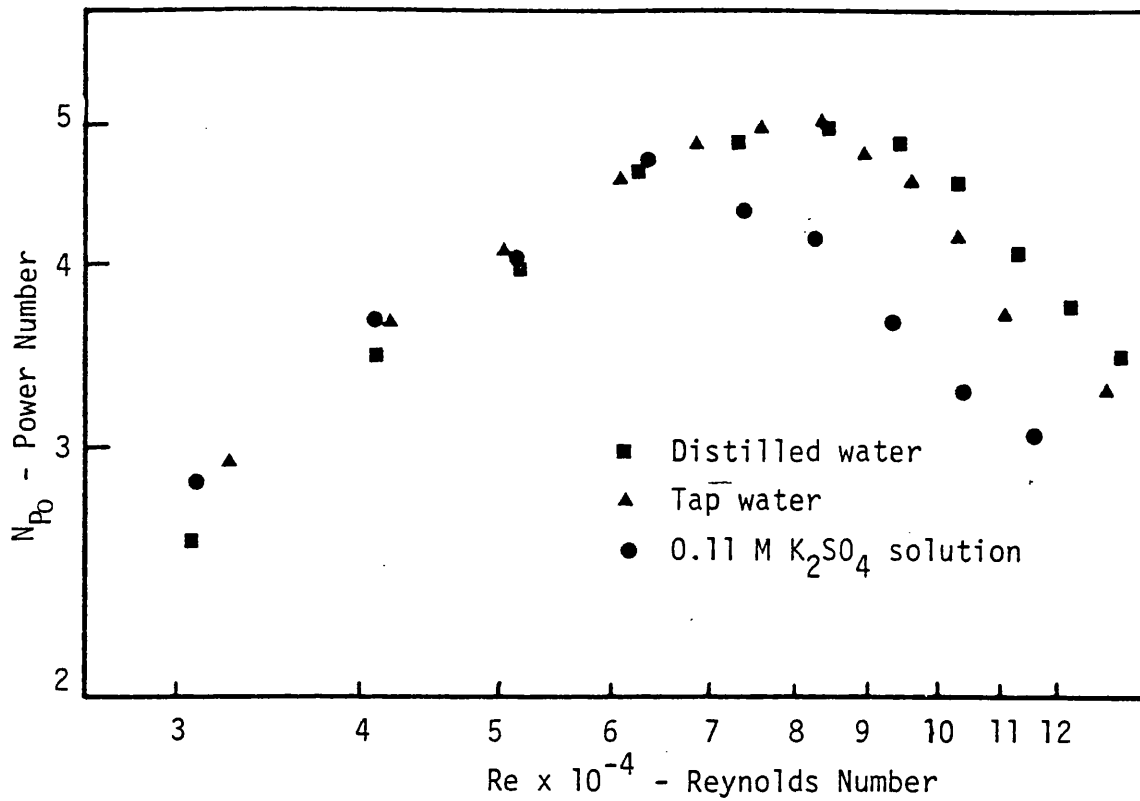
Fig.3.6 Effect of ionic concentration on N_{Po} (D = 0.1016m)
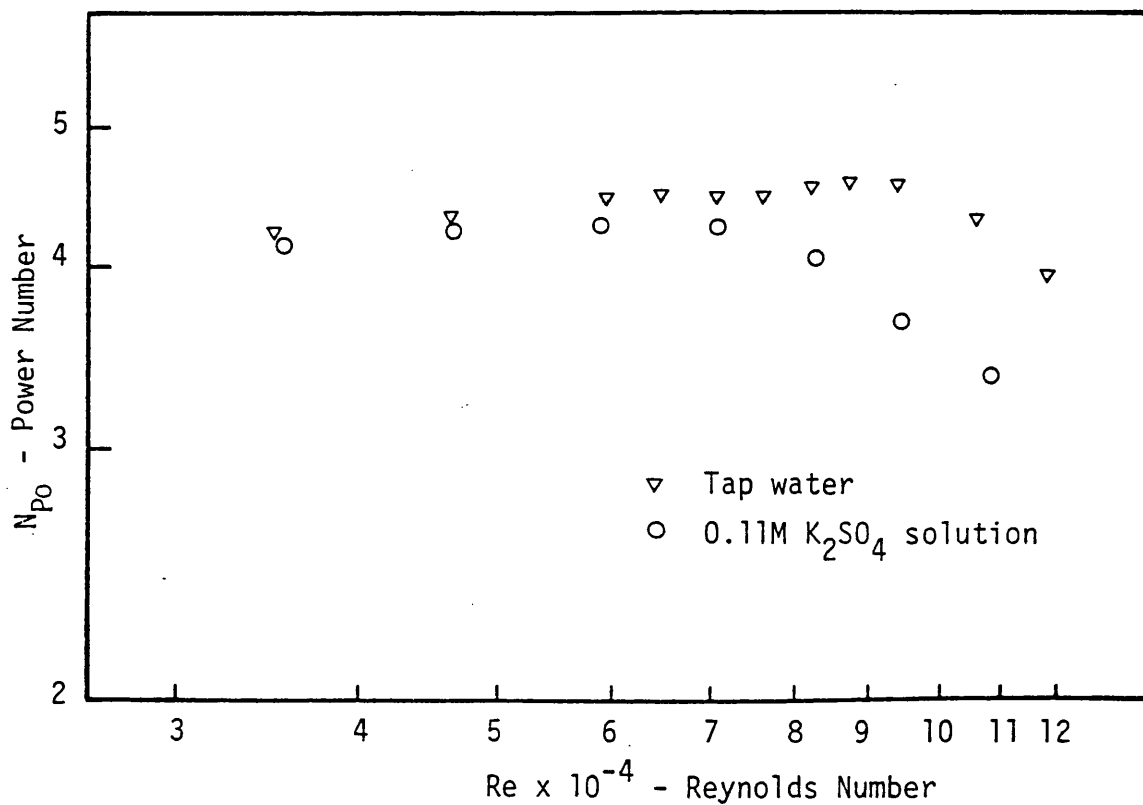
Fig.3.7 Effect of ionic concentration on N_{Po} (D = 0.0762m)

geometrically similar although there were some differences in the material thickness of the blades. This was most pronounced for the largest impeller which had significantly thinner blades compared with the other two impellers (see Table 2.1). Figure 3.3 and 3.4 are two different representations of the same data. The Reynolds number plot clearly shows the effect of small changes in power not readily discernible on the other basis.

Vessel Pressure

It is clear from Figure 3.5 that the increase of vessel pressure up to 20 psig has no effect on the first section of the power curve. However, there is an indication that surface aeration commences at slightly lower impeller speeds as pressure is increased.

Effect of Ionic Concentration

A 0.11 M potassium sulphate solution was used to examine the effect of using an electrolyte solution on the ungassed power consumption. Figures 3.6 and 3.7 show the fall-off in Power number starts at a lower Reynolds number compared with the results for tap water. On the other hand this contrasts with a higher Re condition when distilled water was used, as shown in Figure 3.6.

3.4 DISCUSSION OF RESULTS

The results presented indicate that the power curves for ungassed agitation can be divided into two parts. The first where the Power number increases with Reynolds number, and the second where it shows a decrease.

3.4.1 Initial Rise of Power Number

The initial trend of increase in N_{Po} was first reported by Wisdom (19) and Nienow et al (4). Because of the complexity of the flow around

the impeller, it was decided that the best approach was to concentrate on the conditions which contribute to this effect. In doing so, some of the results of Wisdom (19) will be used alongside the experimental results of this study.

Bates et al (17) attributed the reduction in N_{P_0} with decreasing the impeller clearance to partitioning by the impeller disc of the suction in the impeller region. It is now well known, through the studies of van't Riet (23) that the low pressure region is located immediately behind the turbine blades.

Figures 3.1 and 3.2 show that the initial rise in N_{P_0} is steeper for the smallest impeller clearance (H/4). Wisdom (19) who investigated a wide range of Re also used a small impeller clearance (H/4). Since most of the previous studies were done with the standard impeller clearance of H/3, this may explain why the variation in N_{P_0} was not observed.

Wisdom's results (19), shown in Figure 3.8, indicate an increase of the slope for the initial rise of N_{P_0} with increasing D/T ratio. The same trend is also observed in Figure 3.3 for the two smaller impellers used in this study. However, for the largest impeller the change in N_{P_0} is less steep, which is in contradiction to the results of Wisdom. Therefore, some other factor must be responsible for this effect. The blade thickness to impeller diameter ratio was 0.0074 for the largest impeller and 0.0156 for impeller D2 (D/T=0.5). Thus the reduction in blade thickness may explain the shallower change of N_{P_0} for the largest impeller (Figure 3.3). However, this finding does not agree with Wisdom's results (19) shown in Figure 3.9. In their case, the drop in the maximum Power number was caused by the increase in thickness of the disc. It is significant to note also that the

Fig. 3.8 Effect of impeller diameter on N_{Po} (T=0.29m) Wisdom(19)

—	D/T	a'/T *
A	0.25	0.021
B	0.33	0.016
C	0.625	0.017

	a/T *
A	0.016
B	0.032
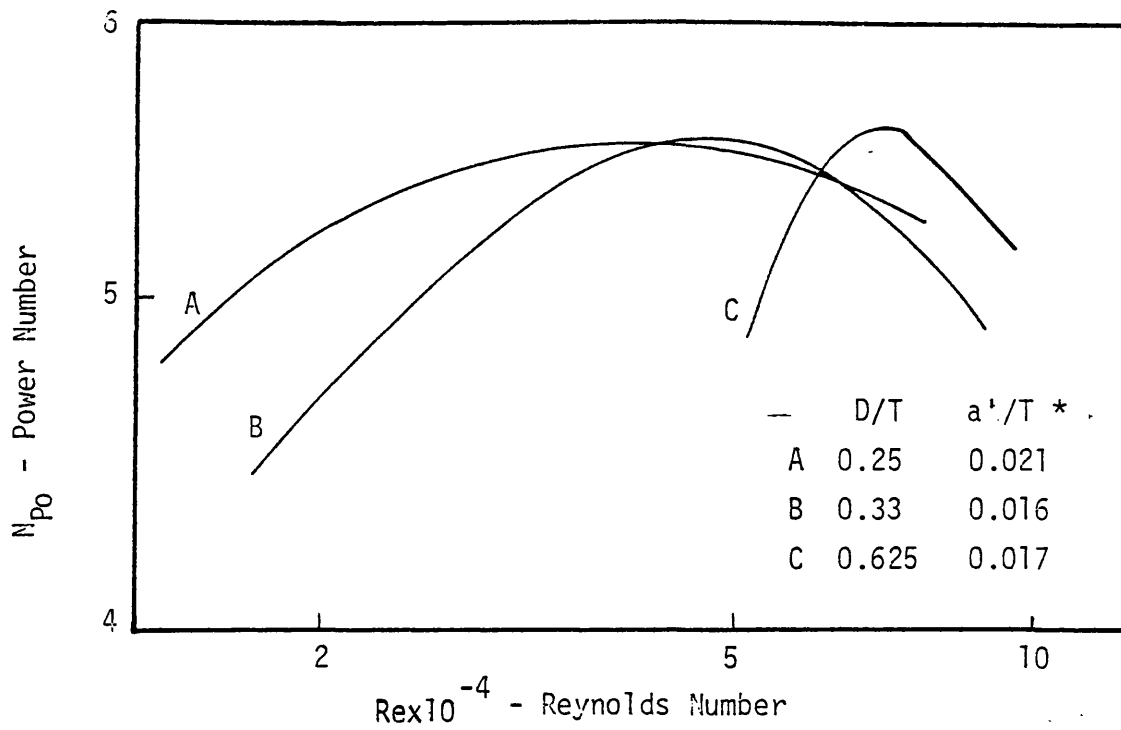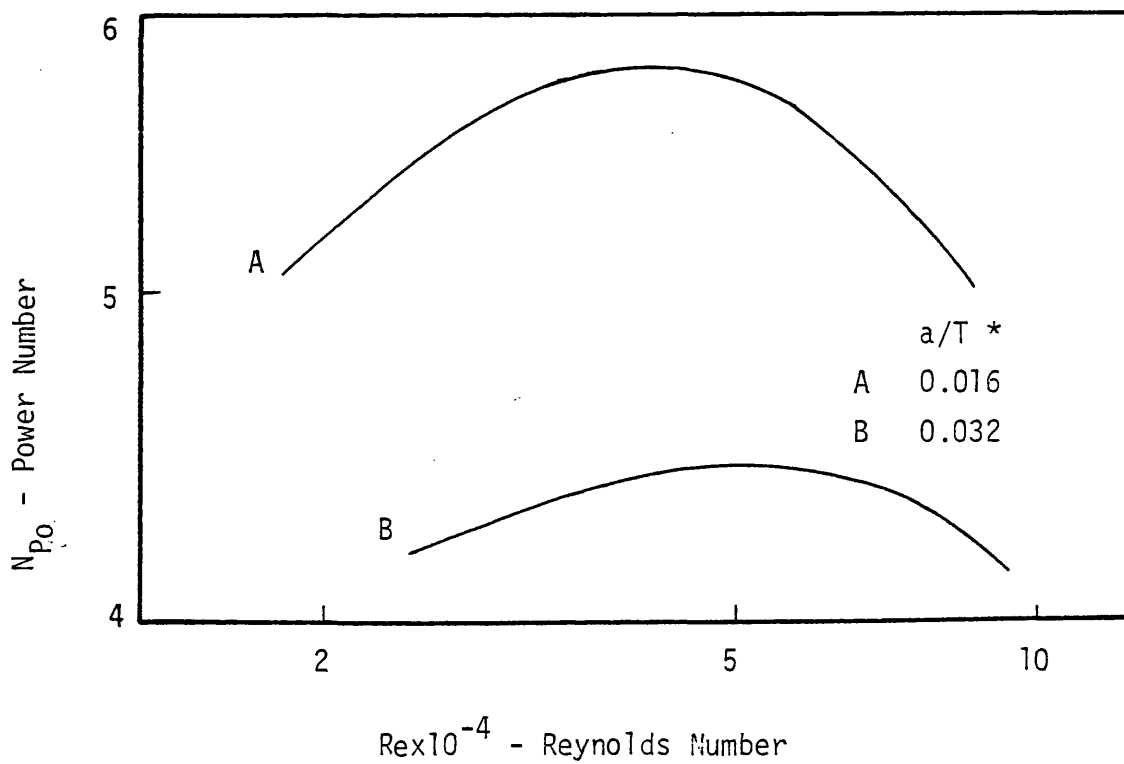
Fig. 3.9 Effect of impeller material thickness on N_{Po}
(D/T = 0.333, T = 0.29 m) Wisdom(19)

* a'= impeller material thickness

studies of continuous flow operation, which are discussed in Chapter 8, confirm the results in Figure 3.3.

From the above discussion, it can be concluded that the initial rise of the Power number with increase in Reynolds number becomes steeper as a result of at least two interacting geometrical factors. These are the reduction of impeller clearance, and increase of the ratio D/T. The blade thickness may also be important. _

3.4.2 Surface Aeration Phenomenon

All of the ungassed power measurements showed a drop in Power number when the Reynolds number exceeded certain limits. The drop occurred at a lower Re when a larger impeller size, impeller clearance, and higher vessel pressure were used. Replacing the tap water with electrolyte solution also produced the same effect. This drop in N_{Po} has been confirmed to be due to air bubbles entrainments at the liquid surface (14, 19).

The mechanism proposed by Clark and Vermeulen (14) for surface aeration, provides some basis for understanding the effect of impeller size and clearance. However it fails to explain the early drop in N_{Po} if electrolyte solution is used, or when the vessel pressure is increased. Although the correlations of Dierendonck (21) (Equations 3.4 and 3.5) include the surface tension as a correlating parameter, it proved unsuccessful in correlating the results of this study. In the absence of any other detailed data about surface aeration in fully baffled agitated vessels, experiments were carried out to obtain more information about this phenomenon.

The technique which was developed for the point bubble size and gas holdup measurement in agitated gas-liquid dispersions (see Chapter 6), was used for studying the surface aeration effect in ungassed agitated liquids. The measuring probe was immersed at a position near to the impeller centre, and at height of 0.038m from the disc (Position S, Figure 3.12.c). This position was carefully selected to lie in the circulating stream of liquid passing close to liquid surface and returning to the impeller. The impeller speed at which bubbles are first detected at the sampling position should be a reliable indication of the lowest speed at which entrainment of gas bubbles from the surface occurs.

The results are shown in Figures 3.10 and 3.11. They were also confirmed visually by observing the measured signal on an oscilloscope. A very small number of fine bubbles were first detected at a low impeller speed. With gradual increase of the speed, the number of bubbles and their size became larger. At speeds above that corresponding to the reduction in N_{P_Q}, no further significant change in bubble size was observed. When sulphate solution was used, the first bubbles were detected at a speed slightly below that obtained with tap water. The change of mean bubble diameter with impeller speed however, is of a much smaller order but the same trend exists. The point gas holdup on the other hand, shows a faster rise. With distilled water the mean bubble size is slightly larger and the point gas holdup is lower compared with tap water.

Further measurements of point bubble size and gas holdup were done at three different positions. These were selected to be near to the liquie surface, and are labelled A, B and C in Figure 3.12.c. Figure 3.12 demonstrates that gas bubbles were first detected in all
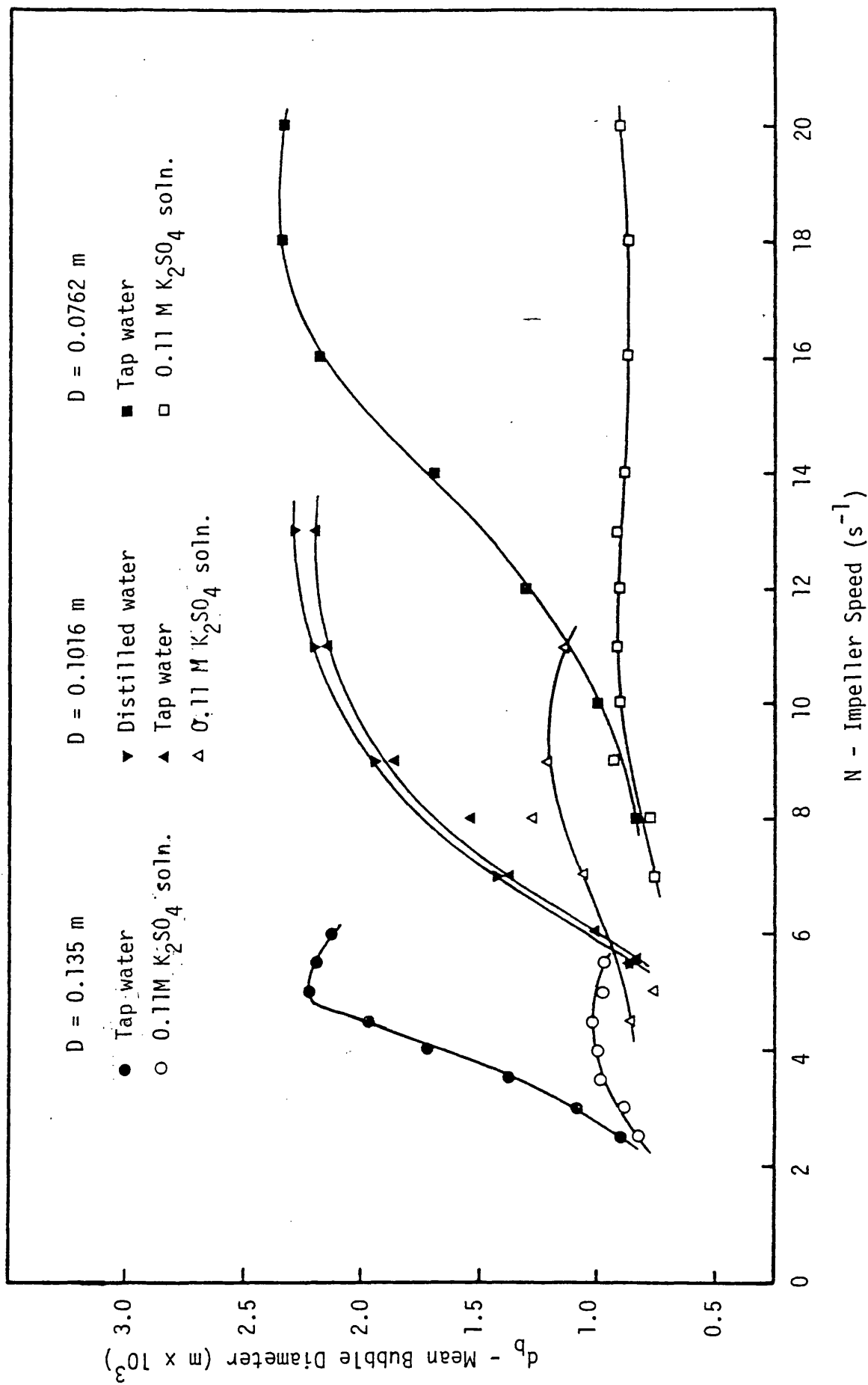
Fig.3.10 Variation of Bubble Size with Impeller Speed at Sampling Position S (Fig. 3.12.c) in Ungassed Liquid
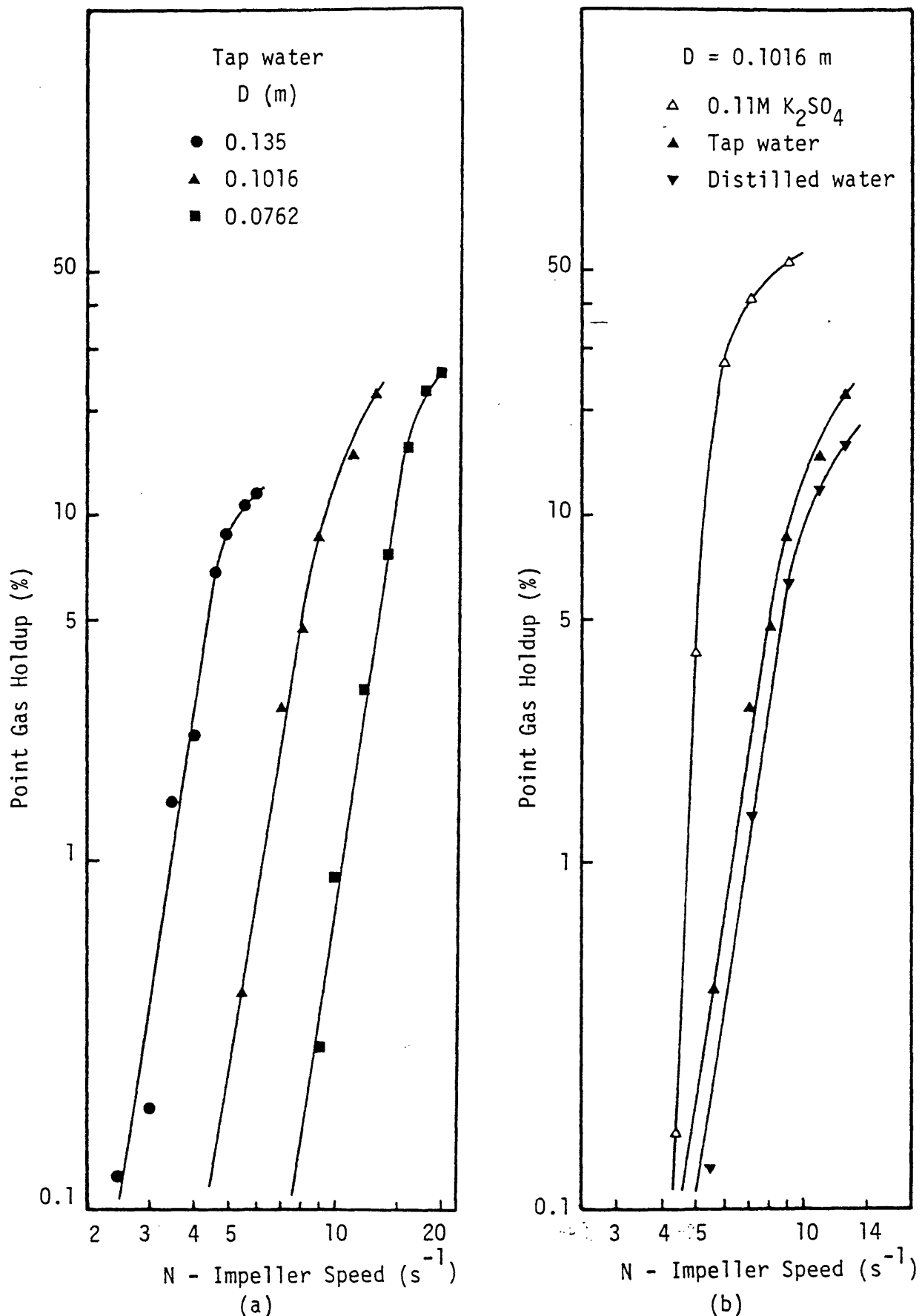
Fig.3.11 Point Gas Holdup against Impeller Speed at Sampling Position S
((Fig.3.12.c) (a) Effect of Impeller Size,(b) Effect of Ionic Concentration

(a)
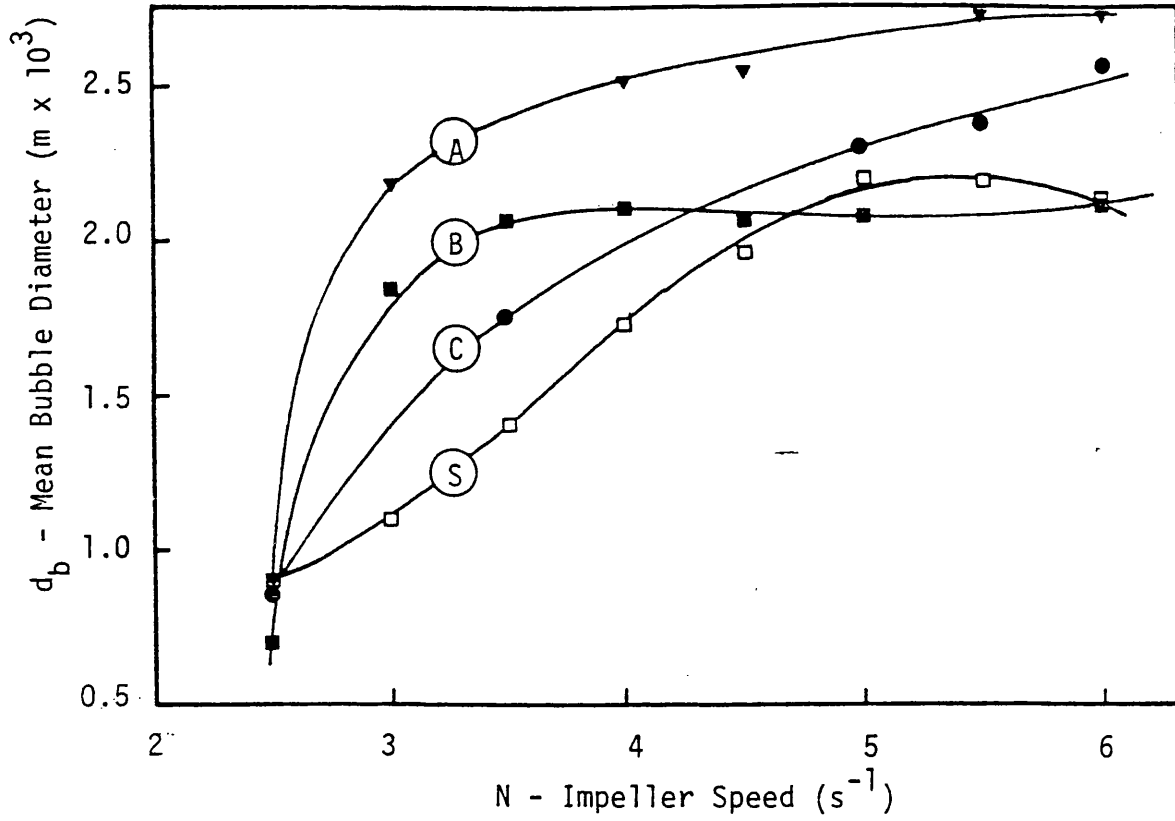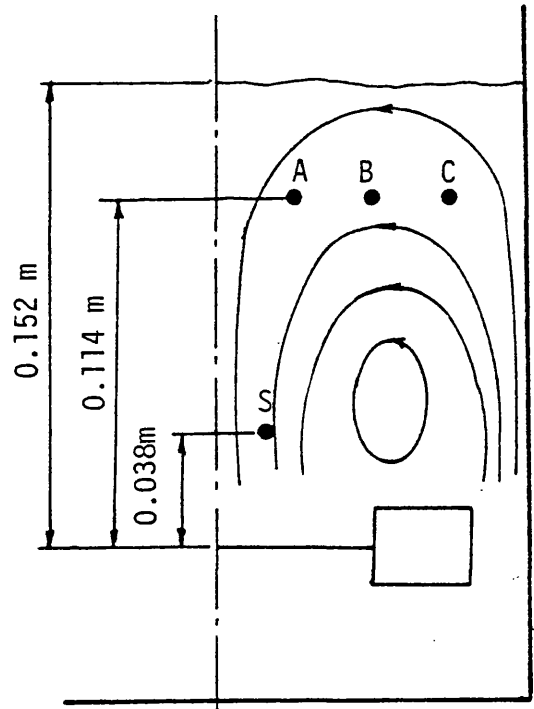
(c) Sampling Positions
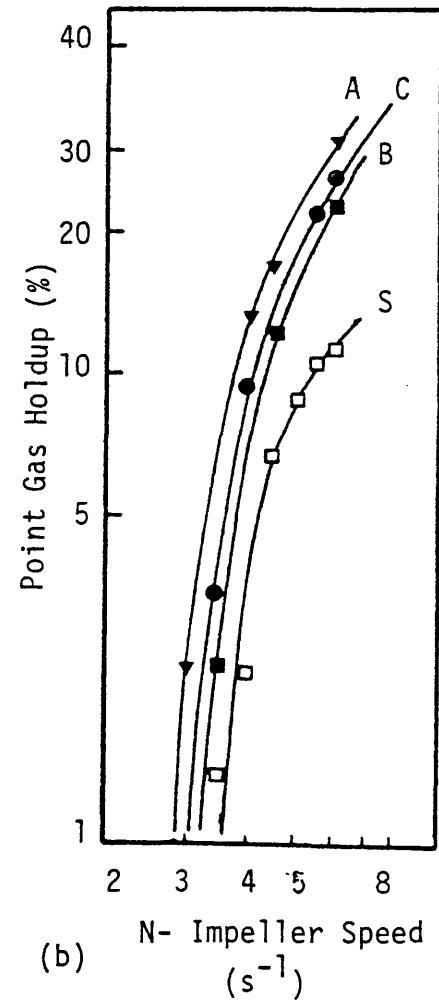
Fig.3.12 Variation of Bubble Size
and Gas Holdup in the Vessel at
Positions A,B,C and S.

(b)

of the sampling positions at virtually the same impeller speed. However the mean bubble size and the point gas holdup are larger at the positions near to the liquid surface.

3.4.2.1 Mechanism

From the previous measurements and observations the following mechanism is proposed for the surface aeration phenomenon in fully baffled tanks.

(i) The initiation of surface aeration takes place at the liquid surface where fine gas bubbles are entrained. It first occurs at low impeller speeds prior to any drop in N_{Po}. From velocity measurements and optical observations, Nagata et al (24) reported the formation of eddies at the liquid surface in a fully baffled tank. The impeller discharge stream impinges on the baffle-plates at the vessel wall, and a large and stable cylindrical eddy A (Figure 3.13) is formed. Thereafter, small eddies B and C are generated. Eddies of type B have a tendency to rotate slowly around the agitator shaft and combine into a stronger eddy forming a hollow vortex on the liquid surface which sucks air bubbles into the bulk liquid.

(ii) The entrained gas bubbles are carried to the impeller region by the stream of the circulating liquid (secondary liquid movement in fully baffled tanks, see Section 3.4.2.2).

(iii) As the impeller speed increases, the eddies residing at the surface grow in intensity. More gas is drawn into the liquid producing a corresponding increase in gas holdup near to the surface. In 'pure' liquids this is accompanied by a rapid increase in the mean bubble size due to coalescence.
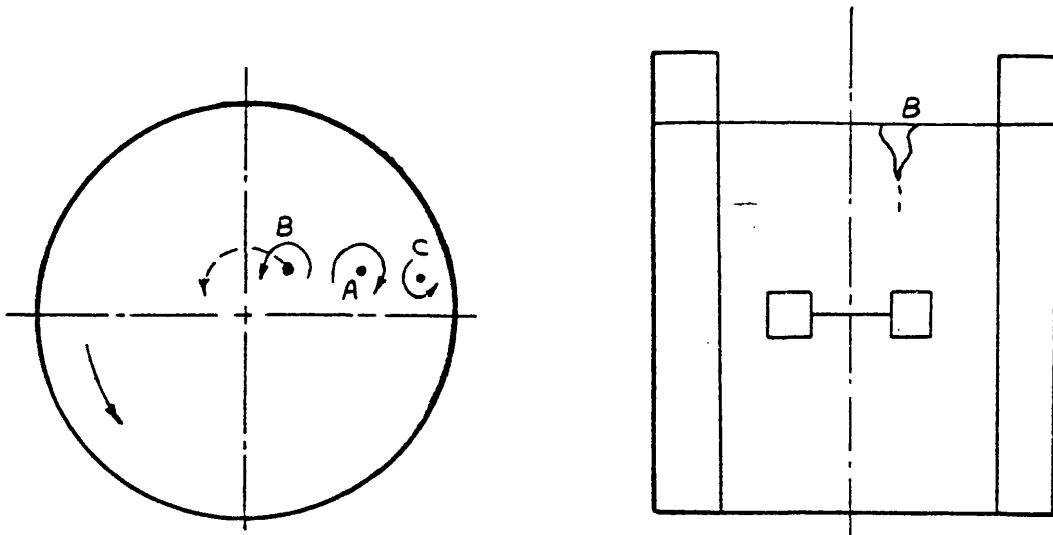
> Fig.3.13 Schematic Representation of Vortex
Formation at Surface of Liquid in a Baffled
Vessel (24)

With electrolyte solutions there is a less dramatic change in bubble size because of the reduced rate of coalescence. These effects are clearly seen in Figures 3.10 and 3.12.

(iv)   Higher liquid circulation velocities develop as the speed of the impeller is increased further. Therefore, larger size and number of bubbles, respectively, are transported to the impeller region in the case of 'pure' liquids and electrolyte solutions. This leads to an increase in the flow rate of gas to the impeller.

(v)   The rate determining process for aeration of the bulk liquid is the capability of the circulating liquid to carry the gas bubbles rather than the strength of the vortexing eddies. Figure 3.12.b shows that the point gas holdup is much larger near to the liquid surface than at the impeller, and this indicates that there is no limitation on the availability of gas from the surface.

(vi)   A drop in the Power number occurs when the flow rate of gas from the surface of the liquid to the impeller region is sufficiently high. This is associated with the formation of clinging cavities behind the impeller blades (25) (see also Chapter 4).

The previous description of surface aeration, points to the important role played by the velocity of the circulating liquid. Therefore, an understanding of the flow pattern in a fully-baffled tank is essential before any correlation based on the physical phenomena involved can be developed.

3.4.2.2 Flow Pattern in a Fully-Baffled Vessel

In a fully-baffled agitated vessel, the 3-dimensional flow of fluid can be described by primary and secondary flow patterns (20, 24-31). The primary movement is the rotational flow of fluid as shown in Figure 3.14.a, which is of minor importance for mixing processes (26). The secondary movement consists of radial and axial components as shown in Figure 3.14.b.   This general flow pattern has been shown to be independent of impeller speed (29) and size (24) in the turbulent region.

The secondary circulation motion could be divided into four zones as shown in Figure 3.15.   Holmes et al (27) showed that the average liquid velocity in zone I could be estimated by

$$\bar{V}_r = C_1 \frac{N D^2}{r} \qquad\qquad 3.6$$

where

$\bar{V}_r$ is the average velocity at a radial distance r from impeller centre line.

Using the data presented by Nagata et al (24) they also found that the average liquid velocity in zones II, III and IV were of the same order but less than the impeller jet velocity near to the wall. Therefore, the average circulating velocity in the tank, apart from the impeller jet region (zone I), can be estimated from :

$$\bar{V} = C_2 \frac{N D^2}{T} \qquad\qquad 3.7$$

Schwartzberg and Treybal (32) who measured the average liquid velocity in a vertical plane, presented the following experimental correlation

(a)

(b)
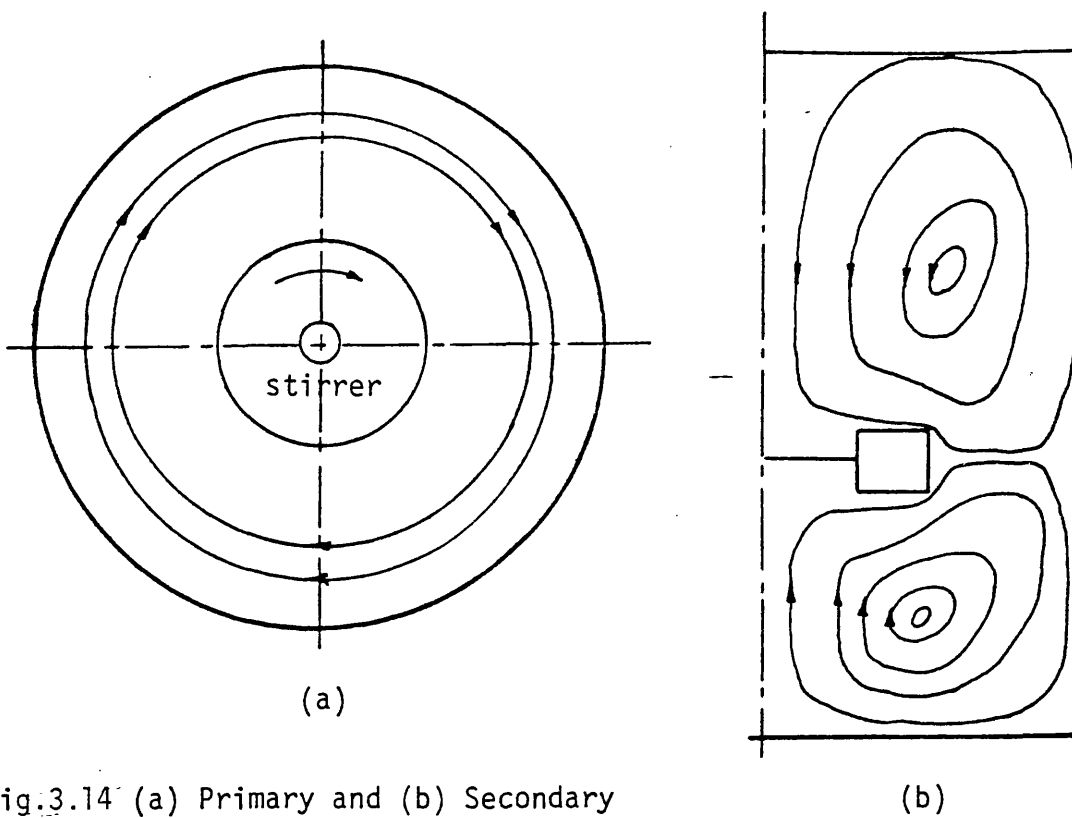
Fig.3.14 (a) Primary and (b) Secondary
Flow Circulation in Mixing Vessel (26)
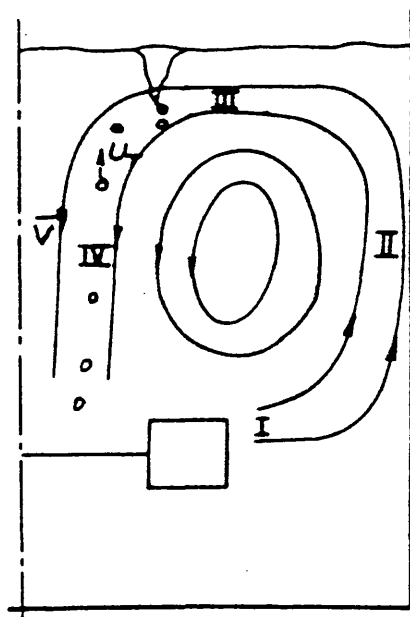
Fig.3.15 Surface Aeration
Mechanism

$$\overline{V}_v = 1.387 \frac{N D^2}{(T^2 H)^{1/3}} \qquad\qquad 3.8$$

where

$\overline{V}_v$ is the average velocity in the vertical plane.

It is clear that Equations 3.7 and 3.8 become identical when H=T, which is the case employed in this study.

3.4.2.3 Correlation for Onset of Surface Aeration

To specify the onset of surface aeration, two impeller speeds are defined. The first, N_{SA1}, is the condition at which air bubbles are first entrained near to the surface by the hollow vortex motion. The second is N_{SA2} which defines the impeller speed at which the first decrease in N_{po} is observed. Since it is not possible to provide an adequate quantitative description for the first process, the approach to be taken first involves developing a correlation for N_{SA2}, then extending it by using the experimental data on N_{SA1}.

As shown in Figure 3.15, the gas bubbles are carried to the impeller region with the vertical downflow of liquid along the tank axis (zone IV). Govier and Aziz (33) have stated that the absolute rise velocity of gas bubble in a flowing stream is equal to the vector sum of the rise velocity in a stagnant fluid and the local absolute velocity of the flowing liquid. Thus if this principle applying to turbulent flow in a pipe is extended to turbulent flow in a stirred vessel, then it can be assumed that the necessary condition for the liquid stream to carry the gas bubbles to the impeller region at $N = N_{SA2}$ is :

$$\overline{v}^* > U_T^*$$

or $$\overline{v}^* = C_3 U_T^* \qquad\qquad 3.9$$

where

$$\bar{v}^* = \bar{v}_V \text{ at } N = N_{SA2} \quad \text{(Equation 3.8)}$$

U_T^* is the terminal velocity corresponding to the average

size of entrained bubbles (near to the impeller, zone IV)

at $N = N_{SA2}$.

Therefore, from Equations 3.8 and 3.9 :

$$N_{SA2} = 0.72 \ C_3 \ U_T^* \ \frac{(T^2 H)^{1/3}}{D^2} \qquad — \qquad 3.10$$

where $C_3 > 1$ by definition (Equation 3.9). Table 3.1 illustrates

values of C_3 for tap and distilled water. For tap water the

average value of C_3 is 2.8, with a maximum deviation of 5% for the

range of impeller sizes used. Here, N_{SA2} was determined from

Figure 3.3 as the impeller speed corresponding to the maximum in the

curve. The average bubble diameter, corresponding to N_{SA2}, was

determined from Figure 3.10, and its terminal velocity was calculated

from the published data of Haberman and Morton (34) shown in Figure 3.16.

The coefficient C_3 in Equation 3.10 includes the effect of the

following system parameters :

1.   Distance from the liquid surface to the impeller. C_3 is

      expected to be larger for the smaller impeller clearance with

      the same liquid height. It is also implicit that a higher

      liquid velocity will be required to carry the gas bubbles

      downward to the impeller. This effect can be expressed as :

      $$C_3 \ \alpha \ (H-C)^C$$

      ie, $$C_3 \ \alpha \ H^C (1 - \frac{C}{H})^C \qquad\qquad 3.11$$

and the exponent c is estimated to have a value of 1/3. When

Equation 3.11 is substituted in Equation 3.10 an additional $H^{1/3}$ term

appears on the R.H.S. of the correlation. This is of particular

Table 3.1   Values of Coefficient C_3 Eq. 3.10
(T=0.203m)

	D m	N_{SA2} s^{-1}	d_B $\times 10^3$ m	U_T^* [+] m s^{-1}	C_3
Tap water	0.0762	15.6	2.1	0.22	2.81
	0.1016	8.3	1.8	0.20	2.93
	0.1350	4.7	2.1	0.22	2.68
Distilled water	0.1016	8.6	1.94	0.30	2.02

+ Haberman and Morton (34)
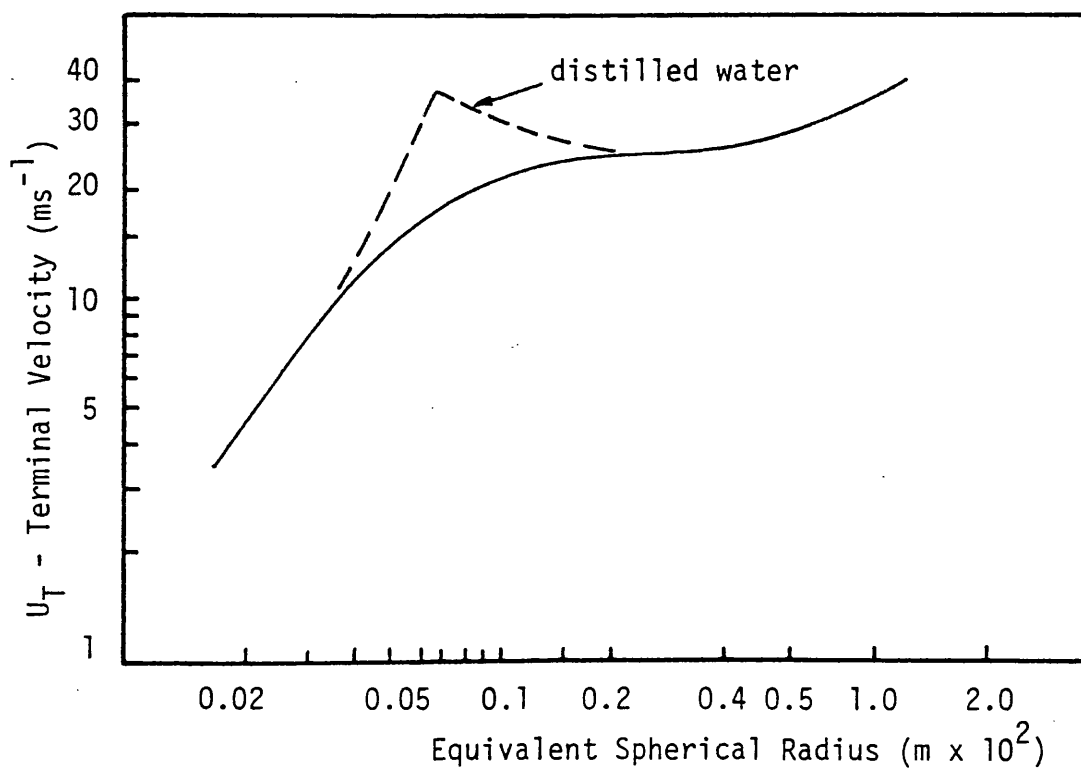
Fig.3.16 Terminal Velocity of Air Bubbles in Tap Water as a Function of Bubble Size (34)

importance regarding scale-up, since it may explain why surface aeration is not observed to occur in large vessels at normal operating speeds (35).

2. Working pressure of the vessel. This effect was correlated by :

$$C_3 \alpha \ (\frac{P}{P_A})^{-0.13} \qquad \qquad 3.12$$

where P   vessel pressure

P_A atmospheric pressure

Sridhar and Potter (6) have recently studied gas-liquid agitation at elevated vessel pressures. They reported a reduction in the average bubble size with increasing vessel pressure. The same effect would be expected for ungassed agitation with surface aeration. The reduction of bubble size and increase in density at higher pressures causes a reduction in the buoyancy force. For this reason the gas bubbles are carried to the impeller region at lower liquid circulating velocities and surface aeration is therefore observed at lower impeller speeds.

3. Liquid media. This effect is rather complex because the bubble size depends on the type of liquid used, ie, whether it is a 'pure' liquid or a solution containing electrolytes or surfactant materials. The degree of interaction between bubbles in the bulk liquid will be affected because of the different volumes of gas drawn in at the surface. Also, the accompanying changes in the physical properties of the dispersion will have an effect on the circulation velocity of the liquid. For simplicity, it is assumed that

$$C_3 \propto C_4 \qquad\qquad 3.13$$

where C_4 is a constant depending on the type of liquid used.

Combining Equations 3.11, 3.12 and 3.13 and then substituting into Equation 3.10 yields the following correlation for N_{SA2}

$$N_{SA2} = C_5 \frac{(T^2 H^2)^{1/3}}{D^2} \left(1 - \frac{C}{H}\right)^{1/3} \left(\frac{P}{P_A}\right)^{-0.13} \qquad 3.14$$

where $C_5 = 0.72 \ C_4 \ \overline{U_T^*}$ $\qquad\qquad 3.15$

The correlation of the experimental results by Equation 3.14 is shown in Figure 3.17. The various values for C_5 are found to be :

0.82 for distilled water

0.80 for tap water

0.62 for 0.11M K_2SO_4 solution

Equation 3.14 has also been used to correlate N_{SA1} which is the impeller speed at which gas bubbles are first detected. Then :

$$N_{SA1} = C_6 \frac{(T^2 H^2)^{1/3}}{D^2} \left(1 - \frac{C}{H}\right)^{1/3} \left(\frac{P}{P_A}\right)^{-0.13} \qquad 3.16$$

where C_6 has the values

0.476 for distilled water

0.429 for tap water

0.375 for 0.11M K_2SO_4 solution.

In Figure 3.17 it can be seen that these are slightly better for N_{SA1} compared to N_{SA2}. This is hardly surprising in view of the fact mentioned previously, concerning the close agreement in impeller speeds for the condition where gas bubbles were first detected near to the liquid surface and at sampling positon S, close to the impeller.
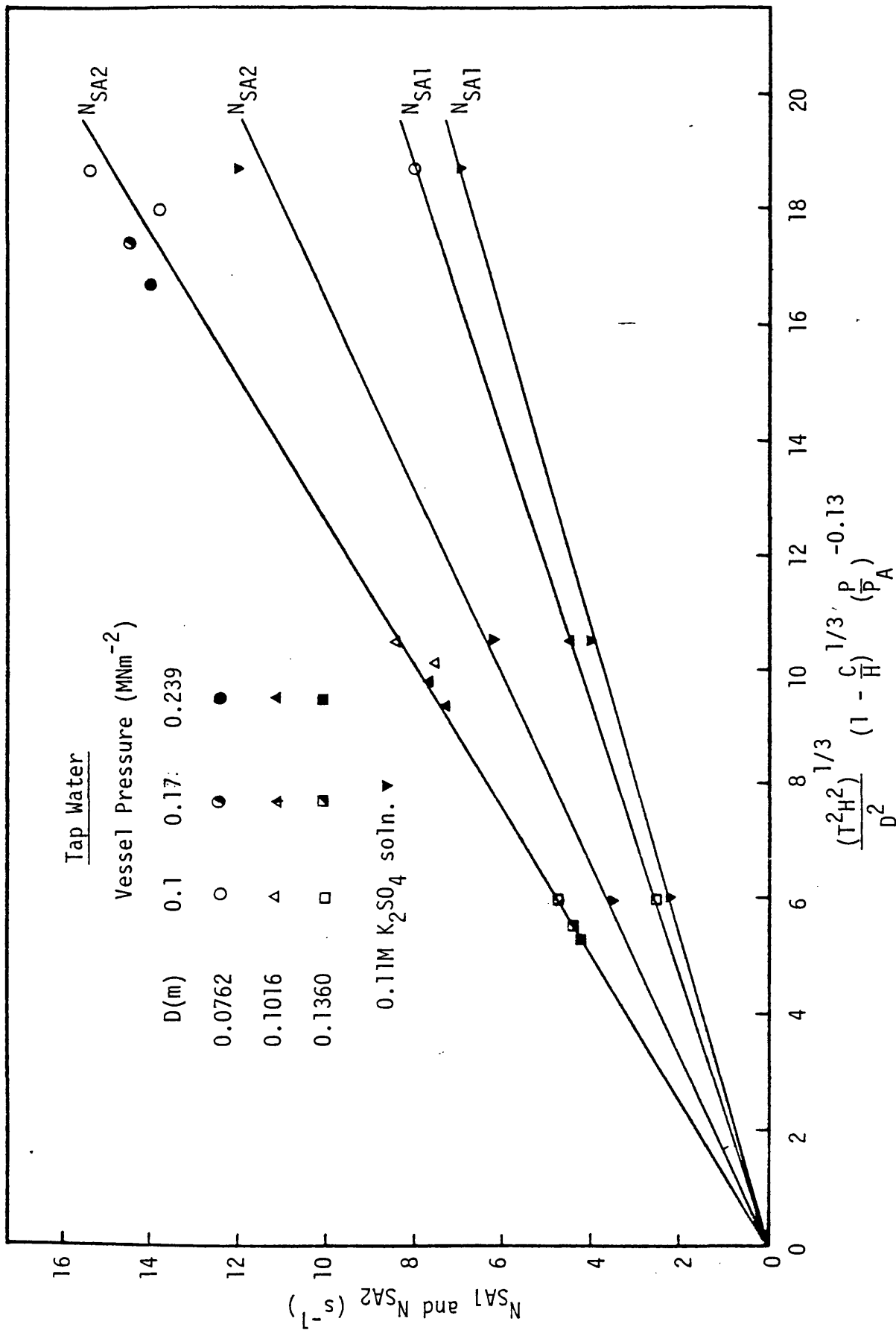
Fig.3.17 Correlation of Critical Impeller Speeds for Start of Surface Aeration: Eqs. 3.14 and 3.16.

From Equations 3.14 and 3.16 it is noticed that the ratio N_{SA1}/N_{SA2} is 0.54 for tap water and 0.6 for sulphate solution. It is apparent therefore that a large error will be incurred if the onset of surface aeration is estimated from the observed drop in N_{P_Q} as was the case previously reported by Clark and Vermeulen (14).

Finally, if we look at the average bubble size for the tap water case, corresponding to the states when bubbles are first observed near to the impeller and when N_{P_Q} first begins to fall, then these are respectively 0.85mm (Figure 3.10) and 2.0mm (Table 3.1 - average for the 3 sizes of impeller). The corresponding terminal velocities estimated from Figure 3.16 are 0.11 and 0.21 ms^{-1}, and the ratio between them is 0.52. This value is close to that obtained for the ratio N_{SA1}/N_{SA2}, confirming that the average size of the bubble carried to the impeller is dependent on the impeller speed, and hence the velocity of the circulating liquid. A similar situation, however, does not apply in the case of the sulphate solution. Here, the increase in impeller speed increases the number rather than the average size of the bubbles which are carried to the impeller region.

3.5   CONCLUSIONS

1 -   In the turbulent region ($Re > 10^4$), the ungassed Power number, N_{Po}, for distilled water, tap water and 0.11 M K_2SO_4 solution, exhibits a characteristic trend with increasing Re. There is first a rise to a maximum value, followed by a falling region. Increasing the impeller size and/or reducing the clearance ratio causes a steepening of the initial part of the curve.

2 -   The drop in N_{Po} was confirmed to be due to surface aeration. A two-stage mechanism has been proposed for this phenomenon

which includes an eddy-capture mechanism for sucking-in air at the liquid surface, followed by circulatory transport of the entrained bubbles to the impeller region.

3 - Entrainment of gas bubbles first occurs at impeller speeds much lower than that which would ordinarily be detected by observing a drop in N_{P_0}. A correlation for the impeller speeds, N_{SA1} and N_{SA2} respectively the conditions at which bubbles are first detected in the circulating flow close to the surface, and when N_{P_0} first begins to fall, showed the ratio between them to be 0.54.

When judged by the ratio of bubble terminal velocities, the value is 0.52, confirming that the average size of bubble which is carried (or recirculated) to the impeller is dependent on the impeller speed, and hence the velocity of the secondary circulating flow. For K_2SO_4 solution, on the other hand, there is an increase in the number of bubbles rather than the average bubble size. This may explain the earlier fall in N_{P_0} experienced for these systems.

CHAPTER 4

POWER CONSUMPTION AND MIXING REGIMES

FOR BATCH GAS-LIQUID REACTORS

4.1   INTRODUCTION

The prediction of impeller power is an important requirement for the design of stirred gas-liquid reactors.   Many of the design correlations used for estimating either the interfacial area or mass transfer coefficient K_La, involve the use of the power quantity in some form, particularly (Pg/V).   In addition the mechanical power requirements will have a critical influence on the design and scaleup of such systems.

Following the literature review, impeller power measurements under gassed conditions are discussed and analysed in this chapter.

4.2   LITERATURE REVIEW

4.2.1   Energy Transfer and Gas Cavities

The transfer of energy from disc turbines in gas-liquid reactors is a complex physical process (26).   Lee and Meyrick (9) were the first to report the dependence of impeller power on the size of large gas bubbles formed behind the impeller blades.   The experimental investigations of Nienow and Wisdom (22), van't Riet and Smith (36) and Bruijin et al (25) have developed a greater understanding of the fundamental processes involved.   These studies have shown that in absence of gas, a low pressure liquid filled regions (36) or low pressure separation bubbles (22) are formed behind the blades of rotating impeller in liquid media.   Once gas is sparged to the system these regions are filled with gas forming what is known as gas cavities. This leads to a rise in pressure behind the blades causing decreased drag effect and reduction in the impeller power consumption (22,36).

For disc impellers rotating at constant speed, three types of gas cavities have been identified (25). At low gas flow rates vortex type cavities are formed, which have no significant effect on impeller power consumption. With increase of the gas inflow, the shape of cavities changes to the form of a clinging cavity causing a continuous drop in the power consumption to about 0.8 of the ungassed value. At higher gas flow rates a large gas cavity is formed behind one blade. This cavity extends as the gassing rate is increased and eventually other cavities are formed behind all the impeller blades. Associated with each cavity formation there is a stepwise drop in impeller power. However, this discontinuity is less distinct with the formation of the last two cavities (fifth and sixth).

The mechanism of gas inflow and bubble dispersion from the cavities have been described by van't Riet (23). The gas bubbles rise from the sparger to the turbine disc. When vortex or clinging cavities are formed the bubbles are carried along by the flow near to the low pressure region behind the blades to be sucked into the cavities. In the case of a large cavity, the bubbles are carried by the flow and pressure field along to the rear of the cavity and coalesce with it. The gas dispersion generated from vortex or clinging cavities is produced by the breakaway of bubbles from the tail of the trailing vortex. Dispersion takes place at the rear of large cavity as a random process, controlled by the flow instabilities and turbulence in the wake region behind the cavity. If a large gas sparger of diameter equal to the impeller size is used, the mechanism of gas inflow to the cavities becomes different. The first large cavity is not formed until a higher Fl value is reached, and part of the sparged gas bypasses the cavity region.

4.2.2 Impeller Speed Limits for Effective Dispersion

Numerous investigators have proposed correlations for the minimum
impeller speed that is required for the effective dispersion of gas
with turbine impellers.   Calderbank (10) attributed a sharp break
which was observed in Pg/Po vs. Fℓ curve to the flooding of the impeller.
In this region of operation the impeller cannot handle the amount of
the gas which is sparged to the vessel, and very inefficient dispersion
performance is obtained.   Westerterp et al (37) measured the interfacial
area by a chemical method.   They found that if the impeller speed was
less than certain value (N_0), the specific absorption rate depended on
the gas load and not on the impeller speed.   They defined this
condition as the minimum speed required for effective dispersion of
the gas and obtained the correlation :

$$\frac{N_0 D}{(\sigma g/\rho)^{0.25}} = 1.22 + 1.25 \frac{T}{D} \qquad\qquad 4.1$$

No was found to occur near to the minimum of $\frac{Pg}{Po}$ vs. Fℓ curve at
constant gas load, but do not coincide (38).

Rushton and Bimbinet (8) defined the flooding point to occur where a
sudden change in the flow pattern took place as the impeller power
was reduced at constant gas flow rate.   Here, the gas holdup decreased
sharply with no gas being dispersed from the impeller in the radial
direction.   Also there was no circulation of gas in the lower half of
the tank.   In addition they identified a sort of hysteresis effect
where the power required to overcome the flooding is higher than that
at which flooding takes place.

Dierendonck et al (21) observed that the stirred tank behaves like a
bubble column at very low impeller speed, where the gas holdup was

independent of the impeller speed. They defined a minimum speed as
that at which the gas holdup starts to increase with increasing the
speed. They proposed the following correlations :

$$No = 0.07(gT)^{\frac{1}{2}} \frac{T}{D^2} \qquad \text{for } T < 1.0m \qquad 4.2.A$$

and

$$No = 2 \frac{\sigma}{\mu} \frac{T}{D^2} \left(\frac{\rho\sigma^3}{g\mu^4}\right)^{-\frac{1}{4}} \left(\frac{H-c}{T}\right)^{\frac{1}{2}} \qquad \text{for } T > 1.0m \qquad 4.2.B$$

which are independent of gas load up to $Vs = \overline{0.03} \ ms^{-1}$.

Smith and coworkers (25) defined a minimum impeller speed as that
required to form a single large gas cavity. This was found to occur
at a Froude number equal to 0.1, ie,

$$\frac{No^2 D}{g} = 0.1 \qquad 4.3$$

However they suggested that the flooding condition would occur after
the complete formation of the six large cavities behind the impeller
blades. It was therefore defined as the condition at which most of
the sparged gas rises vertically without being dispersed (23). In a
later publication (40) they studied the gas recirculation phenomenon.
It was shown that if the impeller speed is high enough gas bubbles in
the bulk of the tank are recirculated back to the impeller region.
The total gas inflow to the gas cavities then becomes equal to the sum
of the sparged and recirculated gas, which causes a further drop in
impeller power. The ratio between the rate of gas recirculation to
the rate of sparging is called the external distribution coefficient α.
It was calculated from the Pg/Po vs. Fℓ curves at constant impeller
speed as illustrated in Fig. 4.1. The power consumption without
recirculation was estimated by using the same impeller in a large tank
which had the effect of minimising any gas recirculation.
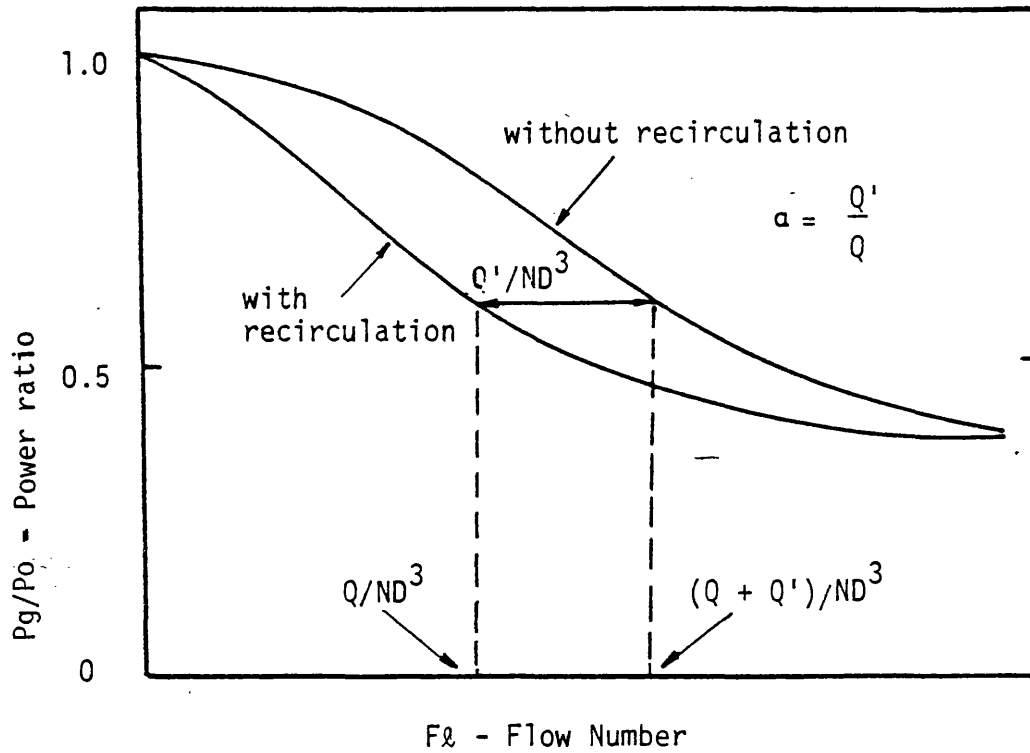
Fig.4.1 Determination of a from gassed power ratio curves at constant impeller speed (40)
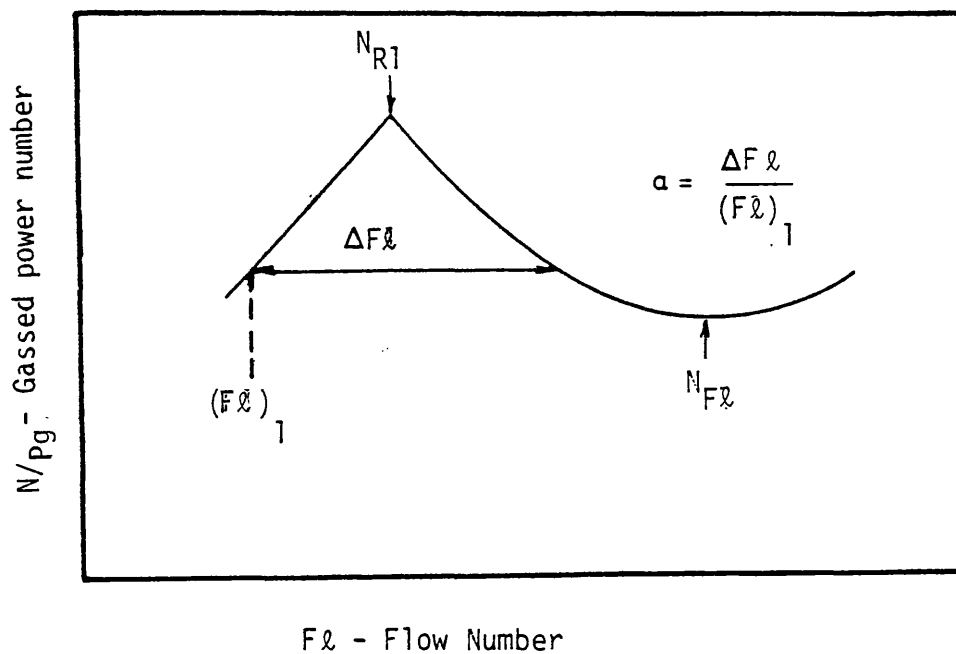
Fig.4.2 Determination of a from gassed power ratio curves at constant sparged gas rate (4)

Nienow et al (4) observed minima and maxima conditions for the N_{Pg} vs. $F\ell$ family of curves at constant gas flow rate (Fig. 4.2). From visual observations, the minimum was found to correspond to a flooding point (N_{F1}). This was defined to be the condition at which the gas is just dispersed in the upper and lower halves of the tank. The maximum point on the curve corresponded to the conditions at which recirculation of gas bubbles commenced (N_{R1}). Increase of the power number with decreasing impeller speed, for $N<\bar{N}_{F1}$, was explained as being due to the disappearance of the gas cavities from the lower part of the blades. The region between the point of flooding and the commencement of recirculation was described as the efficient mixing regime (19). N_{F1} and N_{R1} were correlated from experimental measurements with a range of tank sizes (up to 1.83m diameter), for water and $N_{a2}SO_4$ solution systems as follows

$$N_{F1} = 4 \frac{Q^{0.5}T^{0.2}}{D^2} \qquad\qquad 4.4$$

$$N_{R1} = 1.5 \frac{Q^{0.2}T}{D^2} \qquad\qquad 4.5$$

They also proposed a method for estimating the external distribution coefficient α from the power curve, as shown in Fig. 4.2. Recently Nienow et al (41) have developed a technique for estimating α, based on measuring the concentration of tracer gas in the cavities.

4.2.3 Power Consumption Correlations

The first useful attempt to correlate the impeller power consumption in gas-liquid dispersion was that of Oyama and Endoh (42). They correlated Pg/Po against the flow number ($Q/N D^3$) for a variety of impeller types. Later Calderbank (10) used a similar correlating method and suggested the following correlation for standard Rushton turbine

$$Pg/Po = 1 - 1.26 \frac{Q}{ND^3} \qquad \text{for } Fl < 0.035$$

$$4.6$$

$$Pg/Po = 0.62 - 1.82 \frac{Q}{ND^3} \qquad \text{for } Fl > 0.035$$

This correlation was obtained by varying the gas flow rate at constant impeller speed. However it was reported later (43) that Calderbank had revised his correlation and proposed a single curve similar to that of Oyama and Endoh (42). This was found to hold for large size tanks but with $\frac{D}{T} \leqslant \frac{1}{3}$. Lee and Meyrick (9) found no significant effect of the presence of sodium sulphate as a solute on power consumption using Eqs. 4.6.

In 1962 Michel and Miller (44) presented a correlation which is the most reliable one available to date, but a number of criticisms have been made by different investigators (19,23). It has the form

$$Pg = c M^n \qquad 4.7$$

when

$$M = \left(\frac{Po^2 \, ND^3}{Q^{0.56}}\right)$$

and

$$n = 0.45$$

Later Loiseau and Midoux (45) estimated c = 0.83 and n = 0.45 for non-foaming system and c = 0.69, n = 0.45 if M<2000, and c = 1.88, n = 0.3 if M≥2000 for foaming system. Recently Yung et al (11) found there was no effect of physico-chemical properties or ionic strength on the power requirements. Their experimental measurements were fitted to Eq. 4.7 with c = 0.812 for both water and different electrolyte solutions. It is important to indicate that the accuracy of predicting the power consumption using Eq. 4.7 was never better than $\pm$ 20% (11,44,45).

Pharamond et al (46) tested Eq. 4.7, and reported a dependence of the values of c and n on the tank size and impeller clearance. They also proposed the following correlation

$$Pg/Po = 1 - 1.6 \ Q_{vvm} \ D^{0.63} \qquad \qquad 4.8$$

for $0.19 \leqslant \frac{C}{H} \leqslant 0.33$, and $Q_{vvm} \ D^{0.63} < 0.63$

where

Q_{vvm} = gas volume per minute per volume of liquid in vessel.

From measurements with a wide range of gas flow rate, and various impellers and tank sizes, Nagata (47) showed that the power consumption under aeration is a function of the Flow number, Froude number and Reynolds number. The experimental data were correlated by :

$$Log \ \frac{Pg}{Po} = -192 \ (\frac{D}{T})^{4.38} \ Re^{0.115} \ Fr^{1.96(D/T)} \qquad Fl \qquad 4.9$$

Hassan and Robinson (13) measured the power consumption for aqueous electrolyte solutions, and 'pure' liquids. Using dimensional analysis, they derived the following equation :

$$Pg/Po = c_1 \ We^{-0.38} \ Fl^{-0.22} \ (\frac{\rho}{\rho_D}) \qquad \qquad 4.10$$

where ρ and ρ_D are the liquid and dispersion densities respectively. We is Weber number $(\frac{N^2 D^3 \rho}{\sigma})$ and c_1 was found to depend on the electrolyte nature of the aqueous phase. Recently Luong and Volesky (48) followed a similar approach, but did not include the term $(\frac{\rho}{\rho d})$ in their correlation, which is

$$Pg/Po = 0.497 \ We^{-0.18} \ Fl^{0.38} \qquad \qquad 4.11$$

Bruijn et al (25) found a direct relation between the number of large cavities behind the impeller blades and the relative power consumption Pg/Po.

They presented a graphical relationship between the total number of gas cavities formed and Q/ND^3 for different impeller sizes. From this the relative power consumption can be estimated under no gas recirculation conditions. They also reported no significant change in power consumption when different electrolyte solutions were studied, which is in agreement with Lee and Meyrick (9) and Yung et al (11).

From a simple model of flow through the impeller region, Nienow and Wisdom (49) suggested that

$$Pg = Po \left(1 - 8.5 \frac{Q}{ND^3}\right) \qquad 4.12$$

Equation 4.12 was found to be accurate for $N_{F1} \leq N \leq N_{R1}$. However it does not hold for high gas flow rate.

4.2.4 General Considerations

Correlations for predicting the impeller power under gassed conditions can be divided into two main groups. The first, representing the majority, includes all of the correlations in Sec. 4.2.3 (except Eq. 4.12), following what is called a 'Catch-all points' approach (4). For this type all of the experimental data is used regardless of the prevailing gas-liquid mixing regime, viz. flooding, efficient mixing without recirculation, or recirculation regime. Obviously, the correlations obtained by this approach will have relatively poor accuracy, but more importantly will depend on the operating range covered by the experimental investigations. This explains the variety of correlations which have been obtained. Nevertheless investigators are still producing more correlations of this type even after it became clear from the studies of Nienow, Smith and co-workers (4,19,23,25) that the impeller power consumption depends on the regime of gas-liquid mixing. It is doubtful that continuation along

these lines will lead to generally useful correlations, except to indicate that a universal method for predicting the gassed impeller power may not yet be within reach.

The second approach concentrates on predicting the impeller power for the efficient mixing without recirculation regime -(hereafter called efficient mixing regime). Bruijn et al (25) work, combining power measurements with visual observations of the cavity formation, provides the basis for this approach. Their results have proved to be reasonably accurate when tested for different scales of equipment (4,49). Equation 4.12 is also included in this category, but it does not hold for high gas flow rates. A disadvantage of this approach concerns the difficulty associated with the practical use of graphical data (25,4). Also the data are presented in the form of relative power, ie, Pg/Po, and it has already been shown in Chapter 3, that N_{P_0}, and consequently Po, depends on geometrical factors. Also, the data cannot be used for prediction of power in the recirculation regime, which is necessary to use in certain processes where maximum utilisation of valuable gases is required. Moreover, this approach necessitates that reliable correlations for predicting N_{R1} and N_{F1} be available. These have been correlated in only one study (4) (Eqs. 4.4 and 4.5) although there is reason to believe that the correlations are not sufficiently accurate since they were obtained with mixed experiments. Significant differences in behaviour of coalescing and non-coalescing system have, however, been found to occur (see Sec. 4.3.8).

The objective of the present work, therefore, is not to add a further correlation to the already existing number. Instead, it is to extend the second approach of predicting the power in the efficient mixing

regime to cover the recirculation and the flooding regimes, and also to overcome some of the abovementioned difficulties associated with this approach. Hopefully, this should lead to a better prediction of the impeller power consumption. A necessary prerequisite for this is the establishment of a better understanding of the methods for representing and analysing experimental power data. In the Results and Discussion Section to follow, the specific areas covered are :

representation of experimental data; use of power curves in identifying the different gas-liquid mixing regimes; impeller dispersion efficiency as a measure of the degree of flooding and recirculation; correlation of the conditions N_{F1} and N_{R1} for the onset of flooding and recirculation; development of an improved power correlation; the effects of increasing the vessel pressure on N_{F1} and N_{R1} and impeller power; and effects in 'non-coalescing' electrolyte solutions.

4.3   RESULTS AND DISCUSSION

4.3.1   Representation of Gassed Power Data

In section 3.4.1 the shape of N_{Po} vs R_e curve prior to the onset of surface aeration was shown to be dependent on certain geometrical factors, including the impeller diameter and clearance. It should be reflected, therefore, in the measurements of power consumption with aeration. When the data was examined, it was found to be be a multiplying rather than an additive effect. In other words, to be able to study the effect of adding gas on impeller power consumption, the proper representation of data should be Pg/Po or N_{Pg}/N_{Po}. More-over, at impeller speeds higher than N_{SA2}, N_{Po} drops sharply due to surface aeration. However, when gas is sparged to the vessel, the rate of surface aeration is considerably reduced even at the low gas rates and high power inputs (41). It can be assumed then that N_{Po}

would have maintained its value at N_{Pomax}, providing there is no significant interference from surface aeration. Hence the proper representation for gassed power data at speeds exceeding N_{SA2} would be by N_{Pg}/N_{Pomax}.

To demonstrate these effects, the data for impeller D2 at constant gas flow rate are used. Impeller D2 is selected, where the most dramatic changes in N_{Po} were observed. From Fig. 4.3 it can be noticed for the N_{Pg}/N_{Pomax} vs. Fℓ curve (equivalent to N_{Pg} x constant on the ordinate) the minimum is shifted to the right, leading to underestimation of N_{F1} (as defined by Nienow (4)). This is also clear in Fig. 4.4 where at low gas flow rates the flooding point may disappear altogether. But for N_{Pg}/N_{Po} vs. Fℓ, which is equivalent to Pg/Po vs. Fℓ the maximum in Fig. 4.3 is not observed due to the fall of N_{Po} caused by surface aeration. Curve (A) in Fig. 4.3 demonstrates the correct representation of the data, and both the minimum and the maximum are clear.

Nienow et al (4) have observed a similar influence of surface aeration using $\frac{C}{T} = \frac{D}{T} = \frac{1}{2}$. The onset of surface aeration occurred at a low impeller speed, such that $N_{SA2} < N_{F1}$ indicating a false flooding point prior to reaching its true value. However with standard configuration, ie, $\frac{C}{T} = \frac{1}{3}$ or with $\frac{C}{T} = \frac{1}{4}$ and $\frac{D}{T} \leqslant \frac{1}{3}$, the changes in N_{Po} for $N < N_{SA2}$ are small (Chapter 3) such that N_{Pg} vs. Fℓ would be a sufficiently correct representation for gassed power consumption.

4.3.2 Flooding, Efficient Mixing and Recirculation Regimes

In the present study the power measurement experiments were carried out in the following way. The impeller speed was kept constant and the ungassed power was measured. Gas was then sparged to the vessel and the power was measured at set points of gas flow rate. Then the
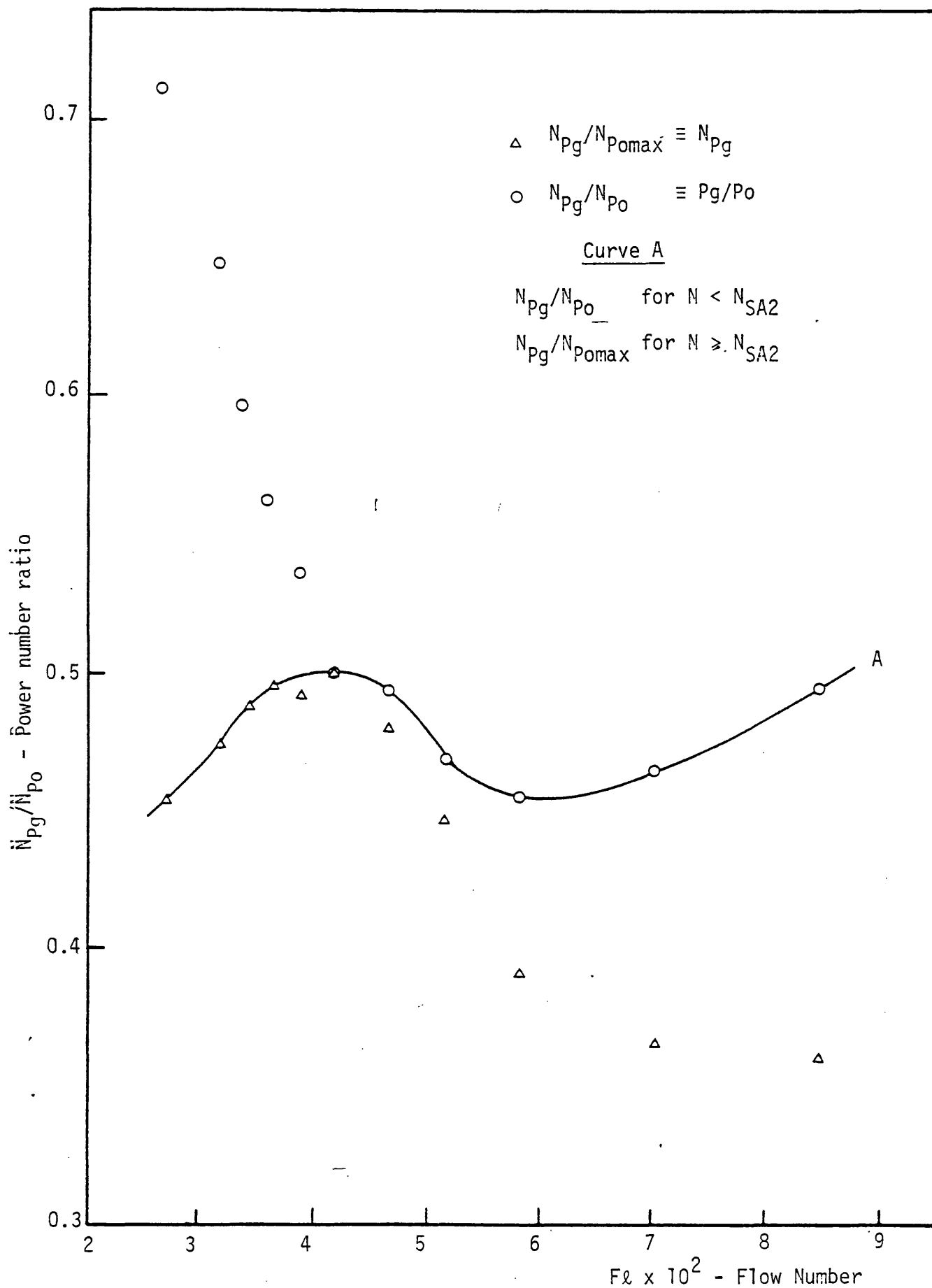
Figure 4.3 : Representation of gassed power data

$(D=0.1016m, \quad Q = 3.61 \times 10^{-4} m^3 s^{-1})$
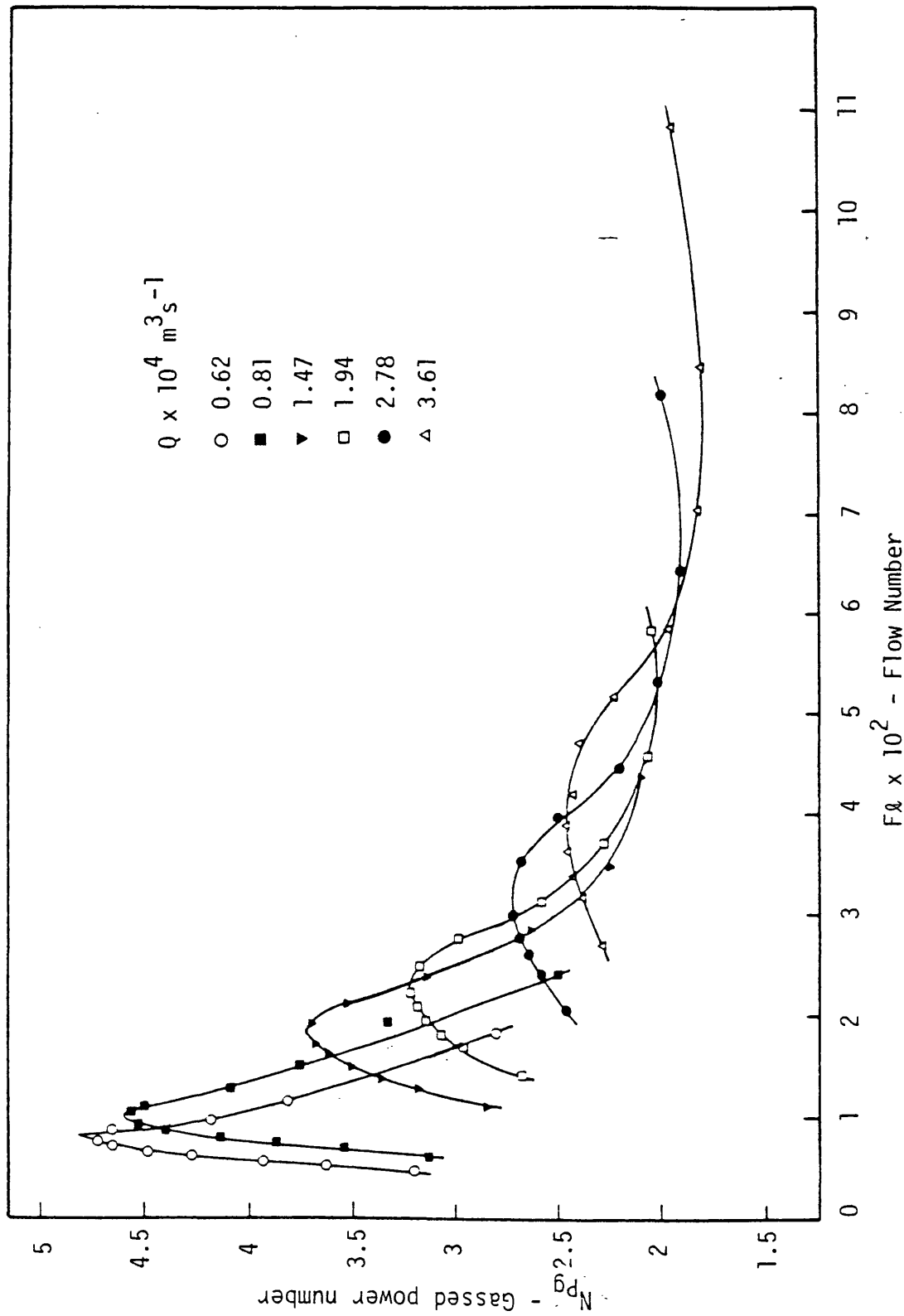
Fig.4.4   Gassed power number against flow number (D = 0.1016 m)

impeller speed was changed and the power was measured under ungassed condition, and at the same gas flow rates. From these measurements it was possible to draw constant speed lines and constant gas flow rate lines on N_{Pg}/N_{Po} vs. $F\ell$ plots by the method described in the previous section (4.3.1). The results for the three impellers used are shown in Figs. 4.5, 4.6 and 4.7.

If a line of constant gas flow rate is examined in any of these, figures, eg, Fig. 4.7, the different regimes of gas mixing as described by Nienow et al (4) can be observed. The region between the minimum and the maximum of each curve is called the efficient mixing regime whereall the sparged gas passes through the impeller just once (19). The region to the right of the minima is called the undeveloped or flooded mixing regime, while that to the left of the maxima is called recirculation regime.

On the other hand, if constant impeller speed lines are examined, it could be noticed that in the efficient mixing zone these lines are close and almost identical for the case of the smaller impeller (Fig. 4.5). This zone is defined by two lines, which are the line connecting the minima, and the line connecting the maxima of the constant gassing rate lines. Within this region the power consumption drops smoothly with decreasing the impeller speed at constant gas rate, and in stepwise when the gas rate is increased at constant impeller speed. In principle, the change in power consumption within this zone is similar to that described by Bruijn et al (25) and is well explained by the cavity formation theory. The smooth drop of power with decreasing the impeller speed for the largest impeller (Fig. 4.7) may be attributed to enlargement of the cavities. With increase of the gas flow rate another large cavity
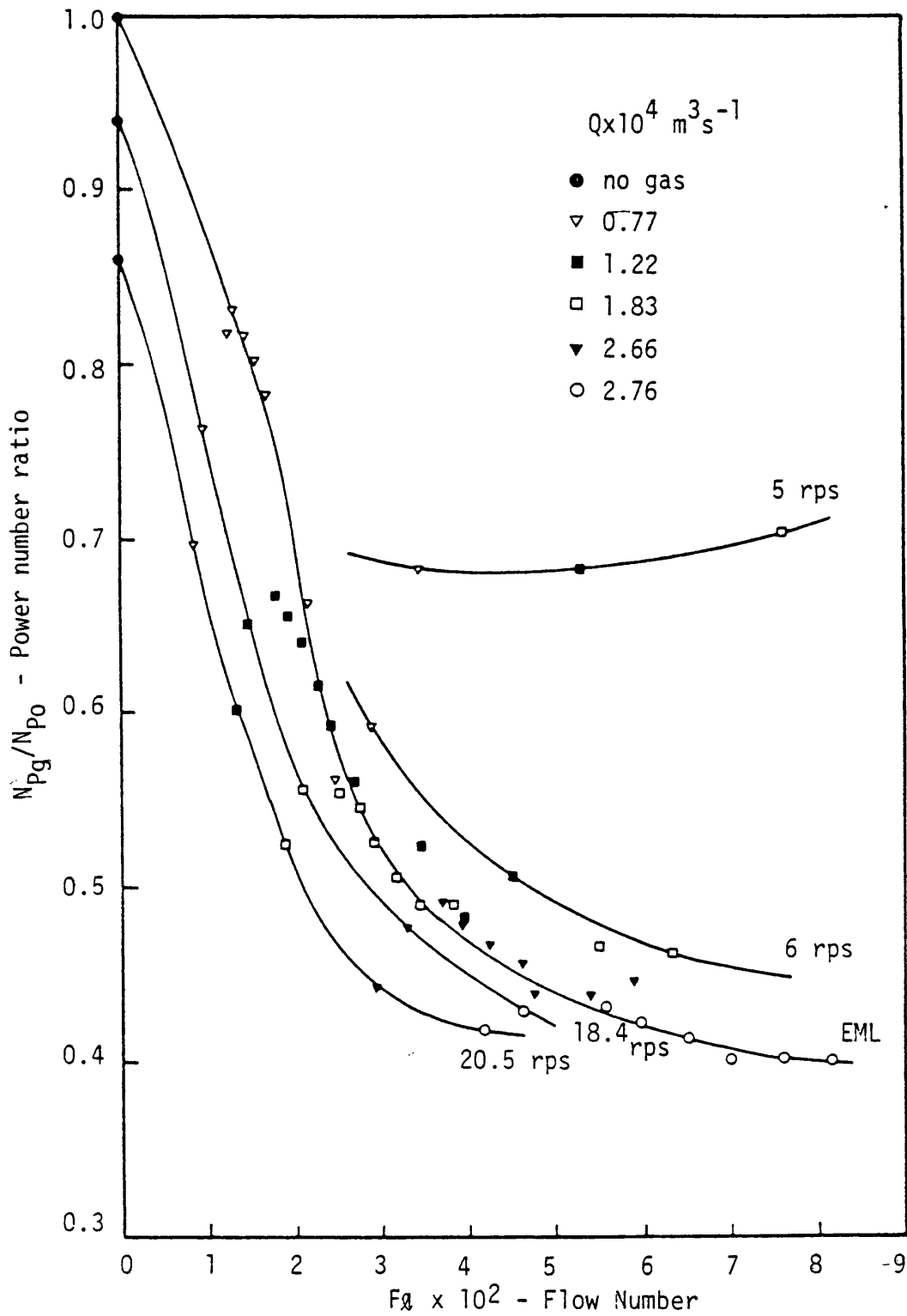
Fig.4.5 N_{Pg}/N_{Po} against Flow Number showing efficient mixing line (D = 0.0762 m)
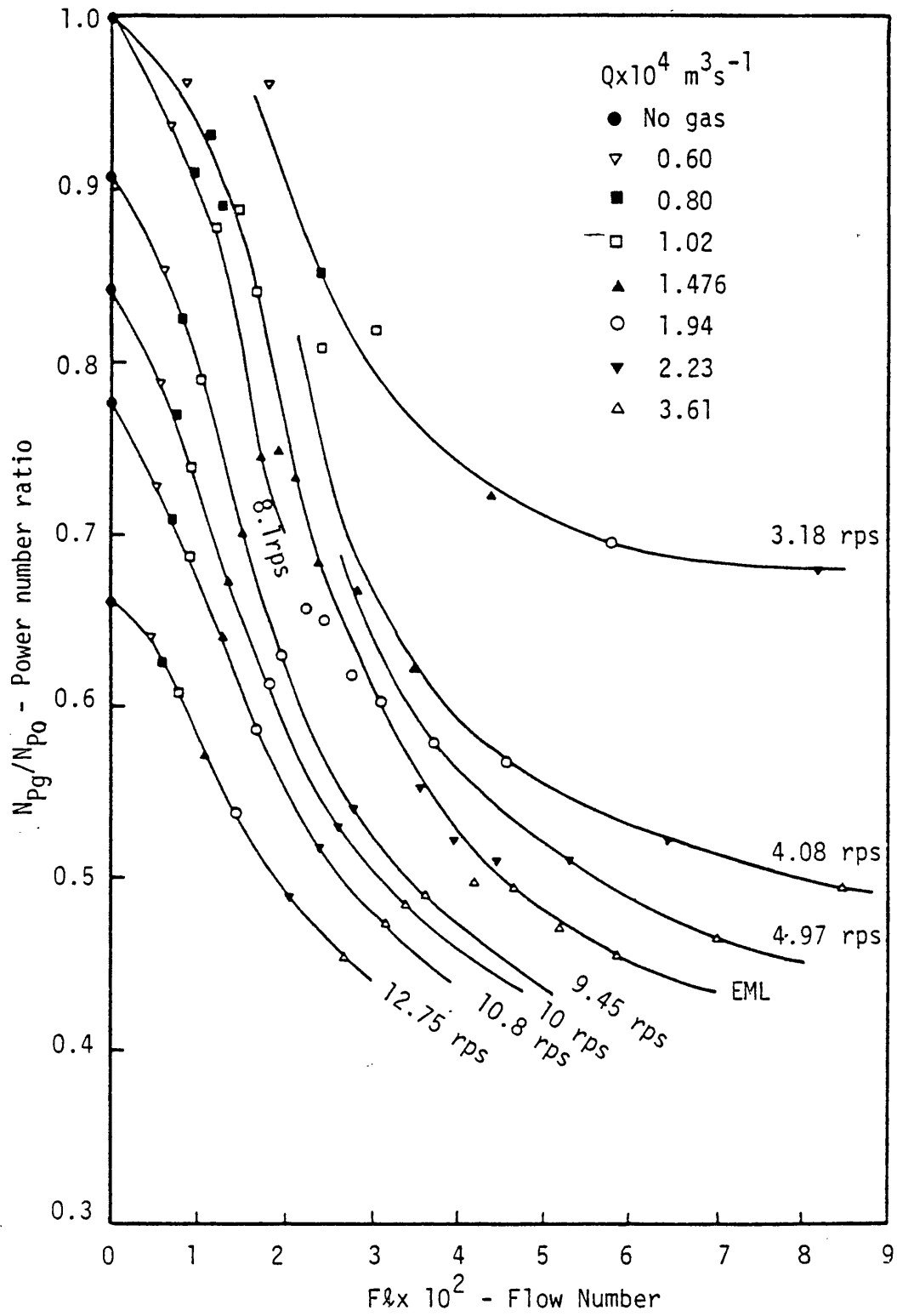
Fig.4.6 N_{Pg}/N_{Po} against Flow number showing efficient mixing line (D = 0.1016 m)
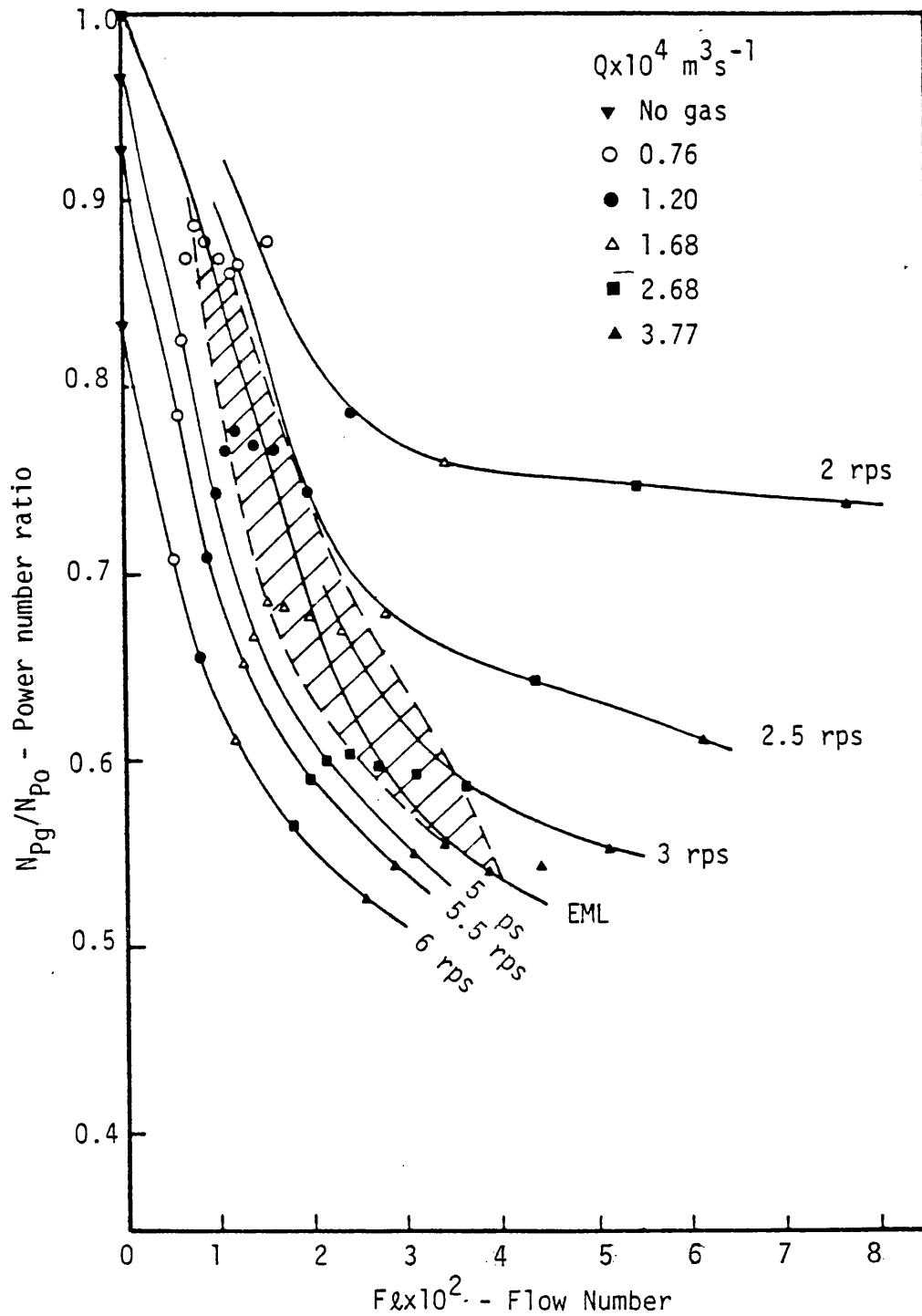
Fig.4.7 N_{Pg}/N_{Po} against Flow Number showing efficient mixing zone (///) and efficient mixing line (D = 0.135 m)

is completed causing a step change in power. However there is a steeper change of power with impeller speed for the smaller impellers D1 and D2 (Fig. 4.5, 4.6). This makes the power curve look continuous and obscures the stepwise change of power which is associated with the formation of large cavities.

The without recirculation curve (40) or what will be called the efficient mixing line (EML) is defined by drawing a line through the centre of the efficient mixing zone. This line for the smallest impeller (D=0.076m, Fig. 4.5) is identical with that estimated from power measurements obtained with a similar impeller size in a large tank (25). The average absolute deviation is 3%.

The constant speed lines to the left of the efficient mixing zone lie in the recirculation regime. These lines intersect the vertical axis (no gas condition) at values less than one, due to surface aeration. However, under gassed conditions the drop in N_{Pg} with increasing impeller speed is due to gas recirculation, and the effect of surface aeration may be neglected as discussed previously.

Those lines which lie to the right of the efficient mixing zone are in the flooded regime. Impeller flooding may occur with any number of large cavities or even with just clinging cavities behind the impeller blades (eg, Q=0.76 10^{-4}, Fig. 4.7). The mechanism of flooding as described by Nienow et al (4) seems to be suitable. However, the continuity of the flooding process, ie, its possible occurrence under any cavity formation conditions, needs further clarification. It appears that the mechanism of gas inflow to the cavities plays an important role in the flooding process. At low impeller speeds a small fraction of the sparged gas coalesces with the formed cavities, and the rest flows through the tank without being dispersed. With

increase of impeller speed at constant sparging rate more gas coalesces with the cavities due to the intensification of the pressure and flow gradients driving the bubbles to the cavities, causing a reduction in N_{Pg}. The flooding point may be described as the point at which all the sparged gas coalesces with the impeller cavities. With further increase of the impeller speed, the rate of gas coalescence with the cavities stays at its maximum, ie, the sparging rate of gas. This is true so long as there is no significant amount of gas being recirculated at $N_{Fl} \leqslant N \leqslant N_{Rl}$ (4 1). Therefore the effective value of Fℓ will be reduced with increasing N, causing reduction in the cavities size (25) and consequently increasing N_{Pg}. This will continue within the efficient mixing zone until further supplies of gas become available. This occurs when the impeller speed is high enough to cause recirculation of gas bubbles back to the impeller. Then a further reduction in N_{Pg} will be observed.

Increase of the gas rate at constant impeller speed, after the formation of all gas cavities, will cause impeller flooding. This is the special case of flooding reported by Bruijn et al (25), and it defines the lower limit of the efficient mixing zone (EMZ). At this limit the EMZ becomes so narrow that it coincides with the efficient mixing line (EML). The upper part of the EMZ is similar and coincides also with the EML. This is caused by the sharp change in power associated with the formation of the clinging cavities (25) and may explain the sharp peaks marking the onset of gas recirculation (49) at low gas flow rates.

4.3.3 Correlation for N_{Rl}

The gas recirculation phenomenon takes place if the liquid velocity in the bulk of the tank becomes high enough to carry the gas bubbles back

to the impeller region. The speed at which gas recirculation commences, N_{R1}, can be defined from the maximum on the N_{Pg}/N_{Po} vs. $F\ell$ curve at constant Q.

There is apparent similarity between surface aeration in ungassed vessels and gas recirculation in gassed vessels. Thus N_{R1} will be correlated in a similar manner to that used for correlating N_{SA2} (see Section 3.4.2). As has been shown in Chapter 3, the average circulating velocity in an ungassed tank in the region away from the impeller zone could be estimated by

$$\bar{V} \alpha \frac{ND^2}{T} \qquad 4.13$$

However, if gas is sparged to the tank the flow pattern of liquid inside the tank may be altered if the gas flow rate is high enough and the impeller speed is low. Oldshue (35) showed that when the impeller is providing four times or more power than the gas flow then a mixer-controlled flow pattern will result. The ratio of the power provided by the impeller to that supplied by the gas flow (Kinetic and expansion) at the condition of com..encement c.' gas recirculation was calculated for the three impellers used. It was found to be 18, 12, and 7 for D1, D2 and D3 respectively, under the worst conditions, ie, the highest gas flow rate. It can be assumed, therefore, that the flow pattern does not change significantly due to the sparging of the gas when gas recirculation commences. Brown and Halsted (50), who estimated mixing model parameters from impulse response experiments for a continuous flow STR at low liquid flow rate, also found very little effect on their overall mixing model for the liquid phase due to gassing of the vessel. The flow pattern may then be represented by Fig. 4.8, and Eq. 4.13 holds. As a first approximation, to define the correct correlating parameters, it can be assumed that the necessary condition

Fig. 4.8   Recirculation of gas bubbles

$$N_{R1} \propto \left(\frac{T}{D^2}\right)^{1.12}$$

$Q \times 10^4 m^3 s^{-1}$	
▲	0.8
●	1.7
■	2.7
▼	3.8
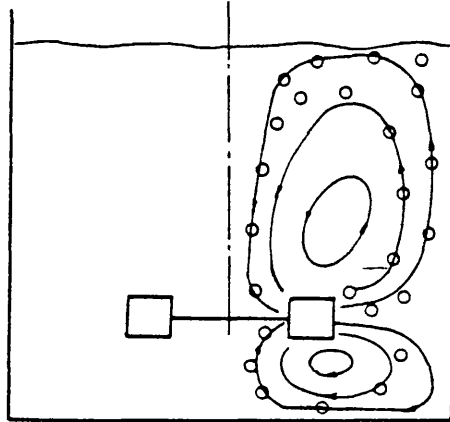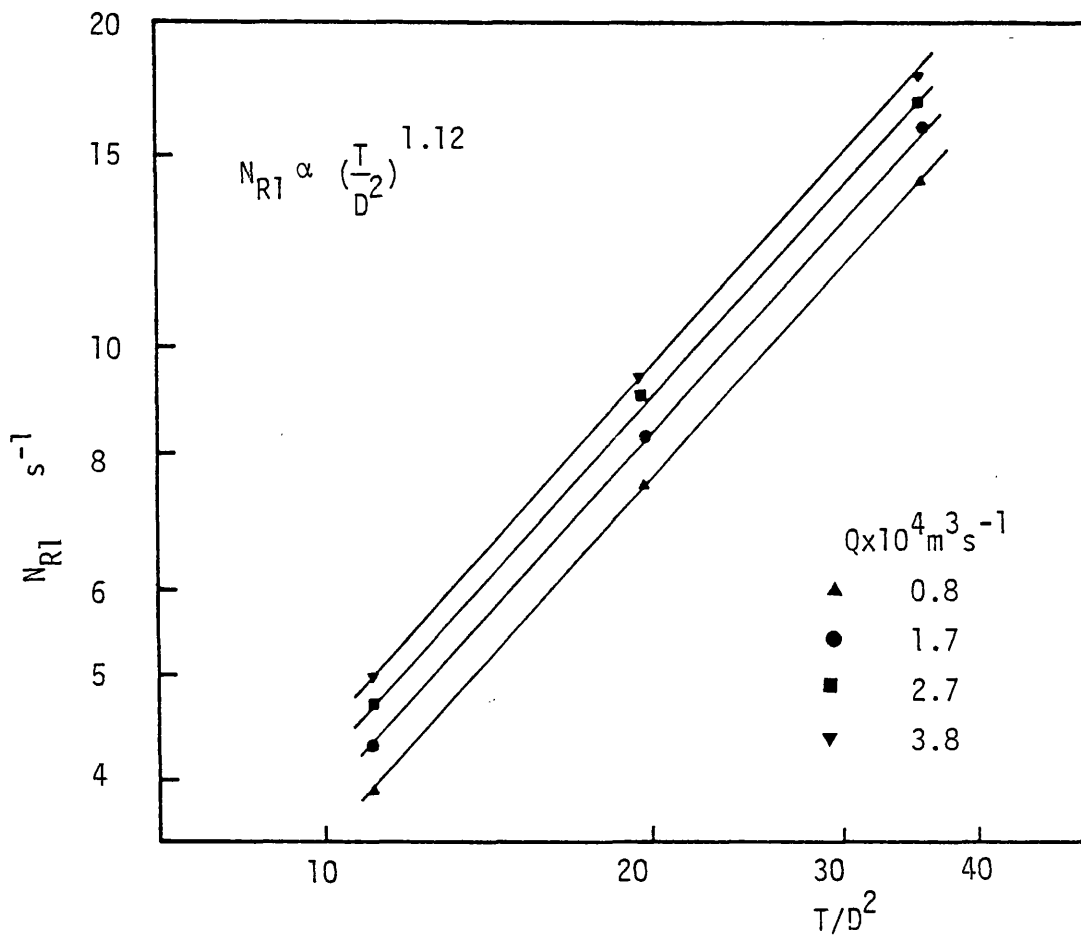
Fig. 4.9 N_{R1} against T/D^2 for different gas flow rates

for the start of gas recirculation (see Section 3.4.2.3) is

$$\bar{V} > U_T \qquad\qquad 4.14$$

where U_T = bubble terminal velocity.

Combining Eqs. 4.13 and 4.14 then

$$N_{R1} \alpha \left(\frac{T}{D^2}\right) \qquad\qquad 4.15$$

where the constant of proportionality will be a function of the average bubble size. To account for the effect of gas load, the Flow number F_ℓ is selected as another correlating parameter, since it relates the gas sparging rate to the impeller discharge, ie,

$$N_{R1} \alpha \left(\frac{Q}{N_{R1} D^3}\right)^X \qquad\qquad 4.16$$

By drawing N_{R1} vs. $\left(\frac{T}{D^2}\right)$ at constant Q (Fig. 4.9), and N_{R1} vs. $\left(\frac{Q}{N_{R1} D^3}\right)$ at constant D (Fig.4.10), in log-log plots, it was found that

$$N_{R1} \alpha \left(\frac{T}{D^2}\right)^{1.12} \left(\frac{Q}{N_{R1} D^3}\right)^{0.15}$$

On rearrangement this gives

$$N_{R1} = 0.57 \frac{T^{0.97} Q^{0.13}}{D^{2.34}} \qquad\qquad 4.17$$

This correlation includes T, although it is based on measurements for a single tank. However, the scaling-up effect is close to that presented by Nienow et al (4), (Eq. 4.5), where their measurements covered a range of equipment sizes (up to T=1.83m). This confirms the proper choice of correlating parameters, and hence the constant of proportionality in Eq. 4.17 is a function of the average bubble size.

$$N_{RI} \; \alpha \; \left(\frac{Q}{N_{RI} \; D^3}\right)^{0.15}$$

D(m)	
■	0.135
●	0.1016
▼	0.0762

Fig. 4.10 N_{RI} against $\dfrac{Q}{N_{RI} \; D^3}$
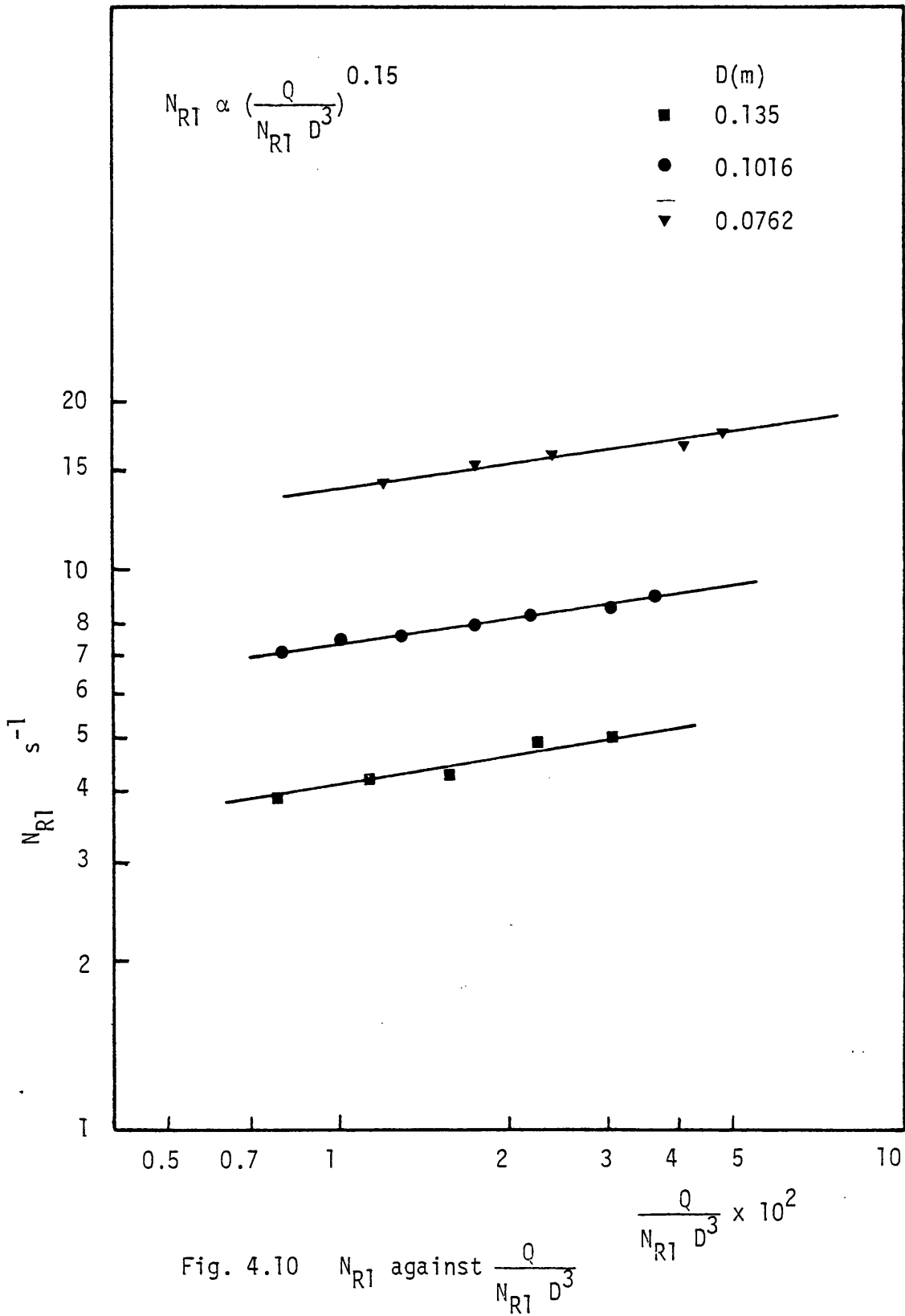
When 0.11M K_2SO_4 solution was studied the constant was found to be 0.48. The effect of added electrolytes will be discussed in more detail in a later section.

4.3.4 Impeller Dispersion Efficiency "η"

As explained before there is an efficient mixing zone for the impeller in which all the sparged gas coalesces and is then dispersed from the cavities behind the impeller blades. In the recirculation regime more gas is recirculated from the bulk of the tank to the impeller. Hence the rate of gas coalescence with the cavities is larger than that sparged. In the flooded regime the gas cavities are capable of capturing only a part of the sparged gas while the rest flows vertically to the surface without being dispersed to the bulk of the tank. The external distribution coefficient α, as defined by van't Riet et al(40), is not suitable to define the disperson performance of the impeller in the flooded regime. Instead, an impeller dispersion efficiency η is defined such that

$$\eta = \frac{\text{Volumetric rate of gas coalescence with the impeller cavities}}{\text{Volumetric sparging rate}} \qquad 4.18$$

where

$\eta = 1$ in the efficient mixing regime

$\eta < 1$ in the flooding regime

$\eta > 1$ in the recirculating regime.

Assume a point in the recirculation regime, ie, lying to the left of the EMZ (Point 2, Fig. 4.11). The rate of gas sparging at that point is Q_2. However, due to gas recirculation the power consumption is equivalent to a condition where the rate of coalescence with the cavities is equal to a gas rate Q_1. Hence

$$\eta_2 = \eta_R = \frac{Q_1}{Q_2}$$

$$\eta_3 = \eta_F = \frac{Q_1}{Q_3}$$
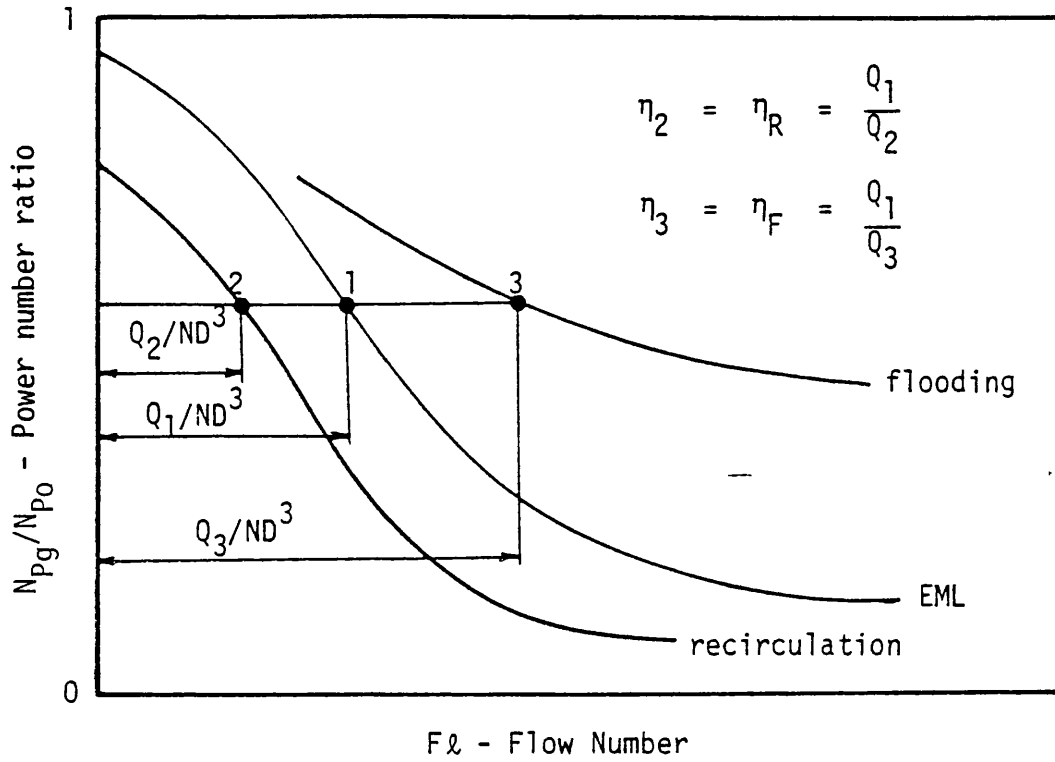
Fig.4.11 Determination of impeller dispersion efficiency from N_{Pg}/N_{Po} against $F\ell$

$$n_2 = n_R = \frac{Q_1}{Q_2} > 1 \qquad\qquad 4.19$$

and $\quad n_R = \alpha+1$

For a point in the flooded regime, point 3 Fig. 4.11, the sparged gas rate is Q_3, while the rate of gas coalescence with the cavities is only Q_1. Therefore :

$$n_3 = n_F = \frac{Q_1}{Q_3} < 1 \qquad\qquad 4.20$$

4.3.5 Correlations for Impeller Efficiency

The impeller dispersion efficiency in the recirculation region n_R was calculated for all the points in that region using Eq. 4.19. When n_R was drawn against Fℓ on a log-log plot, a family of parallel lines was obtained for different values of Q with slopes of -2.53. The intersections of these lines with any one constant Fℓ line were drawn against Q for each impeller. Again they produced 3 parallel lines for the 3 impellers with slopes of 2.2. Finally the intersections of these lines with any constant Q line, when plotted against D in a log-log manner was found to lie on a straight line with slope equal to -1.66. Hence the impeller efficiency in the recirculation region correlates the experimental data as

$$n_R = C1 \ D^{-1.66} \ Q^{2.2} \ \left(\frac{Q}{ND^3}\right)^{-2.53} \qquad\qquad 4.21$$

and on rearrangement

$$n_R = C1 \ \frac{N^{2.53} \ D^{5.93}}{Q^{0.33}} \qquad\qquad 4.22$$

Equation 4.22 does not include a term for the tank diameter T. From the definition of n_R, $n_R \to 1$ when $N \to N_{R1}$. Then by substituting $n_R = 1$ and $N = N_R$ in Eq. 4.22

$$N_{R1} = C2 \frac{Q^{0.13}}{D^{2.34}}$$ 4.23

Equations 4.17 and 4.23 are similar except for the term $T^{0.97}$ which is not present in Eq. 4.23. It is necessary to emphasise that, while Eq. 4.17 was obtained by correlating the experimental points at the onset of gas recirculation, Eq. 4.23 was derived using all the points in the recirculation region. To account for the tank diameter in Eq. 4.22, T is included in the denominator raised to the power (0.97 x 2.53). Thus the correlation for η_R has the general form :

$$\eta_R = 4.13 \frac{N^{2.53} D^{5.93}}{T^{2.45} Q^{0.33}}$$ 4.24

Fig. 4.12 demonstrates that the experimental data are well correlated with Eq. 4.24 within $\pm$ 10%. Also included are the results of van't Riet et al (40) for two impeller sizes. Although the trend is the same, their results are shifted upward by 0.7. It is of interest to note their results for D=0.076 without recirculation are identical to the results of this study with similar impeller size. However, they measured the power consumption with recirculation with an impeller clearance of T/2, and the liquid level was increased to prevent any surface entrainments. This suggests that the rate of gas recirculation in the bottom half of the tank may possibly have been increased because of the increased impeller clearance which is difficult to explain and contradicts the observations of Nienow et al (4).

A similar treatment for the impeller efficiency in the flooded regime η_F, yielded :

$$\eta_F = C3 \frac{N^{2.53} D^{4.4}}{Q^{0.73}}$$ 4.25

Also, since $\eta_F \rightarrow 1$ when $N \rightarrow N_{F1}$, then
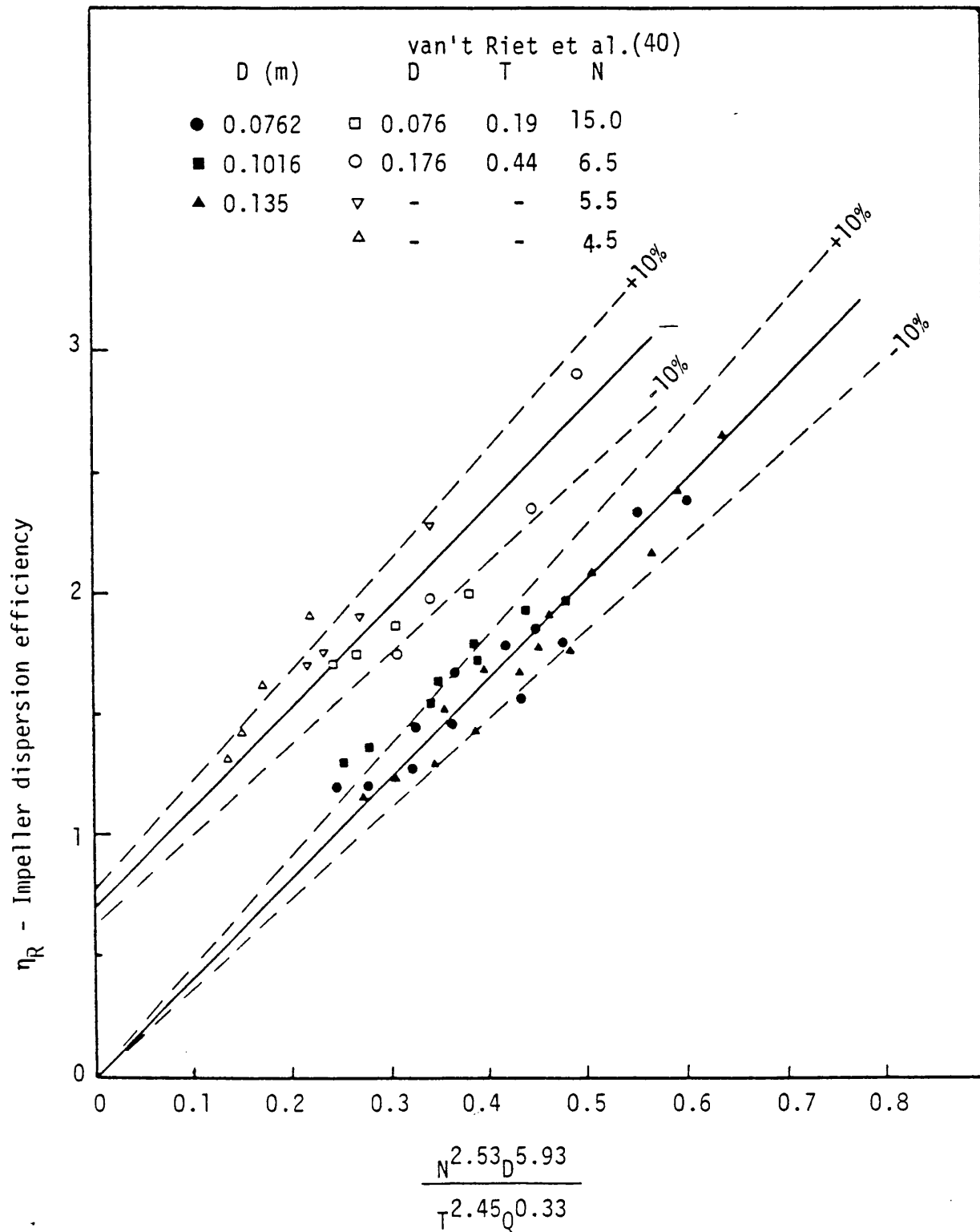
Fig.4.12 Correlation for impeller dipersion efficiency in recirculation region

$$N_{F1} = C4 \frac{Q^{0.29}}{D^{1.74}} \qquad \cdot \qquad 4.26$$

Nienow et al (4) correlated the effect of tank diameter as (see Eq.4.4)

$$N_{F1} \propto T^{0.2}$$

Hence the effect of tank diameter on η_F is accounted for by including $T^{0.2} \times 2.53$ in the denominator of Eq. 4.25. Therefore,

$$\eta_F \propto \frac{N^{2.53} D^{4.4}}{T^{0.5} Q^{0.73}} \qquad - \qquad 4.27$$

Figure 4.13 shows this relationship represented by two straight lines such that :

$$\eta_F = 0.4A \qquad \text{for } A \leqslant 1 \qquad 4.28.a$$

and

$$\eta_F = 0.25 + 0.26A \qquad \text{for } A > 1 \qquad 4.28.b$$

where

$$A = \frac{N^{2.53} D^{4.4}}{T^{0.5} Q^{0.73}}$$

This simplified basis was selected because a single straight line fit was found to be inferior to that of an exponential curve. N_{F1} can be estimated from Eq. 4.28.b by putting $\eta_F = 1$ and $N = N_{F1}$, whence :

$$N_{F1} = 1.52 \frac{T^{0.2} Q^{0.29}}{D^{1.74}} \qquad 4.29$$

An estimation of η_F for 0.61m tank from reference (4) is also shown in Fig. 4.13.

The definition of the impeller efficiency has some useful features.

If η_F(Eqs. 4.28) and η_R(Eq. 4.24) are calculated for certain conditions it will satisfy :

$$\eta_R > 1 \qquad \text{for any point in the recirculation regime}$$
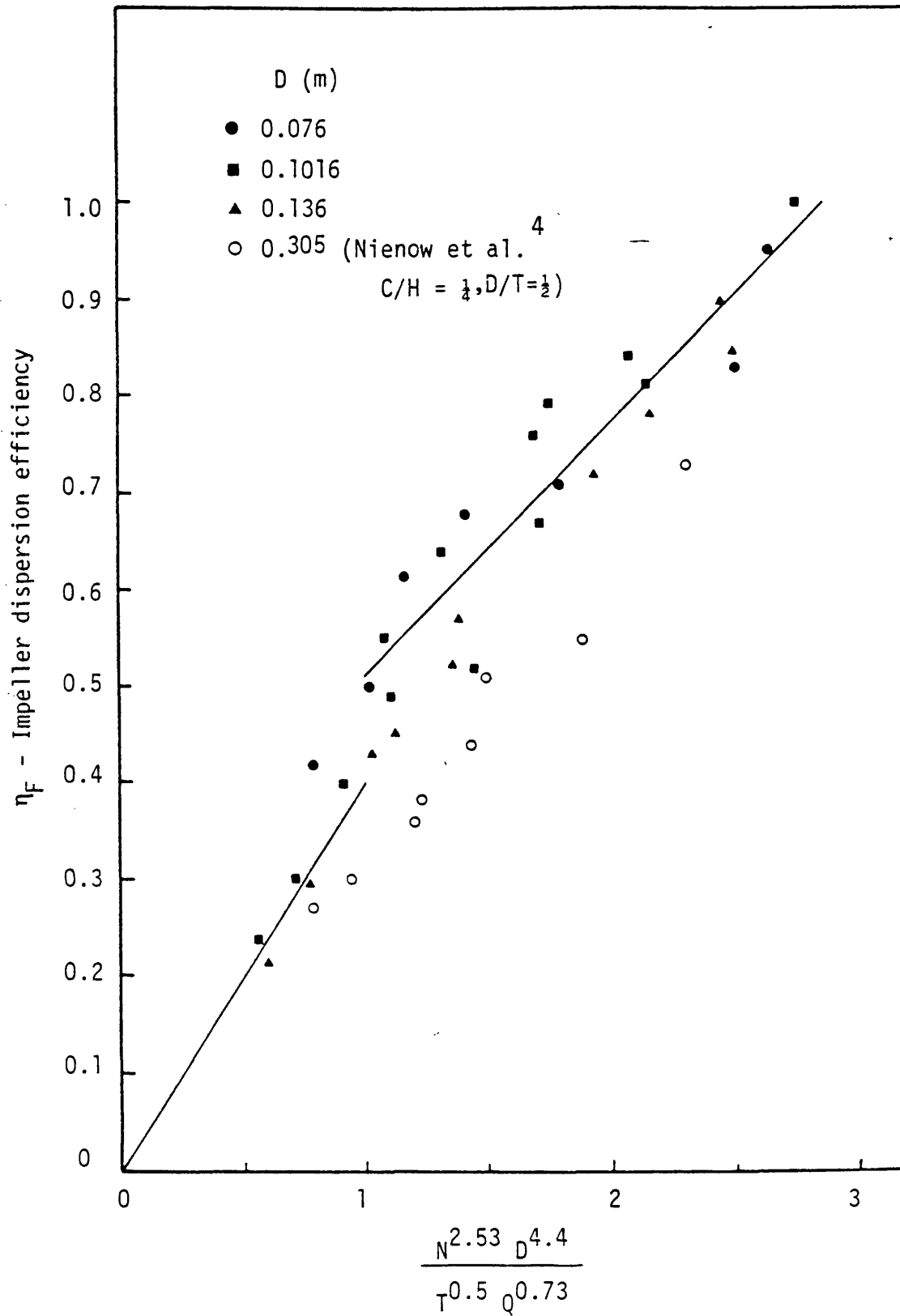
Fig.4.13 Correlation for impeller dispersion efficiency
in the flooding region

$\eta_F < 1$ for any point in the flooding regime

$\eta_R \leqslant 1$ for any point in the efficient

and

$\eta_F \geqslant 1$ mixing regime

The impeller efficiency also has particular importance for correlating the impeller power consumption as will be seen in the following section.

4.3.6   Impeller Power Consumption

The previous analysis (Section 4.3.2) has shown that the impeller power consumption depends on the regime of mixing. However, most of the correlations presented in literature do not discriminate between these regimes. The poor accuracy for these correlations is caused by neglecting the different mixing regimes rather than experimental error in measurements. Moreover all of these correlations (see Section 4.2.3) are correlating the relative power consumption Pg/Po. So it is necessary to estimate Po before Pg can be calculated. This is normally done by using values of the ungassed Power number from literature, which causes further error because N_{Po} changes with R_e for the same system as well as with minor geometrical differences from one system to another.

In this study the power consumption in the efficient mixing regime was correlated separately. The power consumption in this region depends solely on the cavity formation, where all of the sparged gas passes through the cavities just once. Hence the correlating parameters for Pg are N, D and Q. The omission of the tank dimension T implies that any recirculation of gas for $N < N_{R1}$ is neglected. The derivation of N_{R1} correlation previously (Section 4.3.3) indicated that the average size of the bubbles which are recirculated is dependent on the impeller speed. Hence at low impeller speeds only fine bubbles will be carried to the impeller zone, and the volume of the recirculated gas ($Q_R \alpha dp^3$) will be negligible compared with the sparged gas. These conclusions

could be confirmed from the apparent similarity between the gas recirculation and surface aeration phenomena (see Chapter 3).

Any trial to correlate Pg against N, D and Q on log-log plots, will produce a statistically biased correlation. For example, it is hard to find enough experimental data points that have the exact values for N and Q for different impeller sizes. Instead the experimental results were correlated by multiple regression analysis using least squares method. The regression model employed was

$$Pg = ao \ N^{a1} \ D^{a2} \ Q^{a3}$$

All the power data for the three impellers in the efficient mixing zone were used. The result obtained is :

$$Pg = 1007 \ \frac{N^{3.33} \ D^{6.33}}{Q^{0.404}} \qquad\qquad 4.30$$

As shown in Fig. 4.14, Eq. 4.30 provides a good fit of the experimental data, with an accuracy better than $\pm$ 10%. The scattering of the experimental points is caused by two factors. The first is that the efficient mixing regime is best described by a zone rather than a single line, and the second is experimental error. Results for a 0.38m and 0.91m tank(12) are also shown in Fig. 4.14, indicating an excellent fit with Eq. 4.30. However, it can be noticed that for the 0.91m tank, the experimental points lie above the correlating line at low impeller speeds and below the line at high impeller speeds. That is to be expected since these points lie in the flooded and recirculation regimes, respectively.

To calculate the power requirements in both the flooded and recirculation regiems we recall the definition of the impeller dispersion efficiency (Eq. 4.18). The true volumetric rate of gas coalescence with the cavities in these regions is ηQ. Therefore,
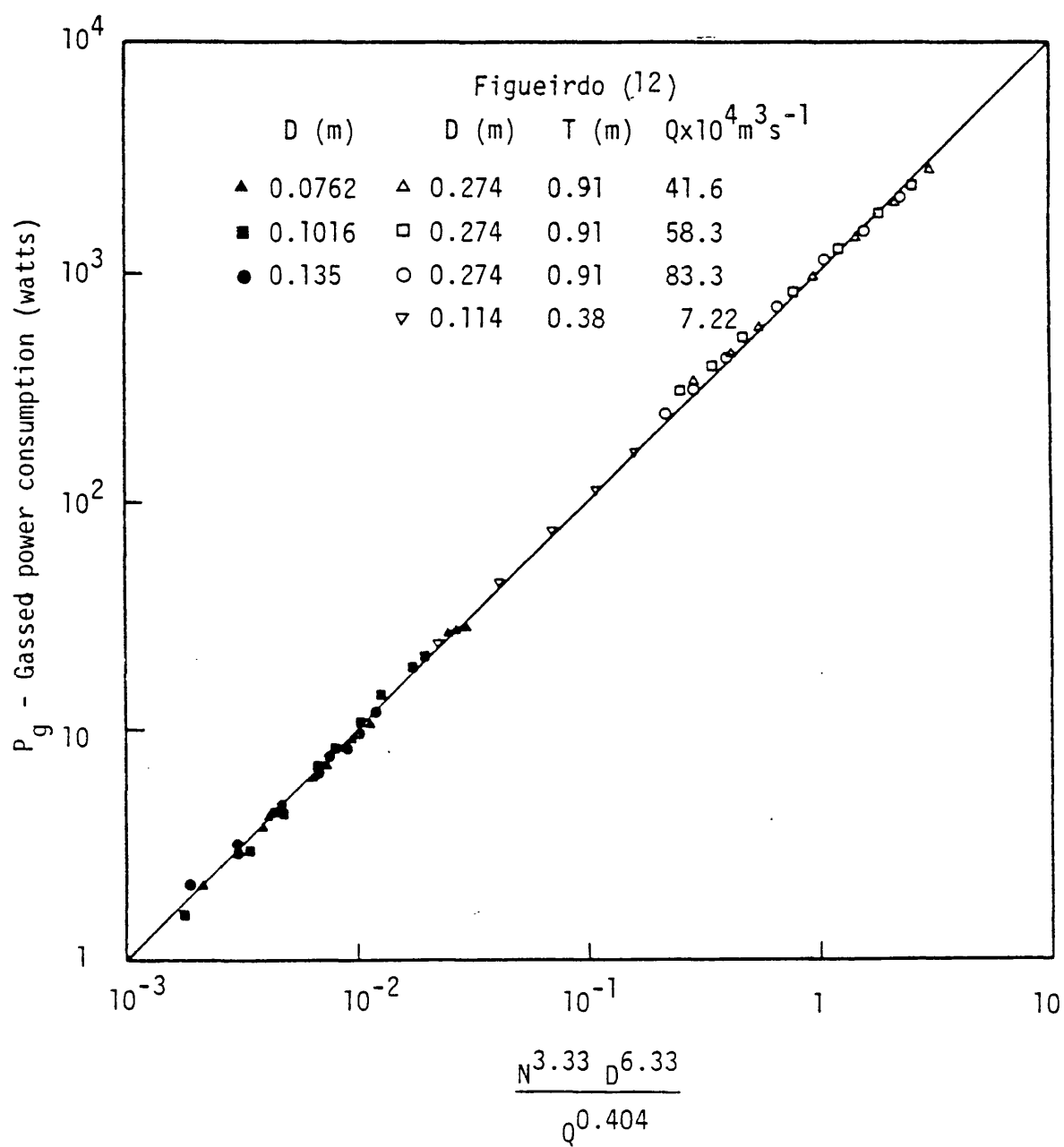
Fig. 4.14 Power consumption in the efficient mixing region

if Q is replaced by ηQ in Eq. 4.30, a general power correlation, which is applicable for any mixing regime, is obtained. Thus

$$Pg = 1007 \cdot \frac{N^{3.33} D^{6.33}}{(\eta Q)^{0.404}} \qquad 4.31$$

where

$\eta = 1$ for $N_{F1} \leqslant N < N_{R1}$

$\eta = \eta_F$ as defined by Eqs. 4.28 for $N < N_{F1}$

$\eta = \eta_R$ as defined by Eq. 4.24 for $N > N_{R1}$

and

N_{F1} is defined by Eq. 4.29

N_{R1} is defined by Eq. 4.17

Figure 4.15 demonstrates a good fit of the experimental results according to the generalised power correlation (Eq. 4.31). The correlation was further examined against the power measurements of Pharamond et al (46) from their 1.0m diameter tank. Table 4.1 shows the measured power as estimated from their graphical results, together with estimates of η and Pg using the correlations presented in this study. The average error in predicting the power is about 4%.

The detailed power measurements of Pollard (51) on a 1.81m tank with $\frac{D}{T} = \frac{C}{T} = \frac{1}{3}$ are also used to test the correlations. Approximate agreement between the calculated and observed N_{F1} and N_{R1} can be noticed from Table 4.2. However, no firm conclusion can be drawn because of the limited number of data points. Tables 4.3.a, b and c demonstrate the values of the impeller efficiency and the accuracy of predicting the impeller power. The total average absolute error in predicting the power is about 13%, but most of the measured power values are higher than those predicted. This may be, in part, attributed to the fact that the sparger was set some distance below the impeller (0.45m),
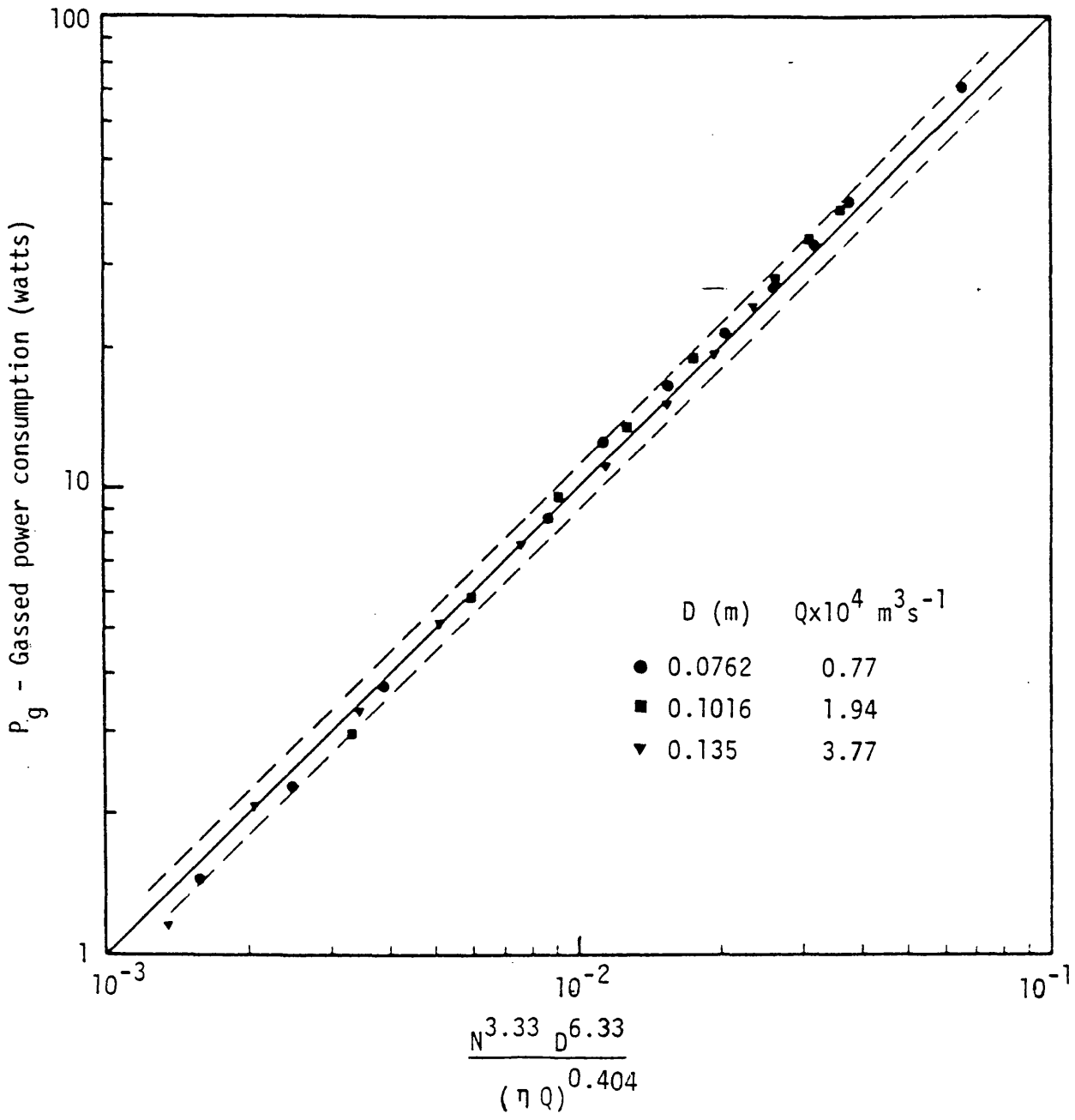
Fig.4.15 Generalised power correlation - Eq.4.31 (Tap water)

Table 4.1 : Power prediction for 1.0m tank

$$(D/T = C/H = 0.33, \quad Q = 8.334 \times 10^{-3}, ^3s^{-1}$$

N s^{-1}	Pg measured* watts	η +	Pg predicted● watts	% difference
1.66	50	0.36	51.0	2.0
2.0	80	0.626	76.0	4.8
2.5	140	0.912	137.6	1.7
3.0	280	1.0	243.0	13.2
3.5	425	1.0	4P6.6	4.3
3.7	505	1.0	489.3	3.1
4.0	630	1.0	634.0	0.6
4.2	740	1.056	729.7	1.4

* Source : Pharamond et al (46)

+ Calculated from Eqs. 4.17, 4.24, 4.28, 4.29

● Calculated from Eq. 4.31

Table 4.2 - Check on predicted values of N_{F1} and N_{R1} for 1.81m tank

$N\ s^{-1}$ \ $Q m^3 s^{-1}$	Pog/Pou^+			
	0.0066	0.0109	0.0183	0.032
0.75	0.95	0.63	0.63	0.685
1.07	0.88	0.77	0.634	0.56
1.34	0.924	0.763	0.59	0.59
1.57	0.92	0.86	0.618	0.574
1.86	0.866	0.88	_0.616	0.523
2.15	0.866	0.85	0.684	0.51
2.51	0.88	0.817	0.688	0.508
N_{F1} *	0.96	1.11	1.29	1.52
N_{R1} *	1.72	1.84	1.96	2.113

Table 4.3.a - Comparison of Predicted and Measured Power Consumption for 1.81m Tank, with Q = 0.0066 $m^3 s^{-1}$

$N\ s^{-1}$	Pg^+ measured watts	η *	Pg^{**} predicted watts	% difference
0.4	25	0.123	34	36
0.75	176	0.645	143	18.7
1.07	472	1.0	393.6	16.6
1.34	970	1.0	832.7	14.2
1.57	1550	1.0	1411	8.9
1.86	2430	1.21	2292	5.7
2.15	3840	1.75	3204	16.5
2.51	6060	2.59	4575	24.5

Average error of predicted power = 17.6%

+ Pollard (51)
* Calculated from Eqns. 4.17, 4.24, 4.28, 4.29
** Calculated from Eqn. 4.31

Table 4.3.b- Comparison of Predicted and Measured Power Consumption for 1.81m
tank, with Q = 0.0183 m^{3}s^{-1}

N s^{-1}	Pg$^+$ measured watts	η *	Pg** predicted watts	% difference
0.4	30	0.059	30.7	2.4
0.75	116	0.29	130.9	12.8
1.07	339	0.71	298	12.2
1.34	620	1.0	549	11.5
1.57	1044	1.0	930	11.0
1.86	1730	1.0	1637	5.3
2.15	2700	1.25	2420	10.3
2.51	4753	1.83	3473	27.0

Average error of predicted power = 11.6%

Table 4.3.c - Comparison of Predicted and Measured Power Consumption for 1.81m
tank, with Q = 0.032 m^{3}s^{-1}

N s^{-1}	Pg$^+$ measured watts	η *	Pg** predicted watts	% difference
0.4	30	0.04	28.7	4.5
0.75	126	0.11	123.8	1.7
1.07	3 0	0.556	262	12.7
1.34	625	0.791	481	23
1.57	970	1.0	741	23
1.86	1469	1.0	1303	11.3
2.15	2215	1.04	2077	6.2
2.51	3507	1.54	2969	15.3

Average error of predicted power = 10.7%

+ Pollard (51)
* Calculated from Eqns. 4.17, 4.24, 4.28, 4.29
** Calculated from Eqn. 4.31

causing some of the gas to escape capture. Also, the gas flow rates in Pollard's study (51) were corrected to the pressure conditions prevailing near to the impeller. These values were used without adjustment and, if corrected, could improve the accuracy of prediction to about 10%.

4.3.7 Effect of Vessel Pressure on Impeller Efficiency and Power Consumption

There is no information in the literature on the impeller power consumption in aerated vessels at pressure higher than the atmospheric pressure. In a recent study of the gas hold up in a pressurised gas-liquid stirred vessel (6) it was assumed that the increase of the vessel pressure had no effect on the impeller power. In the present work, the impeller power consumption was measured at total vessel pressure of 0.17 and 0.239 MNm^{-2} (10 and 20 psig respectively). The power data were treated in the same manner described previously (Section 4.3.1), and the volumetric gas flow rate Q, was adjusted to the condition of pressure inside the vessel. Figure 4.16 shows an example of these results.

From inspection of the experimental results, no change of the impeller power consumption in the efficient mixing regime was observed. Moreover the efficient mixing lines for the same impeller at the higher pressures are close to the atmospheric pressure case. The power correlation for this regime (Eq. 4.30) provides an excellent fit for the experimental data at higher pressures.

The impeller dispersion efficiency was correlated by the same method as described in Section 4.3.5. In the flooded regime the experimental data were scattered around the correlating lines described by Eqs.4.28. For the largest impeller D3 the data lies above the correlating lines,
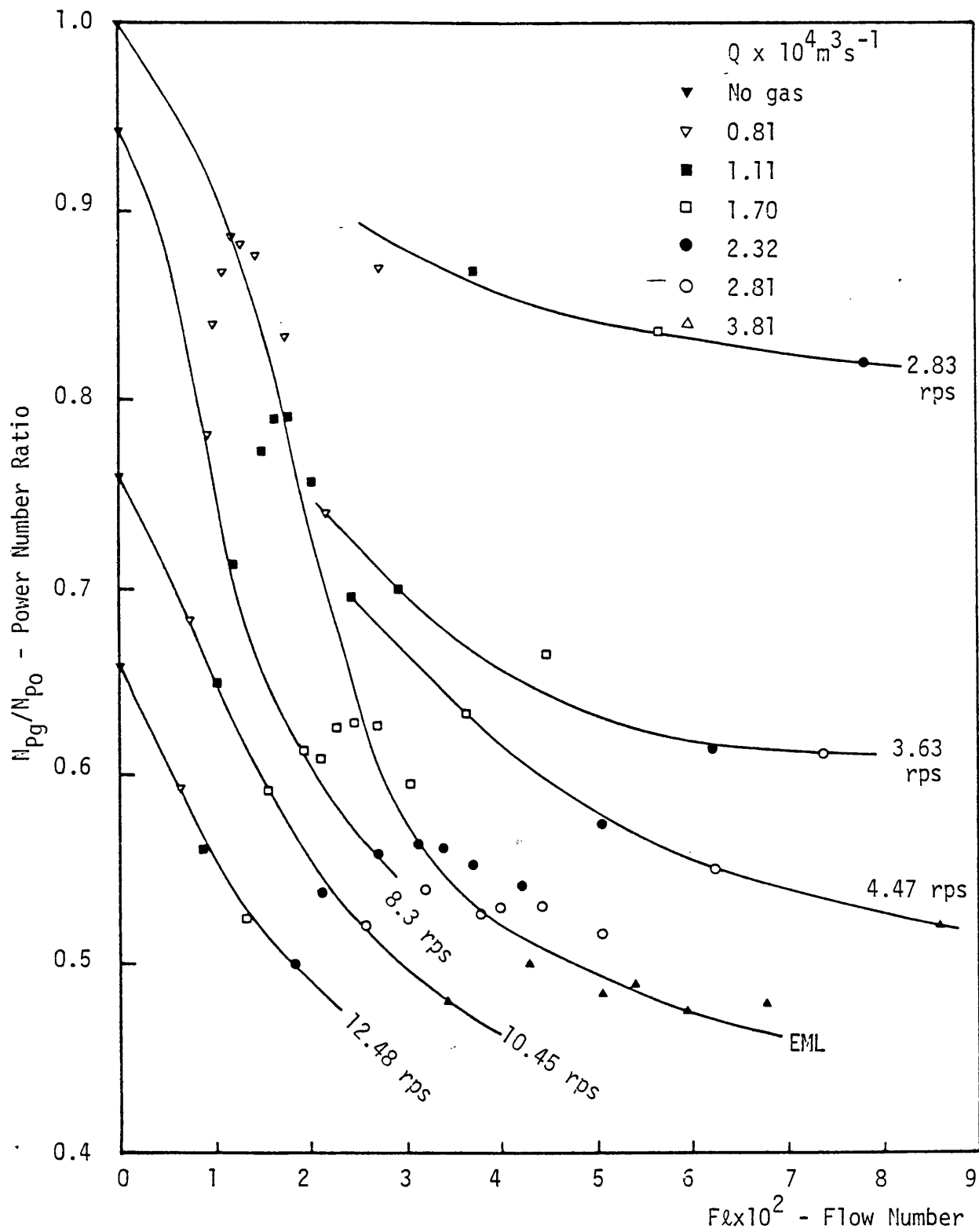
Fig. 4.16 N_{Pg}/N_{Po} against flow number for vessel
pressure of 0.17 MNm^{-2} (D=0.1016m)

while for D2 it lies below. With the smallest impeller D1, the number of experimental points in the flooded regime was small. The scattering of the experimental data is attributed to the degree of uncertainty in measuring the vessel pressure caused by fluctuations in liquid level. This in turn caused an error in estimating the true volumetric gas flow rate. These effects are more apparent in the flooded regime because the impeller power is more sensitive to any changes in the gas flow rate. In addition, the accuracy of measuring the impeller power is lowest under these conditions (about 10%). For the abovementioned reasons, no attempt was made to correlate the effect of pressure on η_F. However, Eq. 4.28 was found to correlate the experimental data within $\pm$ 20%. The speeds at which flooding is overcome, as predicted by Eq. 4.29, are close to the observed values.

In the recirculation regime a definite trend was observed. The speed at which gas recirculation commenced decreased with increase of the vessel pressure, with η_R increasing. Again this is evidence of the similarity between surface aeration under ungassed conditions and gas recirculation in aerated vessels. This is explained by the drop of the average bubble size and the increase in gas density which occurs as the vessel pressure increases (6) (see Section 3.4.2.3). The experimental data were correlated within an accuracy of $\pm$ 10% by

$$\eta_R = 4.13 \left(\frac{P}{P_A}\right)^{0.223} \frac{N^{2.53} D^{5.93}}{T^{2.45} Q^{0.33}} \tag{4.32}$$

$$N_R = 0.57 \left(\frac{P_A}{P}\right)^{0.088} \frac{T^{0.97} Q^{0.13}}{D^{2.34}} \tag{4.33}$$

where   P   vessel pressure

         P_A atmospheric pressure

Figure 4.17 demonstrates a good fit of the experimental data to the generalised power correlation (Eq. 4.31), when η_F was calculated from Eqs. 4.28, and 4.29, and η_R from Eq. 4.32. However, it can be observed that the experimental data lie below the correlating line at its lower part. This part of the curve represents a flooded condition at low impeller speeds and high gas flow rates. It is apparent that Eq.4.28 underestimates η_F for higher vessel pressures. In other words, increase of the vessel pressure leads to the capture of more gas bubbles by the impeller, under the extreme condition of flooding. Nienow et al (4) attributed the reduction of the impeller speed which is required to overcome flooding with the smaller impeller clearance, to the increased linear velocity in the lower circulation loop. This effect, more easily, causes gas recirculation in this region. By analogy then, the effect of increasing the vessel pressure on N_{F1} and η_F can be explained as follows. An increase of the vessel pressure increases the kinetic energy of the gas stream, at the same volumetric gas flow rate because of the increase of the gas density (6). For example, with impeller D3, N = 2 rps, and $Q \simeq 3.8 \times 10^{-4} m^3 s^{-1}$, the ratio between the power supplied by the gas to that supplied by the impeller increased from 1.39 to 2.2 when the vessel pressure increased from atmospheric pressure to 0.17 MN m^{-2} (10 psig). This kinetic energy of the sparged gas is dissipated very close to the sparger exit (52), enhancing the liquid velocity, and causing a greater circulation of the gas bubbles. Hence there is an increasing tendency for bubbles to be captured by the impeller cavities. From this discussion, the effect of pressure on N_{F1} and η_F is expected to be more pronounced at pressures higher than those studied. It is expected, therefore, that Eqs. 4.28 and 4.29 will no longer hold at these conditions.
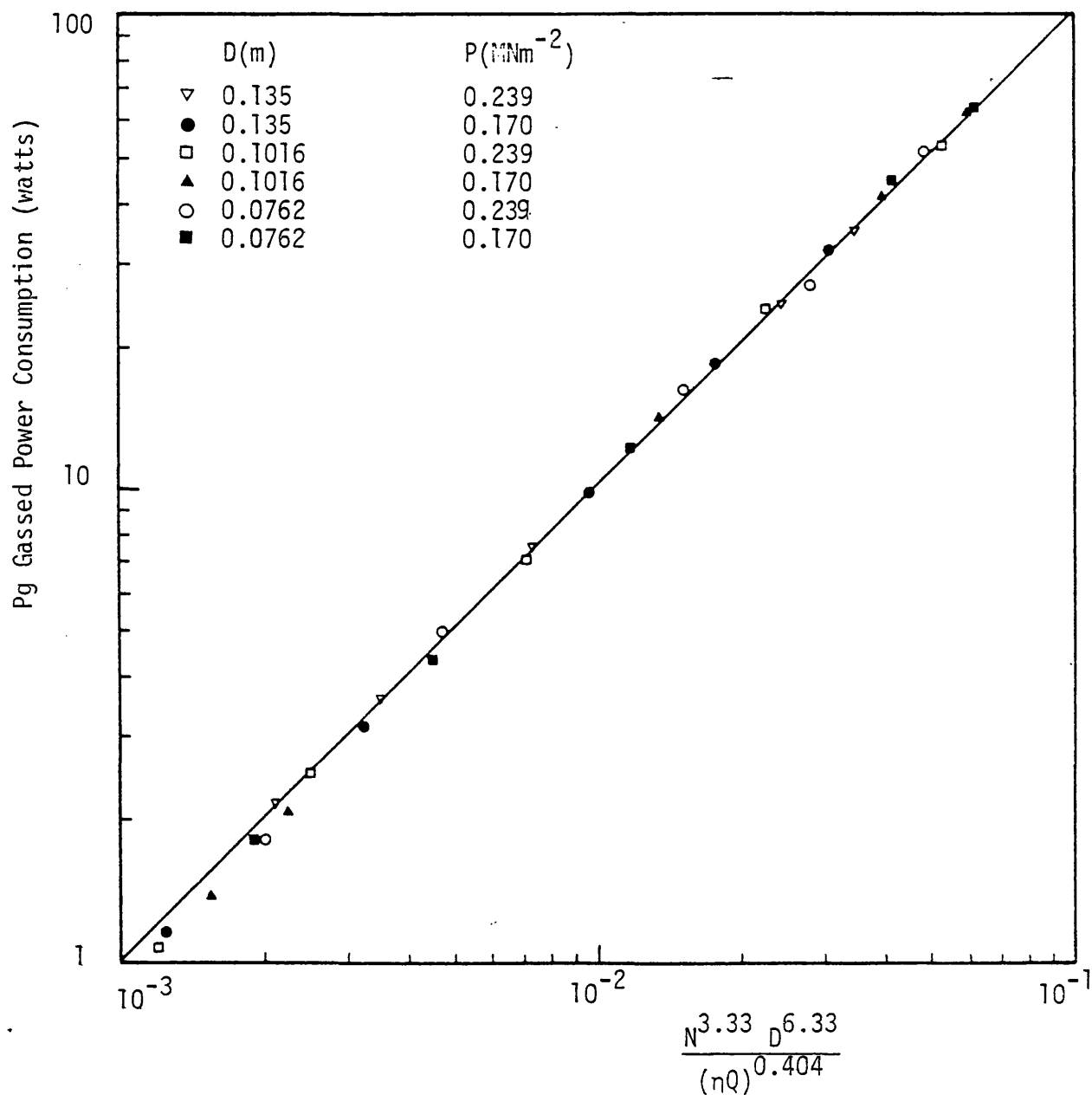
Fig. 4.17   Generalised power correlation under pressurised
vessel condition.

In summary, increasing the vessel pressure reduces N_{R1} and N_{F1}. However, it has no effect on the impeller power consumption in the efficient mixing regime, but the power in both the recirculation and flooded regimes are reduced.

4.3.8   Influence of Ionic Concentration

A 0.11M potassium sulphate solution was used as a 'non-coalescing' system to study the effect of the ionic concentration on impeller dispersion efficiency and power consumption.   This concentration level has been shown to produce a minimum bubble size (53) above which there is no further effect on the specific mass transfer rate $(K_L a)$ (54).

Figure 4.18 shows the power ratio vs. Flow number plot for impeller D3.   A comparison between this figure and Fig. 4.7, for the same impeller with tap water, reveals the effects on power consumption and gas dispersion.   The effective mixing lines are close for both cases, indicating that there is no significant change in impeller power consumption in the efficient mixing regime, which is in agreement with a previous study (25).   However, the efficient mixing zone becomes narrower so that it can be described by a line (EML). This is due to an increase in N_{F1} and reduction in N_{R1} at the same gas flow rate. At the highest gas flow rate (3.77 x $10^{-4} m^3 s^{-1}$), no minimum or maximum can be distinguished, indicating that N_{F1} is greater than N_{R1}.   The physical meaning for this odd situation is that before the impeller reaches a speed at which all of the sparged gas coalesces with the impeller cavities (N_{F1} definition), gas bubbles start to recirculate in the upper region of the tank.   A similar effect has been observed by Nienow et al (4) for a tank of 1.83m diameter and C/H = 2.8, where the flooding conditions appeared never to be prevented.   However, in their case this may have been caused by a drop of N_{R1} and increase of
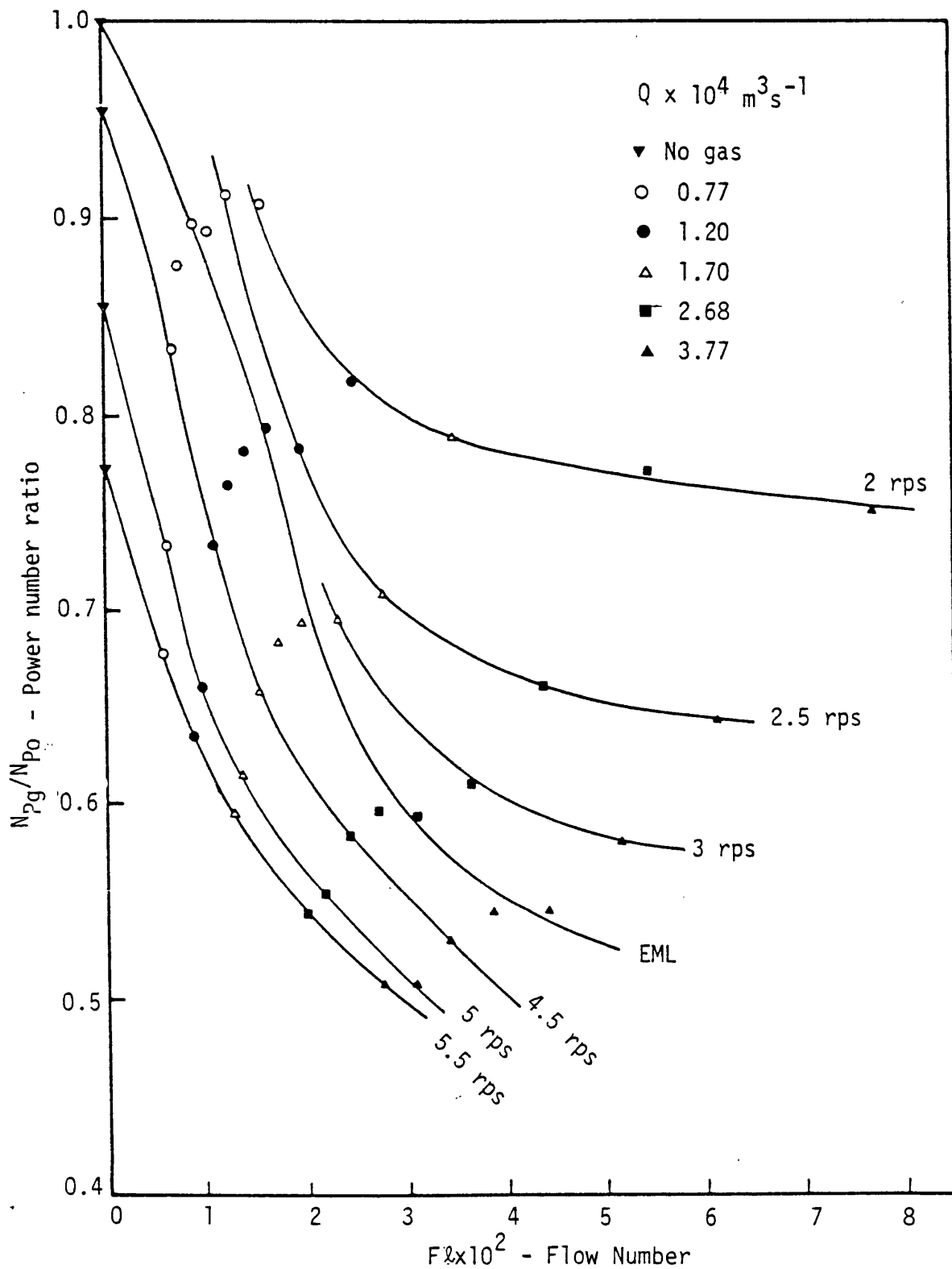
Fig.4.18 $N_{\overline{Pg}}/N_{Po}$ against Flow Number for 0.11 M K_2SO_4 solution (D = 0.135 m)

N_{F1} as a result of increasing the impeller clearance. They also reported that the minima on a Pg/Po vs. Fℓ plot at constant gassing rate appeared when the impeller clearance was reduced. These remarks serve to emphasise the importance of selecting the suitable impeller clearance and diameter, otherwise an efficient mixing regime may never be achieved.

A similar result for impellers D1 and D2 were obtained, but with these smaller impellers a minima and maxima were observed at all gas flow rates. The drop in N_{R1} is not surprising, because with sulphate solution the bubble size is much smaller compared with water system (see Chapter 6). The increase in N_{F1} may be attributed to a hindrance or retardation of coalescence of the sparged gas with the impeller gas cavities when the electrolyte is added.

The correlations for impeller efficiency with sulphate solution are similar to those obtained for the water system, except for the constant values. They are :

$$\eta_R = 6.25 \frac{N^{2.53} D^{5.93}}{T^{2.45} Q^{0.33}} \qquad\qquad 4.34$$

$$\eta_F = 0.35 + 0.18\,A \qquad \text{for } A > 1.5 \qquad\qquad 4.35.A$$

$$\eta_F = 0.4\,A \qquad\qquad \text{for } A \leqslant 1.5 \qquad\qquad 4.35.B$$

where

$$A = \frac{N^{2.53} D^{4.4}}{T^{0.5} Q^{0.73}}$$

and from Eqs. 4.34 and 4.35.A

$$N_{R1} = 0.48 \frac{T^{0.97} Q^{0.13}}{D^{2.34}} \qquad\qquad 4.36$$

$$N_{F1} = 1.66 \frac{T^{0.2} Q^{0.24}}{D^{1.74}} \qquad\qquad 4.37$$

The impeller power consumption is calculated from the generalised power correlation (Eq. 4.31) with the aid of Eqs. 4.34, 4.35, 4.36 and 4.37 for determining the impeller efficiency. Figure 4.19 demonstrates that there is a good fit of the experimental results to the power correlation for impellers D2 and D3. However, the measured power for the smallest impeller D1 is less than the predicted by about 15%. The impeller efficiency is mainly controlled by the strength of the ionic solution which also controls the average bubble size. ¯ Hence, although Eqs. 4.34 and 4.35 are derived for 0.11M K_sSO_4 solution, they can be used with reasonable accuracy for 'non-coalescing' systems with an average bubble size of the same order.

Comparing Eqs. 4.28 and 4.35, it can be seen that there is only a small effect on η_F as a result of adding the electrolyte. Consequently there is only a limited effect on the impeller power in the flooded regime. On the other hand, by comparing Eqs. 4.24 and 4.34, a larger drop in power is to be expected in the recirculation regime (about 15%). This explains the insignificant changes of the impeller power in the study of Lee and Meyrick (9) with different concentrations of sodium sulphate solution. This was because most of their measurements were either in the flooded or in the efficient mixing regimes.

4.3.9   Rate of Surface Entrainment without Sparging

The rate of surface entrainment of gas under ungassed conditions increases rapidly with increasing the impeller speed for $N > N_{SA2}$. The volumetric rate of gas reaching the impeller, and hence its effect on the power requirements, can be determined from N_{Pg}/N_{Po} vs. $F\ell$ Plot as shown in Fig. 4.20. The corresponding values for the three impellers used in this study are shown in Table 4.4.

$$\frac{N^{3.33} D^{6.33}}{(\eta\ Q)^{0.404}}$$
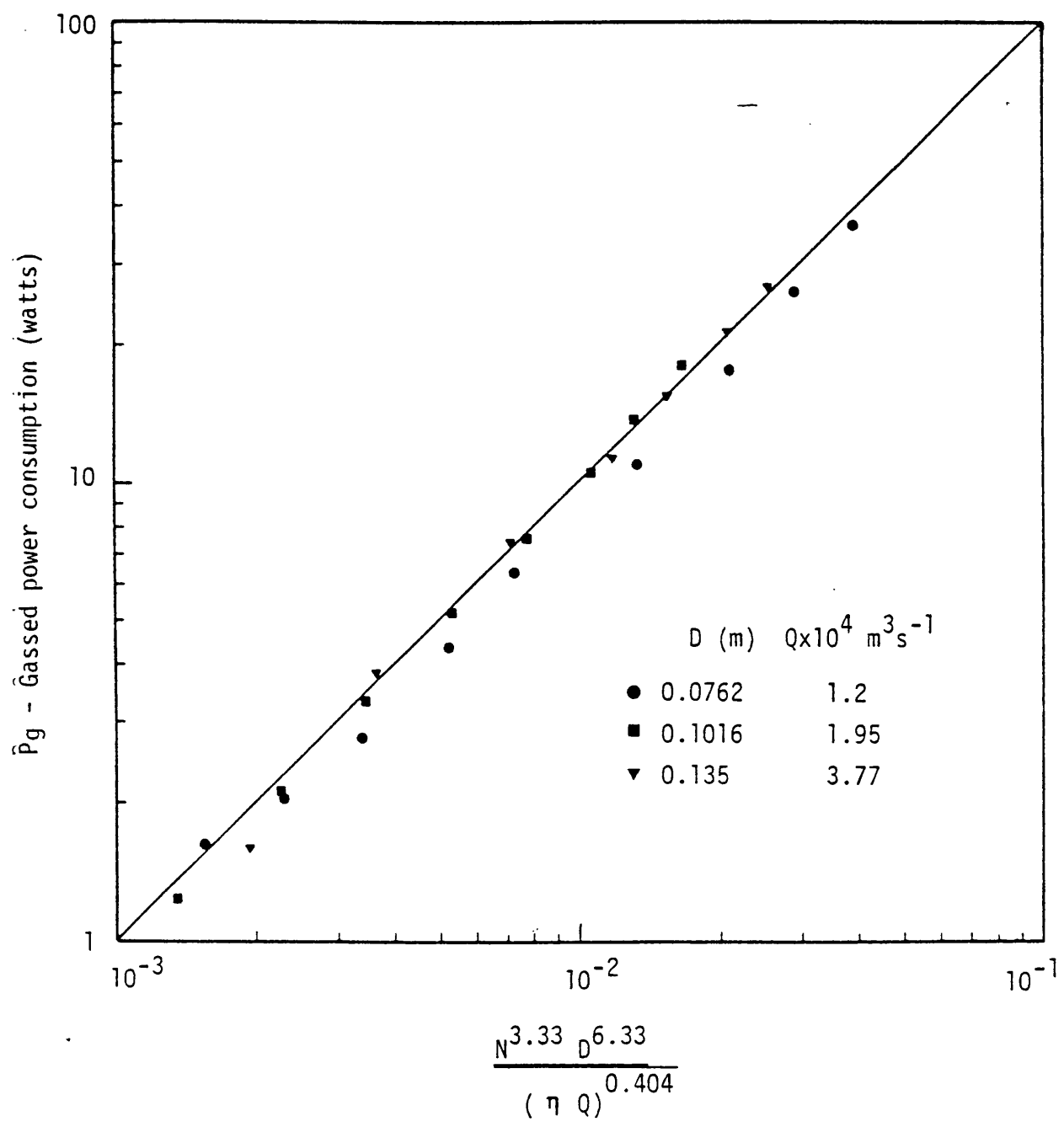
IFig.4.19 Generalised power correlation - Eqn.(4.31)

(0).11 M K_2SO_4 solution)
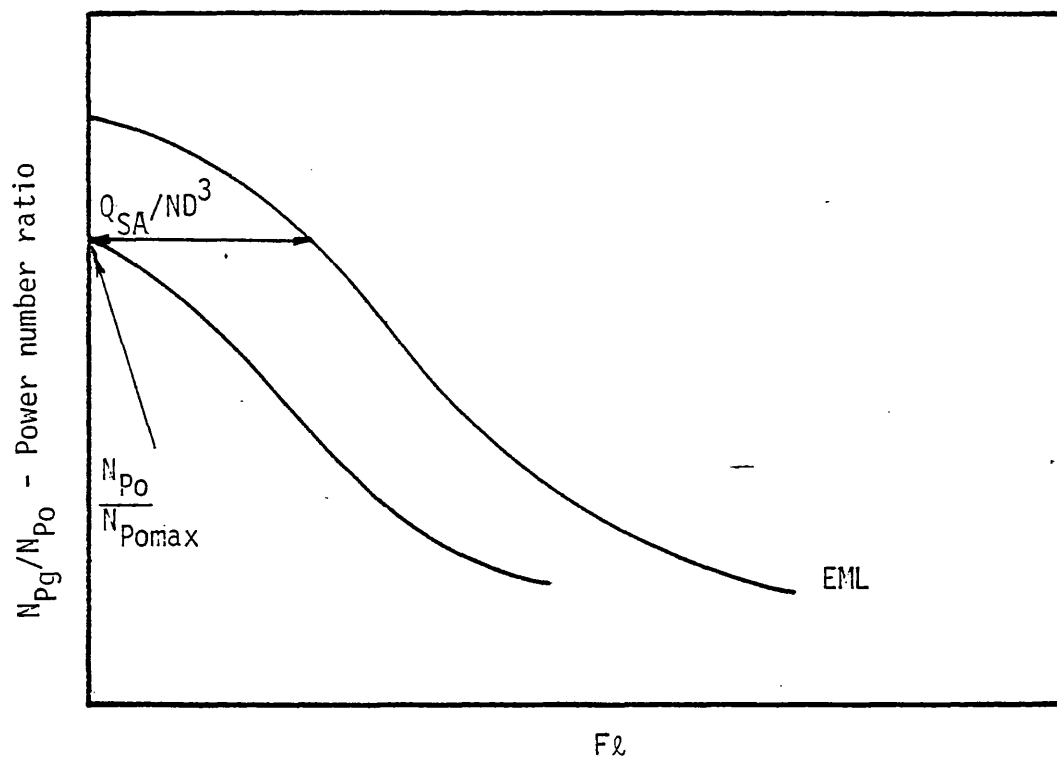
Figure 4.20 Determination of the rate of surface aeration from a plot of N_{Pg}/N_{Po} against $F\ell$.

TTABLE 4.4 Rate of Surface Aeration

	IMPELLERS				
D1		D2		D3	
$N \atop s^{-1}$	$Q_{SA} \times 10^4 \atop m^3 s^{-1}$	$N \atop s^{-1}$	$Q_{SA} \times 10^4 \atop m^3 s^{-1}$	$N \atop s^{-1}$	$Q_{SA} \times 10^4 \atop m^3 s^{-1}$
.18.4	0.45	9.45	1.239	5	0.246
20.5	1.05	10.0	1.783	5.5	0.744
		10.8	2.152	6	1.697
		12.75	3.47		

The dependency on N and D is roughtly correlated by :

$$Q_{SA} \propto N^{10} D^{22}$$ 4.38

for $N > N_{SA2}$

This simply indicates the very high dependency of the surface entrainment rate on N and D. Further results for different tank sizes and impeller clearances are obviously required before any firm conclusions could be drawn.

4.4 CONCLUSIONS

1 - The impeller dispersion efficiency, η, is useful for defining the different regimes of gas-liquid mixing and the degree of flooding and recirculation. Correlations for the speed required to overcome the flooding, N_{F1}, and the speed at which gas recirculation commences, N_{R1}, are readily obtained from those of η. This method is more accurate than determining the point of flooding from the shallow minima in N_{Pg}/N_{Po} vs. $F\ell$ curves, since it makes use of all the points in the flooding region.

2 - The power consumption in the efficient mixing regime was correlated in terms of N, Q, and D. By employing the definition of η, it was possible to generalise this so as to predict the power requirements for any mixing regime. Overall, the accuracy is about $\pm$ 10%. The comparison with data of many scales serves to indicate that accurate measurement and analysis of impeller power on small scale equipment can be successfully applied to larger scale equipment.

3 - Increasing the vessel pressure reduces both N_{R1} and N_{F1}. This is a result of a reduction in the average bubble size and increase in the kinetic energy supplied by the gas stream. The impeller power require-

ment is not affected by the vessel pressure in the efficient mixing regime, but a decrease occurs in both the flooded and recirculation regimes.

4 - In the efficient mixing regime there is no change in the power consumption with aquaeous electrolyte solution (0.11M K_2SO_4) over the water system. However, an increase in N_{F1} and reduction in N_{R1} occurs with electrolyte solution due to the reduced rate of bubble coalescence and the corresponding smaller average bubble size. The power consumption is also higher in the flooded regime and lower in the recirculation regime compared with water.

CHAPTER 5

IMPELLER POWER DYNAMICS

5.1 INTRODUCTION

Very little is known about the dynamical characteristics of the impeller power consumption in stirred-gas-liquid reactors. The study of these characteristics would provide more information about the formation and stripping of the gas cavities behind the impeller blades, and also the associated bubble coalescence and dispersion processes. Additionally, useful information about bulk gas-liquid mixing phenomena, eg, gas recirculation, may be obtained. The intensity of the dynamic loads experienced on start-up and shut-down of the gas to the reactor will also be important, enabling a more rational mechanical treatment of the design of the impeller shaft assembly.

This chapter extends the recent investigation of Greaves and Economides (55). In their study the impeller power response following a positive change in gas flow rate was examined. Three main regions of response were identified. At low impeller speeds prior to the onset of gas recirculation, the response was characterised by high frequency component. Under gas recirculation conditions, however, it was characterised by low frequency component. In the transition between these two regions, both the high and the low frequency components were identified. A method was suggested for estimating the rate of gas recirculation based on the measured time constants from the dynamical tests and the mean residence time of gas in the tank. The external distribution coefficient estimated by this method was higher than the maximum values previously reported.

As will be seen in the subsequent sections, the dynamical behaviour of the impeller power following change in the sparged gas rate, exhibits various types of nonlinearity, making the analysis more complex. Application of linear systems theory therefore can only provide an

approximate basis for analysis. However, the linear system approach

was adopted by describing the process in terms of a number of subsystems.

The response of each of these subsystems can then be studied for

different input disturbances. In other words the impeller power

response following specific change in sparged gas flow rate can be

investigated over a range of impeller speeds. This can be repeated

with various input changes in gas flow rate. A similar approach to

analyse a non-linear system is described by Seinfeld and Lapidus (56).

The advantage of such an approach is that by comparing the responses

of the different subsystems to the different input disturbances, an

appreciation of the changes of the system dynamics with the change of

the operating parameters can be achieved. The alternative to this

approach is to use a 'black box' technique to identify the non-linear

system (Wiener theory, or two level input functions, see section 10

Ref. (56)). These techniques would help to identify a complex

mathematical model to describe the process dynamics. Such models are

valuable for control purposes, rather than for identifying characteristics

of the physical parameters of the process under consideration, which

is the objective of this study.

5.2 EXPERIMENTAL PROCEDURE

The equipment is fully described in Chapter 2 and is further

illustrated in Figure 5.1. Throughout this chapter, all the experimental

results referred to were obtained using tap water at atmospheric pressure.

Before carrying out a dynamical test, the steady state conditions were

previously established. The input disturbance used was a step or

pulse change in gas flow rate, and the output was impeller power response.

The impeller speed was kept constant during the dynamical tests by a

thyristor speed controller. A needle valve (V1)(Fig.5.1) was used to
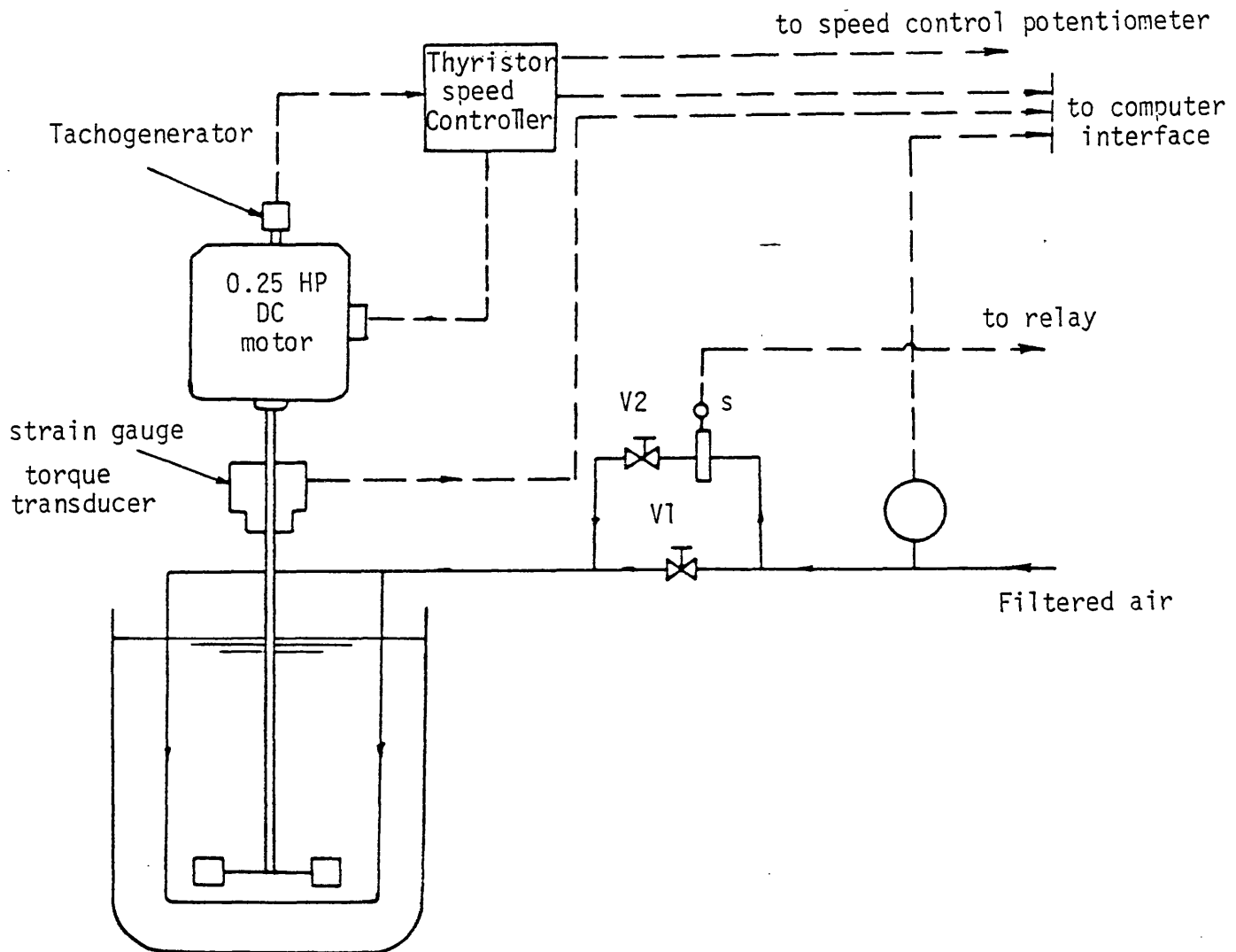
Figure 5.1 :   Instrumentation and control of stirred tank
for dynamic tests.

adjust the steady state level of gas flow rate. A solenoid valve(S)was used to introduce the step or pulse change in gas flow rate, while the height of that change was adjusted by a needle valve (V2).

The MACSYM II data acquisition and analysis system was used to measure the input disturbance and dynamic responses. The speed of sampling was 20 HZ for the step tests, and up to 50 HZ for the pulse tests. The dynamics of the signal conditioning box and the computer circuits were cancelled out as they were used for both the input and the output signals (57). Also the instruments dynamics were much faster compared with those of the process and hence they could be neglected (see Appendix B).

The Macsym system was programmed so that after conducting a series of measurements, further computational processing could be carried out. Included in this were Fourier Transform calculations for the pulse test to obtain the frequency response or Bode plots (see Appendix C). The error in torque measurements was eliminated in the dynamical tests, since the steady state component was subtracted-out of the signal.

5.3   RESULTS AND DISCUSSION

5.3.1   Frequency Domain Analysis

A series of preliminary pulse tests were conducted with one impeller (D=0.1016m), and the full results are reported by Millington (58). The aim of this preliminary investigation was to identify the salient features of the dynamical response of the impeller power and to define the optimum testing conditions, eg, sampling frequency and input pulse duration.

Figure 5.2 demonstrates the effect of sampling rate on the results of the pulse test when the frequency response is represented on a Bode plot. With the low sampling rate, ie, 20 per second, the calculated log-modulus (=20 Log|Magnitude ratio|) starts to undergo a series of meaningless fluctuations at a frequency of 4 radians/second. But with the higher sampling rate (50 HZ), a wider range of frequency response was observable. Lees and Dougherty (59) have examined the convergence of the approximate numerical computations of Fourier Transform to the ideal function in pulse testing. They concluded that the upper bound frequency for convergence was equal to 0.1 π/δ, where δ is the sampling interval. On this basis a sampling interval of 0.02 seconds (sampling rate of 50 HZ), produces convergence in the calculations up to a frequency of about 15.7 rad/s., covering the range of interest in this study.

On the other hand the use of shorter pulses (normally less than 1 sec) was found to reveal more details on the Bode plot. This is expected as the frequency content of a rectangular pulse increases with the reduction of its width (60), and consequently the system dynamics are excited ove. a wider range of frequency values. Millington (58) used the criteria proposed by Clements and Schnelle (60), (ie, a minimum normalised frequency content of 0.3, beyond which deviation would occur) to calculate the limits of frequency deviation for the different pulses used. These values are shown in the last column of Table 5.1, showing a change from 5 to over 10 rad/s according to the pulse width. Figure 5.3 demonstrates the effect of reducing the pulse width under otherwise similar testing conditions. The valley and peak conditions which appeared with the shorter pulse reveal an important feature of the system dynamics as will be discussed in the following analysis.
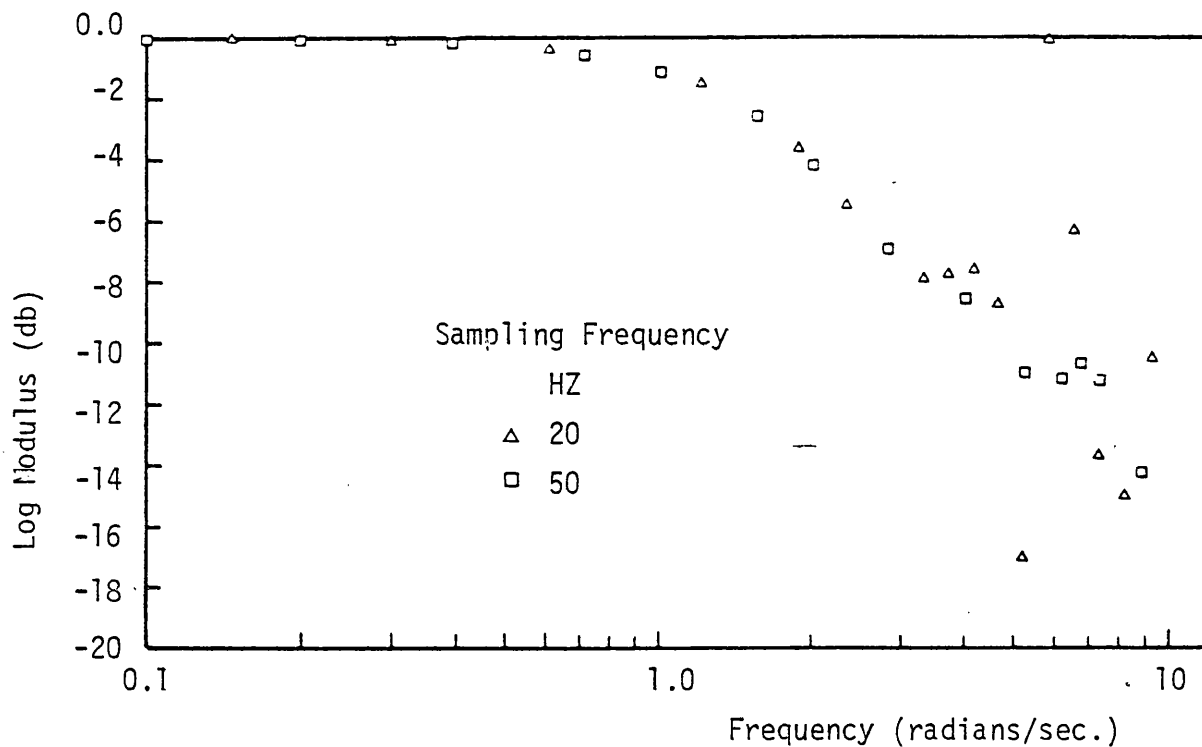
Fig. 5.2 : Effect of sampling frequency on Bode plot

D = 0.1016m N=7 rps

Input pulse 0.8 to 1.95 x10^{-4} m^3 s^{-1}
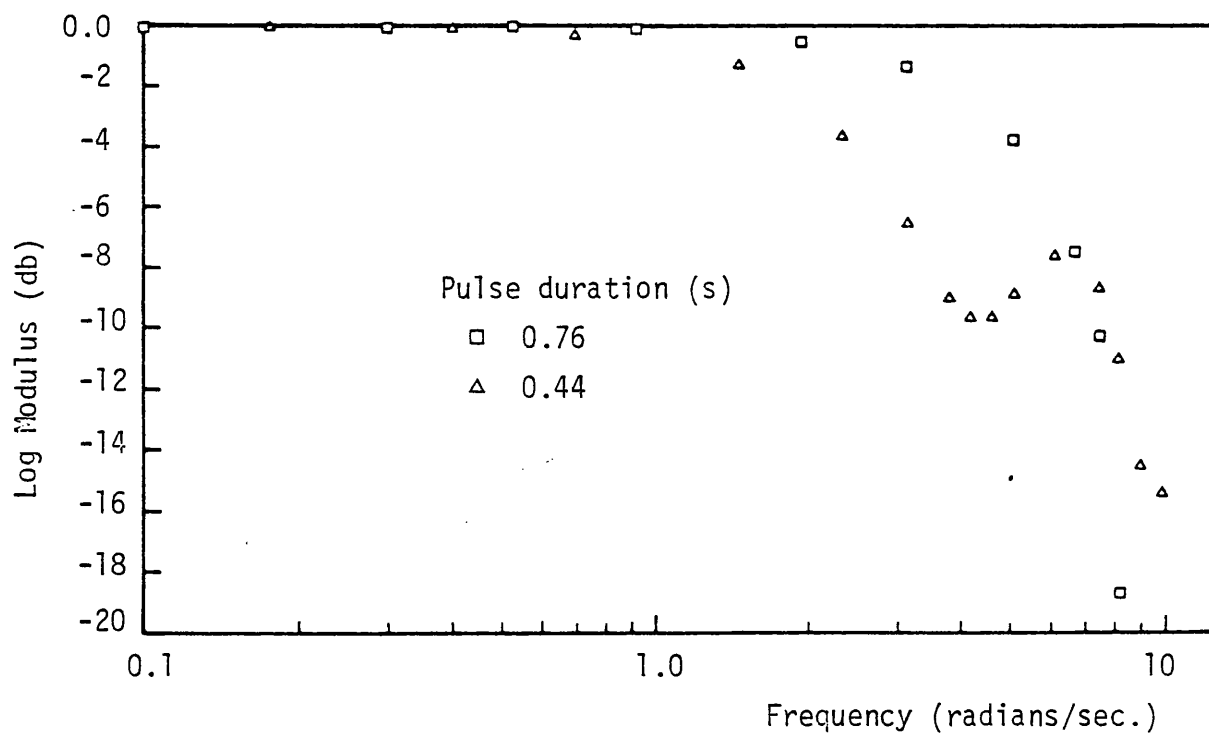
Fig. 5.3 : Effect of input pulse duration on Bode plot.

D = 0.1016m N=7 rps

Input pulse 0.8 to 1.95 x 10^{-4} m^3 s^{-1}

Figure 5.4 shows Bode plots at different impeller speeds. From this figure and similar plots with different pulse heights, the time constants were estimated from the corner frequencies. The summary of these results are given in Table 5.1. The first observation from examining Table 5.1, is the change of the system characteristics (time constants) and slopes with the change of the pulse height. These effects are a clear indication of the nonlinearity of the process (57). Secondly it confirms the dependency of the impeller power dynamical behaviour on the speed (55). However, the changes in the log modulus in the range of the frequencies studied were rather limited (<20db over 2 decades). It is important therefore to stress that the dynamical slopes and the time constants determined from the Bode plots have a certain degree of uncertainty depending on the range of frequency studied. Nevertheless, the trends of the changes of the time constants with the change of the impeller speed is in agreement with the results of Greaves and Economides (55). With reference to Figure 5.4 it can be seen that at the lowest impeller speed (5 rps), a single time constant can be assigned to the curve. At that speed the impeller had just overcome the flooding conditions (see Chapter 4). At an impeller speed of 7 rps, the system is close to the recirculation condition, and at 9 rps the system is well into the gas recirculation regime. At both of these speeds two distinct slopes could be assigned to the log modules curve in the Bode plot. The higher frequency component (low time constant) was claimed to be associated with the onset of gas recirculation (55). At the higher speed of 11 rps only one frequency component can be identified, and corresponds a condition where significant gas recirculation is established.
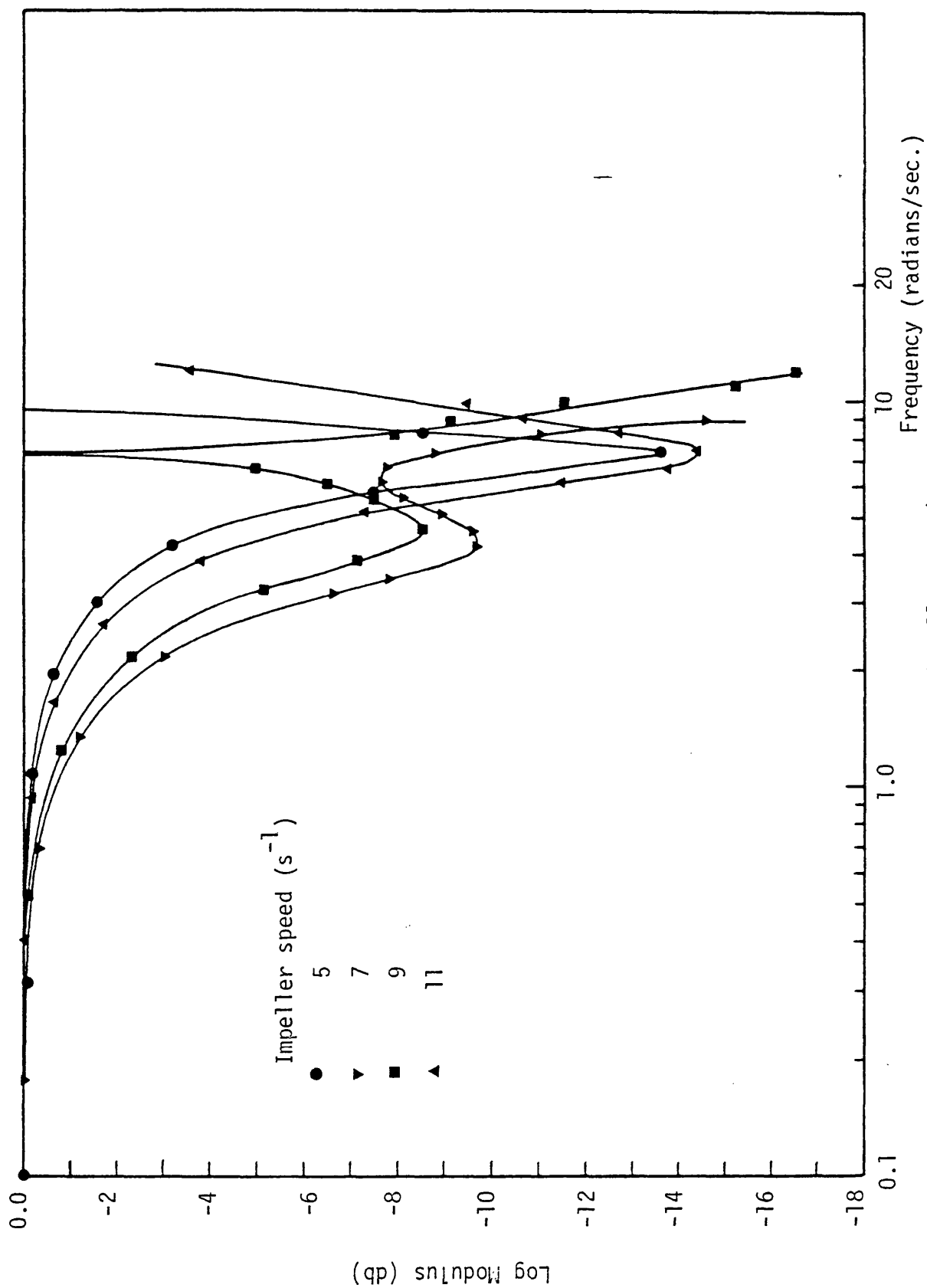
Fig. 5.4 : Bode Plots at different impeller speeds
D = 0.1016m, Input Pulse 0.8 to 1.95 x 10^{-4} m^3 s^{-1}

Table 5.1 : Summary of Results of Frequency Response Analysis (58)

Impeller speed s^{-1}	Input pulse (Gas flow rate) $\times 10^4 m^3 s^{-1}$	Sampling frequency HZ	Pulse height $\times 10^4 m^3 s^{-1}$	Input pulse duration s	Output pulse duration s	Time constant s	Dynamic slope db/decade	Frequency deviation limits
5	0.00→2.78	50	2.78	0.62	0.98	0.22	-52	7.0
5	0.80→1.45	50	1.15	0.69	1.30	0.24	-55	6.1
5	1.95→2.78	50	0.83	0.48	0.60			9.2
7	0.80→2.78	50	1.98	0.76	2.64	0.91, 0.20	-16, -52	5.8
7	0.8 →1.95	50	1.15	0.76	1.42			5.8
7	0.80→1.95	50	1.15	0.44	1.64	0.58, 0.10	-25, -60	10.0
9	0.80→2.78	50	1.98	0.64	2.14	0.87, 0.11	-17, -52	6.9
9	0.80→1.95	50	1.15	0.88	1.98	0.57, 0.09	-24, -50	5.0
11	0.80→2.78	50	1.98	0.43	1.34	0.43	-18	10.2
11	0.8 →1.95	50	1.15	0.54	1.20	0.29	-47	8.2

The valleys and peaks on the Bode plots (Fig. 5.4) are identified as a resonance effect in the system dynamics (57). Cohen and Johnson (61) predicted theroetically and confirmed experimentally the resonance phenomenon for the dynamical response of a double pipe heat exchanger. This phenomenon was observed when the system was forced in a distributed manner. This behaviour occurs with a distributed parameter system which is described by partial differential equations (61). From Fig. 5.4, it can be seen that at speed of 5 rps, a valley appears at frequency of about 7.5 rad/s. When the speed is increased to 7 rps, the valley occurs at a lower frequency of about 4.3 rad/s with a peak at 6.5 rad/s. Further increase of the speed causes the peak to become very sharp at 9 rps, a condition which was not approached until a frequency of 12 rad/s with the highest speed of 11 rps. From these observations, it can be argued that the resonance effect appears at low frequencies with two distinct slopes in the Bode plot, when the rate of gas recirculation is of the same order as the rate of sparging (7,9 rps). Under such conditions the system is therefore affected by both the sparged and recirculated gas, ie, excited or forced in a distributed manner. At low impeller speeds (5 rps), the rate of gas recirculation is very small, and the process is mainly responding to the effect of the sparged gas. In this condition the valley occurs at a high frequency but a peak is not observed. The same effect happened with the highest impeller speed (11 rps) where the gas recirculation was considerably greater. The process behaves as if it was subjected to an input pulse disturbance composed of two components, one for the sparged gas and another for the recirculated gas. This point will be further explained in Section 5.33.

The pulse test results with the smallest impeller, confirmed the previous observations and remarks as shown in Fig. 5.5. However, the valleys and peaks occurred at lower frequencies. The steady state gain increased with increasing impeller speed for the same pulse height, as expected from the steady state measurements (Chapter 4). But at the highest impeller speed (20 rps, Fig. 5.5), it showed a severe drop. This can be explained by the occurrence of surface entrainment of gas.

Figure 5.6 demonstrates the effect of pulse height on the frequency response for the largest impeller. The asymptotic dynamical slopes are again rather difficult to determine because of the limited range. However, the corner frequencies corresponding to the lower frequency components, decreased with increasing pulse height. This implies that there is an increase in the corresponding time constant values or a slower process response as the pulse height increases.

There is a clear discrepancy between the Bode plots as obtained from equal positive and negative pulses, as shown in Fig. 5.7. This indicates a serious type of nonlinearity, ie, hysteresis behaviour and it points to the errors involved using linear system theory to identify a highly nonlinear process. (The use of Fourier Transform analysis pre-assumes a basic linearity for the process). Thus a further development of the pulse response testing will be complex and difficult to analyse. Instead, in what follows in the rest of this chapter, transient response analysis in the time domain is employed. This has advantages over the use of frequency response, that no prior assumption concerning the linearity of the process is required before calculations are carried out. Added to that is the use of positive and negative step changes in gas flow rate, which would further help to identify more features of the process.

Log Modulus (db)

0.0
-2
-4
-6
-8
-10
-12
-14
-16
-18

0.1
1.0
10
20

Frequency (radians/sec.)

Speed 'N'(s^{-1})	Steady State gain ($Nm^{-3}s$)	Time Constant 'τ'(s)
10	-24.9	0.20
12	-46.4	0.44,0.25
14	-94.3	1.3, 0.27
17	-242	1.75,0.32
20	-139	0.33
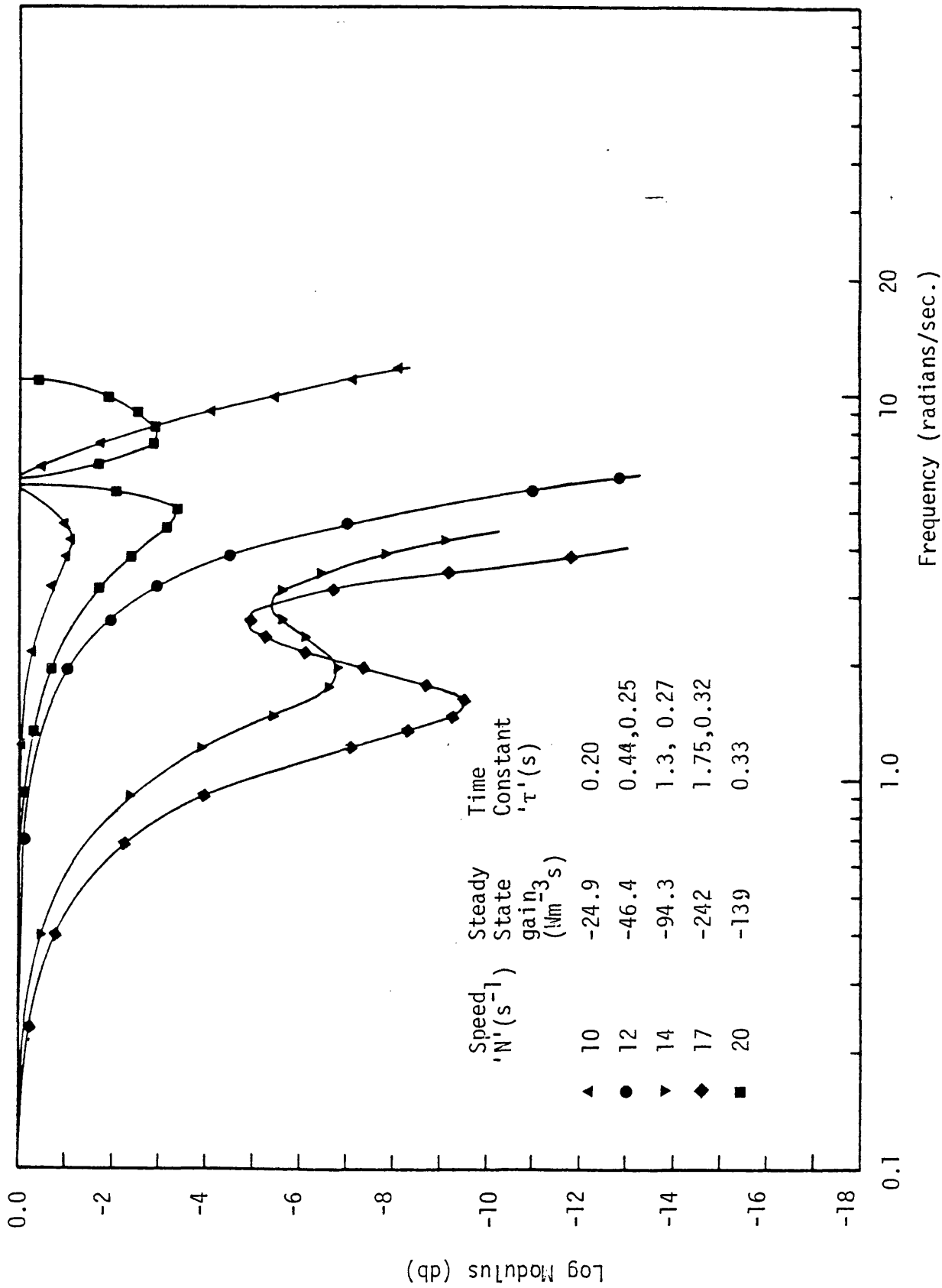
Fig. 5.5 : Bode Plots at different impeller speeds

D = 0.0762m, Input pulse 0.0 to 0.75 x 10^{-4} m^3 s^{-1}
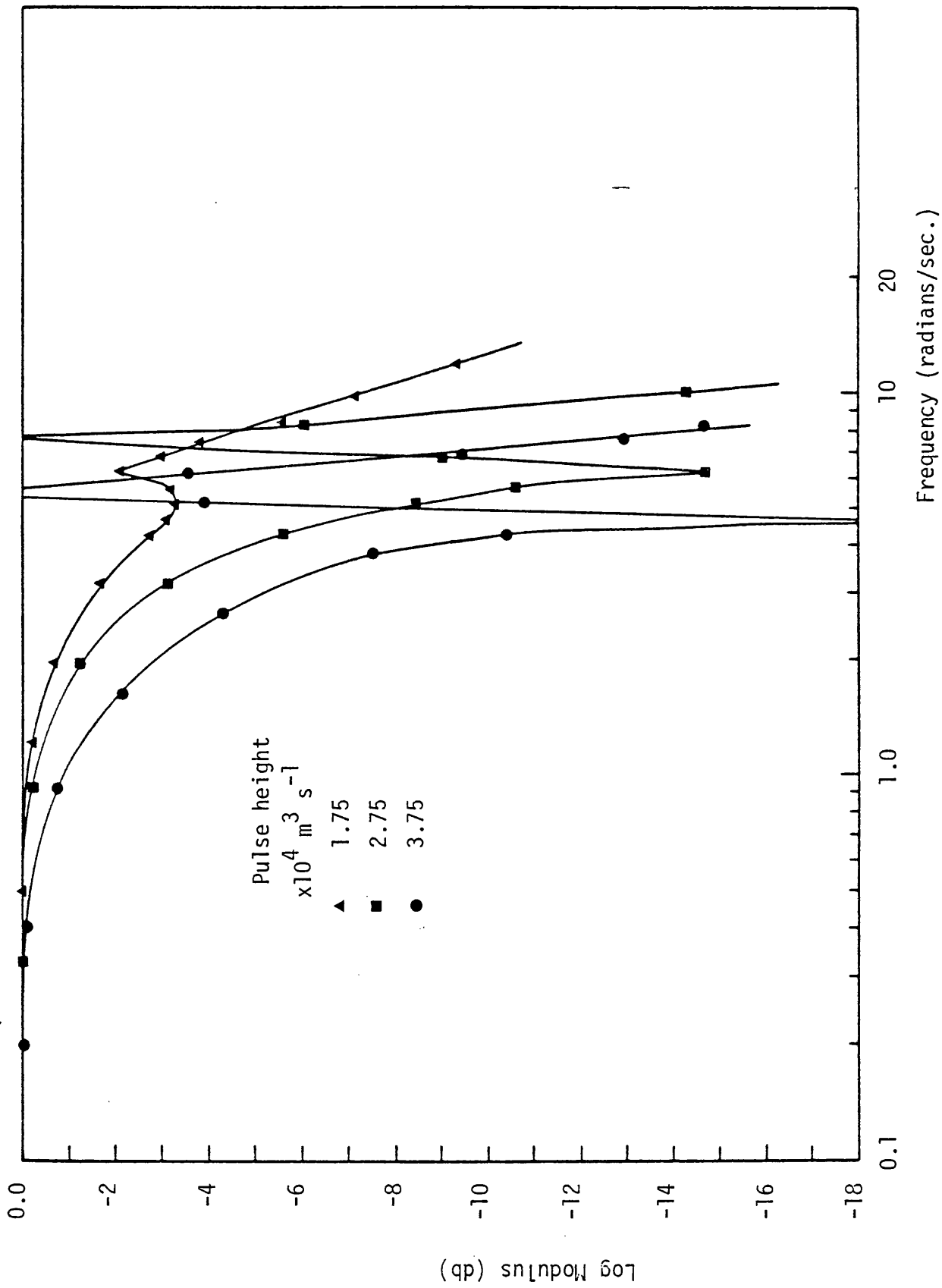
Fig. 5.6 : Effect of pulse height on Bode Plot

D = 0.135m, N=3 rps, Ungassed initial conditions
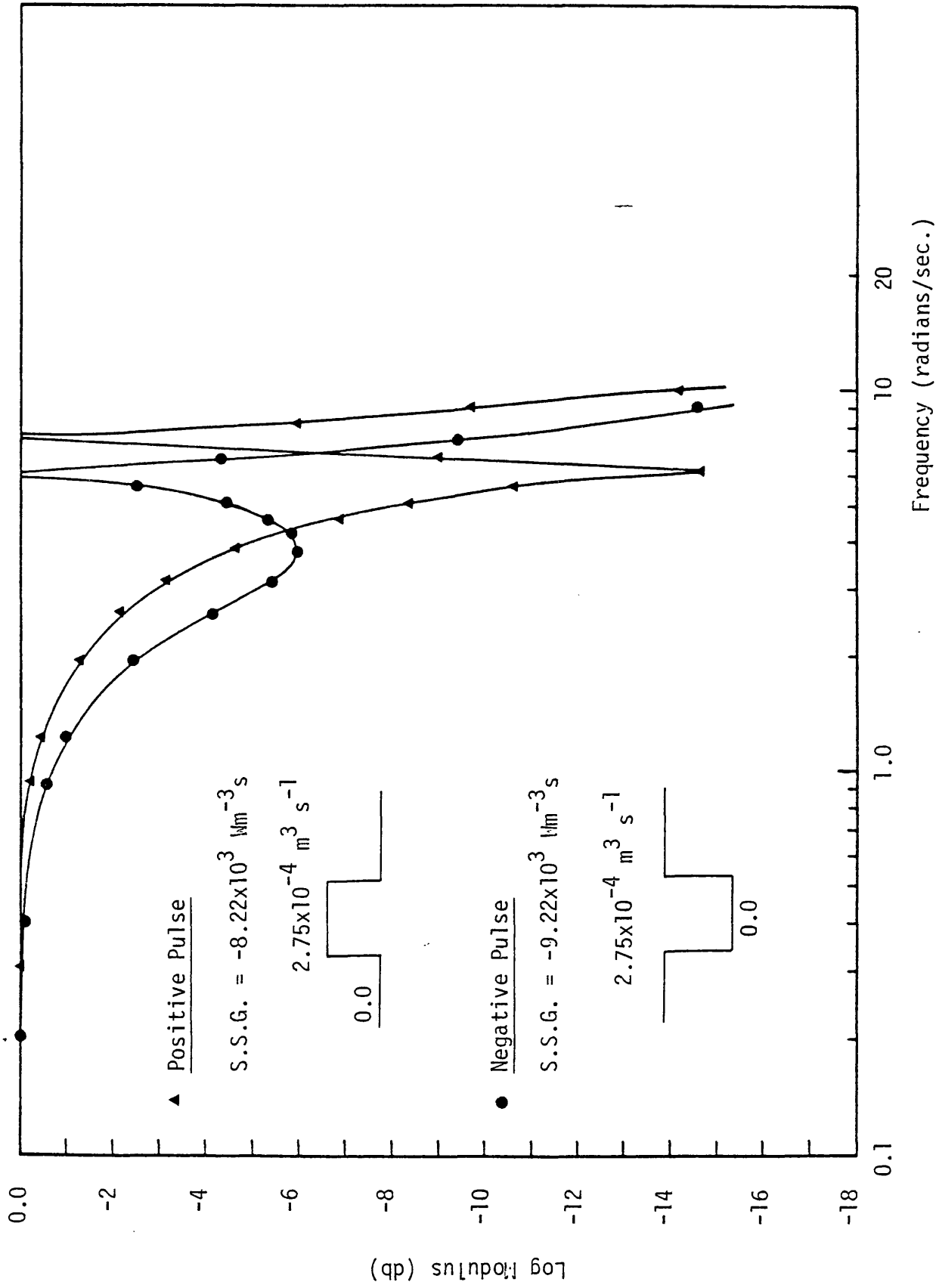
Fig. 5.7 : Bode Plots from positive and negative Pulse tests
D = 0.135m , N=3 rps, 'SSG steady state gain'.

5.3.2 Transient Response and Cavity Formation and Stripping

The appearance of series of damped oscillations in the transient response in preliminary step tests, suggested a possible causal effect associated with the formation of the cavities behind the impeller blades. A series of step tests using impeller D2 were conducted to investigate this phenomenon. The initial and final gas flow rates were carefully selected to cause the formation of a definite number of large gas cavities behind the impeller blades. Bruijn et al (25) related the number of large cavities formed to the relative drop in power consumption (P_g/P_o) as illustrated in Table 5.2. By using these values with the aid of Fig. 4.6 (Chapter 4), the initial gas flow rate and the height of the step change were easily calculated to cause the formation of a desired number of large cavities.

Table 5.2   (After Bruijn et al (25))

Number of large cavities	$P_g/P_o (\pm 5\%)$
1	0.7
2	0.66
3	0.57
4	0.54 .
5	0.51
6	0.48

The impeller speed was selected such that the gas-liquid mixing was in the efficient mixing regime (see Chapter 4). This was a necessary initial precursor to establishing the validity of the values reported in Table 5.2, because vant Riet (23) indicated a possible uncertainty for the condition of forming certain number of large cavities under gas recirculation condition.

Figure 5.8 demonstrates the transient power response associated with the formation of 6 large cavities. A number of peaks (local maxima) are observed in the response. The first four of these are distinct, whereas the last two are less so. It is necessary to indicate that these oscillations are not a result of added noise (say of sinusoidal character) in the response of a first order system which would typically exhibit an exponential form. No oscillations appear in the initial part of response (up to one second), whereas the observed oscillations are decaying with time. Also it is not similar to the sinusoidal response of an underdamped second order system. In the latter case the oscillations fluctuate around a constant value, while for the response in Fig. 5.8 it appears to be like a damped sinusoidal signal imposed on an exponential one. There is a clear correspondence between the number of peaks and the predicted number of large cavities formed. The initial time delay was found to be partially due to the transport delay for the gas through the pipe work from the solenoid valve to the gas sparger (about 1.5m length, Fig.5.1). Also there is a very small time delay between the gas reaching the impeller and the cavity formation response.

Three transient responses for different step heights for an initially ungassed condition are shown in Fig. 5.9. These results further serve to emphasise the relation between the number of large cavities formed and the number of oscillations which appear in the transient response. However for Response (C) there are three oscillations while the predicted number of large cavities from Table 5.2 is two. This could be attributed either to the relatively close Pg/Po value for the formation of the second and third large cavities (see Table 5.2), or else to instabilities of the cavities. This will be explained later.

Fig. 5.8 : Transient power response associated with the formation of 6 large cavities. (D=0.1016m, N=7.5 rps)
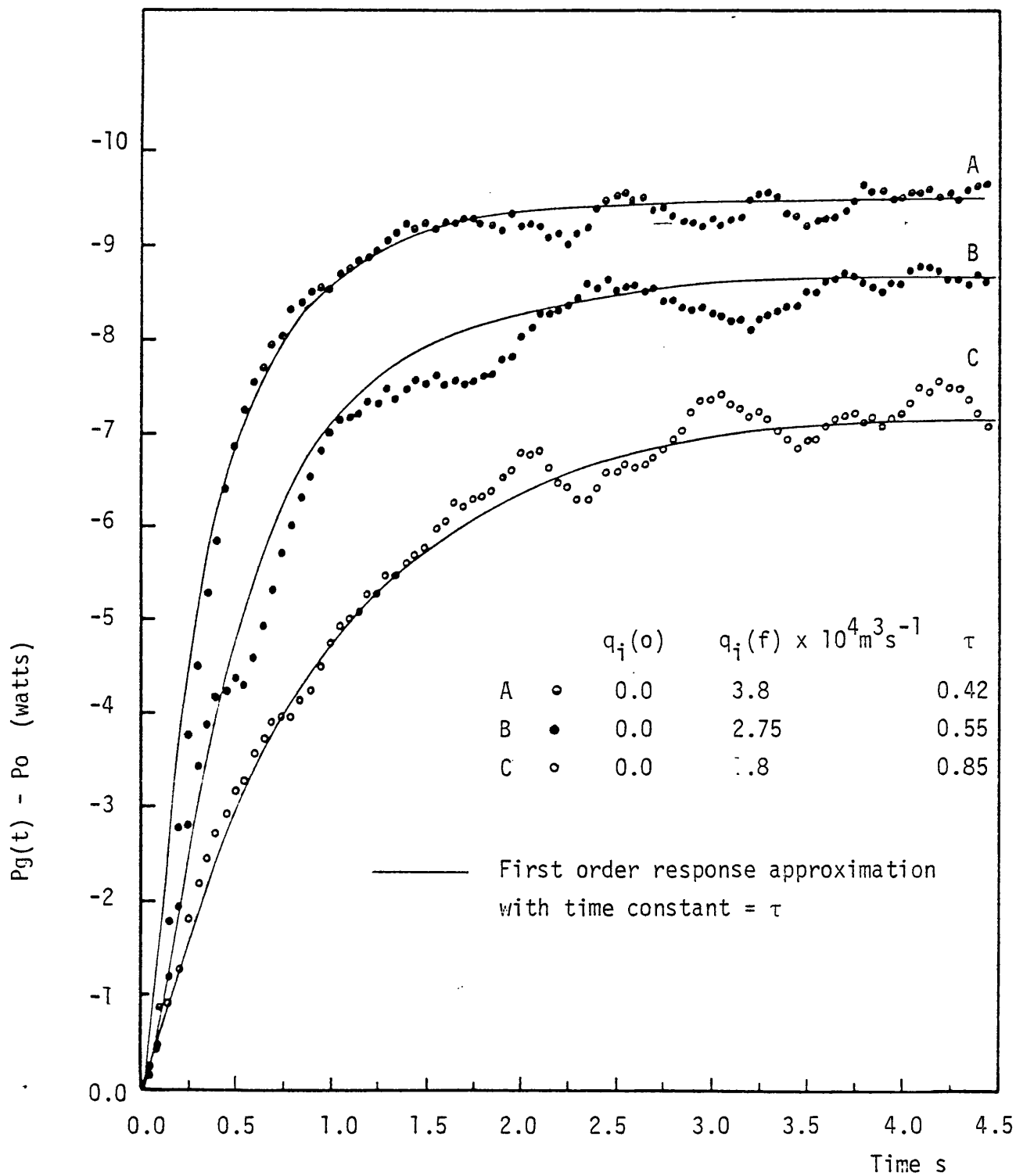
Fig. 5.9 : Transient responses associated with the formation
of 'A' 6 large cavities, 'B' 4 large cavities,
'C' 2 large cavities.
(D=0.1016m, N=7.0 rps)

Response (A) Fig. 5.9 and the response illustrated in Fig. 5.8, are both associated with the formation of the six large gas cavities behind the impeller blades. However, for the latter case the initial condition corresponded to the condition where clinging cavities had already formed, while the former was obtained with an initially un-gassed condition. In this case there were no formed cavities behind the impeller blades. These two responses have a similar shape, but the peaks appear later in Response (A), Fig. 5.9. This may be attributed to the increased time needed to fill the whole cavities. This similarity suggests that under the unsteady state conditions, and if the step increase in gas flow rate is high enough, large cavities will be formed directly. This is unlike the steady state conditions where vortex, clinging and then large gas cavities are formed gradually with increase of the gas flow rate.

The transient power response associated with the formation of each of the first and the second large cavities are shown in Figs. 5.10 and 5.11 respectively. Figure 5.10 demonstrates the instability of the fi: ;t large cavity. Response (A) shows its formation, which is marked by a peak followed by a series of damped sinusoidal oscillations. However, it is different from the response of underdamped second order system since both the amplitude and period of oscillations are damped. Moreover after 2.25 seconds the cavity starts to dissociate as shown by the gradual increase in power which is then followed by reformation of the cavity. The instability of the first large cavity was confirmed when a step with a larger height was imposed (Response (B), Fig. 5.10). In this case, after reaching a maximum indicating the complete formation of the cavity, it undergoes one cycle of damped oscillation. Then this is followed by further drop in power, which indicates the start of formation of the second large cavity. The
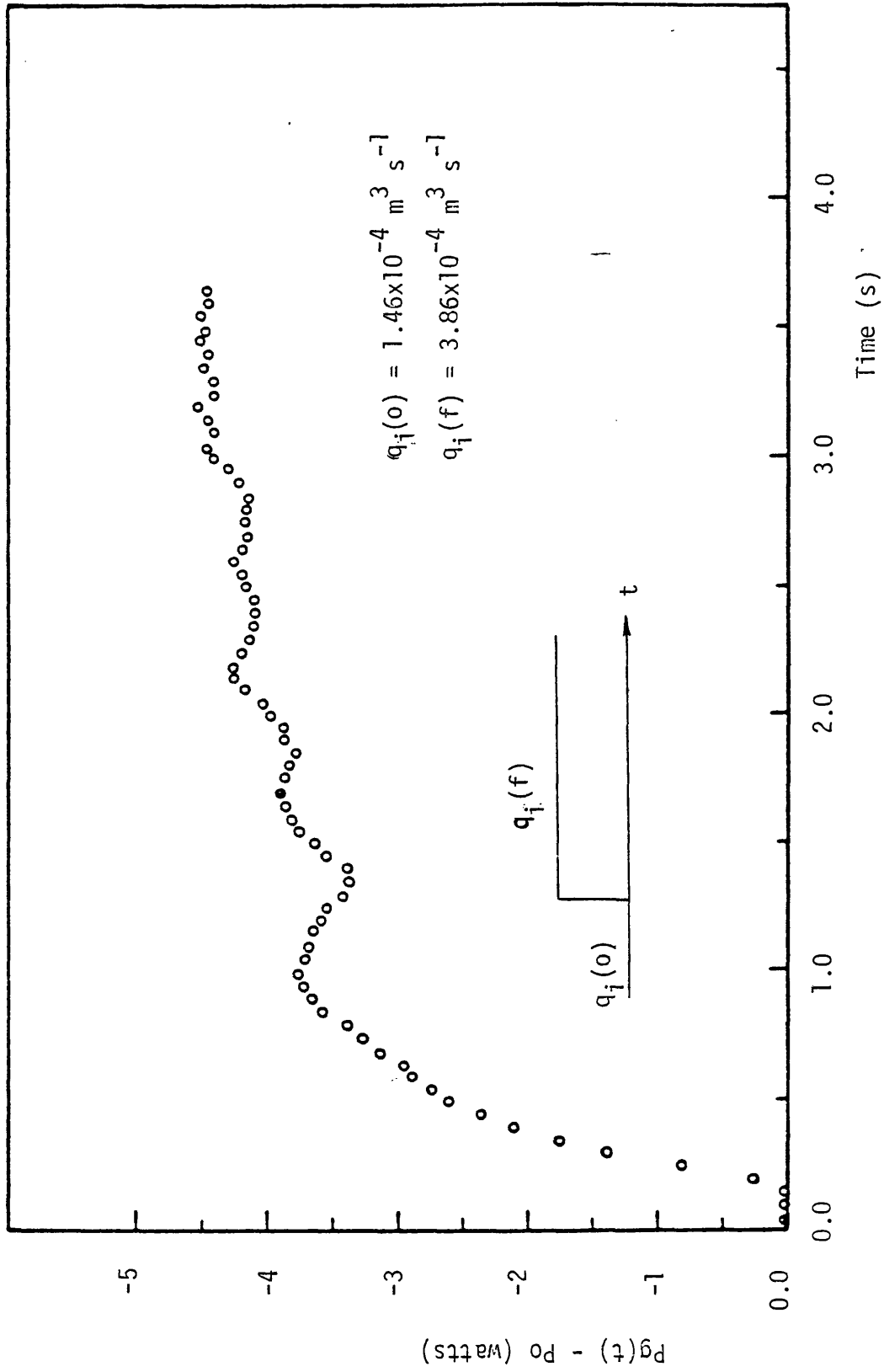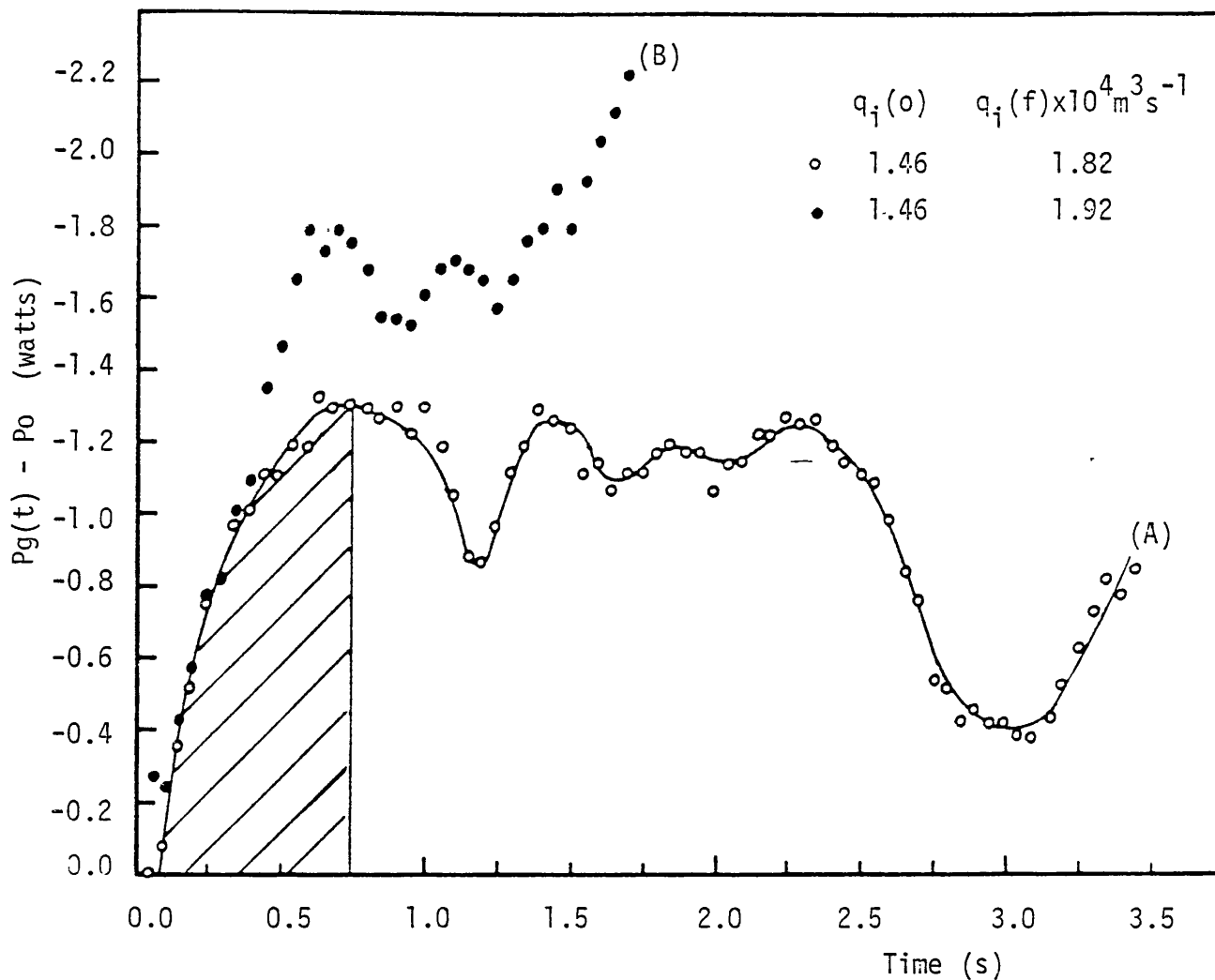
Fig. 5.10 : Transient response associated with the formation
of the first large cavity.
(D=0.1016m, N=7.5 rps)
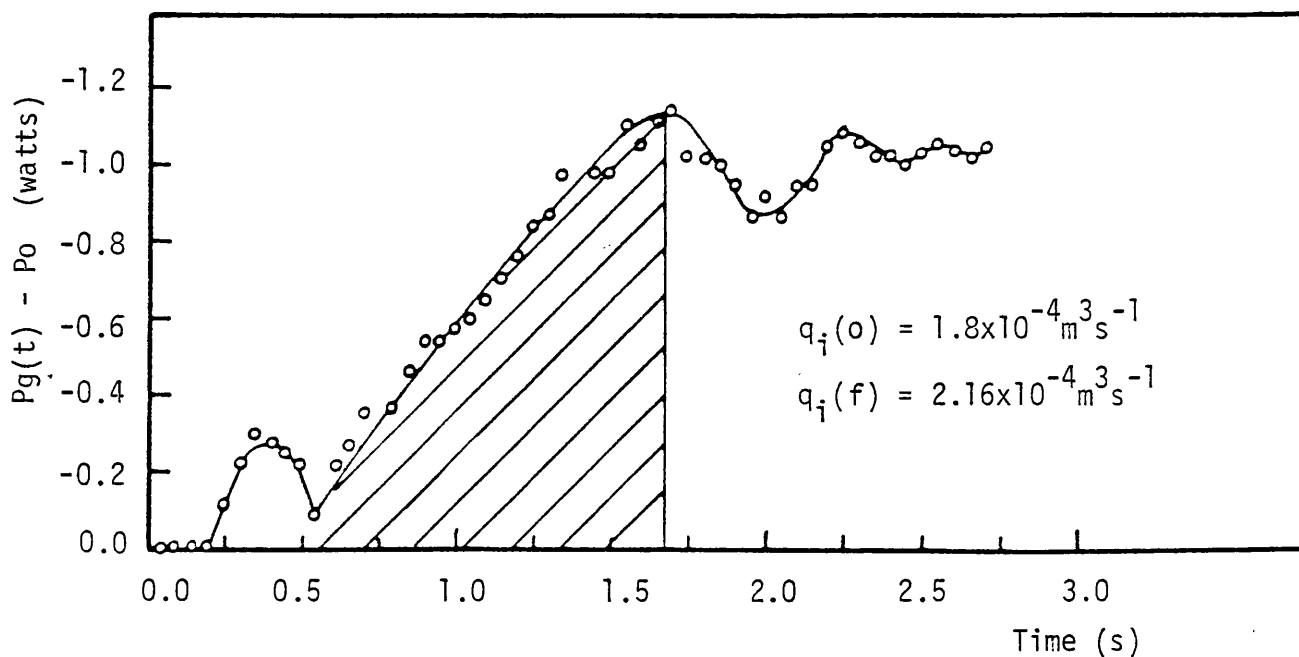
Fig. 5.11 : Transient response associated with the formation
of the second large cavity.
(D=0.1016m, N=7.5 rps)

formation of this cavity exhibited a similar behaviour, ie, peak followed by damped oscillations, as shown in Fig. 5.11. However, a 'hump' revealing an initial time delay is observed, and the speed of cavity formation is slower compared with that of the first cavity. The height of the steps used for studying the first large cavity (Response (A), Fig. 5.10) and that for the second cavity (Fig. 5.11) were of similar size ($0.36m^3s^{-1}$). This indicates that the slower formation of the second cavity compared to the first (as determined by the slopes) is a characteristic of the process rather then due to change in the flow rate of gas to the cavity. However, the total energy dissipated in forming both of these cavities (the hatched area under the curve Figs. 5.10 and 5.11) are almost identical, equal to about 0.6 WS (Joules). A further trial to study the third and subsequent large cavities was less successful, because the drop in power associated with these cavities was smaller (eg, 0.7 watt for the third cavity and less for the others).

The responses associated with the separate formation of the first and second large cavities are combined int) a single response shown in Fig. 5.12. The two clearly distinguishable peaks marked 1 and 2 in this figure indicate the formation of the first and second alrge cavities (comparison with Figs. 5.10 and 5.11). The small 'hump' at the left of the figure, corresponds to the similar event in Fig. 5.11, occurring at the same time. The peak at the extreme right is due to the stripping of the first large cavity (see Fig. 5.10). Figure 5.12 is of particular importance because it shows that the synthesis of the separate responses associated with the formation of the individual cavities reconstructs the peaks which indicate the number of large cavities formed. If Response (C) Fig. 5.9 is re-examined, the appearance of a third peak may now be attributed to the instability of a large
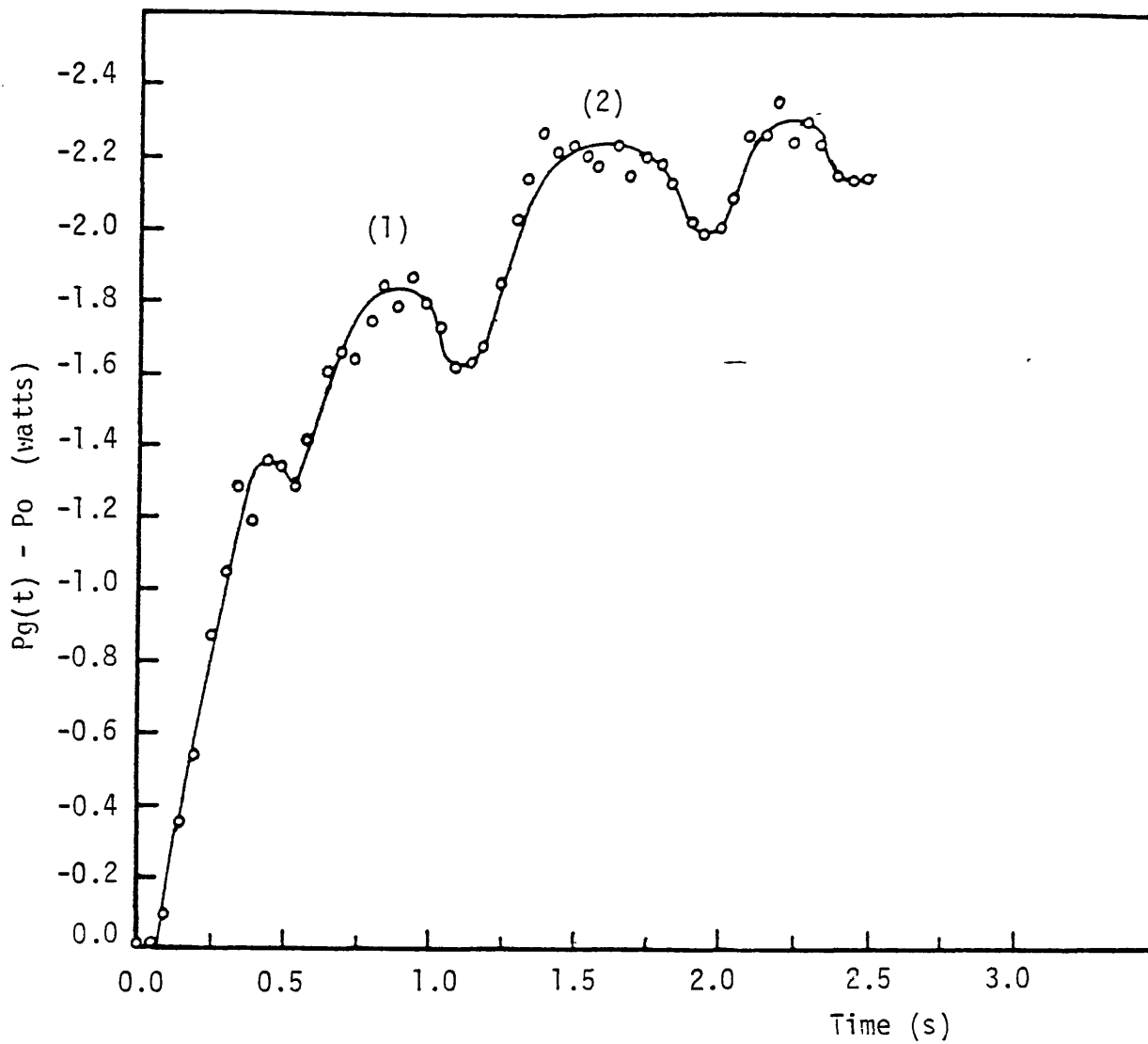
Fig. 5.12 : Synthesised total transient response for the formation of the first and second large gas cavities obtained from the separate responses in Figs. 5.10 and 5.11.

cavity in the same manner. However, the good agreement between the number of peaks and the predicted number of large cavities formed for larger step sizes (Fig. 5.8, and Responses (A) and (B), Fig. 5.9) implies that the cavities are normally stable if the gas supply is high enough. Moreover the small 'hump' shown at the left part of the synthesised response of Fig. 5.12 , (a result of the delay in forming the second large cavity) , can be also observed in Responses (B) and (C) Fig. 5.9 at times of 0.4 and 0.7 seconds, respectively.

The previous observations and remarks can now be put together to give a description of the system dynamical behaviour, and hence used to construct a dynamical model to represent the process.

1 - The transient response associated with the formation of a
     single large cavity contains a peak, followed by a series
of oscillations. The magnitude and the period of these
oscillations respectively decays and decreases with time.

2 - If the step is high enough to cause the formation of more
     than one large cavity, only one f them will start to form.
After a short lapse of time (fraction of a second) a second
cavity starts to form. However, the speed of formation of the
second cavity is slower. This behaviour may be applied to the
formation of the subsequent cavities.

3 - The combined transient response associated with the
     formation of more than one large cavity, is marked by a
number of peaks which indicate the number of formations and/or
strippings of large cavities. The time between the successive
peaks gives indication of the time delay between the start when
these cavities are formed. However this is an approximation
since the speed of formation of the cavities are different.

Figure 5.13 illustrates the synthesis of the impeller power transient response from the responses associated with each large cavity. The system dynamics are then represented by the transfer function block diagram shown in Fig. 5.14. From this, the system transfer function can be expressed in mathematical form as

$$G(s) = \sum_{i=1}^{n} e^{-t_i s} G_i(s) \qquad 5.1$$

where

$G(s)$ transfer function describing the system

$G_i(s)$ transfer function describing the power dynamics of the ith large gas cavity

t_i the time delay of formation of the ith large cavity

n number of large cavities formed

Equation 5.1 indicates the complexity of representing the system by a dynamical model. The number of large cavities and the related transfer functions and time delays are all functions of the impeller speed, the initial gas flow rate, and the characteristic of the input disturbance. For these reasons a first order approximation is employed to describe the process, as described in the following sections.

To examine the dynamics of the reverse process of cavity stripping, a step reduction in gas flow rate was used. Figure 5.15 demonstrates the transient responses following a positive and negative step. The peaks which characterise the cavities formation response, are also observed on the stripping response, while the shift of the peaks to the right suggests a higher time delay for cavity stripping compared with formation. The 'hump' which appears at time of 1.25 seconds in the cavities stripping response points to oscillation precedes the stripping of the large cavity. However, under gas recirculation
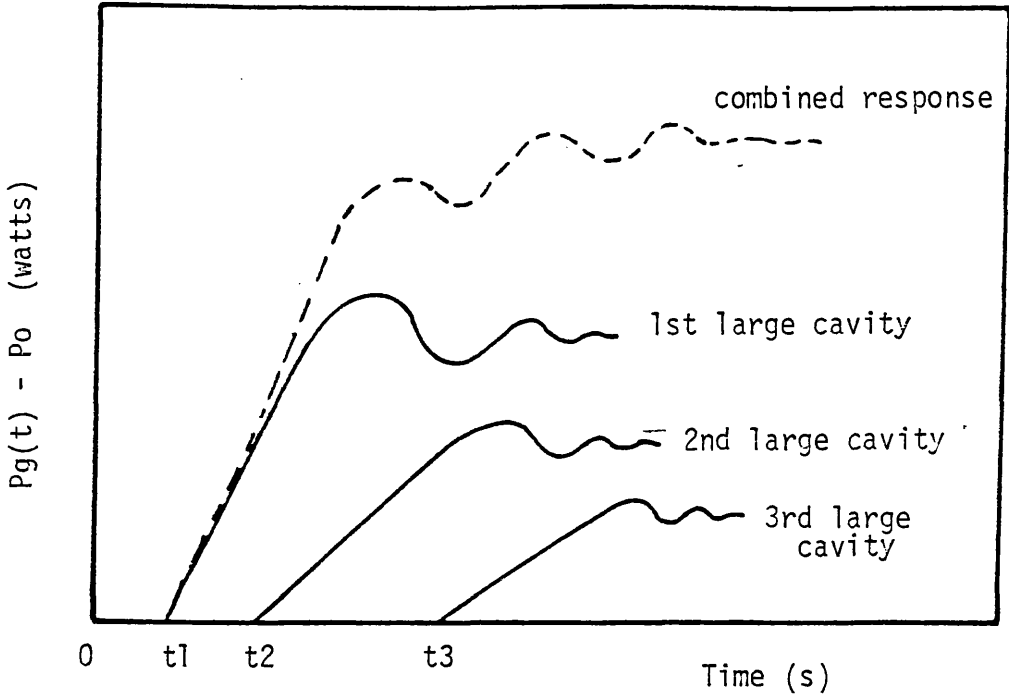
Fig. 5.13 : Schematic diagram for the synthesis of impeller power transient response.
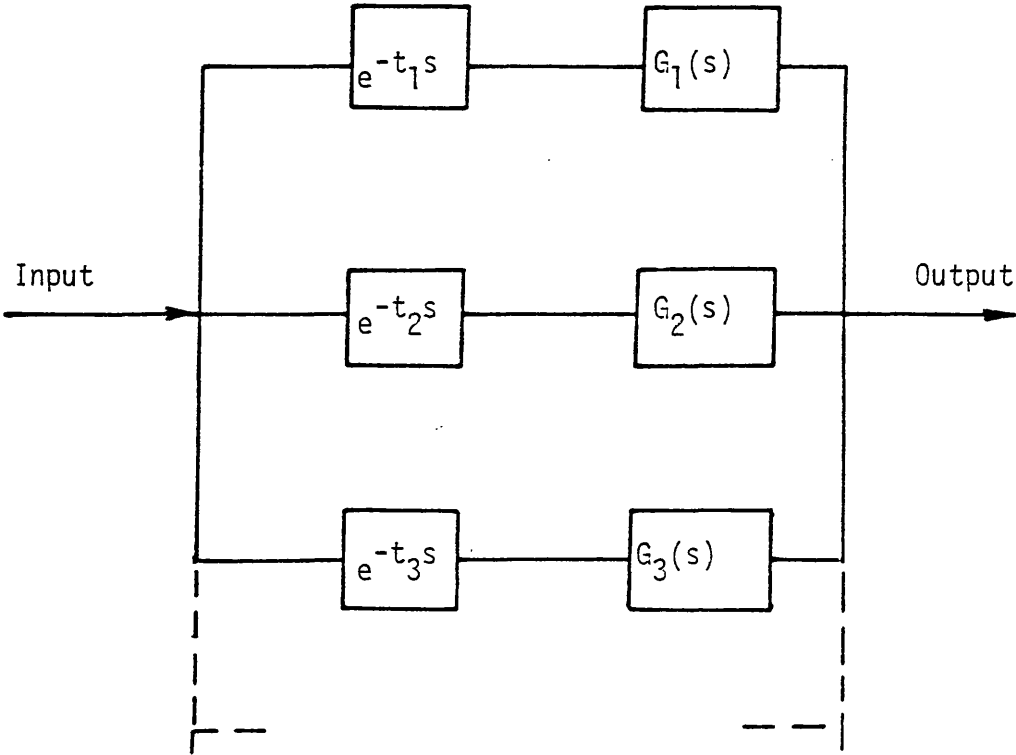
Fig. 5.14 : Transfer function block diagram describing the impeller power dynamical model.

$G_i(s)$ - the transfer function associated with the formation of the ith large cavity

t_i - time delay of formation of ith large cavity.
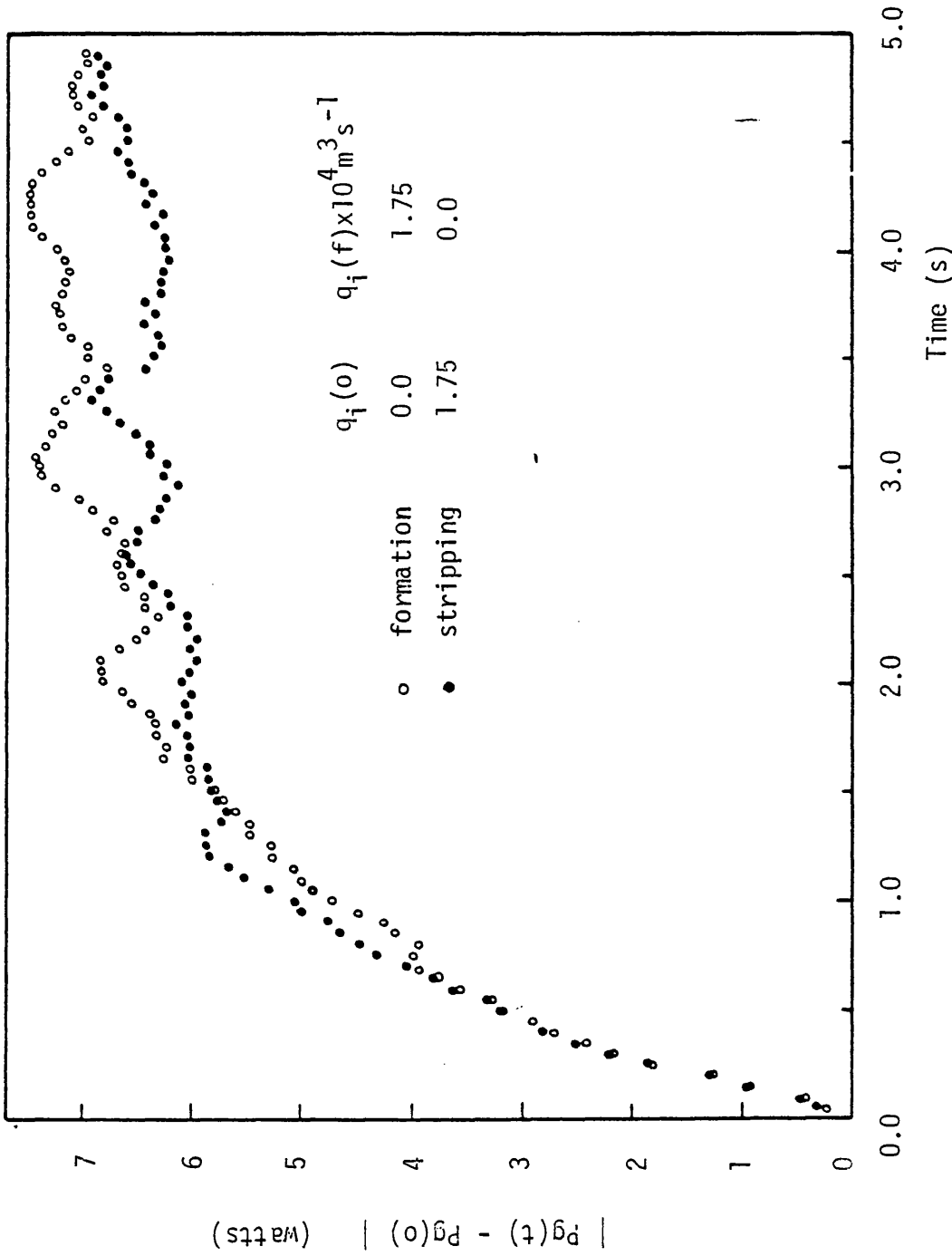
Fig. 5.15 : Transient power responses associated with the formation and stripping of two large cavities. (D= 0.1016m, N=7 rps)

condition, a significant difference between the dynamics of cavity formation and stripping was observed. As shown in Fig. 5.16, the cavity formation response (A), exhibits the same behaviour as that without recirculation condition, except it is faster in approaching the steady state. But the response associated with the cavities stripping (B) is much slower. The large differences between the power levels which correspond to the peaks suggest that cavity stripping with gas recirculation becomes a sequential process. For example, the stripping of the second cavity does not start until the stripping of the first cavity is complete. The difference in the transient responses following positive and negative step change in gas flow rate emphasises the hysteresis nonlinearity which was observed from the pulse test results (Fig. 5.7).

5.3.3 First Order Model Approximation and Gas Recirculation

If the change of the impeller power dynamics with the operating parameters D, N, and the input disturbance is to be quantitatively evaluated, criteria for estimating the system dynamics have to be specified. However, the system dynamical behaviour as described in the previous sections is rather complicated, even for the same operating conditions and input disturbance levels. An exact analysis using the suggested dynamical model (Eq. 5.1) is not feasible within the present limited knowledge of the system. Instead a first order model approximation was employed. In what follows the analysis of this highly nonlinear process was studied using the sub-component approach described in the Introduction (Sec. 5.1). The power responses following a set of step changes in gas flow rate (one at a time) at different impeller speeds were measured and analysed. This was repeated for each of the three impellers used in this study.
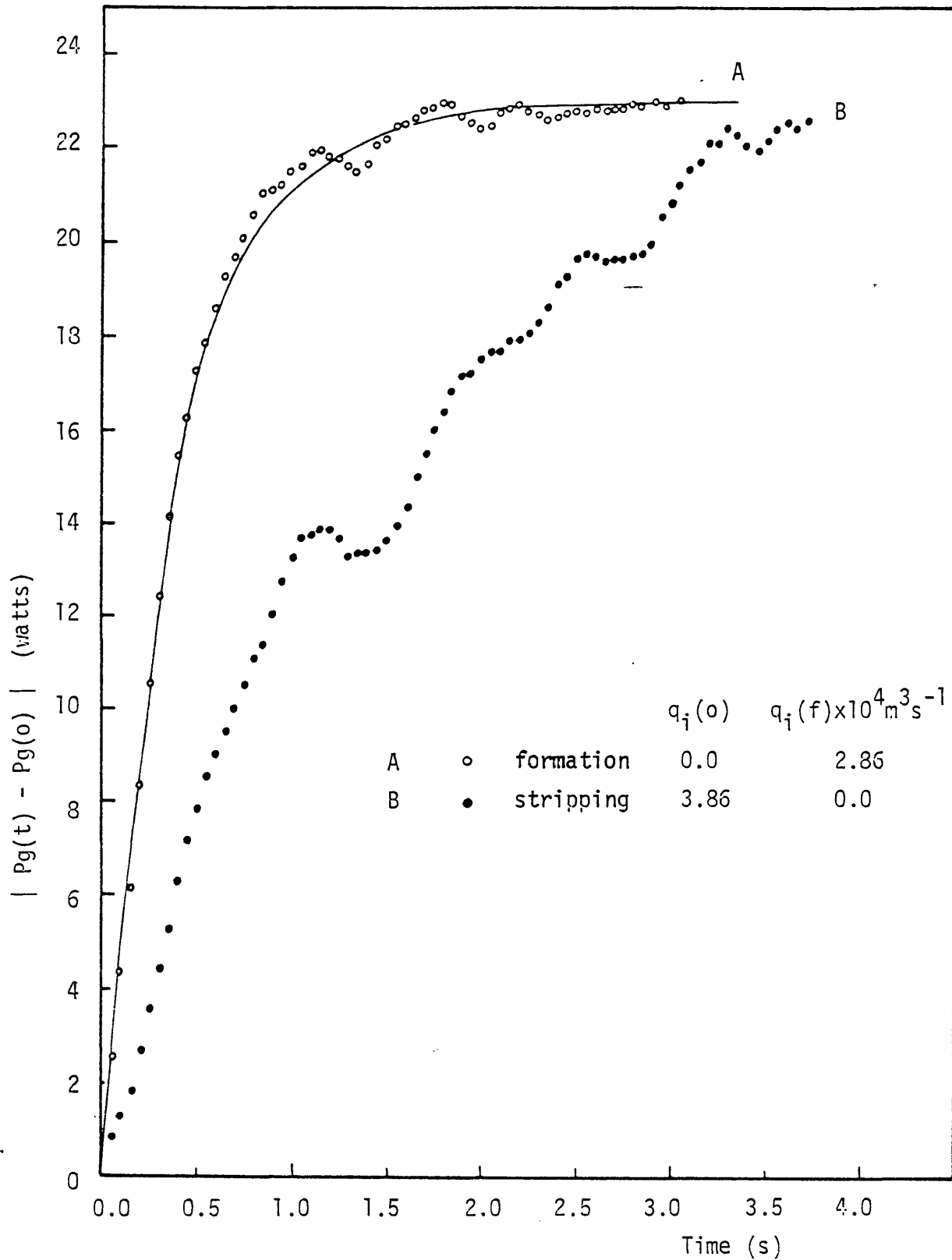
Fig. 5.16 : Transient power response associated with the formation and stripping of 6 large cavities under gas recirculation condition. (D=0.1016m, N=10 rps)

The transient response following a positive step change in gas flow rate with ungassed initial conditions, can be approximated by the response of a first order system. Figures 5.9, 5.16, 5.17 and 5.18 show the true response and the corresponding first order approximation at the various impeller speeds for different sizes of step input. If any of these figures is examined (eg, Fig. 5.18) it can be noticed that the process more rapidly achieves the steady state for the higher step at the same impeller speed. Moreover if responses for the same size step but different impeller speed are examined (eg, Responses (C) in Figs. 5.9, 5.17, 5.18) it can be observed that the responses become faster with the increase of the impeller speed from 5 to 7 rps, and then become slower at N = 9 rps. Figure 5.19 demonstrates the change of the time constant of the corresponding first order approximation (τ) with the step height and the impeller speed for impeller D2. The time constant τ was estimated as the time required for the change of power to achieve 0.632 of its final steady state value which is a standard method of estimating the time constant of first order system(62). The general trend in Fig. 5.19 is similar to that mentioned above for the true response. The speed at which τ starts to decrease is close to the speed at which gas recirculation commences under steady state conditions (Chapter 4). This was confirmed from the results with the other impellers, as shown in Figs. 5.20 and 5.21.

The initial rise of τ with increasing the impeller speed for the same step size may be explained by the increase in the pumping rate of the impeller. This is accompanied by an increase in the rate of gas discharged from the impeller and hence the cavities will need a longer time to form. The increase of τ with the reduction of the step size at the same impeller speeds points to the dependency of the impeller power dynamics on the rate at which the gas cavities are supplied with gas.
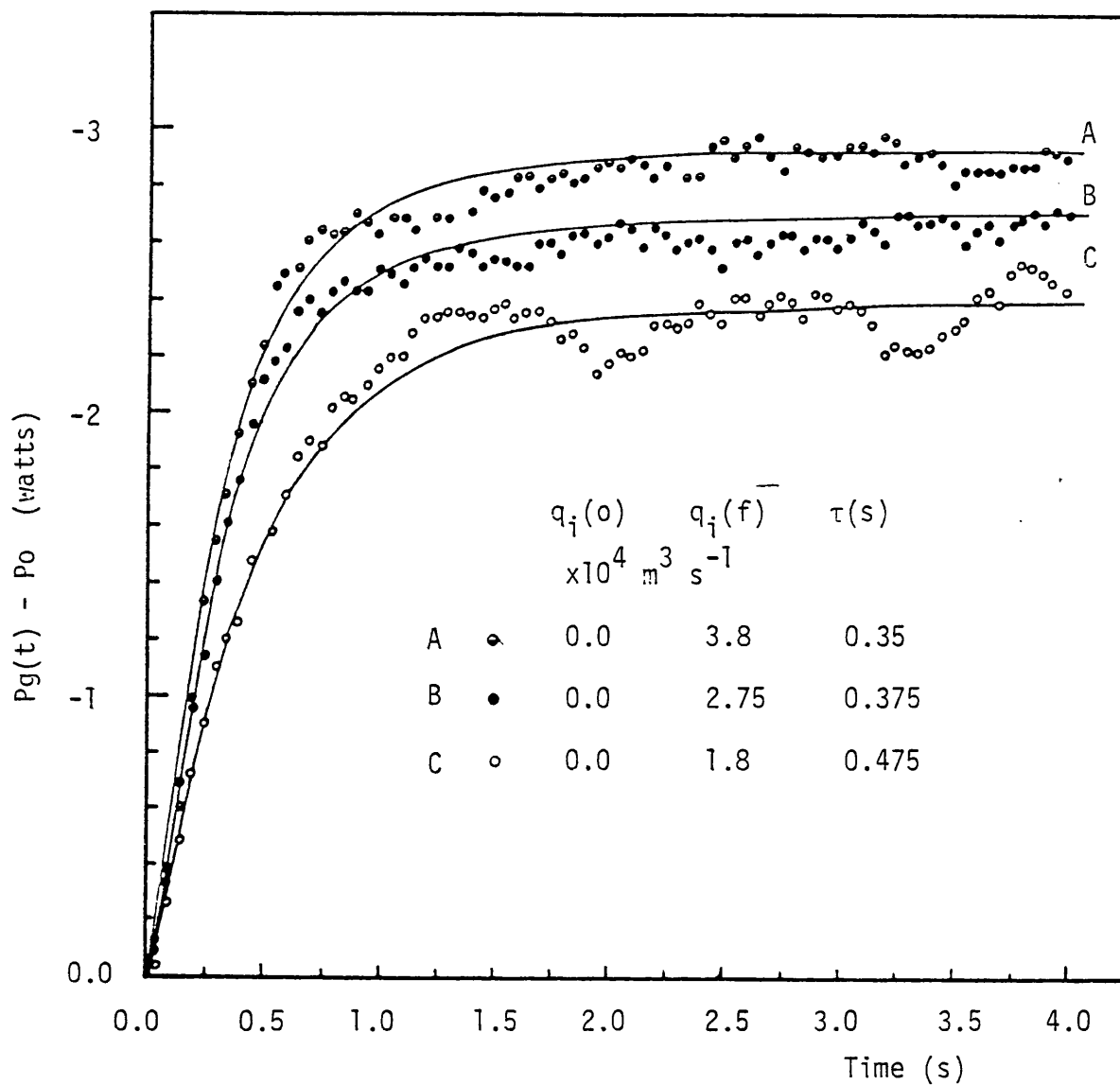
Fig. 5.17 : First order approximation for the impeller
power transient response.
(D=0.1016m N=5 rps)
τ is the time constant of the first order approximation
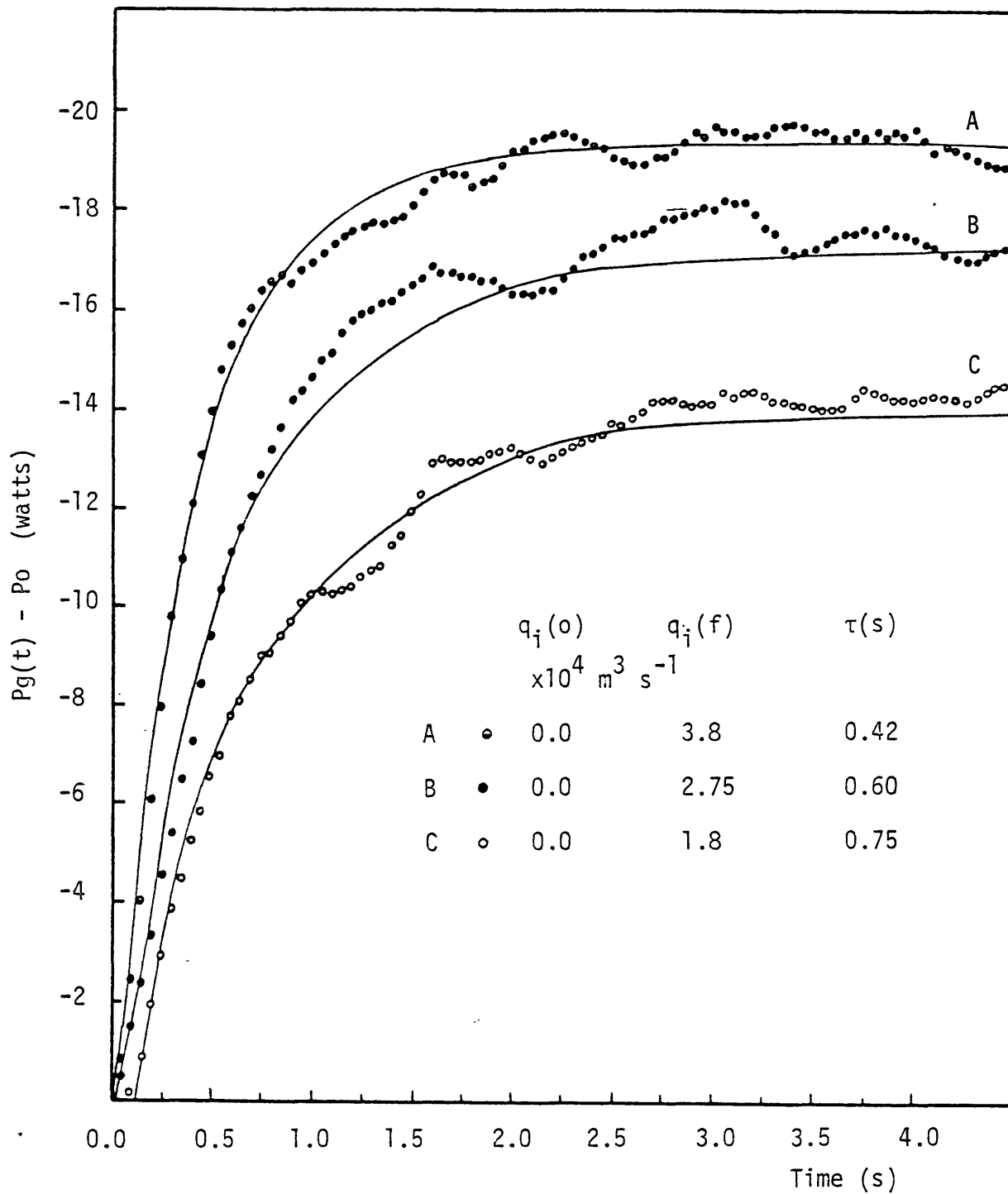
Fig. 5.18 : First order approximation for the impeller power
transient response.
(D=0.1016m N=9 rps)
τ is the time constant of the first order approximation
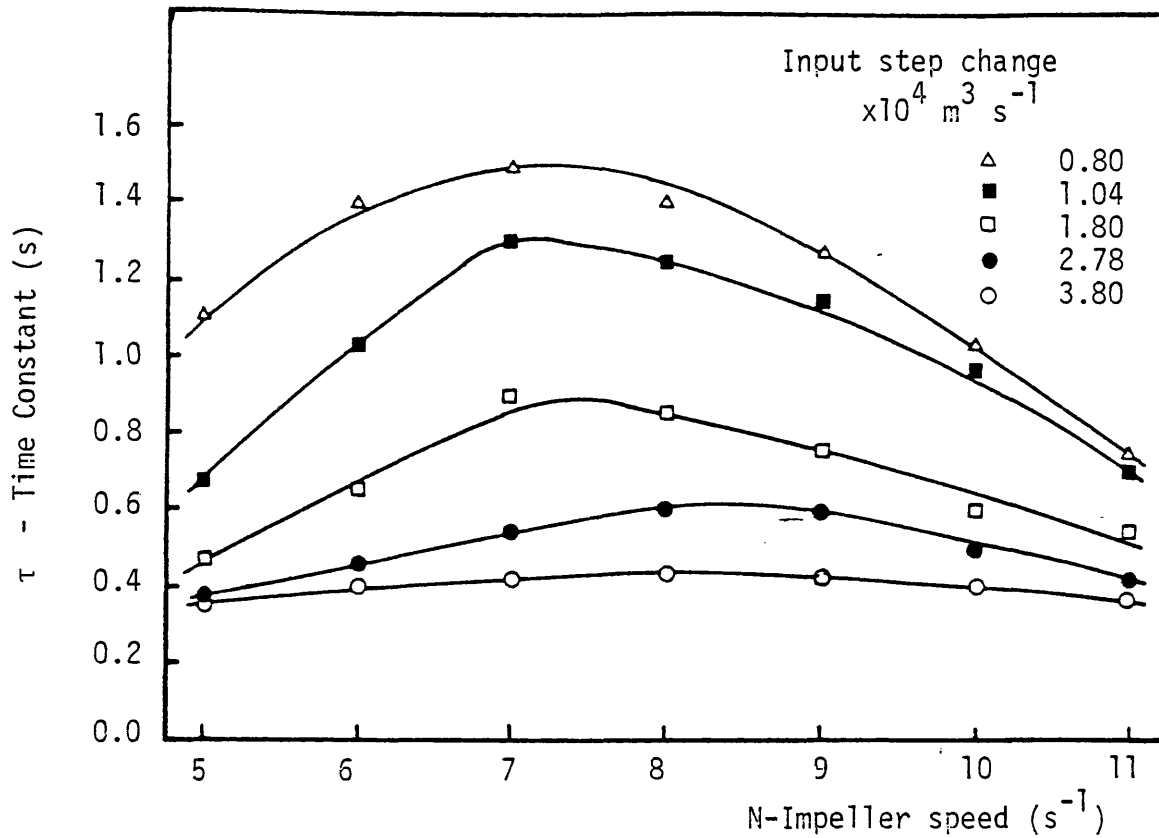
Fig. 5.19 : Time constant of first order approximation against
impeller speed (D=0.1016m).
Ungassed initial conditions.
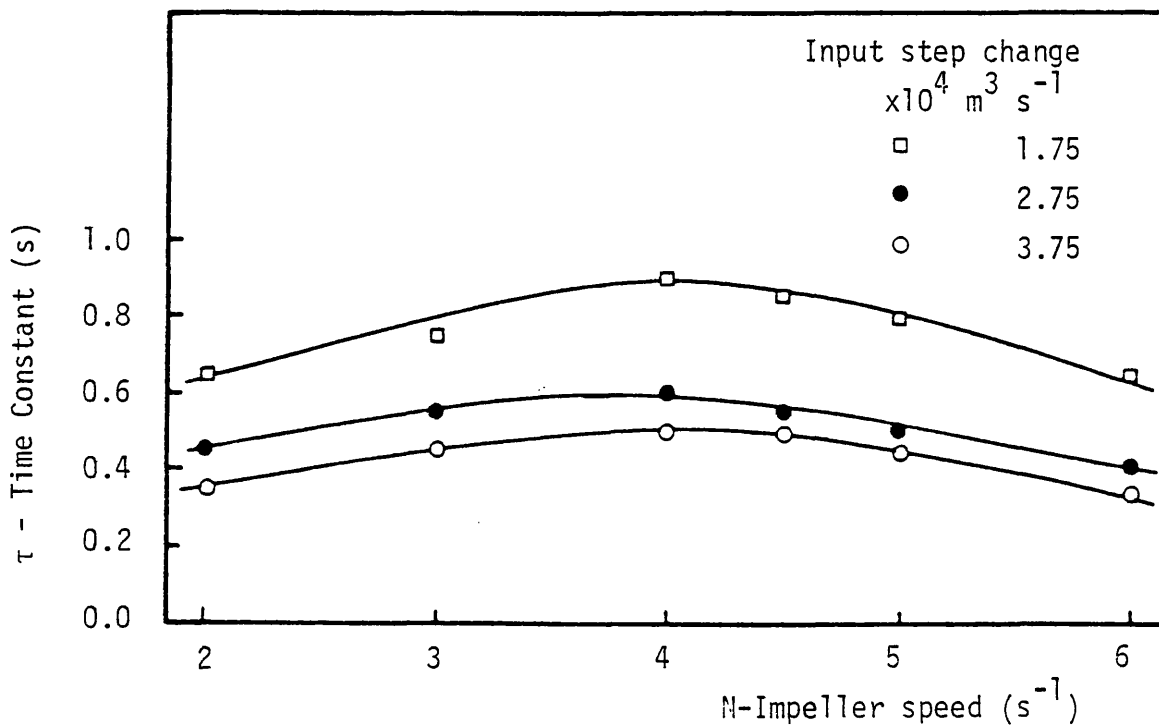
Fig. 5.20 : Time constant of first order approximation against
impeller speed (D=0.135m).
Ungassed initial conditions.
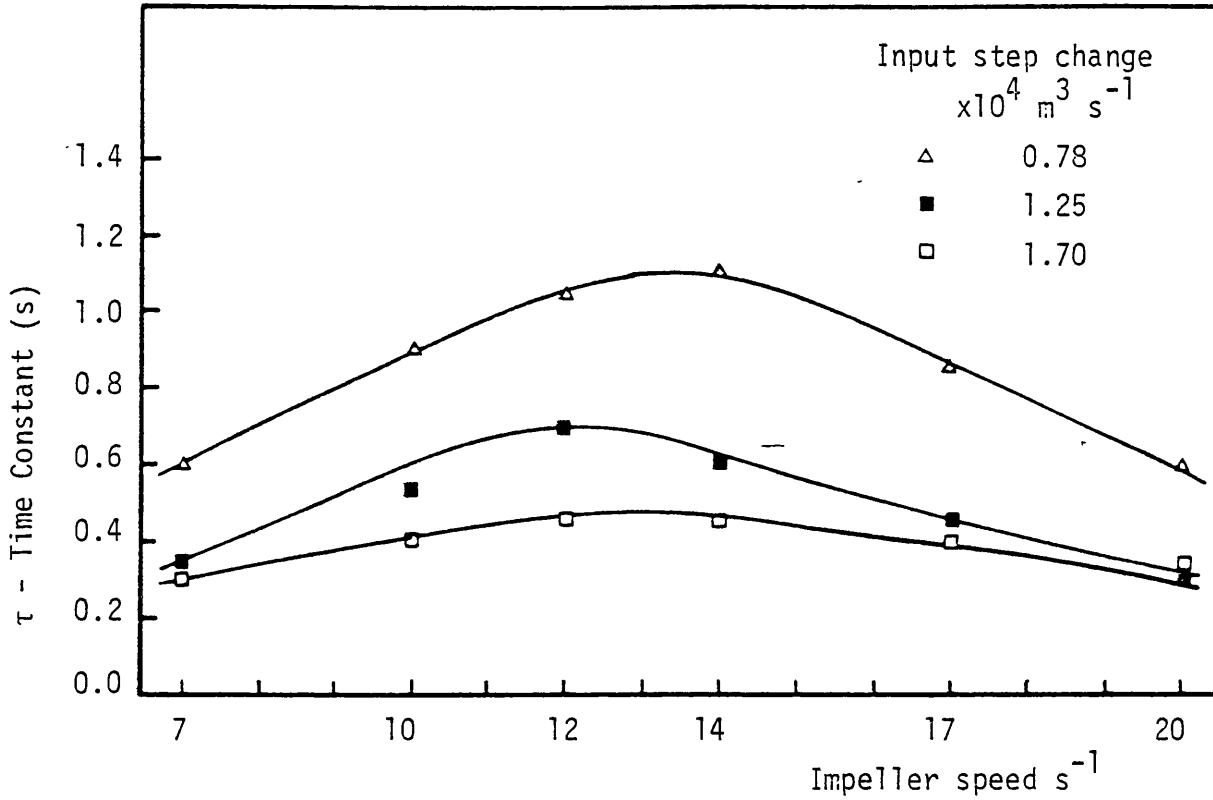
Fig. 5.21 : Time constant at first order approximation against
impeller speed. (D=0.0762m).
Ungassed initial conditions.
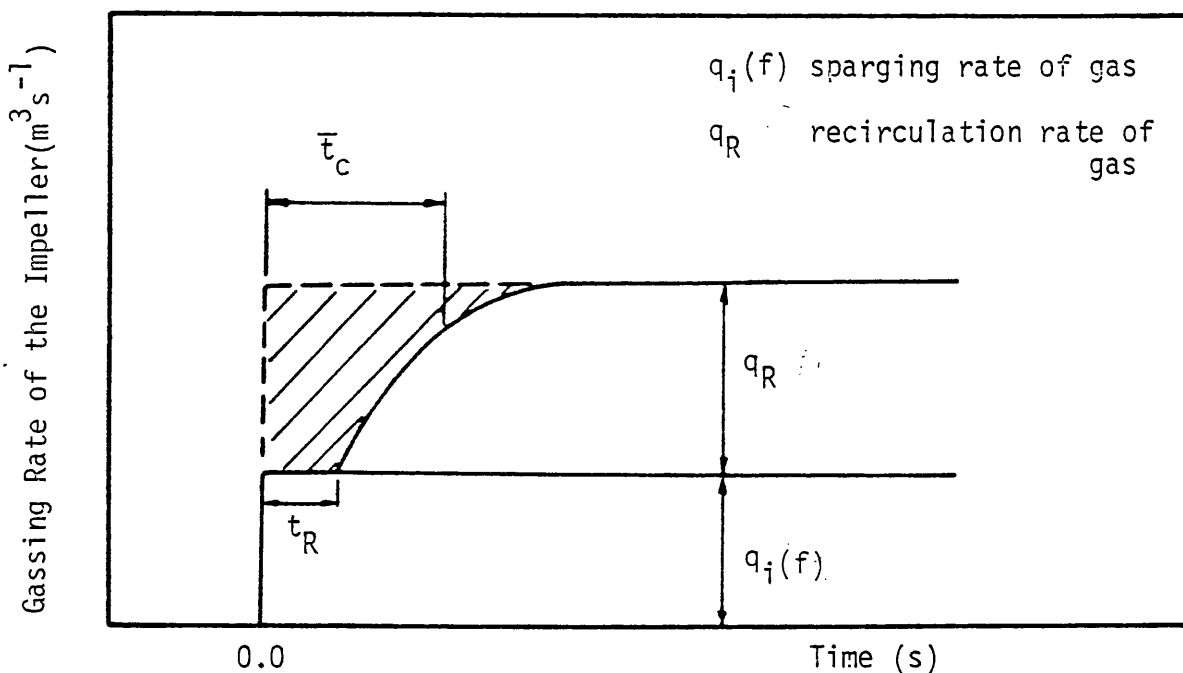
Fig. 5.22 : Input disturbance to the impeller under gas
recirculation conditions.

From the results shown in Figs. 5.19, 5.20 and 5.21 it was found that

$$\tau \, \alpha \, \frac{N}{q_i(f)^{0.9}} \qquad\qquad 5.2$$

where $q_i(f)$ is the step change in gas flow rate from initial ungassed conditions.

The exponent of $q_i(f)$ was lower than 0.9 for the largest impeller (D3), and higher for the smallest one (D1). However a value of 0.9 was estimated as being the best fit for the three impellers. The effect of the impeller diameter is rather difficult to determine from the experimental results, but the values of τ for impellers D1 and D2, at a speed of 7 rps, indicate that

$$\tau \, \alpha \, D^3 \qquad\qquad 5.3$$

Following the region where τ increases with increasing N (for the same step size) the curves start to decrease. The speeds corresponding to the maxima in these curves are close to those achieved for the onset of gas recirculation. Therefore the considerable reduction in τ with further increase of N, can only be explained by the increase of the rate of gas recirculation. Since the recirculated gas constitutes part or all of that which is discharged from the impeller, a time delay is expected before it eventually returns to the impeller region.

Under such recirculation conditions, then the input disturbance comprises two components as mentioned in the section on Frequency response analysis (Section 5.3.1). The first is the step change in the sparged gas flow rate, and the second is that due to the added recirculation gas rate. Figure 5.22 illustrates this composite input disturbance, where t_R is the time delay before any recirculated gas reaches the impeller, as measured from the moment of applying the step

change to the sparged gas flow. The order of this time delay should be smaller than the average recirculation time inside the vessel, as it depends on the shortest circulation loop. Holmes et al (27) measured the average circulation time in an ungassed stirred tank, and found that for $R_e > 2 \times 10^4$:

$$\bar{t}_c = \frac{0.85}{N} \left(\frac{T}{D}\right)^2 \qquad \qquad 5.4$$

where $\bar{t}_c$ is the average circulation time which is defined by

$$\bar{t}_c = \frac{\text{average circulation loop length}}{\text{average local velocity}} \qquad 5.5$$

Recently, Middleton (63), showed experimentally that the aeration of the vessel increases the average circulation time. Bryant and Sadeghzadeh (64) also reported a similar effect and presented the following correlation

$$\bar{t}_c = c \ (1+b/c \ Q) \qquad \qquad 5.6$$

where c and b are constants for the system. Also they indicated that $b/c \alpha N$, but they did not confirm that from their limited results. However, a rough estimation of the quantity (b/c Q) for the working conditions of this study, indicated that the expected increase in the average circulation time due to aeration, as estimated from Eq. 5.6, is about 15% for the highest gas flow rate at the onset conditions of gas recirculation. Nevertheless an approximate value for $\bar{t}_c$ from Eq. 5.4 indicates that $\bar{t}_c$ will be of the same order as τ. This implies therefore that the effect of the recirculated gas on the transient response will appear after a period of time approximately equal to τ. This is in contradiction to the consistently observed effect of the gas recirculation on τ, as shown in Figs. 5.19, 5.20 and 5.21. However $\bar{t}_c$ as defined from Eqs. 5.4 and 5.5 describes the average circulation time of liquid and the above observations point to the

shorter circulation loops of gas which play an important role in reducing τ under the gas recirculation conditions. It can be concluded, therefore, that t_R should be much less than $\bar{t}_c$ as illustrated in Fig. 5.22.

The impeller dispersion efficiency in the recirculation regime, η_R, (as defined in Chapter 4) can also be estimated in an approximate manner from the measured dynamical performance of the impeller. First, assume a point (1), Fig. 5.23, in the recirculation regime, which has a time constant of τ_1. Since τ is proportional to N (Eq. 5.2) in the efficient mixing regime, point (2) in Fig. 5.23 therefore corresponds to point (1), providing there is no gas recirculation. If the quantity of gas represented by the hatched area in Fig. 5.22 is added to the volume of gas which is recirculated, assuming instantaneous gas recirculation, then with the aid of Fig. 5.23 and Eq. 5.2, it can be shown that

$$\frac{\tau_2}{\tau_1} = \left(\frac{q_i(f) + q_R}{q_i(f)}\right)^{0.9}$$

$$= \eta_R^{0.9}$$

or $$\eta_R = \left(\frac{\tau_2}{\tau_1}\right)^{1.11}$$ 5.7

The calculated values of η_R by this approximate method are shown in Fig. 5.24. There is good agreement of the values for η_R as calculated from the dynamical and the steady state measurements for the largest impeller (D3), but only poor agreement in the case of the D2 impeller where the estimates are higher by about 30%. For the smallest impeller (D1) the difference is even larger. These differences could be due to the first order approximation used, and thus the accuracy of estimation is dependent on the time constants values obtained.

$$\eta_{R1} = \left(\frac{\tau_2}{\tau_1}\right)^{1.11}$$

τ – Time Constant (s)

N-Impeller Speed (s^{-1})
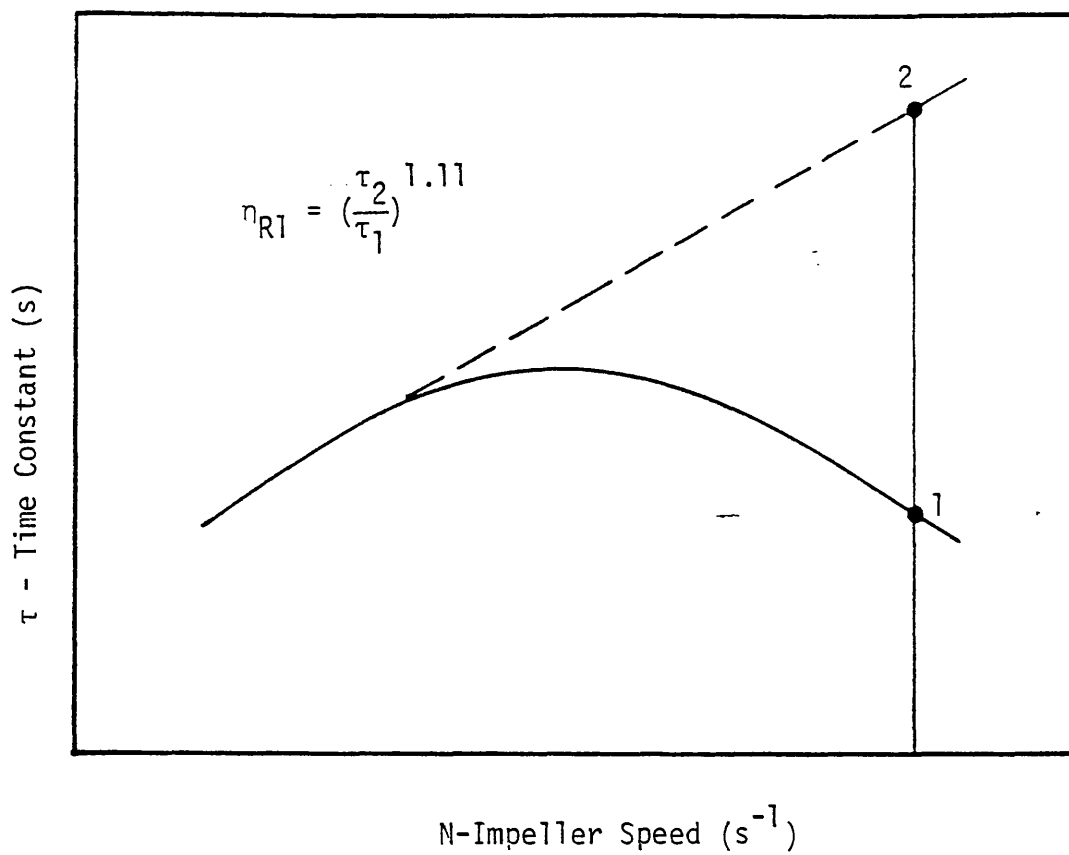
Fig. 5.23 : Approximate estimation of the impeller
dispersion efficiency η_R
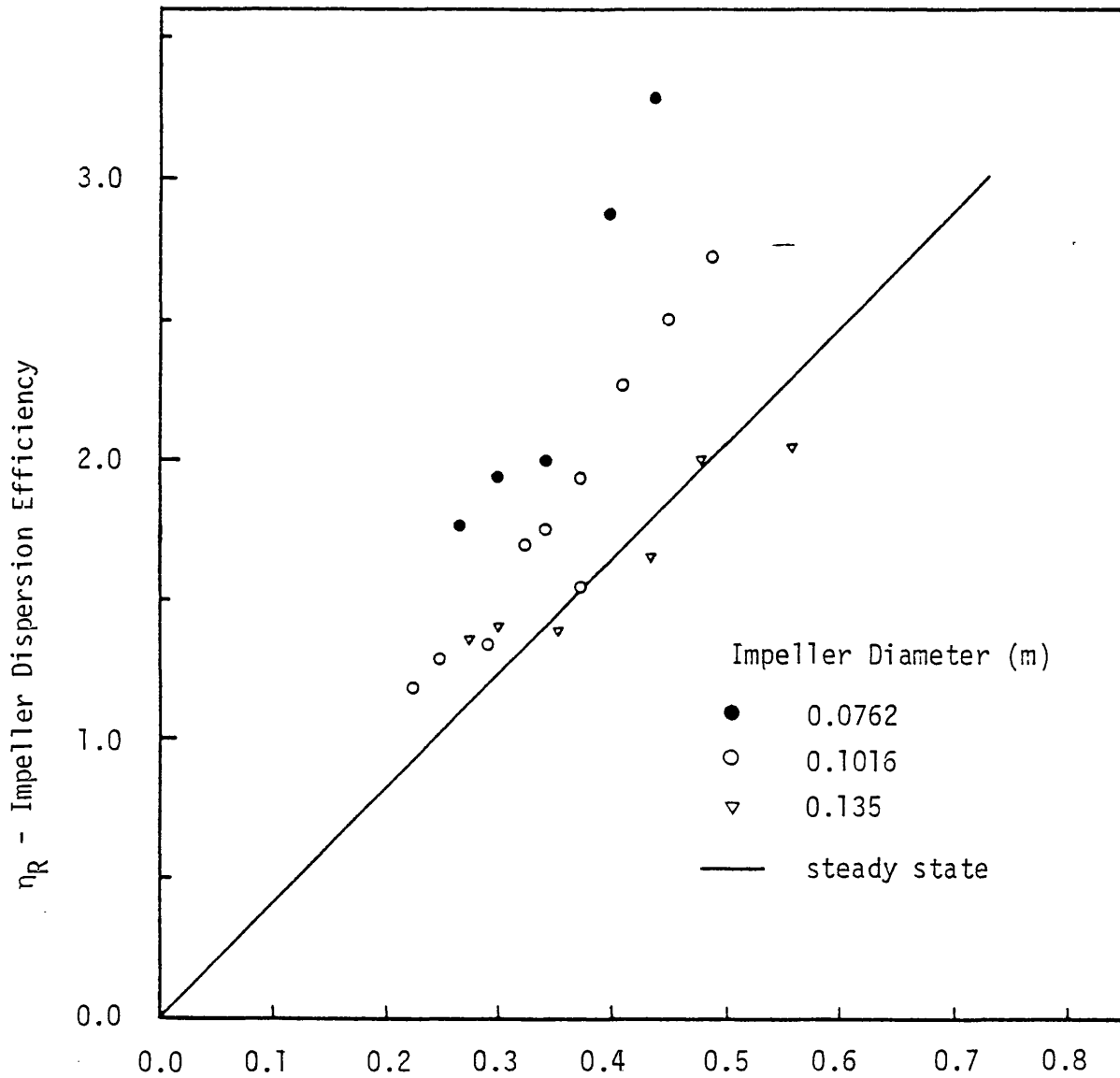
Fig. 5.24 : Estimated values of impeller dispersion efficiency η_R from dynamical tests compared with steady state correlation (Eq. 4.24).

However the general trend showing that n_R is larger when estimated from dynamical measurements is in agreement with the estimation from frequency response analysis (55).

The first order approximation for the cavity stripping response resulting from a negative step input was less successful. The initial slope of the response revealed large deviations from that of a first order system, particularly under gas recirculation conditions (Fig.5.16). However, Fig.5.25 shows a continuous increase of τ for $N > N_{R1}$. By comparing Figs. 5.21 and 5.25 it can be seen that for the cavity stripping response, τ increases with increasing the absolute value of step size which is the opposite of the trend for a positive step. Also the cavity stripping process is in general slower than that of cavity formation. The minima which appear at a speed of about 3 rps in Fig. 5.25, can be identified with the end of the flooding condition. However, this was not confirmed for the other impellers, due to the difficulties in estimating τ in the flooding regime where the change in power was small.

5.3.4 First Order Model of the physical process and its implications

Based on the understanding of the dynamics of the impeller power from the previous sections, a first order model is suggested. The objective is to represent the process by a simple lumped parameter model. This would help to explain the physical implications of using a first order approximation, which yielded a reasonable fit to the measured response data as discussed in the previous section. It should also help to build an overall picture of the gas flow through the impeller region.

Assuming the simple model illustrated in Fig. 5.26, let $q_i(t)$ and $q_o(t)$
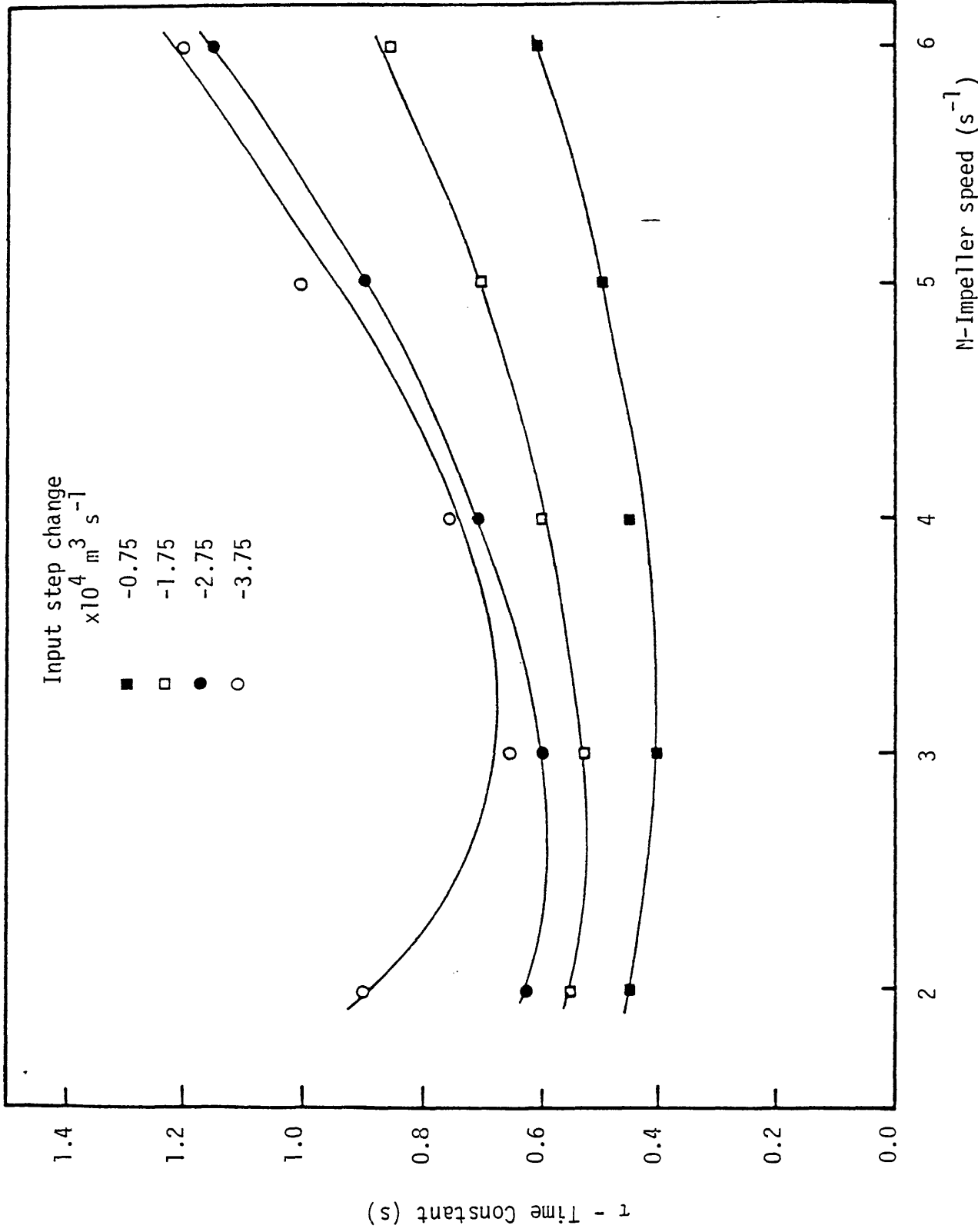
Fig. 5.25 : Time constant of the first order approximation against impeller speed. (D=0.135m). Ungassed final condition.
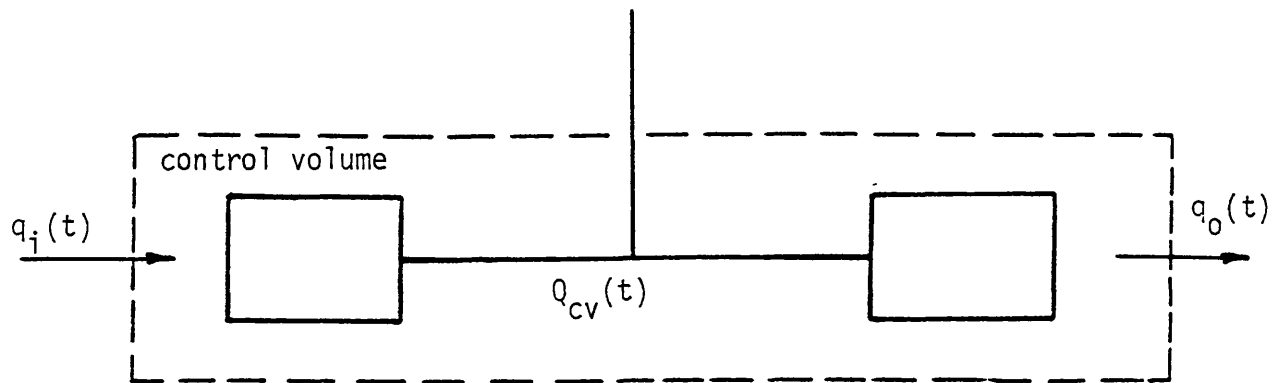
Fig. 5.26 : Transient flow of gas through the impeller cavities.

$Q_{cv}(t)$ total volume of gas cavities at time t.
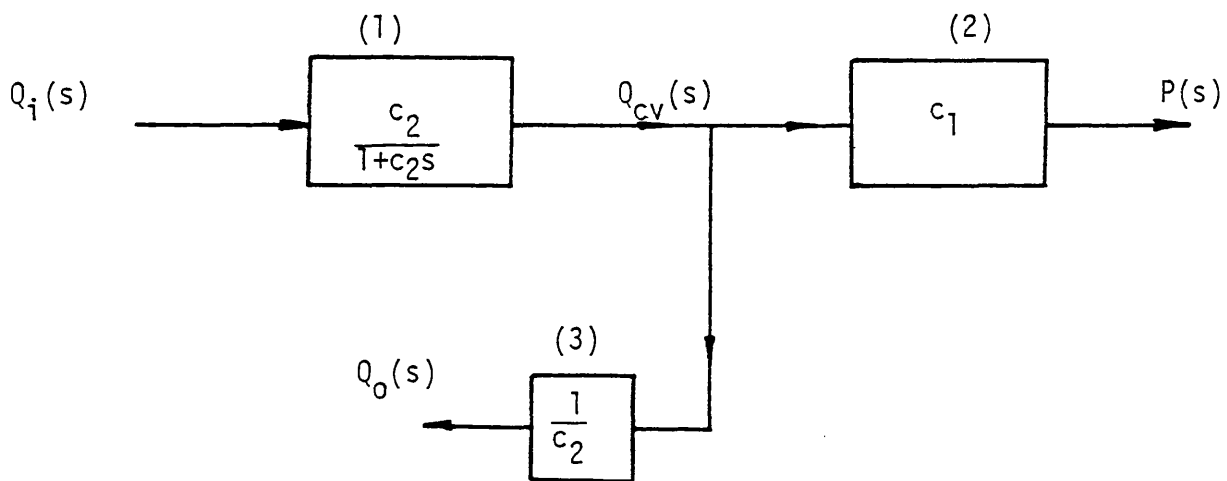
Fig. 5.27 : Block diagram for the first order model.

be the instantaneous gas flow rates into and out of the impeller cavities respectively where $Q_{cv}(t)$ is the total gas volume in all of the formed impeller cavities. By taking a mass balance for gas phase over a control volume enclosing the impeller zone, and assuming constant gas density, then

$$\frac{dQ_{cv}(t)}{dt} = q_i(t) - q_0(t) \qquad\qquad 5.8$$

In order to achieve a model which describes the impeller power dynamical behaviour, the quantities $Q_{cv}(t)$ and $q_0(t)$ in Eq. 5.8, have to be replaced by function expressions in impeller power.

This required the following assumptions :

(1)   Ungassed initial condition

This means

$$Q_{cv}(o) = q_i(o) = q_0(o) = 0 \qquad\qquad 5.9$$
$$\text{for } t<0$$

Defining

$$\bar{P}(t) = Pg(o) - Pg(t) \quad \text{for } t \geqslant 0$$

where $Pg(t)$ is the impeller power at time t measured from applying the change in gas load.

Therefore

$$Pg(o) = Po = \text{Ungassed power consumption at the}$$
$$\text{same impeller speed,}$$

and $$\bar{P}(t) = Po - Pg(t) \qquad\qquad 5.10$$

(2) $$\bar{P}(t) = c_1 Q_{cv}(t) \qquad\qquad 5.11$$

and by differentiation

$$\frac{d\bar{P}(t)}{dt} = c_1 \frac{d Q_{cv}(t)}{dt} \qquad\qquad 5.12$$

This assumption implies that the change in the impeller drag coefficient is a much faster process than that of cavity filling. Hence the dynamics of this can be represented by a simple gain. The constant c_1 is a function of N and D.

(3)
$$q_o(t) = \frac{1}{c_2} Q_{cv}(t) \qquad 5.13$$

This implies that the instantaneous rate of gas discharge from the impeller region is proportional to the instantaneous total gas volume in that region. Also c_2 is a function of N and D.

From Eqs. 5.11 and 5.13

$$q_o(t) = \frac{\overline{P}(t)}{c_1 c_2} \qquad 5.14$$

By substituting 5.12 and 5.14 into 5.8

$$\frac{1}{c_1} \frac{d\overline{P}(t)}{dt} = q_i(t) - \frac{\overline{P}(t)}{c_1 c_2} \qquad 5.15$$

Equation 5.15 is the first order model describing the change of impeller power following a change in gas flow rate. By taking Laplace Transforms of Eq. 5.15, and on rearrangement :

$$\frac{P(s)}{Q_i(s)} = \frac{c_1 c_2}{1 + c_2 s} \qquad 5.16$$

Equation 5.16 is the transfer function of the first order model, where

$c_1 c_2$ is the steady state gain which has units of power per unit gas flow rate as indicated by Eqs. 5.11 and 5.13

c_2 is the time constant which has a unit of time (Eq. 5.13).

Figure 5.27 demonstrates the block diagram for this first order model. Block (1) represents the transfer function describing the process of filling the gas cavities. Block (2) shows the dynamical relationship between the impeller power and the volume of the gas cavities.

Block (3) is merely added to show the dynamical relationship between the gas outflow rate from the impeller cavities and the total volumes of the cavities. From the above description it can be concluded that a first order approximation implies that the process can be represented physically by a process of filling the cavities with the outflow of gas which has a linear resistance (62). The dynamical relationship between the drag reduction and hence the power reduction and the cavities formation is so fast compared with the speed of filling the cavities that it can be neglected. The time constant of the process c_2 can be determined from Eqs. 5.2 and 5.3 as

$$c_2 = \tau \cdot \alpha \frac{ND^3}{q_i(f)}^{0.9} \qquad\qquad 5.17$$

whilst the steady state gain $(c_1 c_2)$ can be estimated from the steady state power correlations presented in Chapter 4.

The model represented in Fig. 5.27 can be extended to include the effects of gas recirculation. Block (4) in Fig. 5.28.a is a gain and time delay element which accounts for the recirculated gas. The time delay represents the circulation time for the gas bubbles before they reach the impeller region, and the gain (c_3) is included to account for the ratio of the recirculated to the sparged gas rates.

The summing point (5) represents the composition of the compound input disturbance described in the previous section and shown in Fig. 5.22. It is also interesting to note that Fig. 5.28.a represents a positive feedback loop, and hence, may indicate possible stability problems for
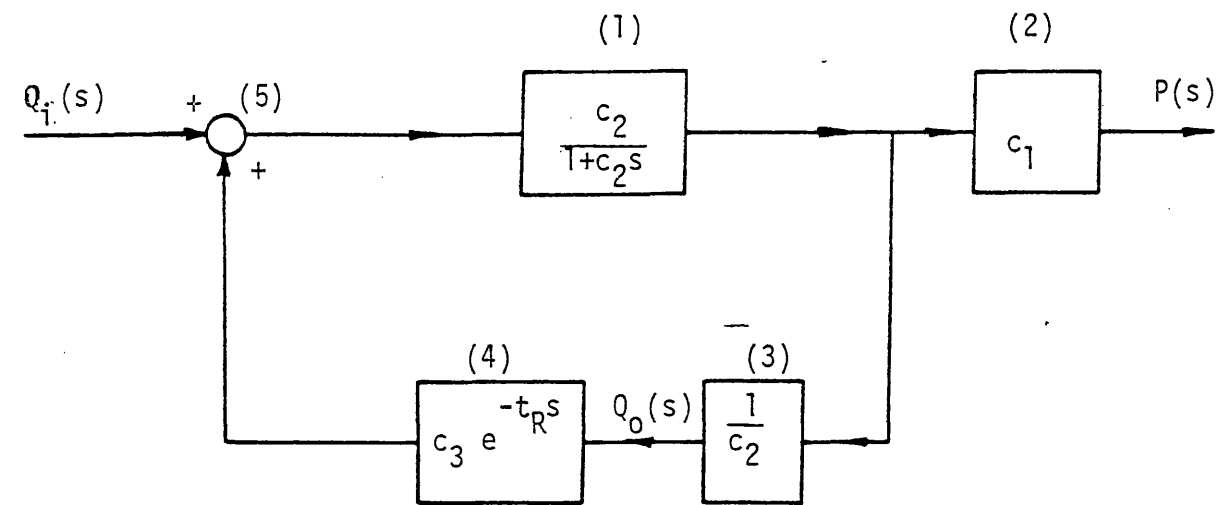
.a
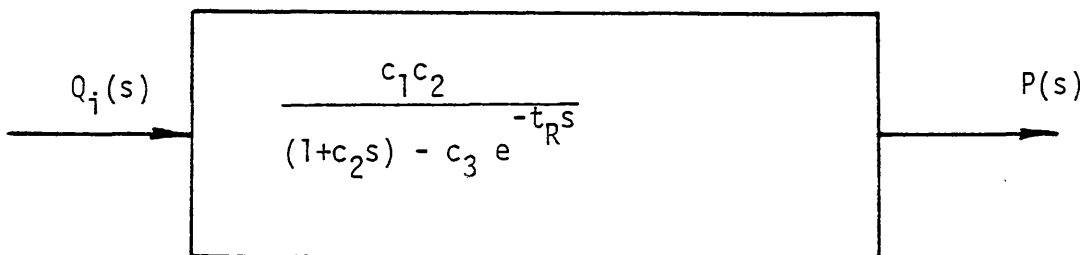
.b

Fig. 5.28 : First order model with gas recirculation.

.a Detailed block diagram

.b Overall transfer function

process of this type. Figure 5.28.b is the overall transfer function as obtained from the detailed block diagram (Fig. 5.28.a) by the standard reduction technique which is used with the closed loop control functions (62). This transfer function has interesting features at two limiting conditions. Firstly, if $t_R \to \infty$, this means a very large circulation time for the gas bubbles, ie, no gas recirculation. In which case, the transfer function is reduced to that describing the original model (see Eq. 5.16). Secondly, if $t_R \to 0$, this means instantaneous recirculation of gas bubbles to the impeller region, an assumption which was used in the approximate estimation for the impeller dispersion efficiency (Section 5.3.4, Eq. 5.7). Under this condition, the transfer function of Fig. 5.28.b can be written as

$$\frac{P(s)}{Q_i(s)} = \frac{c_1 c_2/(1-c_3)}{1+(\frac{c_2}{1-c_3}) s} \qquad 5.18$$

where $\frac{c_2}{1-c_3}$ is the time constant.

As the total input disturbance has increased to $q_i(t) + q_R(t)$ (see Fig. 5.28.a), the value of c_2 will be reduced (Eq. 5.17). In effect, the time constant will be reduced despite any apparent increase contributed by the factor $(\frac{1}{1-c_3})$. This sort of complexity is due to the nonlinear nature of the process and its dependency on the characteristics of the input disturbance, as already stated earlier.

5.4 CONCLUSIONS

1 - The impeller power response resulting from input disturbance in sparged gas flow rate demonstrates a non-linear behaviour which includes a hysteresis type of nonlinearity. Analysis in the frequency domain using linear systems theory clearly identifies salient features of the process dynamics. Included in this

is a resonance phenomenon which is typically found in the response of distributed parameter systems. However, as a result of the hysteresis nonlinearity, the use of Bode plots as obtained from pulse tests, is only capable of providing a qualitative evaluation of the process dynamics.

2 - The impeller power transient response following positive and negative step change in gas flow rate, exhibits a number of peaks which can be related to the number of large gas cavities formed and/or stripped from behind the impeller blades. The general trend is that the cavity formation process is faster than the reverse one of cavity stripping. The cavity formation process becomes faster with the increase in the size of the input disturbance, and also with reduction of the impeller speed and its size. On the other hand, the stripping process becomes faster when the size of the step change in gas flow rate, and/or the impeller speed is increased. The effect of gas recirculation is to increase the speed of gas cavity formation, and to reduce, but to a lesser extent, the speed of cavity stripping.

3 - A first order transient response representation for the gas cavity formation process provided a reasonable agreement with the experimentally determined response. An approximate method for estimating the impeller dispersion efficiency in the recirculation regime obtained from time constant estimates using the first order approximateion, indicated reasonable agreement with the steady state calculations for the case of the largest impeller. However, larger values were obtained for the smaller impellers.

4 - A simple first order lumped parameter model has been developed to describe the process. The first order approximation time constant of this model describes the dynamics of the cavities

filling process, with the outflow of gas represented by a linear

resistance. The impeller drag reduction following the formation of

gas cavities is a much faster process and is represented in the model

by simple gain element.

CHAPTER 6

BUBBLE SIZE

6.1 INTRODUCTION

Mass transfer and chemical reaction in gas liquid dispersions form the basis for many chemical engineering processes. In order to develop design criteria for such processes it is necessary to understand and evaluate some physical properties of the dispersion. Among these are the interfacial area per unit volume, gas volume fraction, and the bubble size distribution.

The physical properties of a dispersion vary from point to point in an agitated vessel, depending on the geometry and size of the impeller and vessel, impeller speed, properties of the dispersed and the continuous phases, and their flow rates. This situation therefore represents a very complex task for theoretical analysis. Instead most previous work has tended to concentrate attention on the determination of the average properties of the dispersion from experimental measurement. Few studies have looked at the distribution of bubble size, although development of a suitable measurement technique has been a difficulty.

The subject matter of this chapter is the bubble size and its distribution in an agitated vessel. A technique developed for measuring the point bubble size and gas holdup is described first, then bubble size measurements in air-water and air-electrolyte systems are reviewed. Correlations have also been developed for the sauter mean bubble diameter for both systems.

6.2 LITERATURE REVIEW

When gas and liquid are brought into contact in agitated vessel, a dispersion is formed as a result of two competing rate processes. These are the rate of break-up of the bulk gas to produce fine bubbles

and the rate of coalescence of these bubbles.   If the agitation

continues for a long enough period of time, a dynamical equilibrium is

established between the break-up and coalescence.   Under such

equilibrium conditions a bubble size distribution for the dispersion is

established for specific operating conditions at a certain location and

also for the tank as a whole.

In a turbulent fluid field, three forces are involved in splitting the

gas bubbles, namely, surface tension, viscous and inertial forces.

For agitated vessels at large Reynolds number (the case in this study)

the viscous effects are negligible.   In 1949 Kolmogorov(65/66)

published his fundamental study on the disintegration of drops in a

turbulent flow.   He showed that whenever the viscous forces are

negligible but the inertial and capillary forces are dominant, the

splitting of gas bubbles depends upon a critical Weber number.   Later

in 1955 Hinze (67) reached a similar conclusion.   By assuming the

simplest case of isotropic homogeneous turbulence he derived the

following relationship for the maximum stable bubble size.

$$d \; max = C \; \frac{\sigma^{0.6}}{\rho^{0.6} \, \varepsilon^{0.4}} \qquad\qquad 6.1$$

where

ε = energy dissipation per unit mass

σ = interfacial tension

ρ = density of the continuous phase

Several experimental studies have been carried out to investigate the

bubble size in gas-liquid agitated dispersions.   Vermeulen et al (68)

measured the specific interfacial area in a closed agitated vessel using

a light transmission method.   Their measurements were conducted at one

position near to the impeller.   The bubble size was estimated by Eq.6.2.

$$d_{32} = \frac{6h}{a} \qquad\qquad 6.2$$

where

d_{32} = sauter mean bubble diameter

h = gas holdup

a = specific interfacial area

They proposed the following correlation :

$$d_{32} = 4.3 \times 10^{-3} \frac{\sigma f \, \mu^{0.25}}{N^{1.5} \, D \, \rho^{0.5} \, \mu_d^{0.75}} \qquad\qquad 6.3$$

where f is a function of the gas holdup and was found to be

$$f = 2.5h + 0.75$$

Calderbank (10) carried out bubble size measurements in geometrically similar mixing vessels. He employed a method of measurement similar to that of Vermeulen et al (68) but repeated the measurements at many different locations in the tank. For air dispersed in 'pure' liquids, he found that :

$$d_{32} = 4.15 \left[\frac{\sigma^{0.6}}{(P/V)^{0.4} \, \rho^{0.2}} \right] h^{0.5} + 9 \times 10^{-4} \qquad\qquad 6.4$$

Equation 6.4 is similar to Eq. 6.1, except for the term for gas holdup ($h^{0.5}$) which accounts for the coalescence of gas bubbles. This effect is explained by the expected dependency of the frequency of bubble coalescence upon their relative proximity and hence upon h (9). Comparison between Eqs. 6.1 and 6.4 reveals that :

$$d_{32} \propto d_{max} \qquad\qquad 6.5$$

Calderbank (10) also measured the bubble size in electrolyte solutions. He observed a progressive drop in bubble size with increase in the amount of solute at fixed impeller speed. At a certain electrolyte concentration a minimum size was reached beyond which further addition

of solute had no effect. The bubble size measured under these
conditions was correlated by

$$d_{32} = 2.25 \left[\frac{\sigma^{0.6}}{(Pg/V)^{0.4} \rho^{0.2}} \right] h^{0.4} \left(\frac{\mu_d}{\mu} \right)^{0.25} \qquad 6.6$$

Lee and Meyrick (9) who used the same light transmission method for
measuring the bubble size in water and different concentrations of
sodium sulphate and sodium chloride solutions, found that :

$$d_{32} = (0.229 + Kh) \left[\frac{\sigma^{0.6}}{(Pgt/V)^{0.4} \rho^{0.2}} \right] \qquad 6.7$$

where K is a constant which decreases as the concentration of the
solution increases, and Pgt is the total power supplied by the impeller
and the gas stream. For pure water, the constant K has a larger
value, but the best fit was found to be :

$$d_{32} = 4.25 \left[\frac{\sigma^{0.6}}{(Pg/V)^{0.4} \rho^{0.2}} \right] h^{\frac{1}{2}} \qquad 6.8$$

which is very similar to Calderbank's correlation.

Recently, Sridhar and Potter (6) using the same light transmission
technique verified and extended Calderbank's correlation (Eq.6.4) to
account for the effect of increasing the vessel pressure. Their
proposed modification is

$$d_{32} = 4.15 \left[\frac{\sigma^{0.6}}{(Pg/V)^{0.4} \rho^{0.2}} \right] \left(\frac{Pg}{Pgt} \right) \left(\frac{\rho a}{\rho g} \right)^{0.16} h^{0.5} + 9 \times 10^{-4} \qquad 6.9$$

where ρa = density of air at operating conditions

ρg = gas density at system conditions

Equation 6.9 implies that the bubble size becomes smaller with increasing
vessel pressure. They used the following expression to calculate the

power supplied by the gas stream Pgs

$$Pgs = 0.5 \ Q\rho_g u^2 + \rho g H Q \qquad\qquad 6.10$$

where u is the velocity of gas at sparger exit.   This equation predicts relatively large value for Pgs if small sparger orifice is used. Discussion of this point is extended in Chapter 7.

Kawecki et al (69) used a photographic method-to measure the bubble size in the impeller discharge stream.   They found that the bubble surface area is best fitted by an Erlang distribution.   Figueiredo and Calderbank (12,70) measured the bubble size in a relatively large size tank of 0.91m diameter using a light transmission technique and an electroresistevity compound probe.   Both methods gave the same bubble size under all operating conditions being almost independent of the position in the tank.   Figueiredo (12) also presented a histogram of the bubble size distribution.

In a very recent study, Weiland et al (71) used a photoelectric probe to measure the bubble size distribution in agitated vessel using fermentation media and water.   They reported a reduction in the bubble size of the order of 10% when the power input was increased from 1 to 10KW/m^3 in the water system.   This was accompanied by increase of h by a factor of three.   These changes, however, do not agree with Calderbank's correlation which predicts a reduction of bubble size by about 30%.   The change of bubble size in the fermentation media was found to be insignificant.

6.3   MEASUREMENT TECHNIQUE FOR BUBBLE SIZE AND POINT GAS HOLDUP

6.3.1   Review of Previous Experimental Techniques

The bubble size in agitated dispersion can be determined by direct or indirect method.   The indirect method involves measuring the specific interfacial area and the gas holdup, from which the bubble size is then estimated from Eq. 6.2.   Such techniques provide only an estimate of the average surface volume (sauter) mean bubble diameter, but information about the mean bubble size or its distribution cannot be obtained. Furthermore, methods which are used to measure the specific interfacial area have certain drawbacks.   The light transmission technique used by many workers (6,9,10,68) is not suitable for high values of gas holdup owing to the effect of multiple scattering (4,18).   It has also been recently suggested that the mass-transfer-effective specific interfacial area is smaller than the total specific interfacial area (72).   Therefore, d_{32} may be overestimated if based on a as measured by a chemical method.

Several methods have been developed for the direct measurement of bubble size in agitated vessels.   Kawecki et al (69) utilised the pumping action of the impeller to transport a sample of bubbles from the reactor through a tube connected to square section column.   The bubbles were then photographed and subsequently measured.   Although this is one of few studies to measure directly the bubble size distribution, it has been criticised.   Despite the tedious effort required, the photographic technique does not provide high accuracy. There may also have been problems due to coalescence (19) in their experiments.   In addition there is doubt whether their measurements were representative of the whole of the tank since the samples were taken at only one position.

Wisdom (19) designed a suction probe to withdraw samples of dispersion. This incorporated a special narrow tip fitted with two electrodes separated by a small distance (1.6×10^{-3}m). These electrodes were connected to a constant voltage supply and resistance. A sample of dispersion was withdrawn using a peristaltic pump. The significantly different conductivities of the two phases caused binary fluctuations in the voltage across the resistance and by feeding this binary signal to pulse counter, the number of bubbles in the sample was determined. By separating the dispersion in a collecting vessel, the volumes of water and air were measured. From these measurements the point gas holdup and the volume average bubble diameter at the point of sampling were estimated.

Figueiredo (12) used an electroresistivity probe which was developed by Burgess and Calderbank (73) for determining bubble size, velocity and shape on a sieve tray and in freely bubbling gas-fluidised beds. The probe used by Figueiredo (12) was of smaller size and had four channels. Each channel formed an individual resistivity circuit conrected to DC power supply. Pulses are obtained as the circuits are broken and made by the passage of a bubble through the array. The signals were fed to a computer and converted into discrete digital representation for analysis by a series of sophisticated logic decisions. This then gave as output the bubble velocity and diameter. Figueiredo's (12) evaluation of the use of this technique in an agitated vessel showed that a successful bubble-probe encounter is a relatively rare event making it a very slow technique in practice. For example, it was reported that the measurements of a sample of 200 bubbles took about 3-4 hours. Another major disadvantage of this technique is that the smallest bubble which can be measured is 0.98×10^{-3}m.

In 1980 Weiland et al (71) published their study for measuring the bubble size by using a photoelectric probe. This technique is similar to the one used in this study. A fine glass capillary tube was used for drawing samples of dispersion from the vessel. Two photoelectric sensors were fitted at set locations along the capillary tube. The speed and length of the bubble slug passing through the capillary were measured from the time elapsed between the detection of the bubble by each of the two sensors and the time for the bubble to pass across one sensor. From these measurements the volume of the bubble was estimated. The probe used was designed so that its response signal was influenced essentially by light absorption. Therefore, it was suitable for measuring the bubble size in fermentation media where the light intensity is weakened due to the presence of micro-organisms. However they did not consider the complex pattern of slug flow in short capillaries (see Appendix A) and particularly the well known effect of the liquid film which surrounds the gas bubbles while they travel through the capillary. This oversimplification of the technique may have led to significant errors in their results. One of the major limitations of their technique was that it was not found to be successful for dispersions with high values of gas holdup. Also the technique did not allow the point gas holdup to be measured.

6.3.2 Capillary Probe Technique

A precision capillary tube was used as a sampling probe for the dispersion. This was connected to vacuum pump via a vacuum jar which incorporated a pressure gauge. A CL155 optical switch made by Clarex Electronics (see Appendix B) was fitted near to the end of the capillary tube by perspex block holder. Figure 6.1 shows the experimental setup, and Figure 6.2 the electrical circuit connections
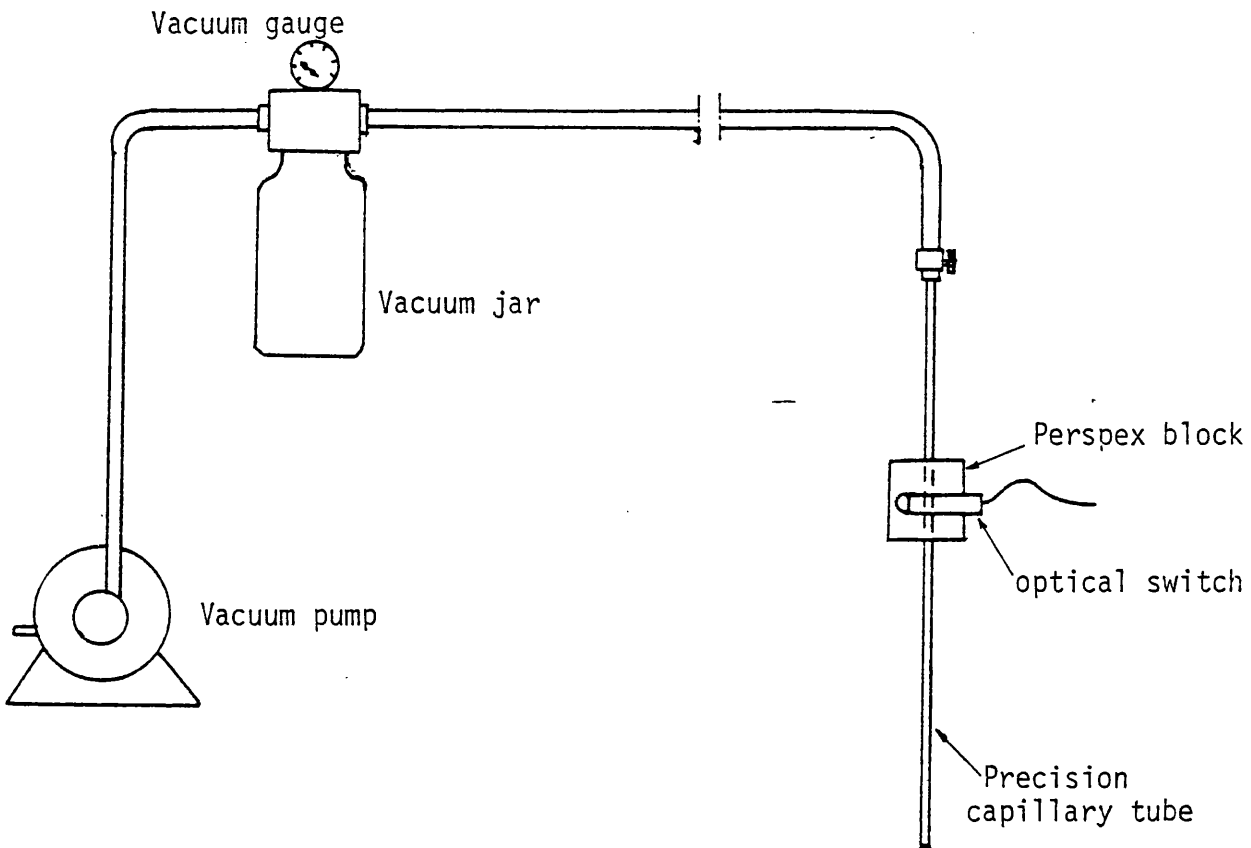
Fig. 6.1 : Experimental setup for measuring bubble size and
point gas holdup.
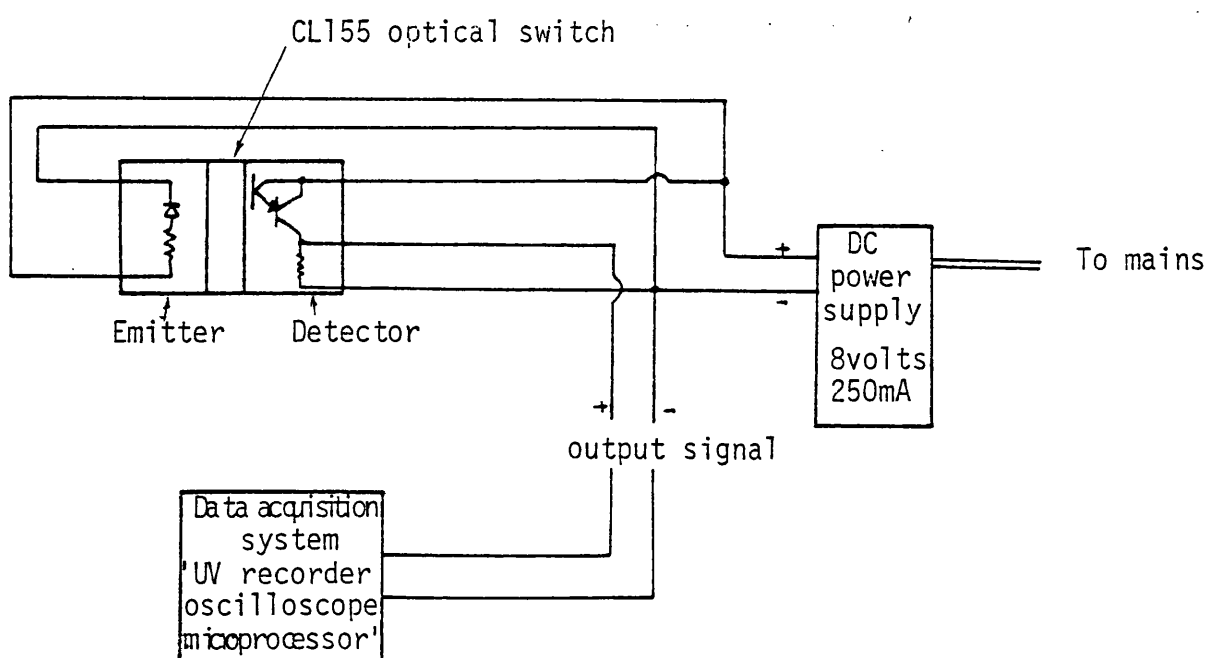
Fig. 6.2: Electronic circuit for measurements and data
acquisition.

to the optical switch. Where the optical switch was positioned, the capillary was wrapped with black tape leaving two windows for the collimated light beam from the emitter to pass to the detector.

The principle of operation is as follows. The funnel-shaped tip of the capillary tube was immersed at the sampling point by vertically traversing through the cover plate on the agitated vessel. A continuous sample of dispersion was drawn through the capillary tube by the vacuum pump. Inside the capillary tube the gas bubbles elongate into a cylindrical shape. The difference in the intensity of light transmitted when an air bubble travels across the light beam from the optical switch causes an increase in the output voltage signal. For continuous flow of the dispersion, the output signal from the optical switch is like a binary signal. The high level voltage represents a gas bubble passing and the low level voltage represents water slug. The signal was then converted into digital form, recorded and processed with the aid of on-line microprocessor. A typical output signal as recorded on a U.V. recorder is shown in Fig. 6.3 (also see Appendix A).

The complexity of the two phase flow inside the capillary tube necessitated calibration of the instrument. The free end of the capillary tube was immersed in water contained in a glass beaker and air bubbles were generated just below the tip using an Agla Micrometer syringe. A variety of hypodermic needles and fine glass capillaries enabled a range of bubbles with accurately known volumes to be produced. The time t_b for each gas bubble was measured by the microprocessor to the nearest 10^{-3}s (PROG(4), Appendix C). These measurements were then used to draw a calibration curve. The calibration procedures were repeated for each capillary tube used for different total pressure

Time

air bubble

water slug

t_s

t_b

t_2 t_1
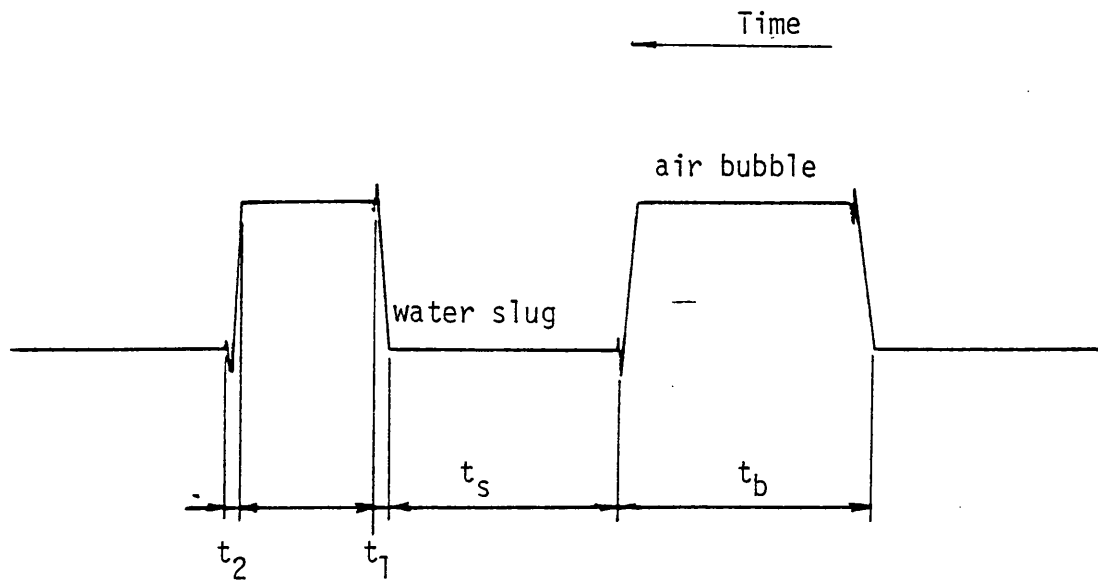
Fig. 6.3 :   Typical output voltage signal from the optical
            switch as recorded with a UV recorder.

t_b time for gas bubble to flow across the detection point

t_s time for slug of water to flow across the detection
            point

t_1, t_2 rise and fall time, respectively, of optical
            switch signal

$$t_1 = t_2 = 0.3 \times 10^{-3} s$$

drops over the capillary tube length. Figure 6.4 demonstrates calibration curves for the three different sizes of capillary tubes used in this study. It is worthwhile to mention that an increase of the pressure drop for tube of the same size shifts the calibration curve to the left relative to the axes.

In practice the calibration curve for each capillary tube at a given pressure drop was fitted to third order polynomial. The bubble volume is then determined from Eq. 6.11

$$V_b = x\ t_b + y\ t_b^2 + z\ t_b^3 \qquad\qquad 6.11$$

where

V_b = bubble volume

t_b = time for gas bubble to pass the detection point

x,y,z = constants depending on capillary tube size, and pressure drop.

It will be shown in forthcoming discussion, that there is a need to sample at different rates in order to estimate the true point gas holdup. For this reason each of the coefficients of the polynomial of Eq. 6.11 was fitted to a second order polynomial as a function of the pressure drop. The general form of the calibration equation is

$$V_b = \sum_{i=1}^{3} (a_i + b_i Pc + c_i Pc^2)\ t_b^i \qquad\qquad 6.12$$

where

Pc = pressure drop over the capillary

For each capillary tube used, a calibration equation of the form of Eq. 6.12 was obtained. If the pressure drop Pc, and the time t_b are measured then the volume of the bubble can be calculated.

Having calibrated the capillary tubes, the use of the technique in
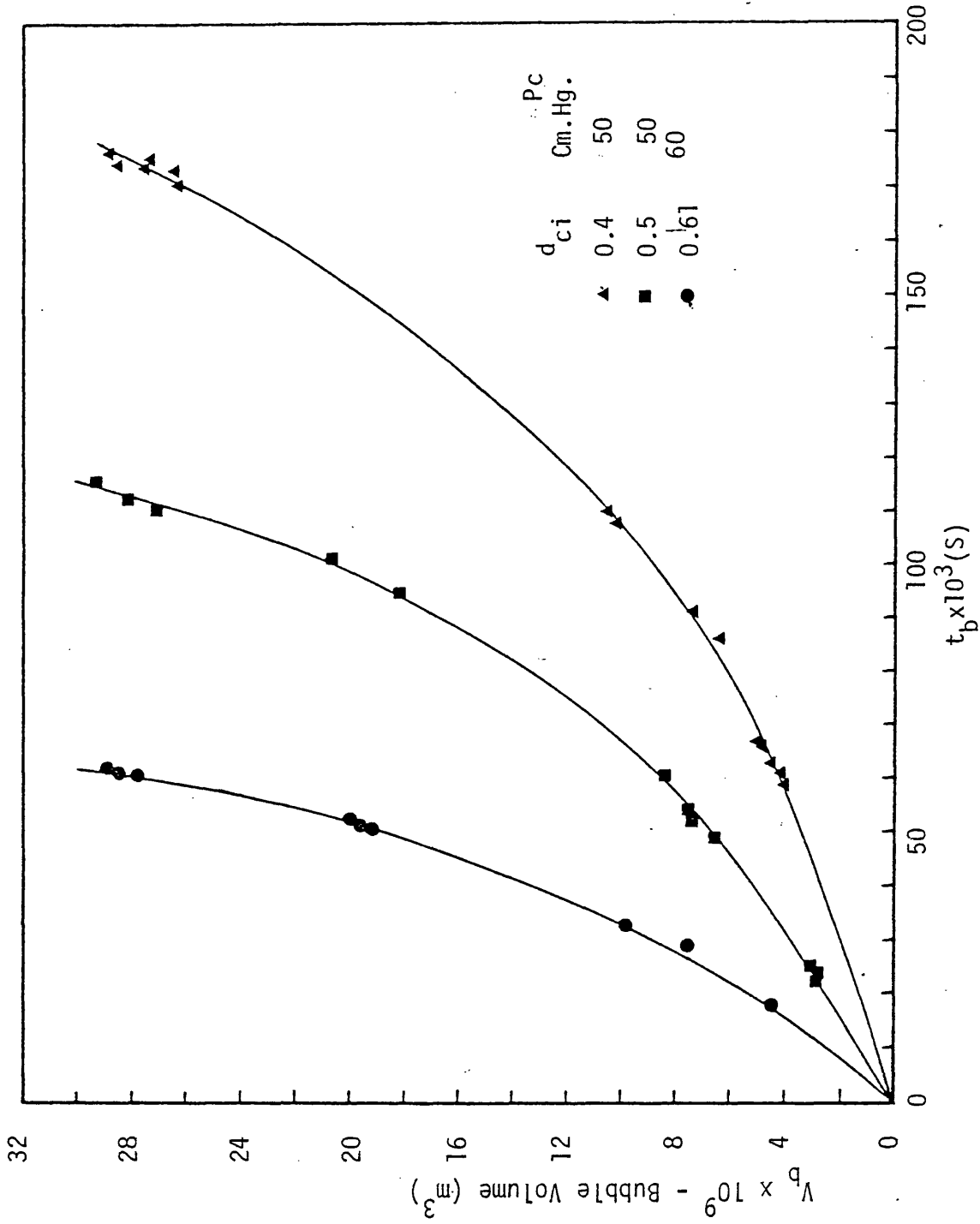
Fig. 6.4 : Calibration curves for capillary tubes of different sizes.

d_{ci} = capillary tube inner diameter x 10^3m, Pc pressure drop over the capillary tube

measuring the bubble size is simple. The tip of the capillary tube
is placed at the desired position for sampling in the agitated vessel.
The vacuum pressure which controls the pressure drop over the capillary
and hence the sampling rate, is adjusted using the regulator valves on
top of the vacuum jar (Fig.6.1). A computer program was written to
sample the output signal of the optical switch at a high rate (PROG(5)
Appendix C). This sampled signal is then processed by the computer
identifying the bubbles and slugs of water from the voltage level of
the signal. The time of each bubble t_b and that of the slugs of
water are determined and by using Eq. 6.12 the volume of each bubble is
calculated. From this, the equivalent spherical bubble diameter is
estimated. The bubbles in the sample are then classified according
to size, and the mean bubble diameter (d_{10}) and the sauter mean bubble
diameter (d_{32}) for the sample are also calculated. Results are then
printed out on a teletype.

The technique was further developed to estimate the gas holdup at the
point of sampling in the dispersion. The representation of the output
signal of the optical switch is as shown in Fig. 6.5. This signal
represents a sample of dispersion taken in a period of time t_t, and
consists of 3 bubbles and four slugs of water. The time taken by the
water slugs to flow across the detection point is

$$t_s = \Sigma t_s = t_t - \Sigma t_b \qquad\qquad 6.13$$

If the average water flow rate through the capillary tube at the same
conditions of sampling is estimated from the total volume of water
collected in the vacuum jar, then

$$h_p = \frac{\Sigma V_b}{\Sigma V_b + t_t \, q_w} \qquad\qquad 6.14$$
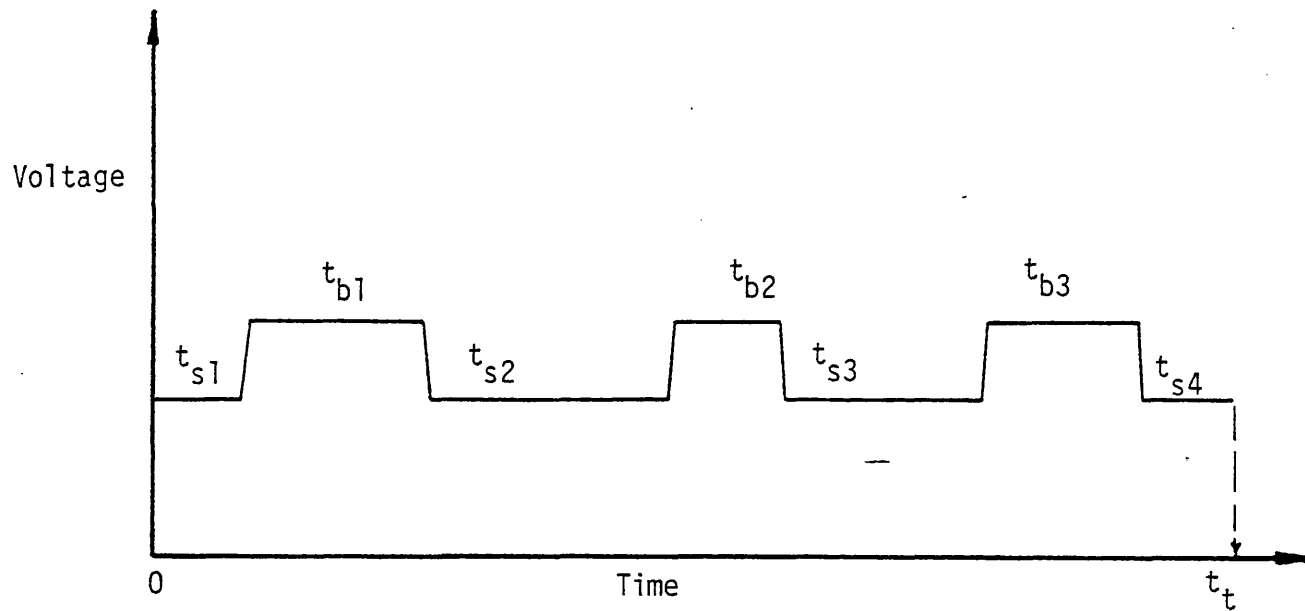
Fig. 6.5 :   Typical output signal of the optical switch during sampling period t_t.
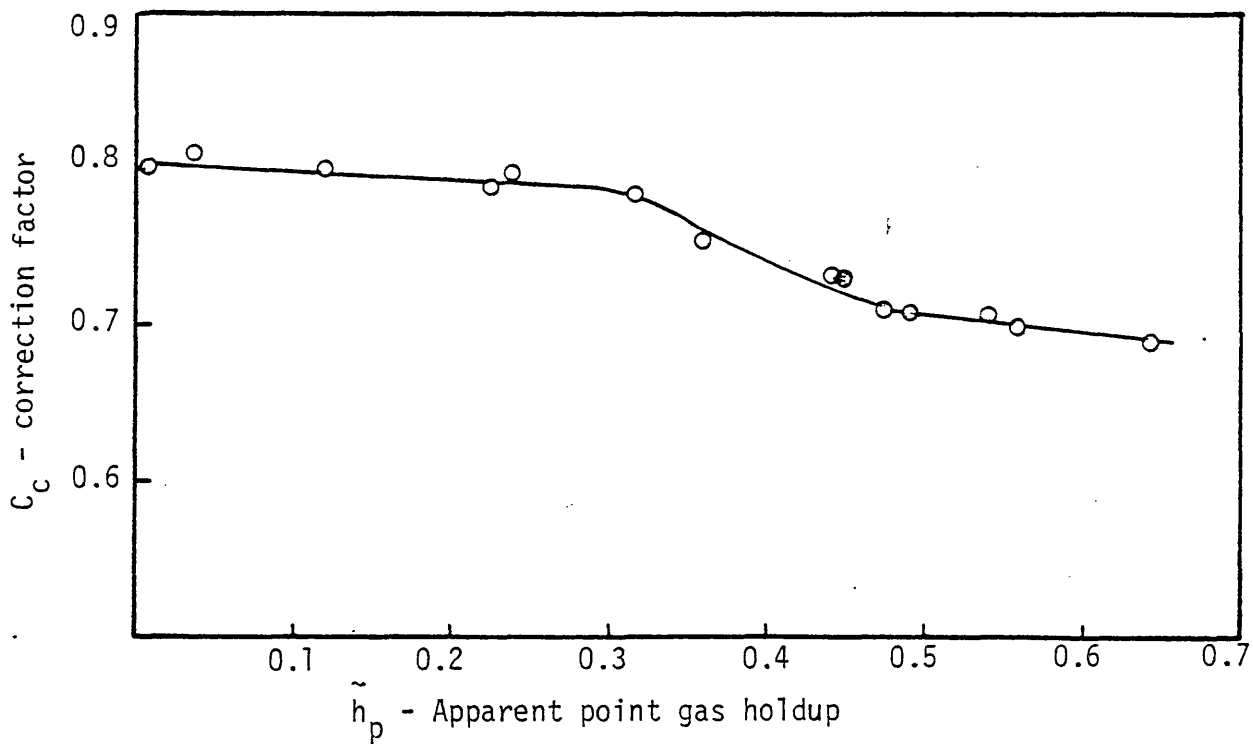
Fig. 6.6 :   Correction factor for estimating point gas holdup for sampling from dispersion of air-0.11M K_2SO_4.

when h_p point gas holdup

ΣV_b total volume of the gas bubbles passing through the capillary during sampling time t_t

q_w average flow rate of water during sampling period.

Equation 6.14 provides a means of estimating the point gas holdup. However, estimating q_w for every sampling run is time consuming and would give poor results if the sampling period is not large enough. For this reason an approximation of the point gas holdup was first calculated.

Let $\quad \tilde{h}_p = \dfrac{\Sigma V_b}{\Sigma V_b + t_s\, q_w'}$ 6.15

where $\tilde{h}_p$ first approximation of h_p

q_w' water only flow rate at the same sampling condition

t_s estimated by Eq. 6.13

By sampling water only by the capillary tubes, it was found

$$q_w' = x'\, p^{y'} \qquad\qquad 6.16$$

where y' equal to 1.3 for the three capillary tube sizes used (inner diameter of 0.4, 0.5 and 0.6×10^{-3} m), while x' increases sharply with increasing the capillary diameter. It is clear that $\tilde{h}_p$ can be estimated with the aid of Eqs. 6.15 and 6.16 without need to estimate the water sampling rate during sampling period.

To calculate h_p from Eq. 6.14 a correction factor was introduced. A number of dispersion samples were taken, and for each h_p and $\tilde{h}_p$ were calculated by Eqs. 6.14 and 6.15 respectively. The correction factor was estimated by

$$C_c = h_p / \tilde{h}_p \qquad\qquad 6.17$$

Figure 6.6 demonstrates the correction factor against $\tilde{h}_p$ when samples were taken from an air - 0.11M K_2SO_4 dispersion. It is important to indicate that the correction factor for sampling from tap water was close to one. It is not easy to explain the apparent different values for C_c for air-water and air-electrolyte solution dispersions. However, it may be attributed to a larger error incurred in measuring t_b for thesmaller bubbles in the case of air-electrolyte solution dispersions, which may have caused a larger error in estimating $\overline{t}_s$ which is used in Eq. 6.15 to calculate $\tilde{h}_p$.

By combining Eqs. 6.15 and 6.17

$$h_p = C_c \frac{\Sigma V_b}{\Sigma V_b + t_s \ q_w^r} \qquad\qquad 6.18$$

In practice the computer program (PROG(5) Appendix C) was supplied with Eqs. 6.15 and 6.16 and the approximate gas holdup $\tilde{h}_p$ was one of the outputs. The corrected gas holdup h_p was estimated with the aid of the correction factor curves (Fig. 6.6).

Calderbank (10) and Wisdom (19) used different sized sampling probes to measure the point gas holdup in agitated vessels. Calderbank (10) did not report any effect for the sampling rate on the measured values of point gas holdup. Wisdom (19) and later Nienow et al (4) discussed this point. Wisdom (19) indicated that the use of too slow a sampling rate would allow bubbles to be swept away from the sampling intake. On the other hand, if it is too fast it would cause bubbles to be preferentially attracted to the sampling region. Having studied a range of sampling rates, the latter effect was found to be less significant, and Wisdom (19) decided to choose a sampling rate such that the velocity in the probe throat was larger than the impeller tip speed. Nienow et al (4) pointed to the difficulties in achieving

isokinetic sampling in stirred tank.

To study the sampling rate effect, the entrance zone at the capillary tube tip was first examined. Fine bubbles were generated near to the capillary tube tip in stagnant water. It was found that the capture zone at the entrance covers almost half-a-sphere extending from the periphery of the funnel tip. If the bubble trajectory does not cross this attraction zone, it will not enter the capillary tube. This is in agreement with aforementioned observations of Wisdom (19), ie, preferential attraction of bubbles at high sampling rate is not significant. Figure 6.7 demonstrates measurements of the point gas holdup using Eq.6.18, against the total pressure drop in the capillary tube. The apparent point gas holdup increases with increasing sampling flow rate (function of pressure drop) and, after reaching a maximum, it starts to drop. This phenomenon is interpreted schematically in Fig. 6.8. The gas sampling rate q_g increases as the total sampling rate of dispersion increases up to critical point (1) after which it becomes constant. At this critical sampling rate, every bubble passing by the attraction zone of the probe is sucked in. Any further increase in the sampling rate leads to an increase of the water flow rate through the tube, with no further increase in the rate at which gas bubbles are sampled. This explains the drop in the apparent gas holdup after reaching a peak (point (2)).

It could be argued that the sampling rate which gives true indication of the point gas holdup should be when every bubble reaching the tip of the probe is sucked in to the tube, and the sampling rate of the gas bubbles should just equal the rate at which bubbles arrive at the point of sampling. Point (1) on the q_g curve in Fig. 6.8 is the only point which satisfys these conditions. The maximum in the apparent gas
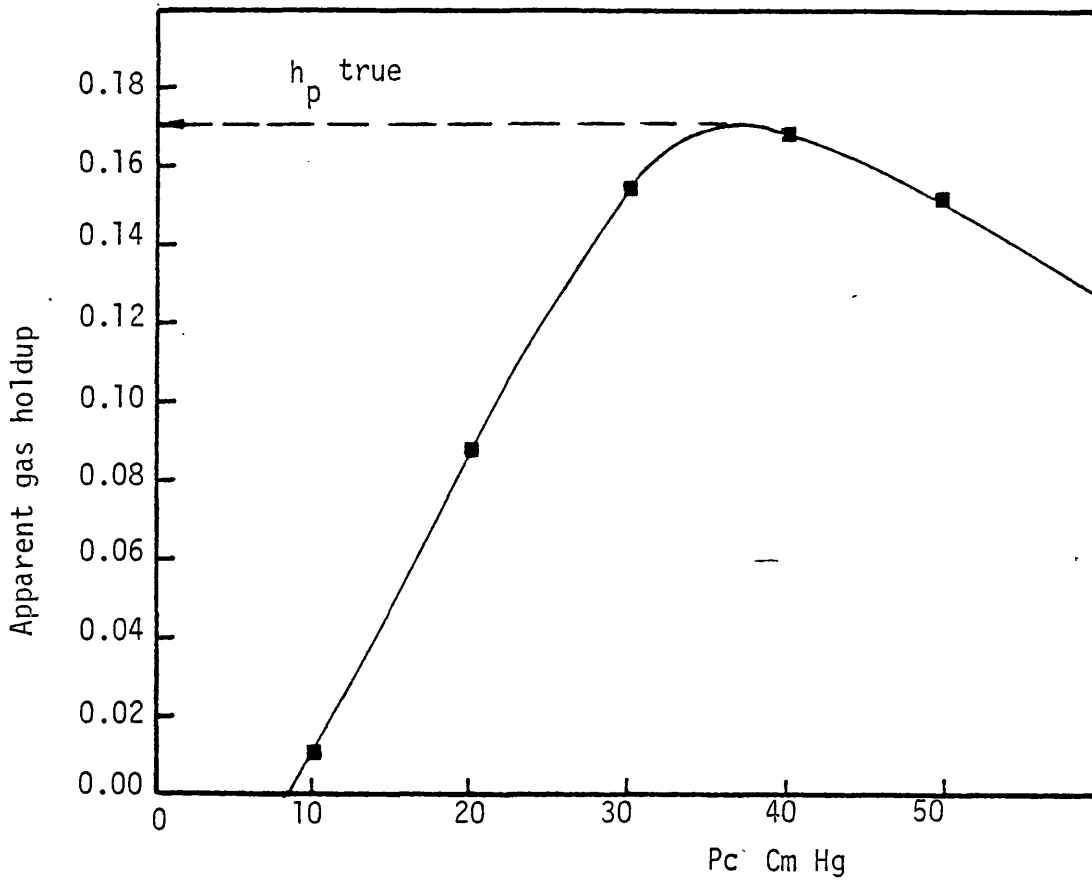
Fig. 6.7 : Apparent gas holdup against total pressure drop in
the capillary tube, sampling at a point in the
agitated vessel.
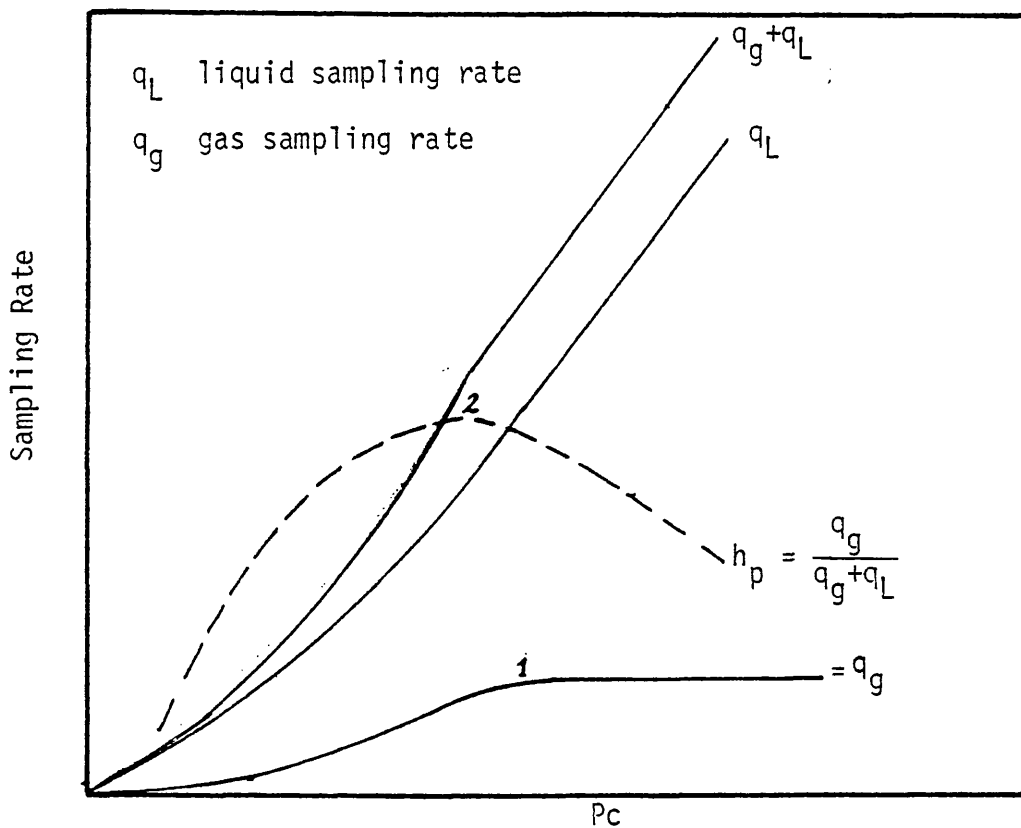
Fig. 6.8 : Schematic diagram to illustrate the
the change of the measured point gas holdup
with the total pressure drop in the capillary tube.

holdup curve (point (2), Fig. 6.8) is close to point (1), but they do
not necessarily coincide. It was concluded, therefore, that the
maximum gas holdup measured at different sampling flow rates should be
a good estimate of the true gas holdup at that point. In practice,
the sampling from any point in the tank was repeated at different
sampling rates and the maximum was calculated. However, it is important
to mention that, irrespective of the sampling rate, the bubble size is
correctly determined by the calibration equation (Eq. 6.12), which
includes the effect of sampling rate.

6.3.3 Accuracy and Reproducibility

The technique which has been described in Section 6.3.2 raises a number
of points concerning its use for the sampling and measurement of gas
bubbles from a two-phase turbulent dispersion in an agitated vessel.
Prior to establishing the direct calibration of the device, the
technique was checked thoroughly by examining the nature of the two-
phase flow inside the capillary tube. For convenience of presentation,
critical review of the relevant literature on the capillary slug flow
is included in Appendix A. The derivation of a semi-empirical
relationship between the volume of the bubble and the time required for
it to pass a given location in the capillary tube (detection point) is
given in this appendix. When this relationship was compared with the
calibration curve, a reasonable agreement was found.

(1) Dynamic pressure effect at sampling point

As explained previously the calibration curves were
obtained by sampling bubbles with known volumes from a stagnant liquid.
In the real sampling process of the dispersion from an agitated tank,
however, dynamical pressure gradients exist. To study this effect,
the sampling rate of water only, from stagnant liquid, and from an

agitated tank with the impeller rotating at maximum speed, were measured and compared. No significant change of the water sampling flow rate was observed for these two cases when the pressure gauge on the vacuum jar (Fig. 6.1) indicated the same reading. Therefore it was concluded that the dynamical pressure is small compared to the total pressure drop in the capillary tube and consequently has negligible effect on the sampling process. On the other hand, the effect on sampling the gas bubbles is automatically taken care of by the method of sampling at the optimal sampling rate described previously. In general, the optimal sampling rate depends on the impeller speed, gas flow rate, the location of sampling, and the direction of the flow at the location relative to the orientation of the capillary tube.

(2) <u>Bubble interaction effects inside capillary tube</u>

Calibration of the probe was done with only a single bubble passing through the tube, but when sampling the dispersion, more than one bubble could be flowing inside the capillary tube. This leads to a complicating effect because of axial interaction between the bubbles. To investigate this, two optical switches were used to observe the gas bubble slugs at two different positions along the capillary tube. By examining the simultaneously recorded output signals, it was found that

(a) more than 80% of the bubbles in the sample behaved as though only a single bubble were flowing inside the tube, and hence any axial interaction effect could be neglected.

(b) for the remainder of the sample, axial interaction between bubbles was observed to take place. Thus the trailing

bubble accelerates due to the wake effect of the leading bubble, while the leading bubble accelerates due to the expansion of the trailing one.

This type of axial interaction effect was found to be proportional to the size of the bubbles. The estimated error caused by these phenomena was found to be less than 10% underestimation of the total gas volume in a sample. The measured bubble size distribution is also expected to be slightly skewed to the right.

(3) Breakage and coalescence of bubbles inside the capillary tube

Two optical switches were also used to observe the gas bubbles near to the capillary tube entrance and at the exit. It was found that the coalescence of gas bubbles never occurred during the wide range of sampling experiments conducted in this study. However, breakage of bubbles did frequently occur if the bubble volume exceeded a critical volume. This volume was found to be dependent on both the capillary tube internal diameter and the sampling rate. Bubble break-up inside the capillary tube produced smaller bubbles which then continued to travel close together. The distance separating successive pairs of secondary bubbles was found to be very small compared with that separating the original bubbles. Based on this observation, a simple solution for the bubble breakage problem was found. In processing the output signal from the optical switch, the computer program (PROG(5), Appendix C) was designed to measure the time between every two successive bubbles in the sample. If that time was less than certain value (9×10^{-3}s) these bubbles were considered to be the result of breakage of a larger bubble. Subsequently, the width of the pulses associated with these bubbles are added and processed as one pulse representing one bubble.

The bubble size measuring technique has been used successfully with air-water as well as with the air-electrolyte solution dispersions. The range of the bubble size differs significantly for these two systems.

With the 0.4, 0.5 and 0.61 x 10^{-3}m internal diameter capillary tubes

used as the sampling probes in this study, it was possible to measure

bubbles with equivalent diameter of 0.4 x 10^{-3} to 5.0 x 10^{-3}m. An

important factor which determines the accuracy of measurements is the

rate of sampling of the output analog signal from the optical switch.

For air-water system a sampling rate of 1000 per second was found to

be sufficient, while for the air-electrolyte system, where smaller

bubbles are observed, the sampling rate was increased to 2000 per

second.

A main advantage of this technique, in addition to the wide range of

the bubble size that can be measured, is the high speed with which the

bubbles are sampled and measured.   Naturally the speed of the technique

depends on the point gas holdup at the position of sampling, ie, the

availability of bubbles and their sizes.   For example, the average

number of bubbles found in a sampling period of 5 seconds from an air-

water dispersion was about 30.   The processing of the data required

about 3 minutes on the high speed microprocessor.   This means that a

sample of 200 bubbles would require about 20 minutes for sampling,

processing and printing out the results, ie, about 10 times faster than

the electroresistivity probe technique which was used by Figueiredo (12).

For air-electrolyte solution system, the size of bubbles was much

smaller, and the number much larger.   On average 200 bubbles were

detected in a sampling period of 2 seconds, which needed about 5 minutes

for data acquisition and analysis.   It is evident that the technique

is about four times faster when used with a 'non-coalescing' system as

may be typically employed in industrial applications.   It should also

be mentioned that the sampling time was limited by the capacity of the

computer to store the sampled data (32K words RAM).   Therefore, to

obtain a large enough sample of bubbles which were representative of the conditions at the sampling point, sampling was repeated until a sufficiently large sample was obtained.

An important measure of any experimental measuring technique concerns the reproducibility of results. Figure 6.9 demonstrates the bubble size distribution obtained for two successive samples from air-electrolyte dispersion. It is clear from the distributions and the relevant statistics illustrated on the figure, the good reproducibility of measurements. For air-water system larger deviations were observed when the measurements were repeated. Figure 6.10 shows bubble size distributions for two samples from air-water dispersion performed under identical conditions but taken 3 days apart. The differences between the two distributions may be attributed partly to the sensitivity of the bubble coalescence rate in pure liquids to any impurities in the system and to the relatively small size of the samples.

6.4   RESULTS AND DISCUSSION

The bubble size was measured at 15 different locations in the agitated tank, as indicated in Fig. 6.11. At each location the measurements were repeated at five or six impeller speeds, and at three gas flow rates in each case. Two impellers were used with $\frac{D}{T}$ = 0.375 and 0.5. Two different liquids were used. Tap water is an example of a 'pure' liquid where the bubble coalescence rate is high and the average bubble size relatively large, and potassium sulphate solution a 'non-coalescing' system. Results for each of these two systems are discussed separately.
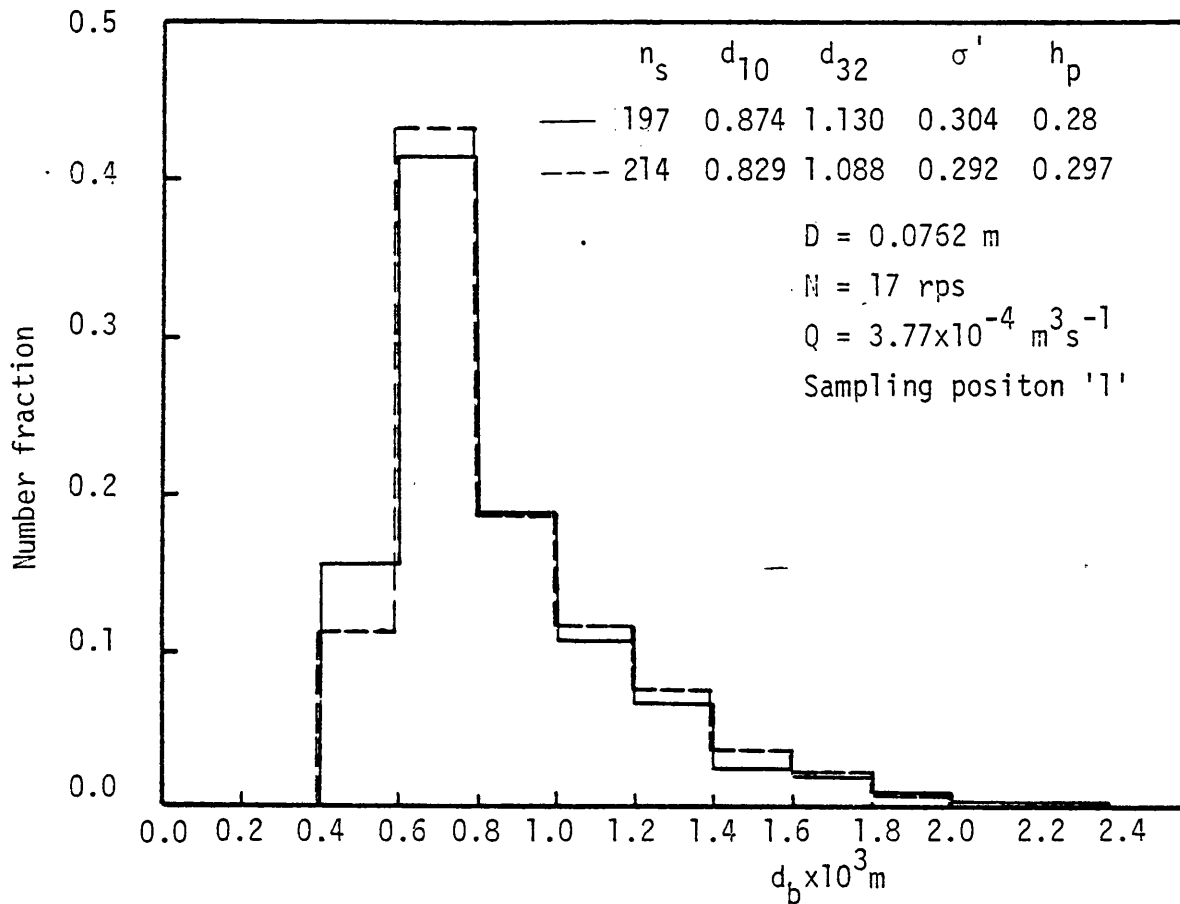
Fig. 6.9 : Bubble size distribution of two successive samples from air-0.11M k_2SO_4 dispersion.

n_s = sample size (bubbles), σ' = standard deviation.
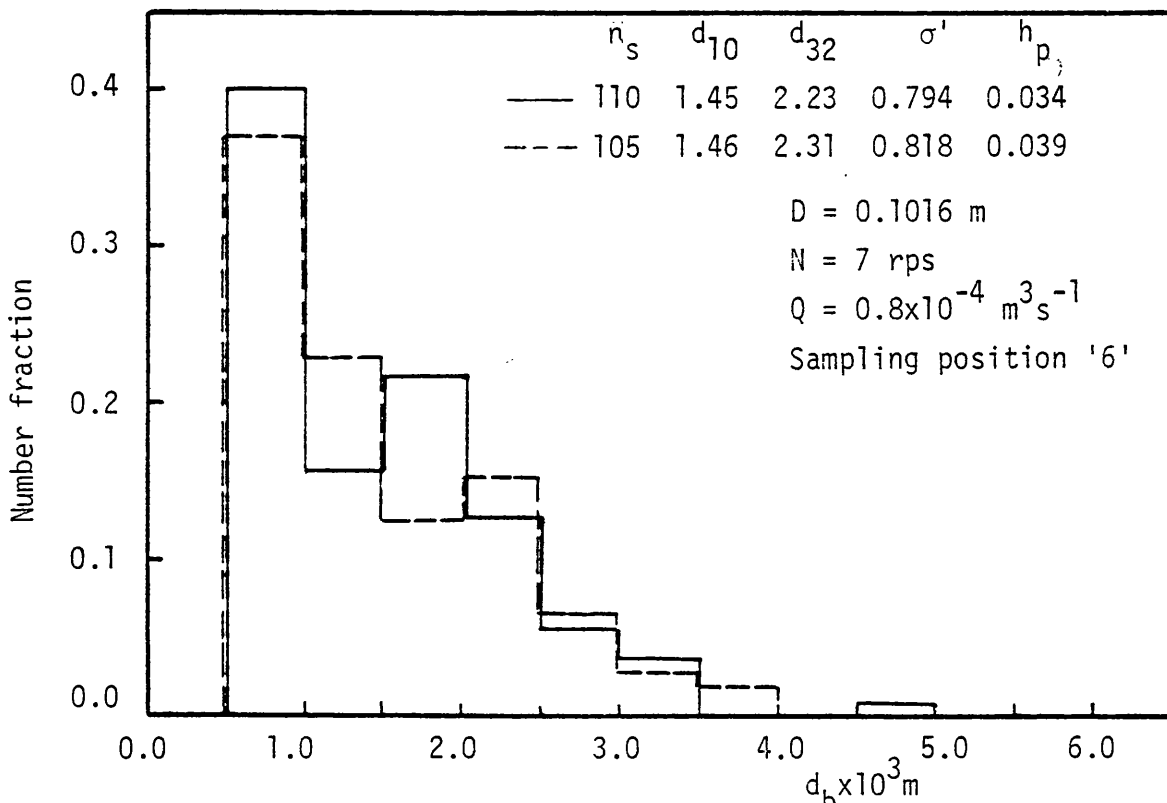
Fig. 6.10 : Two bubble size distributions taken 3 days apart. air-tap water dispersion. n_s = sample size (bubbles) σ' = standard deviation
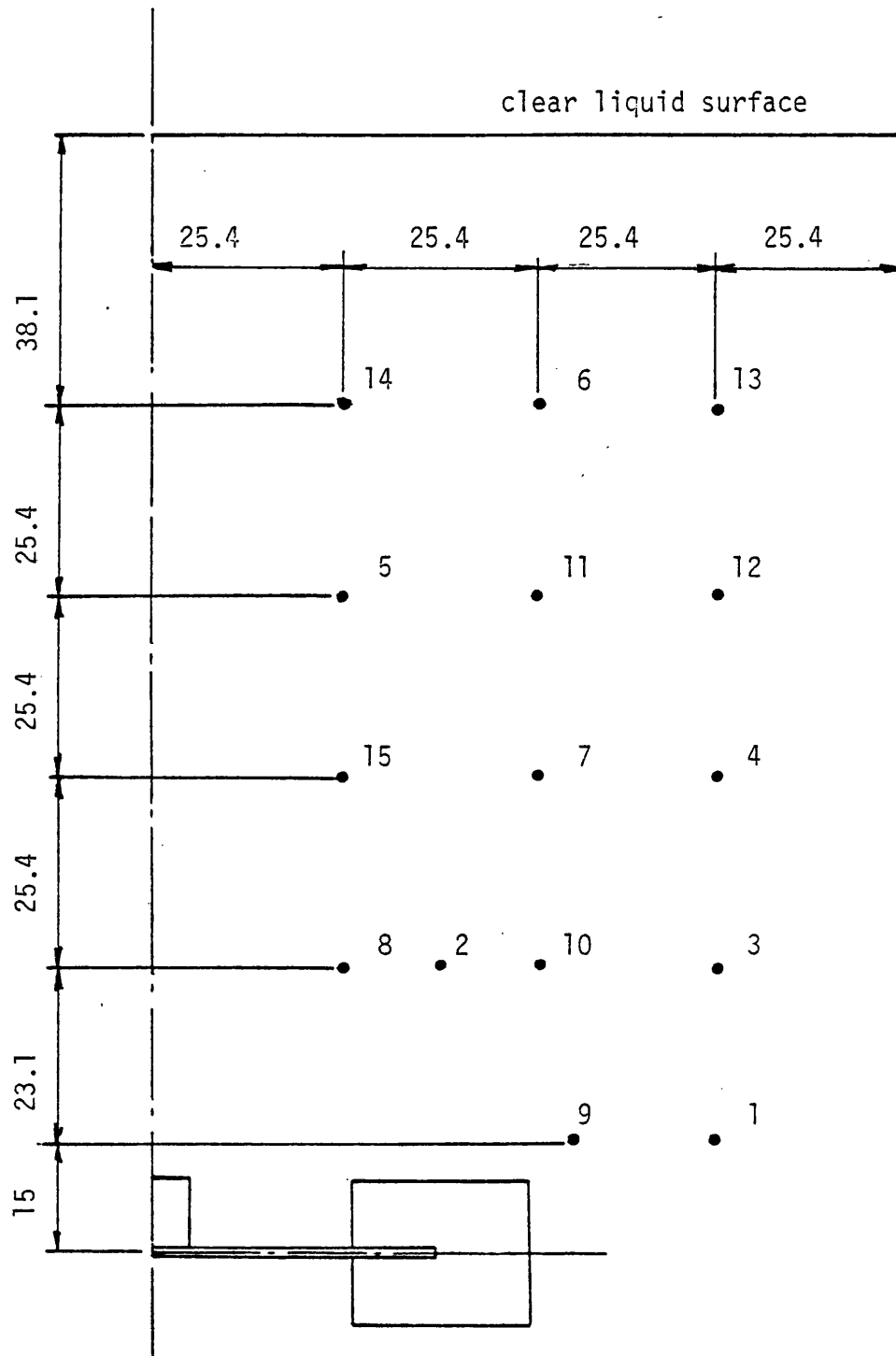
Fig. 6.11 : Sampling locations in the agitated vessel.
Scale 1:1 (dimension in $m \times 10^{-3}$)

Before discussing the results, it is important to clarify some points regarding the calculations and presentation of the experimental measurements. For each histogram (hereafter called bubble size distribution) a number of statistics are given. These statistics were calculated from the samples and not from the grouped data as presented in the form of histograms. The number of classes in each histogram is rather limited. Therefore, if these grouped data were used to calculate the statistics of the distributions biased estimates would have been obtained. The statistics which are calculated for each sample are

(1) Mean Equivalent bubble diameter d_{10}

$$d_{10} = \frac{\sum\limits_{i=1}^{n_s} d_{bi}}{n_s} \qquad 6.19$$

where

d_b equivalent bubble diameter assuming its shape is spherical

$d_b = \sqrt[3]{\frac{6}{\pi} V_b}$

V_b =   the measured volume of bubble

n_s =   number of bubbles in the sample

(2) Sauter Mean bubble diameter d_{32}

$$d_{32} = \frac{\sum\limits_{i=1}^{n_s} d_{bi}^3}{\sum\limits_{i=1}^{n_s} d_{bi}^2} \qquad 6.20$$

(3) Coefficient of variation C_v

The coefficient of variation was selected to measure the spread of the distribution relative to its mean. It is calculated by Eq. 6.21

$$C_v = \frac{\sigma'}{d_{10}} \qquad 6.21$$

where

$\sigma' =$ standard deviation

$$\sigma'^2 = \frac{\sum\limits_{i=1}^{n_s} (d_{bi} - d_{10})^2}{n_s}$$

For some distributions, and for convenience of calculation, these statistics were estimated from the grouped data. That will be referred to when used.

6.4.1 Tap-water-Coalescing System

6.4.1.1 Bubble size distributions

The point measurements of bubble size in the air-water dispersion reveal that the bubble size depends on the position of sampling in the tank, the impeller speed and size, and the gas flow rate. This is in contradiction to the reported observations of the recent study of Figueiredo and Calderbank (70). Figures 6.12 and 6.13 show the change of point bubble size with location in the tank and impeller speed for two impeller sizes. These results show that the smallest bubble size is normally observ~d in the impeller r gion and near to the tank walls. The impeller zone seems to cover a small proportion of the tank volume. The spatial distribution of bubble size depends on the impeller speed and the regime of gas-liquid mixing.

In the flooding regime (N=3 and 5 s^{-1} in Figs. 6.12 and 6.13 respectively) the largest bubbles are at the mid radial locations (positions 10, 7, 11, 6, Fig. 6.11). For these locations the bubble size increases as the liquid surface is approached. The bubbles rise more or less vertically past the impeller disc and hence the ensuing coalescence produces larger bubbles.

speed = 3 s^{-1}

$\overline{d_{32} = 2.73}$

3.0	3.5	3.2
2.5	2.9	2.3
1.1	3.1	2.6
2.9	2.0	2.5
	2.5	2.3

speed = 5 s^{-1}

$\overline{d_{32} = 3.29}$

	3.3	
3.7		3.1
3.6	3.3	3.3
3.3	3.3	3.1
3.4	3.4	3.1
	3.0	2.0

speed = 7 s^{-1}

$\overline{d_{32} = 3.3}$

3.2	3.3	3.6
3.5	3.2	3.2
3.3	3.3	2.8
3.7	3.7	2.8
	3.1	1.9

speed = 9 s^{-1}

$\overline{d_{32} = 3.07 \ s^{-1}}$

3.4	3.1	3.5
3.3	3.0	3.0
3.1	3.3	2.5
3.1	3.4	2.5
	2.4	1.5

speed = 11 s^{-1}

$\overline{d_{32} = 2.81}$

3.0	2.8	3.1
3.4	3.1	2.3
2.8	2.8	2.3
3.0	2.9	2.3
	2.0	
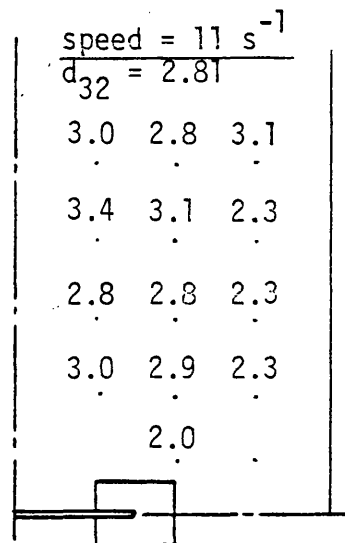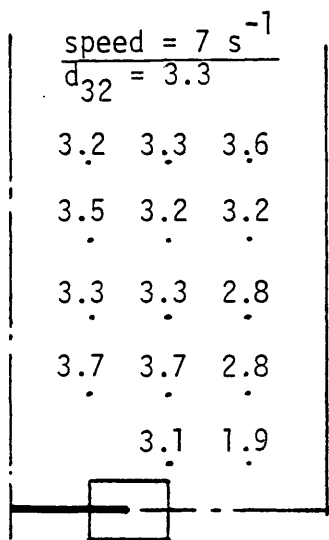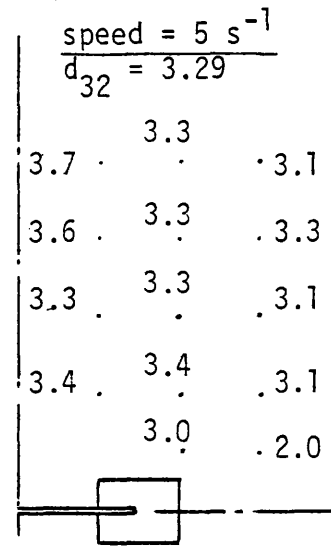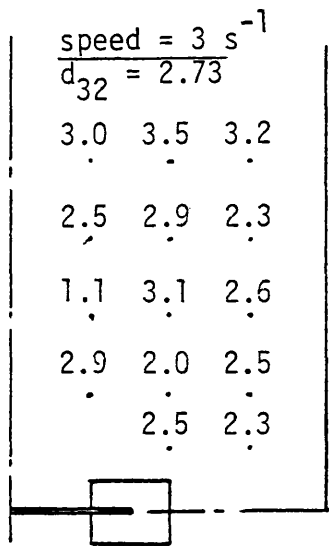
Fig. 6.12 : Matrix of point surface volume mean diameter($\times 10^3$m)

D = 0.1016m , Q = 1.95$\times 10^{-4}$ m^{3}s^{-1}

Air-tap water system

d_{32} = Average bubble diameter over the tank x 10^3m

speed = 5 s^{-1}

d_{32} = 2.91

2.8	3.5	3.0
2.7	3.1	2.8
3.2	2.9	2.3
3.0	2.3	2.9
	2.7	3.1

speed = 8 s^{-1}

d_{32} = 3.32

3.2	3.2	3.0
3.5	3.2	3.2
3.6	3.6	3.1
3.6	3.4	3.0
	3.2	3.2

speed = 11 s^{-1}

d_{32} = 3.46

3.4	3.5	3.4
3.8	3.5	3.3
3.4	3.4	2.9
4.0	3.7	3.2
	3.4	3.0

speed = 14 s^{-1}

d_{32} = 3.47

3.7	3.6	3.5
3.9	3.5	3.3
2.8	3.4	3.1
3.9	3.8	3.1
	3.3	2.9

speed = 17 s^{-1}

d_{32} = 3.29

3.7	3.4	3.3
3.8	3.2	3.1
3.9	3.2	2.7
3.8	3.7	2.9
	2.8	2.7

speed = 20 s^{-1}

d_{32} = 3.27

3.7	3.2	3.2
3.6	2.9	2.7
3.8	3.3	2.6
3.2	3.2	2.7
	2.6	2.5
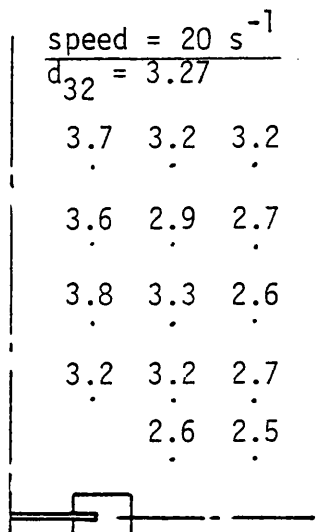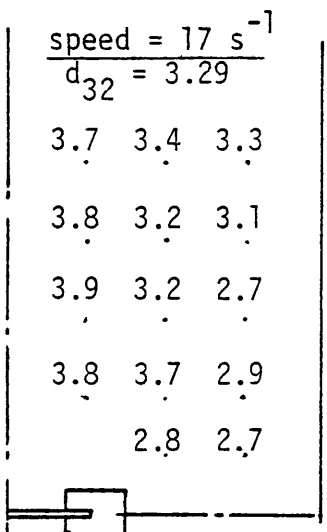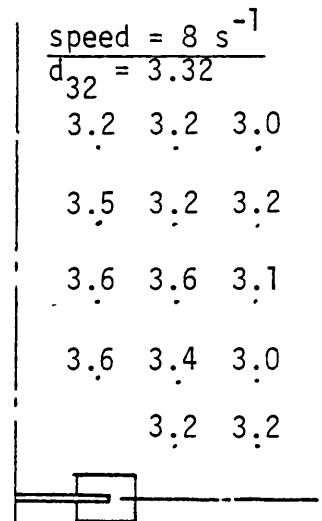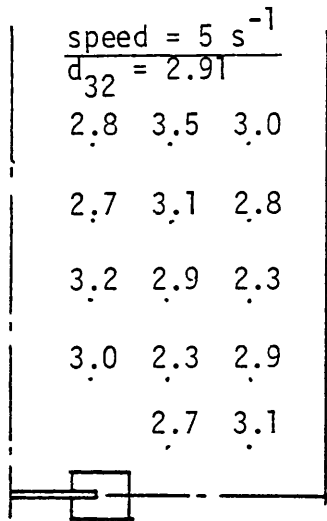
Fig. 6.13 : Matrix of point surface volume mean diameter ($\times 10^3$m)

D = 0.0762m , Q = 2.67$\times 10^{-4}$ m^{3}s^{-1}

Air-tap water system

d_{32} = average bubble diameter over the tank $\times 10^3$m.

In the efficient mixing regime (N=7, 14 s^{-1}, Figs. 6.12 and 6.13) the bubble size in the impeller discharge stream (position 1, Fig. 6.11) becomes noticeably smaller compared with the rest of the tank. Larger bubbles are now observed near to the vessel axis (positions 8, 15, 5, 14), increasing in size near to the impeller. The largest bubbles are observ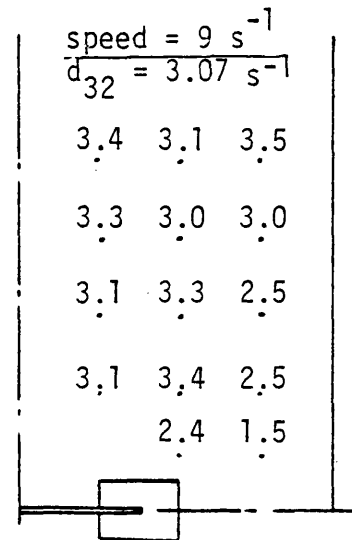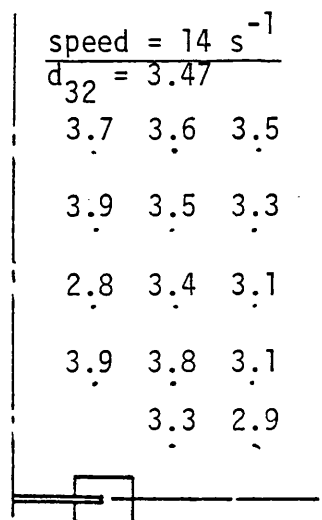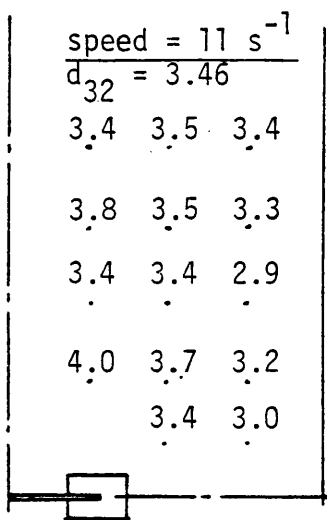ed at positions 8 and 10. Position 8, lies in the circulating liquid stream to the impeller, while position 10 could be considered to be at the centre of this circulation path. This suggests that recirculation of bubbles starts at speeds lower than those predicted by the impeller power consumption(N_{R1}) (Chapter 4). Further increase of the impeller speed, under gas recirculation conditions (speeds 11, 20 s^{-1}, Figs. 6.12, 6.13) causes the bubble size distribution over the tank to become more uniform. Large bubbles are, however, still observed near to the tank axis.

The bubble size distribution at a particular location in the tank was found to be strongly dependent on the impeller speed and gas flow rate. For example, distributions at three different locations in the tank are illustrated in Figs. 6.14, 6.15 and 6.16. It can be seen that none of these distributions follows any known statistical distribution. The number of bubbles in the lowest class, however, constitutes a large fraction of the total number of bubbles in the sample. Another general observation is that the mean bubble diameter (d_{10} and d_{32}) at the same location and the same impeller speed increases with increasing gas flow rate. An exception to this occurs for the lowest impeller speed of 3 s^{-1}. In this case the power supplied by the impeller at gas flow rates of 0.8 and $3.61 \times 10^{-4} m^3 s^{-1}$ is 0.8 and 0.52 watts respectively. The corresponding power supplied by the gas stream is 0.13 and 1.5 watts, respectively. Thus increasing the total power input as the gas flow rate increases leads to reduction
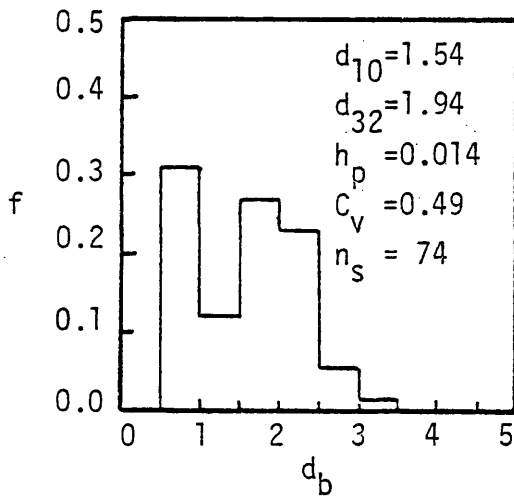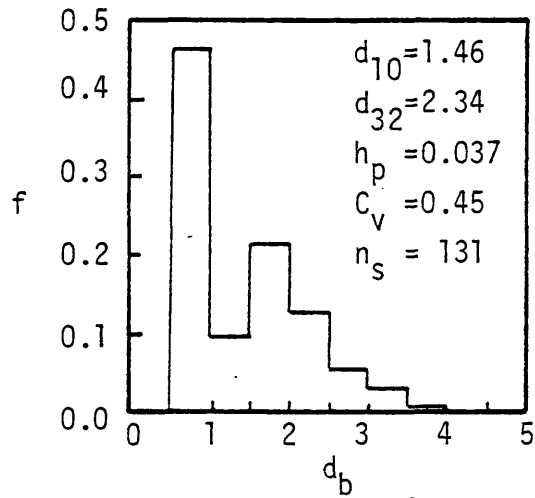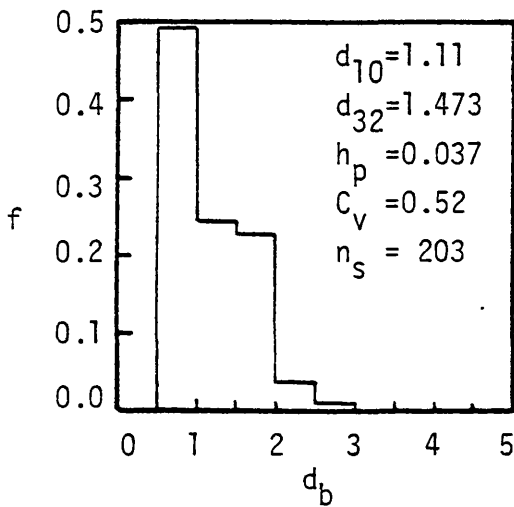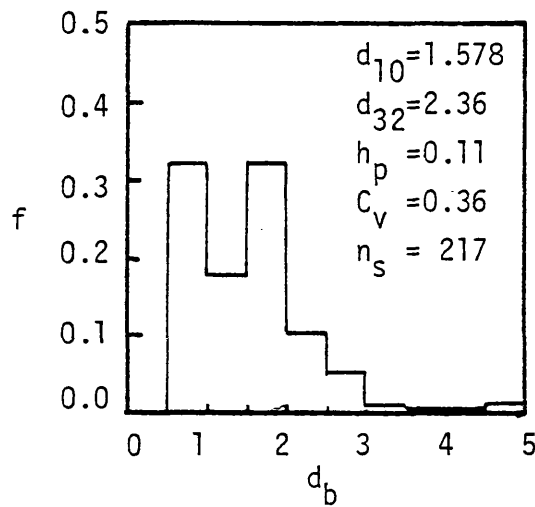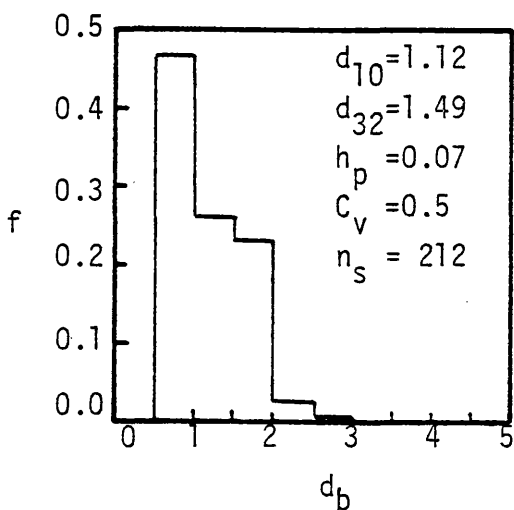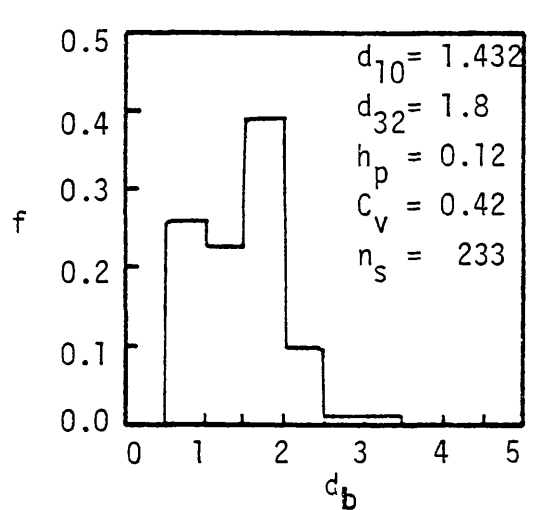
Fig. 6.14 : Bubble size distribution near to the impeller (Position 1, Fig.6.11). Tap water, D = 0.1016m, N = impeller speed rps, Q = gas flow rate x $10^4 m^3 s^{-1}$, C_v = coefficient of variation = $\frac{\sigma'}{d_{10}}$, n_s = sample size (bubbles), h_p = point gas holdup. f = number fraction, d_b = bubble diameter $mx10^{-3}$
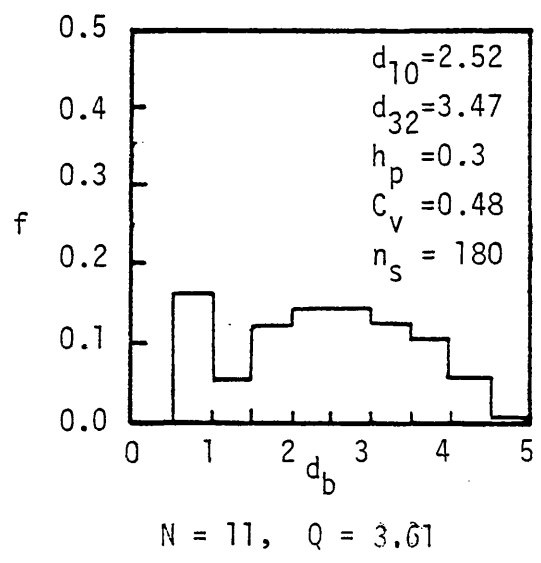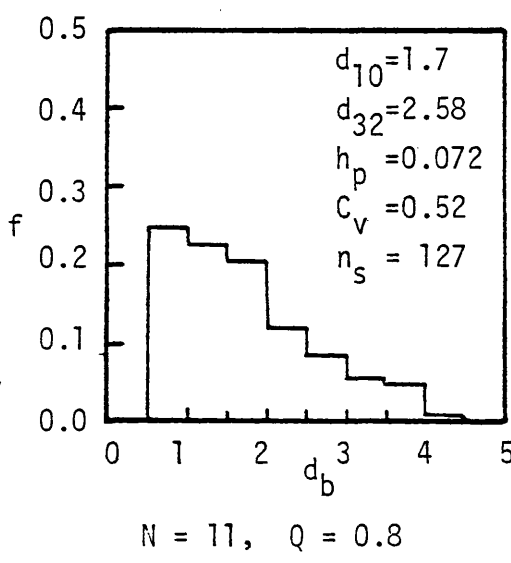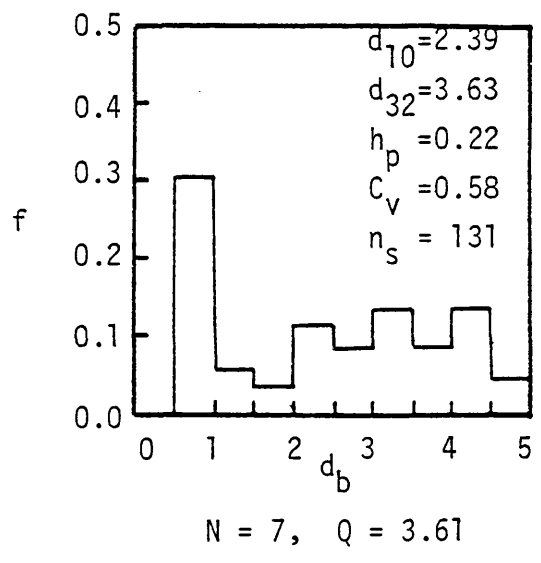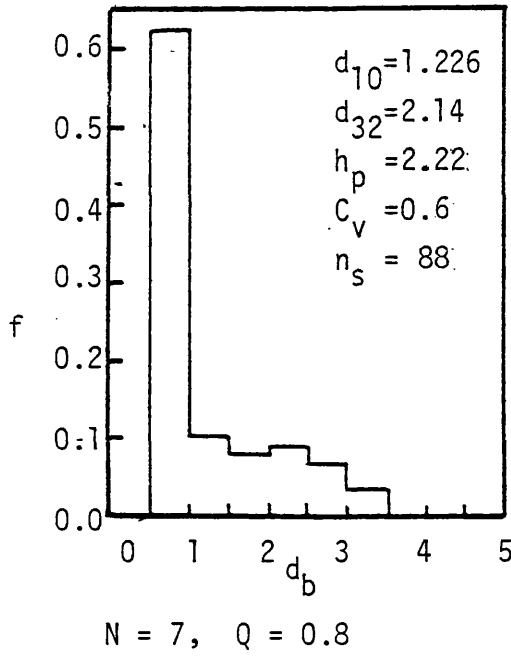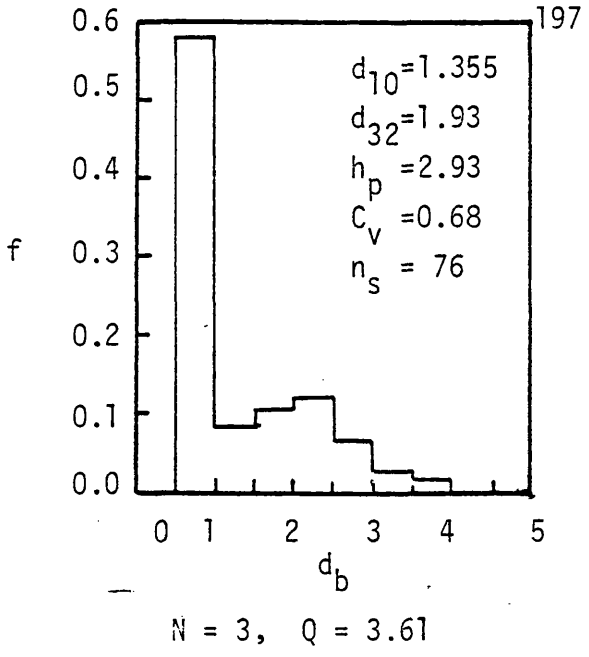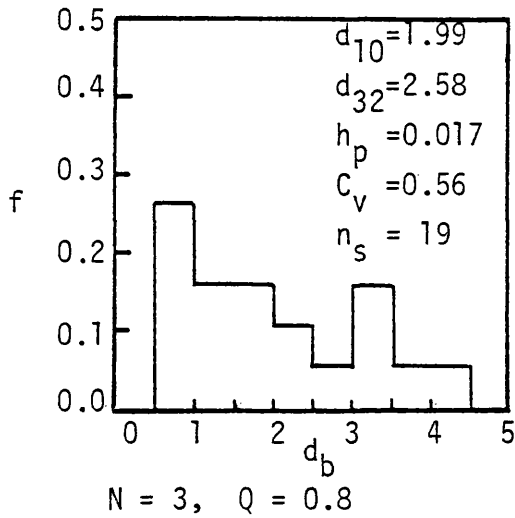
Fig. 6.15 : Bubble size distribution at a centre position in the tank
(Position 7, Fig. 6.11). Tap water, D = 0.1016m,
N = impeller speed rps, Q = gas flow rate x $10^4 m^3 s^{-1}$
C_v = coefficient of variation $\frac{\sigma'}{d_{10}}$ n_s = sample size (bubbles)

f = Number fraction, d_b, d_{10}, d_{32} in $mx10^3$ h_p = point gas holdup.
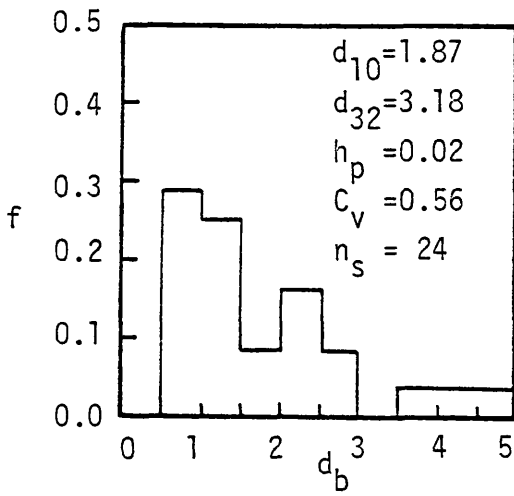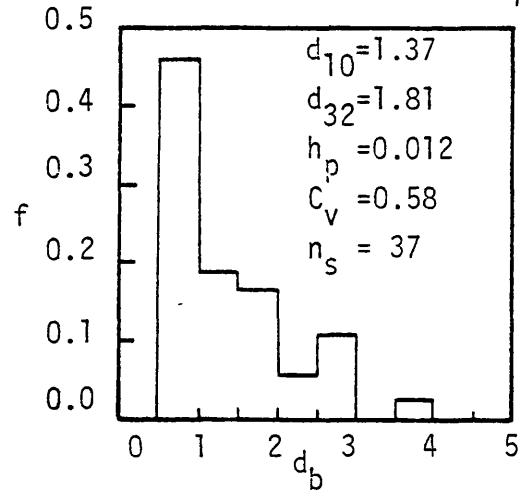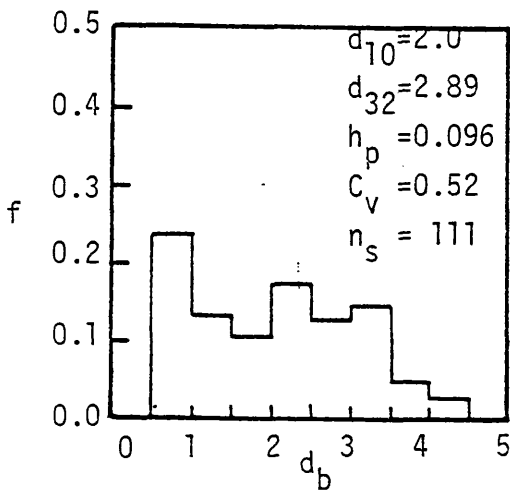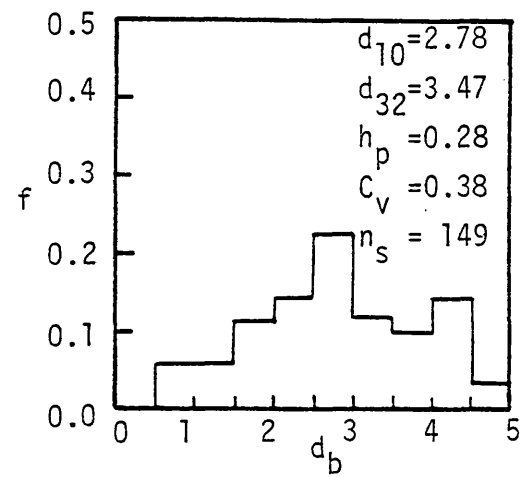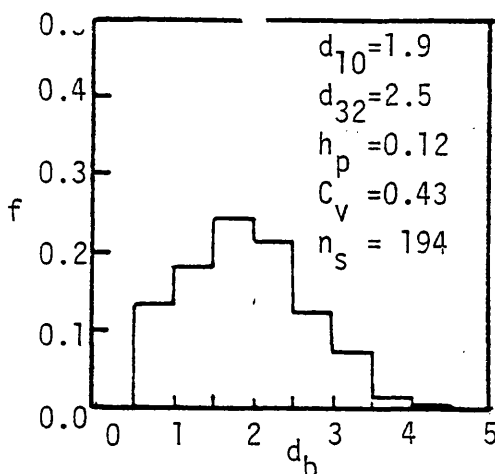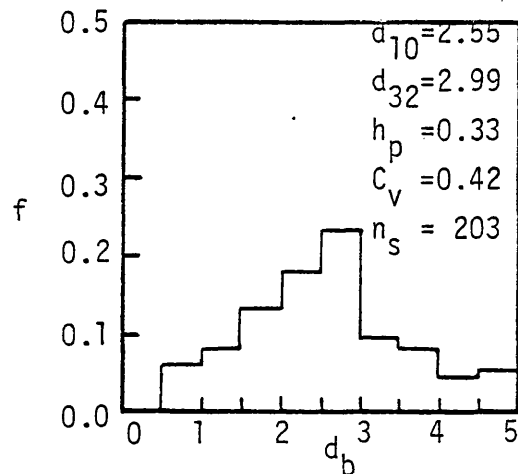
Fig. 6.16 : Bubble size distribution near to the liquid surface (position 6, Fig.6.11). Tap water, D = 0.1016m, N = Impeller speed rps, Q = gas flow rate x $10^4 m^3 s^{-1}$, C_v = coefficient of variation $\frac{\sigma'}{d_{10}}$ n_s = sample size (bubbles), h_p = point gas holdup. f = number fraction, d_b = bubble diameter mx10^{-3}
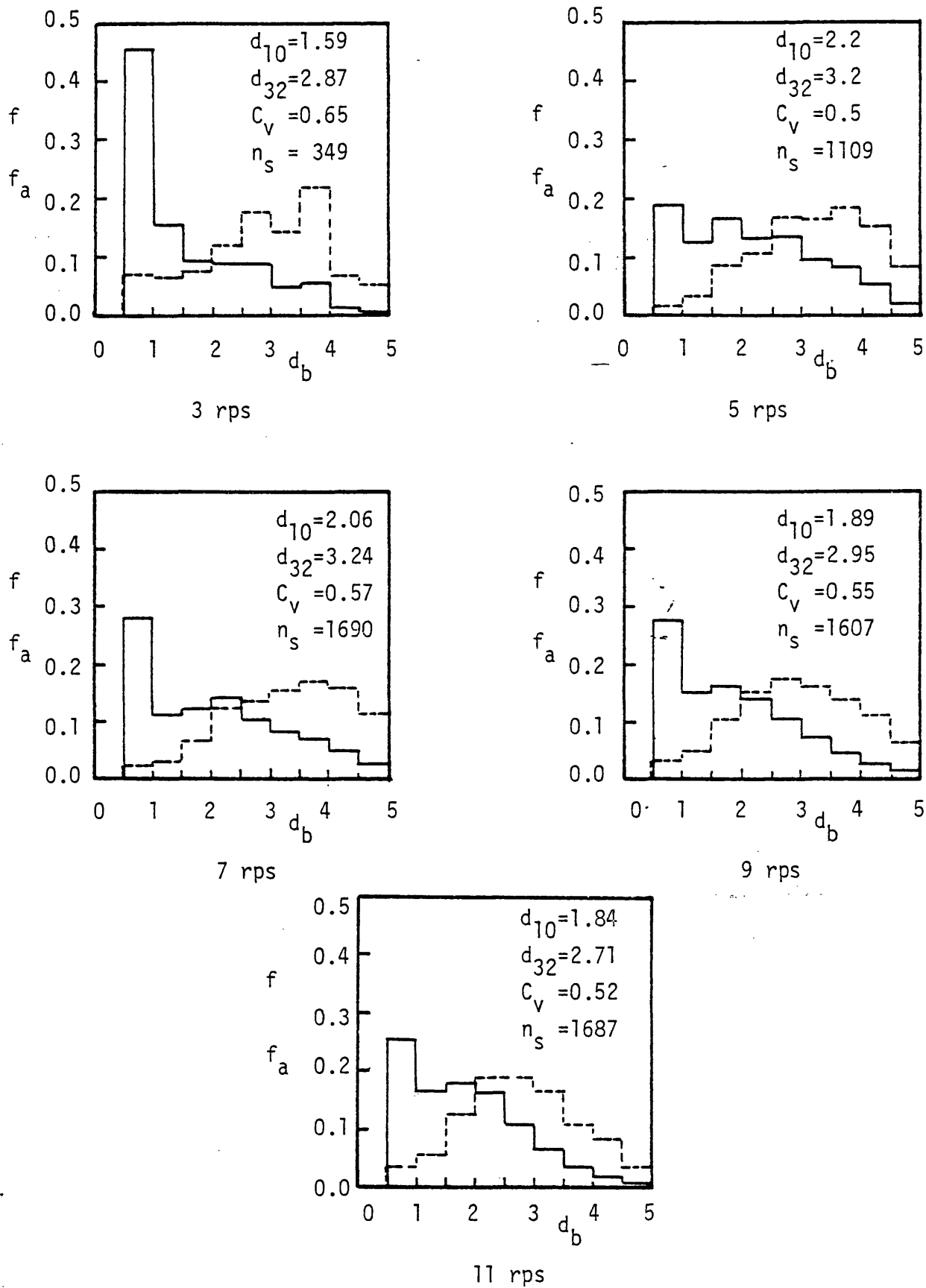
Fig. 6.17 : Bubble size and bubble surface area distribution in the
whole tank when samples drawn from different positions.
Tap water, D = 0.1016m, Q = 1.95x10^{-4}. f — Number fraction,
f$_a$ --- surface area fraction, n$_s$ sample size, d$_b$, d$_{10}$, d$_{32}$ in mx10^{-3}

of the bubble size throughout the tank. The contribution of the power

supplied by the gas stream is particularly important at lower impeller

speeds and high gas flow rates. Figures 6.14, 6.15 and 6.16 also

show that the maximum bubble size is smaller nearest to the impeller

(Fig. 6.14). The number of bubbles in the largest class increased

significantly near to the surface (Fig. 6.16). These findings are

expected since the rate of energy dissipation per unit volume in the

impeller stream is much greater than that in the rest of the tank (74)

and therefore the maximum stable bubble size in this region should be

smaller according to Eq. 6.1.

Combining the samples measured at the different locations for the same

operating conditions of N and Q, provides distributions for the whole

tank. The statistics of these distributions were then calculated

from the combined data. Figure 6.17 demonstrates the effect of

impeller speed at the same gas flow rate. It can be seen that the

number fraction has the same trend for all speeds, ie, reducing with

increasing bubble size. Except for the lowest impeller speed of $3 \ s^{-1}$,

the coefficient of variation is close to 0.5 for all impeller speeds

higher than this. This means that the standard deviation is about

half the average bubble size for both the efficient and the recirculation

mixing regimes.

The bubble surface area distributions were calculated by Eq. 6.22

$$f_{ai} = \frac{f_{ni} \ d_{bi}^2}{\Sigma \ f_{ni} \ d_{bi}^2} \qquad\qquad 6.22$$

where f_{ai} = surface area fraction of bubbles in increment i

   f_{ni} = number fraction of bubbles in increment i

   d_{bi} = mean bubble diameter in increment i.

These distributions are also shown in Fig. 6.17. The most interesting observation is that although the number fraction of bubbles in the smallest class (0.5-1.0mm) constitutes a considerable fraction of the total number of bubbles in the sample, it has a much smaller effect on the surface area. Therefore, the very small bubbles of diameter less than 0.5mm which were either not detected by the measuring probe, or possibly overestimated and included in the next class (0.5-1.0mm), have a negligible effect on the total surface area of the bubbles in the sample.

The effect of gas flow rate and impeller speed on the surface area distribution is shown in Fig. 6.18. It is clear that as the impeller speed increases or the gas flow rate is reduced, the surface area contribution by the smallest size bubbles increases. The effect of the impeller speed, however, is less significant, particularly at high gas flow rates.

6.4.1.2 Correlation of Bubble Size

The theoretical equation of Hinze (Eq. 6.1) for the maximum stable bubble size in a 'non-coalescing' system with an isotropic homogeneous turbulent flow field is the basis for most of the correlations of sauter mean diameter in agitated vessels. Most of the investigators, however, implicitly assumed a linear relation between d_{32} and d_{max}. The large size of data available from this study has made it possible to check this assumption. Figure 6.19 shows the relation between d_{max} and d_{32} for samples of dispersion for air-tap water. The result verifies that there is a linear relationship between d_{max} and d_{32}. From the best fit of the data :

$$d_{32} = 0.73 \, d_{max} \qquad\qquad 6.23$$
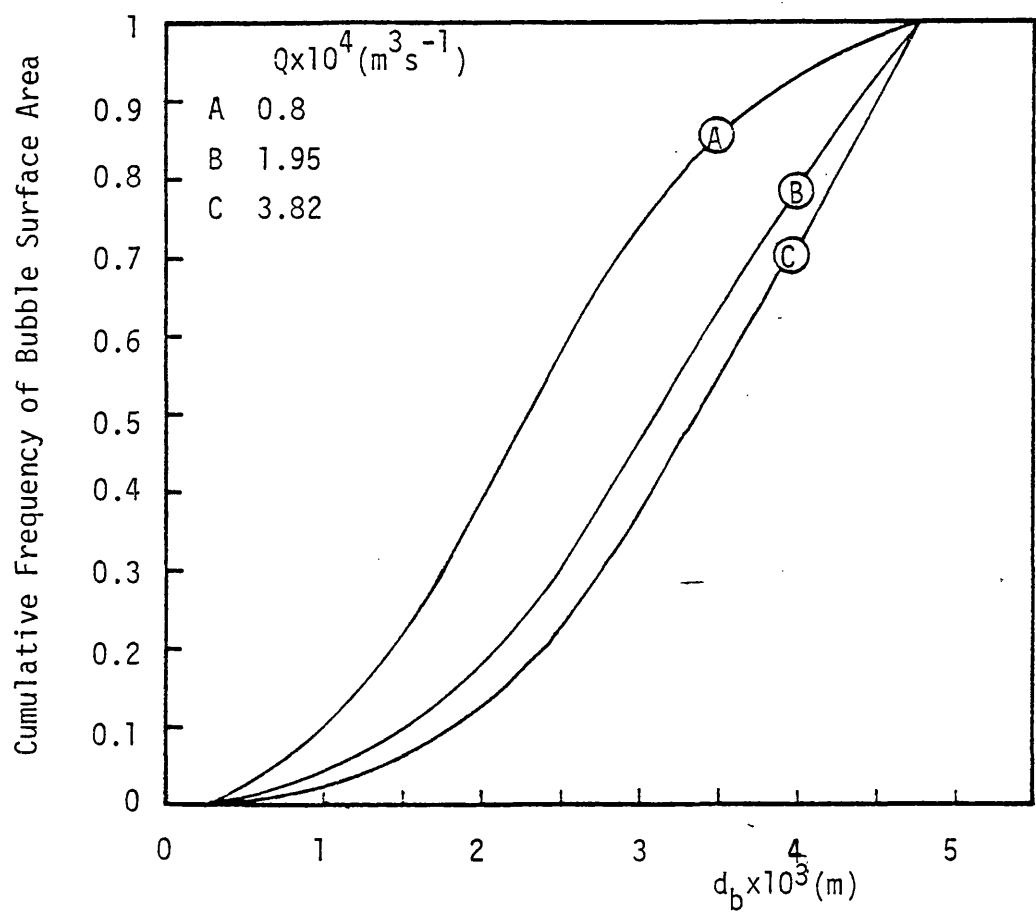
(a) Effect of gas flow rate (N=7 rps)
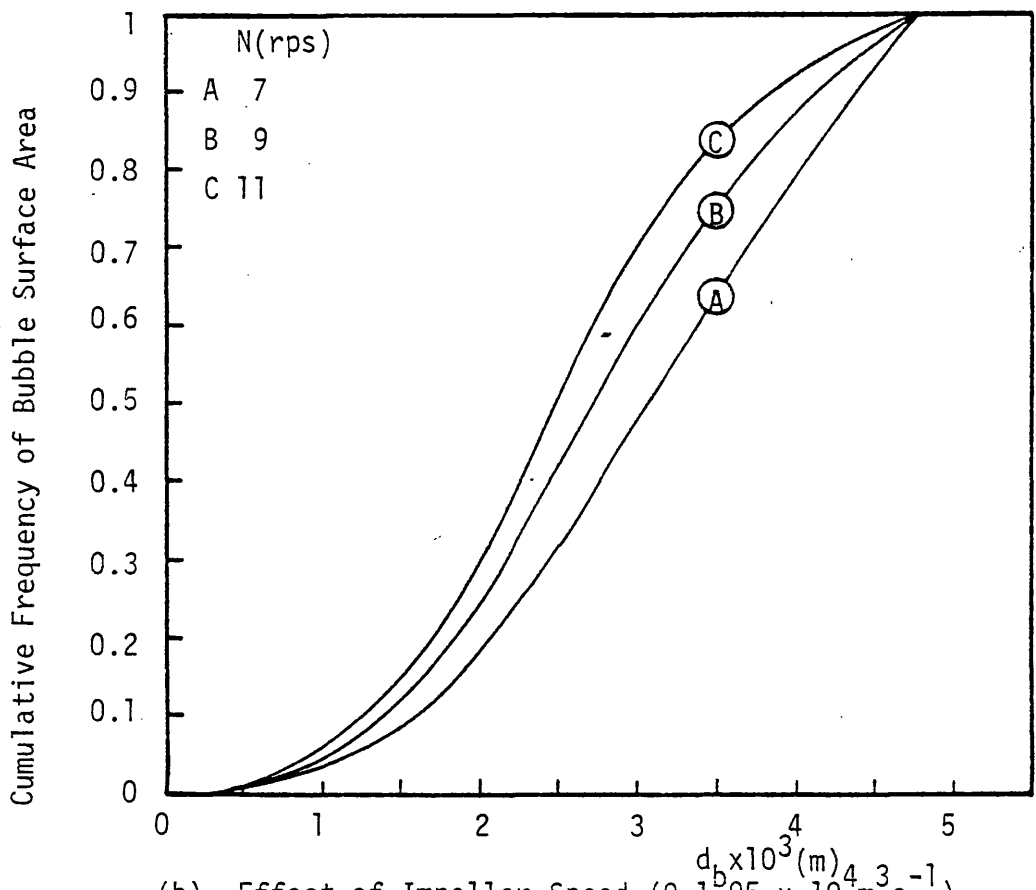
(b) Effect of Impeller Speed (Q=1.95 x $10^4 m^3 s^{-1}$)

Fig. 6.18 : Bubble surface area cumulative distribution for air-water system over the whole tank. D = 0.1016m.
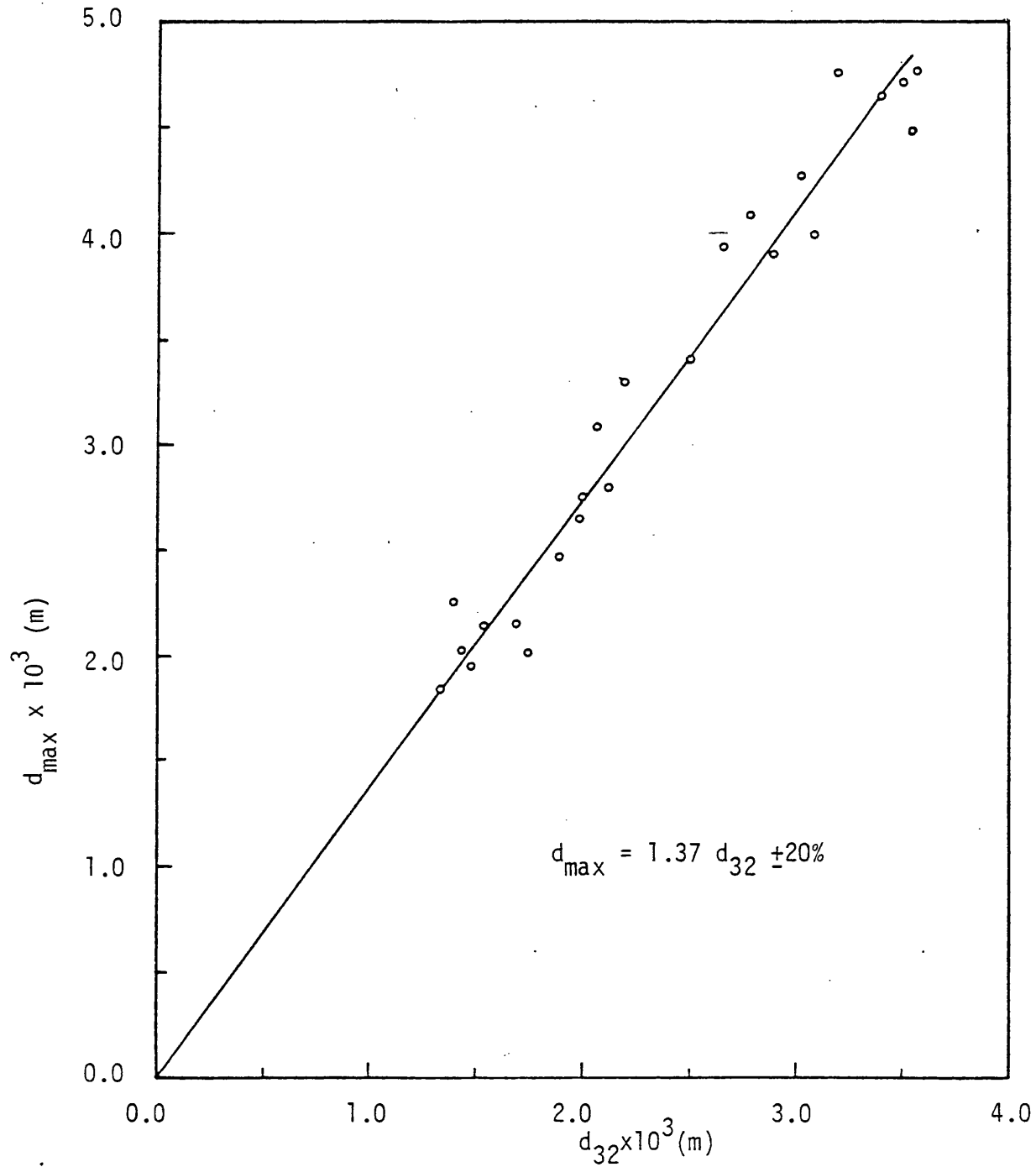
Fig. 6.19 : Maximum bubble diameter against sauter mean bubble
diameter of dispersion sample drawn from air-water system.

It is interesting to note that Eq. 6.23 also holds for samples of much smaller bubbles obtained with air-electrolyte solution.

Because of the uneven distribution of bubble size over the tank volume, it was decided to estimate d_{10} and d_{32} for the whole tank by averaging the point measurements over all of the sample locations weighted by the respective point gas holdups. The following equations were used to calculate d_{10} and d_{32}.

$$d_{10} = \sum_{j=1}^{15} h_{Pj} \, d_{10j} / \sum_{j=1}^{15} h_{Pj}$$

6.24

$$\text{and} \quad d_{32} = \sum_{j=1}^{15} h_{Pj} \, d_{32j} / \sum_{j=1}^{15} h_{Pj}$$

where d_{10j}, d_{32j} and h_{Pj} are the local mean diameter, sauter mean diameter, and point gas holdup at location j in the tank, respectively.

Figures 6.20 and 6.21 show d_{10} and d_{32} against the Flow number $\frac{Q}{N \, D^3}$. For high gas flow rates, the bubble size increases with increasing impeller speed up to a maximum and then starts to decrease. This trend is attributed to the change in the rates of bubble breakage and coalescence as the impeller speed increases. On the other hand, there is indication of a continuous increase in the average bubble diameter at the lowest gas flow rate and high impeller speed. This was accompanied by a larger increase in the gas holdup compared to the situation at higher gas flow rates (see Fig. 7.2) which may explain this trend. The trend exhibited by the two impeller sizes in Figs. 6.20 and 6.21 are similar. d_{10} and d_{32} were found to vary linearly as shown in Fig. 6.22.

$$d_{32} = 0.85 \, d_{10} + 1.33 \times 10^{-3}$$

6.25
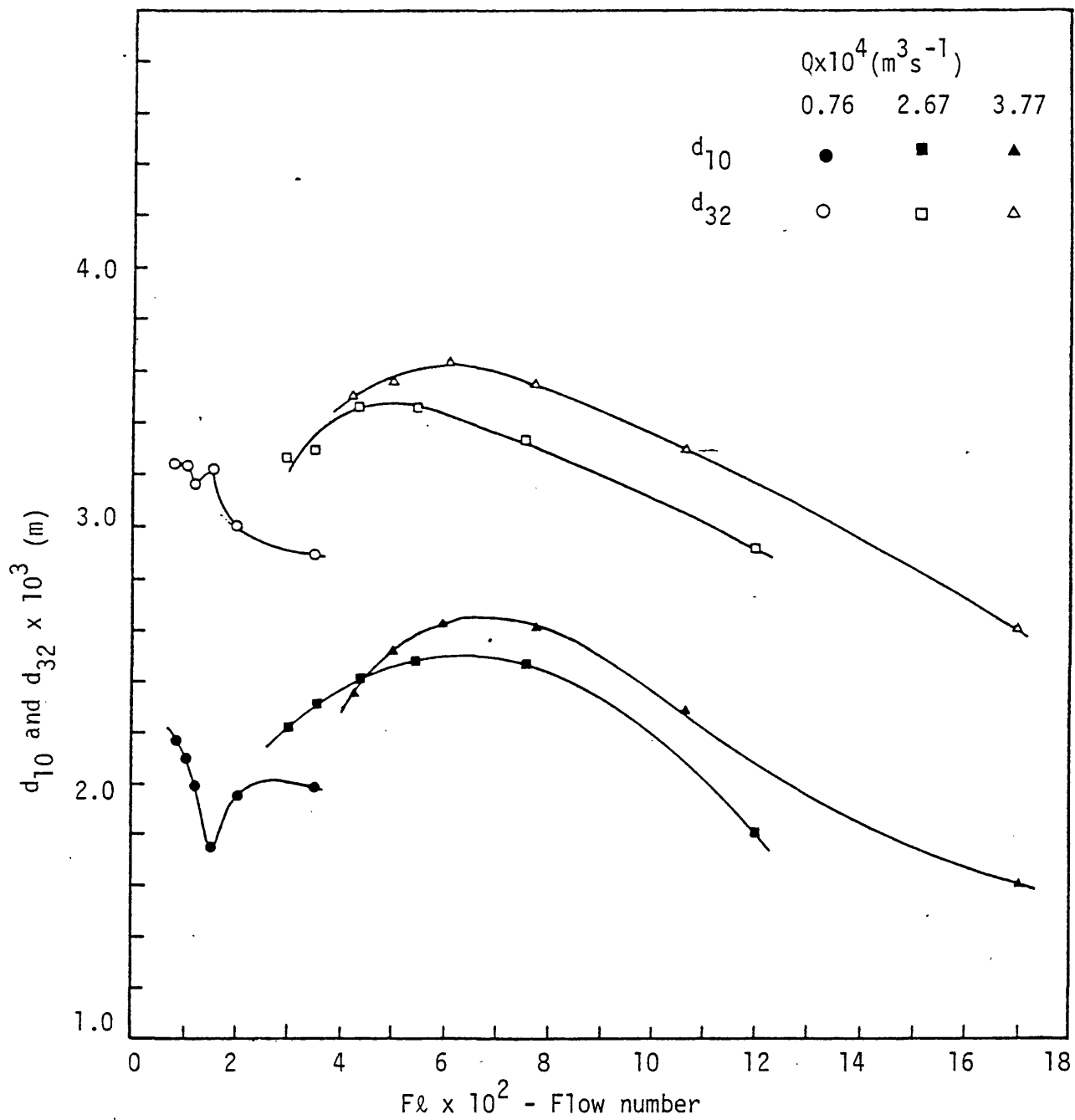
Fig. 6.20 : d_{10} and d_{32} against $F\ell$.

D = 0.0762m, Air-water dispersion.
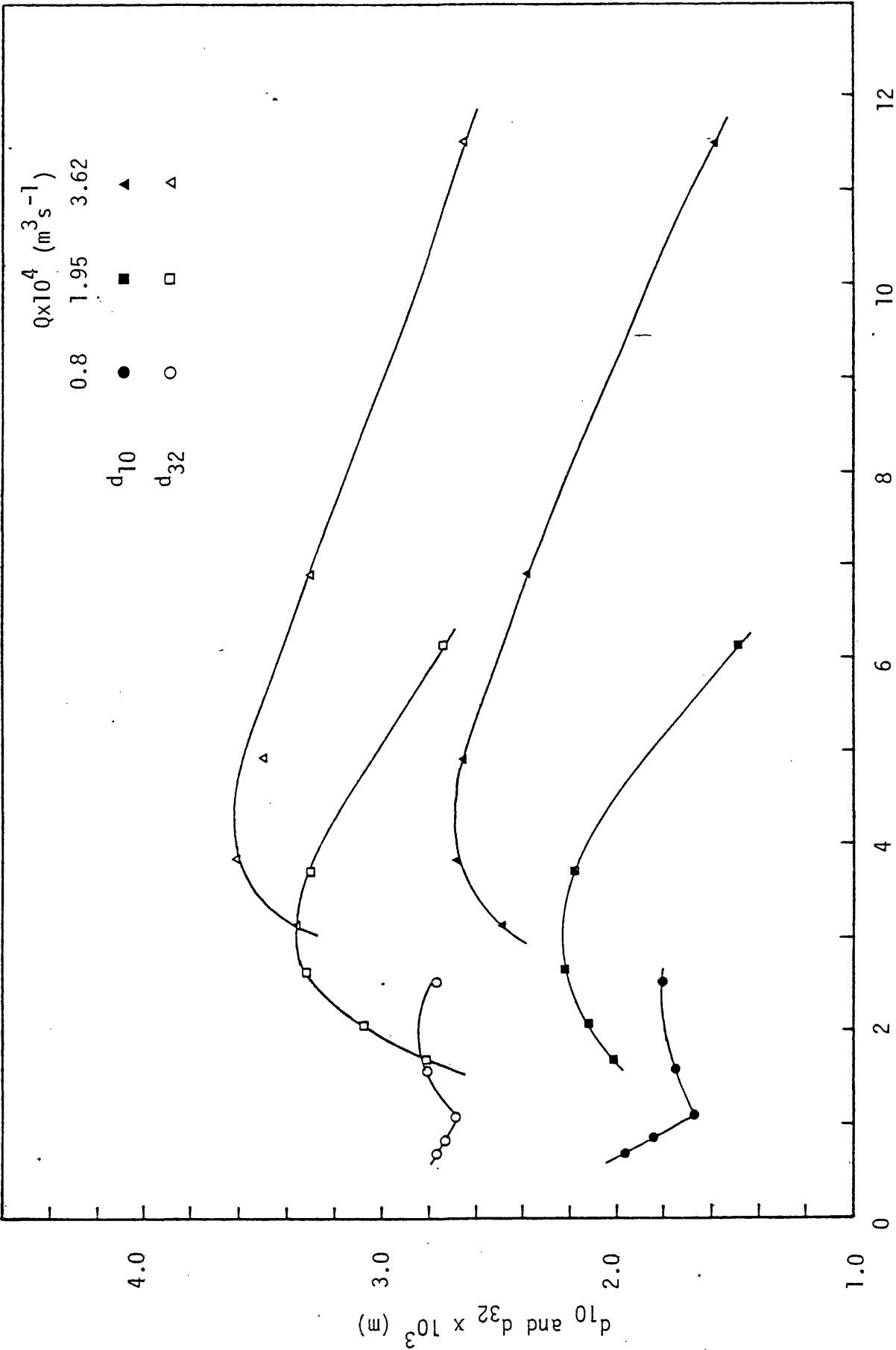
Fig. 6.21 : d_{10} and d_{32} against $F\ell$. $D = 0.1016m$, Air-water dispersion.
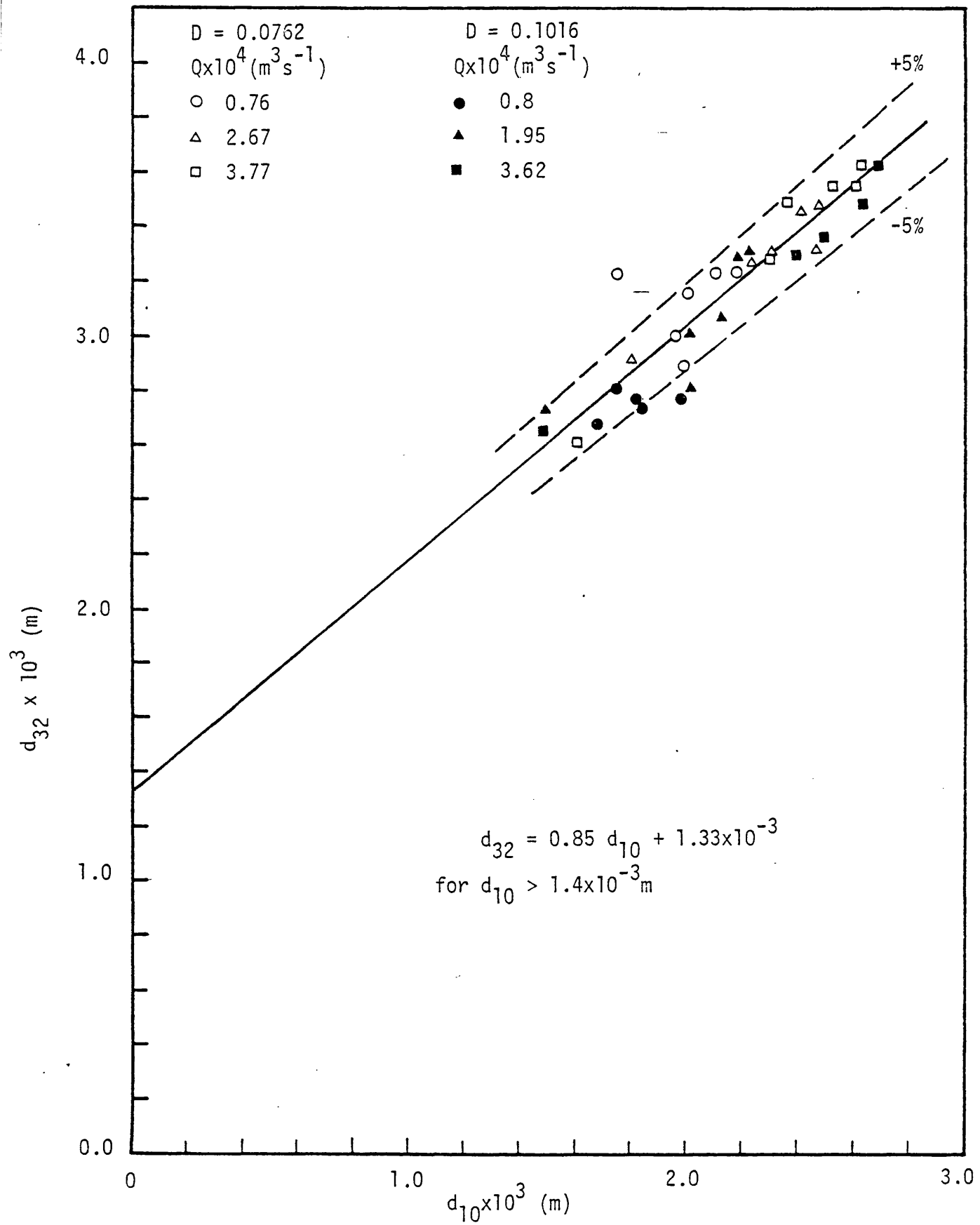
Fig. 6.22 : d_{32} against d_{10}, for air-water dispersion.

There is general agreement between Eqs. 5.23 and 6.25 and Sprow's results obtained for liquid-liquid dispersion (75). He proposed that

$$d_{Pq} = C\, d_{max} \qquad\qquad 6.26$$

for various P and q, so that

$$d_{32} = 0.38\, d_{max} \qquad\qquad 6.27$$

Comparing Eqs. 6.23 and 6.27 provides some indication of the effect of bubble coalescence since Eq. 6.27 was obtained for a non-coalescing system.

Following on from the previous studies of Calderbank (10), Lee and Meyrick (9) and Sridhar and Potter (6), many trials were conducted to correlate the group $d_{32}/\left[\sigma^{0.6}/(P/v)^{0.4}\, \rho^{0.2}\right]$ against the gas holdup. The power quantity P was either Pg or Pgt, or Pg with the group multiplied by Pg/Pgt. All of the trials gave a poor correlation result and in general, this quantity was found to be proportional to h, rather than $h^{\frac{1}{2}}$. The best fit for this type of correlation with the experimental data is

$$d_{32} = 15.7 \left[\frac{\sigma^{0.6}}{(Pg/v)^{0.4}\rho^{0.2}}\right] \left[\frac{Pg}{Pgt}\right] h \qquad 6.28$$

This is shown in Fig. 6.23 along with correlation proposed by Sridhar and Potter (6).

It is important to note that the range of experimental data used to test Eq. 6.28 was d_{32} = 2.6 to 3.6mm. For a bubble of size 3mm to lie within the accuracy limits, it could have a diameter between 1.95 and 4.05mm. Thus the limits of accuracy are wider than the measurement range, which therefore raises doubts about the validity of Eq. 6.28. The same reservation applies to Sridhar and Potter's (6) correlation (Eq. 6.9). They put accuracy limits of $\pm 25\%$ for a range of measured
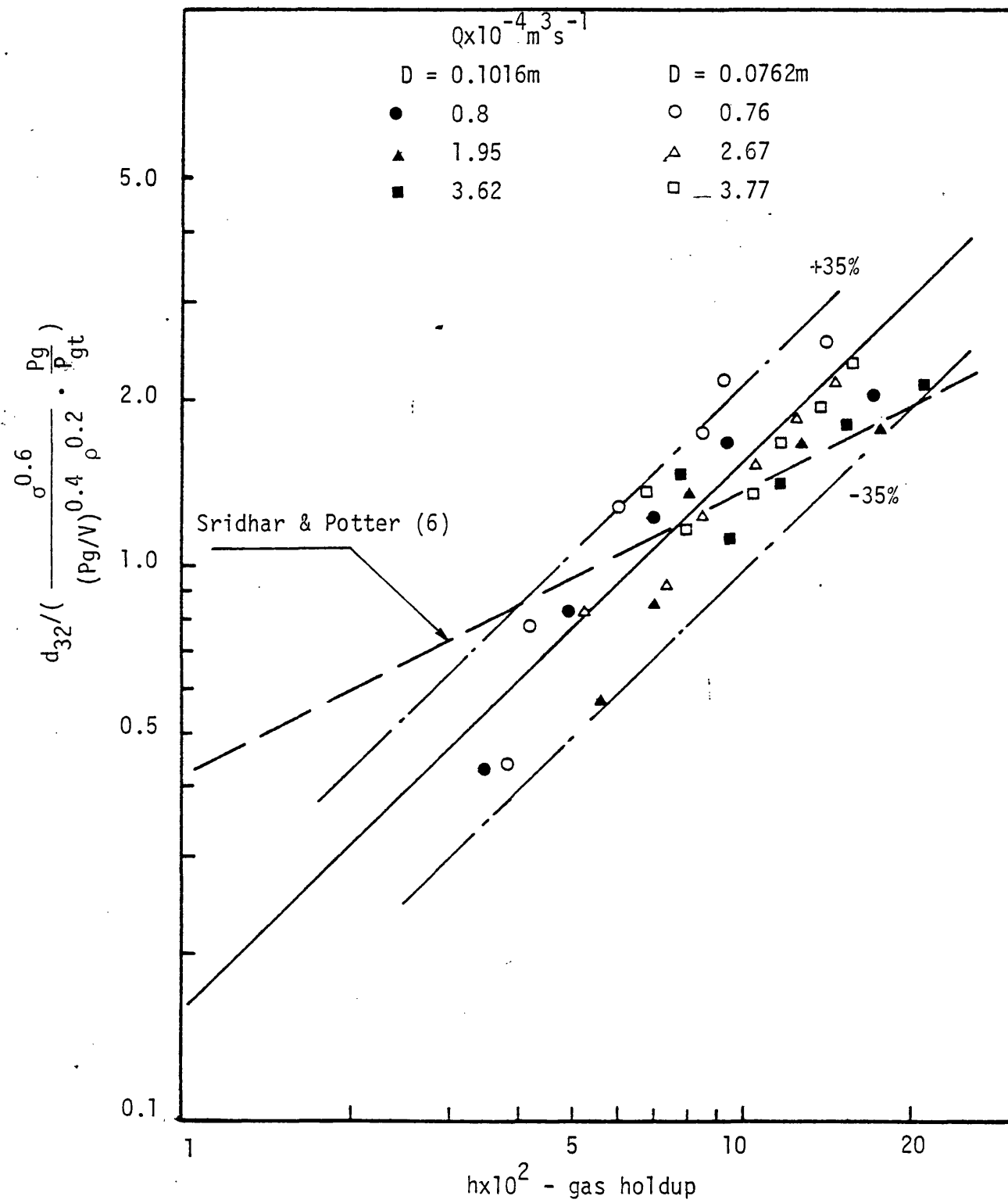
Fig.6.23 : Correlation of d_{32} 'air-water dispersion'.

bubble size from 2 to 4mm.

The recent theoretical investigation of the turbulent flow by Harvey (76) and experimental measurements of turbulence parameters by Nishikawa et al (77) and others, have shown that although the turbulence in the impeller stream deviates greatly from a condition of isotropy and homogeneity, the assumption of local isotropy in the whole of the vessel is applicable as a first approximation. This suggests that Eq. 6.1 can be used if there is no coalescence. These conclusions, however, apply mainly to single-phase systems. The physical properties and holdup fraction of a second phase may have a significant effect on the local turbulence properties of the flow field (78). This is expected to be most pronounced for high values of gas holdup, which is the case in this study. Hence it should be emphasised that the use of the correlating group $\left[\dfrac{\sigma^{0.6}}{(Pg/v)^{0.4} \rho^{0.2}} \right]$ gives at best only a rough estimate for the maximum stable bubble size in the turbulent flow field of a stirred tank.

Regarding the use of the term of the gas holdup "$h^{\frac{1}{2}}$" to account for the coalescence of gas bubbles (6, 9, 10), it should be pointed out that there is no theoretical justification for this, except for the explanation advanced by Lee and Meyrick (9). In addition, since the gas bubbles are nonuniformly distributed in the tank, the frequency of coalescence is expected to be dependent on location. A major drawback of using gas holdup values to correlate d_{32} is the lack of a universal correlation that can be used with sufficient accuracy to predict the gas holdup (see Chapter 7.)

Within the scope of the present study, the object was to find a correlation to fit the extensive bubble size measurements made rather

than to examine in detail the complex physical phenomena of bubble coalescence, etc, in an agitated tank. Since the gas holdup is a dependent variable for the process, it was excluded from the analysis. Instead, the independent parameters N, Q and D were used to correlate the group $d_{32} / \dfrac{\sigma^{0.6}}{(Pgt/v)^{0.4} \rho^{0.2}}$ by using log-log plots. It was

found that

$$\frac{d_{32}}{\left(\dfrac{\sigma^{0.6}}{(Pgt/v)^{0.4} \rho^{0.2}} \right)} \ \alpha \ N^{1.2} \ D^{2.4}$$

with no dependence on Q. Using the least squares method, the following correlation was obtained :

$$d_{32} = 17.7 \left(\frac{\sigma^{0.6}}{(Pgt/v)^{0.4} \rho^{0.2}} \right) (ND^2)^{1.2} + 1.3 \times 10^{-3} \qquad 6.29$$

Figure 6.24 demonstrates that there is a good fit of the experimental data and improvement of the accuracy limits compared with Eq. 6.28. It is worthwhile to mention that the 33 experimental points shown in Fig. 6.24 represent a total of 33,322 bubbles measured at 33 different operating conditions, and that each point is the average of sampling from 15 different positions in the tank. The main drawback of Eq. 6.29 is that it is not dimensionally sound and it would predict very large bubble size if used for larger sized tank. The appearance of the term (ND^2) suggests that the average circulating velocity of liquid $(V\alpha \frac{ND^2}{T}$, see Eq. 3.7). might be used for correlation purposes. This group has been used successfully for correlating the conditions for the onset of surface aeration and gas recirculation in this study (Chapters 3 and 4). Schwartzberg and Treybol (32), have recommended the use of this group as a criterion for scale up for mass and heat transfer in turbulent agitated vessels. Hence modifying Eq. 6.29 on
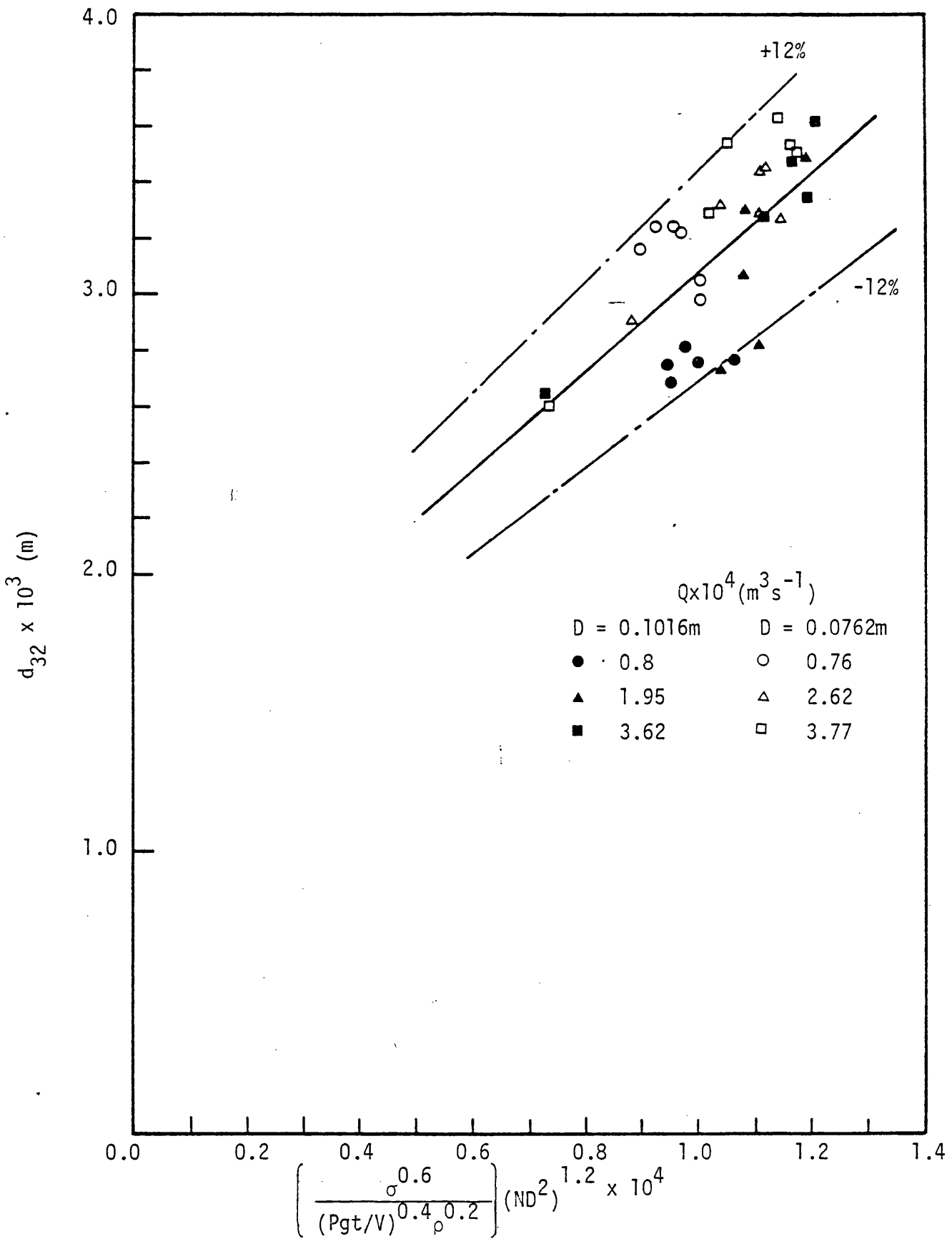
Fig. 6.24 : Correlation of d_{32} 'air-water dispersion.

this basis, then :

$$d_{32} = K^1 \left[\frac{\sigma^{0.6}}{(Pgt/v)^{0.4} \rho^{0.2}} \right] \left[(\frac{ND^2}{T})/U_T \right]^{1.2} + 1.3 \times 10^{-3}$$ 6.30

where U_T is the bubble terminal velocity.

Equation 6.30 is now dimensionally sound, but since U_T is almost constant for the bubble range studied (see Fig. 3.16), it is included in the constant K^1, and Eq. 6.30 is stated as—

$$d_{32} = C \left[\frac{\sigma^{0.6}}{(Pgt/v)^{0.4} \rho^{0.2}} \right] (\frac{ND^2}{T}) + 1.3 \times 10^{-3}$$ 6.31

where $C = 2.61 \quad m^{-1.2} s^{1.2}$

The rather intuitive way in which the effect of the tank diameter is included in Eq. 6.31 needs to be checked further with different size equipment if Eq. 6.31 is to be of any use. Table 6.1 compares the results of Figueiredo's (12) study using two different techniques for measuring d_{32} in 0.91m diameter tank, and the predicted values using Eq. 6.31. The maximum deviation between her results is 30% with an average absolute error of 20%, while the deviations between the predicted values using Eq. 6.31 and those measured with the aid of Eq. 6.2 are also of the same order. Therefore, this does not confirm either way the validity of Eq. 6.31. Further measurements on larger scale equipment, using the bubble size measuring technique developed in this study, are needed before more firm conclusions regarding the validity of Eq. 6.31 can be made.

Table 6.1 :   Comparison of bubble size measurements in 0.91m tank(12),

with the predicted values using Eq. 6.31

$Q \times 10^3$ $(m^3 s^{-1})$	N (s^{-1})	$d_{32} \times 10^3 m$			
		Point measurements *	Eq. 6.2 +	Eq. 6.5 •	Eq. 6.31
4.16	5.00	2.85	3.75	3.76	4.16
	6.67	2.86	3.62	— 3.15	4.11 ·
	8.83	3.00	3.36	2.81	4.14
8.33	5.00	2.87	3.49	4.91	4.40
	6.67	2.89	3.42	3.90	4.41
	8.83	3.02	3.47	3.47	4.43

*   Point measurements using electroresistivity probe

+   From measurements of gas holdup and interfacial area

•   Using Calderbank's correlation (10).

6.4.2 'Non-coalescing' System

It is well known that the addition of small quantities of electrolyte to water substantially reduces the bubble size in gas liquid contactors. The small changes in the physical properties of the solution including the surface tension do not have a significant influence on the break-up of gas bubbles in turbulent fluid field (Eq. 6.1). Thus the main action of the electrolyte solution is to inhibit the coalsecence of the gas bubbles creating a smaller mean bubble size (9).

Marrucci and Nicodemo (53) suggested that the inhibited state of coalescence in electrolyte solutions, is mainly due to electrical repulsive force. Lee and Meyrick (9) attributed this phenomenon to the increase of the surface tension caused by the increase of the electrolyte concentration in the stretched liquid film between bubbles.

'Non-coalescing' systems are more commonly observed in industrial applications, eg, fermentation media. It was considered important, therefore, to study the bubble size in this type of system and 0.11M potassium sulphate solution was selected (see also Chapter 4).

6.4.2.1 Distribution of Bubble Size

Figure 6.25 demonstrates how the bubble size varies at different locations in the tank as the impeller speed changes. At speed lower than N_{F1} (5 s^{-1}), the bubble size throughout the tank is relatively large. In the efficient mixing regime (8 and 11 s^{-1}), the bubble size is smaller. In the early stages of gas recirculation mixing regime (N=14 s^{-1}) a slight increase in bubble size is observed. This may be due mainly to the increase of the residence time of the gas bubbles in the tank which leads to an increase in the coalsesence rate. The general trend is that the smallest bubble size is observed near to the impeller, and the largest is observed near to the liquid surface.

speed=5 s^{-1}
d_{32} = 2.29

2.6
15.8

2.06
12.6

1.32   2.5
2.2   14.4

1.9
5.1

2.1
2.14

speed = 8 s^{-1}
d_{32} = 1.53

1.66
3.1

1.43
24.4

1.2   1.87
16.6   20.5

1.56
24.8

1.23
9.4

speed = 11 s^{-1}
d_{32} = 1.175

1.29
34

1.23
21

1.14   1.07
25.9   12.3

1.12
23.7

0.94
7.35

speed = 14 s^{-1}
d_{32} = 1.23

1.4
35

1.2
22.6

1.07   1.03
24.5   14

1.3
33   1.05
          10.5

speed = 17 s^{-1}
d_{32} = 1.122

1.1
23

1.2
14.4

1.2   1.03
23   10

1.15
31.4   0.96
          21.7

speed = 20 s^{-1}
d_{32} = 1.075

1.2
27

0.92
16.8

1.1   0.96
26.3   15.6

1.13
26.9

0.95
18
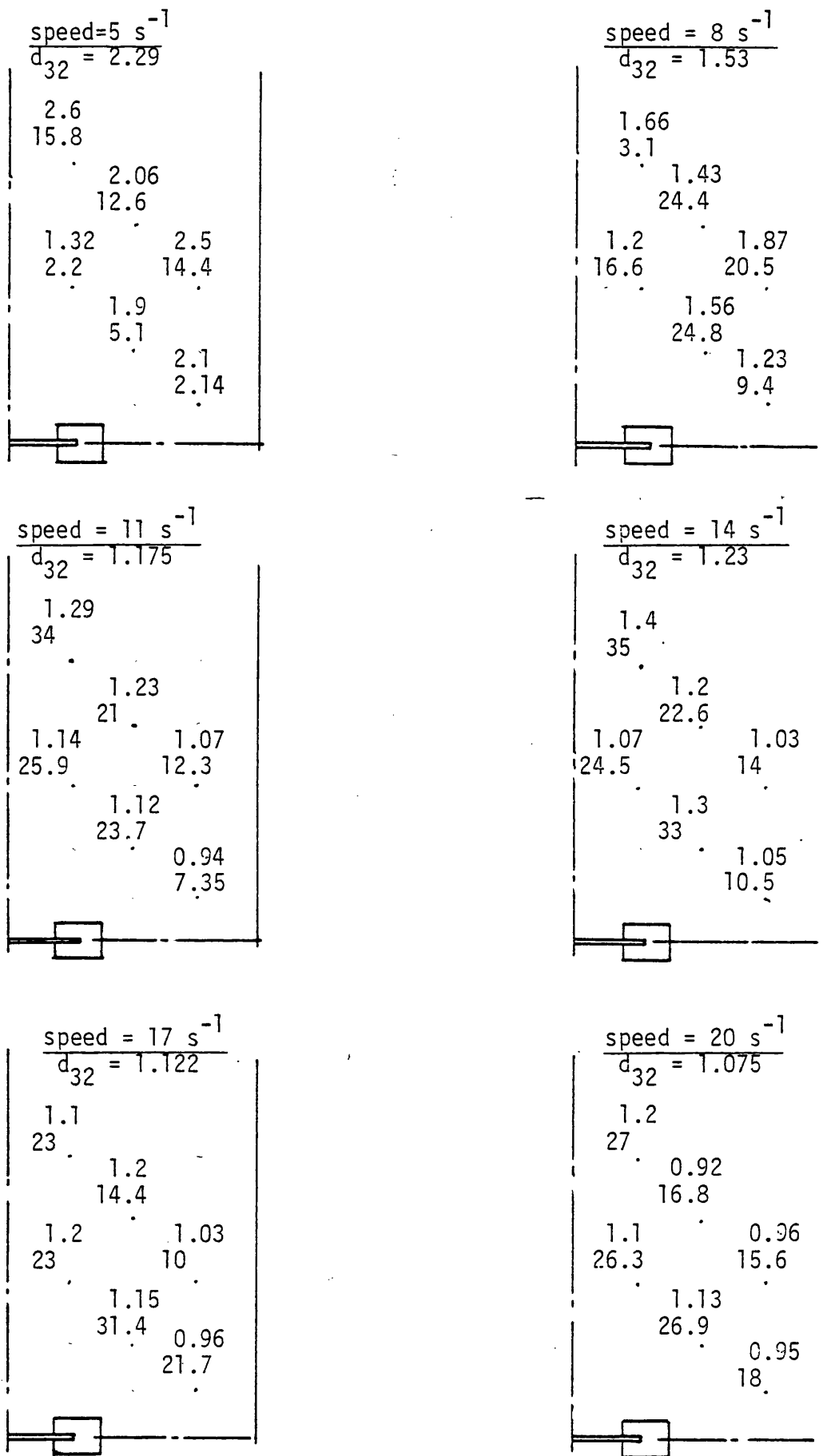
Fig. 6.25 :   Sauter mean bubble diameter (mx10^3) and point gas holdup(%)
in the tank. air-0.11 K_2SO_4 solution.   D = 0.0762m,
Q = 0.76x10^{-4}m^{3}s^{-1}, N_{F1} = 6.8 s^{-1}, N_{R1} = 12.3 s^{-1}.

However, the variation of the average bubble size within the tank is much less compared to that of tap water.

The bubble size distributions at different locations in the tank for the same operating conditions using impellers D1 and D2 are shown in Figs. 6.26 and 6.27, respectively. These distributions are more symmetrical than those obtained for the air-water system. At position 1 near to the impeller, d_{max} is about 1.6mm, while near to the liquid surface (position 14 Fig. 6.26 and postion 5 Fig. 6.27) it is about 2.4mm.

Figure 6.28 demonstrates distributions at one location in the tank (position 4) for different operating conditions. Comparison between Fig. 6.26 and Fig. 6.28 indicates that there is a more marked change in the bubble size distribution with location than there is with any change in operating condition. That serves to emphasise that the turbulent flow field in an agitated tank deviates from a condition of isotropy and homogeneity.

The bubble size distribution for the whole tank is obtained by adding together all of the separate distributions at the different locations in the tank. Figures 6.29 and 6.30 show how the distribution changes with impeller speed and with gas flow rate (represented by the bubble surface area cumulative distribution function). Figures 6.29.a and 6.30.a indicate that at impeller speeds above N_{F1}, the surface area distribution becomes almost independent of the impeller speed, whilst Figs. 6.29.b and 6.30.b show that there is less significant dependence of the distributions on the gas flow rate.

All of the distributions mentioned above for impeller speeds higher than N_{F1} have been added together as shown in Fig. 6.31 to illustrate
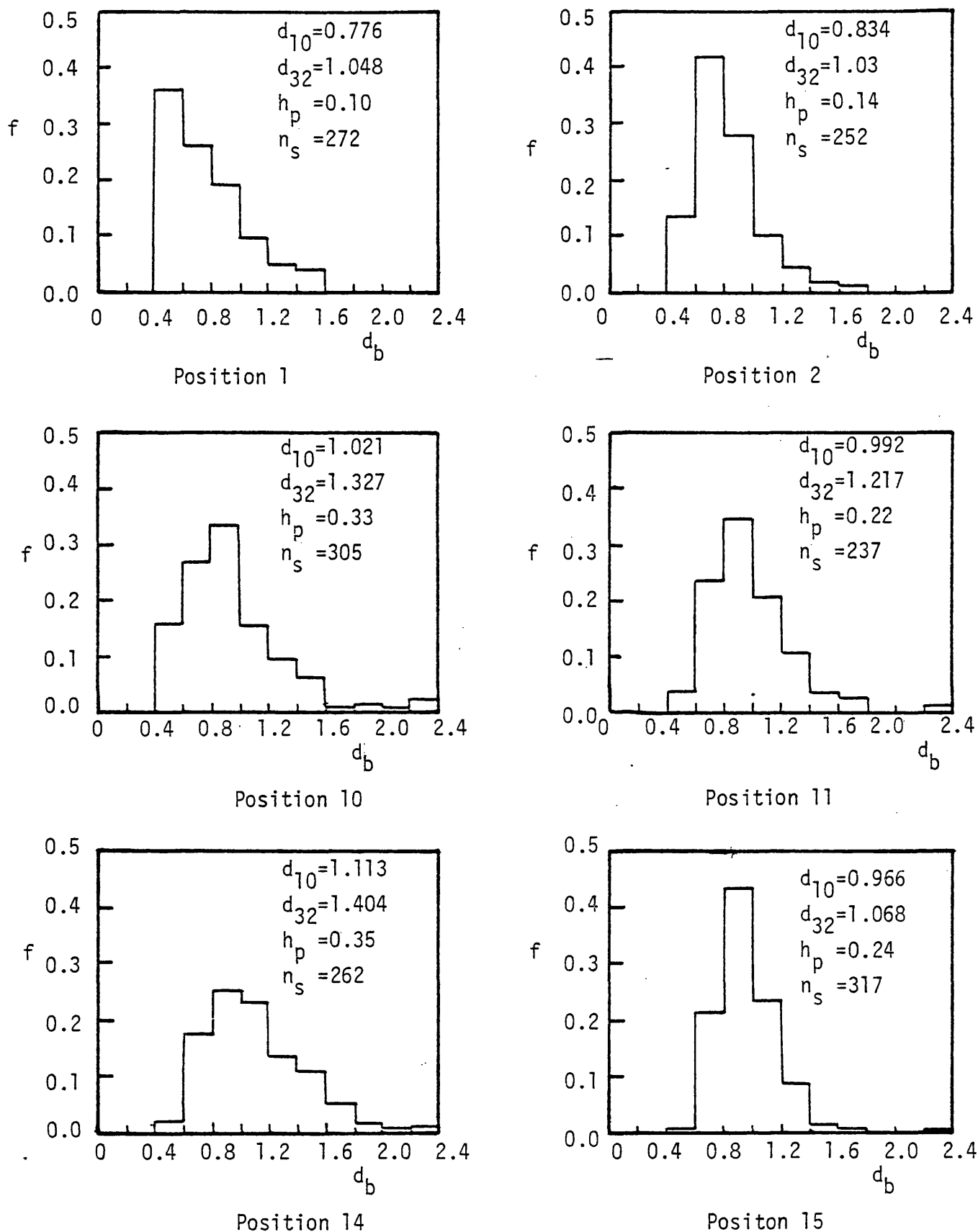
Fig. 6.26 : Bubble size distributon in the tank. D = 0.0762m, air-0.11 K_2SO_4 solution. f number fraction, N = 14 rps, Q = $0.76 \times 10^{-4} m^3 s^{-1}$

d_b, d_{10}, d_{32} in $m \times 10^{-3}$ - (Key for positions: Fig. 6.11).

n_s = sample size (bubbles)
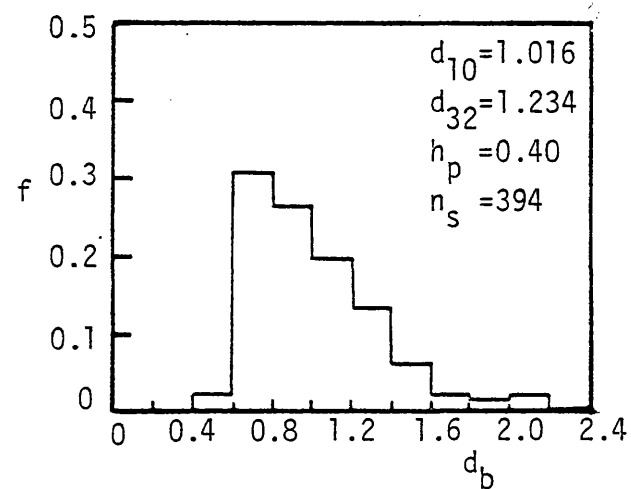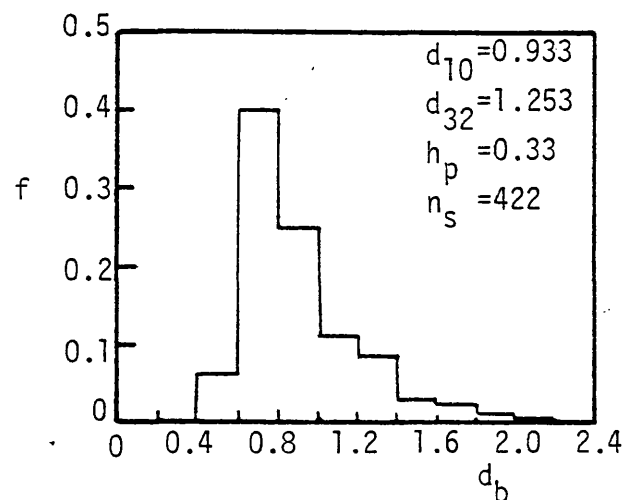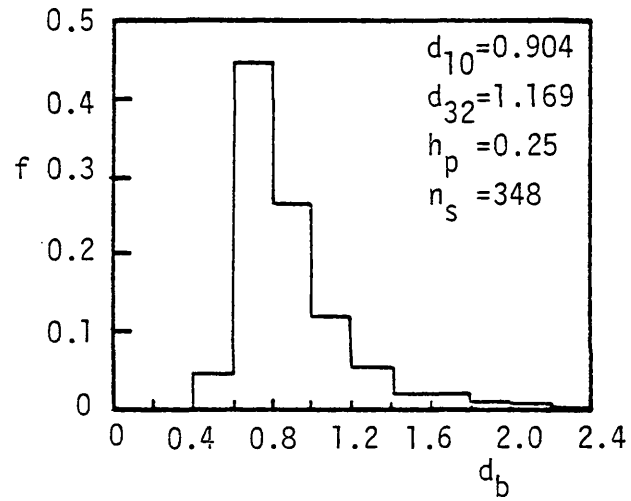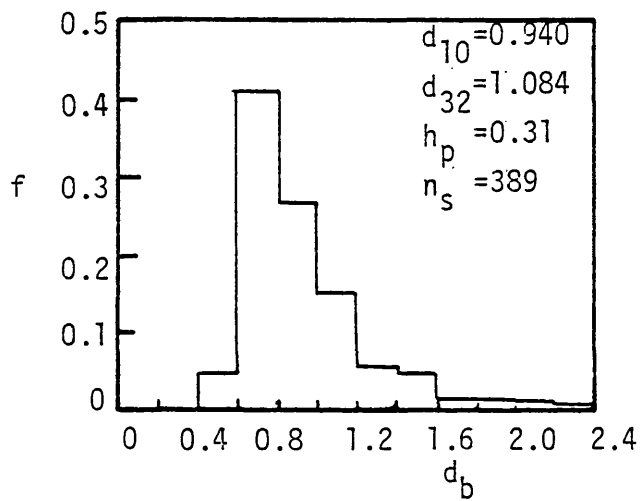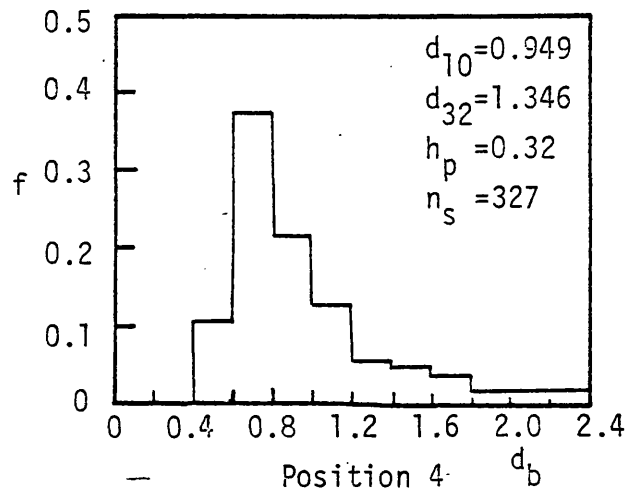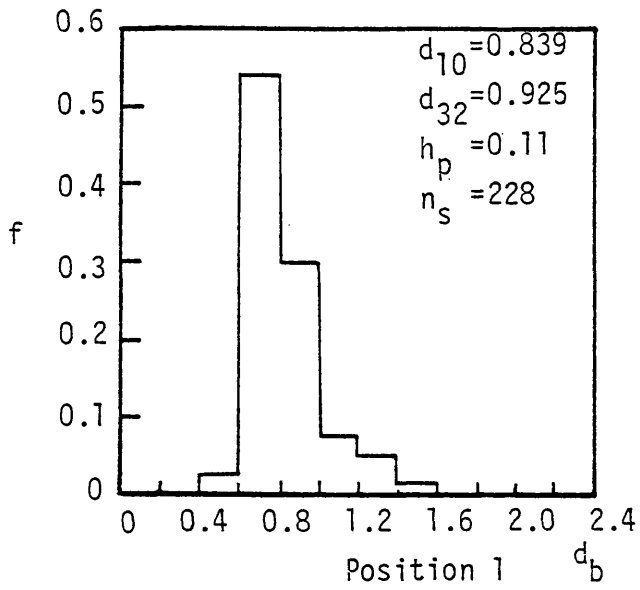
Fig. 6.27 : Bubble size distribution in the tank, D = 0.1016m,
0.11 K_2SO_4 solution. N = 7 rps, Q = $1.95 \times 10^{-4} m^3 s^{-1}$,
d_b, d_{10}, and d_{32} in $m \times 10^3$ - (Key for positions :Fig. 6.11)
f = number fraction. n_s = sample size (bubbles)
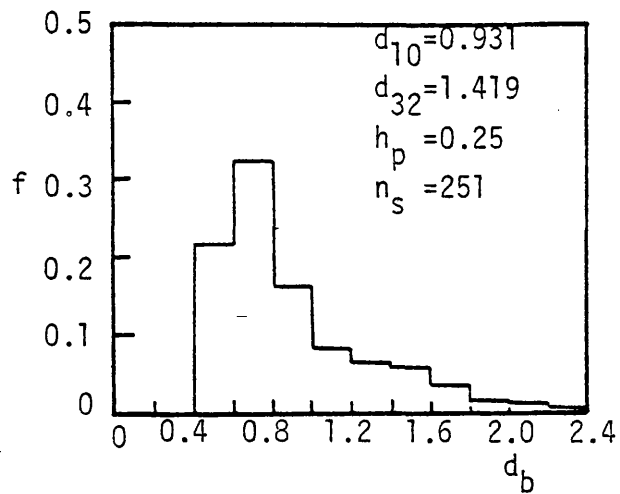
a.1. N=11 rps
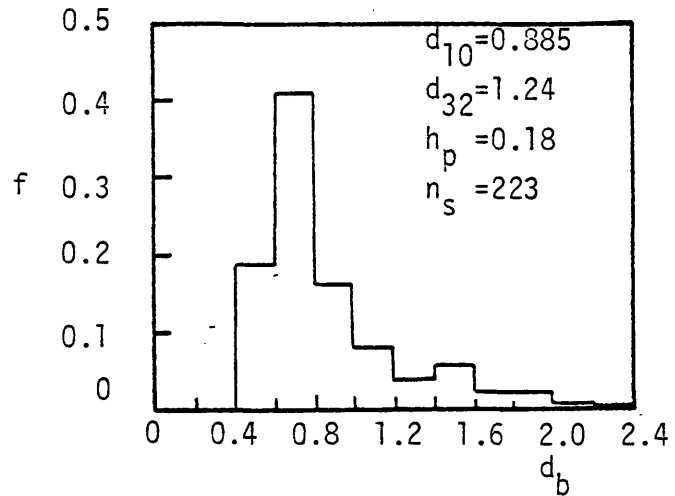
b.1. N=11 rps
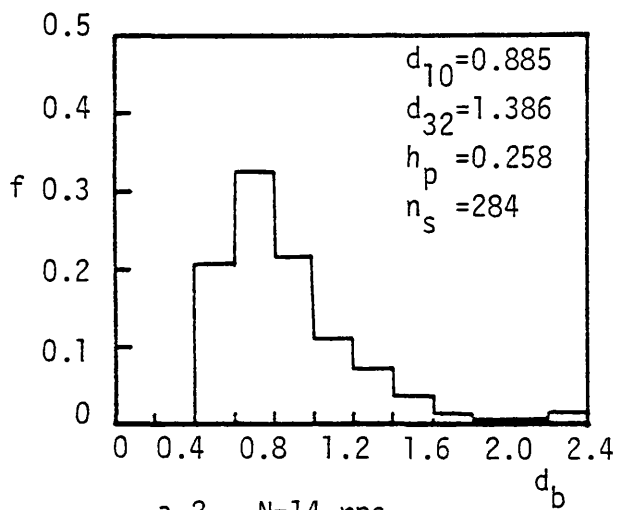
a.2. N=14 rps
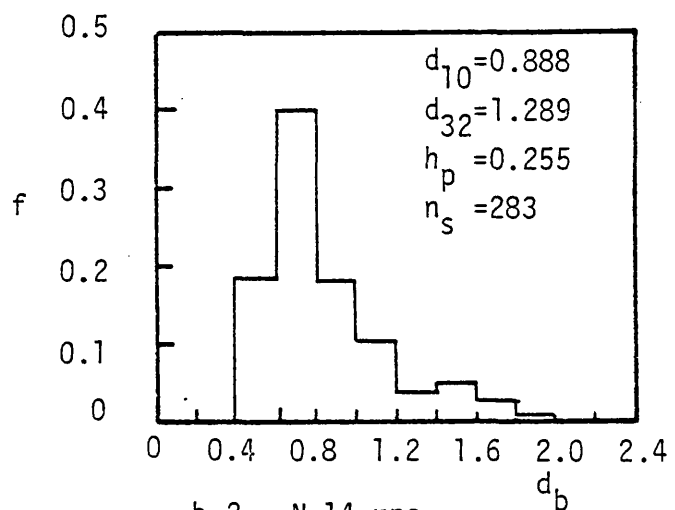
b.2. N=14 rps
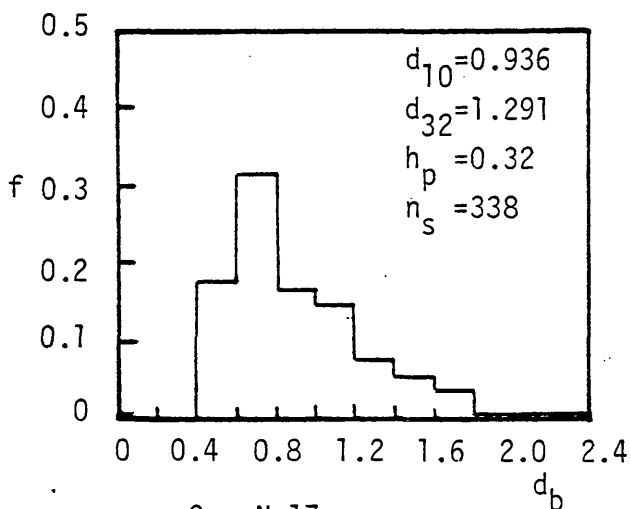
a.3. N=17 rps

a. Q = 2.67x10^{-4}m^{3}s^{-1}
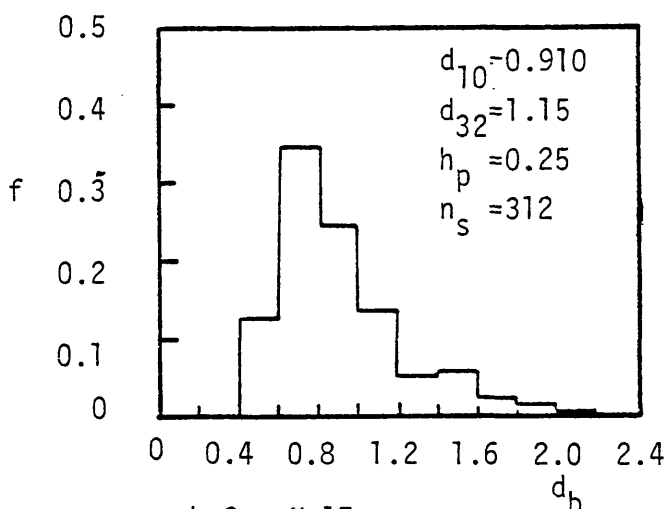
b.3. N=17 rps

b. Q = 3.77x10^{-4}m^{3}s-1

Fig. 6.28 : Bubble size distributions at Position 4(see Fig. 6.11) for
two gas flow rates at different impeller speeds. D = 0.0762m.
Air-0.11 K$_2$SO$_4$ solution, d_b,d_{10}, and d_{32} in mx10^3
f = number fraction. n_s = sample size (bubbles)
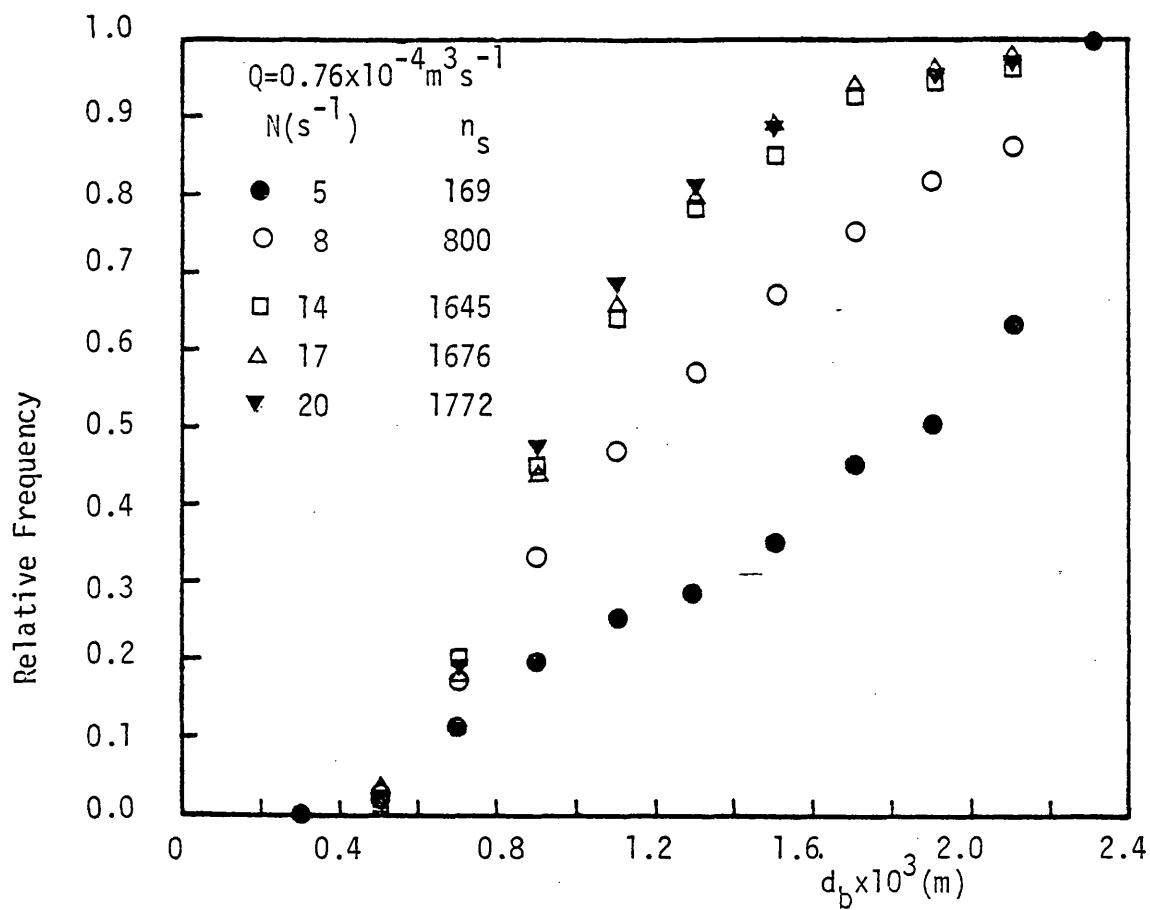
a. Effect of impeller speed.
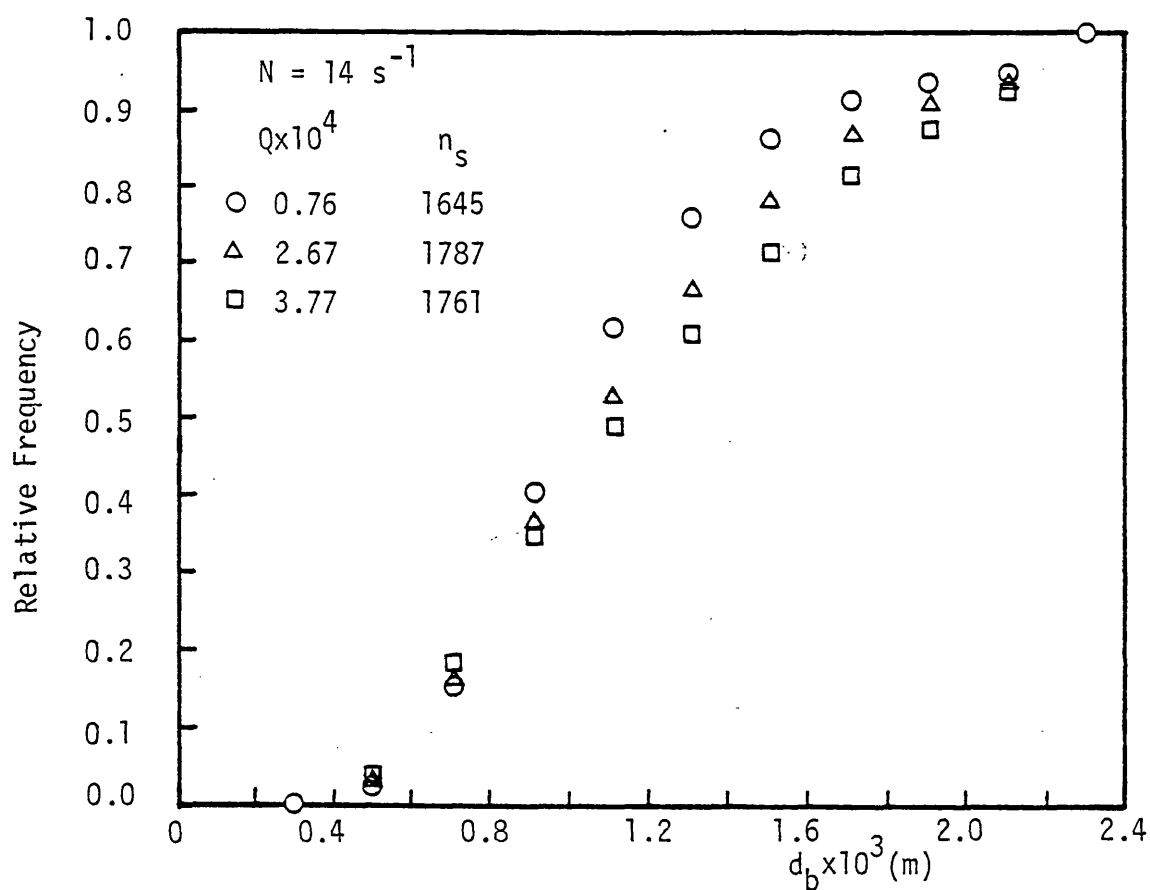
b. Effect of gas flow rate

Fig. 6.29 : Bubble surface area cumulative distribution function.

D = 0.0762m, air-0.11M K_2SO_4 solution.

n_s = sample size (bubbles)
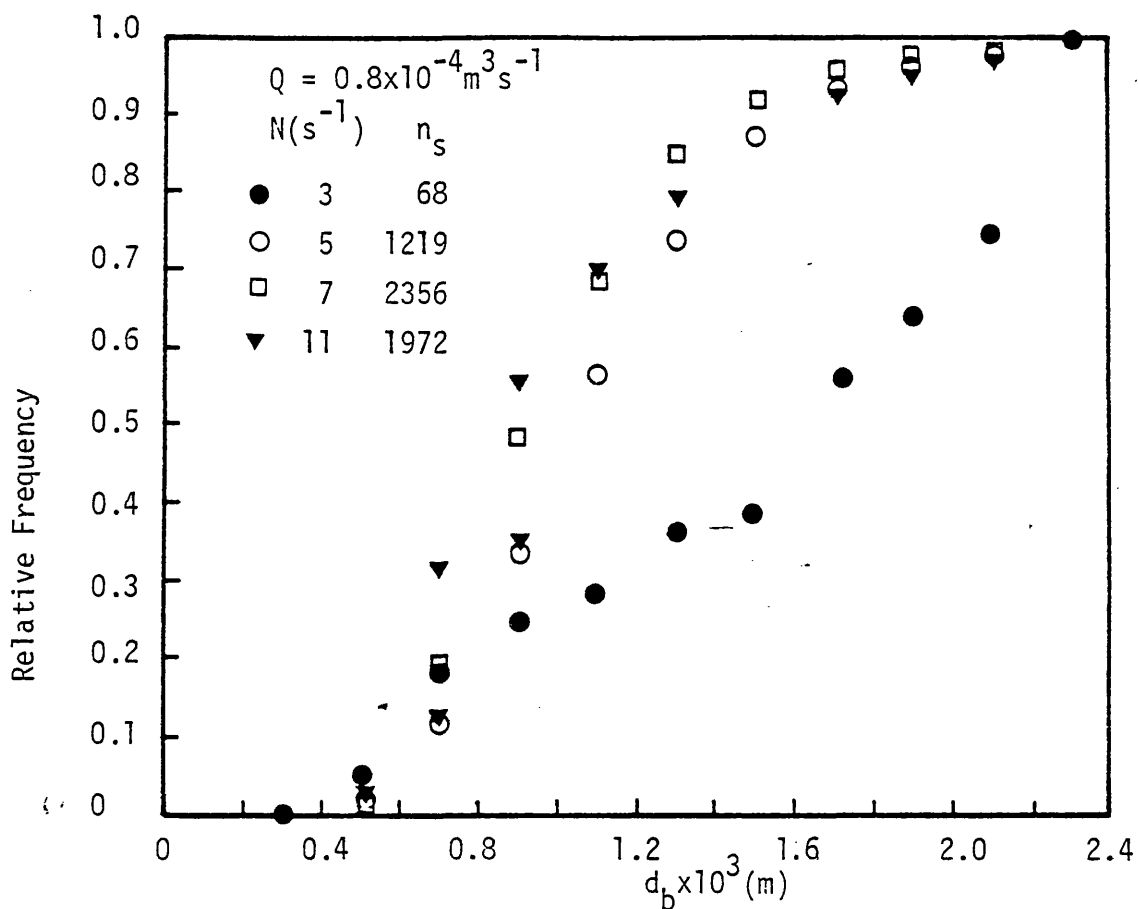
a. Effect of impeller speed
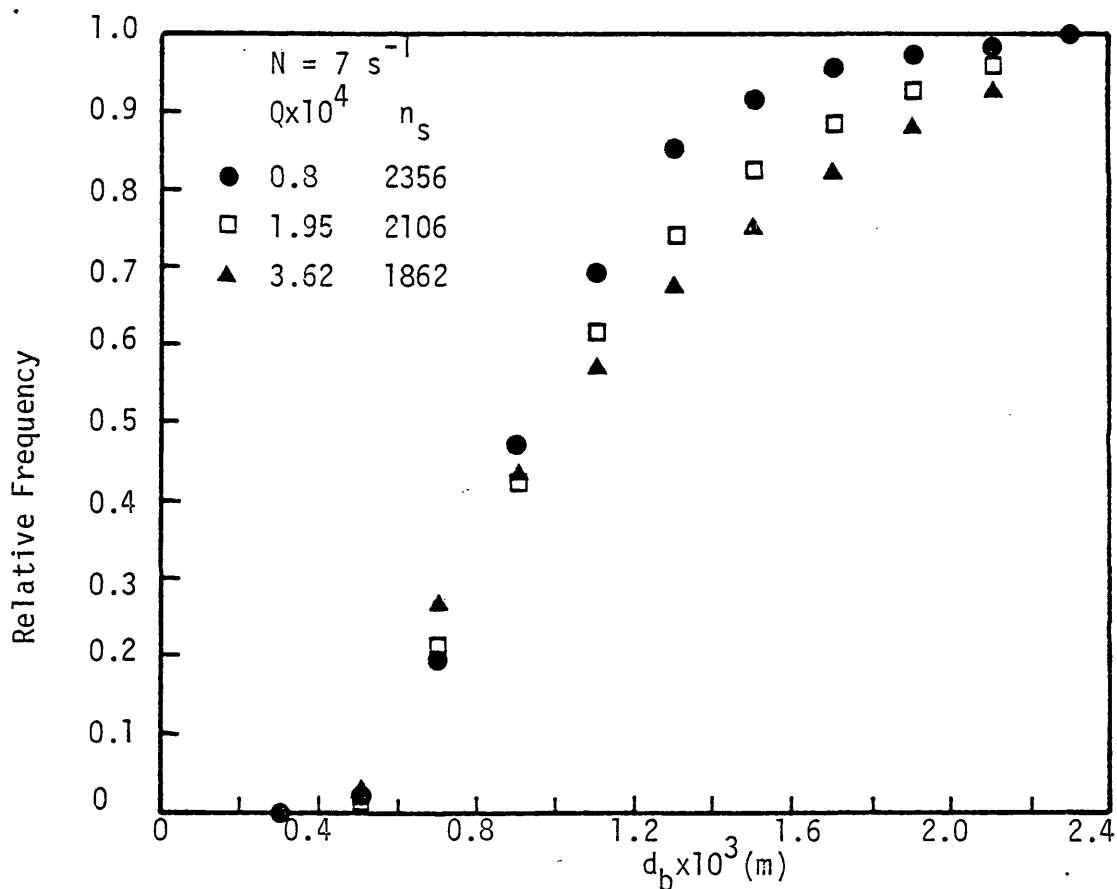
b. Effect of gas flow rate

Fig. 6.30 : Bubble surface area cumulative distribution function.

D = 0.1016m, air-0.11 K_2SO_4 solution

n_s = sample size (bubbles)
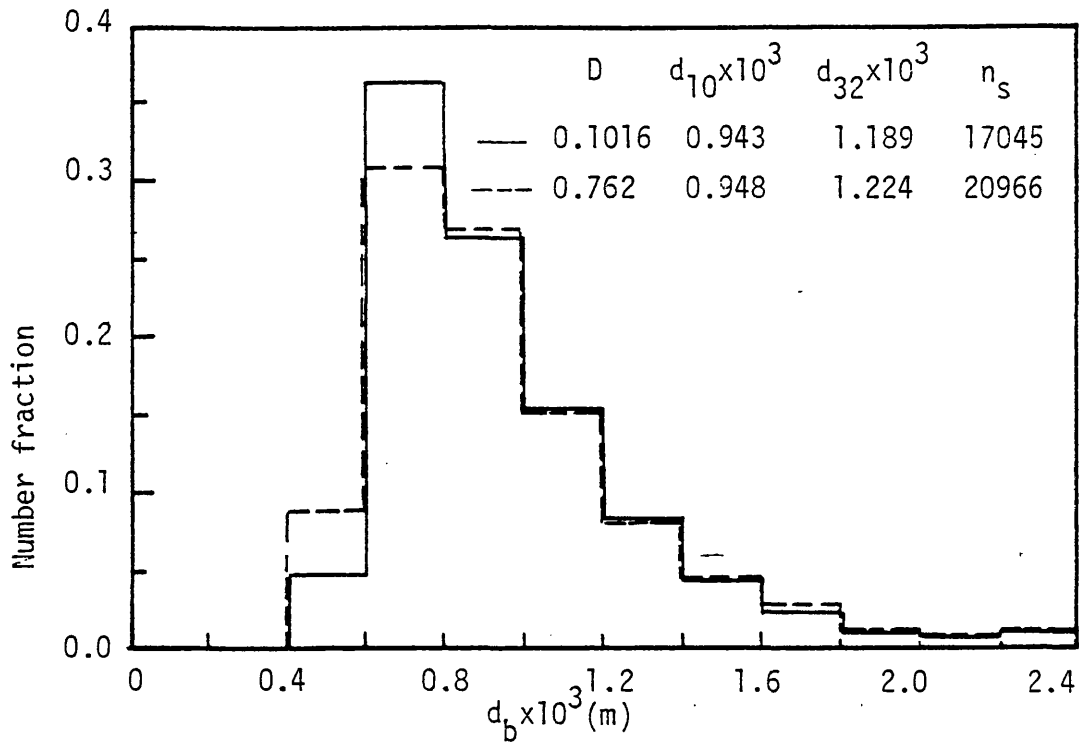
Fig. 6.31 : Bubble size distribution in the whole tank with different
Q and N (N > N_{F1}) for impellers D1 and D2.
Air-0.11M K_2SO_4 solution.
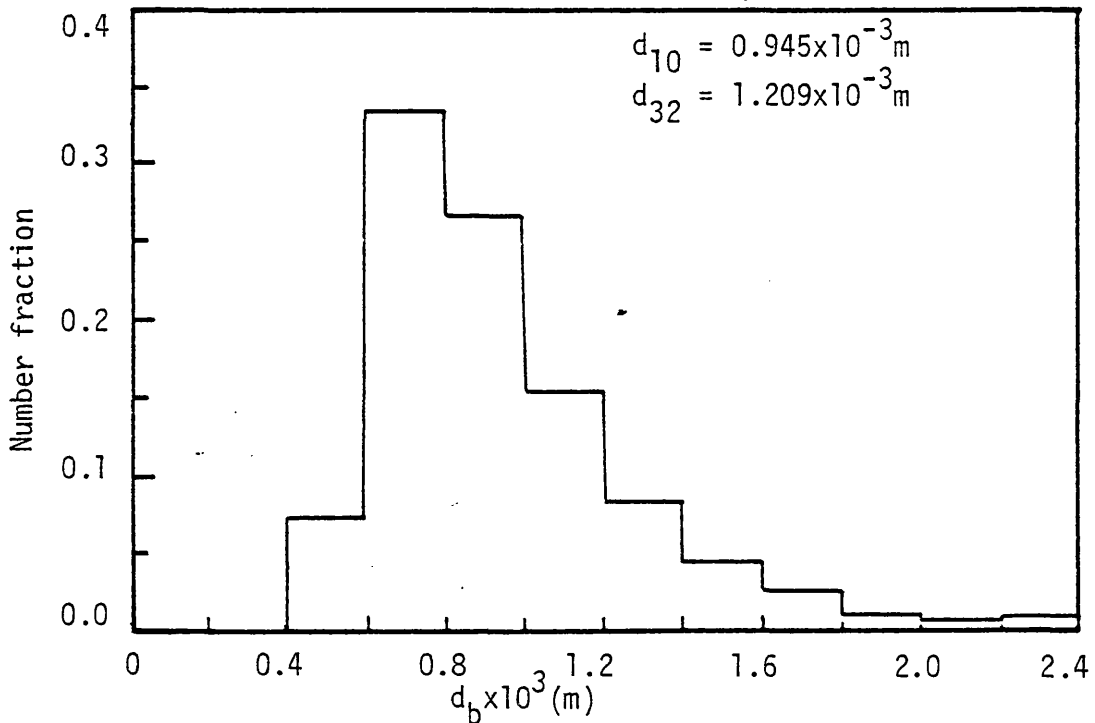
Fig. 6.32 : Bubble size distribution covering all operating conditions
at N > N_{F1} with impellers D1 and D2. air-0.11 K_2SO_4 solution.
sample size 38,011 bubbles.

the close distributions for the two sizes of impeller. In the case of impeller D1 the sampling was done at positions 1, 4, 10, 11, 14, and 15, and for impeller D2 at positions 1, 4, 5, 6, 7, and 8 (see Fig. 6.11). These two distributions are added together to create a general bubble size distribution for the air-0.11M K_2SO_4 dispersion for the condition $N > N_{F1}$ as shown in Fig. 6.32. The mean bubble size is 0.945mm, which is about 2.4 times that which was measured in bubble column for the same solution using a photographic method (53). The corresponding bubble surface area cumulative distribution is shown in Fig. 6.33 together with a similar distribution for a fermentation media as measured by Weiland et al (71) using photoelectric probe technique similar to the one used here. The agreement between these two distributions suggests that the measurements of bubble size obtained for the electrolyte solution could be used to simulate industrial applications which use 'non-coalescing' systems.

The deviations between these two distributions may in fact be attributable mainly to error in measurement. Weiland et al (71) measured very small bubbles in their system and they would have needed to use a very fine capillary tube of about 0.1mm inner diameter for sampling. The larger bubbles measured in this study (d_b=1.6-2.4mm) would probably have broken up inside a capillary of this fine dimension. Thus, it is apparent that they did not consider the bubble breakage phenomenon inside the capillary tank.

6.4.2.2 Correlation for Bubble Diameter

The measured mean sauter bubble diameter did not show any measure of dependence on gas holdup. Calderbank's correlation (10), Eq. 6.6, and that of Lee and Meyrick (9), Eq. 6.7, were both unsuccessful in correlating the results of this study. However, by drawing d_{32} against the total power input on a log-log plot, a linear relationship was
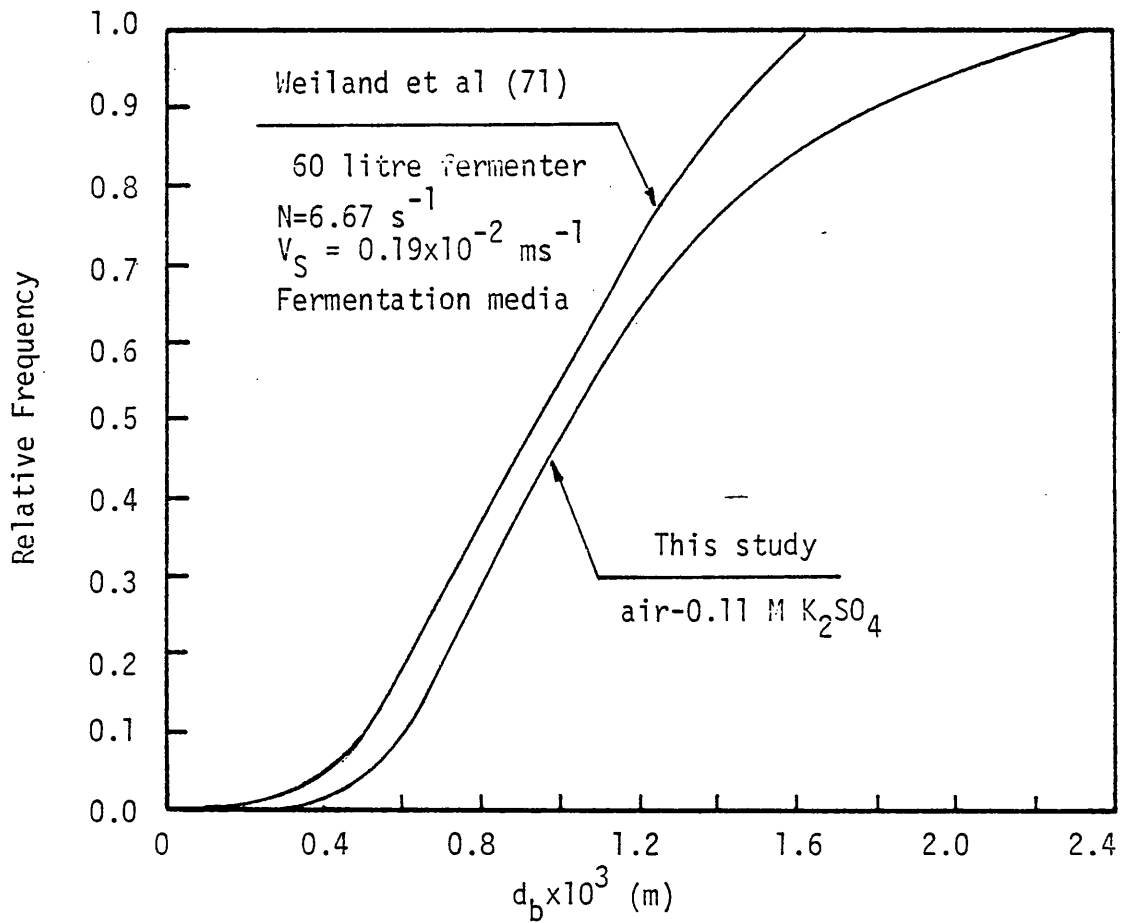
Fig. 6.33 : Bubble surface area cumulative distribution covering
all operating conditions at $N > N_{F1}$ with impellers
D1 and D2.   Sample size 38,011 bubbles.

obtained as shown in Fig. 4.34. This relation can be expressed in terms of the power dissipation per unit volume of liquid :

$$d_{32} = 3.52 \times 10^{-3} \left(\frac{Pg\cdot t}{V} \right)^{-0.13}$$

6.32

In the absence of any other detailed data it is difficult to judge the validity of Eq. 6.32 for larger scale equipment. However, as a rough check, the single measurement of Weiland et al (71) for their fermentation media, indicates that d_{32} is close to the average value obtained here, ie, 1.2mm (see Fig. 6.32). In their study a 60-litre fermenter fitted with 6-blade turbine was used. Assuming standard dimensions for the fermenter, ie, T=H=3D, the detailed dimensions of their equipment could be estimated. Using the power correlations for the sulphate solution which are presented in Chapter 4, it was found that they were operating within the efficient mixing zone. By estimating the impeller power consumption and using Eq. 6.32, d_{32} was found to be 1.44mm, which is about 20% higher than their measured value.

Finally it is important to mention that Eq. 6.32 was obtained for 0.11M K_2SO_4 solution. For lower concentrations Eq. 6.32 is expected to underestimate d_{32}. The large bubble sizes measured in this study compared with the measurements of Marrucci and Nicodemo (53) in bubble column with the same solution, points to an increased effect of bubble coalescence in the agitated tank. Thus it seems that measurements on bubble columns (53) are not really valid for agitated vessels. It would not be wise, therefore, to exclude the possibility that a further reduction in bubble size may occur with increase of the electrolyte concentration beyond the 0.11M used in this study without experimental evidence. However, given the reasonable success achieved in predicting the bubble size for the fermentation media then it can be considered that the power correlations given in Chapter 4, and the bubble size
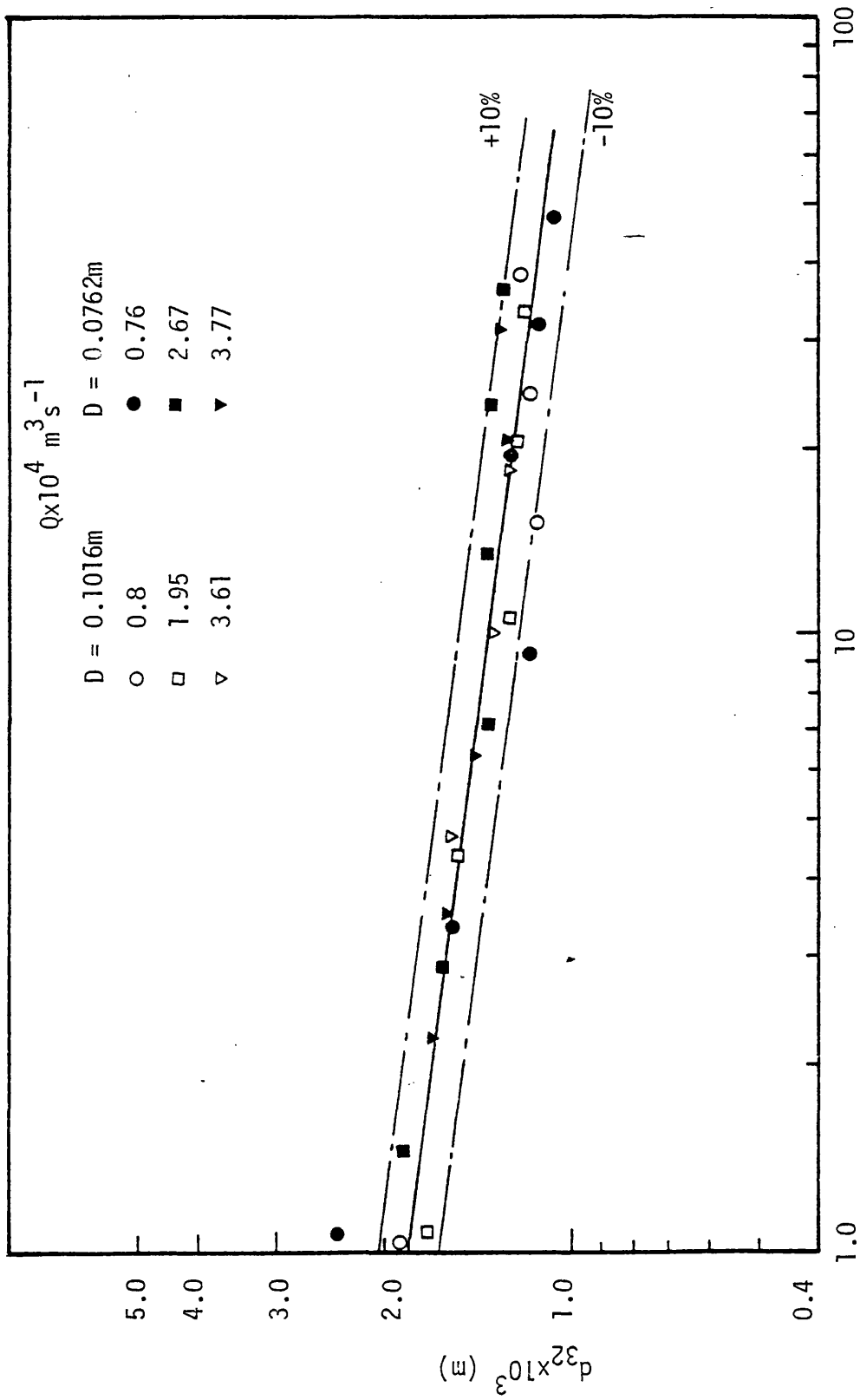
Fig. 6.34 : Correlation of bubble size (air-0.11M K_2SO_4)

correlation (Eq. 6.32) are capable of predicting d_{32} to a reasonable accuracy, which may be a good enough estimate for design.

6.5   CONCLUSIONS

1 - A capillary tube measurement technique for bubble size has been developed and used successfully for measuring the bubble size in 'coalescing' and 'non-coalescing' gas-liquid dispersions in an agitated vessel.   The photoelectric probe when coupled to a computer, provides fast and accurate results and is simple to use.   The fact that this technique has also been developed to measure point gas holdup and hence to give a direct estimate of the point interfacial area, points to its potential application as an effective instrument for control in industrial processes.

2 - The bubble size measurements in air-water dispersions show that there is a strong dependence on the location of sampling and the operating parameters, ie, N, D, Q, and T.   For the range of impeller speeds and gas loads investigated, the mean equivalent bubble diameter, d_{10}, varied from 1.5 to 2.7mm, while the range of Sauter mean bubble diameters was 2.6 to 3.6mm.   A correlation for d_{32} has been proposed, but further measurement in larger scale equipment is needed to verify the suitability of this correlation.

3 - For air-0.11M k_2SO_4 solution, much smaller bubbles were produced. The bubble surface area cumulative distribution function was found to be almost independent of N and Q for $N > N_{F1}$. d_{32} for this condition has average value of 1.2mm.   When this distribution was compared with published results on fermentation media there was a reasonable agreement.

The mean bubble size was found to be independent of gas holdup and a function only of the total power dissipation per unit volume of liquid. The measurements of d_{32} obtained in this study have been correlated within $\pm 10\%$. The proposed correlation is expected to give reasonable estimate for bubble size in 'non-coalescing' agitated dispersions.

CHAPTER 7

GAS HOLDUP AND INTERFACIAL AREA

7.1   INTRODUCTION

One of the main functions of the stirrer in an agitated vessel is to break-up and distribute the gas into the bulk liquid.   Dispersion of the gas is required to generate the gas-liquid interfacial area in order to promote mass transfer across the gas-liquid interface.   On the other hand, the gas holdup which is produced is a measure of the effectiveness of gas-liquid agitation.   Because of their importance as design parameters, therefore, the gas holdup and specific interfacial area have been studied in detail.

The overall gas holdup was measured from the change of the liquid level in the vessel following the introduction of gas (see Chapter 2).   For the point gas holdup and the corresponding specific interfacial area, the capillary probe method (described in Chapter 6) was used.   The total specific interfacial area was estimated from the bubble size measurements presented in Chapter 6, and the measurements of the over-all gas holdup.   Impeller power measurements and correlations which are presented in Chapter 4, are used to develop correlations for the gas holdup and specific interfacial area.   Some of the correlations for bubble size presented in Chapter 6 are also used in this chapter.

It is important to point out that there is very widespread literature pertaining to this subject.   In the review which is to follow, therefore, emphasis is given to fundamental aspects and the most recently published studies.

7.2   LITERATURE REVIEW

7.2.1   Gas Holdup

The lack of agreement in measurements and the variety of forms of correlations for gas holdup, h, available in the literature can be

mainly attributed to experimental errors. A discussion of the techniques used for measuring h and the possible causes of errors is presented in Section 2.4.2. The following review concentrates on the more important correlation forms rather than attempting critically to analyse the deficiencies in other techniques. To complete the discussion of results, a comparison with other published data is made.

In their early study, Foust et al (7) used the impeller power consumption per unit liquid volume (Pg/V) and the superficial gas velocity Vs to correlate gas holdup. The agitated vessels were equipped with disc turbines having blades of special shape. They found

$$h \alpha (Pg/V)^{0.47} Vs^{0.53} \qquad 7.1$$

This type of correlation has subsequently been employed by many other workers.

Calderbank (10) measured the gas holdup in stirred tanks fitted with a standard 6-bladed disc turbine. Using different sizes of equipment and also different liquids, he proposed the following correlation

$$h = (\frac{Vs \ h}{U_T})^{\frac{1}{2}} + 0.0216 \left[\frac{(Pg/V)^{0.4} \rho^{0.2}}{\sigma^{0.6}} \right] (Vs/U_T)^{\frac{1}{2}} \qquad 7.2$$

At large rates of power dissipation, Eq. 7.2 reduces to

$$h \alpha (Pg/V)^{0.4} Vs^{0.5} \qquad 7.3$$

which is in reasonable agreement with Eq. 7.1.

In their recent study, Sridhar and Potter (6) measured the gas holdup in an agitated vessel at elevated pressures. They proposed the following modification to Calderbank's correlation

$$h = (\frac{V_s \, h}{U_T})^{\frac{1}{2}} + 0.0216 \left[\frac{(P_g/V)^{0.4} \, \rho^{0.2}}{\sigma^{0.6}} \right] \left[\frac{V_s}{U_T} \right]^{\frac{1}{2}} \left[\frac{P_{gt}}{P_g} \right] \left[\frac{\rho_g}{\rho_a} \right]^{0.16} \qquad 7.4$$

where

ρ_g = gas density at system conditions

ρ_a = density of air at operating temperature

At high power inputs, and assuming ideal gas behaviour, the effect of vessel pressure may be expressed as —

$$h \; \alpha \; (\frac{P}{P_A})^{0.16} \qquad 7.5$$

where

P = vessel pressure

P_A = atmospheric pressure

Rushton and Bimbinet (8) who investigated gas holdup over a range of equipment size, with T = 0.228 to 0.91m and D/T = 0.222 to 0.53, found that

$$\frac{h}{1-h} = C_1 \; (\frac{P_{gt}}{V})^{C_2} \; V_s^{0.6} \qquad 7.6$$

where C_1 and C_2 are constants which depend on D and T. In calculating the power supplied by the gas stream, they considered only the expansion energy, ie, the second term of Eq. 6.10.

Hassan and Robinson (13) measured the gas holdup in small size tanks (T = 0.152 and 0.291m) using different types of impellers. They proposed the following correlation

$$h = C_3 \; (\frac{QN^2}{\sigma})^{C_4} \qquad 7.7$$

The constants C_3 and C_4 were found to depend on the impeller type and the nature of the aqueous electrolyte.

Lee and Meyrick (9) studied the gas holdup in electrolyte solutions with different concentrations. They found the parameter C_o $(d\sigma/dc)^2 \emptyset$ * to be promising in correlating the gas holdup as well as the specific interfacial area. Their results were presented in graphical form and an iterative method was proposed to estimate h.

In a recent publication Yung et al (11) used dimensional analysis to correlate h. Using different 'pure' liquids they found

$$h = C_5 \ F\ell^{0.5} \ We^{0.65} \ (\tfrac{D}{T})^{1.4} \qquad\qquad 7.8$$

where C_5 equals 0.0052 for flat bottomed tank fitted with a 6-blade turbine. They examined the data of Kawecki et al (69) and Maini (79/11), which exhibited a similar trend to that described by Eq. 7.8, but was larger than their own results by a factor of 3 and 1.6 respectively. They attributed this discrepancy to surface aeration. For electrolyte solutions, the following correlation has been proposed

$$h \ \alpha \ Q^{0.5} \ N^{0.8} \ D^{1.4} \qquad\qquad 7.9$$

The latest study on this subject is that of Botton et al (80) where h is correlated with the impeller tip velocity as follows

$$h = (\tfrac{VP}{VPf})^{C_5} \qquad\qquad 7.10$$

where

VP = tip velocity of stirrer $(=\pi ND)$

VPf = fictitious value of VP at h=1.

---

* C_o concentration of the solute in the solution

C   concentration of solute in film

$\emptyset$ activity coefficient function $\emptyset = (1+dInf/dInc)^{-1}$

f   activity coefficient

The value of C_5 was found to depend only on the ratio $\frac{Vs}{Vs_f}$, where Vs_f is a fictitious value of superficial gas velocity at h=1.

Further studies on gas holdup can be found in the investigations of Yoshide and Miura (81), van Dierendonck et al (21), Reith and Beek (82), Miller (83), Joshi and Sharma (84), Smith et al (54), and Loiseau and Midoux (45).

7.2.2 Interfacial Area

The specific interfacial area, a, in agitated vessels has been investigated by many workers. However, there is no general correlation for predicting a, nor any agreement concerning the most suitable method for measuring this quantity.

The methods for measuring a can be classified as either physical or chemical. Excluding the photographic technique, which has often been criticised (85), the light scattering techniques are the only reliable physical methods so far employed. Different light scattering techniques have been used but they all make use of the light scattering properties of the dispersion. Details of these techniques can be found elsewhere (10,85). The chemical method has also been widely used. This method makes use of a fast reaction between two phases. The rate of absorption can be predicted from the theory of absorption with chemical reaction, and the interfacial area can be calculated from measured absorption rates.

During 1980 several studies were published on the specific interfacial area in stirred tanks. Sridhar and Potter (85) who used the light scattering technique, pointed to the following drawbacks of the chemical method. They stated that although the chemical method provides a sophisticated way of determining a, it has the disadvantage

of requiring time consuming investigations of the kinetics. This means that a systematic investigation of the effects of the liquid phase properties such as σ and μ is virtually impossible. Therefore, despite its widespread use, the chemical method has not led to any generalised correlation for predicting a. However, Hassan and Robinson (72) have advocated the use of the chemical method on the basis that it determines an integral value of a, which represents the sum of only those surface area elements across which mass transfer actually takes place. In comparison the light scattering method is only capable of providing local values of a, unless a complete traverse of the dispersion volume is carried out. They also claimed that the presence of the light transmission/reception probe in the dispersion disturbs the fluid flow pattern in the vicinity of the probe. Hofer and Mersmann (86) compared the measured a using physical and chemical absorption methods in various types of gas-liquid contactors, including stirred vessels. They found that the chemical method yields a lower value compared with the physical method. This was attributed to depletion effects in the gas bubbles at very high mass transfer rates. To prevent this depletion effect, it was suggested that in using the chemical method the rate of mass transfer should be kept as small as possible. They also indicated that physically determined values of a are appropriate for physical absorption processes, whilst in the case of chemical absorption it is necessary to use a as measured by a chemical method in estimating rates of mass transfer.

From the above discussion, it is evident that the values of the specific interfacial area obtained will depend on the method of measurement. However, the work of Hassan and Robinson (72) and Hofer and Mersmann (86) indicates that there is a need to use both the physical and the chemical methods to determine the total and

the effective specific interfacial area.

Physical Methods

In 1955 Vermeulen et al (68) presented the first correlation for a in agitated gas-liquid vessels which was based on measurements obtained by using the light scattering method. Calderbank (10) claimed that the results were not representative since only one location in the tank close to the impeller tip was studied. ⁻Using a light obscuration method, Calderbank (10) was able to measure a at many points in the tank, demonstrating that there was a wide variation in the local values of a. His correlation for pure liquids and non-electrolyte solutions is :

$$a = 1.44 \frac{(Pg/V)^{0.4} \rho^{0.2}}{\sigma^{0.6}} (\frac{Vs}{U_T})^{\frac{1}{2}} \qquad 7.11$$

Sridhar and Potter (85) also verified this correlation and proposed a modification to account for the vessel pressure and temperature (multiplying L.H.S. of Eq. 7.11 by $(\frac{Pgt}{Pg}) \cdot (\frac{\rho_g}{\rho_a})^{0.16}$, see Eq. 7.4).

Kawecki et al (69) estimated a from Eq. 6.2. These results when presented on an a Vs. N plot gave a series of parallel lines for different gas loads. However, both the photographic technique used and the restriction of sampling to the impeller region, has been criticised (85).

Lee and Meyrick (9) used the light transmission method to study the effect of electrolyte concentration on a. Less variation in the local values of a was observed compared to Calderbank's (10) results for pure liquids. They attributed this to the smaller bubble size produced in electrolyte solution causing an increase in the rate of recirculation of bubbles and therefore greater homogenity of the

tank contents. A large increase of a occurred with increasing concentration of electrolyte, which became more pronounced at higher impeller speeds.

Chemical Methods

Westerterp et al (37) defined a minimum impeller speed N_0 (Eq. 4.1, Chapter 4) below which a was found not to change with N. They proposed the following correlation for $N>N_0$ —

$$a = c \frac{(1-h)}{H} D \left(\frac{\rho T}{\sigma}\right)^{\frac{1}{2}} (N-N_0) \qquad 7.12$$

where c is a constant which depends on the liquid viscosity. The kinetic data and assumptions made have, however, been the subject of some criticism (5,82,87).

A wide investigation to study the effect of several parameters on a, was conducted by Metha and Sharma (87). Different systems were employed, including the absorption of CO_2-air mixture into aqueous alkaline solutions of NaOH KOH and $Ba(OH)_2$. The effects of impeller speed was found to be in agreement with the results of Westerterp et al (37). The considerable increase in a found with increase in the ionic strength of the solution is in agreement with Lee and Meyrick's (9) result. However, they reached the conclusion that the effective interfacial area could not be predicted a priori because of the high sensitivity of the process to changes in system parameters.

Reith and Beek (82) measured a in sodium sulphate solution and observed an increase of a with increasing gas load at low impeller speeds. At high impeller speeds the opposite effect was observed. This was explained as being due to the ineffectiveness of the impeller at high impeller speeds. Using three sizes of tank (T=0.191, 0.45, and 1.20m) they found that a scaling rule, based on

constant power input per unit volume, applied over the range of operating conditions used ($Vs = 4.7 - 15.8 \times 10^{-2} \, ms^{-1}$).

A technique for simultaneous evaluation of k_L and a in stirred tank was developed by Robinson and Wilke (5). It involved cocurrent chemical absorption of carbon dioxide and desorption of oxygen in aqueous solution of inorganic electrolytes. They found that a increases with increasing the ionic strength, I. Also the dependency of a upon Pg/V increased somewhat with increasing I. For $KOH-K_2CO_3$ with $I = 0.0965$ mol ion/L, a varied as $(Pg/V)^{0.89}$ and in $KCL-KOH-K_2CO_3$ ($I = 0.221$), a was proportional to $(Pg/V)^{1.06}$. Only one gas load was investigated ($Vs = 4.57 \times 10^{-3} \, ms^{-1}$). Recently Hassan and Robinson (72) stated that the previous measurements of a (5) were overestimated. This was because the assumption of perfect mixing of the gas phase if applied in systems in which there is significant solute gas depletion, results in underestimation of the actual time-average driving force. After making correction for this effect then over a range of ionic concentration ($I = 0.1$ to 1.2) they found

$$a \, \alpha \, (Pg/V)^{0.9} \, Vs^{0.4} \qquad\qquad 7.13$$

In contrast to the finding of previous studies (5,9,87), they found a to be independent of the ionic strength of the solution (for $I>0.1$). Their explanation for this was that Lee and Meyrick's (9) measurements using the light scattering method represented the total specific interfacial area and not the mass-transfer-effective specific interfacial area. Since Lee and Meyrick's (9) values were higher than theirs, they therefore concluded that the effective a is less than the total a. The use of the effectiveness factor defined by Joosten and Danckwerts (88) was recommended for further investigations.

The method recently proposed by El Shawarby and Eissa (89) based on the impeller power, contains a number of assumptions regarding the mechanism of energy dissipation in ungassed and gassed agitated liquids. Although there is no experimental evidence to support these assumptions, their measurements of a for air-water system lie within the acceptable range.

7.3   RESULTS AND DISCUSSION

7.3.1   Gas Holdup

7.3.1.1   Point Gas Holdup

The measurements of point gas holdup for air-water dispersion are shown in Fig. 7.1.   In general, the gas distribution in the vessel is in a good agreement with the visual observations and measurements of Nienow et al (4).   In the flooding regime ($N=5$ s^{-1}) the gas bubbles rise vertically, with little dispersion occurring towards the walls of the tank.   In the efficient mixing regime ($N=11,14$ s^{-1}) a toroidal flow loop (4) starts to appear.   Near to the upper limit of the efficient mixing regime, and in the gas recirculation regime (17 and 20 s^{-1}), the circulation loop contracts in size and its centre appears to coincide with Position (10) (see Fig. 6.11).   This applies to all the gas flow rates with the two sizes of impeller used.

The coefficient of variation $\sigma'_{h_p}/\bar{h}_p$ is used as a measure of the spread of the spatial distribution of the gas bubbles in the liquid volume in the tank.   Figures 7.2 and 7.3 illustrate the change of $\sigma'_{h_p}/\bar{h}_p$ with N and Q for impellers D1 and D2.   These results show that at constant gas flow rate, $\sigma'_{h_p}/\bar{h}_p$ has high values for $N<N_{F1}$. This indicates that there is relatively poor distribution of the gas. As the impeller speed is increased $\sigma'_{h_p}/\bar{h}_p$ decreases, and a minimum is reached when $N_{F1}<N<N_{R1}$, ie, in the efficient mixing regime

N = 5 s^{-1}

1.9 1.6 4.0

5.2 3.8 1.9

4.2 0.3 3.0

2.7 0.4 1.7

     1.1 1.0

N = 8 s^{-1}

12.3 8.5 11.0

9.8 15.6 8.4

16.3 16.0 7.9

11.0 15.0 10.8

     4.3 4.2

N = 11 s^{-1}

14.9 19.0 9.2

29.0 21.0 10.4

19.5 21.8 9.5

19.9 21.3 21.2

     16.5 17.8

N = 14 s^{-1}

30.7 16.8 12.3

21.3 23.9 12.5

24.8 20.8 8.5

28.5 28.3 17.9

     23.0 15.6

N = 17 s^{-1}

25.3 13.7 4.3

38.2 24.6 7.4

21.4 12.6 7.1

22.5 30.9 9.3

     13.0 13.0

N = 20 s^{-1}

22.2 15.3 4.9

29.5 16.7 8.0

24.3 15.5 8.0

30.8 29.5 10.0

     10.6 12.5
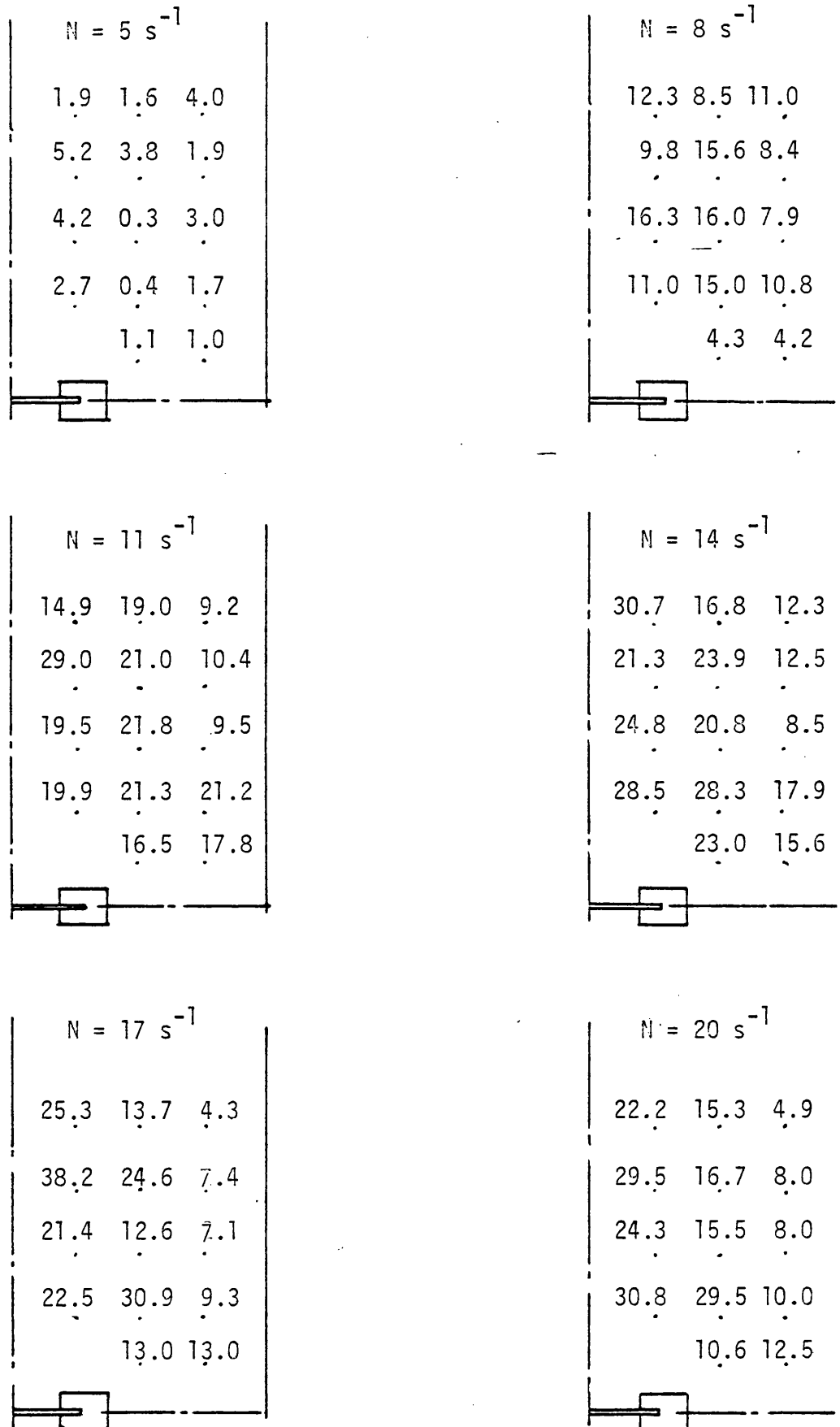
Fig. 7.1   Matrix of point gas holdup values (%) for
Air-tap water dispersion.
D = 0.0762m, Q = 3.77 x 10^{-4} m^{3}s^{-1}
N_{F1} = 9.9 s^{-1}, N_{R1} = 18 s^{-1}
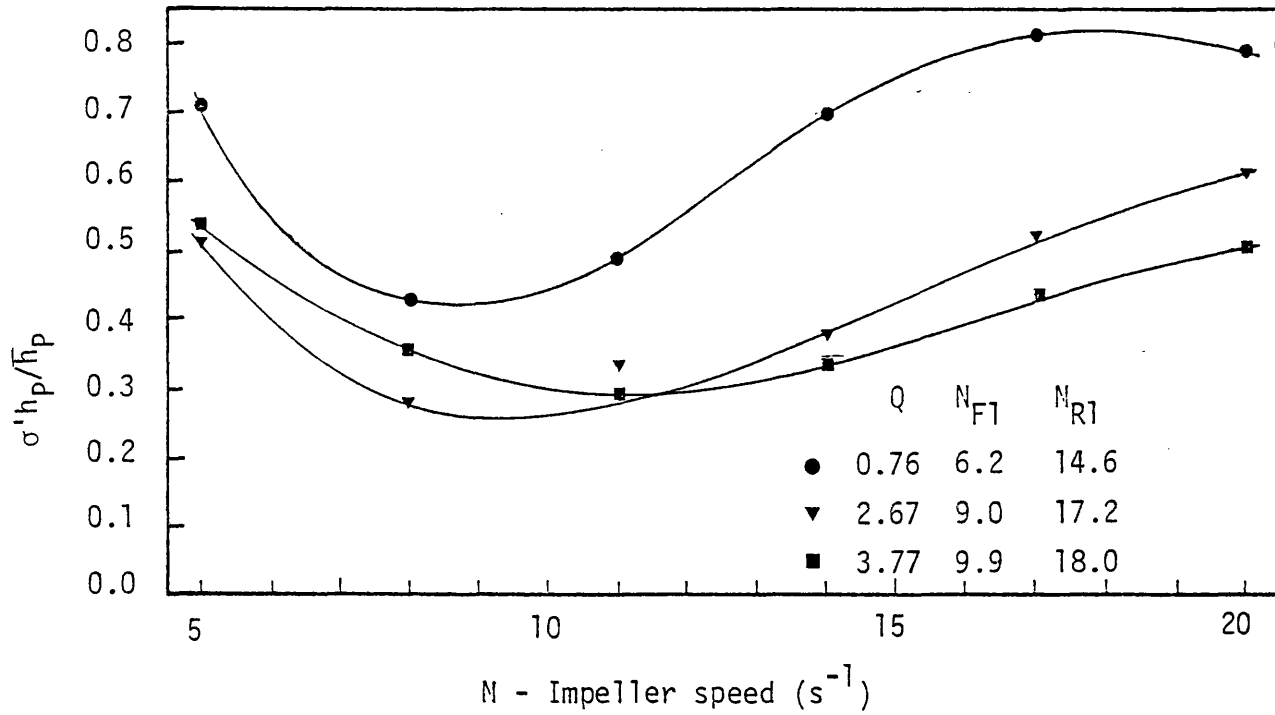
Fig. 7.2   Coefficient of variation of point gas holdup against the
impeller speed.   D = 0.0762m, air-water dispersion.
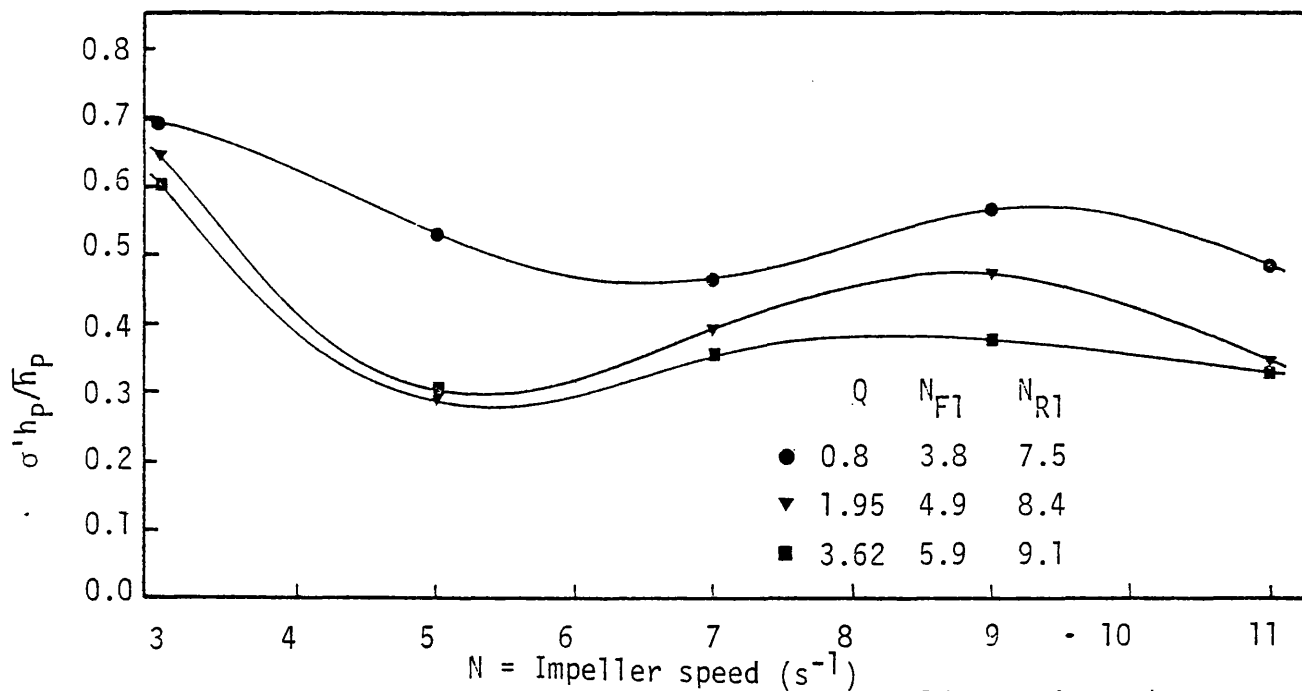
Fig. 7.3   Coefficient of variation of point gas holdup against the
impeller speed.   D = 0.762m, air-water dispersion.

but close to the flooding point. At this minimum value of $\sigma'_{h_p}/\bar{h}_p$, the gas-liquid dispersion achieves its highest quality in terms of uniformity of gas dispersion in the liquid. Further increase of the impeller speed causes $\sigma'_{h_p}/\bar{h}_p$ to increase, ie, the dispersion becomes less uniform.

In the case of an air-electrolyte solution dispersion, the distribution of point gas holdup showed a similar behaviour to that of air-water system (see Fig. 6.2, Chapter 6). The higher values of point gas holdup of the air-electrolyte compared to the air-water dispersion are confirmed by the overall gas holdup measurements. However, the change in the coefficient of variation with the impeller speed showed a different trend. Figures 7.4 and 7.5 demonstrate that there is a continuous reduction of $\sigma'_{h_p}/\bar{h}_p$ with increasing N. This means that there is continual improvement in the uniformity of dispersion.

Comparing Figs. 7.2 and 7.3 and Figs. 7.4 and 7.5, it can be inferred that at low impeller speeds ($N<N_{F1}$) the dispersion of gas bubbles is more uniform in water than in electrolyte solution. However at higher impeller speeds, ie, in the efficient and the gas recirculation mixing regimes, the opposite behaviour is observed.

7.3.1.2 Overall Gas Holdup

Two types of correlation for h are selected to examine the results of this study. These are Eq. 7.1 which is based on power consumption and superficial gas velocity, and the correlation derived from dimensional analysis, ie, Eq. 7.8.

Figure 7.6 shows h against Pg/V for impeller D1. Similar results were also obtained with the other two impellers. This figure shows that the constant gas flow rate lines are not parallel. Also for a
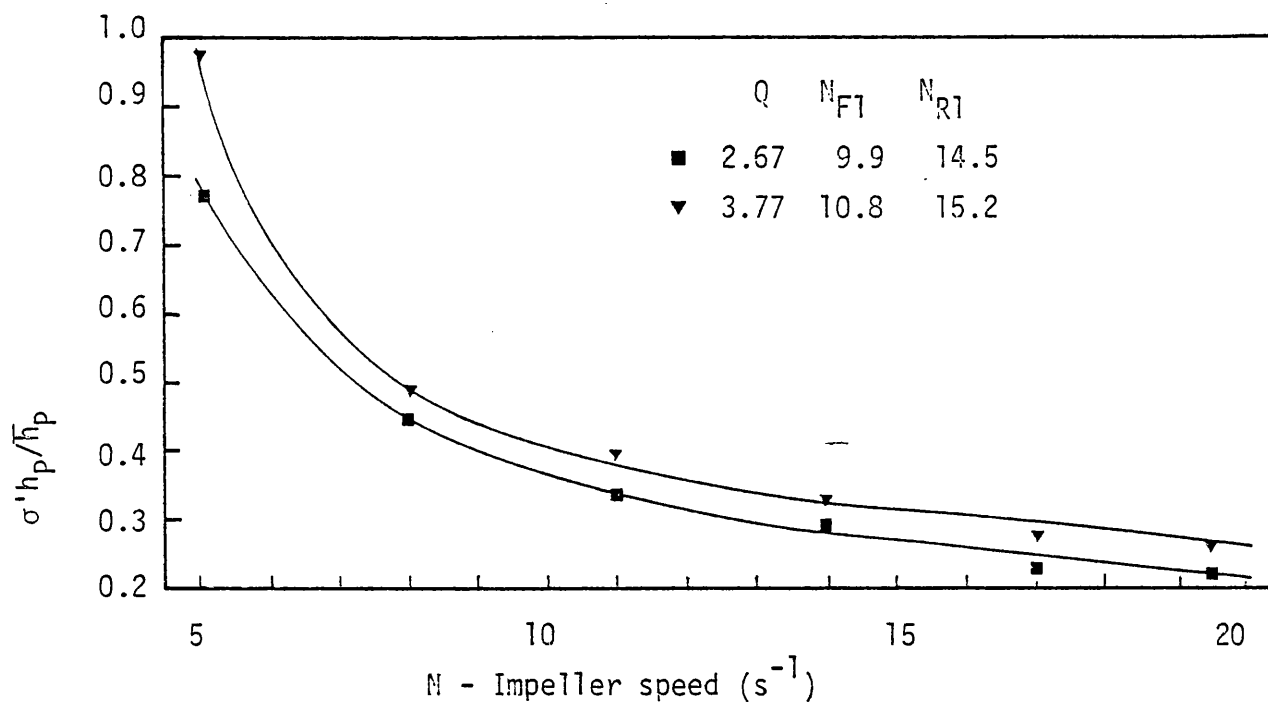
Fig. 7.4   Coefficient of variation of point gas holdup against the
impeller speed. D = 0.0762m, air-0.11 K_2SO_4 dispersion.
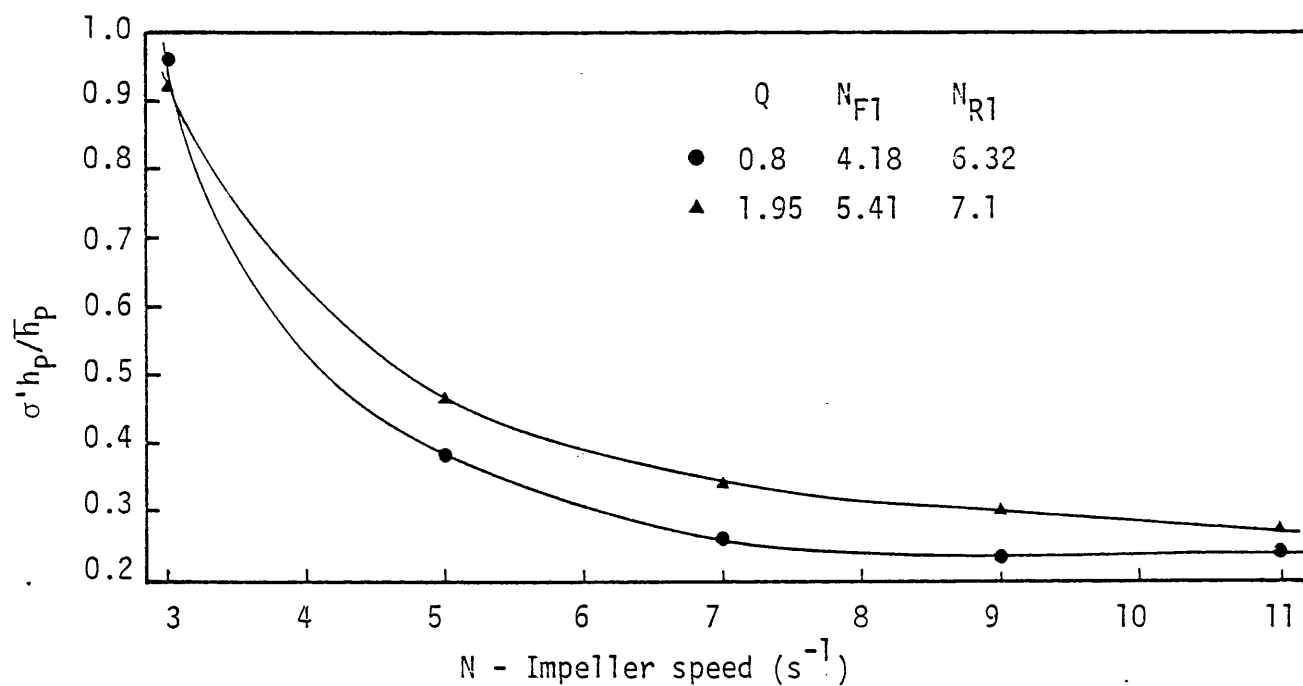
Fig. 7.5   Coefficient of variation of point gas holdup against the
impeller speed. D = 0.1016m, air-0.11 K_2SO_4 dispersion.
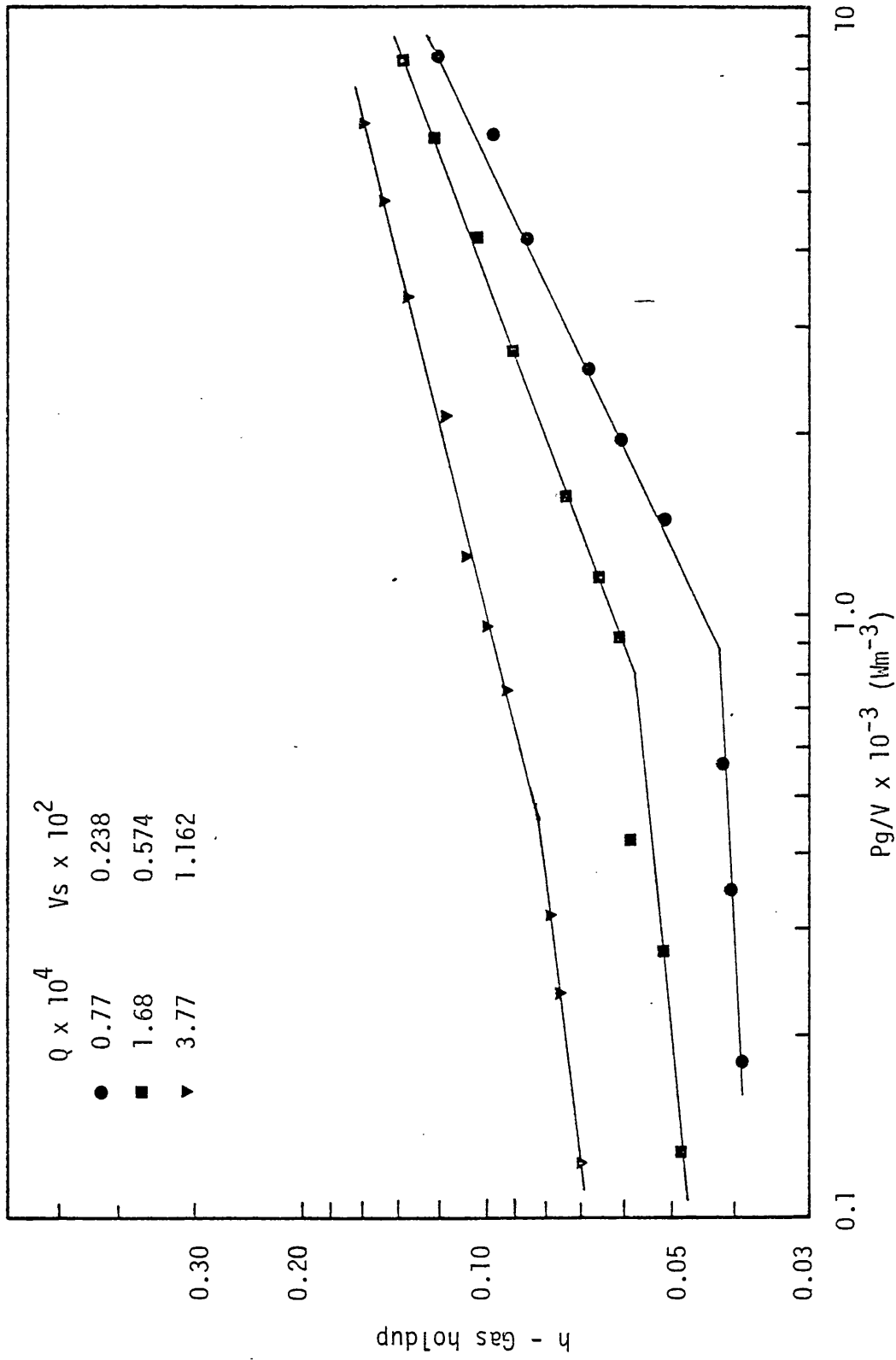
Fig. 7.6 Gas holdup against power per unit volume of liquid.
air-water dispersion (D = 0.0762m)

a particular gas flow rate there is a change in the slope of the curve.
This, therefore, precludes the use of a logarithmic plot for obtaining
a correlation of the type of Eq. 7.1. What is more important, however,
are the reasons for these distinct trends.

The h vs. N curves in Fig. 7.7 (same data used in Fig. 7.6) show that
there is an increase in gas holdup with increasing impeller speed
over the first section of the curve. This, therefore, excludes the
possibility that the break point in the curve corresponds to the
minimum impeller speed which was defined by Dierendonck et al (21)
(Eq. 4.2.A). On the other hand, the minimum impeller speed N_o, as
defined by Westerterp et al (37) (Eq. 4.1), gives a reasonable
prediction for the impeller speed at the break point condition.
However, the specific interfacial area was found to increase with the
impeller speed for $N<N_o$ which contradicts their definition. The
definition of the flooding point as employed in this study has also
been examined. For all the impellers, the speed corresponding to
the break point in h vs. N curve at constant Q is always higher than
N_{F1} and lower than N_{R1}.

Yoshida and Miura (81) obtained a family of curves similar to those
of Fig. 7.7. They suggested that the increase in slope at high
impeller speeds may be caused by surface aeration. The increase in
the slope as the gas flow rate decreases (Fig. 7.7) tends to
substantiate this opinion. A further examination of this point is
made by considering the rate of surface aeration measured in two
previous studies.

It was referred to previously (Chapter 4) that Nienow et al (41)
reported a very rapid decrease in the rate of surface aeration with
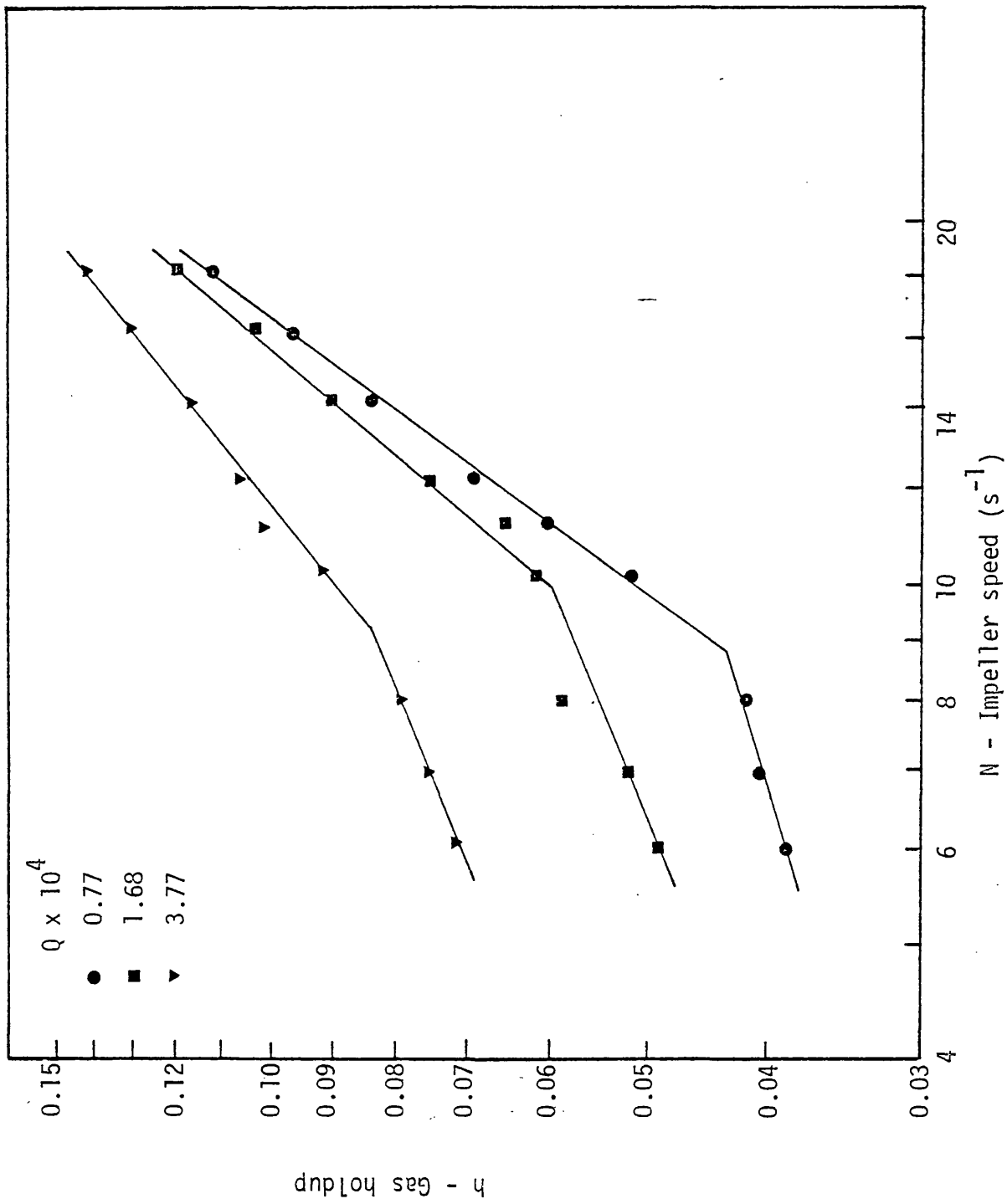
Fig. 7.7 Gas holdup against impeller speed. air-water dispersion (D = 0.0762m)

increase of the sparged gas rate.   For example, at Vs = 5.71 x 10^{-3}ms^{-1},

and power input of 6.5 x 10^{-3} Wm^{-3} the surface aeration rate was found

to represent only 4.7% of the sparge rate.   On this basis, if the trend

shown in Fig. 7.6 is to be attributed to surface aeration only, then

there should not be any distinct difference between the slopes at the

two higher gas flow rates.   Calderbank (90) also investigated the

surface aeration phenomenon by stripping dissolved sulphur dioxide

in water with air.   The flow rate of air participating in the

absorption was estimated and compared with the sparge rate.   His

correlations can be stated in the following forms :

$$N_{gSA1} = 1.5 \times 10^4 \left(\frac{D^2\rho}{\mu}\right)^{-0.7} \left(\frac{D}{Vs}\right)^{0.3} \qquad 7.14$$

$$N_{gSA2} = 6.0 \times 10^4 \left(\frac{D^2\rho}{\mu}\right)^{-0.7} \left(\frac{D}{Vs}\right)^{0.3} \qquad 7.15$$

where

N_{gSA1} = impeller speed for the onset of surface aeration
in aerated vessel.

N_{gSA2} = impeller speed for the complete development of
surface aeration in aerated vessel.

Table 7.1   Characteristic impeller speeds for surface aeration
in aerated vessel.   D=0.0762m,   T=0.203m

$Qx10^4$ m^3s^{-1}	0.76	1.68	3.76
N_{gSA1} (s^{-1})	12.5	16.0	19.8
N_{gSA2} (s^{-1})	50.0	64.0	79.2

Table 7.1 shows values of N_{gSA1} and N_{gSA2} corresponding to the results shown in Figs. 7.6 and 7.7. From Table 7.1 and Fig. 7.7 it can be seen that the increased slopes at high impeller speeds are well established before any surface entrainments take place.

This discussion suggests that surface aeration is not the main cause and other effects must make a major contribution to the observed trend of gas holdup as shown in Figs. 7.6 and 7.7._ A principal candidate is gas recirculation. The inference is that gas recirculation starts at $N<N_{R1}$, as was suggested previously in Section 6.4.1.1. It has also been proposed by Nienow et al (4,41). Given the previous description of the gas-liquid mixing regimes in Chapter 4, it can be assumed that at $N<N_{R1}$ the recirculated gas does not coalesce with the gas cavities behind the impeller blades and there is no effect on impeller power.

Figure 7.8 demonstrates how h varies with Pgt/V. Thus, when the power supplied by the gas stream is included, a straight line is obtained at high gas flow rates for the three impellers. Therefore

$$h \propto (Pgt/V)^b$$

where the exponent b increases with increasing D/T and/or decreasing Q. The dependence of b on the ratio D/T was also observed by Rushton and Bimbinet (8) in their extensive experiments.

In order to correlate the gas holdup, multiple regression analysis using the least squares method was used. The following correlation was obtained

$$h = 0.051 \ (Pgt/V)^{0.36} \ (Vs)^{0.27} \ (D/T)^{0.85} \qquad 7.16$$

The accuracy limit of this correlation is $\pm$ 20% as shown in Fig. 7.9. The main contributing factor to the error in prediction is caused by

	D/T	Q x 10^4
●	0.375	0.77
■	0.375	1.68
▶	0.375	3.76
◆	0.500	3.62
◀	0.665	3.76
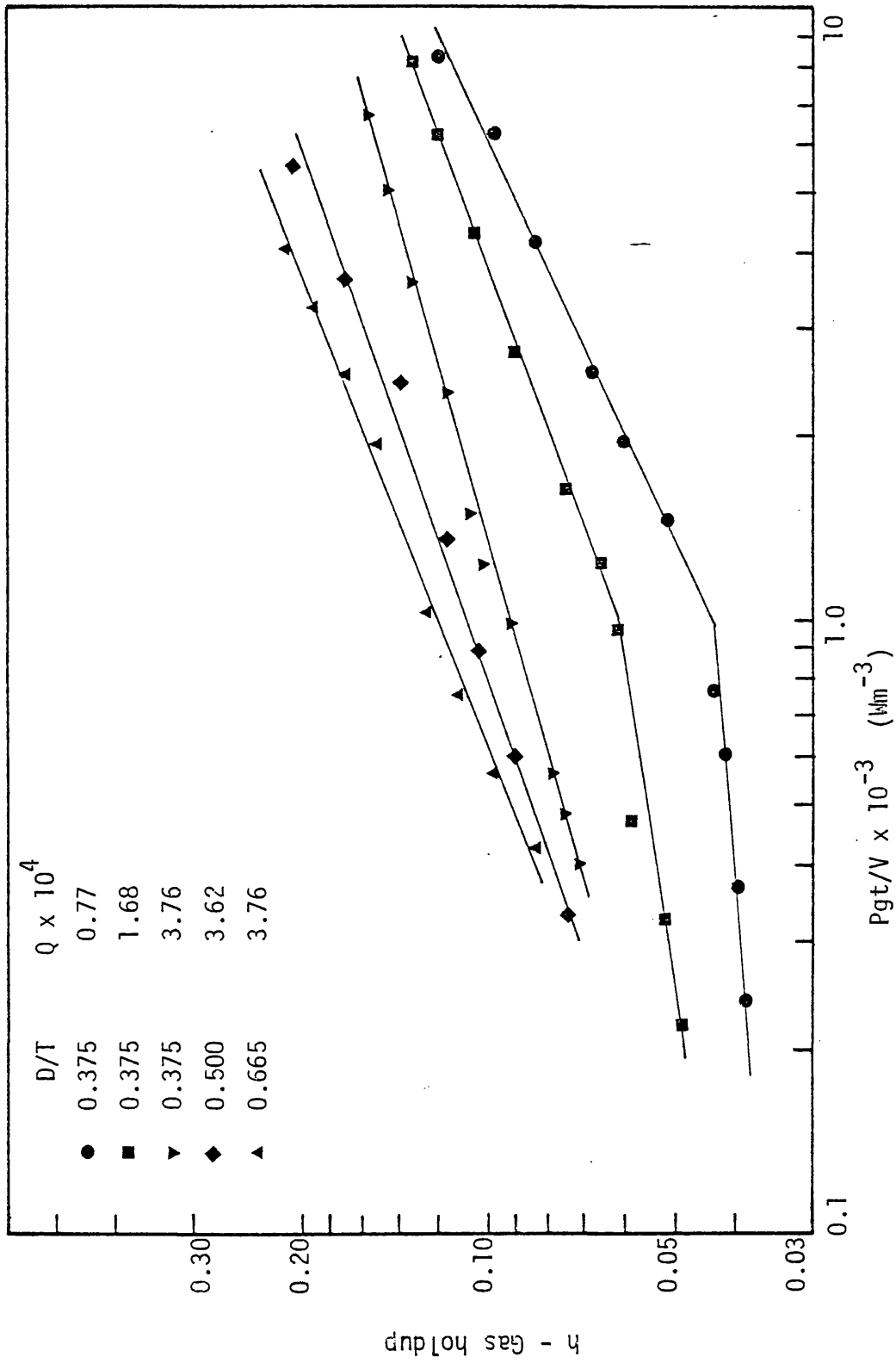
Fig. 7.8   h against Pgt/V.   air-water dispersion (T = 0.203m)
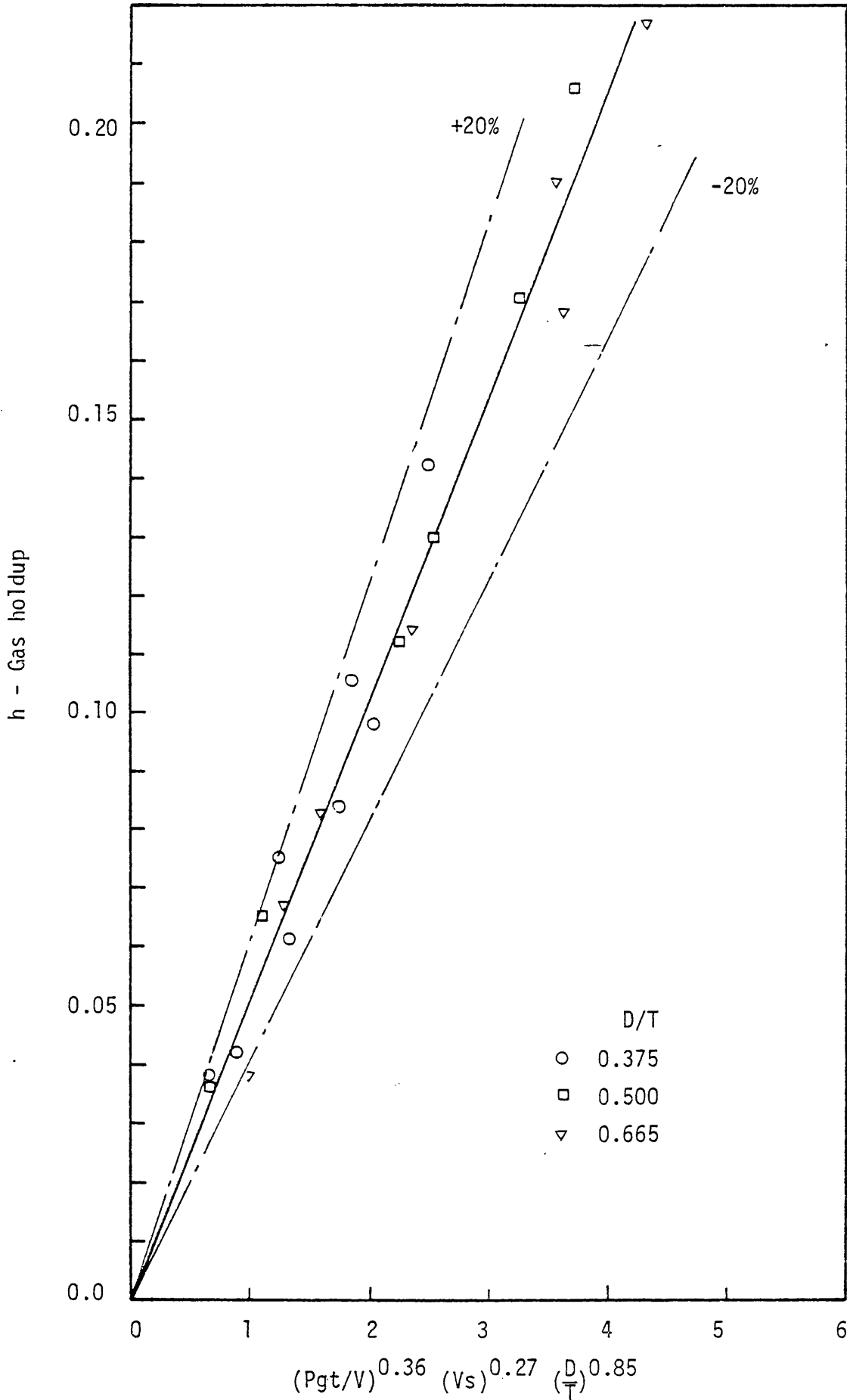
Fig. 7.9   Correlation for gas holdup.   air-water dispersion
(T = 0.203m)

the reduced dependency between h and (Pgt/V) at low gas flow rates
and impeller speeds (see Fig. 7.8).

The effect of vessel pressure on gas holdup is illustrated in Fig. 7.10.
This effect can be stated as

$$h \propto \left(\frac{P}{P_A}\right)^{0.15} \qquad 7.17$$

Equation 7.17 is in good agreement with the results of Sridhar and
Potter (6) at high power inputs (see Eq. 7.5). By combining Eqs.
7.16 and 7.17, the following correlation of h,which includes the
effect of vessel pressure, is obtained

$$h = 0.051 \left(\frac{Pgt}{V}\right)^{0.36} (Vs)^{0.27} \left(\frac{D}{T}\right)^{0.85} \left(\frac{P}{P_A}\right)^{0.15} \qquad 7.18$$

The exponent of the power term in Eq. 7.18 is in reasonable agreement
with the results of other studies (6,10,39). However, the exponent
of Vs is much lower than previously reported. Figure 7.11 compares
the gas holdup measurements of this study for the small sized tank
(T = 0.203m) with the correlation obtained by Smith et al (54)
for tw larger si :ed vessels (T = 0.91, 1.83m). With $\frac{D}{T}$ = 0.5
there is a reasonable agreement with their correlation. However,
for the largest impeller the experimental points lie above the
correlating line and for the smallest impeller most of the points lie
below the line. This emphasises the effect of the ratio D/T which
is included in Eq. 7.18.

An interesting result is also obtained when the measurements of gas
holdup are compared with Eq. 7.8 obtained by Yung et al (11).
Fig. 7.12 shows that the experimental results follow the same trend
of their correlation, and correlate within ± 30% according to

$$h = 0.022 \; Fl^{0.5} \; We^{0.65} \left(\frac{D}{T}\right)^{1.4} \qquad 7.19$$
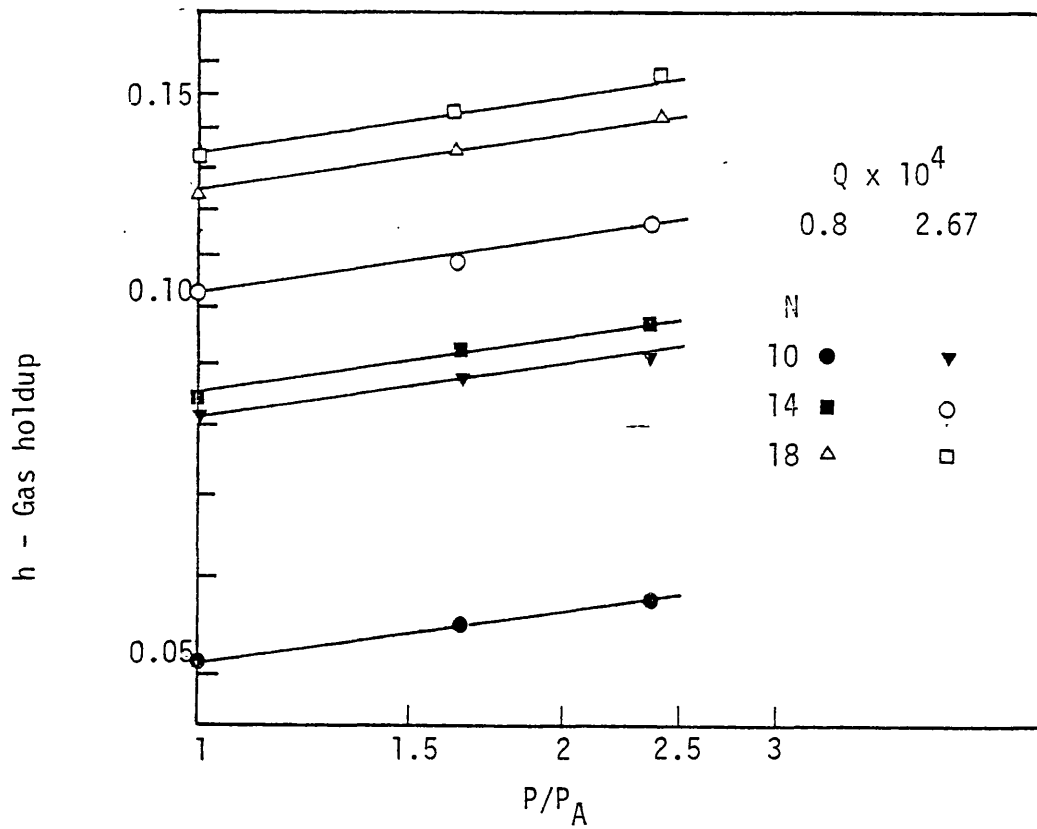
Fig. 7.10   Effect of vessel pressure on gas holdup (D = 0.0762m)
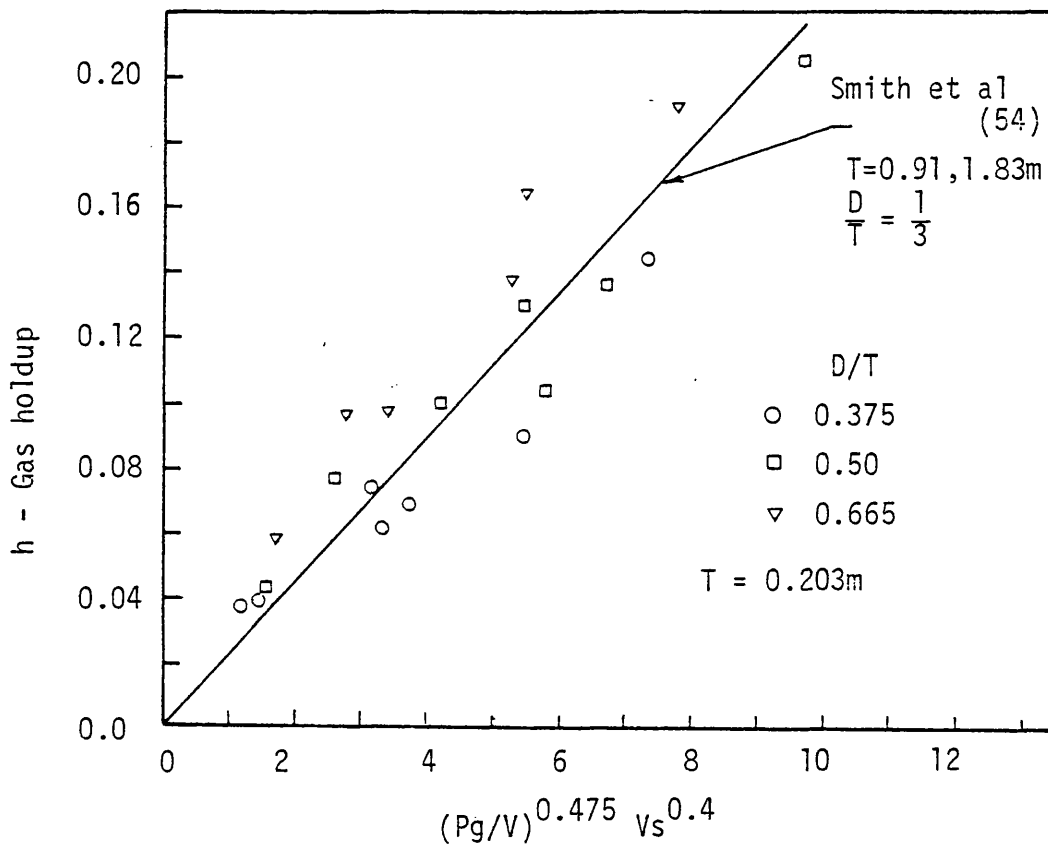
Fig. 7.11   Comparison of gas holdup measurements in small
and large size tanks.
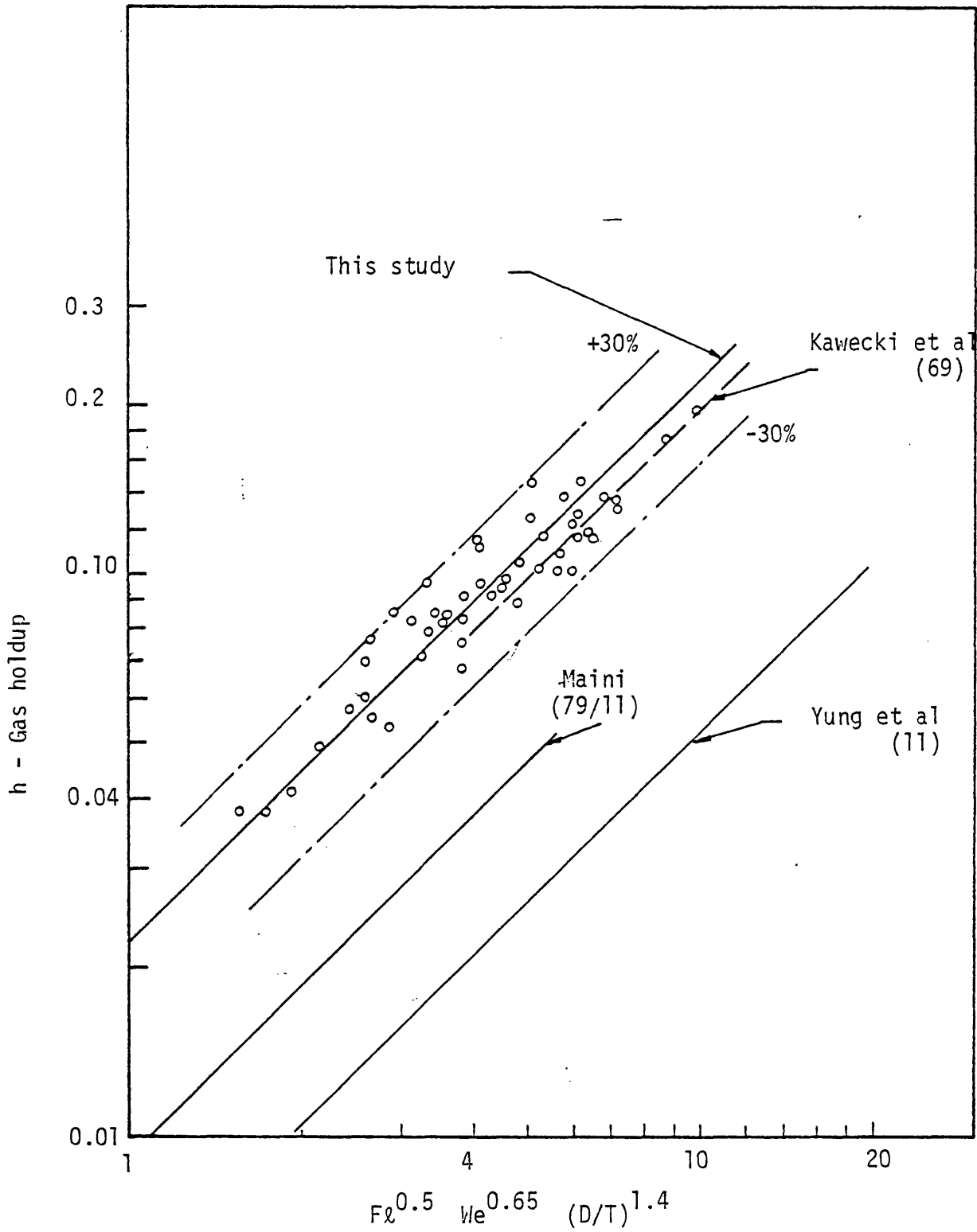
Fig. 7.12   Test of the gas holdup measurements against the
            correlation of Yung et al (11).

The constant of proportionality is about four times greater than the value they reported. There is however close agreement with the results of Kawecki et al (69).

The considerably lower values of gas holdup obtained by Yung et al (11), compared to those of Kawecki et al (69), Smith et al (54), and the results of this study, is believed to be due to experimental error in measurements. Yung et al (11) stated that they measured h by the manometric method described by Robinson and Wilke (5). The latter authors, as explained in Sec. 2.4.2, observed an increase in the manometer readings under agitated ungassed condition and attributed this to a dynamic pressure effect, without any consideration of surface aeration effects. The correction which was employed, therefore, could lead to considerable underestimation of h. It is of interest to note that Robinson and Wilke (5) started to observe an increase of the manometer reading at impeller speed of 8.33 s^{-1}, whilst Eq. 3.16 predicts a speed of 9.38 s^{-1} for the onset of surface aeration for their experimental conditions. On the other hand, the effect of surface aeration under gassed conditions cannot be fully excluded for the results of Smith, Kawecki, and this study. For the operating conditions used by Smith, and in this study, surface aeration may have taken place at the lower range of gas loads according to Eq. 7.14 of Calderbank (90). However the characteristic impeller speed for the onset of surface aeration, N_{gSA1}, was not achieved either by Kawecki or Yung, though Kawecki used an impeller clearance of T/2, which may have caused surface aeration to take place at lower impeller speeds.

It is worthwhile to mention that although the accuracy achieved by Eq. 7.19 for correlating h is the same as that obtained by Yung et al (11),

a parallel series of lines of constant $F\ell$ and We were not obtained on log-log plot as was reported for their results. Equation 7.19 also shows a similar level of accuracy in correlating the gas holdup measurements at higher vessel pressures but with a larger constant of proportionality. At a vessel pressure of 0.239 MNm^{-2} this constant is 2.5 which confirms the effect of pressure as expressed by Eq. 7.17. Therefore Eq. 7.19 can be stated as

$$h = 0.022 \ F\ell^{0.5} \ We^{0.65} \ (\frac{D}{T})^{1.4} \ (\frac{P}{P_A})^{0.15} \qquad\qquad 7.20$$

The measurements of gas holdup in air-electrolyte solution system are compared with the correlation obtained by Smith et al (54) who used the same solution (0.11 K_2SO_4) but in larger sized equipment. As shown in Fig. 7.13, there is a good agreement between the two studies, though for the result of this study the replacement of Pg by Pgt improves the accuracy at low values of N and Q. The correlation obtained is

$$h = 0.045 \ (\frac{Pgt}{V})^{0.475} \ (Vs)^{0.4} \qquad\qquad 7.21$$

A comparison of the results shown in Figs. 7.11 and 7.13 demonstrates that the gas holdup in the air-electrolyte system is about two times that for air-water over the same range. On a log-log plot of h against (Pgt/V) a series of parallel lines is obtained for different values of Q with a slope of 0.475. The disappearance of the break point in this case can be attributed to the early start of gas recirculation.

7.3.1.3 Gas Holdup and Mixing Regimes

The results on gas holdup do not readily relate to the different gas-liquid mixing regimes identified from impeller power measurements in Chapter 4. In the flooding regime the degree of flooding (which is a gradual process) can be estimated from the impeller dispersion
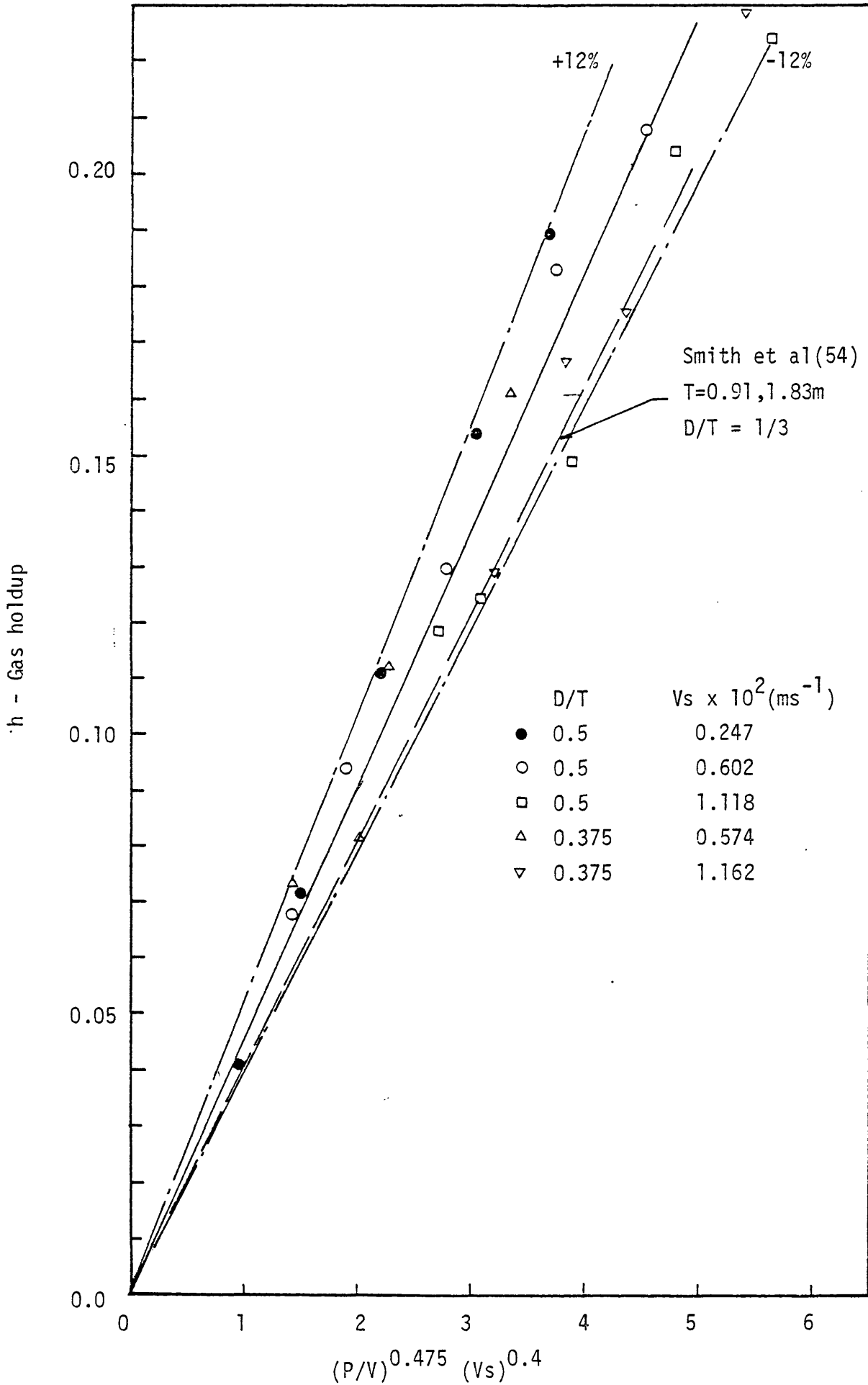
Fig. 7.13   Correlation for gas holdup for air-0.11K₂SO₄ dispersion

P = Pgt for this study

P = Pg for Smith et al (54)

efficiency η_F. As the impeller speed increased at constant gas flow rate more gas is dispersed causing the residence time of the bubbles, and hence the gas holdup, to increase. This is consistent with the observed trend of continuously increasing gas holdup shown in Fig.7.7.

In the efficient mixing regime, although there is no recirculation of gas bubbles back to the impeller, recirculation does take place in the bulk liquid. This is evident from the steepening effect of the curves in a plot of h against (Pg/V) or N at constant Q. The trend of gas holdup which is established in the efficient mixing regime continues through into the gas recirculation regime.

In summary, the measurements of gas holdup confirm qualitatively some aspects of the behaviour expected in the different regimes of gas-liquid mixing. There is also additional evidence concerning the onset of gas recirculation, ie, prior to any drop in N_{Pg}. The relatively high margin of uncertainty associated with the correlations developed in Section 7.3.1.2 does, however, point to the need for a deeper and wider range of experiments to investigate quantitatively the causal relationship between the different impeller mixing regimes and the gas holdup.

7.3.2   Interfacial Area

7.3.2.1   Point Measurements

The point specific interfacial area a_p was measured by the capillary technique described in Chapter 6. By averaging the point gas holdup and the point bubble size for several samples taken at the same location, a_p was calculated by

$$a_p = \frac{6h_p}{d_{32}}$$

7.22

The vertical and radial distributions of a_p obtained for air-water dispersion have shown good agreement with the results of Calderbank (10). Figure 7.14 demonstrates the distribution of specific interfacial area at different impeller speeds for air-$0.11K_2SO_4$ dispersion. Comparing $\bar{a}_p$ and a (illustrated on the figure) indicates that there is good agreement at high impeller speeds. At low impeller speeds, the discrepancy is more apparent. This may be attributed to the fact that a_p was measured at a small number of positions in the tank, and that all of them lie in the upper region above the impeller level. From Nienow's et al (4) visual observations it is clear that at N < N_{F1} virtually no gas exists in the region below the impeller, and hence $\bar{a}_p$ in the upper region of the tank should therefore over-estimate a.

The coefficient of variation $\sigma'a_p/\bar{a}_p$ is used as a measure of the spread of a throughout the tank. Figures 7.15 and 7.16 show the changes of $\sigma'a_p/\bar{a}_p$ with N, which are similar to those of $\sigma'h_p/\bar{h}_p$ previously discussed in Section 7.3.1.1. The figures also indicate that the variation of a_p for the electrolyte solution is less than for water which is in agreement with the observations of Lee and Meyrick (9).

7.3.2.2 Total Specific Interfacial Area

The total specific interfacial area a, was calculated from

$$a = \frac{6h}{d_{32}} \qquad 7.23$$

where h is the overall gas holdup measured by the level probe, and d_{32} is the Sauter mean bubble diameter calculated from Eq. 6.24.

The results for the air-water system are first examined against those of other studies. Calderbank's correlation (Eq. 7.11) was selected for this purpose since it is virtually the only complete and reliable

N=5
$\bar{a}_p$=310
a=253

365
.

179
.

84   1133
.   .

65
.

34
.

N=8
$\bar{a}_p$=763
a=485

862
.

654
.

980   847
.   .

907
.

328
.

N=11
$\bar{a}_p$=1081
a=873

1355
.

1207
.

1513   880
.   .

1095
.

440 .

N=14
$\bar{a}p$=1345
a=1319

1679
.

1176
.

1674   1187
.   .

1305
.

1047

N=17
$\bar{a}_p$=1554
a_p=1532

1436
.

1706
.

1528   1283
.   .

1806
.

1565
.

N=20
$\bar{a}_p$=1547
a=1454

1604
.

1304
.

1477   1061
.   .

1792
.

1552
.
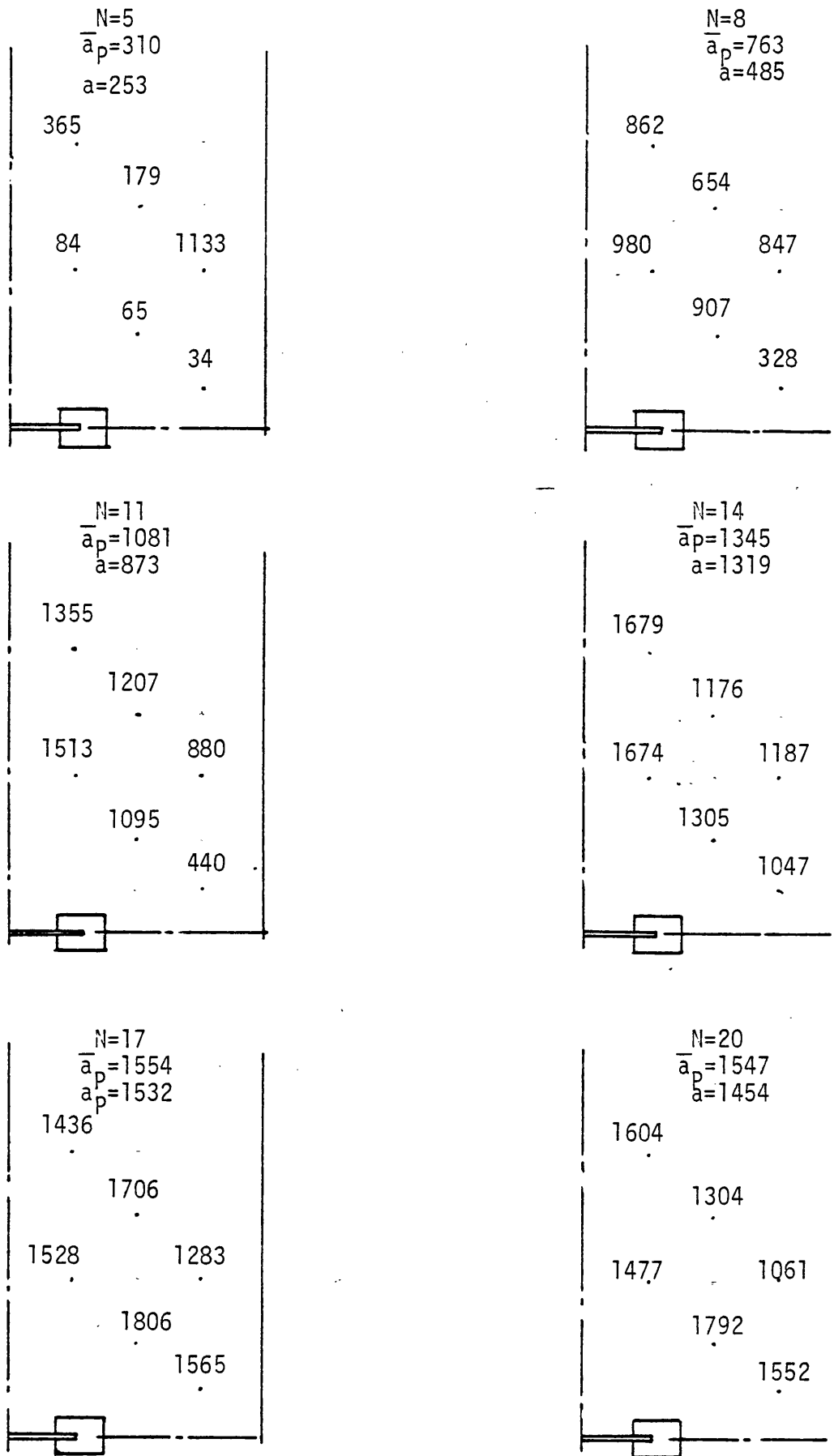
Fig. 7.14   Matrix of point specific interfacial area (m^{-1}).
D=0.0762m, Q=3.77x$10^{-4}m^3s^{-1}$, air-0.11K_2SO_4 dispersion.
$\bar{a}_p$ = average point specific interfacial area
a   = overall specific interfacial area
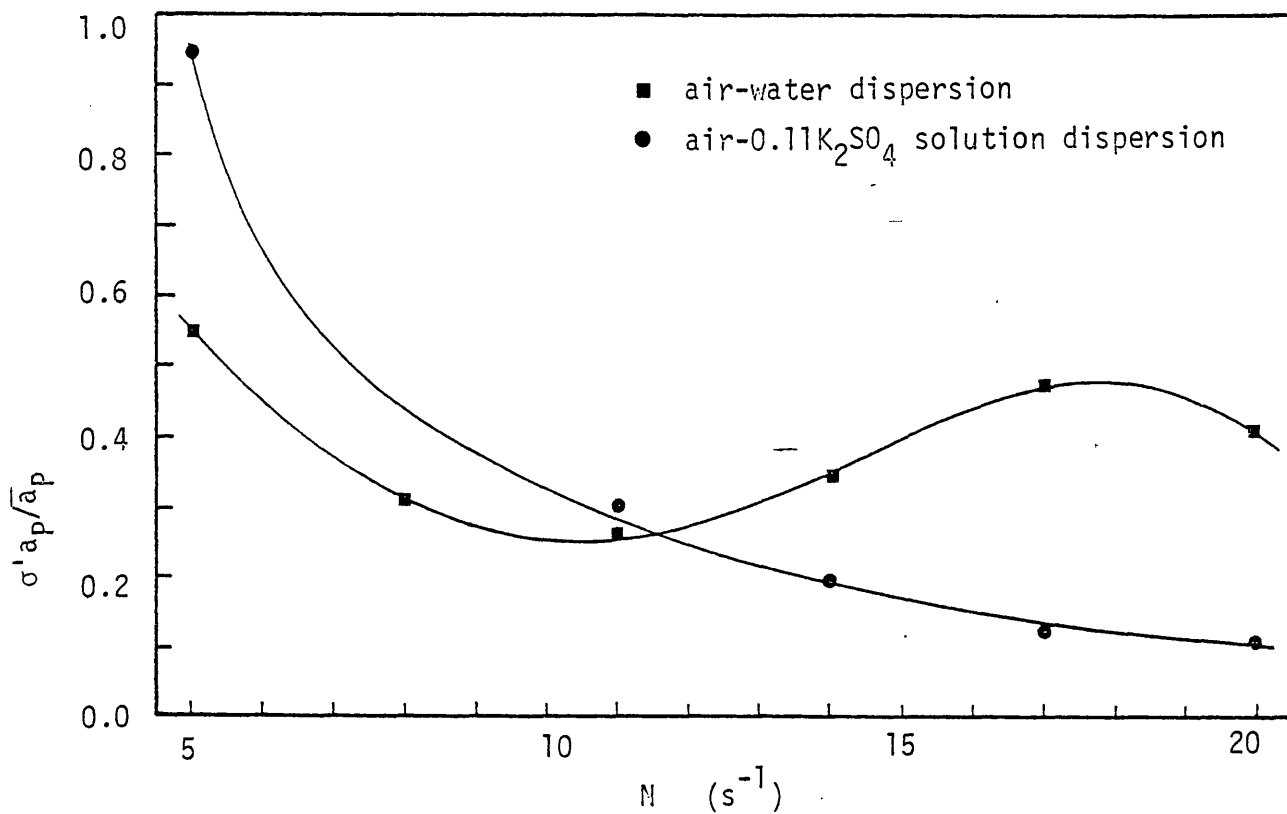
Fig. 7.15   Coefficient of variation of point specific interfacial
area against the impeller speed.   D= 0.0762m,
$Q = 3.77 \times 10^{-4} m^3 s^{-1}$
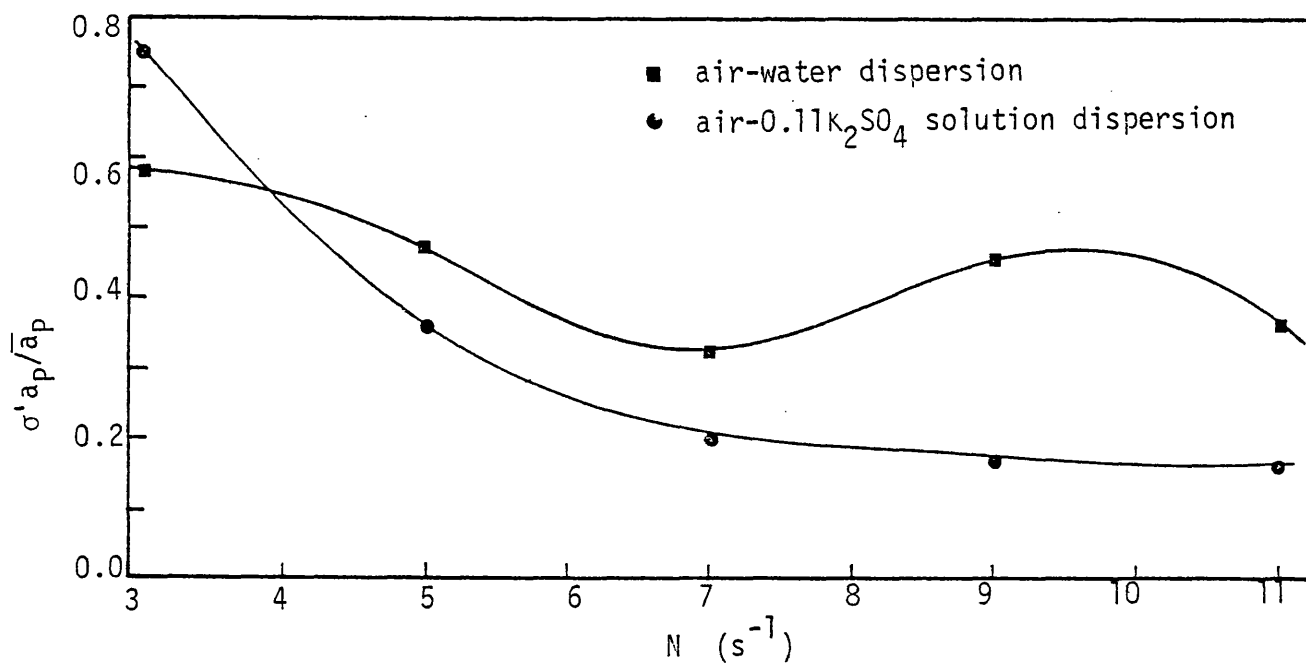
Fig. 7.16   Coefficient of variation of point specific interfacial
area against the impeller speed.

correlation for predicting a (85). The results are shown in Fig.7.17.

It is clear that the values obtained are greater than those of

Calderbank (10) but are generally lower than those of Dierendonck et

al (21), Kawecki et al (69) and El Shawarby and Eissa (89). To obtain

correlation of the type proposed by Calderbank (10) a line of slope

equal to unity was drawn through the experimental points in Fig. 7.17.

The resulting correlation is

$$a = 2.8 \left[\frac{(Pg/V)^{0.4} \rho^{0.2}}{\sigma^{0.6}} \right] (\frac{Vs}{U_T})^{0.5} \qquad 7.24$$

with an accuracy of $\pm 30\%$. The constant of proportionality in Eq. 7.24

was found to be 1.44 by Calderbank (10) which indicates that the

results of this study are higher by a factor of 2. According to

Calderbank (10,90) such an increase of a is caused by surface aeration.

However, in Fig. 7.17, the deviation from Calderbank's correlation is

larger at low than at high impeller speeds. This cannot possibly be

the result of either surface entrainment or gas recirculation. The

smaller bubble size (see Fig. 6.23) and larger gas holdup measurements

of this study have both contributed to produce larger values of a

compared to those predicted from Calderbank's (10) correlation.

Although a correlation for a can be obtained by substituting d_{32} from

Eq. 6.29 and h from Eq. 7.16 into Eq. 7.23, the expression obtained

is cumbersome. A more simplified form of correlation can be obtained

by a multiple regression analysis. The result is

$$a = 78.6 \ (\frac{Pgt}{V})^{0.278} \ Vs^{0.245} \qquad 7.25$$

This relationship is also illustrated in Fig. 7.18.
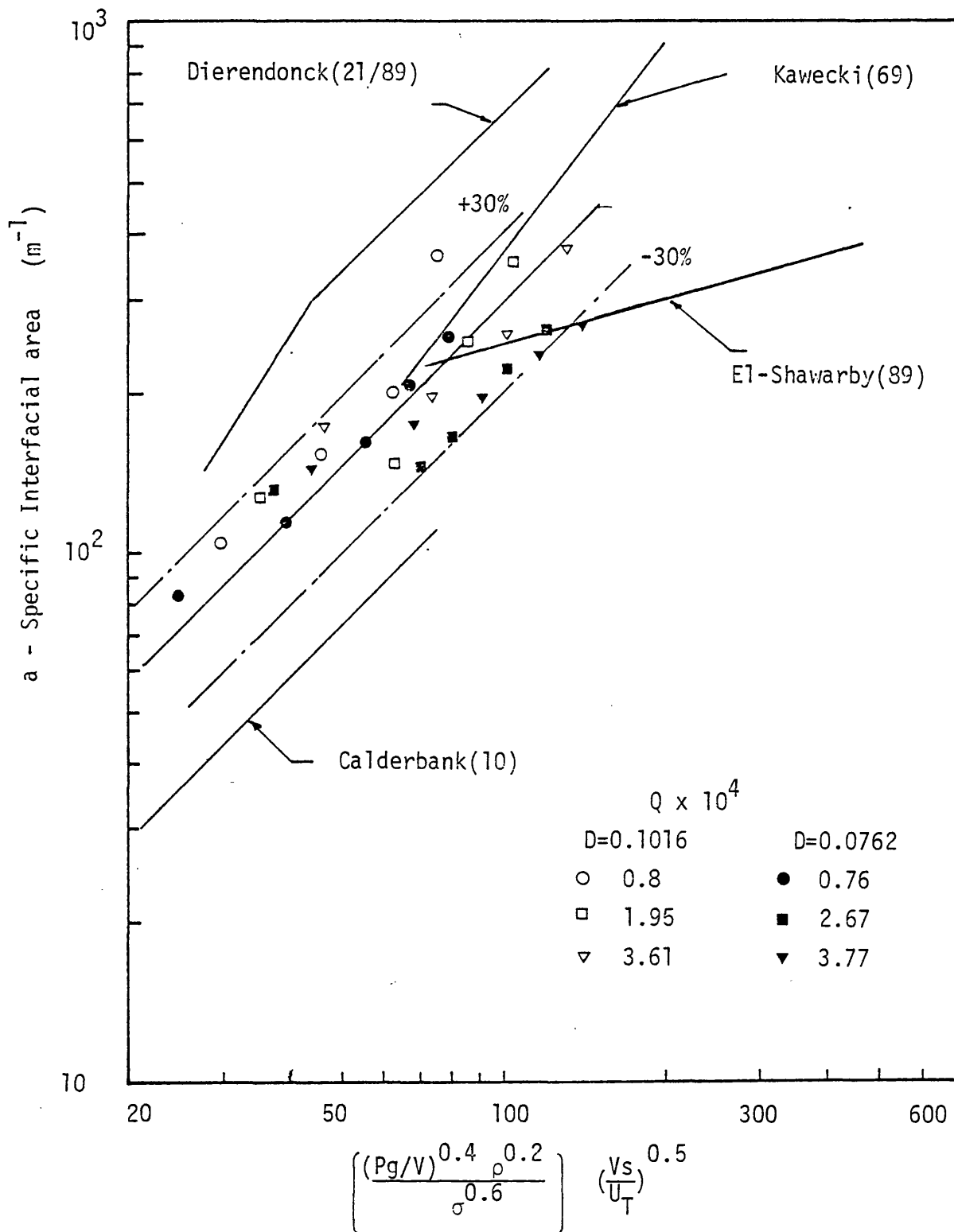
Fig. 7.17 Comparison of measurements of a with other published
results using Calderbank's correlation (Eq.7.11).
air-water dispersion.
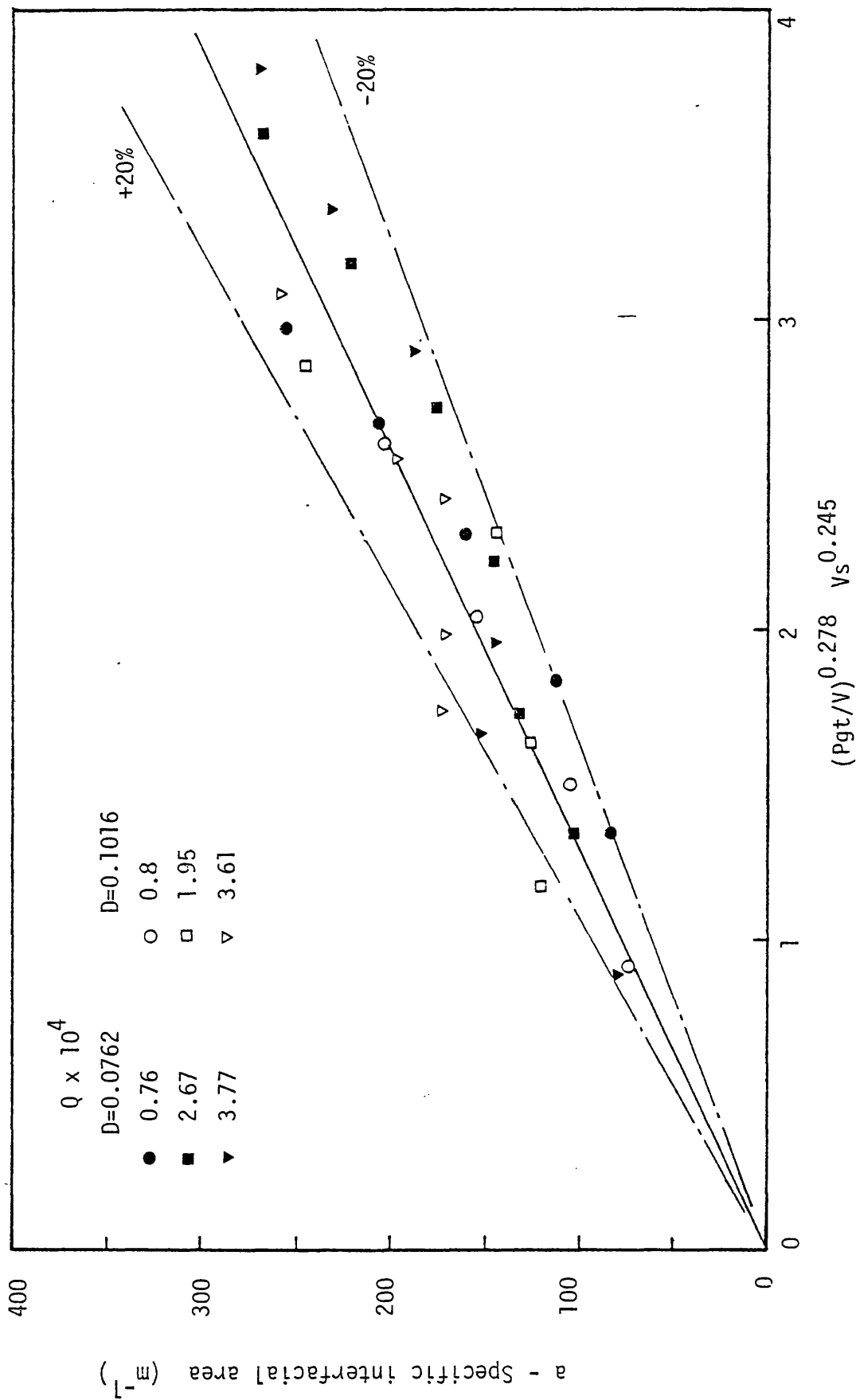
Fig. 7.18   Correlation for specific interfacial area.   air-water dispersion.
(Average absolute deviation = 13.8%)

The exponent of the power term in Eq. 7.25 is lower than that found

by Calderbank (10) but it is in close agreement with the results of

Figueiredo (12). For her largest tank (T = 0.91m), she found

$$a \propto (\frac{Pg}{V})^{0.29} Vs^{0.73} \qquad 7.26$$

On the other hand, the exponent of Vs is very low by comparison, but

it is consistent with the value obtained for the gas holdup correlation

(Eq. 7.16). The only comparable value is that reported by Joshi and

Sharma (84) for a gas inducing type of agitator (a $\propto$ Vs$^{0.25}$ for

Vs > 0.005).

For the air-electrolyte dispersion, the measured values of a were much

larger than those for the air-water dispersion. This is in agreement

with previous studies (9,10,87) and is due to the high values of gas

holdup and the smaller bubble size. A simple correlation can be

obtained using the correlations of h and d_{32} (Eq. 7.21 and Eq. 6.32,

respectively). Therefore

$$a = 76.7 (\frac{Pgt}{V})^{0.605} Vs^{0.4} \qquad 7.27$$

Figure 7.19 shows the scatter of the experimental points around the

correlating line. Since the bubble size and gas holdup in an

electrolyte solution depends on its concentration, Eq. 7.27 is

expected to provide an overestimate of a for potassium sulphate

solution of concentrations less than 0.11M. The hypothesis that a

increases with increasing concentration of electrolyte until a maximum

is reached (given all other operating parameters are kept constant)

is supported by the experimental measurements of Lee and Meyrick (9),

although it was not stated by them. Their results also imply that

the maximum values of a achieved in Na_2SO_4 solution are higher than
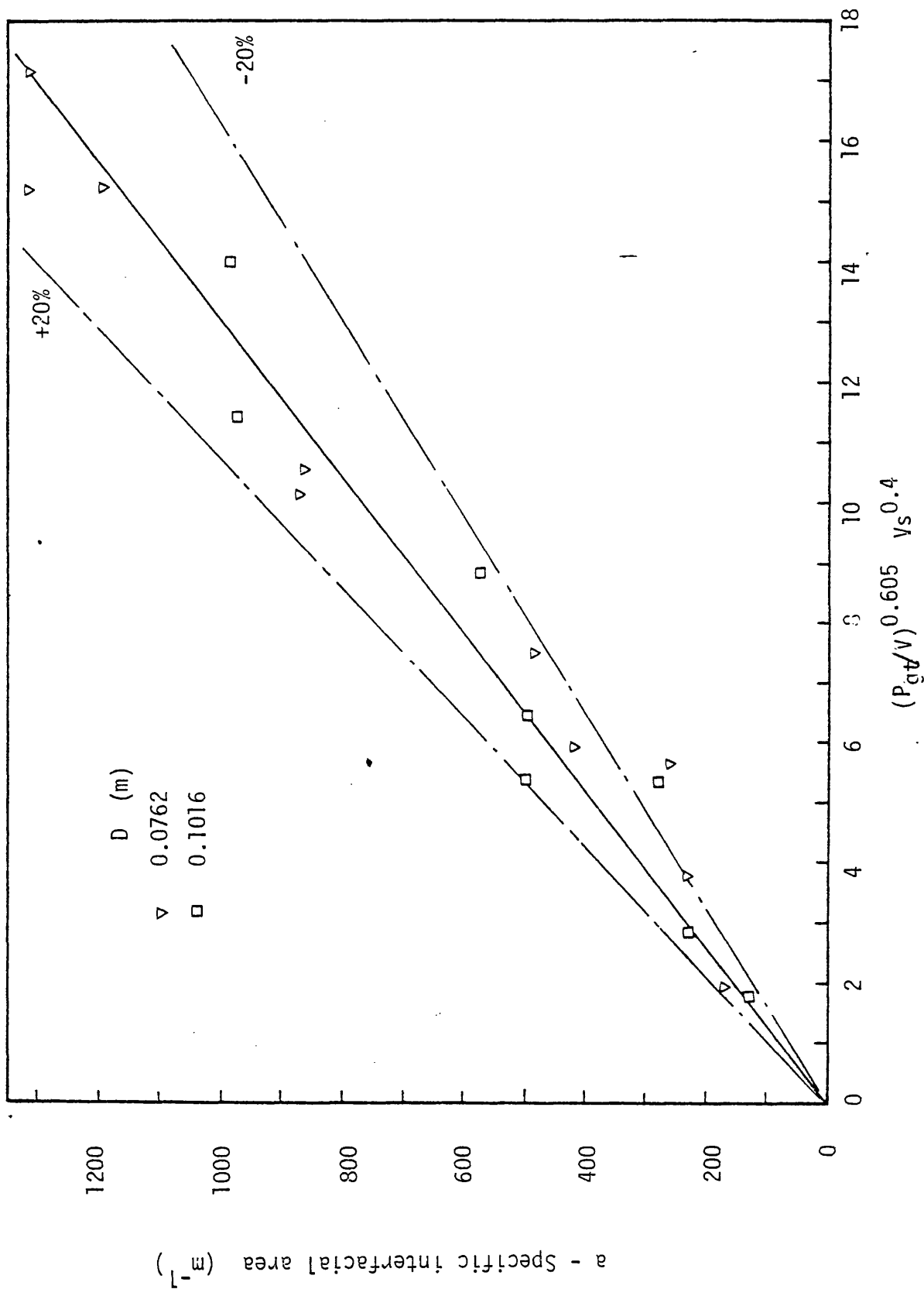
Fig. 7.19 Test of correlation of specific interfacial area for air-0.11K$_2$SO$_4$ solution dispersion.

those obtained with NaCl solution. Given the previously mentioned experimental evidence of other studies (10,53,54), that the bubble size and $K_L a$ reach a plateau value with increasing the electrolyte concentration (0.11M for K_2SO_4 solution), there is the indication, therefore, that Eq. 7.27 predicts the plateau value of a for K_2SO_4 solution and possibly for other electrolytes. It is important, however, to point out the reservation given previously in Sec. 6.4.2.2 regarding the possibility that a 0.11M concentration of K_2SO_4 does not produce minimum bubble size in an agitated vessel.

To test this corollary, Eq. 7.27 was examined against the experimental measurements of other workers who used different electrolyte solutions. Those of Robinson and Wilke (5), Lee and Meyrick (9), and Hassan and Robinson (72) were selected for this purpose. Since Lee and Meyrick (9) did not publish the details of impeller power consumption, the correlations of power consumption for electrolyte solution which are presented in Sec. 4.3.8 are used. To estimate the power supplied by the gas stream, Eq. 6.10 proposed by Sridhar and Potter (6) was tried. Since the gas spargers used in the three studies (5,9,72) were narrow orifices of 1/16 or 1/8 inch diameter, the kinetic energy calculated by Eq. 6.10 was excessively large. For example, for the study of Lee and Meyrick (9) at $N = 10$ s^{-1} and with $Q = 2.67 \times 10^{-4}$ and $6.67 \times 10^{-4} m^3 s^{-1}$, the predicted impeller powers are 31 and 19 watts respectively, while the corresponding kinetic energy calcualted from Eq. 6.10 is 3 and 49 watts. It is important to indicate, however, that Eq. 6.10 does give reasonable values for the conditions of the present study. This is because of the relatively large size of gas sparger used. Here, the power supplied by the gas stream at the lowest and highest gas flow rates were found to be 0.12 and 1.65 watts respectively.

The alternative expression for estimating the power supplied by the gas stream, is that derived by Leher (91) in a study of 'Gas agitation of liquids' which was used by Miller (83) for agitated vessels. Miller (83) multiplied the kinetic energy term by an efficiency factor representing the fraction of the jet energy transmitted to bulk liquid. He also employed a correction factor which was dependent on the size of the sparger and the tank. In this way, the kinetic energy estimated from Miller's expression is less than 0.02 of that estimated by Eq. 6.10. When Miller's expression was tested, it was found to give reasonable kinetic energy for the studies where a narrow sparger orifice is used (5,9,72). However, for the present study it predicts negligible values which do not account for the noticeable reduction of bubble size with increasing the gas load at low impeller speeds (see Figs. 6.20 and 6.21).

It is apparent that neither of the two expressions available in literature gives an acceptable prediction of the energy supplied by the gas stream for all sizes of spargers. Since this power contribution was significant compared with the impeller power only at the lowest impeller speeds and the highest gas flow rates in this study, Pgt is therefore replaced by Pg in Eq. 7.27, which becomes

$$a = 76.7 \ (\frac{Pg}{V})^{0.605} \ Vs^{0.4} \qquad\qquad 7.28$$

Figure 7.20 shows that Eq. 7.28 holds for the highest gas flow rates, the conditions which would be affected most by replacing Pgt by Pg.

Lee and Meyrick's (9) results with Na_2SO_4 solution (concentrations greater than 0.2M) are also shown in Fig. 7.20. It is clear that their results lie just on, or below, the lower accuracy limit of Eq. 7.28. Table 7.2 gives details of how their results compare with
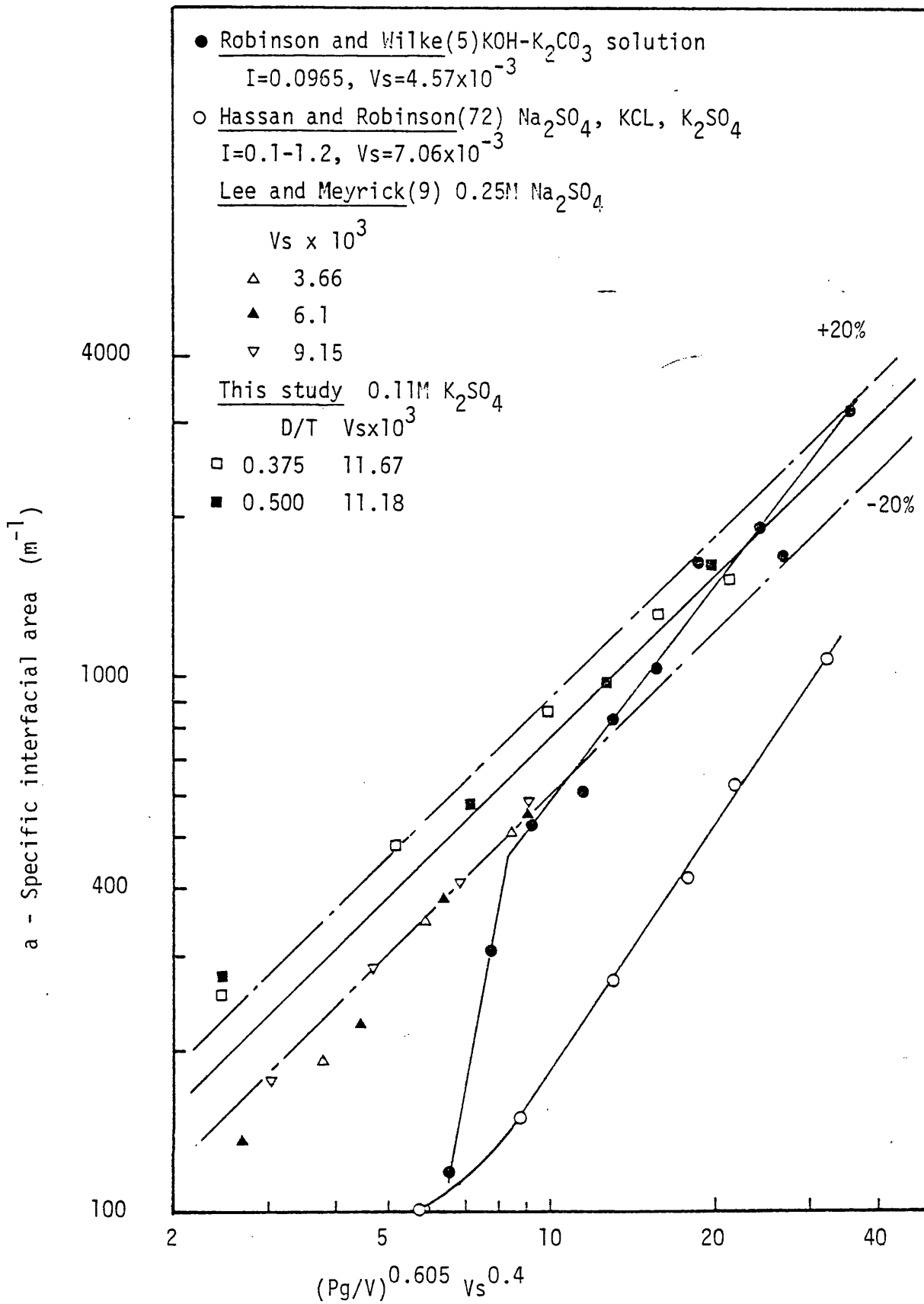
Fig. 7.20   Test of correlation (Eq. 7.28) for specific
interfacial area.   air-electrolyte solution dispersions.

Table 7.2. Prediction of the results of Lee and Meyrick (9) for Na_2SO_4 solution with $c \geqslant 0.2$ g.mol/ℓ (I $\geqslant 0.6$ mol ion/L) D = 0.1016m, T = 0.305m.

N (s^{-1})	$Vsx10^3$ (ms^{-1})	η +	Pg * Predicted (watts)	a · measured (m^{-1})	a ° Predicted (m^{-1})	% difference
5.0	3.66	0.68	3.59	85	176	107
6.67	3.66	1.0	8.02	190	286	50
8.34	3.66	1.0	16.85	350	449	28
10.0	3.66	1.0	30.93	510	648	27
5.0	6.1	0.51	3.29	132	204	54
6.67	6.1	0.82	7.06	225	327	44
8.34	6.1	1.0	13.71	385	485	26
10.0	6.1	1.0	25.16	550	701	27
5.0	9.15	0.38	3.14	176	234	33
6.67	9.15	0.70	6.4	285	360	26
8.34	9.15	0.97	11.78	405	521	28
10.0	9.15	1.0	19.2	565	701	24
Average absolute error of predicting a = 39.5%						

\+ Calculated from Eqs. 4.34, 4.35, 4.36, 4.37

* Calculated from Eq. 4.31

· Lee and Meyrick (9)

o Calculated from Eq. 7.28

the predictions obtained from correlations presented in this study.

The average error is about 40% which accounts for accumulating errors

for predicting the impeller dispersion efficiency, the impeller power

and the use of Eq. 7.28 for predicting a (has accuracy limits of $\pm$20%).

In the present state of development, such a reasonable agreement tends

to confirm that the correlations presented in this study for the

'noncoalescing' system are reasonably accurate.   The maximum value of

a measured for the sodium chloride solution by Lee and Meyrick (9)

is about 0.75 of those achieved with the sodium sulphate solution.

This means that the predicted values of a using Eq. 7.28 are 55%

higher than their measurements, or these measured values deviate by

35% from Eq. 7.28.

Considering now the measurements of Robinson and Wilke (5); it can be

seen in Fig. 7.20 that most of their experimental points lie within

the accuracy limits of Eq. 7.28, but at the lowest two impeller speeds,

an increasingly larger deviation exists.   It is interesting to note

that the ionic strength of the $KOH-K_2CO_3$ solution used by them was

0.0965 mol ion/L.   For the study of Lee and Meyrick (9) the maximum

interfacial area was achieved at an ionic concentration of about 0.4

and 0.6 mol ion/ for NaCl and Na_2SO_4 solutions respectively.   In

this study, the ionic strength of the K_2SO_4 solution used was 0.33.

It seems therefore that there is no apparent relationship between the

ionic strength and the concentration of the electrolyte solution

required to achieve maximum interfacial area.

Fig. 6.20 also shows the relatively lower results of Hassan and

Robinson (72).   Considering the degree of agreement between the results

of Robinson and Wilke (5) and those of Lee and Meyrick (9), and this

study, their results are rather difficult to judge.   However, if the

results of Robinson and Wilke (5) are proved to be erroneous, then
the explanation given by Hassan and Robinson (72) concerning the
difference between the total and effective a can certainly be
substantiated, particularly in the light of the most recent study in
this subject of Hofer and Mersmann (86). The measurements of this
study and those of Lee and Meyrick (9), both obtained using physical
methods, and are in reasonable agreement, are therefore indicative
of the total or the geometrical specific interfacial area. The
correlation proposed in this study (Eq. 7.28), therefore, is useful
for predicting a for physical absorption processes. The results of
Hassan and Robinson (72), however, are more representative of the
effective a in chemical absorption (86). The agreement achieved by
Hofer and Mersmann (86) in estimating a by physical absorption and
chemical methods after applying the enhancement factor (the ratio of
mass transfer in the presence of a chemical reaction to that in a
purely physical process, calculated theoretically) is very encouraging.
Wider investigations along these lines, ie, using physical and
chemical methods, should help to establish more understanding and
narrow the existing differences.

7.4   CONCLUSIONS

1 -   The spread of the point gas holdup through the vessel was
estimated by the coefficient of variation $\frac{\sigma' h_p}{\bar{h}_p}$. For air-water
dispersion, $\frac{\sigma h_p}{\bar{h}_p}$ achieved a minimum at an impeller speed condition
$N_{F1} \leqslant N \leqslant N_{R1}$. This means that the degree of uniformity achieved
by the gas-liquid dispersion is highest in the efficient mixing
regime. For air-electrolyte dispersions, however, the gas
distribution becomes more uniform with increasing impeller speed.
In general, the air-electrolyte dispersion is more uniform than the

air-water dispersion at the same operating conditions, provided $N > N_{F1}$.
The point specific interfacial area also showed similar trends.

2 - The overall gas holdup measurements for air-water dispersion
showed a distinct trend. A plot of log h against $\log(\frac{Pg}{V})$ at constant
gas load exhibits two slope conditions. It is concluded that the
break point on this curve indicates the start of gas recirculation in
the bulk liquid. This occurred at impeller-speed less than N_{RT} and
is less than that predicted from impeller power measurements. The
holdup measurements for both air-water and air-0.11M K_2SO_4 dispersion
compared very favourably with the results of Smith et al (54),
obtained with larger size vessels (T = 0.91, 1.83). The difficulty
of obtaining a scaling rule for gas holdup, however, is because the
different gas liquid mixing regimes and the interference effect of
surface aeration are neglected.

3 - The measurements of specific interfacial area for air-water
dispersion are larger than the values predicted by Calderbank's (10)
correlation, but lower than the results of other studies (21,69,89).
The high values of a measured in this study at low impeller speeds
cannot be explained by the presence of surface aeration or gas
recirculation. It is apparent, therefore, that Calderbank's (10)
correlation underestimates a.

For the air-electrolyte system, it was found that

$$a = 76.7 \ (\frac{Pg}{V})^{0.605} \ Vs^{0.4}$$

When tested against Lee and Meyrick's (9) results for 0.25M
Na_2SO_4 solution, the average error is 40%. At the present level
of development, therefore, this correlation is useful for predicting

the geometrical specific interfacial area for 'non-coalescing'

systems. The relatively lower values of a measured by the chemical

method (72) emphasises the significant difference between the

geometrical and effective a in agitated vessels.

CHAPTER 8

POWER CONSUMPTION AND GAS HOLDUP

FOR CONTINUOUS-FLOW SYSTEM

8.1   INTRODUCTION

Agitated vessels are widely used in continuous-flow processes in industry, for mixing, heat transfer and chemical reaction (1).   Very little is known, however, concerning the effects of the continuous-flow of liquid on the important design aspects of these systems.   In this chapter, a study is made of the impeller power consumption in an agitated vessel operated with continuous liquid flow, considering both ungassed and gassed considitons.   For the latter case, the effect of the liquid flow on the gas holdup is also investigated.

The effect of continuous-flow of liquid on the impeller power consumption for ungassed systems has been investigated by Laity and Treybal (92) and Ito et al (1).   In both studies, closed tanks were used.   There was no air-liquid interface since the tanks were full of liquid.   Laity and Treybal (92) used a standard six-bladed disc-turbine impeller positioned at the midpoint of the vessel (C = H/2).   The water flow through the tank was from the bottom to the top.   For the case of an unbaffled vessel they found the Power number increased linearly with the ratio of water flow rate to vessel diameter.   For vessels fitted with 16.7% baffles, the flow rate of liquid was found to have only a negligible effect.

In the recent study of Ito et al (1) an unbaffled vessel of diameter 0.196m was used.   It was equipped with six-bladed paddle stirrer with D/T = 0.51, 0.70 and 0.78.   The liquids used were water and an aqueous glycerin solution, at feed rates of 1.0 to 13.6 litre/min.   Two cases were studied;   in the first the liquid was fed through a pipe at the bottom of the tank with the outlet through a side pipe.   For this case, the Power number was found to increase with increasing the liquid flow rate, which is in agreement with the observations of Laity and Treybal (92).   They also found no effects for the diameter of the inlet and

outlet pipes or the height of the outlet pipe from the bottom of the

tank. In the second case, the liquid entry was through a side inlet

pipe and the exit through bottom pipe. At low values of Liquid Flow

number, $F\ell_L = \frac{Q_L}{ND^3} < 0.04$, the Power number was found to decrease

linearly with $F\ell_L$. With the inlet side pipe in a higher position

from the tank bottom, a larger drop in Power number was observed.

Further increases of $F\ell_L$ (> 0.04) caused an increase of N_{Po}. The

exception to this was the case where the inlet side pipe was at the

same level as the impeller, ie, H/2. For this condition, N_{Po}

exhibited a continuous decrease with increasing water flow rate. Ito

et al (1) also correlated the effects of the liquid flow rate (Q_L) on

N_{Po}.

Apart from these studies, no other experimental information was reported

in the literature concerning power consumption or gas holdup in

continuous-flow agitated vessels. Brown and Halsted's (50) study of

a gas-liquid continuous-flow system incorporated an air-liquid interface.

However, they used only a low liquid flow rate (1.365 1/m) with the

assumption that it would not significantly disturb the batch flow

pattern in the vessel. Their measured gas holdups obtained from batch

runs were assumed to be representative of the continuous-flow system

at the same operating conditions. This has proved to be an acceptable

assumption as will be seen in the following analysis.

The work of both Ito et al (1) and Laity and Treybal (92), although not

directly similar to this study, points to the importance of the system

design and the operating conditions. Any minor change in system

parameters may significantly affect the results obtained. Details of

the system studied in this work are given in the following section.

8.2　DETAILS OF CONTINUOUS-FLOW SYSTEM

The main details of the equipment are included in Chapter 2.
The liquid dispersion level in the fully baffled vessel was kept constant
during the runs at height equal to the tank diameter.　Only tap water
was used and the vessel pressure was kept constant at 0.205 MNm^{-2} (15 psig)
during all runs.　The impeller clearance was fixed at T/4 for the
reasons explained in Chapter 3.　　　—

Two cases were studied.　In the first the liquid inlet was through the
side pipe of the vessel and outlet through the bottom pipe (see Fig.2.6).
For the second case the inelt and exit positions were reversed.　The
water flow rate was varied over the range 0.31 to 2.48 m^3s^{-1} x 10^4
(1.86 - 14.88 lit/min).　These are equivalent to liquid residence
times of 212 to 26.5 seconds.　The gas flow rate was varied over the
range 0.3 to 2.58 m^3s^{-1} x 10^4 (Vs = 0.92 x 10^{-3} to 7.97 x 10^{-3} ms^{-1}).
Thus the combined residence time of gas and liquid varied from 108 to
13 seconds.

8.3　RESULTS AND DISCUSSION

8.3.1　Case I - Liquid Inlet through Side and Outlet through Bottom of
Vessel

Figures 8.1 and 8.2 demonstrate some of the experimental results for
ungassed runs, using impellers D1 and D2.　A comparison with batch
system measurements　- which are also shown in these figures -
indicates that there is a negligible effect due to the continuous-flow
of liquid on the initial rising part of the power curve.　The small
deviations exhibited for the different water flow rates have no
monotonic trend and can be attributed to experimental errors.　In
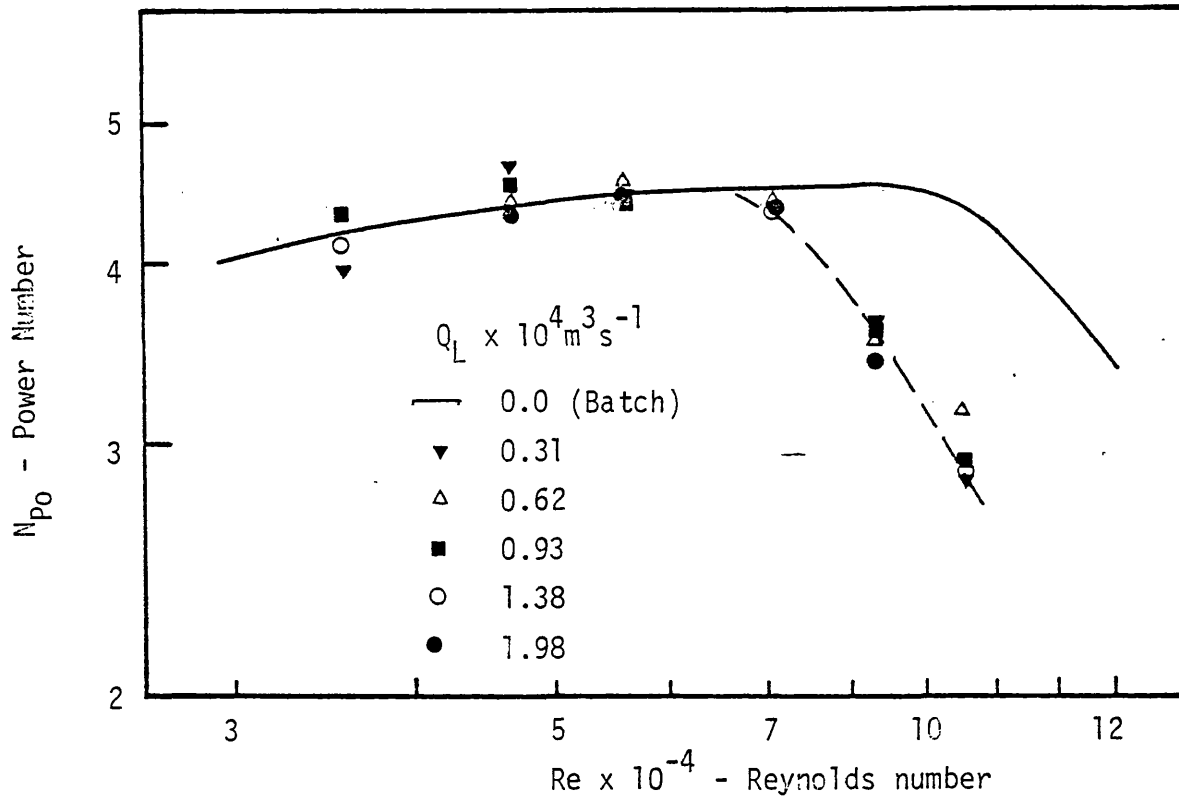
Fig. 8.1   Effect of water flow rate on N_{Po}.
(D = 0.0762 m)
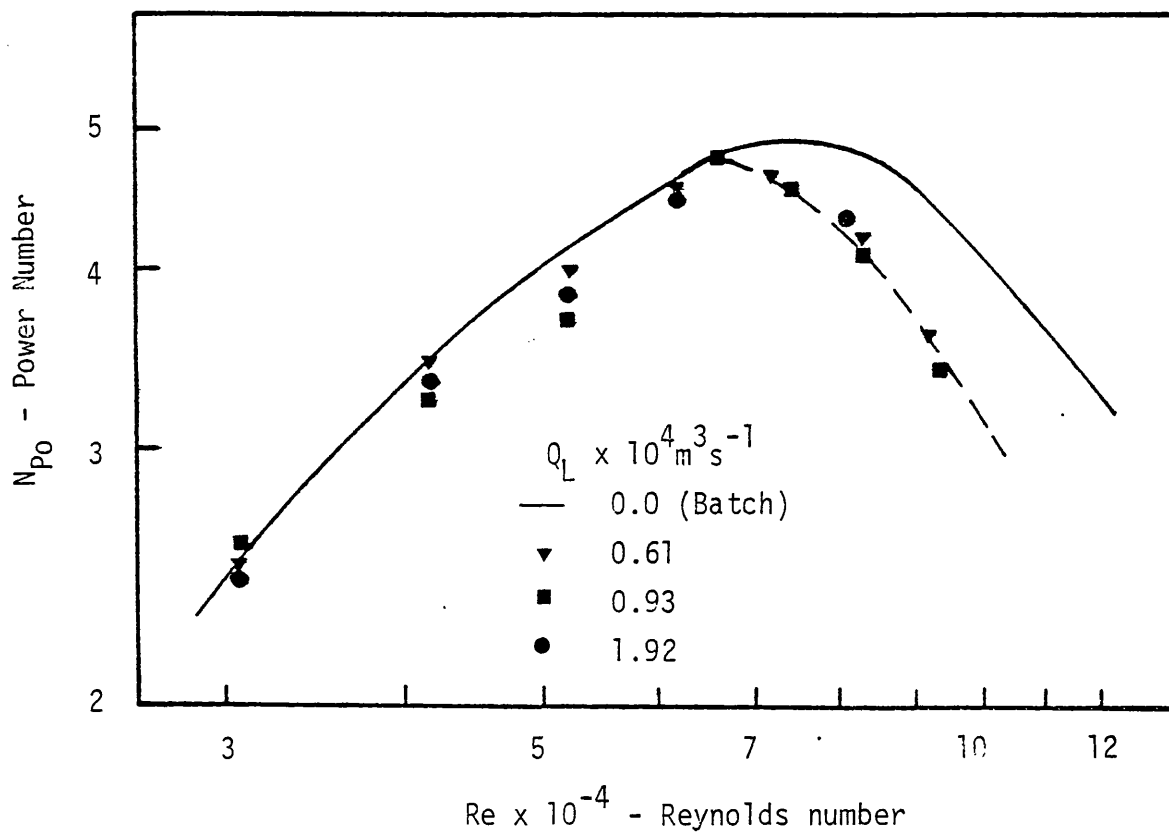
Fig. 8.2   Effect of water flow rate on N_{Po}
(D = 0.1016 m)

this mode of operation, it was observed (from the liquid level indicator of the level controller, see Fig. 2.8) that the liquid level fluctuations were larger compared with bath operation, and also Case II, where the liquid inlet pipe was at the tank bottom. These fluctuations produced similar disturbances in the vessel pressure causing uncertainties in the friction torque. This component becomes significantly greater at the lower end of the power measurement range.

Figures 8.1 and 8.2 also reveal that the decrease in N_{Po} first occurs at lower Re than with batch system. However, this value of Re is not dependent on the liquid flow rate. It is therefore deduced that this trend is due to the system design. This may be explained by the fact that with level control the liquid level is not allowed to increase when surface aeration takes place at low impeller speeds (see Chapter 3). Therefore it is concluded that the continuous-flow of liquid in this case has no direct effect on the impeller power consumption in the ungassed system in the range of water flow rates studied.

On the other hand the same mode of operation does exhibit significant effects in the gas-liquid system. Figures 8.3 and 8.4 show the effect on impeller power consumption at the same gas flow rate. The representation of power data in these Figures is done on the same basis as described in Section 4.3.1 for the batch system. The efficient mixing lines shown (EML) are those obtained for the batch data (Figs. 4.5 and 4.6).

A comparison between the batch power curve and the curve at the lowest water flow rate (0.31×10^{-4} m^3s^{-1}) in Fig. 8.3, indicates that in the flooding region the impeller power consumption is reduced by the continuous-flow of liquid. An explanation for this is that the opposing effect of the inlet flow against the outwards circulation flow from the impeller may have carried some of the dispersed gas back into
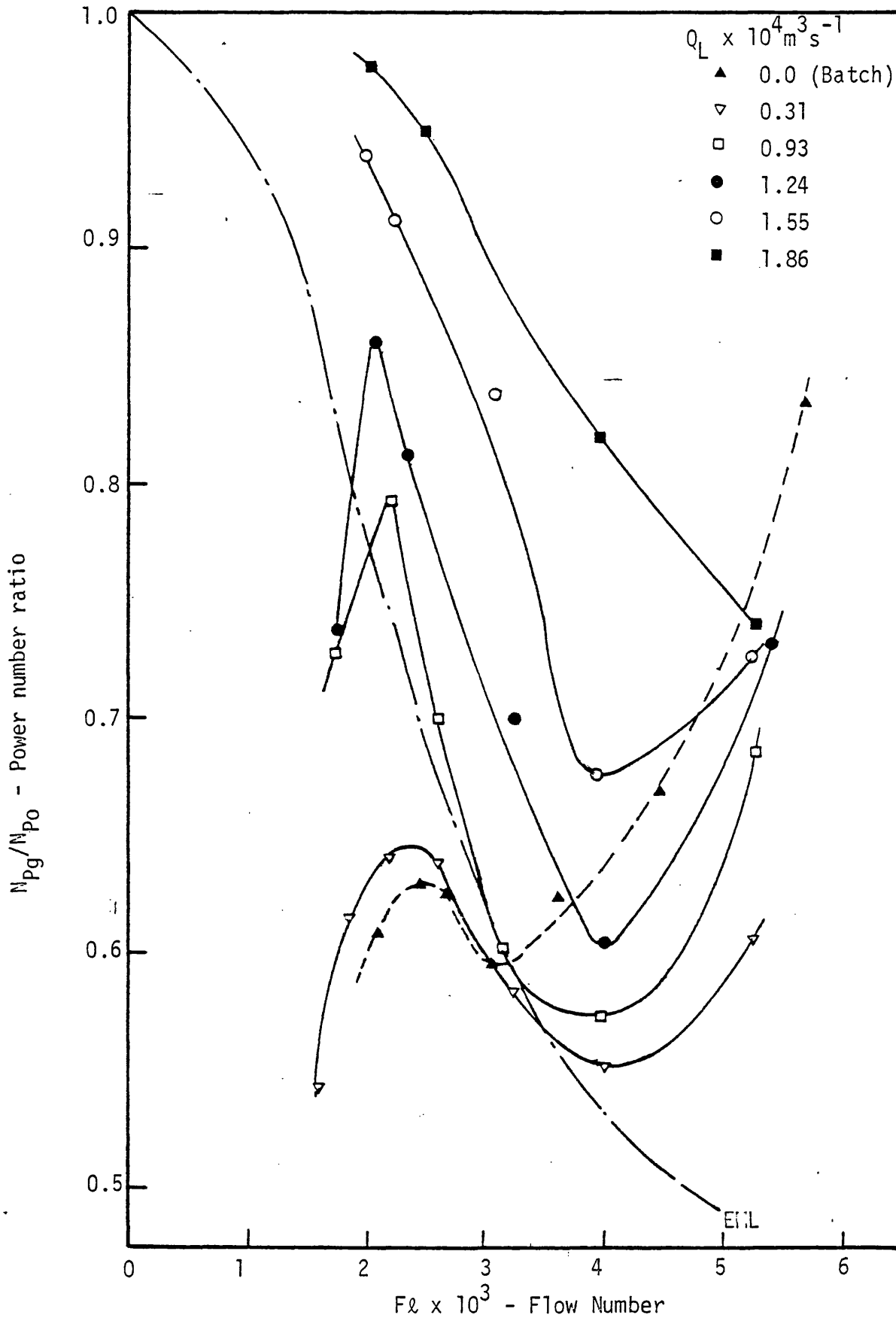
Fig. 8.3   Effect of water flow rate on gassed power consumption.
D = 0.1016 m,   Q = 1.65 x $10^{-4}m^3s^{-1}$
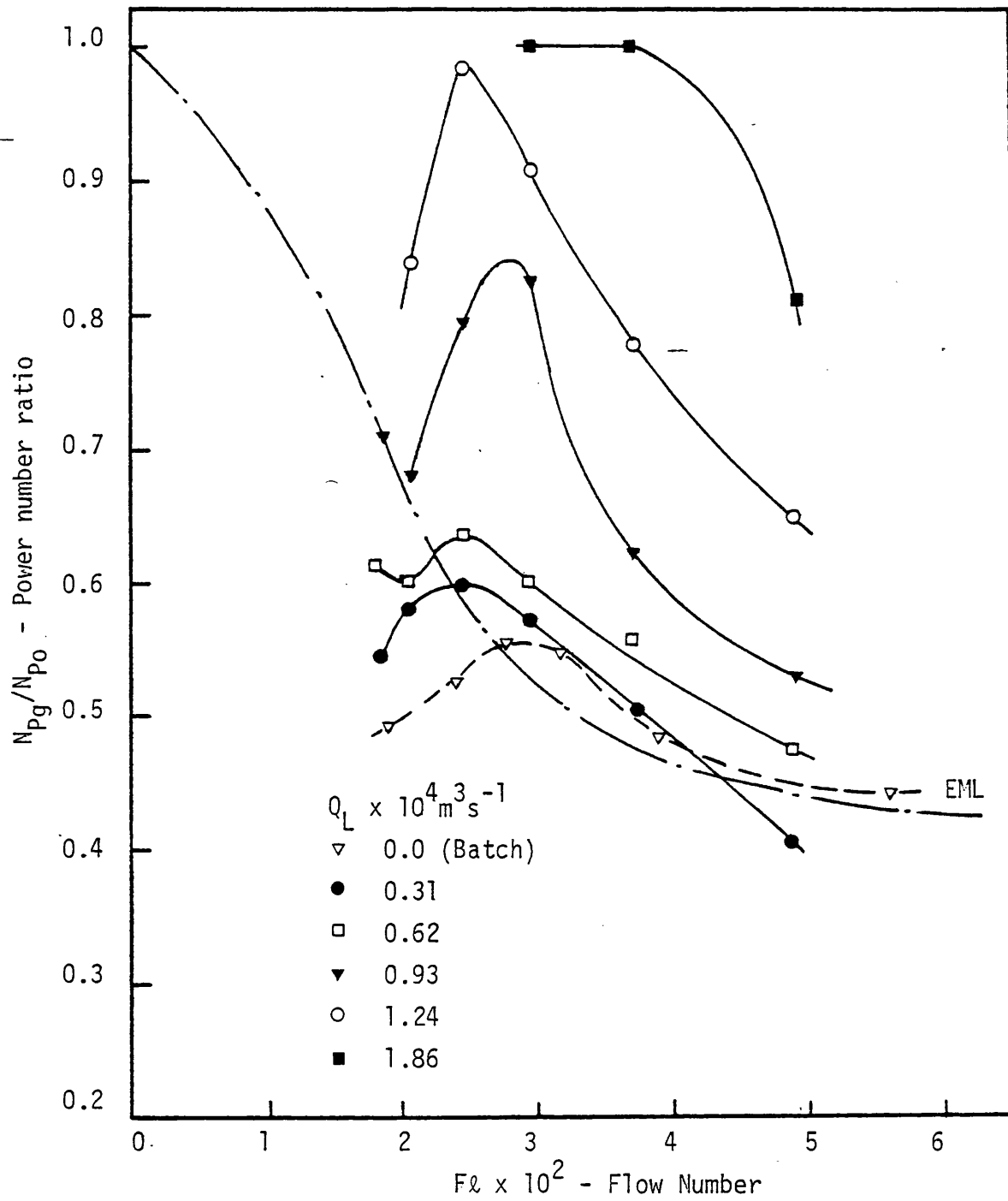
Fig. 8.4   Effect of water flow rate on gassed power consumption.
$D = 0.0762$ m, $Q = 1.32 \times 10^{-4} m^3 s^{-1}$

the impeller.   Thus an additional quantity of gas coalesces with the impeller cavities, reducing the impeller power.   It is important to indicate that since the minimum in the continuous-flow case is close to the EML this indicates that the rate of gas coalescence at this condition is equal to the sparging rate.   However, this is not necessarily all freshly sparged gas.   Figures 8.3 and 8.4 also show that there is a good agreement between the efficient mixing lines for batch and continuous-flow at the lowest water flow rate.   On the other hand, gas recirculation starts at lower speeds for the batch system, indicating that there is a lower rate of gas recirculation in the continuous-flow case.

With increasing the water flow rate the power curves shift upwards. As an example, at a water flow rate of $1.24 \times 10^{-4} \, m^3 s^{-1}$ (Figs. 8.3 and 8.4) minima and maxima appear, and both lie in the flooding region. Hence, they do not correspond to the conditions N_{F1} and N_{R1}, respectively.   The minimum indicates that the rate of gas coalescence with the impeller cavities has reached a local maximum, whilst the maximum indicates that the rate of gas coalescence has reached a local minimum.   Since both conditions lie in the flooding region, this means that the corresponding rates of gas coalescence are both less than the sparged rate.

With further increase of the water flow rate to $1.55 \times 10^{-4} \, m^3 s^{-1}$, (impeller D2, Fig. 8.3), the minimum still appears at the same speed, but the power consumption increases, indicating that there is now a reduction in rate of gas coalescence with the cavities.   As the impeller speed increases, ie, reducing $F\ell$, the power increases sharply and the system reaches a condition of instability at $F\ell \simeq 0.02$.

At this condition attempts to further increase the impeller speed, or the gas flow rate, caused a sudden increase of the liquid level and pressure inside the vessel.   Similar observations were also found to occur with the smaller impeller (Fig. 8.4).   At the highest water flow rate, N_{Pg}/N_{Po} reached a value of 1.0, indicating a complete absence of gas coalescence with the cavities.   Figure 8.5 shows the power curves at different gas flow rate for the highest water flow rate with impeller D2.   It is clear that most of the power measurements, over a relatively wide range of gas flow rates, all lie in the flooding region.   This again indicates that the rate of gas coalescence with the impeller cavities is much less than the corresponding sparged rate.

The interpretation given above based on analysis of the power curves is also confirmed from measurements of the exit gas flow rate from the vessel (see Fig. 2.2).   From a simple mass balance of gas flow through the vessel, it is clear that

$$\overline{Q} = Q - Q_o \qquad\qquad 8.1$$

where

$\qquad\qquad$ Q $\;$ = volumetric sparging rate

$\qquad\qquad$ Q_o = gas flow rate out of the top of the vessel

$\qquad\qquad$ $\overline{Q}$ $\;$ = fraction of gas which escapes with the liquid

$\qquad\qquad\qquad$ flowing out of the vessel.

Q, Q_o, and $\overline{Q}$ are all measured at the vessel operating pressure.

From simultaneous measurements of Q and Q_o, the ratio F was calculated, where

$$F = \frac{\text{rate of gas escaping with liquid}}{\text{rate of gas sparging}}$$

or $\qquad\qquad$ $F = \dfrac{\overline{Q}}{Q}$ $\qquad\qquad\qquad$ 8.2
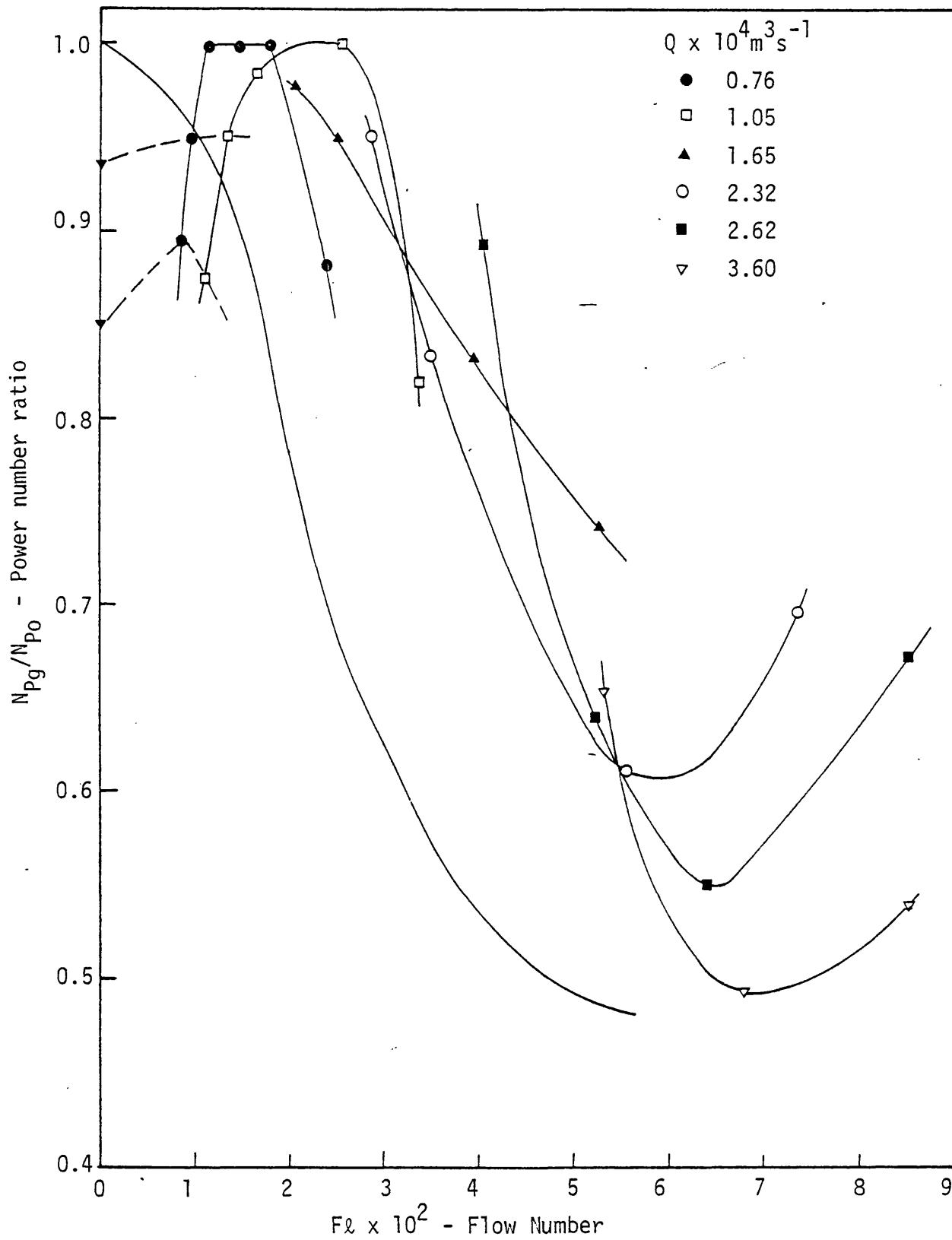
Fig. 8.5   Effect of gas flow rate on gassed power consumption
at high liquid flow rate. $D = 0.1016$ m, $Q_L = 1.86 \times 10^{-4} m^3 s^{-1}$

Figures 8.6 and 8.7 show the change of F with the water flow rate.
It can be seen that, with increasing the water flow rate, a larger
fraction of the sparged gas is carried out with the water flow.   It
is evident from the foregoing analysis of the power curves that since
the gas sparger lies beneath the impeller, the escaping sparged gas
is carried out before it reaches the impeller.   It is also interesting
to note that the maximum liquid superficial velocity was about 0.6
cm/sec.   This value is very small compared to the bubble terminal
velocity, and hence cannot fully explain why the gas escapes with the
liquid flowing out from the tank bottom.   On the other hand, the
liquid velocity inside the outlet pipe (15 mm inner diameter) was in
the range 17.5 to 105 cm/sec.   The flow field created near to the
entrance of the bottom outlet pipe is therefore most likely responsible
for causing this effect.   Also there was only a relatively short
distance between the gas sparger and the bottom of the tank (3.5 cm).
Moreover, the difficulties of controlling the liquid level at high
liquid and gas flow rates can now be explained as being due to the
increased rate of two-phase flow through the outlet pipe.

Typical gas holdup measurements are shown in Fig. 8.8.   They indicate
that at the same gas flow rate and impeller speed, the gas holdup
increases gradually with increasing the water flow rate up to a
maximum value.   Any further increase in the liquid flow rate causes
a drop in gas holdup.   The initial increase of gas holdup compared to
the batch system is difficult to explain, particularly in view of the
previous observations regarding the power consumption and the rate
of escape of gas.
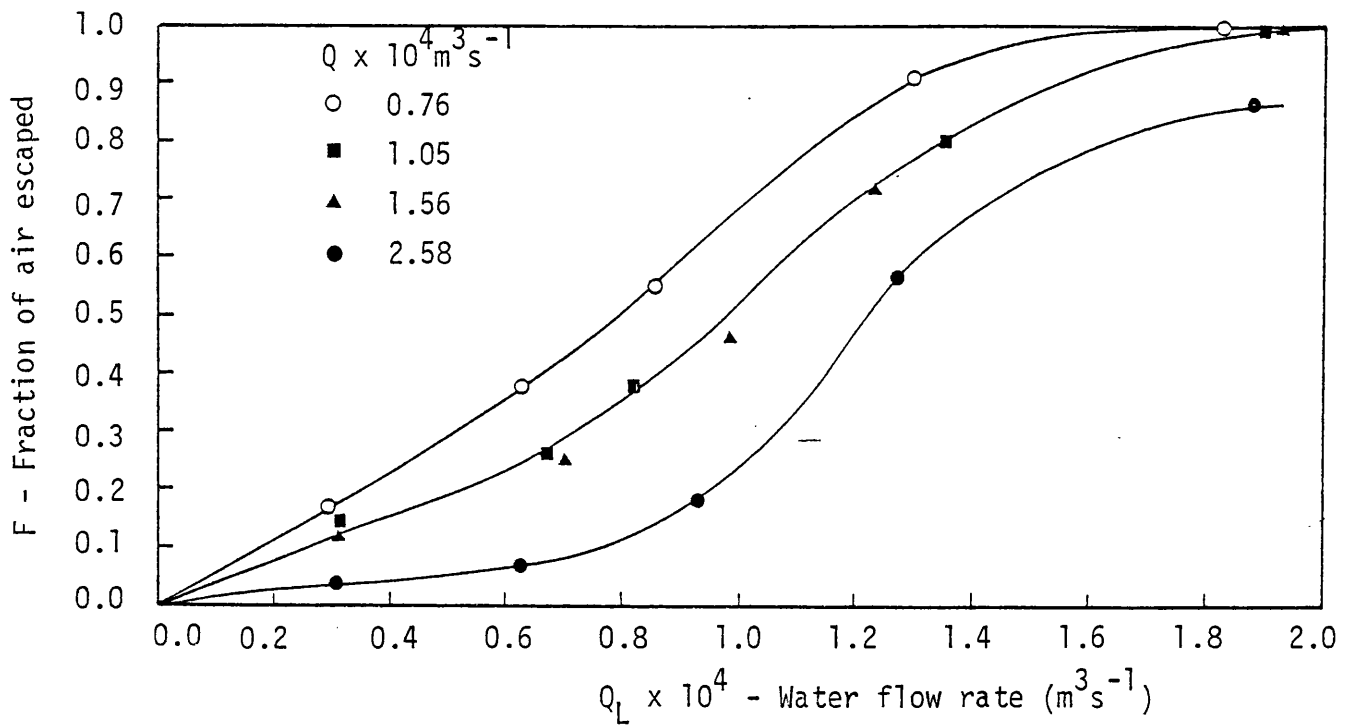
Fig. 8.6 Effect of gas flow rate on fraction of gas which escapes with water F. D = 0.0762m, N = 10 rps.
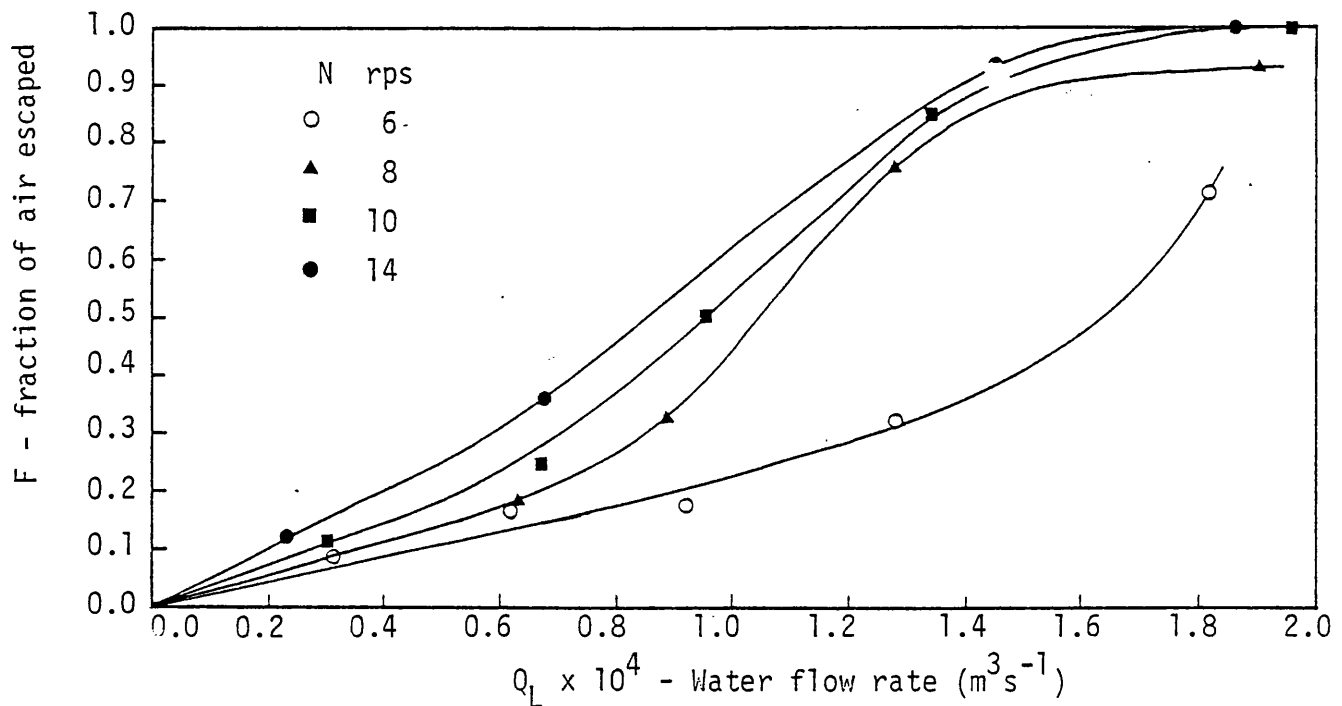
Fig. 8.7 Effect of impeller speed on fraction of gas which escapes with water F. D = 0.0762m, Q = $1.32 \times 10^{-4} m^3 s^{-1}$
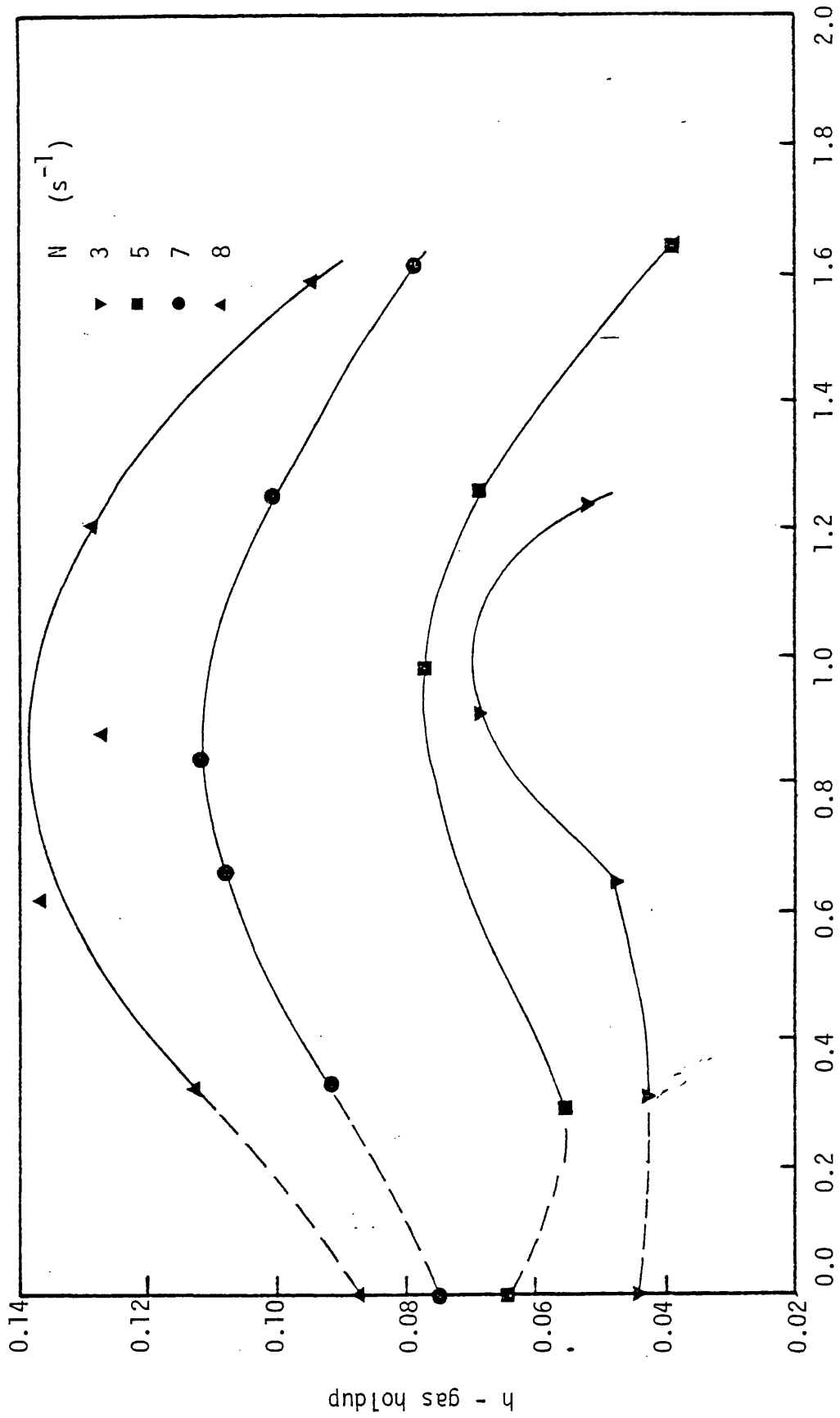
Fig. 8.8   Gas holdup against water flow rate. $D = 0.1016m$, $Q = 1.66 \times 10^{-4} s^{-1}$

$Q_L \times 10^4$ - Water flow rate ($m^3 s^{-1}$)

h - gas holdup

N	(s^{-1})
▼	3
■	5
●	7
◀	8

With side-entry of liquid, a considerable fraction of the sparged gas escapes with water, thereby reducing the efficiency of the reactor as a gas-liquid contactor. This behaviour is not desirable in industrial systems since reactant gas can escape with the product. In addition, the impeller power consumption is high and the impeller dispersion efficiency is very poor. Therefore, it is not recommended that this mode of operation be used in practice. The noticeable improvement achieved when the liquid inlet and outlet pipes were reversed led to attention being concentrated on Case II, which is described in the next section.

8.3.2 Case II. Liquid Inlet through Bottom and Outlet through Side of Vessel

8.3.2.1 Ungassed Power

Figures 8.9, 8.10, and 8.11 show the ungassed power measurements for the three impellers used. It can be seen that an increase of water flow rate, Q_L, causes an increase in N_{Po} at all values of Re. For the initial part of the power curve, there is a gradual increase of N_{Po} with Q_L, and the batch run can be considered a special case, with $Q_L = 0$. The trends are similar to those observed for unbaffled vessels in the absence of a gas-liquid interface (1,92).

The decrease of N_{Po} for $Q_L > 0$ starts at higher Re with increasing Q_L. This effect is most pronounced for the two larger impellers (Figs. 8.10 and 8.11) and may be explained by the escape of part of the entrained gas with the liquid flowing out of the vessel. On the other hand, the decrease of N_{Po} for batch runs first occurs at higher Re compared to the continuous-flow case. The earlier drop of N_{Po} in continuous-flow is therefore due to the control of the liquid level (see Sec. 8.3.1).
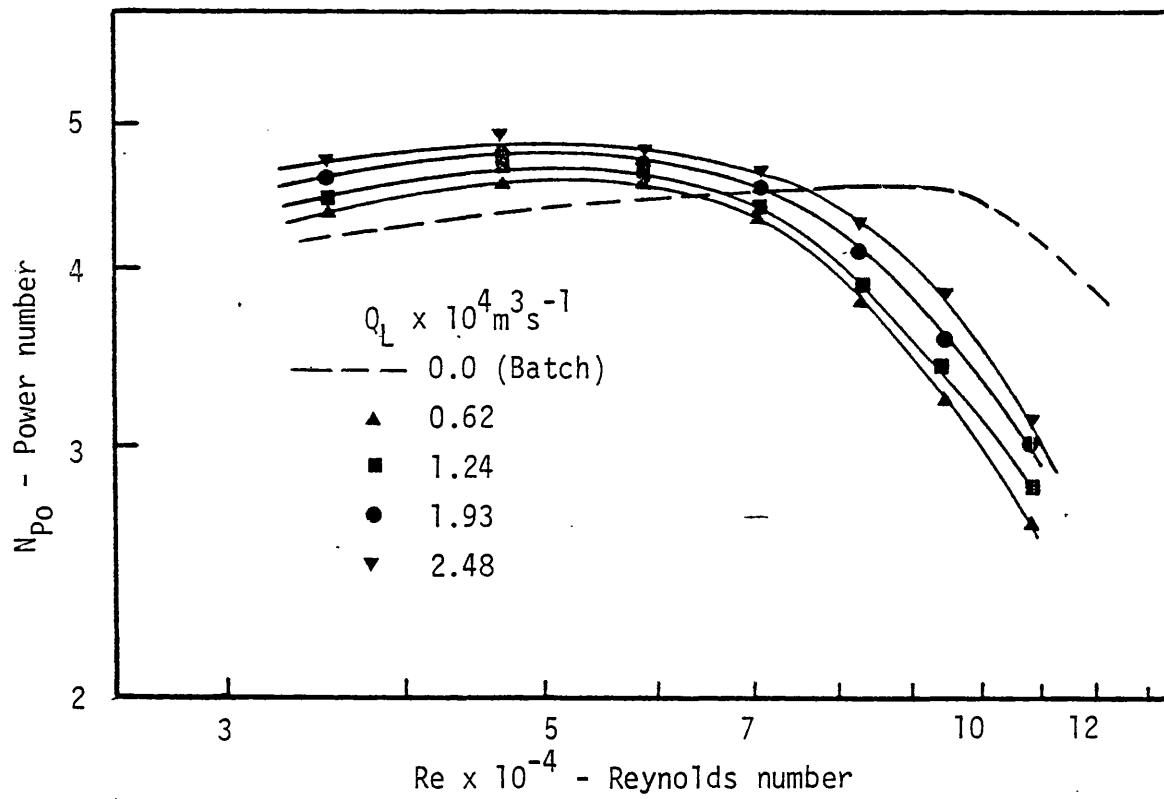
Fig. 8.9   Effect of water flow rate on N_{Po}.
(D = 0.0762 m)
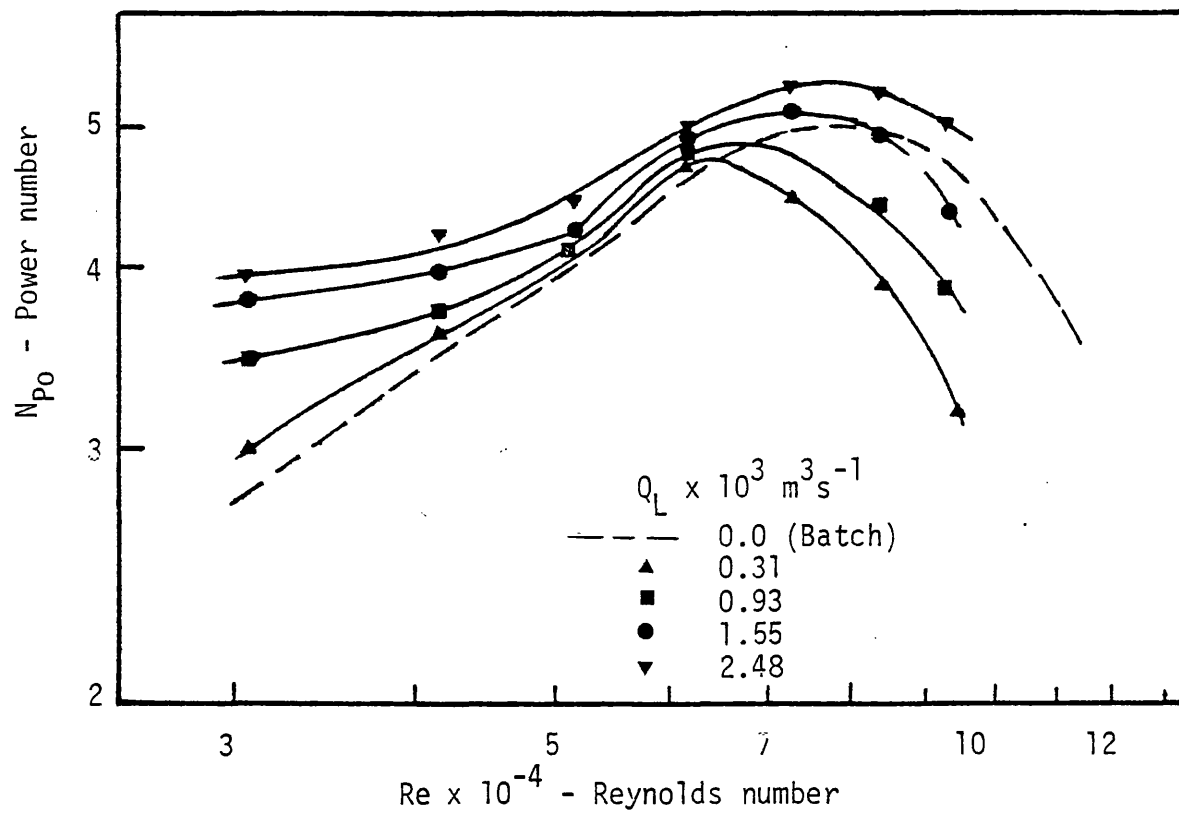
Fig. 8.10   Effect of water flow rate on N_{Po}.
(D = 0.1016 m)
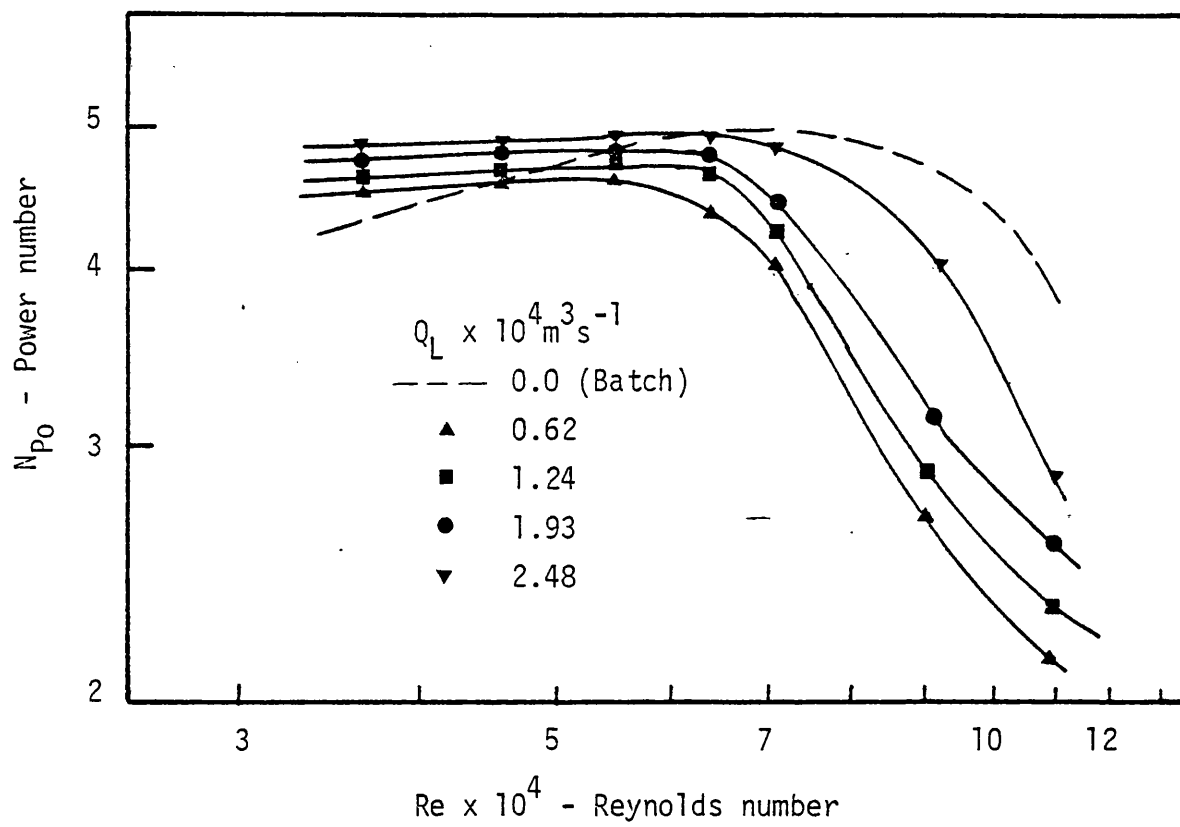
Fig. 8.11   Effect of water flow rate on N_{Po}.
(D = 0.135 m)

The early start of surface aeration for the continuous-flow system, with the present arrangement, restricted the useful range of the power curves. This makes it more difficult for correlating the effect of the water flow rate on N_{Po}. With the largest impeller, the entrainment of gas bubbles first occurred in the batch run at N = 2.5 rps (see Fig. 3.10), ie, at Re $\simeq$ 4.5 x 10^4. The earlier start of gas entrainment expected in continuous-flow caused a relative reduction in N_{Po} (Fig. 8.11). This was lower than the corresponding $\overline{N_{Po}}$ for batch runs, even before any drop in N_{Po} occurred (Q_L = 0.62 and 1.24 x 10^{-4} m^3s^{-1} at Re = 5.45 x 10^4). In addition, impeller D2 (Fig. 8.10) still shows a steeper increase of N_{Po} at low Re. As explained in Chapter 3, the relatively thinner blades of the D3 impeller (Fig. 8.11) may have caused the flattening of the power curve.

At this point, it is relevant to mention the study of Molen and Mannen (93), concerning turbulent flow in the impeller stream region. Using a Laser-Doppler velocimeter they found that the periodic component of the circulating velocity in the trailing vortices is very sensitive to the impeller geometry, and in particular to the thickness of the blade. A reduction of the blade thickness from 1.5 to 0.5 mm (For D = 0.12m) was found to cause a considerable increase in the vertical periodic component. This observation, coupled with the reported dependency of the impeller power on the mean velocity within the trailing vortex (23), tends to support the explanation for the above-mentioned effects of the blade thickness on the power curve.

8.3.2.3 Gas-Liquid Power Consumption

To illustrate the effect of the continuous-flow of liquid on gassed power measurements, some of the results for impellers D2 and D3 are shown in Figs. 8.12 and 8.13 respectively. It is clear that increase
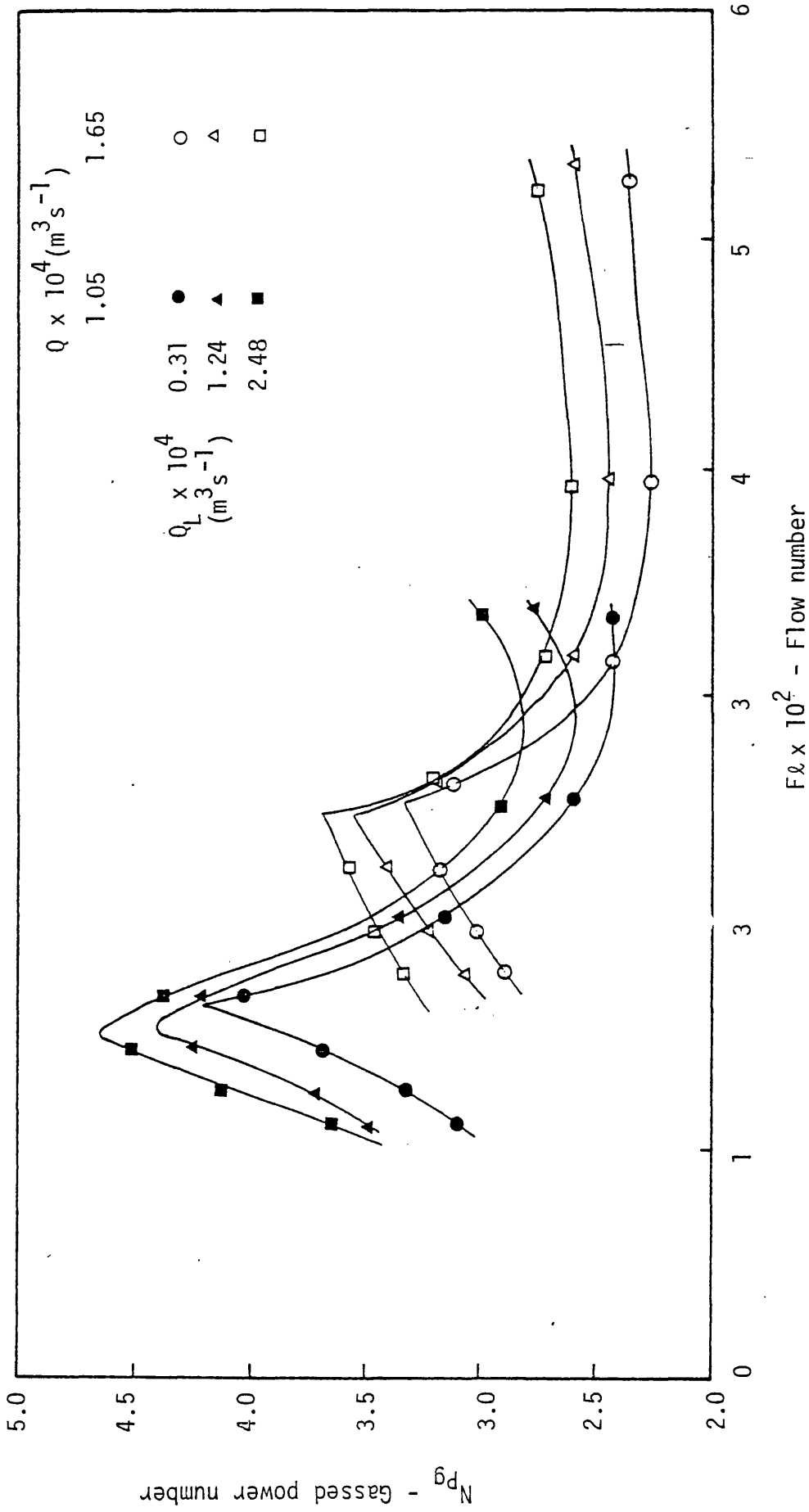
Fig. 8.12 N_{Pg} against $F\ell$ at different water flow rates. (D = 0.1016)
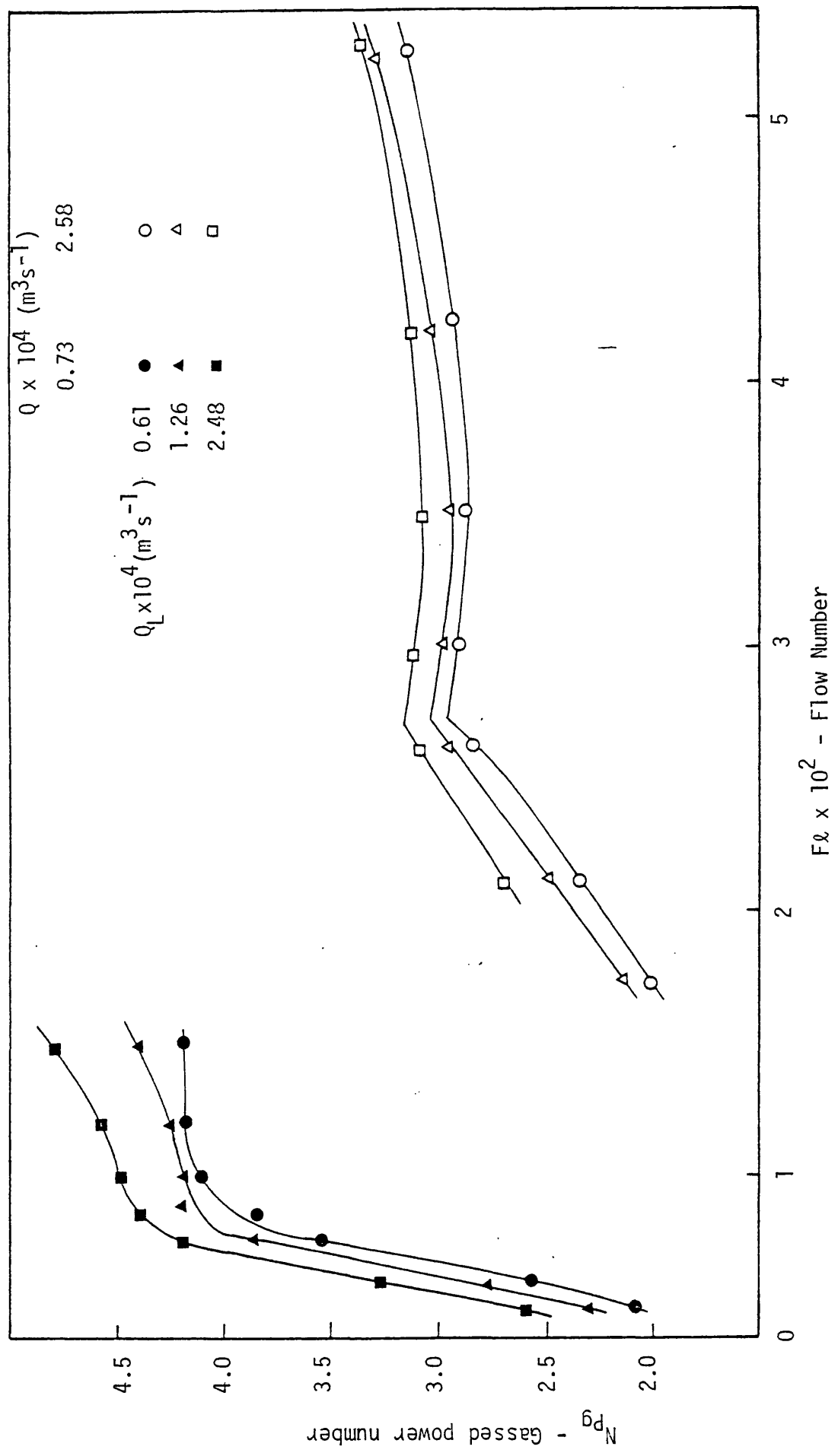
Fig. 8.13 N_{Pg} against $F\ell$ at different water flow·rates. (D = 0.135 m)

of the water flow rate causes an increase in N_{Pg}. However, N_{R1} does not change significantly with the water flow rate.

The method discussed in Section 4.3.1 for representation of gassed power data is used here. Since the ungassed power for this case of continuous-flow was found to change with the water flow rate, the gassed power measurements have to be referred to the ungassed power at the same water flow rate. In other words, in calculating N_{Pg}/N_{Po}, both of these quantities should be measured at the same water flow rate as well as at similar impeller speeds. A large number of results were obtained for these runs and therefore a few only are seclected to illustrate the main effects. These are shown in Figs. 8.14, 8.15, and 8.16.

Figures 8.14 and 8.15 indicate that difference between the power curves at different values of Q_L is small. The maximum variation of N_{Pg}/N_{Po} at the same Fℓ, when the water flow rate was increased from 0.3 to 2.48 $m^3 s^{-1}$ x 10^{-4} is about 10%. To compare these results with the batch system, the efficient mixing lines obtained from batch runs (Section 4.3.2) are placed on Figs. 8.14, 8.15 and 8.16. It is clear that these EMLs describe the power consumption for continuous system reasonably well. Furthermore, to compare the limits of the efficient mixing regime, the correlations developed in Chapter 4 have been used (N_{F1} from Eq. 4.29 and N_{R1} from Eq. 4.33). The arrows shown in Figs. 8.14 and 8.15 indicate the values obtained for N_{R1} and N_{F1}. The flooding point is predicted quite well but the impeller speed at the onset of gas recirculation (N_{R1}) is overestimated. This is particularly pronounced for the lower gas flow rates. In general then, the effect of sparging gas on impeller power is similar to the batch system, within the operating conditions of this study.
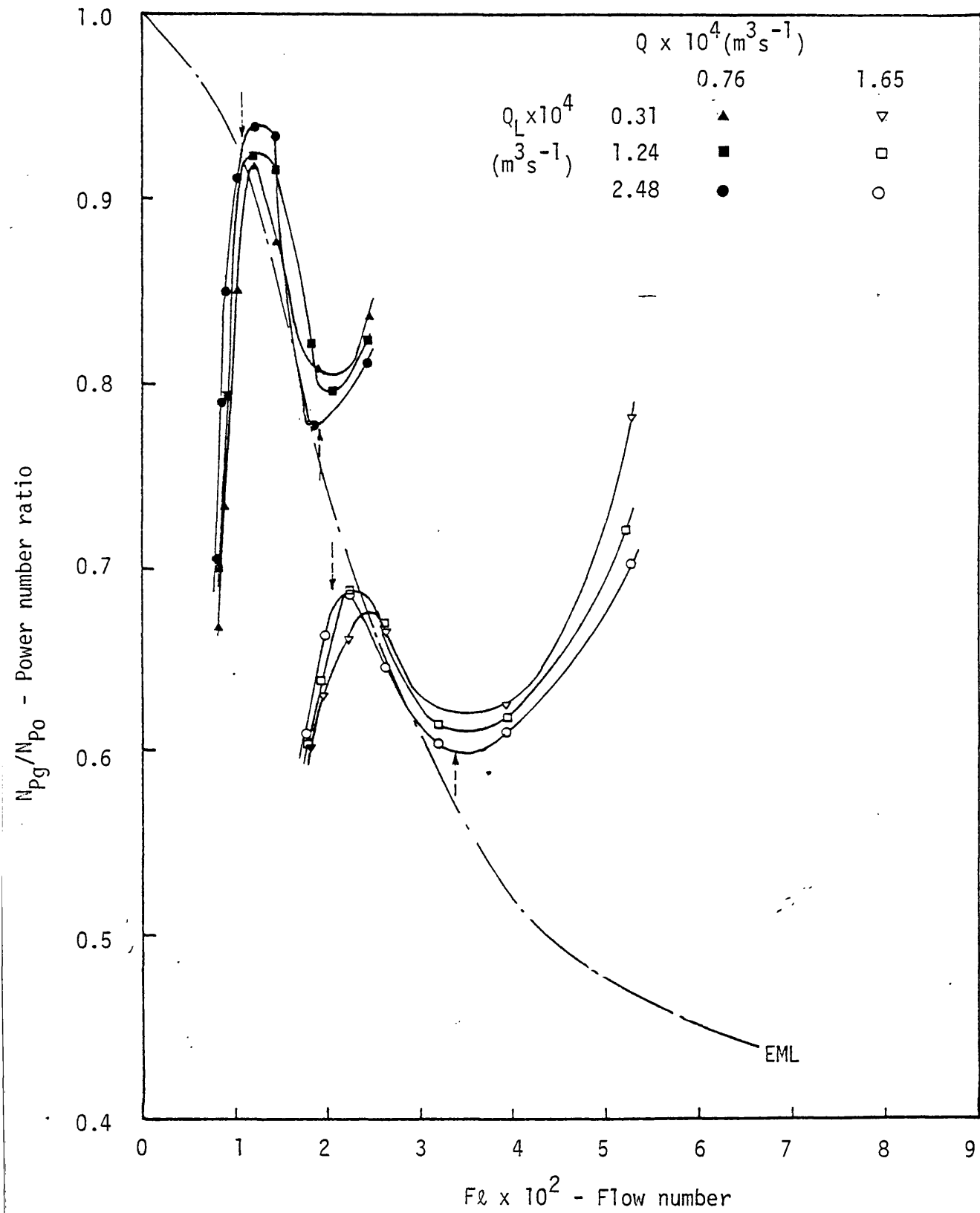
Fig. 8.14 N_{Pg}/N_{Po} against $F\ell$ at different water flow rates
(D = 0.1016).
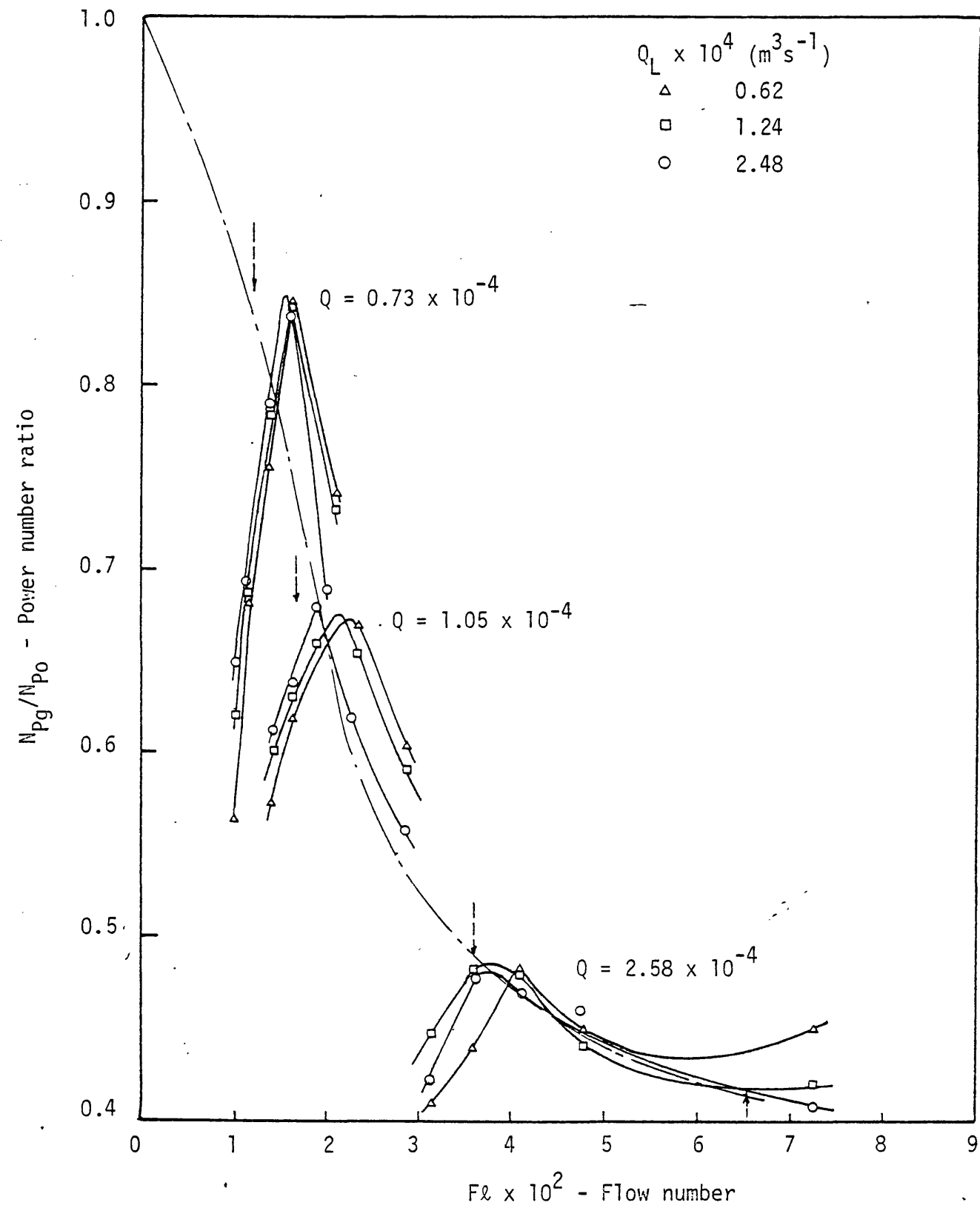
Fig. 8.15 N_{Pg}/N_{Po} against $F\ell$ at different water flow rates.
(D = 0.0762 m)
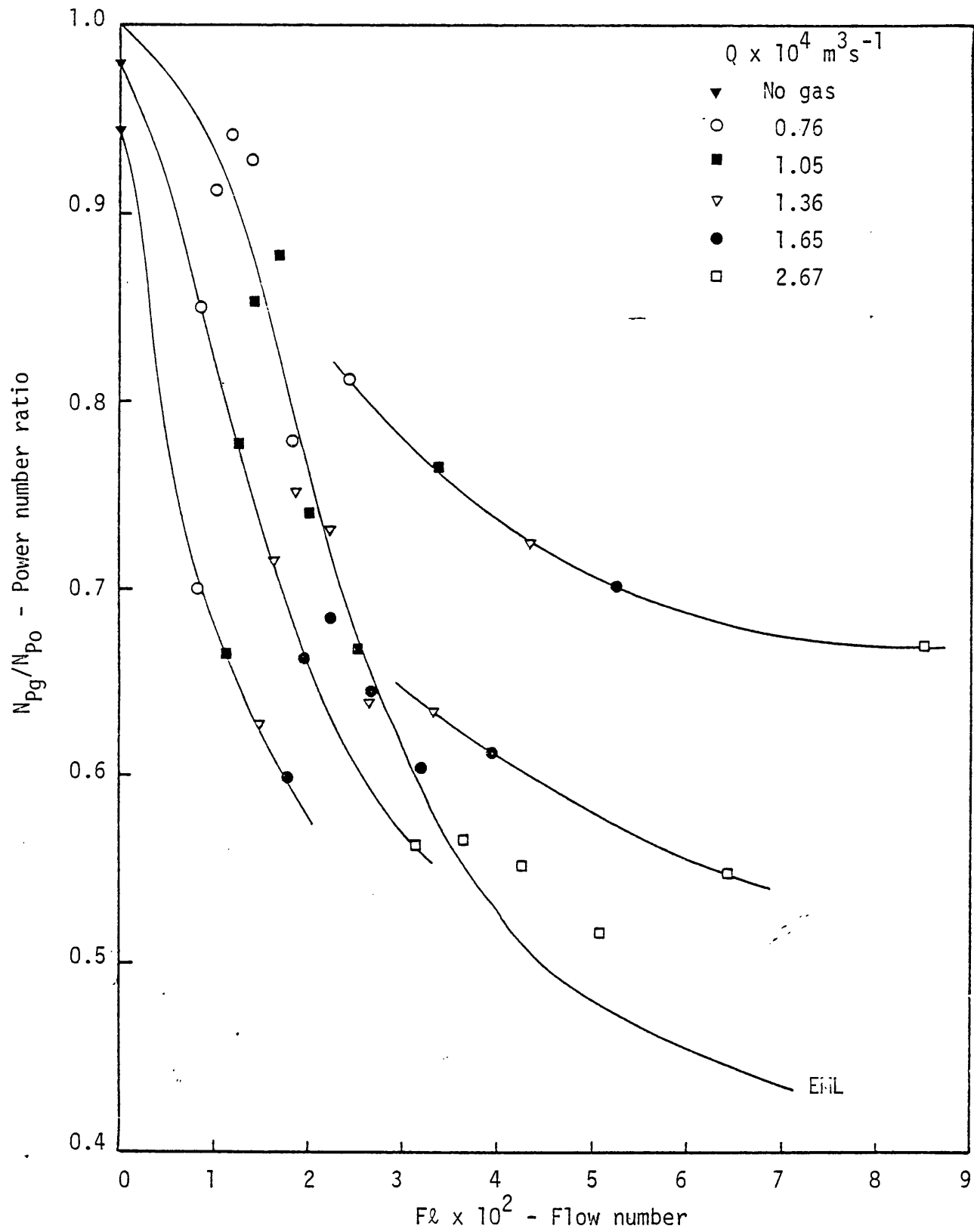
Fig. 8.16 N_{Pg}/N_{Po} against $F\ell$ at maximum water flow rate.
$Q_L = 2.48 \times 10^{-4} \ m^3 s^{-1}$ (D = 0.1016 m)

To correlate the gassed power data, the absolute increase of power with increasing the water flow rate (Figs. 8.12 and 8.13) needs to be considered. The power measurements in the efficient mixing regime are plotted against the Liquid Flow number $Fl_L (\frac{Q_L}{ND^3})$ in log-log manner as shown in Fig. 8.17. It was found that

$$Pg \ \alpha \ (\frac{Q_L}{ND^3})^{0.06} \qquad\qquad 8.3$$

For $Q_L > 0$.

Since the exponent on this group is very small and also the fact that the EML obtained for the batch system represents quite accurately the continuous-flow data, it is anticipated that the analysis carried out previously (Chapter 4) should be applicable here. Thus using Eq. 4.30

$$Pg \ \alpha \ \left(\frac{N^{3.33} \ D^{6.33}}{Q^{0.404}}\right) \qquad\qquad 8.4$$

and combining with Eq. 8.3 :

$$Pg \ \alpha \ \left(\frac{N^{3.33} \ D^{6.33}}{Q^{0.404}}\right) \ (\frac{Q_L}{ND^3})^{0.06} \qquad\qquad 8.5$$

This relationship is shown in Fig. 8.18, which gives the result :

$$Pg = 1250 \ \left(\frac{N^{3.33} \ D^{6.33}}{Q^{0.404}}\right) \left(\frac{Q_L}{ND^3}\right)^{0.06}$$

or

$$Pg = 1250 \ \frac{N^{3.27} \ D^{6.33} \ Q_L^{0.06}}{Q^{0.404}} \qquad\qquad 8.6$$

for $Q_L > 0$.
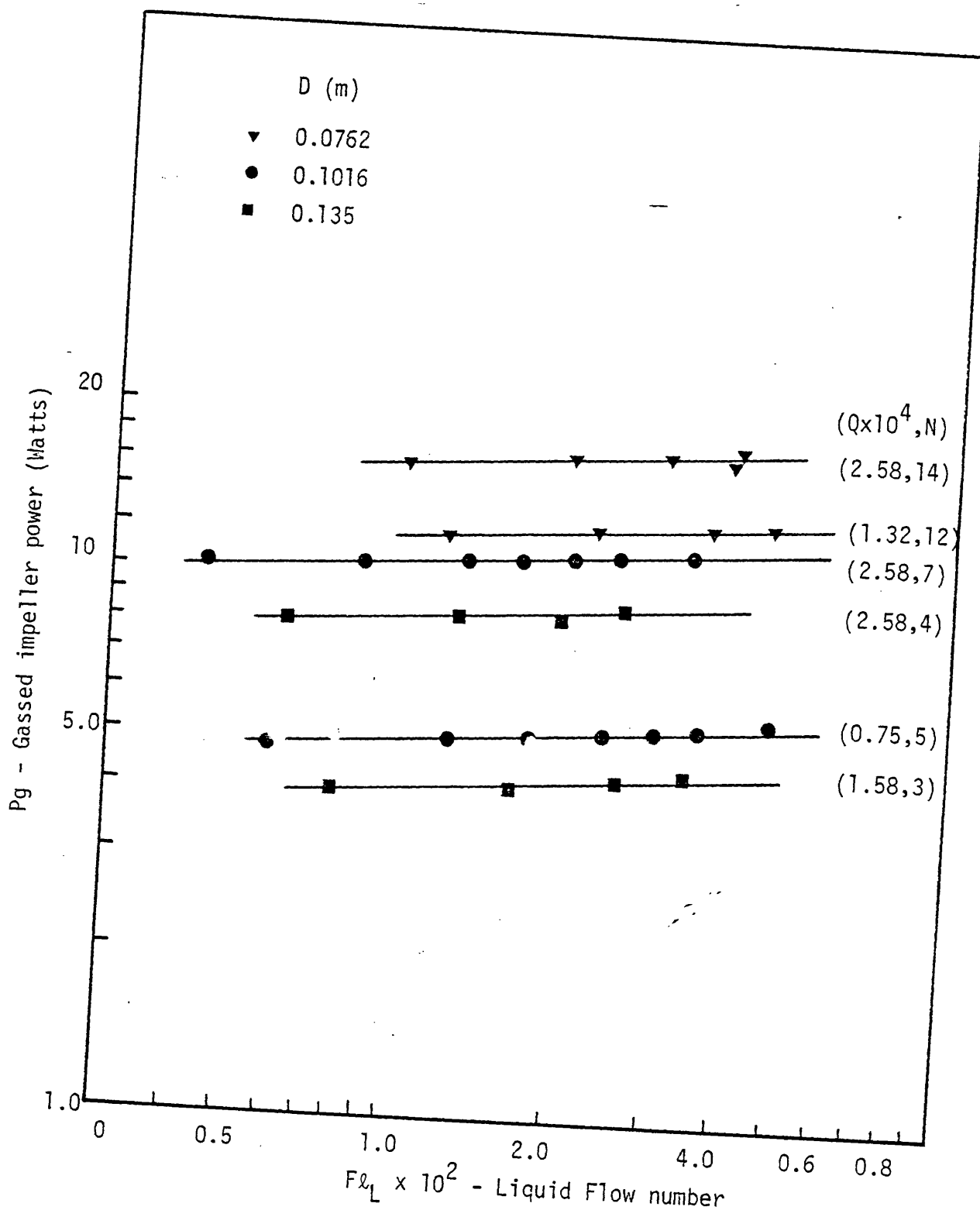
Fig. 8.17   Effect of water flow rate on impeller power
consumption in the efficient mixing regime.
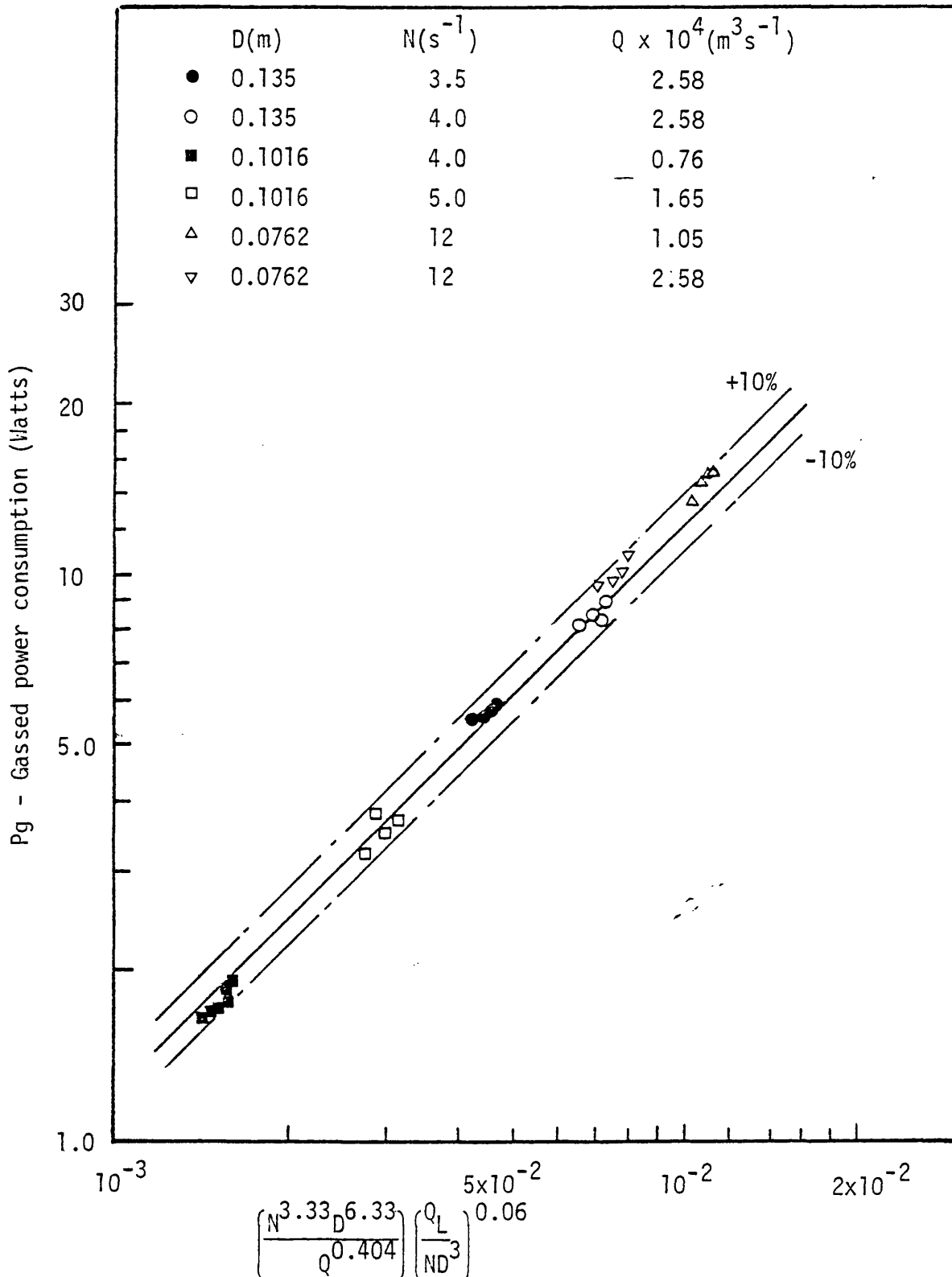
Fig. 8.18   Power consumption in the efficient mixing regime.
(Each symbol represents number of runs with different
water flow rate, Q_L = 0.31 - 2.48 x 10^{-4}).

Equation 8.6 predicts the power in the efficient mixing regime within $\pm$ 10%, ie, the same accuracy of Eq. 4.30 for batch system. Comparing Eq. 8.6 and Eq. 4.30 for batch system, it can be shown that at the lowest Q_L value the ratio (Pg continuous/Pg batch) at otherwise similar operating conditions equals 0.9, and at the highest Q_L value it is 1.03. In general then, the difference between the batch and continuous-flow systems in this region is small.

To extend Eq. 8.6 to correlate the power in the flooding and recirculation regimes, the impeller dispersion efficiency is used in a manner similar to Sec. 4.3.6. Therefore Eq. 8.6 can be generalised by replacing Q by ηQ to become

$$Pg = 1250 \frac{N^{3.27} D^{6.33} Q_L^{0.06}}{(\eta Q)^{0.404}} \qquad 8.7$$

Since the correlations for predicting N_{F1} and N_{R1} for batch system give a reasonable prediction for continuous-flow, the correlations for η obtained previously can also be used. Hence η in Eq. 8.7 has characteristics similar to those stated for Eq. 4.31 for the batch system. The effect of vessel pressure is also accounted for by using the correlations presented in Sec. 4.3.7. Figure 8.19 shows that Eq. 8.7 correlates Pg within $\pm$ 15%.

Finally it is important to mention that since the correlations developed for η from batch runs give a good prediction for continuous-flow in the case of tap water, it is expected that a similar situation applies to the non-coalescing system. Therefore, for a non-coalescing continuous-flow system, Eq. 8.7 together with Eqs. 4.34 - 4.37 (see Section 8.3.8) can be employed to predict the impeller power consumption.
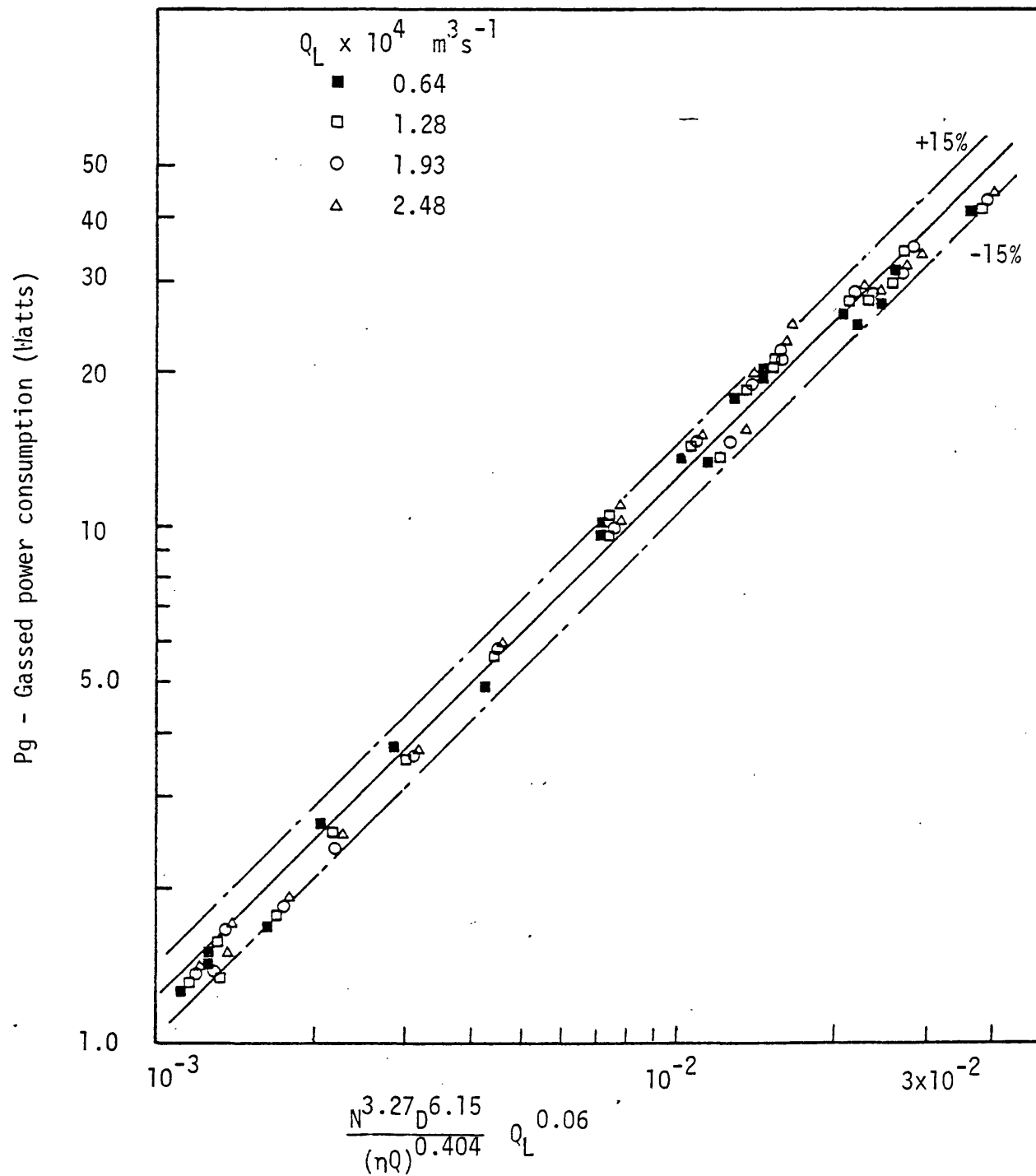
Fig. 8.19   Test of generalised power correlation for continuous
flow system, using impellers D1, D2, and D3.

8.3.2.3 Gas Holdup

The liquid flow rate was found to have negligible effect on the gas

holdup.   Figures 8.20 and 8.21 are examples of the gas holdup

measurements using impellers D1 and D2.   The scatter of the experimental

points has no specific trend and is attributed to experimental error.

Equation 7.22 which was used to correlate the batch system results was

also used to correlate the results of this case of continuous-flow

system.   As shown in Fig. 8.22, this correlation fits the experimental

results with the same accuracy found for the batch system, ie, $\pm$ 30%.

8.4   CONCLUSIONS

1 -   The arrangement of feeding liquid through the tank side and

discharging from the bottom pipe has no significant effect on

the ungassed power consumption.   For gas-liquid system, however, a

large fraction of the sparged gas escapes with liquid discharge.

This causes considerable reduction in the rate at which gas coalesces

with the impeller cavities.   This is also accompanied by severe

reduction in the impeller dispersion efficiency, η, with a consequent

increase of the power requirement.   Because of the poor performance

achieved by this arrangement, it is not recommended as a practical

design for continuous-flow gas-liquid contacting.

2 -   The alternative arrangement of feeding the liquid through the

bottom of the vessel and discharging through side pipe, produces

an increase in N_{Po} and N_{SA2} as the liquid flow rate is increased.

For gas-liquid operation, N_{Pg} also increases with the liquid flow rate.

The increase is basically caused by the corresponding increase of

N_{Po}.   Indeed, the representation of gassed power data on N_{Pg}/N_{Po} vs. $F\ell$

revealed only minor changes over the whole range of water flow rate.

In general, the performance of a gassed agitated vessel with continuous-
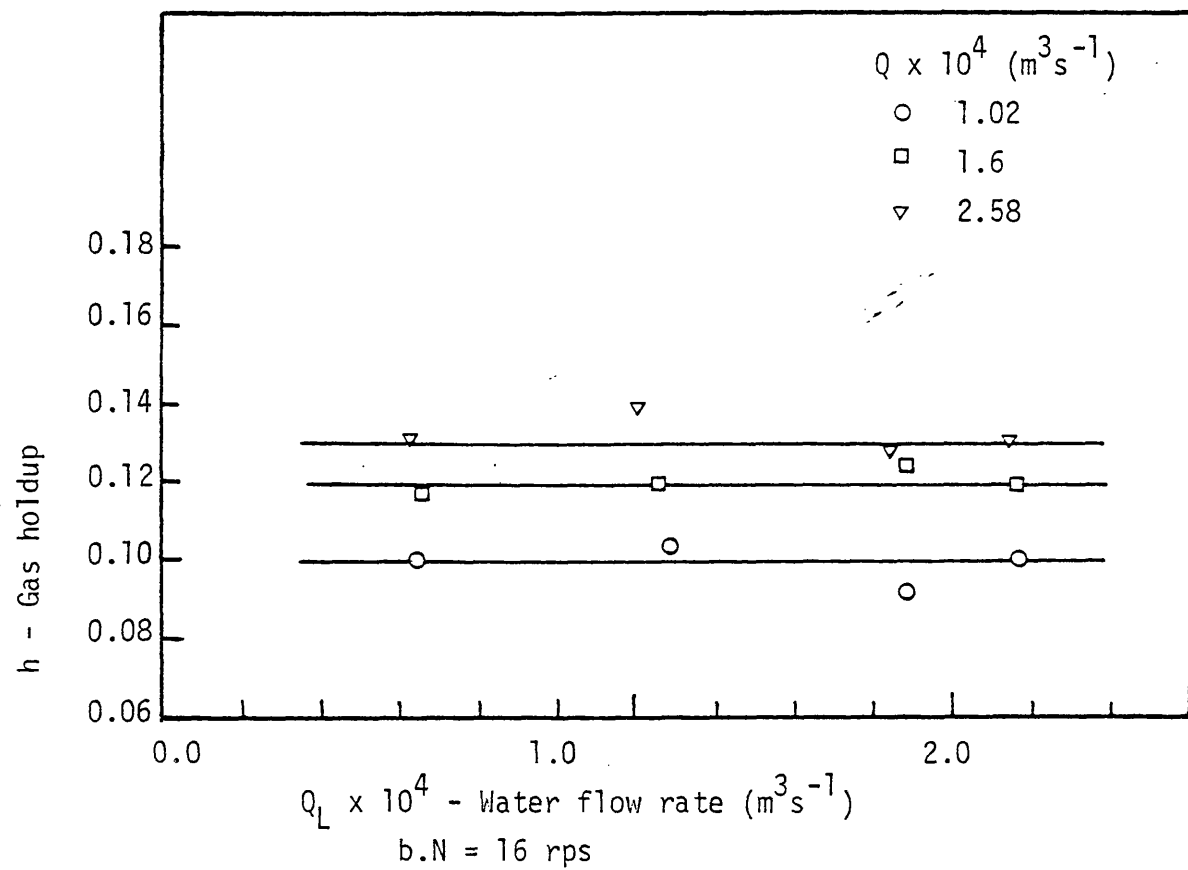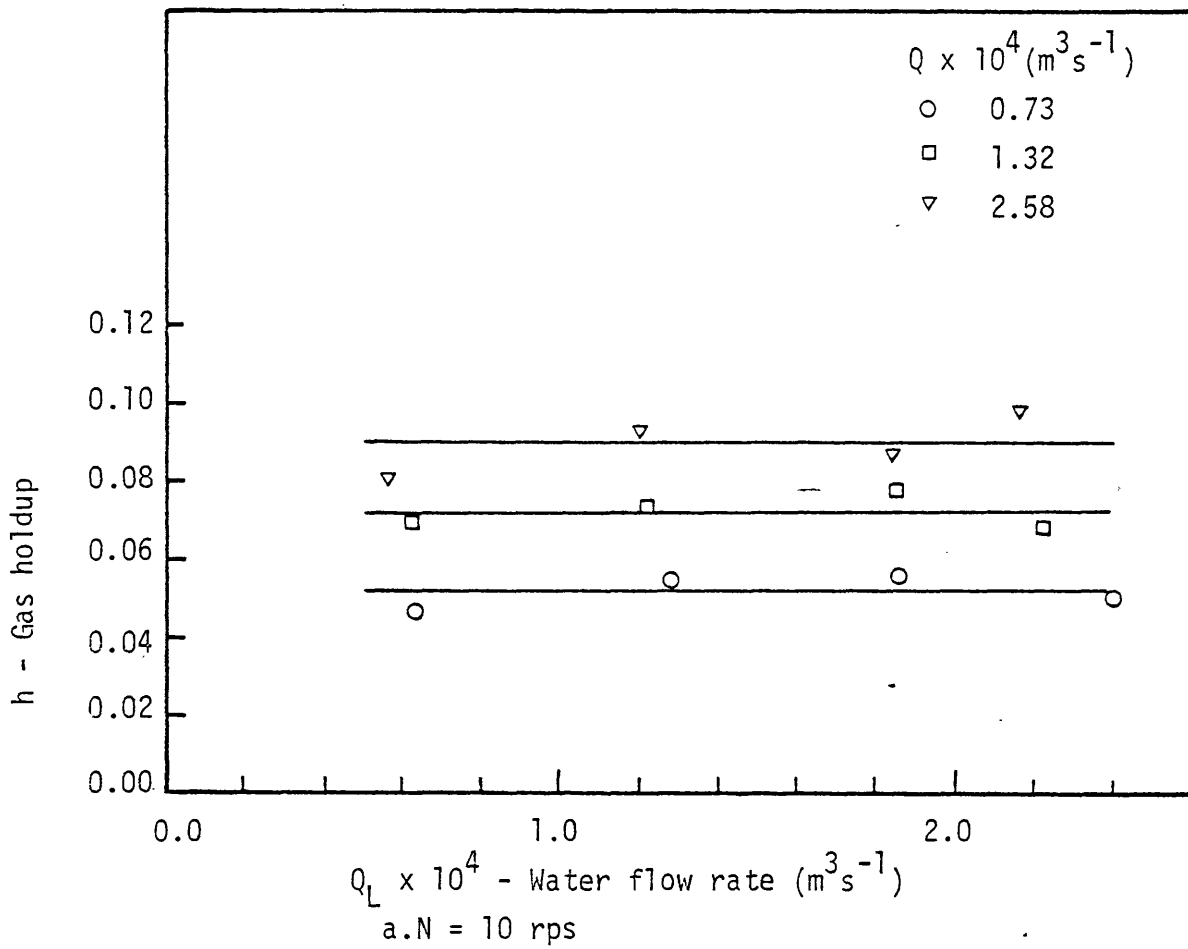
Fig. 8.20   h against Q_L (D = 0.0762 m)
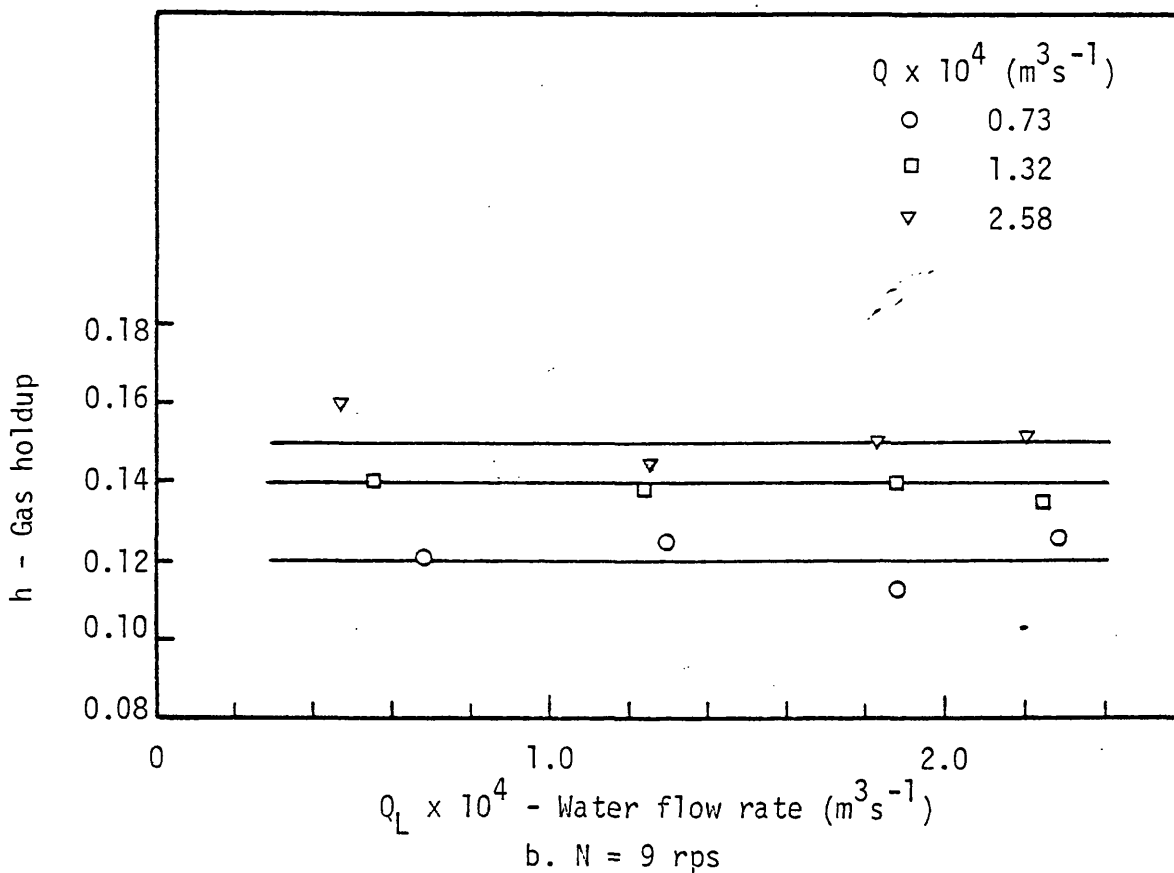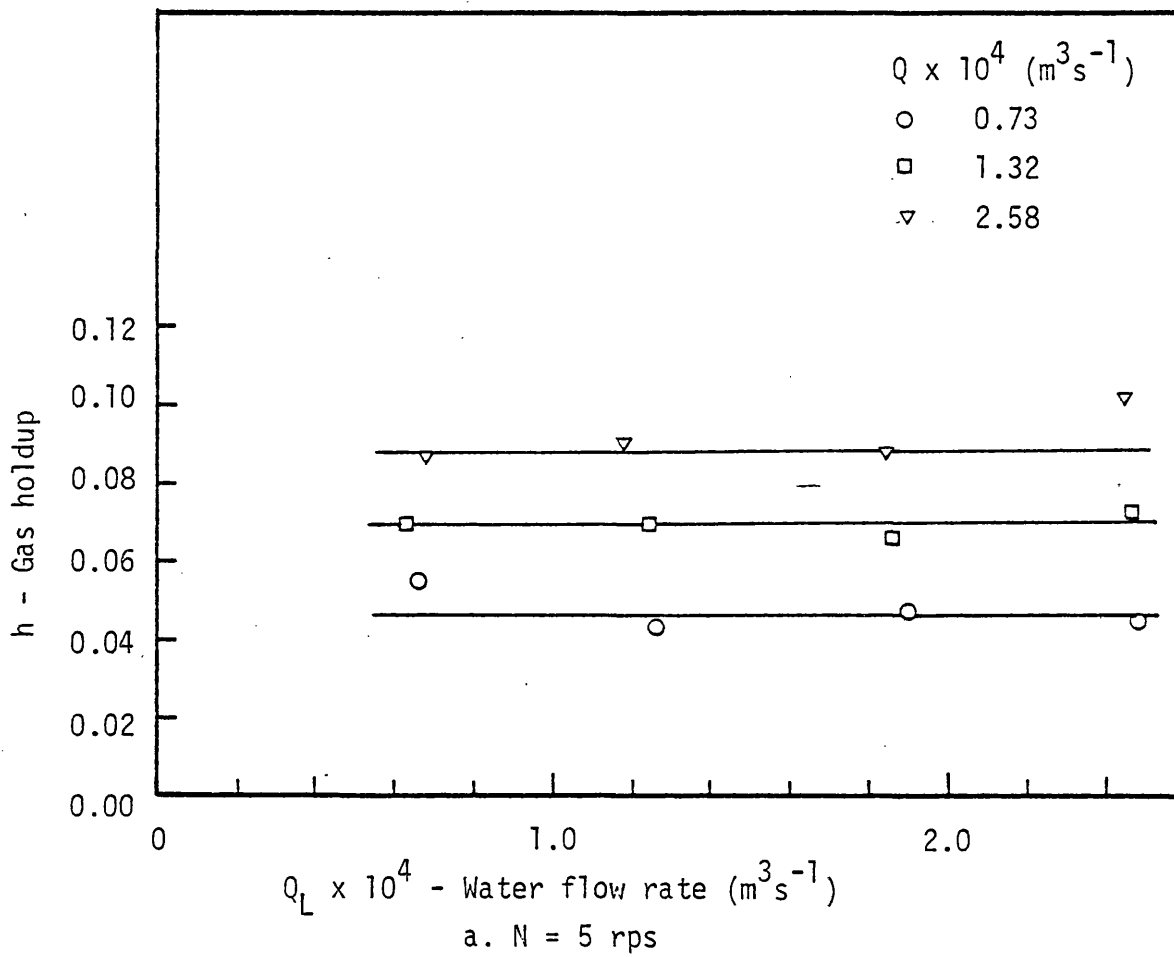
Fig. 8.21   h against Q_L (D = 0.1016)
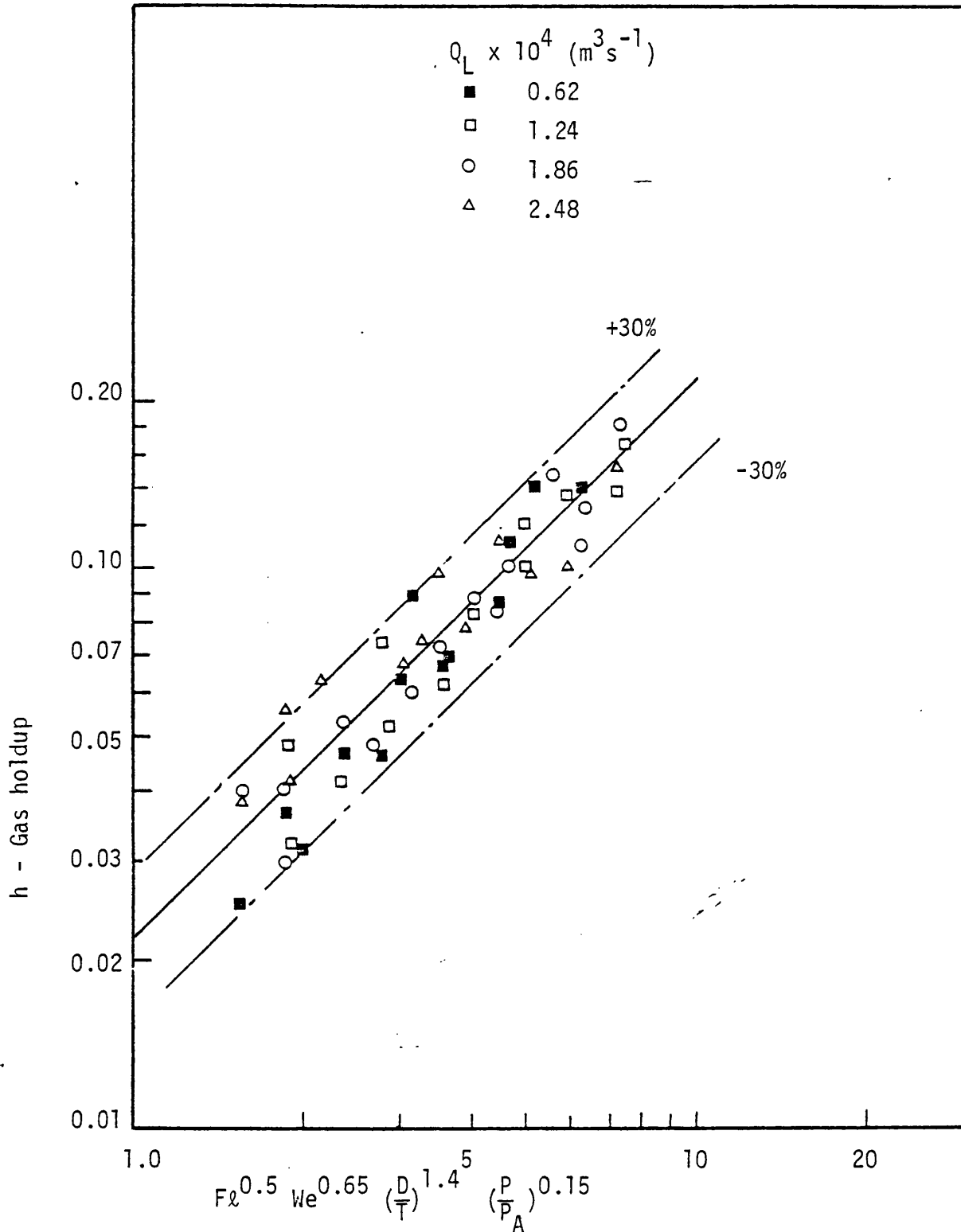
Fig. 8.22   Correlation for gas holdup. (Using impellers D1,D2 and D3)

flow of liquid is very similar to that of the batch system. Thus, the analysis of batch systems can be very useful in understanding and estimating the important design parameters of continuous-flow systems. The power correlations developed from batch data have been modified to account for the relatively small effect of the continuous-flow of liquid. The change in gas holdup from batch system was found to be insignificant.

CHAPTER 9

RECOMMENDATIONS FOR FUTURE WORK

Having studied the different aspects of power consumption and gas dispersion in agitated vessels, it became clear that further work is still required to investigate more thoroughly some specific topics. These are :

(1)   Effect of material thickness of the impeller on the ungassed power consumption with particular reference to the blade thickness.

(2)   The effect of impeller clearance and increasing the liquid height (above the standard level, H=T) on the conditions for onset of surface aeration in ungassed vessels.

(3)   Surface aeration in gassed agitated vessels with reference to the work of Calderbank (90) and Nienow et al (41).

(4)   There is a strong indication that the impeller clearance may have a considerable effect on the impeller dispersion efficiency, and hence, N_{F1} and N_{R1}. A study of this parameter and also a more detailed understanding of the effect of increasing the vessel pressure on N_{F1} are needed.

(5)   Further development of the impeller power dynamics (Chapter 5) should be undertaken. System identification can be divided into two phases, namely, modelling and parameter estimation. In this study emphasis was given to the modelling phase. The system parameters were also estimated, but only using simple approximation methods. The present approach in analysing the system, whereby an understanding of the physical phenomena was combined with measurements, was necessary in order to achieve a conceptual model for the process. The main requirement was to reduce the problem from the very complex process identification

state, with unknown model and parameters, to the more amenable

one of parameter estimation. Further investigations, therefore,

should be more systematic and make use of the advanced theory of

System Identification. On-line measurements and analysis of

a high order are, of course, essential if this approach is to

be implemented.

The problem should be approached gradually so that an understanding

of the physical meaning of the parameters can be developed.

Firstly, starting with a first order model (see Sec. 5.3.4),more

accurate estimates of the time constant and gain element can be

obtained. Secondly, a more advanced model (eg, Eq. 5.1) can

then be used. This will enable estimation of the transfer

functions associated with the formation of each cavity behind the

impeller blades and hence a greater understanding of the

mechanisms of energy transfer can be achieved.

(6) A wide range of experiments is required to investigate the effect

of impeller mixing regime, ie, flooding, efficient mixing and

gas recirculation, on the gas holdup.

(7) The effect of electrolyte concentration on bubble size and

interfacial area should be investigated using the capillary tube

measurement technique. In particular, the concentrations which

yield minimum bubble size and maximum specific interfacial area

are most important. References (9) and (53) should be the

starting point for such research.

(8) It is strongly recommended in future investigations of continuous-

flow mixing (using similar equipment and with a controlled liquid

level) that the liquid or dispersion height should be increased

to about 1.25, the tank diameter.   By suppressing or inhibiting surface entrainment in this way, it should be possible to study ungassed Power number over a wider range of Reynolds number. Further work, using different combinations of inlet and outlet positions, is required on gas-liquid systems.   This could also be extended to 3-phase slurry reactors to investigate the optional positions required for efficient use of the gas and suspension of of the solid particles.

NOMENCLATURE

The symbols represent the following, unless stated otherwise :

a	interfacial area per unit volume of liquid	$m^2 m^{-3}$
a_p	point value of a	$m^2 m^{-3}$
$\bar{a}_p$	a_p averaged over the tank volume	$m^3 m^{-3}$
a'	material thickness of turbine blade	m
b'	material thickness of turbine disc	m
C	clearance of impeller above tank base	m
Ci	constant; $i=1,2,3,...$	( )
c'	impeller boss diameter	m
c_v	coefficient of variation (Eq. 6.21)	-
D	overall impeller diameter	m
d'	diameter of turbine disc	m
d_b	equivalent bubble diameter assuming its shape is spherical	m
d_{ci}	capillary tube (probe) inner diameter	m
d_{max}	maximum stable bubble size	m
d_{10}	mean equivalent bubble diameter	m
d_{32}	Sauter mean bubble diameter	m
e'	height of impeller boss	m
Fl	gas Flow number $(\frac{Q}{ND^3})$	-
Fl_L	liquid Flow number $(\frac{Q_L}{ND^3})$	-
Fr	Froude number $(\frac{N^2 D}{g})$	-
f	number fraction (bubble size dist.; Ch.6)	-
fa	surface area fraction (bubble size dist.; Ch.6)	-
f'	diameter of impeller shaft	m
$G(s)$	transfer function describing the power dynamics of impeller (Dynamics Ch.5)	
$G_i(s)$	transfer function describing the power dynamics of ith large cavity (Ch.5)	

g	gravitational acceleration	ms^{-2}
H	height of the ungassed unagitated liquid in vessel	m
H'	height of the aerated liquid in vessel	m
h	gas holdup	-
h_p	point gas holdup	-
$\bar{h}_p$	h_p averaged over the tank volume	-
$\tilde{h}_p$	first approximation of h_p	-
I	ionic strength; $I=\frac{1}{2} \sum_j Z_j^2 C_j$	
	(Z_j charge on ionic species, C_j concentration)	Kg ion m^{-3}
K,k	constant	( )
K_L	liquid phase mass transfer coefficient	ms^{-1}
N	impeller speed	s^{-1}
N_o	minimum agitation speed (see Sec.4.2.2)	s^{-1}
N_p	power number ($\frac{P}{\rho N^3 D^5}$)	-
n_s	sample size (bubbles)	-
P	power consumption of impeller	W
P_{gs}	power supplied by gas stream	W
P_{gt}	total power supplied by the impeller and gas stream	W
$P_g(t)$	instantaneous gassed power consumption at time t	W
p	vessel pressure	$N\ m^{-2}$
p_A	atmospheric pressure	$N\ m^{-2}$
p_c	pressure drop over the capillary tube (probe, see Ch. 6)	$N\ m^{-2}$
Q	gas flow rate through the sparger	$m^3 s^{-1}$
Q_L	liquid flow rate in continuous flow vessel(see Ch.8)	$m^3 s^{-1}$
$Q_{cv}(t)$	total volume of gas cavities at time t (see Ch.5)	m^3
$q_i(t)$	instantaneous gas flow rate through the sparger at time t; (o) initial and (f) final	$m^3 s^{-1}$
q_R	instantaneous coalescing recirculating gas rate	$m^3 s^{-1}$
$q_o(t)$	instantaneous gas flow rate out of the impeller cavities at time t	$m^3 s^{-1}$
Re	Reynolds number ($\frac{\rho N D^2}{\mu}$)	-
s	Laplace transform variable; $\mathcal{L} f(t) = \int_o^\infty f(t)e^{-st}\ dt = F(s)$, $\mathcal{L}$ Laplace operator (dynamics, see Ch.5)	
T	tank diameter	m
T_f	friction torque	mN

T_i	torque exerted on the impeller	mN
T_m	measured torque by the transducer	mN
t	time measured from applying disturbance in gas load (Dynamics, Ch.5)	s
t_b	time for gas bubble to pass across detection point on the capillary probe (Ch.6)	s
$\bar{t}_c$	average circulation time of liquid	s
t_i	time delay of formation of ith large cavity (Dynamics, Ch.5)	s
t_s	time of slug of water to pass across detection point on the capillary probe (Ch.6)	s
U_T	bubble terminal velocity	ms^{-1}
u	velocity of gas at sparger exit	ms^{-1}
V	liquid volume in the vessel	m^3
$\bar{V}$	average circulation velocity of liquid	ms^{-1}
V_b	bubble volume	m^3
Vs	superficial gas velocity	ms^{-1}
W	impeller blade width	m
We	Weber number $(\frac{\rho N^2 D^3}{\sigma})$	-

Greek :

α	external distribution coefficient	-
ε	energy dissipation per unit mass	WKg^{-1}
μ	liquid dynamic viscosity	NSm^{-2}
μ_d	dispersed phase viscosity	NSm^{-2}
η	impeller dispersion efficiency	-
ρ	liquid density	$Kg\ m^{-3}$
ρ_D	dispersion density	$Kg\ m^{-3}$
ρ_g	gas density	$Kg\ m^{-3}$
σ	surface tension	$N\ m^{-1}$
σ'	standard deviation	( )
$\sigma' a_p$	standard deviation of a_p at different locations in the vessel	$m^2 m^{-3}$
$\sigma' h_p$	standard deviation of h_p at different locations in the vessel	-
τ	time constant of first order approximation (Dynamics, Ch. 5)	s

Subscripts :

F	flooding region
F1	flooding point
g	gassed
o	ungassed
R	recirculation region
R1	recirculation point
SA	surface aeration under ungassed condition;
	1 - onset, 2 - dropin N_{Po}
gSA	surface aeration under gassed condition;
	1 - onset, 2 - fully developed

REFERENCES

(1)   Ito, R, Hirata, Y, Sakata, K, and Nakahara, I, International
        Chem.Eng., Vol.19, No.4, p.605 (1979)

(2)   Verhoff, F H, Ross,S L, & Curl, R L, Ind.Eng.Chem.Fundam., Vol.16,
        No.3, p.371 (1977).

(3)   Anandha Rao, M and Brodkey, R S, Chem.Eng.Sci., Vol.27, p.137 (1972).

(4)   Nienow, A W, Wisdom, D J and Middleton, J C, Preprints of Second
        Europ.Conf. on Mixing, Cambridge (1977).

(5)   Robinson, C W and Wilke, C R, AIChE Journal, Vol.20, No.2,
        p.285 (1974).

(6)   Sridhar, T and Potter, O E, Ind.Eng.Chem.Fundam., Vol.19, No.1,
        p.21 (1980).

(7)   Foust, H C, Mack, D E and Rushton, J H, Ind.Eng.Chem., Vol.36,
        No.6, p.517 (1944).

(8)   Rushton, J H and Bimbinet, J J, Can.J.Chem.Eng., Vol.46, p.16(1968).

(9)   Lee, J C and Meyrick, D L, Trans.Instn.Chem.Engrs., Vol.48,
        p.T37 (1970).

(10)   Calderbank, P H, Trans.Instn.Chem.Engrs., Vol.36, p.443 (1958).

(11)   Yung, C N, Wong, C W and Chang, C L, Can.J.Chem.Eng., Vol.57,
        p.672 (1979).

(12)   de Figueiredo, M M L, PhD thesis, University of Edinburgh,UK(1978).

(13)   Hassan, I T M and Robinson, C W, AIChE Journal, Vol.23, No.1,
        p.48 (1977).

(14)   Clark, M W and Vermeulen, T, AIChE Journal, Vol.10 No.3,p.420(1964).

(15)   Rushton, J H, Costich, E W and Everett, H J, Chem.Eng.Progr.,
        Vol.46, No.8, p.395 & P.467 (1950).

(16)   Dickey, D S and Fenic, J C, Chem.Eng., Jan.5 (1976).

(17)   Bates, R L, Fondy, P L and Corpstein, R R, Ind.Eng.Chem.Process
        Des.Develop., Vol.2, No.4, p.310 (1963).

(18)   Nienow, A W and Miles, D, Ind.Eng.Chem.Process Des.Develop.,
        Vol.10, No.1, P.41 (1971).

(19)   Wisdom, D J, PhD thesis, University of London, UK (1974).

(20)   Metzner, A B and Taylor, J S, AIChE Journal, Vol.6, No.1,p.109(1960).

(21)   van Dierendonck, L L, Fortuin, J M H and Venderbos, D, Proc.4th
        Eur.Chem.Reaction Symp., Brussels, p.205 (1968).

(22)   Nienow, A W and Wisdom, D J, Chem.Eng.Sci., Vol.29,p.1997 (1974).

(23) van't Riet, K, PhD thesis, Delft University of Technology, Netherlands (1975).

(24) Nagata, S, Yamamoto, K, Hashimoto, K and Naruse, Y, Mem.Fac. Engng.Kyoto, Vol.21, p.260,(1959).

(25) Bruijn, W, van't Riet, K and Smith, J M, Trans.Instn.Chem.Engrs., Vol.52, p.88 (1974).

(26) Brauer, H, Advances In Biochem.Eng., Vol.13, p.87 (1979).

(27) Holmes, D B, Voncken, R M and Dekker, J A, Chem.Eng.Sci., Vol.19, p.201 (1964).

(28) Rushton, J H and Oldshue, J Y, Chem.Eng.Progr., Vol.49, No.4, p.161, and No.5, p.267 (1953).

(29) Aiba, S, AIChE Journal, Vol.4, No.4, p.485 (1958).

(30) Desouza, A and Pike, R W, Can.J.Chem.Eng., Vol.50, p.15 (1972).

(31) Ambegaonkar, A S, Dhruv, A S and Tavlarides, L L, Can.J.Chem. Eng., Vol.55, p.414 (1977).

(32) Schwartzberg, H G and Treybal, R E, I & EC Fundamentals, Vol.7, No.1, p.1 (1968).

(33) Govier, G W and Aziz, K, "The Flow of Complex Mixtures in Pipes" van Nostrand Reinhold Co., New York (1972) pp.379,380.

(34) Haberman, W L and Morton, R K, David Taylor Model Basin, Report 802 (1953).

(35) Oldshue, Y J, CEP, p.60, June (1980).

(36) van't Riet, K and Smith, J M, Chem.Eng.Sci., Vol.28,p.1031 (1973).

(37) Westerterp, K R, van Dierendonck, L L and Kraa, J A, Chem.Eng. Sci., Vol.18, p.157 (1963).

(38) Westerterp, K R, Chem.Eng.Sci., Vol.18,p.495 (1963).

(40) van't Riet, K, Boom, J M and Smith, J M, Trans.Instn.Chem.Eng., Vol.54, p.124 (1976).

(41) Nienow, A W, Chapman, C M and Middleton, J C, Chem.Eng. Journal, Vol.17, p.111 (1979).

(42) Oyama, Y and Endoh, K, Chem.Eng. (Japan),Vol.19, p.2 (1955).

(43) Uhl, V W and Gray, J B, "Mixing-Theory and practice", Academic Press Inc., London (1967), p.146, Vol.1.

(44) Michel, B J and Miller, S A, AIChE Journal, Vol.8, No.2,p.262(1962).

(45) Loiseau, B and Midoux, N, AIChE Journal, Vol.23,No.6, p.931(1977).

(46)   Pharamond, J C, Roustan, M and Roques, H, Chem.Eng.Sci.,
        Vol.30, p.907 (1975).

(47)   Nagata, S, "Mixing Principles and Applications", Kodansha Ltd.
        (1975), p.60.

(48)   Luong, H T and Volesky, B, AIChE Journal, Vol.25,No.5,p.893(1979).

(49)   Nienow, A W and Wisdom, D J, Institution of Chem.Engrs. 3rd
        Annual Research Meeting, Salford (1976).

(50)   Brown, D E and Halsted, D J, Chem.Eng.Sci., Vol.34, p.853(1979).

(51)   Pollard, G J, Preprints of Int.Symp. on Mixing Mons (1978).

(52)   Abramovich, G N, "Theory of Turbulent Jets", MIT,Cambridge(1963).

(53)   Marrucci, G and Nicodemo, L, Chem.Eng.Sci., Vol.22,p.1257 (1967).

(54)   Smith, J M, van't Riet, K and Middleton, J C, Preprints of Second
        Europ.Conf. on Mixing, Cambridge (1977).

(55)   Greaves, M and Economides, C A, Preprints of Third Europ.Conf.
        on Mixing, York (1979).

(56)   Seinfeld, J H and Lapidus, L, "Mathematical Methods in Chemical
        Engineering", Vol.3, Prentice-Hall Inc., New Jersey (1974).

(57)   Pollock, G G, and Johnson, A I, Can.J.Chem.Eng.,Vol.47,
        p.565 (1969).

(58)   Millington, G C, Experimental Project Report for the BSc Degree
        in Chem.Eng., School of Chem.Eng., University of Bath (1980).

(59)   Lees, S and Dougherty, R C. Journal of Basic Eng., Trans. of the
        ASME, p.445 (1967).

(60)   Clements, W C and Schnelle, K, Ind.Eng.Chem. Process Des.
        Develop., Vol.2, No.2, p.94 (1963).

(61)   Cohen, W C and Johnson, E F, Chem.Eng.Prog.Symp.Series, Vol.57,
        No.36, p.86 (1961).

(62)   Coughanowr, D R and Koppel, L B, "Process System Analysis and
        Control", McGraw-Hill Inc., (1965) p.60 and 133.

(63)   Middleton, J C, Preprints of Third Europ.Conf. on Mixing,York(1979).

(64)   Bryant, J and Sadeghzadeh, S, Preprints of Third Europ.Conf.on
        Mixing, York (1979).

(65)   Kolmogorov, A N, Doklady Akad.Nauk, SSSR, Vol.66,p.825 (1949).

(66)   Sevik, M and Park, S H, JOurnal of Fluids Eng., Trans. of the
        ASME, p.53 (1973).

(67)   Hinze, J O, AIChE Journal,Vol.1,No.3,p.289 (1955).

(68)　Vermeulen, T, Williams, G M and Langlois, G E, Chem.Eng.Progr., Vol.51, No.2, p.85-F (1955).

(69)　Kawecki, W, Reith, T, van Heuven, J W and Beek, W J, Chem.Eng. Sci., Vol.22, p.1519 (1967).

(70)　de Figueiredo, M M L and Calderbank, P H, Chem.Eng.Sci., Vol.34, p.1333 (1979).

(71)　Weiland, P, Brentrup, L and Onken, U, Ger.Chem.Eng.,Vol.3,p.296 (1980).

(72)　Hassan, I T M and Robinson, C W, Chem.Eng.Sci., Vol.35,p.1277(1980).

(73)　Burgess, J M and Calderbank, P H, Chem.Eng.Sci.,Vol.30, p.743, 1107, 1511 (1975).

(74)　Cutter, L A, AIChE Journal, Vol.12,No.1, p.35 (1966).

(75)　Sprow, F B, Chem.Eng.Sci., Vol.22, p.435 (1967).

(76)　Harvey, P S, PhD, thesis, University of Bath, UK (1980).

(77)　Nishikawa, M, Okamoto, Y, Hashimoto, K and Nagata, S, J.Chem.Eng. of Japan, Vol.9, No.6, p.489 (1976).

(78)　Coulaloglou, C A and Tavlarides, L L, Chem.Eng.Sci., Vol.32, p.1289 (1977).

(79)　Maini, B B, PhD Diss., Univ.Washington, USA (1976).

(80)　Botton, R, Cosserat, D, and Charpentier, J C, Chem.Eng.Sci., Vol.35, p.82 (1980).

(81)　Yoshida, F and Miura, Y, Ind.Eng.Chem.Process Des.Develop., Vol.2, No.4, p.263 (1963).

(82)　Reith, T and Beek, W J, Proc.4th Eur.Chem.Reaction Symp. Brussels, p.191 (1968).

(33)　Miller, D N, AIChE Journal, Vol.20,No.3,p.445 (1974).

(84)　Joshi, J B and Sharma, M M, Can.J.Chem.Eng., Vol.55,p.683 (1977).

(85)　Sridhar, T and Potter, O E, Chem.Eng.Sci., Vol.35,p.683(1980).

(86)　Hofer, H and Mersmann, A, Ger.Chem.Eng.,Vol.3,p.347 (1980).

(87)　Metha, V D and Sharma, M M, Chem.Eng.Sci., Vol.26,p.461(1971).

(88)　Joosteen, G E H, and Danckwerts, P V, Chem.Eng.Sci., Vol.28, p.453 (1973).

(89)　El-Shawarby, S I and Eissa, S H, Ind.Eng.Chem.Process Des. Dev. Vol.19, No.3, p.469 (1980).

(90)　Calderbank, P H, Trans.Instn.Chem.Engrs., Vol.37,p.173 (1959).

(91)   Lehrer, L H, Ind.Eng.Chem.Process Des.Dev., Vol.7, No.2,
        p.226 (1968).

(92)   Laity, D S and Treybal, R E, AIChE Journal, Vol.3, No.2,
        p.176 (1957).

(93)   van der Molen, K and van Maanen, H R E, Chem.Eng.Sci., Vol.33,
        p.1161 (1978).

APPENDIX A

CAPILLARY SLUG FLOW

A.1   INTRODUCTION

It was necessary before using the capillary probe for measurement of bubble size (see Chapter 6) to understand the nature of the two-phase slug flow in the capillary tube.   This was very useful for identifying the causes and order of errors in measurement.

Initially, the method involved the measurement of bubble speed by determining the passage of the bubble interface at two locations along the capillary.   From this, the bubble volume could be estimated (this method has been used in its simplest form in a recent publication (71)). This particular method was developed to account for the liquid film surrounding the bubble inside the capillary and for the expansion of the bubbles as they passed through.   Eventually, the method was superseded by a simpler and more accurate technique that was based on direct calibration of the instrument.   (See Sec. 6.3.2 for details)..

Although this Appendix is not directly relevant to the main subject matter, it is included for two reasons.   Firstly, it supports certain observations mentioned in the main text (Chapter 6), and secondly it constitutes a basis for future development of the capillary probe technique.

A.2   PREVIOUS WORK

A number of investigators have studied aspects of gas-liquid slug flow in capillary tubes.   In most of these studies the pattern of flow was simplified.   The bubble expansion and acceleration effects have barely received any consideration.   In most cases steady-state flow with no axial interaction between bubbles was assumed.

Starting with a simple steady-state model; if the bubbles and liquid slugs are flowing with steady speeds of U_b and U, respectively, it can be argued that if viscosity ratio ($\mu/\mu g$) is very large, the liquid film around the bubble does not move (A.1). Using the law of continuity, it can be shown that

$$m = \frac{U_b - U}{U_b} \qquad A.1$$

where m is the fraction of tube cross section covered with liquid film.

In 1935 Fairbrother and Stubbs (A.2) measured U and U_b in a 1m length of 2.25mm diameter tube using different liquids. They found that, providing the bubble length is greater than $1\frac{1}{2}$ times the diameter of the tube, U_b becomes independent of the bubble length. They proved the following empirical relationship for low bubble speeds

$$m = \left(\frac{\mu U_b}{\sigma}\right)^{\frac{1}{2}} \qquad A.2$$

Later in 1961, Taylor (A.3) showed that Eq. A.2 is only valid for $m \leqslant 0.09$. He established a graphical correlation between m and $\frac{\mu U_b}{\sigma}$, which indicates that m reaches a limiting value above 0.56 when the stresses due to the viscosity become much greater than those due to surface tension.

Bretherton (A.4) presented a theoretical treatment for this flow and indicated that m is uniquely determined by the conditions near the leading interface (nose of bubble). For very small tube radius r, such that gravitational effects are negligible, it was shown theoretically that

$$m \simeq 1.29 \left(\frac{3\mu U_b}{\sigma}\right)^{2/3} \qquad \text{as} \quad \frac{\mu U_b}{\sigma} \rightarrow 0 \qquad A.3$$

and the pressure drop across the bubble is given by

$$\Delta P = 3.58 \left(\frac{3\mu \, U_b}{\sigma}\right)^{2/3} \frac{\sigma}{r} \quad as \quad \frac{\mu U_b}{\sigma} \rightarrow 0 \qquad A.4$$

The results of photographic measurements on a 1mm diameter capillary showed large deviations from Eq. A.3.

Suo and Griffith (A.1) studied the two-phase flow in capillary tubes using a photographic technique. Their results are presented in the form of a plot of (1-m) against $\frac{\mu U_b}{\sigma}$. A useful plot is also presented for defining the limits of the different flow regimes, ie, annular, slug, and bubbly-slug flow. In a later study Suo (A.5) measured simultaneously the pressure drop and the bubble velocity of capillary slug flow. He showed that if the viscosity and density of the gas are much less than that of the liquid, then each bubble is almost a region of constant pressure. The pressure drop per slug ΔPs was correlated by

$$\Delta Ps = \left(\frac{8U}{\pi r^2}\right)\left(\frac{\mu U_b}{r}\right) + 4 \frac{\mu U_b}{r} \quad for \ Re_b < 270 \qquad A.5$$

and

$$\Delta Ps = \left(\frac{8U}{\pi r^2}\right)\left(\frac{\mu U_b}{r}\right) + 0.163 \, \rho U_b^2 \quad for \ 270 < Re_b < 630 \qquad A.6$$

where Re_b is Reynolds number based on the bubble velocity, liquid viscosity and tube radius. In Eqs. A.5 and A.6, the first term is the pressure drop in the slug calculated as if the flow were in fully developed laminar flow. The second term is an end effect of the bubble ends.

Capillary tubes are widely used in refrigeration equipment, as restrictors. Among studies in this area are those of Mikol (A.6) and Whitesel (A.7). The former observed a pulsating mode of flow with the bubbles enlarging as they move downstream. The latter

presented a simplified model for air-water slug flow in a capillary
considering the acceleration and expansion of the air bubbles.

A.3   OBSERVATION OF THE FLOW USING OPTICAL SWITCHES

The use of two optical switches to observe the bubble at two locations
along the capillary tube provides a very useful method for studying
the capillary slug flow (see Sec. 6.3.2 for details of equipment).
Figures A.1 and A.2 show typical output signals of the optical switches
recorded by a UV recorder.   Pulses I, II, III and IV represent the
time taken by bubbles to pass across the detection point (ie,
collimated light beam from optical switch) near to the capillary
sampling tip (upstream position).   I', II', III' and IV' are the
corresponding pulse recordings for the same bubbles detected at a
distance of 0.3m downstream from the tip.   If the time of a pulse is
t_b, then

$$t_b = \frac{L}{U_b}$$ A.7

where L and U_b are the length and the average speed of the bubble,
respectively.   This is defined by the condition when the nose or
leading interface of the bubble is just at the point of observation.

Firstly, considering bubble I in Figs. A.1 and A.2, it can be seen
that no other bubbles were detected close to them.   Therefore, these
bubbles can be considered to be free of axial interaction effects.
It is also evident that the width of pulse I' is larger than pulse I.
This means that either the bubble length L has increased, or else
its speed U_b has decreased (Eq. A.7).   The bubble velocity inside
the capillary tube was measured by the method illustrated in Fig. A.3.
Figure A.4 shows that the bubble velocity downstream is larger than
upstream (at the observation points 4 & 1 respectively).   Therefore
it is evident that the increase of pulse width (pulses I, I', Figs.
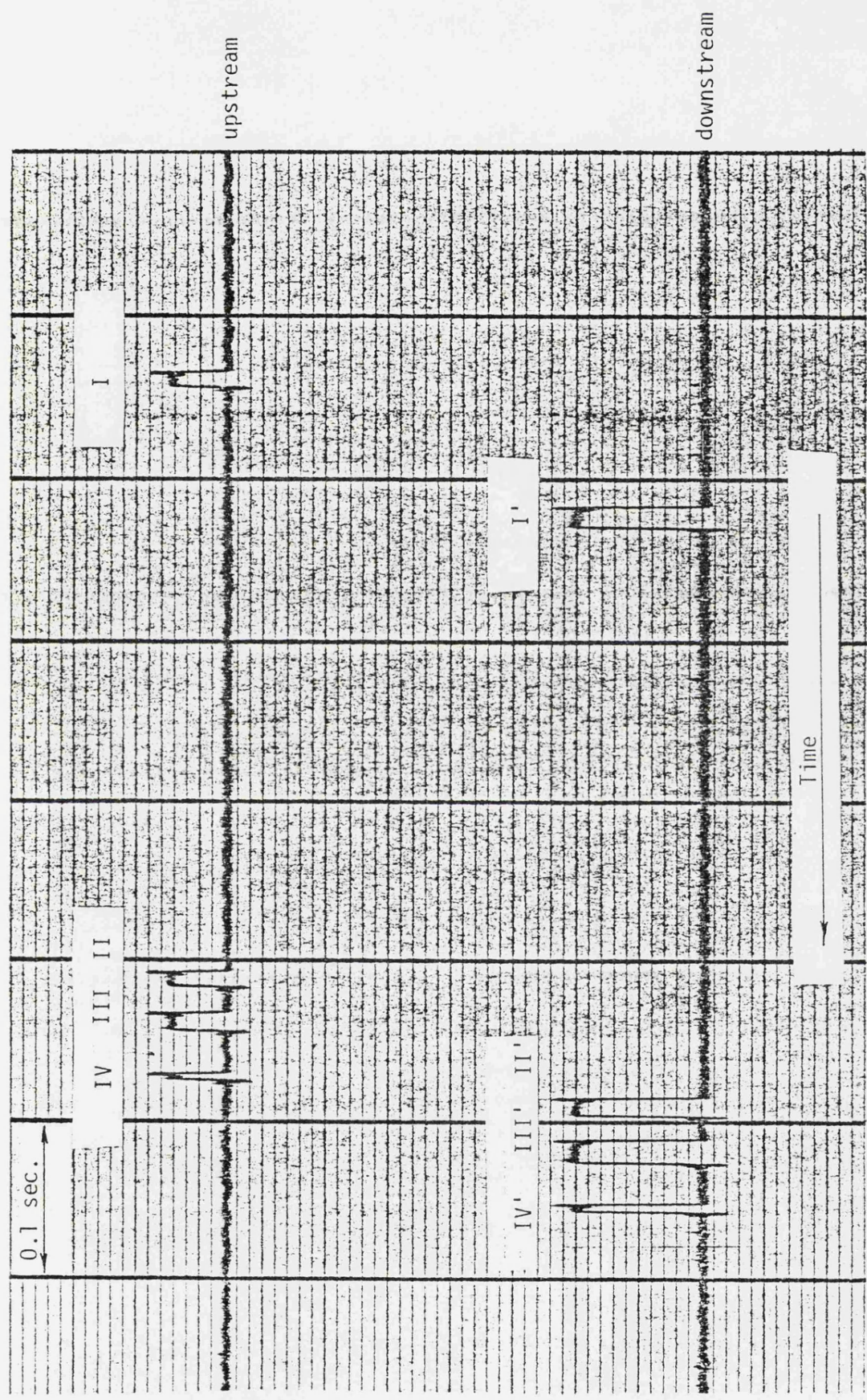
Fig. A.1 Output signals of two optical switches simultaneously recorded by UV recorder. Capillary diameter = 0.61x10⁻³m, capillary length = 0.35m. Optical switch positions: upstream at 0.08m from sampling tip; downstream at 0.3m from sampling tip.
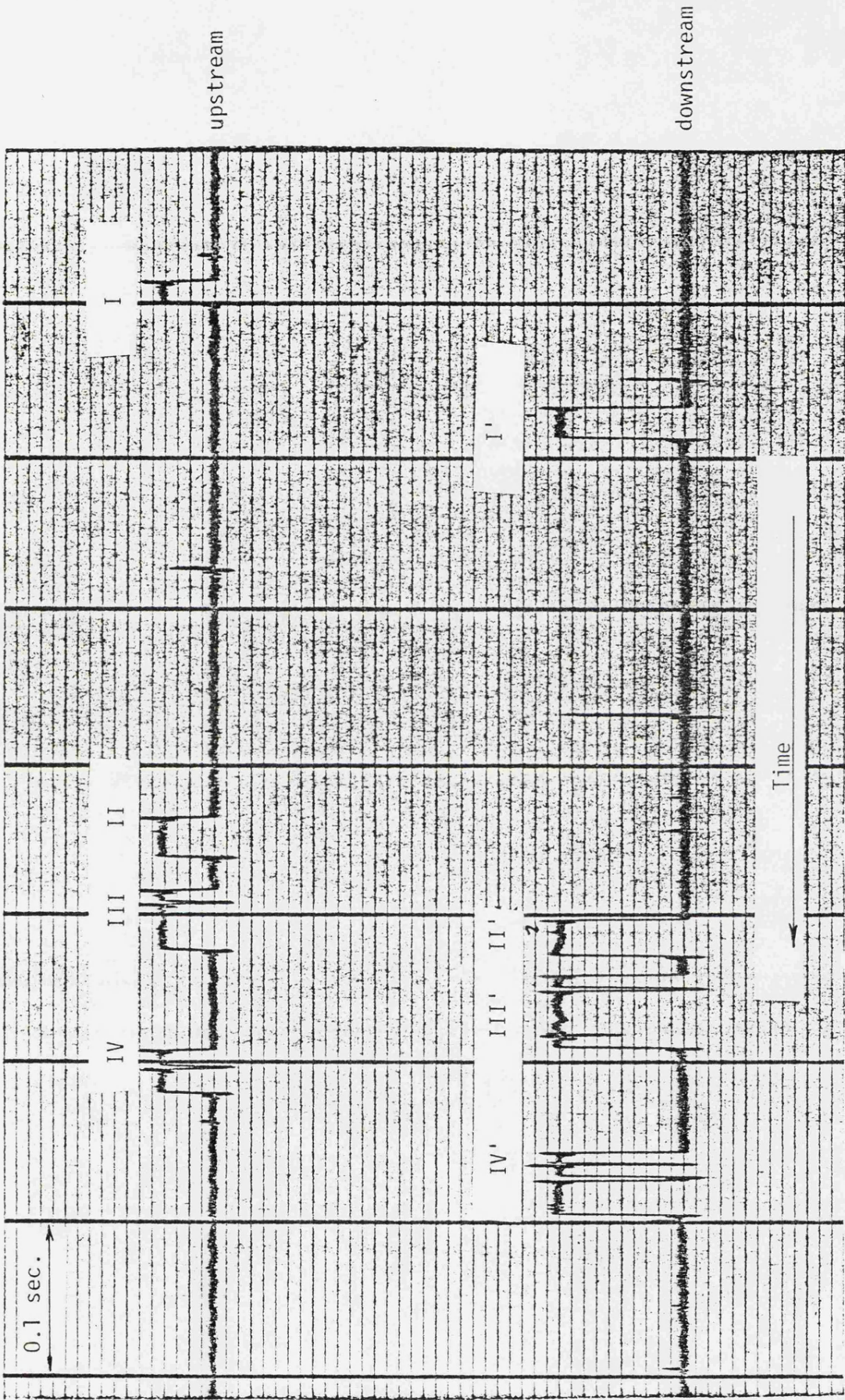
Fig. A.2 Output signals of two optical switches simultaneously recorded by UV recorder. Capillary diameter = 0.61×10^{-3}m, capillary length = 0.35m. Optical switch positions : upstream at 0.08m from sampling tip; downstream at 0.30m from sampling tip.
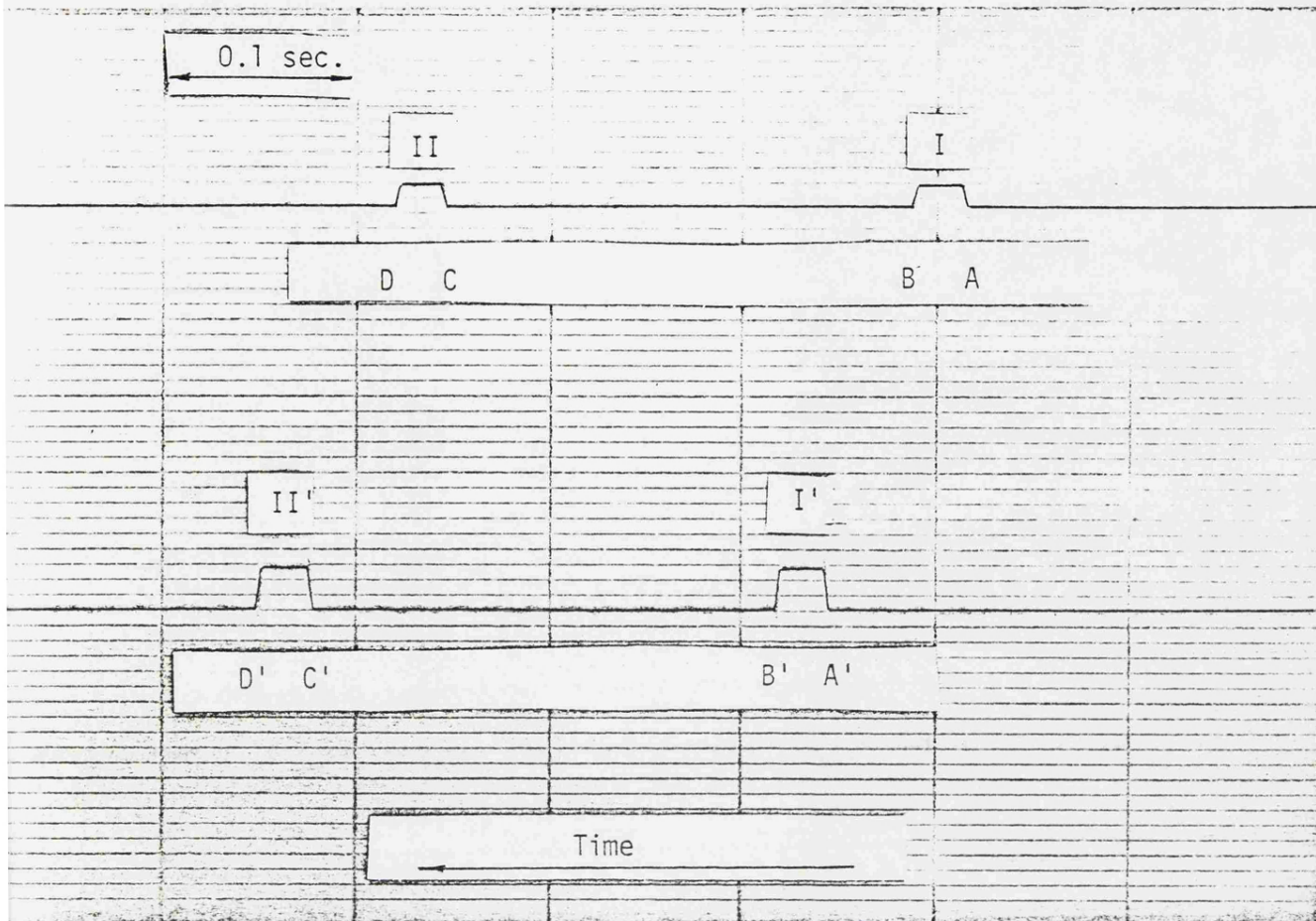
Fig. A.3   Method of measuring the average bubble velocity in capillary
           tube using two optical switches.

(i)   Since the time elapsed between the detection of the ends of the two
      bubbles is the same for the two optical switches, ie

$$BD = B'D'$$

and $$C'D' > CD$$

therefore the expansion of the bubbles occurs in the direction of flow.

(ii) Based on this conclusion, then

$$U_b = \frac{\ell}{t}$$

where U_b = average bubble velocity in the section of the capillary tube
             between the two optical switches

      ℓ = distance between the two optical switches

      t = time elapsed between the detection of the end of the same
            bubble by the two optical switches
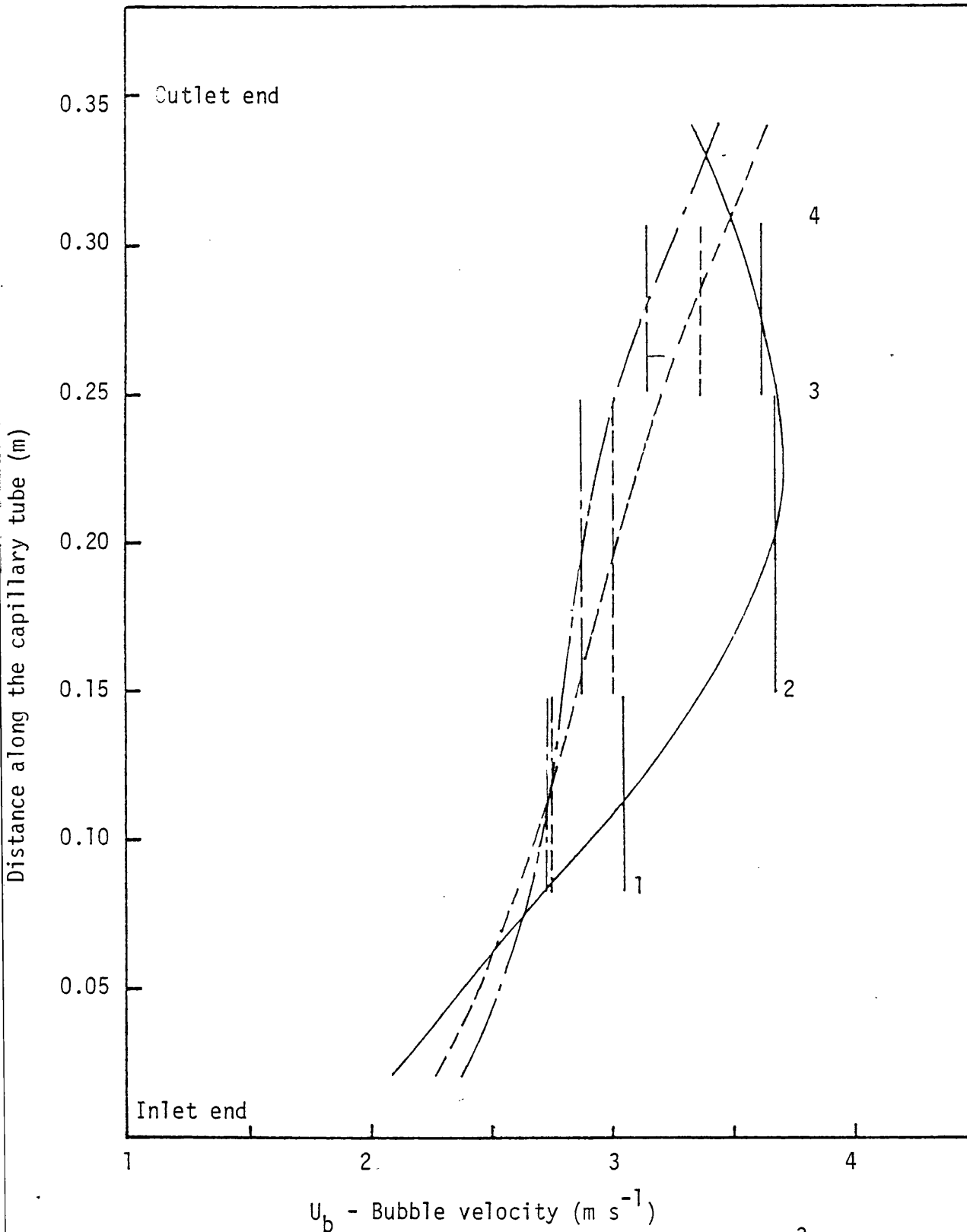
Fig. A.4   Change of bubble velocity inside 0.61×10^{-3}m diameter
capillary tube of 0.35m length. (1,2,3 and 4 observation
points of optical switches).

———— $d_b = 3.62 \times 10^{-3}$m

—·——— $d_b = s.53 \times 10^{-3}$m

—·—— $d_b = 1.79 \times 10^{-3}$m

A.1 and A.2) is caused by expansion of the bubble as it travels inside the capillary.

Pulses II, III and IV in Figs. A.1 and A.2 illustrate two different classes of the axial interaction effect between bubbles, which is discussed in Sec. 6.3.2. Pulses II, III and IV in Fig. A.1 represent the first class, where the average bubble diameter of the group of bubbles is less than twice the capillary tube diameter. Here the trailing bubble accelerates due to the wake effect of the leading one and the leading bubble accelerates due to the expansion of the trailing one. In this case, the change in bubble speed due to axial interaction never exceeded 10% (estimated by comparing the speed of the bubble with that of free-axial-interaction bubble of the same size). This leads to underestimation of the bubble volume by the same order when the calibration graph (see Fig. 6.4) is used for measurements. Pulses II, III and IV in Fig. A.2 represent the second class, where one or more of the bubbles is larger than the rest of the bubbles in the group and has diameter over three times the capillary tube diameter. The largest axial interaction effect occurs when a bubble is trailed by a larger one. The acceleration of the leading bubble due to the relatively large expansion of the trailing bubble becomes quite considerable and can lead to underestimation of the bubble size by up to 30%. The error in estimating the size of the larger trailing bubble, however, remains in the region of 10%. Pulses II and III (Fig. A.2) demonstrate these effects. The acceleration of the leading bubble, Pulse II, is very significant to the extent that Pulse II' becomes shorter, obscuring the opposite effect of bubble elongation.

The break-up of bubbles inside the capillary, previously described
in Sec. 6.3.2, can also be observed for bubbles III and IV in Fig. A.2.
Using this method of flow observation, a wide range of experiments
was carried out covering different capillary tube sizes and sampling
flow rates.   The results of this study are summarised in Sec. 6.3.2.

A.4   RELATIONSHIP BETWEEN THE TRUE BUBBLE VOLUME AND U_b and t_b

As explained in the previous section, it is possible to measure the
bubble velocity U_b and the time t_b required for it to pass a given
location in the capillary.   The sequence of pulse from the optical
-witch is processed by a fast data acquisition system.   However, to
estimate from these quantities the true bubble volume V_b at the point
of sampling, the expansion of the bubble in the capillary and the
thickness of the surrounding liquid film have to be considered.
In the analysis to follow, a relation between V_b and the measured
quantities U_b and t_b is derived.   It is assumed, however, that there
is only one bubble flowing in the capillary at one time, ie, any axial
interaction effect between bubbles inside the capillary is neglected.

Assume that V_b is the true volume of a bubble at the entry to the
capillary tube.   After travelling a distance inside the capillary
the bubble expands.   Let V_b^* and L^* be the bubble volume and length
when its leading end is just at the point of observation (see Fig.
A.5.a).

Therefore

$$V_b^* = K^*(V) \ V_b \qquad\qquad A.8$$

and   .

$$V_b^* = L^*(1-m^*)A \qquad\qquad A.9$$

where K*(V) is an expansion factor which depends on the bubble volume and A is the capillary tube cross section area. m* is the corresponding fraction of the tube cross section occupied by the liquid film. From Eqs. A.8 and A.9

$$L* = \frac{K*(V)\ V_b}{(1-m*)A}$$ A.10

by substituting m from Eq. A.2 into Eq. A.10, then

$$L* = \frac{K*(V)\ V_b}{\left[1-\left(\frac{\mu U_b*}{\sigma}\right)^{\frac{1}{2}}\right]A}$$ A.11

From Eqs. A.7 and A.11, we obtain

$$V_b = \frac{t_b*\ U_b*}{K*(V)}\left[1-\left(\frac{\mu U_b*}{\sigma}\right)^{\frac{1}{2}}\right]A$$ A.12

To estimate the expansion factor K*(V) in Eq. A.12, a simple pressure drop model shown in Fig. A.5.b is used. Further, assuming that the bubbles expand according to ideal gas law behaviour, then from Eq.A.8

$$K*(V) = \frac{V_b*}{V_b} = \frac{P_A}{P*}$$ A.13

From Eq. A.6, the pressure drop due to the end effect of the bubble ends is

$$\Delta P_b = 0.163\ \rho U_b^2$$ A.14

Using Eq. A.14 in conjunction with Fig. A.5, it can be shown that

$$P* = P_A - \frac{z}{\ell c - L*}\left[P_A - P_v - 0.163\frac{\rho U_b*^2}{g_c}\right]$$ A.15
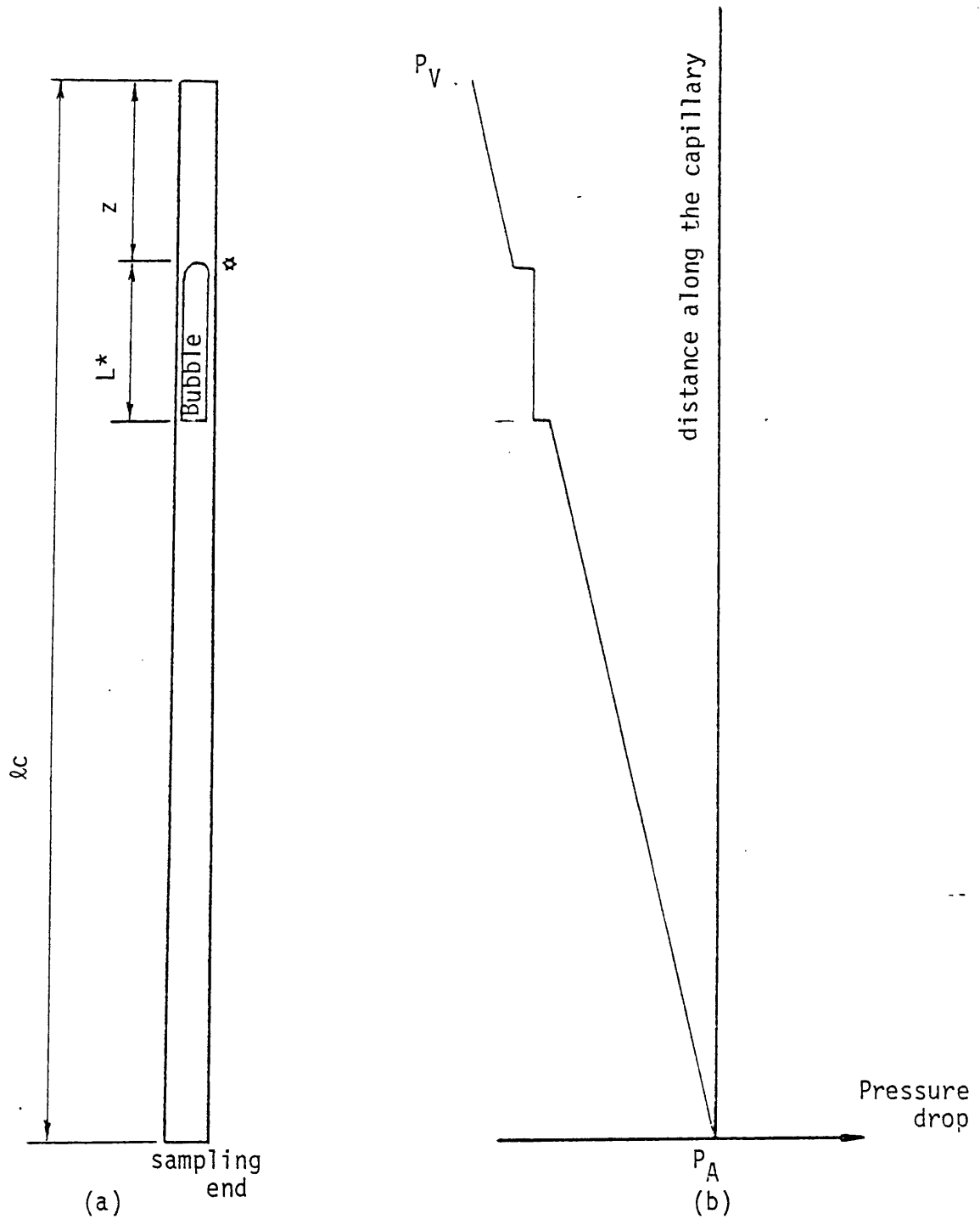
Fig. A.5   Pressure drop along the capillary tube.

✿   point of observation (position of optical switch)

ℓc   capillary tube length

z   distance between the point of observation and the outlet end of the capillary tube

L   bubble length at point of observation

P_A pressure at point of sampling (assumed equal to atmospheric, neglecting hydrostatic pressure).

P_V pressure at the outlet end of the capillary tube (vacuum pressure).

By substituting Eq. A.15 into Eq. A.13, then

$$K^*(V) = \frac{P_A}{P_A - \frac{z}{\ell c - L^*}\left(P_A - P_V - 0.163 \frac{\rho U_b^{*2}}{g_c}\right)} \qquad A.16$$

Substituting L* from Eq. A.7 into Eq. A.16 and then into Eq. A.12, the final result is :

$$V_b = \frac{t_b^* U_b^* A}{P_A}\left[1 - \left(\frac{\mu U_b^*}{\sigma}\right)^{\frac{1}{2}}\right] \quad - $$

$$\left[P_A - \frac{z}{\ell c - t_b^* U_b^*}\left(P_A - P_V - \frac{0.163 \rho U_b^{*2}}{g_c}\right)\right] \qquad A.17$$

Equation A.17 relates the bubble volume at the point of sampling V_b to the following variables :

t_b^* time required for the bubble to pass observation point along the capillary

U_b^* speed of the bubble when its leading end at the point of observation

$\ell c, A$ capillary tube length and cross section area

$(\ell c - z)$ distance from the sampling end of the capillary tube to the observation point

P_A pressure at point of sampling

$P_A - P_V$ pressure drop over the capillary

ρ, μ liquid density and viscosity

σ surface tension

g_c conversion constant = 9.81 Kg.m/Kgf.sec^2

Equation A.17 can be used instead of the calibration graph of the

capillary probe (see Sec. 6.3.2.1) for measuring the bubble size.

Figure A.6 shows the comparison between the bubble volume calcualted

from Eq. A.17 and the true bubble volume measured by an Alga

microsyringe.   It is clear that Eq. A.17 overestimates the bubble

volume by about 40% and hence the equivalent spherical bubble diameter

by about 12%.   This error is attributed mainly to the use of Eqs.A.2

and A.6, the assumptions made in estimating the expansion coefficient

K(V), and any possible inaccuracy in measuring U_b.

As a result of the above analysis, it was decided to use the more

simple and accurate calibration method described previously in Sec.

6.3.2.   However, future development of the method based on Eq. A.17

could have significant benefits.   It would save on the time required

to obtain a calibration curve for the capillary probe.   Moreover,

the computing time required to analyse the output signal of the

optical switch (see the polynomial of Eq. 6.12) could be appreciably

reduced.
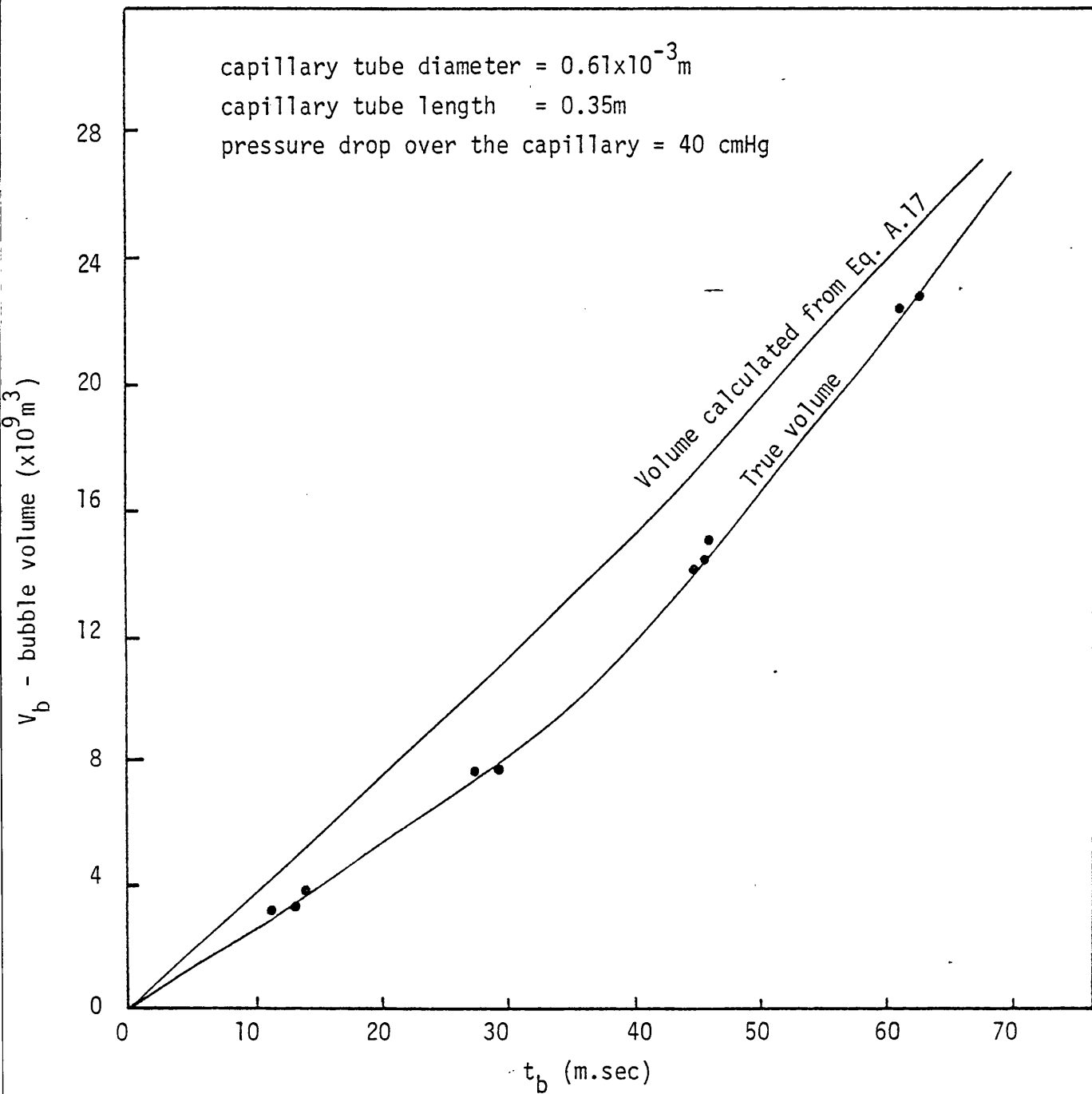
Fig. A.6   Comparison between the bubble volume calculated from Eq.A.17
and the true bubble volume measured by microsyringe.
(Air-water system)

Literature cited

(A.1) Suo, M and Griffith, P, Journal of Basic Engineering, Trans. ASME, Series D, Vol.86, p.576 (1964).

(A.2) Fairbrother, F and Stubbs, A E, J. of Chemical Society, part 1, p.527 (1935).

(A.3) Taylor, G I, J. of Fluid Mechanics, Vol.10, part 2, p.161(1961).

(A.4) Bretherton, F P, J. of Fluid Mechanics, Vol.10, part 2, p.166 (1961).

(A.5) Suo, M, Journal of Basic Eng., Trans.ASME, series D,p.140(1968).

(A.6) Mikol, E P, Proc.Ashrae Semiannual Meeting, New York, NY, Vol.69, p.213 (1963).

(A.7) Whitesel, H A, Refrigeration Eng., Vol.65, p.42 (1957).

APPENDIX B
MEASURING INSTRUMENTS SPECIFICATIONS
AND CALIBRATION

This appendix deals with the specifications of the main instruments used in this study. Only the main specifications which are related to the accuracy of measurements in this study are listed. For further details about these instruments the reader is referred to the manuals issued by the manufacturers.

A.   THE MICROPROCESSOR
(source :   MACSYM II SYSTEM MANUAL)

Make	Analog Devices Ltd
Model	MACSYM II

ADIO CONTROLLER
Analog/Digital Converter

Non-linearity Error	$\pm \frac{1}{2}$ lsb
Gain Temperature	± 15 ppm ^{o}C max
A/D Conversion Time	25 μ.sec max

CENTRAL PROCESSOR UNIT (CPU)

Word length	16 bit
Memory	32 K words
Execution speed	
Arithmetic/Logic Instructions	1.2 μ.s.
Memory Reference Instructions	1.8 μ.s.

ANALOG INPUT CARD (MUX)

Number of Inputs	32 single ended or 16 true differential, software selectable
Gain	1, 16, 256
Gain Accuracy	$\pm 0.02\%$
Gain/Temp. Coefficient	± 30 ppm/^{o}C
Linearity	$\pm 0.001\%$
Settling Time	25 μ.sec. G=1
	25 μ.sec. G=16
	50 μ.sec. G=256

PACER CLOCK CARD

It allows a programmable number of A/D measurements to be made at accurately controlled time intervals.

Time Interval   20 µ.sec. to 42949.672 sec. in
                              10 µ.sec. steps

Delay Time   20 µ.sec. to 0.65536 sec. in
                              10 µ.sec. steps

Interval and Delay Accuracy   ± 30 µ.sec. max

B.   TORQUE TRANSDUCER

(source : Operating and Service Manual BLH/TM-TPU-2 March 75)

Principles of Operation : The use of Wheatstone bridge principle to produce a variable voltage as a linear function of applied torque.

Make   BLH Electronics, Inc. 42 Fourth Avenue
                              Waltham, Mass. 02154
Model   A-002
Capacity   20 In.lb.
Max. speed   3600 rps

PERFORMANCE :

Output at Rated Torque (RT)   1.5 mv/v
Calibration Accuracy   0.25% RT
Non-Linearity   0.10% RT
Repeatability   0.05% RT
Hysteresis   0.15% RT

TEMPERATURE :

Compensated Range   0 to 140°F
Effect on Rated Torque   0.005% reading per °F
Effect on Zero Balance   0.0025% RT per °F

CALIBRATION :

Using test resistor (factory supplied) to simulate a torque output of 80% of full scale

$$T = 2.0879 \ V_T$$

where

T torque (inch-lb)

V_T output signal of signal conditioning box (volts)

C.   GAS FLOW METER

(source :   Instruction Manuals for TEKFLO TF issue 4, 73, and for
            TR2 issue 1, 74)

Principle of Operation : Measuring pressure drop across a venturi
                          nozzle.   The differential pressure trans-
                          ducer incorporates a four-arm Wheatstone
                          bridge principle.

VENTURI NOZZLE :

Make	TEKFLO LTD, Albany Road, Granby Industrial Estate, Weymouth, Dorset.
Model	CVO 250
Material	Stainless Steel
Accuracy	$\pm$ 0.5% of Reading
Repeatability	0.1%

TRANSDUCER :

Make	TEKFLO LTD
Model	TF2 10-150
Max. Pressure	83 MN/m^2
Total Error and Nonlinearity	Better than $\pm$ 0.5% full scale
Hysteresis and Repeatability	0.1%

DYNAMIC CHARACTERISTICS :

Measured for the coupled venturi-transducer with the microprocessor.
"Ref. Moulder N.E., Final Year Project, School of Chem.Eng. Bath Univ.
1980."

Order of the System	First Order
Time delay	1.0 m.sec.
Time constant	24-43 m.sec.

CALIBRATION :

$Q = K.V^A$

where

Q   Air flow rate at atmospheric pressure m^3/sec.

V   Output signal from signal conditioning box (volts)

K & A   Calibration constants, 'dependent on the pressure before
        and after the venturi."

D.   MAGNETIC-FLOW METER

(source : Technical Manuals TM5-05-00/Rev.1 and TM5-05-16/Rev.1)

Principle of Operation : The flow of liquid through a metering tube
cuts a magnetic field and develops an induced
voltage in the liquid which is picked off by
two electrodes in the walls of the metering
tube. The induced voltage is proportional
to the flow velocity multiplied by the magnetic
field strength. It is fed to converter to
provide output current directly proportional
to flow velocity.

DETECTOR HEAD :

Make	KENT INSTRUMENTS, Bath Road, Stroud, Gloucestershire, England.
Model	VAA 0862111740, $\frac{3}{8}$ in. N.B.
Accuracy	Better than $\pm$ 1% of induced reading
Suitable Fluids	Liquids and slurries having a conductivity not less than 10 μ ohm/cm
Material	Stainless Steel

CONVERTER :

Make	KENT INSTRUMENTS
Model	VCA
Range	0.6 to 12 m/sec.
Output	4-20 mA
Response Time	3 sec.
Calibration Accuracy	$\pm$ 0.2% of increment switch reading.

CALIBRATION :

Factory calibrated such that

$$F = 0.04712.V.d^2$$

where

F   flow rate of liquid litre/minute

V   velocity of flow   m/sec.

d   nominal bore   mm

The output signal from the conditioning box was 1-5 volts.   When the range of the converter was adjusted at 7 m/sec. the calibration equation is

$$F = 1.2468 \ (v-1) \ 10^{-4} \ m^3/sec.$$

where v is the output signal of the signal conditioning box.

E.   THYRISTOR MOTOR SPEED CONTROLLER

It operates with DC shunt wound motor, by supplying two rectified mains supplies to the armature and field circuits.   The feed back signal is derived from tachogenerator mounted—on the non-drive end of the motor.

Make	Electro-Comp, 36B, Stanstead Road, Hertford, Herts, SG13 7HY
Model	RMB-50T
Speed Range	100-1
Regulation	Typically $\pm$ 0.3% of full speed, no load to full load
Temperature	The speed increases 0.01% of set speed per ^{o}C increase in ambient temperature
Supply Volts	The speed will change 0.001% for a 10% change in mains supply voltage

F.   LEVEL TRANSMITTER
(source :   Installation and Operating Instructions, No.909-605-176D,1977)

It is a two wire capacitance to current transmitter which produces a standard 4-20 mA DC current output signal directly proportional to the input capacitance.

Make	Robertshaw SKIL LTD, Skelmersdale, Lancs, WN8 9SB
Model	160
Linearity	$\pm$ 0.25% for 10 to 500 p.f. span
Temperature Effect	
Span	0.01% /^{o}F (0.018%/^{o}C)
Zero	0.01% /^{o}F
Max.Output Ripple	0.25% peak to peak
Response Time	100 milliseconds
Stability	1% max/30 days, non-cumulative

LEVEL PROBE

A miniature level probe was manufactured in the University workshop.

Electrode	$\frac{1}{8}$" diameter brass rod of q in. length
Insulation	$\frac{1}{4}$" outer diameter, made of PTFE

Calibration

$$L = L_o + K\ (V-V_o)$$

where

L	level to be measured mm
L_o	datum level mm
V	output voltage at measured level mm
V_o	output voltage at datum level mm
K	calibration constant, changes with adjusting the span (18-27 mm/volts)

G.   ELECTRONIC CONTROLLER
(source: Installation Bulletin : 53EL4000 Rev. 2)

It is utilised to control the level of liquid inside the mixing vessel for continuous flow runs.

Make	Fisher & Porter Co., Workington, Cumberland
Model	53EL 4431B-KBAE
Input Signal	4-20 mA
Output Range	4-20 mA
Set Point Accuracy	$\pm$ 0.4% of span (at reference conditions)
Temperature Effect	Less than 0.5% per 28^oC

Mode Ranges

Proportional	3 to 500% Std.w/auto reset or manual reset
Reset	0.02 to 50 minutes (12 steps)
Derivative	0.01 to 8 minutes (11 steps and off)

H.   PRESSURE TRANSDUCER

Transduction Principle : Integrated silicon strain gauge bridge.

Make	Druck Limited, Fir Tree Lane, Granby, Leicestershire LE6 OFH
Model	PDCR-10
Range	3 BAR
Sensitivity	100 mv Nominal
Non-Linearity and Hysteresis	$\pm$ 0.06% B.S.L.
Compensated temp. range	0 to + 50^oC

J.   OPTICAL SWITCH

Make	CLAIREX ELECTRONICS USA (Hird Brown Ltd,UK)
Model	CL 155
Emitter	infrared light-emitting diode
Sensor	npn darlington phototransistor
Max. Temperature	$-55^{\circ}C$ to $+ 150^{\circ}C$
Rise or Fall time	300 μ.sec. Typical.

APPENDIX C

COMPUTER PROGRAMS

A MACSYM II Microprocessor (Analog Devices Ltd) was used for measurements and analysis of the experimental results. The programming language developed for the MACSYM II is MACBASIC. MACBASIC is a high level interactive programming language based on Standard Dartmouth Basic, and optimised for measurements and control applications.

In what follows we shall describe three real time statements of MACSYM extensions to Basic which have been used for measurements in the present study. This will make it easier for the reader who has a knowledge of the standard BASIC to follow the computer programs listed in this Appendix. For more details, the reader is referred to the MACSYM II SYSTEM MANUAL.

AIN (s, c, g, m)

This statement is used to measure analog input signal, where

s = 1 (the slot number in the I/O card cage where the card is physically located)

c is the card channel number. In the present work specific channel has been selected for the output signal of each measuring device such that :

I/O Card Channel number	Measuring device
0	Input liquid flow meter
1	Output liquid flow meter
2	Input gas flow meter
3	Output gas flow meter
4	Torque Transducer
5	Tachogenerator (for measuring impeller speed)
6	Liquid level transmitter
9	Pressure transducer

g is the gain code

when g = -1 auto ranging (default)

     = 0 Gain = 1

     = 1 Gain = 2

      :

     = 11 Gain = 2048

m = 1 (differential mode)

Example :

```
10        X = AIN (1,4,1)
20        PRINT X
```

This program when executed will measure the output signal of torque transducer (channel 4) in volts, and assign the value to variable X. This variable can be treated as any normal variable in computer program, eg, in statement 20 the value of X will be printed.

The AIN statement has been used for signal measurements in dynamical tests (see PROGS (6) and (7)).

AVG (s, c, g, n, t)

This statement averages the value of measured analog signal over a period of time, where

```
s, c, g          as defined for AIN (   )
n =              number of readings to be acquired
t =              time (in seconds) between readings.
```

Example :

```
10        A = AVG (1,2,0,1000,0.01)
20        PRINT A
```

Statement 10 when executed will measure analog signal from channel 2 with gain = 1 (g=0) 1000 times with time period of 0.01 seconds between every two readings. The average value of these 1000 readings will be assigned to variable A.

The AVG statement has been used for measuring the output signals of the measuring devices in the 'steady state' experiments. The averaging process with suitable sampling frequency has the advantage of eliminating any noise effect.

This statement may be used only with TASK has been assigned a priority of 2 or greater. Thus, in every computer program using this statement, it will be noticed that a TASK of priority 2 has been created (see PROGS (1), (2) and (3)).

<u>COLLECT (s, c, g, n, t) INTO X(J)</u>

where s, c, g, n as defined for AVG (   )

t = time (in seconds) between readings within the scan   (default is 0.25 sec)

X   a real array into which the analog values (in volts) are to be placed in order

J   first array element to receive the data collected.

This statement allows the acquisition of a number of readings automatically from a single analog input channel.   When executed, MACBASIC performs n readings of the channel specified.   The resulting data is placed in order in array X.

The main advantage of this statement is that it measures a signal with high accuracy at a very high speed (up to 4000 measurements per second). This statement was used for bubble size measurements (see PROGS (4) and (5).)

PROGRAM (1)

```
 10 REM PROG(1)
 20 REM PROGRAM FOR POWER  AND GAS HOLDUP MEASUREMENTS FOR
 30 REM BATCH EXPERIMENT
 40 REM
 45 REM
 50 REM THIS PROGRAM IS DESIGNED TO MEASURE AND CALCULATE
 60 REM THE POWER AND GAS HOLDUP FRACTION AT STEADY STATE
 70 REM CONDITIONS IN BATCH GAS-LIQGID MIXING EXPERIMENT
 80 REM
 90 REM ADJUST THE IMPELLER SPEED AND THE GAS FLOW RATE
100 REM AT THE DESIRED VALUES.
110 REM RUN THE COMPUTER PROGRAM.
120 REM
130 REM INPUT:
140 REM      A- VARIABLES:
150 REM       P0 UNGASSED POWER AT SAME SPEED  WATTS
160 REM          T3 FRICTION TORQUE   VOLTS
170 REM      B- SIGNALS (MEASURED IN VOLTS):
180 REM           N1  OUTPUT SIGNAL OF THE TACHOGENERATOR
190 REM              (FOR MEASURING IMPELLER SPEED)
200 REM          T1 OUTPUT SIGNAL OF TORQUE TRANSDUCER
210 REM           A  OUTPUT SIGNAL OF INPUT GAS FLOWMETER
220 REM           L  OUTPUT SIGNAL OF LEVEL TRANSMITTER
230 REM          P9  OUTPUT SIGNAL OF PRESSURE TRANSDUCER
240 REM OUTPUT:
250 REM       Q   GAS FLOW RATE *10+4  M3/SEC
260 REM       PG  GASSED IMPELLER POWER   WATT
270 REM      PG/P0  GASSED POER RATIO
280 REM      P/V IMPELLER POWER PER UNIT VOLUM *10+3 W/M+3
290 REM      NP  POWER NUMBER
300 REM      NQ  AREATION NUMBER
310 REM      NR REYNOLDS NUMBER
320 REM      H  GAS HOLDUP FRACTION
330 REM      N   IMPELLER SPEED  RPS
340 REM      P8 MIXING VESSEL PRESSURE  PSIG
350 REM P2 IS P0
360 INPUT P2
370 REM L2= LEVEL TRANSMITTER OUTPUT SIGNAL WITH NO GAS FLOW
380 L2=2.75
390 TASK 1,430,2
400 ACTIVATE 1
410 END
420 REM MEASURING THE INPUT SIGNALS
430 N1=AVG(1,5,3,5000,.001)
440 T1=AVG1,4,1,4000,.01)
450 A=AVG(1,2,0,1000,.01)
460 L=AVG(1,6,0,1000,.005)
470 P9=AVG(1,9,4,100,.02)
480 PRINT "TYPE RUN 520"
```

```
490 KILL SELF
500 REM CALCULATING MIXING PARAMETERS
510 PRINT "SPEED VOLTS TORQUE V. Q VOLTS LEVEL V    PRESSER V."
520 PRINT N1, T1, A, L, P9
530 REM T3 IS THE FRICTION TORQUE
540 INPUT T3
550 REM N2 IS THE SPEED REVS/S
560 N2=3.89827+42.3837*N1-49.5773*N1↑2+44.7202*N1↑3
570 IF N2<5 THEN  PRINT "SPEED RPS" INPUT N2
580 Q=.595*1.865*A↑.4647
590 T2 =T1-T3
600 P=1.4822*T2
              N2
610 P1=P/P2
620 REM N6=POWER NUMBER FOR 4" IMPELLER
                                        630 N6=136.5*T2/N2↑2
640 REM L1=CHANGE IN LEVEL MM
650 REM  IN STATMENT 670 ,18.33 IS A CALIBRATION CONSTANT
660 L1=18.33*(L-L2)
670 PRINT "↑L MM=",L1
680 PRINT "Q 10↑4 M3S-1" ,Q
690 REM P8=PRESSURE IN PSIG
700 REM IN STATMENT 720 ,435 IS A CALIBRATION CONSTANT
710 P8=435*(P9-.004)
720 REM N7=AREATION NUMBER FOR 4" IMPELLER
730 N7=.09534*Q/N2
740 REM N8=REYNOLDS NUMBER FOR 4" IMPELLER
750 N8=10322.5*N2
760 PRINT "PG=",P,"PG/P0=",P1,"P/V=",P/6.589
770 PRINT "NP=",N6,"NQ=",N7,";NR=",N8
780 REM H IS THE GAS HOLDUP
790 PRINT "H=",L1/(203.2+L1)
800 PRINT "SPEED SPS",N2
810 PRINT "PRESSER PSIG=",P8
820 REM
830 REM
840 REM    =THIS IS THE END OF THE FILE=
```

PROGRAM (2)

```
 10  REM  PROG(2)
 20  REM  PROG FOR POWER MEASUREMENTS FOR COTINUOUS FLOW
 30  REM  GAS-LIQUID EXPERIMENT
 40  REM
 50  REM
 60  REM  THIS PROGRAM IS DESIGNED TO MEASUR AND CALCULATE
 70  REM  THE POWER AT STEADY STATE CONDITIONS IN CONTINOUES
 80  REM  FLOW GAS-LIQUID MIXING EXPERIMENT
 90  REM
100  REM  ADJUST THE IMPELLER SPEED , THA GAS AND LIQUID
110  REM  FLOW RATES AT THE DESIRED VALUES
120  REM  RUN THE COMPUTER PROGRAM
130  REM
140  REM  INPUT:
150  REM     A-VARIAELES:
160  REM        P0   UNGASSED POWER AT SAMESPEED WATTS
170  REM        T3   FRICTION TORQUE    VOLTS
180  REM     B-SIGNALS (MEASURED IN VOLTS):
190  REM        N1 OUTPUT SIGNAL OF THE TACHOGENERATOR
200  REM           (FOR MEASURING IMPELLER SPEED)
210  REM        T1   OUTPUT SIGNAL OF TORQUE TRANSDUCER
220  REM        A   OUTPUT SIGNAL OF INLET GAS FLOWMETER
230  REM        A1  OUTPUT SIGNAL OF OUTLET GAS FLOWMETER
240  REM        F   OUTPUT SIGNAL OF LIQUID FLOWMETER
250  REM        P9   OUTPUT SIGNAL OF PRESSURE TRANSDUCER
260  REM  OUTPUT:
270  REM        Q INLET GAS FLOW RATE *10↑4 M3/SEC
280  REM        Q1  OUTLET GAS FLOW RATE *10↑4 M3/SEC
290  REM        PG  GASSED IMPELLER POWER   WATTS
300  REM        PG/PO  GASSED POWER RATIO
310  REM        P/V  IMPELLER POWER PER UNIT VOLUM *1000 W/M↑3
320  REM        NP POWER NUMEER
330  REM        NQ AREATION NUMBER
340  REM        NR  REYNOLDS NUMBER
350  REM        NFL LIQUID FLOW NUMBER
360  REM        F  GAS FRACTION ESCAPED WITH WATER
370  REM        N IMPELLER SPEED  RPS
380  REM        P8  MIXING VESSEL PRESSURE  PSIG
390  REM  P2 IS P0
400  INPUT P2
410  INPUT T3
420  REM
430  REM  MEASURING THE INPUT SIGNALS
440  TASK 1,470,2
450  ACTIVATE 1
460  END
470  N1=AVG(1,5,3,5000,.001)
480  T1=AVG(1,4,1,4000,.01)
```

```
490  A=AVG(1,2,0,1000,.01)
500  F=AVG(1,0,0,1000,.005)
510  P9=AVG(1,9,4,100,.02)
520  PRINT "TYPE (RUN 550)"
530  KILL SELF
540  REM
550  REM  CALCULATING MIXING PARAMETERS
560  PRINT "SPEED VOL. TORQUE V Q VOL. FW VOL  PRESSURE V"
570  PRINT N1,T1,A,F,P9
580  REM N2 IS THE SPEED REVS/S
590  N2=3.89827+42.3837*N1-49.5773*N1↑2+44.7202*N1↑3
600  IF N2<5 THEN  PRINT "SPEED" INPUT N2
610  PRINT "SCALE OF GAS M  S?"
620  INPUT S
630  IF S=1 Q=.595*3.177*A↑.430463 GOTO 650
640  Q=.595*1.865*A↑.46475
650  T2 = T1-T3
660  P=1.4822*T2*N2
670  P1=P/P2
680  REM N6 =POWER NUMBER FOR 4" IMPELLER
690  N6=136.5*T2/N2↑2
700  REM F1 IS THE WATER FLOW RATE  *10-4 M3?SEC
710  F1=1.2468*(F-1)
720  PRINT "WATER F R M3/S=",F1
730  PRINT "Q 10↑4 M3S-1" ,Q
740  REM P8 IS PRESSER IN PSIG
750  P8=435*(P9-.004)
760  REM N7=AREATION NUMBER FOR 4" IMPELLER
770  N7=.09534*Q/N2
780  REM N8 IS RENOLD NO.
790  N8=10322.5*N2
800  PRINT "PG=",P,"PG/P0="P1,"P/V=",P/6.589
810  PRINT "NP=",N6,"NQ=",N7,";NR=",N8
820  REM NF=LIQUID FLOWNUMBER FOR 4" IMPELLER
830  PRINT "NF=",.09534*F1/N2
840  PRINT "SPEED SPS",N2
850  PRINT "PRESSAR PSIG=",P8
860  REM
870  REM
880  REM    =THIS IS THE END OF THE FILE=
```

PROGRAM (3)

```
10 REM PROG(3)
20REM PROGRAM FOR MEASURING GAS HOLDUP FRACTION FOR
30 REM CONTINUOUS FLOW GAS LIQUID EXPERIMENT
40 REM
50 REM
60 REM THIS PROGRAM IS DESIGNED TO MEASURE ANDCALCULATE
70 REM THE GAS HOLDUP FRACTION AT STEADY STATE CONDITIONS
80 REM IN CONTINOUES FLOW GAS LIQUID MIXING EXPERIMENT
90 REM
100 REM ADJUST THE IMPELLER SPEED,AND THE GAS AND LIQUID
110 REM FLOW RATES AT THE DESIRED VALUES
120 REM AFTER MEASURING THE STEADY STATE VARIAELES,THE
130 REM PROGRAM WILL STOP.TYPE "RUN 550" TO EXCUTE THE
140 REI CALCULATIONS.THE PROGRAM WILL STOP AT STATMENT
150 REM 670. SWITCH ON THE RELAY TO SHUT THE LIQUID FLOW
160 REM TO ANDOUT OF THE MIXING VESSEL.STOP THA
170 REM IMPELLER AND SHUT THE GAS VALVE. AFTER THE LIQUID
180 REM LEVEL SITTLE AT SOME VALUE, TYPE "RUN 690" TO
190 REM EXCUTE THE MEASURMENT OF THE LIQUID LEVEL AFTER
200 REM SHUT OFF,AND THE CALCULATIONS OF THE GAS HOLDUP
210 REM FRACTION
220 REM        SIGNALS (MEASURED IN VOLTS):
230 REM            N1  OUTPUT SIGNAL OFTHE TACHOGENERATOR
240REM                 (FOR MEASURINGIMPELLER SPEED)
250 REM            L  DISPERSION LEVEL AT STEADY STATECODITIONS
260 REM            A  OUTPUT SIGNAL OF THE INLET GAS FLOWMETER
270 REM            A1  OUTPUT SIGNAL OF THE OUTLET GAS FLOWMETER
280 REM            F OUTPUT SIGNAL OF THE LIQUID FLOWMETER
290 REM            P9 OUTPUT SIGNAL OF PRESSURE TRANSDUCER
300 REM            L1 LIQUID LEVELAFTER SHUTOFF
310 REM OUTPUT:
320 REM            Q INLET GAS FLOW RATE *10+4  M3/SEC
330 REM            Q1  OUTLET GAS FLOW RATE *10+4  M3/SEC
340 REM            H  GAS HOLDQP FRACTION
350 REM            NQ AREATION NUMBER
360 REM            NR REYNOLDS NUMBER
370 REM            NFL  LIQUID FLOW NUMBER
380 REM            FG  GAS FRACTION ESCAPED WITH WATER
390 REM            N  IMPELLER SPEED  RPS
400 REM            P8 MIXING VESSEL PRESSURE     PSIG
410 REM   MEASURING THE INPUT SIGNALS
420 TASK 1,450,2
430 ACTIVATE 1
440 END
450 N1=AVG1,5,3,5000,.001)
460L=AVG(1,6,0,1000,.005)
470 A=AVG(1,2,0,1000,.01)
480 A1=AVG1,3,0,1000,.01)
```

```
490 F=AVG(1,0,0,1000,.005)
500 P9=AVG(1,9,4,100,.02)
510 PRINT "TYPE(RUN 550)"
520 KILL SELF
530 REM
540 REM   CALCULATING MIXING PARAMETERS
550 PRINT"SPEED V LEVEL V Q IN   Q0UT FW VOL PRESSUREV"
560 PRINTN1,LA,A1,F,P9
570 REM N2 IS THE SPEED REVS/S
580 N2=3.89827+42.3837*N1-49.5773*N1↑2+447202*N1↑3
590 IF N2<5.3 THEN  PRINT "SPEED" INPUT N2
600 PRINT "SCALE OF GA IN S,SCALE OF GAS OUT S1"          \
610 INPUT S,S1
620 IF S=1 Q=.495*3.67589*A↑.418136 GOTO 640
630 Q=.495*2.13013*A↑.490802
640 IF S1=2 Q1=.495*3.34188*A1↑.49019 GOTO 660
650 Q1=.495*1.91887*A1↑.512557
660 PRINT "TYPE (RUN 690)"
670 STOP
680 REM SHUT OFF THE FLOW AND STOP THE IMPELLER
690 L1=0
700 FOR G=1 TO 100
710    L1=L1+AIN(1,6,1)
720    WAIT .02
730 NEXT G
740 L1=L1100
750 H=18.33*(L-L1)/(203.2+(L-2.75)*18.33
760 REM F1 IS THE WATER FLOW RATE  *10-4 M3?SEC
)  770 F1=1.2468*(F
780 PRINT "WATER F R M3/S=",F1
790 PRINT "Q 10↑4 M3S-1" ,Q
800 REM P8 IS PRESSER IN PSIG
810 P8=435*(P9-.004)
820 REM N7 IS AREATION NO.
830 N7=.09534*Q/N2
840 REM N8=REYNOLDS NUMBER FOR 4" IMPELLER
850 N8=10322.5*N2
860 PRINT "GAS HOLDUP H=",H
870 PRINT "LEVEL L1 VOLTS=",L1
880 PRINT "NQ=",N7,"NR=",N8
890 REM NFL=THE WATER FLOW NUMBER FOR 4"IMPELLER
900 PRINT "NFL=,.09534*F1/N2
910 PRINT "SPEED SPS",N2
920 PRINT "GAS OUT M3/S *10↑4=",Q1
930 PRINT "GAS OUT WITH WATER M3/S*10↑4=",Q-Q1
940 PRINT "GAS FRACTION ESCAPED WITH WATER F=",(Q-Q1)/Q
950 PRINT "PRESSURE PSIG=",P8
960 REM
970 REM
980 REM      =THIS IS THE END OFTHE FILE=
```

PROGRAM (4)

```
  10 REM  PROG(4)
  20 REM CAPILLARY CALIBRATION PROGRAM
  30 REM
  40 REM
  50 REM THIS PROGRAM IS DESIGNED TO MEASURE THE TIME FOR
  60 REM A BUBBLE WITH KNOWN SIZE TO FLOW INSIDE CAPILLARY
  70 REM TUBE ACROSS A POINT WHERE OPTICAL SWITCH IS
  80 REM POSITIONED.
  90 REM
 100 REM RUN THE PROGRAM. AT STATMENT 310 THE COMPUTER WILL
 110 REM GIVE AUDIBLE ALARM, INJECT THE BUBBLE FROM THE
 120 REM MICROSYRANGE AT THE TIP OF THE CAPILLARY TUBE.
 130 REM
 140 REM INPUT:
 150 REM      THE COMPUTER SCANS THE OUTPUT SIGNAL OF THE
 160 REM      OPTICAL SWITCH FOR 2 SECONDS AT A RATE OF
 170 REM      1000 READINGS PER SECOND, AND STORS THE
 180 REM      THE MEASURED VALUES IN ARRAY A.
 190 REM OUTPUT:
 200 REM      B = TIME FOR THE BUBBLE TO FLOW ACROSS
 210 REM          OPTICAL SWITCH            M.S.
 220 REM      X(K)= POINTS IN THE TIME WHERE THE BUBBLE
 230 REM            IS FLOWING ACROSS THE OPTICAL SWITCH.
 240 REM            THAT SEQUENCE OF NUMBERS GIVES INDICATION
 250 REM            OF ANY POSSIBLE BUBBLE BREAKAGE INSIDE
 260 REM            THE CAPILLARY TUBE.
 270 REM
 280 J=1
 290 DIM A(2000),X(300)
 300 WAIT 5
 310 PNT 7
 320 COLLECT (1,11,0,2000,.001) INTO A(1)
 330 B=0
 340 FOR I=2 TO 2000
 350    IF A(I) <= A(1)-.1 THEN  B=B+1 X(J)=I J=J+1
 360 NEXT I
 370 PRINT B
 380 FOR K=1 TO J-1
 390   PRINT X(K),
 400 NEXT K
 410 REM
 420 REM
 430 REM    =THIS IS THE END OF THE FILE=
```

PROGRAM (5)

```
  10 REM PROG(5)
  20 REM PROGRAM FOR BUBBLE SIZE AND POINT GAS HOLDUP
  30 REM FRACTION MEASUREMENTS
  40 REM
  50 REM
  60 REM THIS PROGRAM IS DESIGNED TO DETECT THE BUBBLES
  70 REM WHICH ARE SAMPLED BY THE CAPILLARY TUBE,COUNTS
  80 REM ITS NUMBER,MEASURE ITS SIZE ,AND CALCULATE THE
  90 REM POINT GAS HOLDUP FRACTION.
 100 REM
 110 REM
 120 REM THIS PROGRAM IS TAKING ACCONT OF ANY POSSIBLE
 130 REM BREAKAGE OF BUBBLES INSIDE THE CAPILLARY TUBE
 140 REMIF THE TIME BETWEEN ANY TWO BUBBLES IS LESS THAN
 150 REM 8 MS, THEY ARE CONSIDERED AS ONE BUBBLE (STAT 800).
 160 REM
 170 REM INPUT:
 180 REM      P  PRESSURE DROP ALONG THE CAPILLARY TUBE CM HG
 190 REM      ANALOG SIGNAL FROM THE OPTICAL SWITCH.
 200 REM OUTPUT:
 210 REM       I  NUMBER OF BUBBLES IN SAMPLE
 220 REM       THE SIZE DISTRIBUTION (PRINTED IN TABLE)
 230 REM       H  POINT GAS HOLDUP FRACTION
 240 REM       D10  MEAN BUBBLE DIAMETER    MM
 250 REM       D32  SAUTER MEAN DIAMETER    MM
 260 REM      LISTING THE DIAMETERS OF BUBBLES IN MM.
 270 REM
 280 REM IF P<5 THE PROG. JUMPS TO STAT(1690) TO MEASURE
 290 REM AND CALCULATE THE MIXING PARAMETERS.
 300 PRINT "P"
 310 INPUT P
 320 REM C1 ,C2 AND C3 ARE CALIBRATION COEFFICENTS FOR
 330 REM .6 MM  CAPILLARY TUBE
 340 C1=-.10931+7.97837E-3*P-1.77226E-5*P↑2
 350 C2=0168739-4.03514E-4*P+9.97666E-7*P↑2
 360 C3=-1.109827E-4+5.32094E-7*P+5.04687E-8*P↑2
 370 Z1=5000
 380 Z2=200
 390 DIM A(Z1,B(Z2),S(Z2),V(Z2,D1(3*Z24)
 400 IF P<5 GO TO 1700
 410 WAIT 5
 420 PNT 7
 430 REM SAMPLING THE ANALOGSIGNAL
 440 COLLECT (1,10,0,5000,.001) INTO A(1)
 450 REM
 460 REM SEARCH FOR THE FIRST BUBBLE IN THE SAMPLE
 470 FOR I=1 TO 150
 480    S(I)=0
```

```
490 E(I)=0
500 V(I)=0
510 NEXT I
520 A=A(1)
530 FOR L=2 TO 100
540    IF A(3*L)>A A=A(3*L)
550 NEXT L
560 J=0
570 J=J+1
580 IF J>5000 GOTO 1670
590 IF A(J) >A-.1 GOTO 570
600 REM FIRST BUBBLE IS LOCATED
610 REM
620 REM IDENTIFICATION OF BUBBLES AND LIQUID SLUGS
630 E(1)=1
640 I=1
650 K=1
660 J=J+1
670 IF J>5000 GOTO 780
680 IF A(J)>A-.1 GOTO 730
690 IF E(I) > .1 E(I)=BI)+1 GOTO 660
700 K=K+1
710 E(I)=1
720 GOTO 660
730 IF S(K) >.1 S(K)=S(K)+1 GOTO 660
740
750 I=I+1
760 S(K)=1
770 GOTO 660
780 I9=I
790 FOR J=1 TO K
800    IF S(J)<8 B(J+1)=B(J+1)+B(J) A(J)=0 GOTO 820
810    A(J)=1
820    A(J+1)=1
830 NEXT J
840 N=0
850 U=0
860 REM
870 REM CALCULATINGTHE VOLUMS AND DIAMETERS OF BUBBLES
880 FOR M=1 TO I9
890    U=U+B(M)*A(M)
900    V(M)=C1*B(M)+C2*B(M)↑2+C3*B(M)↑3
910    V(M)9A(M)*V(M)
920    IF V(M)>0 N=N+1 D1(N)=(1.9098*V(M))↑.33334
930 NEXT M
940 PRINT "I=",I9,"N=",N
950 REM
960 REM CLASSIFICATION OF BUBBLES INTO SIZE GROUPS
```

```
 970 N1=0
 980 N2=0
 990 N3=0
1000 N4=0
1010 N5=0
1020 N6=0
1030 N7=0
1040 N8=0
1050N9=0
1060 M9=0
1070 FOR G=1 TO N
1080    IF D1(G)>4.5 GOTO 1270
1090    IF D1(G)>4 GOTO 1260
1100    IF D1(G)>3.5 GOTO 1250
1110    IF D1(G)>3 GOTO1240
1120    IF D1(G)>2.5 GOTO 1230
1130    IF D1G)>2 GOTO 1220
1140
1150    IF D1(G)>1.5 GOTO1210
1160    IF D1(G)>1 GOTO 1200
1170    IF D1(G)>.5 GOTO 1190
1180    N1=N1+1 GOPO 1280
1190    N2=N2+1 GOTO 1280
1200    N3=N3+1 GOTO1280
1210    N4=N4+1 GOTO 1280
1220    N5=N5+1 GOTO 1280
1230    N6=N6+1 GOTO 1280
1240    N7=N7+1 GOTO 1280
1250    N8=N8+1 GOTO 1280
1260    N9=N9+1 GOTO 1280
1270    M9=M9+
1280    X=G
1290 NEXT G
1300 REM
1310 REM PRINTINGTHE RESULTS
1320 PRINT "NØ OF BUES .5>D>0",N1,
1330 PRINT "NØ. OF BUBS 1>D>.5",N2
1340 PRINT NØ OF BUBS 1.5>D>1",N3,
1350 PRINT "NØ.OF BUBS 2>D>1.5",N4
1360 PRINT "NØ OF BUBS 2.5>D>2",N5,
1370 PRINT "NØ. OF BUBS 3>D>25",N6
1380 PRINT "NØ OF BUBS 3.5>D>3",N7,
1390 PRINT NØ. OF BUBS 4 >D>3.5"N8
1400 PRINT "NØ OF BUBS 4.5>D>4",N9,
1410 PRINT "NØ. OF BUBS  D>4.5",M9
1420 S=0
1430 FOR M=1 TO I9
1440    S=S+V(M)
```

```
1440  S= S+V(M)
1450  NEXT M
1460  PRINT "TOTAL VOL OF GAS MM3=", S
1470  L7=(5- U/1000)*1.23921*P+1.35302
1480  PRINT "H=", S/(S+2*L7)
1490  S1=0
1500  S2=0
1510  S3=0
1520  FOR W=1 TO N
1530     S1=S1+D1(W)
1540     S2 = S2+D1(W)+2
1550     S3=S3+D1(W)+3
1560  NEXT W
1570  PRINT "MEAN D MM=", S1/N
1580  PRINT "D32=", S3/S2, "S2=", S2, "S3=", S3
1590  FOR W2=1 TO 5
1600     FOR W1=8*(W2-1)+1 TO 8*W2
1610        PRINT D1(W1),
1620        D1(W1)=0
1630     NEXT W1
1640     PRINT W1
1650  NEXT W2
1660  STOP
1670  PRINT " SORRY NO BUBBLES IN THE SAMPLE"
1680  STOP
1690  REM MEASURINGIMPELLER SPEED AND GAS FLOW RATE
1700  REM SPEED RPS R
1710  INPUT R
1720  A=AIN(1,2,1)
1730  Q=1.931*A+.391
1740  PRINT "Q+10+4 MM3/S=", Q
1750  PRINT "SPEED RPS=", R
1760  PRINT NQ=", .09534*Q/R
1770  REM
1780  REM
1790  REM      =THIS IS THE END OF THE FILE=
```

PROGRAM (6)

```
 10 REM PROG(6)
 20 REM STEP TEST PROGRAM
 30 REM
 40 REM THIS PROGRAM IS DESIGNED TO MEASURE A STEP
 50 REM CHANGE IN GAS FLOW RATE AND THE RESPONSE OF
 60 REM IMPELLER POWER.
 70 REM RATE OF SAMPLING = 20 PER SECOND
 80 REM
 90 REM RUN THE PROGRAM AND INTRODUCE THE STEP CHANGE
100 REM IN THE SPARGED GAS FLOW RATE BY SWITCHING THE RELAY.
110 REM INPUT:
120 REM       VARIABLES: N SPEED OF IMPELLER   RPS
130 REM       SIGNALS (MEASURED IN VOLTS):
140 REM           Q(I)  GAS FLOWMETER OUTPUT SIGNAL AT
150 REM              TIME I*.05 SEC FROM START OF SAMPLING
160 REM           T(I)  OUTPUT SIGNAL OF TORQUE TRANSDUCER
170 REM              AT TIME I*.05 S. FROM START OF SAMPLING
180 REM OUTPUT:
190 REM       Q(L)  GAS FLOW RATE *10↑4 M3/SEC AFTER START
200 REM              OF SAMPLING BY .05*L SEC.
210 REM       P(L)  IMPELLER POWER W , AFTER START OF
220 REM              SAMPLING BY .05*L SEC.
230 DIM Q(200),T(200),P(200)
240 PRINT "SPEED RPS" INPUT N
250 REM MEASURING THE INPUT SIGNALS
260 FOR I=1 TO 200
270    Q(I)=AIN(1,2,1) T(I)=AIN(1,4,1)
280    WAIT .05
290 NEXT I
300 REM CALCULATING THE RESPONSE
310 FOR J=1 TO 10
320    T1=T1+T(J)
330 NEXT J
340 T1=T1/10
350 FOR K=1 TO 200
360    IF Q(K)<0 THEN  Q(K)=0
370    P(K)=(T(K)-T1)*1.4822*N
380    Q(K)=1.6921*Q(K)↑.4981
390 NEXT K
400 P1=0
410 REM CALCULATING THE AVARAGE STEADY STATE POWER
420 FOR M=161 TO 200
430    P1=P1P(M)
440 NEXT M
450 P2=P1/40
460 P3=.632*P2
470 REM PRINTING THE RESULTS
480 PRINT "P .632=",P3
490 PRINT "N Q*10↑4 M3/SEC ↑P P(L)/PSS"
500 FOR L=1 TO 80
510    PRINT L,Q(L),P(L),P(L)/P2
520 NEXT L
530 REM
540 REM       =THIS IS THE END OF THE FILE=
```

PROGRAM (7)

```
 10 REM PROG(7)
 20 REM PULSE TEST PROGRAM
 30 REM
 40 REM
 50 REM THIS PROGRAM IS DESIGNED TO MEASURE INPUT PULSE
 60 REM DISTURBANCE IN GAS FLOW RATE AND THE FOLLOWING
 70 REM RESPONSE OF IMPELLER POWER. THESE MEASURED INPUT
 80 REM AND OUTPUT SIGNALS ARE USED TO EVALUATE THE
 90 REM FREQUENCY RESPONSE USINGFOURIER TRANSFORM.
100 REM
110 REM AFTER SAMPLING THE SIGNALS, THE PROGRAM WILL
120 REM SEARCH AUTOMATICALY FOR THE START AND END OF
130 REM BOTH THE DISTURBANCE AND RESPONSE. THE NUMBER
140 REM OF POINTS ON THESE CURVES WILL BE CALCULATED
150 REM AND FED TO THE FOURIER TRANSFORM.
160 REM
170 REM INPUT:
180 REM      MEASURED SIGNALS (IN VOLTS):
190 REM          U(T)  OUTPUT SIGNAL OF GAS FLOWMETER
200 REM                AT TIME T
210 REM          X(T)  OUTPUT SIGNAL OF THE TORQUE
220 REM                TRANSDUCER AT TIME T.
230 REM OUTPUT:
240 REM      INPUT DISTURBANCE AND OUTPUT RESPONSE
250 REM          IN TIME DOMAIN.
260 REM      STEADY STATE GAIN  W/L OF GAS
270 REM      FREQUENCY RESPONSE RESULTS.
280 REM
290 REM
300 REM  W2 LOWEST FREQUENCY TO BE STUDIED      HZ
310 REM  W4 HIGHEST FREQUENCY TO BE STUDIED     HZ
320 REM  W3 STEP CHANGE IN FREQUENCY       W<1 HZ
330 REM  W5 STEP CHANGE IN FREQUENCY       W>1 HZ
340 REM  T TIMEPERIOD BETWEEN MEASURMENTS   SEC.
350 W2=.1
360 W3=1.2
370 W4=12
380 W5=1.1
390 DIM U(500),X(500),W9(500),D9(500),G9(500)
400 PRINT "INPQT IN RPS "
410 INPUT V1
420 REM
430 REM MEASURING AND CALCULATINGTHE INPUT AND OUTPUT
440 REM IN TIME DOMAIN.
450 PNT 7
460 S1=0
470 WAIT 1
480 FOR I =1 TO 200
```

```
490 U(I)=AIN(1,2,1)
500 X(I) =AIN(1,4,1)
510 WAIT 0.02
520 NEXT I
530 S=0
540 FOR Z=1 TO 10
550    S1=S1+X(Z)
560    S=S+U(Z)
570 NEXT Z
580 U=S/10
590 IF U<0 THEN  U=.0001
600 X=S1/10
610 FOR J =2 TO 200
620    IF U(J)<0 THEN  U(J)=.001
630    U(J)=U(J)↑.4981-U↑.4981
640    U(J)=.16921*U(J)
650    X(J)=X(J)-X
660 NEXT J
670 J1=1
680 J1=J1+1  .
690 IF U(J1)>.05 T1=J1 GOTO710
700 GO TO 680
710 J2=T1
720 J2=J2+1
730 IF U(J2)<.02 T2=J2-1 GOTO 750
740 GO TO 720
750 J3=T2
760 J3=J3+1
770IF ABS(X(J3))<.025 T3=J3 GO TO  790
780 GO TO 760
790 M=T2-T1+1
800 N=T3-T1+1
810 FOR K2=1 TO N
820    U(K2) = U(T1K2-1)
830 NEXT K2
840 FOR K3 = 1 TO N
850    X(K3)=14822*V1*X(T1+K3-1)
860 NEXT K3
870 X(1)=X(2)
880 N9=1
890 REM
900 REM COMPUTING STEADY STATE GAIN
910 S1=X(1)*T/2
920 FOR Z=2 TO N
930    S1=S1+X(Z)+X(Z-1))*T/2
940 NEXT Z
950 S2=U(1)*T/2
960 FOR V=2 TO M
```

```
 970  S2=S2+(U(V)+U(V-1))*T/2
 980  NEXT V
 990  S=S1/S2
1000  REM
1010  REM FOURIER TRANSFORM AND FREQUENCY RESPONSE EVALUATION.
1020  W=W2
1030  R2=0
1040  N9=N9+1
1050  I2=0
1060  R1=COS(W*T)
1070  I1=SIN(W*T)
1080  FOR K=2 TO N
1090     R2=R2-(X(K)-X(K-1))*R1
1100     I2=I2-(X(K)-X(K-1))*I1
1110     W1=W*K*T
1120     IF W1<=360 THEN GOTO 1150
1130     W1=W1-360
1140     GOTO 1120
1150     R1=COS(W1)
1160     I1=SIN(W1)
1170     R2=R2+(X(K)-X(K-1))*R1
1180     I2=I2+(X(K)-X(K-1))*I1
1190  NEXT K
1200  R=X(N)/W*SIN(W1)+X(1)/(W↑2*T)*(COS(W*T)-1)
1210  R=R+R2/(W↑2*T)
1220  I=-X(N)/W*COS(W1)+X(1)/(W↑2*T)*(SIN(W*T))
1230  I=I+I2/(W↑2*T)
1240  A=R
1250  B=I
1260  R2=0
1270  I2=0
1280  R1=COS(W*T)
1290  I1=SIN(W*T)
1300  FOR K=2 TO M
1310     R2=R2-(U(K)-U(K-1))*R1
1320     I2=I2-(U(K)-U(K-1))*I1
1330     W1=W*K*T
1340     IF W1<=360 THEN GOTO 1370
1350     W1=W1-360
1360     GOTO 1340
1370     R1=COS(W1)
1380     I1=SIN(W1)
1390     R2=R2+(U(K)-U(K-1))*R1
1400     I2=I2+(U(K)-U(K-1))*I1
1410  NEXT K
1420  R=U(M)/W*SIN(W1)+U(1)/(W↑2*T)*(COS(W*T)-1)
1430  R=R+R2/W↑2*T)
1440  I=-U(M)/W*COS(W1)+U(1)/(W↑2*T)*(SIN(W*T))
```

```
1450  I=I+I2/(W↑2*T)
1460  C=R
1470  D=I
1480  E=(A*C+B*D)/(C↑2+D↑2
1490  F=(A*D-B*C)/(C↑2+D↑2)
1500  D1=20*.43429*LOG(ABS(SQR(F↑2+E↑2))/ABS(S))
1510  G1=ATN(F/E)*180/3.1416
1520  IF (E/S)<0 G1=G1-180
1530  W9(N9)=W
1540  D9(N9)=D1
1550  G9(N9)=G1
1560  IF W<=1 W=W3*W
1570  W=W5*W
1580  IF W<=W4 GOTO 1030
1590  REM
1600  REM PRINTING THE RESULTS
1610  PRINT " S. S. GAIN = ",S
1620  PRINT " FREQUENCY    LOG MOD (DB)    ANGLE(DEG) "
1630  FOR N8=1 TO N9
1640     PRINT W9(N8),D9(N8),G9(N8)
1650  NEXT N8
1660  PRINT "N0.          U           X"
1670  FOR I=1 TO N
1680     PRINT I,U(I),X(I)
1690  NEXT I
1700  PRINT 'M=",M,'N=",N
1710  REM
1720  REM
1730  REM       =THIS IS THE END OF THE FILE=
```

APPENDIX D

ANALYSIS OF THE WATER SUPPLYING

THE UNIVERSITY OF BATH

Wessex Water
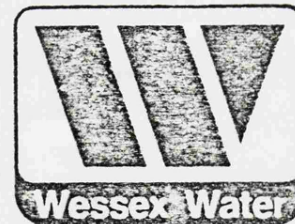
Mr K Kobbacy
School of Chemical Engineering
Bath University
Claverton Down
BATH

Bristol Avon Division
P O Box 95
The Ambury
Bath BA1 2YP
Telephone Bath
(0225) 313500

Our ref: BC/MAP

Your ref:

Date: 16th July 1979

Dear Mr Kobbacy

Further to our telephone conversation, analysis of the water supplying
the University is as follows:

		Mean	Max	Min
Turbidity	FTU	0.37	0.87	0.12
pH		7.4	7.6	7.1
Conductivity	µs/cm	643	770	530
Alkalinity	mgCaCo$_3$/litre	231	250	205
Total Hardness	"	339	352	326
Non-Carbonate Hardness	"	108	147	76
Calcium Hardness	"	313	324	298
Magnesium Hardness	"	28	44	20
Total Organic Carbon	mgC/litre	1.6	2.5	0.75
Ammonia	mgN/litre	0.02	0.09	0.01
Nitrate	mgN/litre	4.7	7.0	2.6
Nitrite	mgN/litre	0.01	0.02	0.01
Silica	mgS/litre	3.4	4.3	2.9
Total Phosphate	mgP/litre	0.05	0.05	0.05
Chloride	mgCl/litre	23	28	18
Fluoride	mgF/litre	0.12	0.2	0.07
Sulphate	mgSO$_4$/litre	85	100	76
Sodium	mgNa/litre	11	16	6
Potassium	mgK/litre	2.4	3.0	1.8
Iron	mgFe/litre	0.03	0.055	0.01
Lead	mgPb/litre	0.005	0.005	0.005
Copper	mgCu/litre	0.017	0.03	0.111
Zinc	mgZn/litre	0.02	0.02	0.02
Manganese	mgMn/litre	0.002	0.002	0.002

Yours sincerely

D J PALMER
Divisional Supply Scientist

Wessex Water Authority

APPENDIX E

PUBLISHED WORK

SURFACE AERATION IN AGITATED VESSELS

M. Greaves[+] and K.A.H. Kobbacy[+]

Surface aeration effects in ungassed liquid systems have been investigated using tap water, distilled water and 0.11M K_2SO_4 solution. The reduction in maximum power number, as the Reynolds number is increased, was confirmed to be due to surface aeration. Measurements of bubble size and gas holdup at sample locations close to the liquid surface and near to the turbine impeller, revealed that the onset of surface aeration begins before there is any drop in Pou. A mechanism has been proposed for the surface aeration process and correlations developed to predict two impeller speed conditions, $N_{SA,1}$ and $N_{SA,2}$, determining when gas bubbles are first entrained and when Pou first begins to fall. 'Pure' liquids and electrolyte solutions have been found to exhibit significantly different surface aeration behaviour.

INTRODUCTION

Many investigators have, in their studies of mixing in ungassed liquids, noticed the existence of surface aeration, but an adequate description of it has not been presented. Most results on power consumption have been obtained for batch vessels and, although the general characteristics are well known, discrepancies between the various data exist. The value of the power number, Pou, is known to be sensitive to any minor changes in impeller geometry. A reduction in its value from 5.7 to 4.4 was noti-ed by Wisdom (1) when using a turbine made of thicker guage material. In unbaffled vessels there is a continuous reduction in Pou when the Reynolds number is increased, due to the vortex at the shaft. Clark and Vermeulen (2), who identified the onset of surface aeration by a sudden drop in Pou, extended this concept to fully-baffled vessels. There reasoning was, that a continuous increase of the volumetric ratio, D^2W/T^2H, should bring the system into a region where the baffling effect is overcome. It is unlikely, however, that such a trend could contribute significantly to surface aeration, except possibly at very high impeller speeds, lying outside the normal operating range.

Dierendonck et al (3) defined two impeller speeds for the onset of surface aeration : (i) N^*, the minimum stirrer speed at which gas is sucked into the liquid by vortices on the liquid surface and (ii) No^*, the characteristic impeller speed for bubble aspiration, obtained from gas holdup measurements. Neither their correlation, nor Vermeulen's, proved to be satisfactory and a further investigation of the surface aeration effect in ungassed systems was therefore undertaken.

+ School of Chemical Engineering, University of Bath, Claverton Down, Bath, BA2 7AY.

Surface aeration effects may also be significant when interpreting data on gas-liquid, 3-phase, and continuous flow reactors. In gas-liquid systems, it is normal to operate the reactor so that the sparged gas is well distributed throughout the vessel volume. Nienow et al (4) have recently shown that re-entrainment of gas by surface aeration is reduced considerably when gas is sparged to the vessel. Even at a relatively high power input and moderate gas load, surface aeration represented only a few per cent of the sparged gas flow. The extent to which 'old' recirculated gas is mixed with new gas in the impeller cavities will, of course, depend also on the rate of recirculation.   Thus, further detail on surface aeration effects may shed light on the question as to whether recirculation of gas begins before a certain critical speed N_{R1} is reached. Whilst determination of surface aeration under ungassed conditions cannot satisfactorily relate what will happen in a sparged reactor there are, additionally, details regarding mechanical geometry and also any differences between 'pure' and ionic or surfactant solutions, which need to be investigated.

EXPERIMENTAL

Experiments were carried out in a fully-baffled flat-bottomed tank, 0.203m diameter, with a nominal liquid capacity of 6 litres. Three sizes of disc blade turbine were used having diameters Dl = 0.0762m, D2 = 0.106m and D3 - 0.135m. Other details of the equipment and materials used have been fully described in another paper (5).   The liquids used were filtered tap water, distilled water, and 0.11m potassium sulphate solution.

On-line measurement and data acquisition was employed with the aid of a Macsym II microcomputer. A strain guage transducer was used to measure the shaft torque, and a directly coupled D.C. tachogenerator provided the

impeller speed measurement. Typically, the error in speed measurement was less than 0.7%, whilst for the torque the error was a variable quantity. This ranged from about 10% for a combination of low speed and the smallest impeller, to less than 1% for the largest impeller. Measurements of bubble size were also made using a capillary probe equipped with photo-transistor detectors. Sampling points were located near to the impeller and in the circulating flow close to the surface of the liquid. Local gas holdup values were also estimated from this data.

Details of the technique are given by Kobbacy (6), and are to be included in a forthcoming publication. The effect of vessel pressure was investigated by raising the pressure to 0.239 MNm^{-2}. An accurate strain guage transducer was used to measure the pressure.

RESULTS AND DISCUSSION

Impeller Power

The effect on impeller power consumption of changing the impeller clearance, impeller diameter, total vessel pressure and the type of liquid is shown in Figs. 1 to 7. Results presented for the smaller tank in Fig. 1 formed part of a preliminary investigation, and because it was noticed that the fall-off in Pou occurred at lower impeller speeds, it was decided not to include it in further parts of the investigation. Excepting this case, the trends exhibited against Reynolds number, in Figs. 1, 2 and 3, are similar to those obtained by Wisdom (1) and Nienow et al (7). Thus, there is an initial rise of Pou up to a maximum value, and then a decrease. Increasing the impeller clearance has two effects. First, there is an upward shift in the rising part of the curve, which also becomes less steep. Secondly, the drop in Pou occurs at a lower Reynolds number, i.e. surface aeration starts at a lower impeller speed. For this reasons, the clearance was fixed at H/4 throughout the rest of the investigation. Since most previous studies used the standard clearance of H/3, this may explain why the variation in Pou was not observed.

Fig. 4 and Fig. 3 are different reprsentations of the same data, and serve to show that small changes in power are only readily discernable on the Reynolds number basis. The maximum values of Pou achieved for the three sizes of impeller are all relatively close, ranging from 4.6 to 5.05. For the D2 impeller (D/T = 0.5), however, there is a steeper variation in Pou up to the maximum. Although this trend for the two smaller sizes of impeller is consistent with Wisdom's work (1), the much less marked variation observed for the larger impeller (D) is quite different - a result which we have also confirmed in studies of continuous flow mixing. Wisdom also observed a drop in maximum Pou due to increase in thickness of the impeller disc. In our case, a reduction in the blade thickness/diameter from 0.0156 (D2) to 0.0074 (D3), may be the reason for the shallower change in Pou observed for the D3 impeller. Overall, then, there is an initial rise in Pou as the Reynolds number increases and steepening effect due to interacting geometrical factors. These are reduction of impeller clearance (C/H) and increase of the ratio D/T. The material thickness of the impeller blades is also an important factor, but the complex effects here need further investigation.

From Fig. 5, it is evident that there is no effect of raising the vessel pressure up to 0.239 MNm^{-2} (20 psig) on the first part of the power curve. However, the results do seem to indicate that surface aeration commences at slightly lower impeller speeds as the pressure is increased. The effect of

changing the ionic concentration is shown in Figs. 6 and 7. Thus, compared to tap water, the fall-off in Pou starts earlier for 0.11M K_2SO_4 solution, whereas a slightly higher Reynolds number is reached in the case of distilled water. Further details on this effect are discussed below.

Bubble Size and Gas Holdup

The capillary probe was first located at position S near to the impeller, as shown in Fig. 10c. This sampling position lies in the circulation path of liquid which passes close to the surface before returning to the impeller region. The detection of bubbles at this point should, therefore, be a reliable indication of the lowest impeller speed at which entrainment of gas (bubbles) from the surface first occurs. Fig. 8 shows the results obtained for tap water, distilled water and 0.11m K_2SO_4 solution. A very small number of fine bubbles are first detected at low impeller speeds then, gradually, as the speed is increased, the number and size of bubbles becomes larger. The corresponding variation of gas holdup is shown in Fig. 9 Above an impeller corresponding to the condition where Pou first begins to fall, there is no further significant change in the bubble size. In the case of 0.11m K_2SO_4 solution, bubbles are first detected at impeller speeds which are slightly below those obtained for tap water. Although the variation of mean bubble diameter is, in this case, much smaller, the same overall trend exists. On the other hand, the gas holdup shows a much faster increase. With distilled water, the mean bubble size is slightly larger and the gas holdup lower, compared with tap water.

Further measurements of bubble size and holdup are shown in Fig. 10 and correspond to the 3 sampling locations A, B and C close to the liquid surface, as identified in Fig. 10C. The variation of bubble size in Fig. 10a shows that bubbles are first detected in all of the sampling positions at virtually the same impeller speed. Comparing between the two sampling regions, larger mean bubble sizes and higher gas holdup values are found at A, B and C. On the basis of these measurements and observations, a mechanism for surface aeration in fully-baffled tanks is developed in the following section.

Surface Aeration Mechanism

(i)   Surface aeration starts at a low impeller speed prior to any drop in Pou. Gas is drawn-in at the surface of the liquid by the process depicted in Fig.11 and circulation of fine bubbles takes place in the bulk liquid. In the figure, A represents a large stable cylindrical eddy, formed from the resulting flow effect generated by the impeller discharge interacting with the baffled wall of the vessel (8). Thereafter, small eddies B and C are formed. Eddies of type B have a tendency to rotate slowly around the agitator shaft and then combine into a stronger eddy to form a hollow vortex - shown as B at the liquid surface.

(ii)   Entrained gas bubbles are carried down to the impeller region by the circulating liquid.

(iii)   As the impeller speed increases, the eddies residing at the surface grow in intensity. More gas is drawn into the liquid producing a corresponding increase in gas holdup near to the surface. In 'pure' liquids this is accompanied by a rapid increase in the mean bubble size due to coalescence. With electrolyte solutions there is a less dramatic change in bubble size because of the reduced rate of coalescence. These effects are clearly seen in Fig. 8.

(iv)   Higher liquid circulation velocities develop as the speed of the impeller is increased further. Therefore, larger sizes and numbers of bubbles, respectively, are transported to the impeller region in the case of 'pure' liquids and electrolyte solutions. This leads to an increase in the flow rate of gas to the impeller.

(v)   There is no limitation on the availability of gas from the surface of the liquid, as evidenced by the much larger gas holdup there compared to the impeller region (Fig. 10b). The rate determining step for aeration of the bulk liquid is therefore the capability of the circulating liquid to carry gas, rather than the strength of the vortexing eddies.

(vi)   A drop in the power number occurs when the flow rate of gas from the surface of the liquid to the impeller region is sufficiently high. This is associated with the formation of clinging cavities behind the impeller blades.

Liquid Flow Patterns

The previous description of surface aeration points to the important role played by the velocity of the circulating liquid. Therefore, before attempting any correlation of the factors governing the process, it is necessary to develop an understanding of the flow patterns produced. In a fully-baffled vessel, equipped with a turbine agitator, the three-dimensional flow can be described in terms of primary and secondary flow patterns (8, 9, 10). These are shown in Fig. 12. Whilst the rotational primary flow is of minor importance for mixing processes, the secondary circulation comprises radial and axial components. This general flow pattern (Fig. 12 b) has been shown to be independent of both the size (8) and speed of the impeller (11) in the turbulent region.

The secondary circulation in the vessel can be divided into the four regions shown in Fig. 13. Holmes et al (12) showed that the average velocity of the liquid in zone I could be estimated from :

$$\overline{V}_r = C_1 \frac{ND^2}{r} \qquad (1)$$

where $\overline{V}_r$ is the average velocity at radial distance r from the impeller centre line. Using Nagata's et al data (8), they found that the average liquid velocities in the other three zones were of the same order, but less than $\overline{V}_r$ near to the wall. Apart from the impeller jet region then, the average velocity of the circulating flow in the tank can be estimated from

$$\bar{V} \quad = \quad C_2 \frac{ND^2}{T} \qquad (2)$$

Schwartzberg and Treybal (13) have also presented a correlation for this velocity condition:

$$\bar{V} \quad = \quad 1.387 \frac{ND^2}{\left(T^2H\right)^{1/3}} \qquad (3)$$

Equations (2) and (3) are identical when $H = T$, which is the case employed in this study.

Onset of Surface Aeration

The onset of surface aeration requires specification of two impeller speeds; namely, $N_{SA\,1}$ and $N_{SA\,2}$. $N_{SA\,1}$ is the condition at which air bubbles are first entrained near to the surface of the liquid by the hollow vortex motion. The second condition, $N_{SA\,2}$, defines the impeller speed when Pou decrease in Pou first occurs. Since it is not possible to provide an adequate quantitative description for the first process, the approach to be taken first involves developing a correlation for $N_{SA\,2}$, then extending it by using the experimental data on $N_{SA\,1}$.

Govier and Aziz (14) state that the absolute rise velocity of a bubble in a flowing stream is equal to the vector sum of the rise velocity in a stagnant fluid and the local absolute velocity of the flowing liquid. Thus, if we extend this principle applying to turbulent flow in a pipe, to turbulent flow in a stirred vessel, then the necessary condition for a gas bubble to be transported downwards into the liquid, near to the impeller axis (zone lV) is :

$$\bar{V} \quad > \quad U_T$$

$$\qquad (4)$$

$$\text{or} \quad \bar{V} \quad = \quad C_3 U_T$$

where $\bar{V}$ is the average vertical plane velocity of the liquid and U_T is the terminal bubble velocity corresponding to the average size of entrained bubbles at the impeller speed condition N_{SA2} - defined by Equation (3).

Therefore, from Equations (3) and (4) :

$$N_{SA2} \quad = \quad 0.72 \ C_3 U_T \ \frac{\left(T^2H\right)^{1/3}}{D^2} \qquad (5)$$

where $C_3 > 1$ by definition. Values of $N_{SA\,2}$ were taken from Fig. 8 and substituted into Equation (5), together with the corresponding terminal

velocities calculated from Haberman and Mortons' data (15), shown in Fig. 14. The calculated values of C_3 are given in Table 1, and the average value for tap water is 2.8, with a maximum deviation of 5% for the range of impeller sizes used.

TABLE 1 - Values of coefficient C_3 in Equation (5)

(T = 0.203m)

	D m	N_{SA2} s^{-1}	d_b $\times 10^3 m$	U_T^* MS^{-1}	C_3
	0.0762	15.6	2.1	0.22	2.81
Tap	0.1016	8.3	1.8	0.20	2.93
Water	0.1350	4.7	2.1	0.22	2.66
Distilled Water	0.1016	8.6	1.94	0.30	2.02

* Haberman and Morton (15)

The coefficient C_3 in Equation (5) includes the effect of the following system parameters:

1. Distance from the liquid surface to the impeller. C_3 is expected to be larger for smaller impeller clearances with the same liquid height. Similarly, it is also implicit that a higher liquid velocity will be required to carry the bubbles down to the impeller. This effect can be expressed as :

$$C_3 \ \alpha \ \left(H - c \right)^a$$

$$i.e. \quad C_3 \ \alpha \ H^a \left(1 - \frac{c}{H} \right)^a \tag{6}$$

and the exponent a is estimated to have a value of 1/3. When Eqn (6) is substituted into Eqn. (5) an additional $H^{1/3}$ term appears on the R.H.S of the correlation. This is of particular importance regarding scale-up, since it may explain why surface aeration is not observed to occur in large vessels at normal operating speeds (16).

2. Working pressure of the vessel. This effect was correlated by :

$$C_3 \ \alpha \ \left(\frac{p}{P_A} \right)^{-0.13} \tag{7}$$

where p is the vessel operating pressure and P_A the atmospheric

pressure. Sridhar and Potter (17) observed a reduction in the average bubble size with increasing vessel pressure. The same effec would be expected for ungassed agitation with surface aeration. At higher pressures, therefore, the net rise velocity of bubbles will be reduced and lower liquid circulation velocities required to carry them to the impeller region. Thus, surface aeration will commence at lower impeller speeds compared to atmospheric operation.

3. Liquid media. This parameter is rather complex since bubble size is also dependent on the type of liquid used, i.e. whether it is a 'pure' liquid or a solution containing electrolytes or surfactant materials. The degree of interaction between bubbles in the bulk liquid will be affected because of the different volumes of gas drawn-in at the surface. Also, the accompanying changes in the physical properties of the dispersion will have an affect on the circulation velocity of the liquid. For simplicity, it is assumed that

$$C_3 \quad \alpha \quad C_4 \tag{8}$$

where C_4 is a constant depending on the type of liquid used.

Combining Equations (6), (7) and (8) and then substituting into Equation (5) yields the following relationship for N_{SA2}, predicting the onset of surface aeration:

$$N_{SA2} = C_5 \frac{\left(T^2 H^2\right)^{1/3}}{D^2} \left(1 - \frac{C}{H}\right)^{1/3} \left(\frac{P}{P_A}\right)^{-0.13} \tag{9}$$

$$\text{where } C_5 = 0.72 \ C_4 \ U_T \tag{10}$$

The correlation of the experimental results by Equation (9) is shown in Fig. 15. The various values for C_5 are found to be 0.82 for distilled water, 0.80 for tap water and 0.62 for 0.11m K_2SO_4 solution. Equation (9) has also been used to correlate N_{SA1} which is the impeller speed at which gas bubbles are first detected. Then :

$$N_{SA1} = C_6 \frac{\left(T^2 H^2\right)^{1/3}}{D^2} \left(1 - \frac{C}{H}\right)^{1/3} \left(\frac{P}{P_A}\right)^{-0.13} \tag{11}$$

where C_6 has the values

0.476   for distilled water

0.429   for tap water

0.375   for 0.11 M K_2SO_4 solution.

In Fig.15 it can be seen that there is a slightly better fit for N_{SA1} compared to N_{SA2}. This is hardly surprising in view of the fact mentioned previously, concerning the close agreement in impeller speeds for the condition where gas bubbles were first detected near to the liquid surface and at sample point S, close to the impeller.

From Equations (9) and (1 1) it is noticed that the ratio N_{SA1} / N_{SA2}

is 0.54 for tap water and 0.6 for sulphate solution. This suggests that a large error will be incurred if the observed drop in Pou is used to estimate the onset of surface aeration. Finally, if we look at the average bubble size for the tap water case, corresponding to the states when bubbles are first observed near to the impeller and when Pou first begins to fall, then these are respectively, 0.85 mm (Fig.8) and 2.0mm (Table 1 - average for the 3 sizes of impeller). The corresponding terminal velocities estimated from Fig. 14 are 0.11 and 0.21 MS^{-1}, and the ratio between them is 0.52. This value is close to that obtained for the ratio N_{SA1} / N_{SA2} , confirming

that the average size of the bubble carried to the impeller is dependent on the impeller speed, and hence the velocity of the circulating liquid. A similar situation, however, does not apply in the case of K_2SO_4 solution,

where it is the number rather than increase in bubble size produced when the impeller speed is increased.

Conclusions

In the turbulent region $\left(Re > 10^4 \right)$, the ungassed power number, Pou, for distilled water, tap water and 0.11 M K_2SO_4 solution, exhibits a characteristic trend with increasing Re. There is first a rise to a maximum value, followed by a falling region. Increasing the impeller size and/or reducing the clearance ratio causes a steepening of the initial part of the curve. The drop in Pou was confirmed to be due to surface aeration. A two-stage process has been proposed for this, which includes an eddy-caputre mechanism for sucking-in air at the liquid surface, followed by circulatory transport of the entrained bubbles to the impeller region. Entrainment of gas bubbles first occurs at impeller speeds much lower than those which would ordinarily be detected by observing a drop in Pou. A correlation for the impeller speeds, N_{SA1} and

N_{SA2} , respectively the conditions at which bubbles are first detected in the circulating flow close to the surface, and when Pou first begins to fall, showed the ratio between them to be 0.54. When judged by the ratio of bubble terminal velocities, the value is 0.52, confirming that the average size of bubble which is carried (or recirculated) to the impeller is dependent on the impeller speed, and hence the velocity of the secondary circulating flow. For K_2SO_4 solution, on the other hand, there is an increase in the number of bubbles rather than the average bubble size. This may explain the earlier fall in Pou experienced for these systems as the impeller speed is increased (increasing liquid circulation velocity).

Acknowledgements

SYMBOLS USED

a	–	thickness of turbine blades (m)
C	–	impeller clearance (m)
d_b	–	spherical bubble diameter (m)
D	–	impeller diameter (m)
H	–	height of clear liquid (m)
N	–	impeller rotational speed $(s^{-1}$
p	–	vessel pressure MNm^{-2}
P	–	impeller power (watts)
Po	–	power number (dimensionless)
r	–	radial distance from impeller axis (m)
Re	–	Reynolds number (dimensionless)
T	–	tank diameter (m)
U_T	–	bubble terminal velocity $(ms^{-1}$
$\bar{V}$	–	average liquid circulation velocity $(ms^{-1}$
W	–	width of turbine blades (m)

Subscripts

A	–	atmospheric
SA	–	surface aeration; 1 – onset, 2 – drop in Pou
U	–	ungassed

REFERENCES

1.   Wisdom, D.J., 1974, Ph.D. Thesis, University of London.

2.   Clark, M.W. and Vermeulen, T., 1964, A.I.Ch.E. Journal 10, No.3, 420.

3.   van Dierendonck, L.L. Fortuin, J.M.H., and Vendertos, D., 1968,
       Proc. 4th Euro. Chem. Reaction Symp., Brussels, p. 205

4.   Nienow, A.W., Chapman, C.M. and Middleton, J.C., 1979, The Chem.Eng.
       Journal 17, 111

5.   Greaves, M. and Kobbacy, K.A.H., 1981, "Power Consumption and Impeller
       Dispersion Efficiency in Gas-Liquid Mixing". Paper to be presented
       at I.Chem.E. Symposium on Mixing, University of Bradford.

REFERENCES (CONTINUED)

6.   Kobbacy, K.A.H., Ph.D., Thesis, University of Bath (to be published).

7.   Nienow, A.W., Wisdom, D.J., and Middleton, J.C., 1977, "The Effect of Scale and Geometry on Flooding, Recirculation, and Power in Gassed Stirred Vessels". Paper Fl, Second European Conference on Mixing, St John's College, Cambridge.

8.   Nagata, S., Yamamoto, K., Hashimoto, K., and Naruse, Y., 1959 and 1960 Mem. Fac. Engng., Kyoto, 21 - 260 and 22 - 68.

9.   Bruijn, W.,Van't Riet, K. and Smith, J.M., 1974, Trans. Instn. Chem. Engrs. 52, 88.

10.   Brauer, H., 1979, "Power Consumption in Aerated Stirred Tank Reactor Systems", in Advances in Biochem. Eng., Vol.13, Springer-Verlag, Frankfurt.

11.   Aiba, S., 1958, A.I.Ch.E. Journal 4, No.4, 485.

12,   Holmes, D.B., Vouken, R.M., and Dekker, J.A., 1964, Chem.Eng.Sci. 19, 201.

13.   Swartzberg, H.G. and Treybal, R.E., 1968, IEC Fundamentals 17, No. 1, 1.

14.   Govier, G.W. and Aziz, K., 1972, "The Flow of Complex Mixtures in Pipes", van Nostrand Reinhold Co., New York.

15.   Haberman, W.L. and Morton, R.K., 1953, David Taylor Model Basin Report No. 802.

16.   Oldshue, J.Y., 1980, CEP, 64

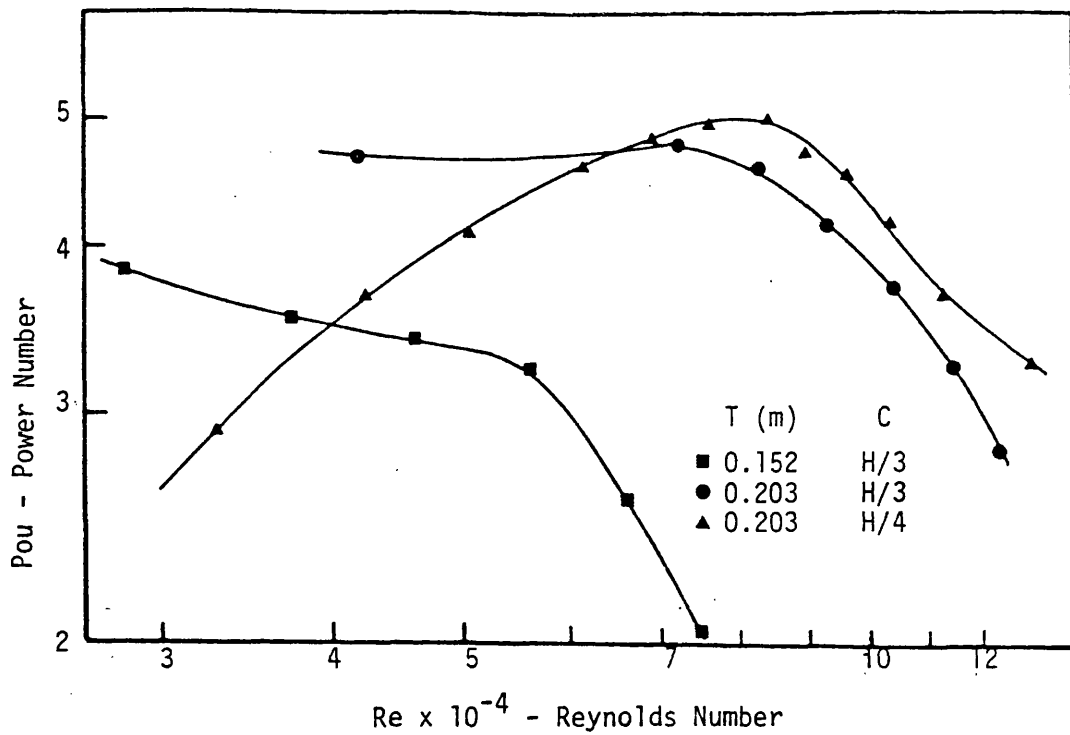17.   Sridhar, T. and Potter, O.E., 1980, IEC Fundamentals 19, No. 1, 21.

Figure 1 Effect of Tank Diameter and Impeller Clearance on Pou
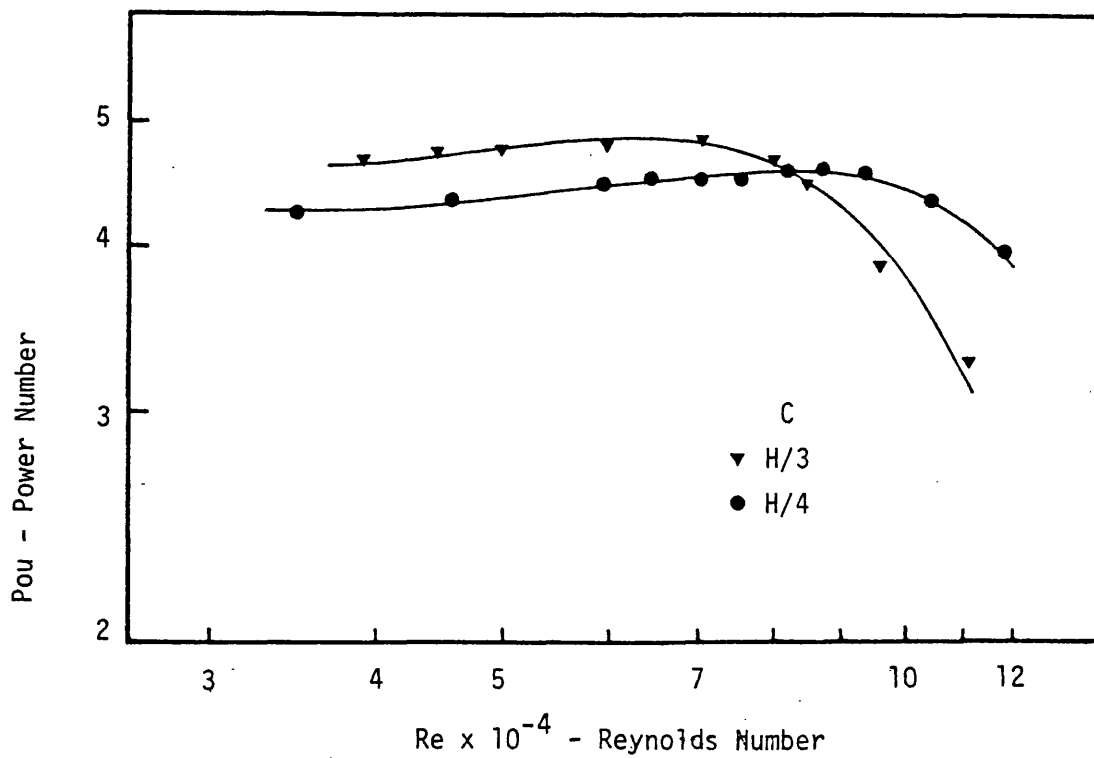(D = 0.1016 m)

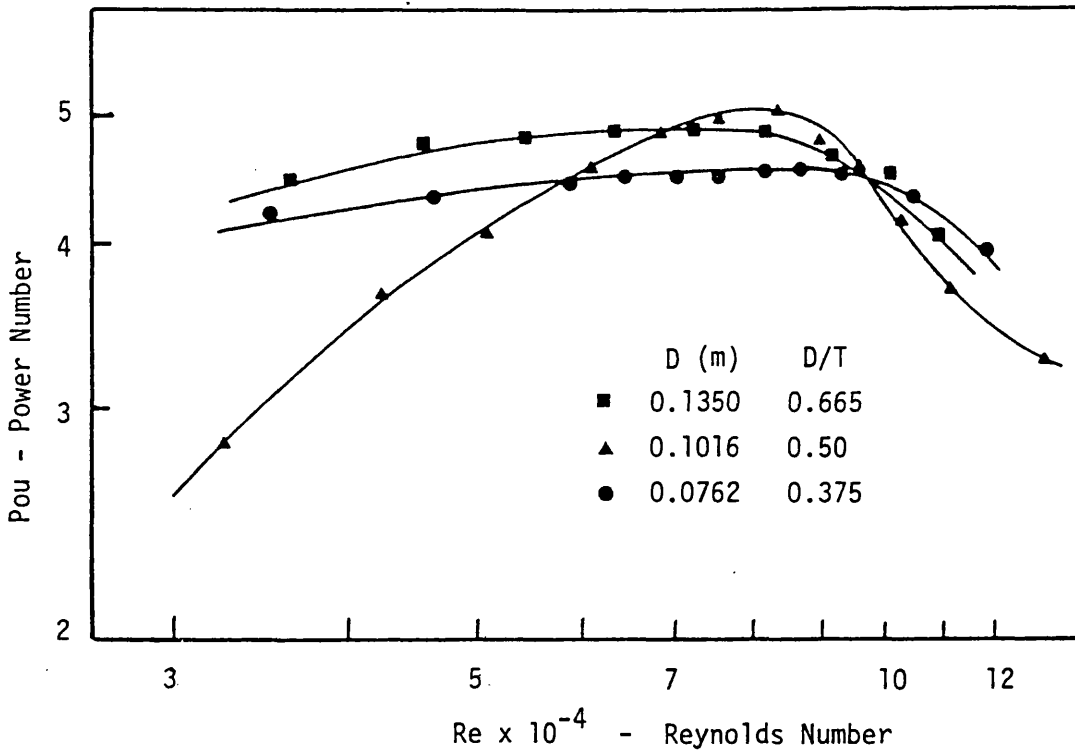Figure 2 Effect of Impeller Clearance on Pou (D = 0.0762m,T = 0.203m)

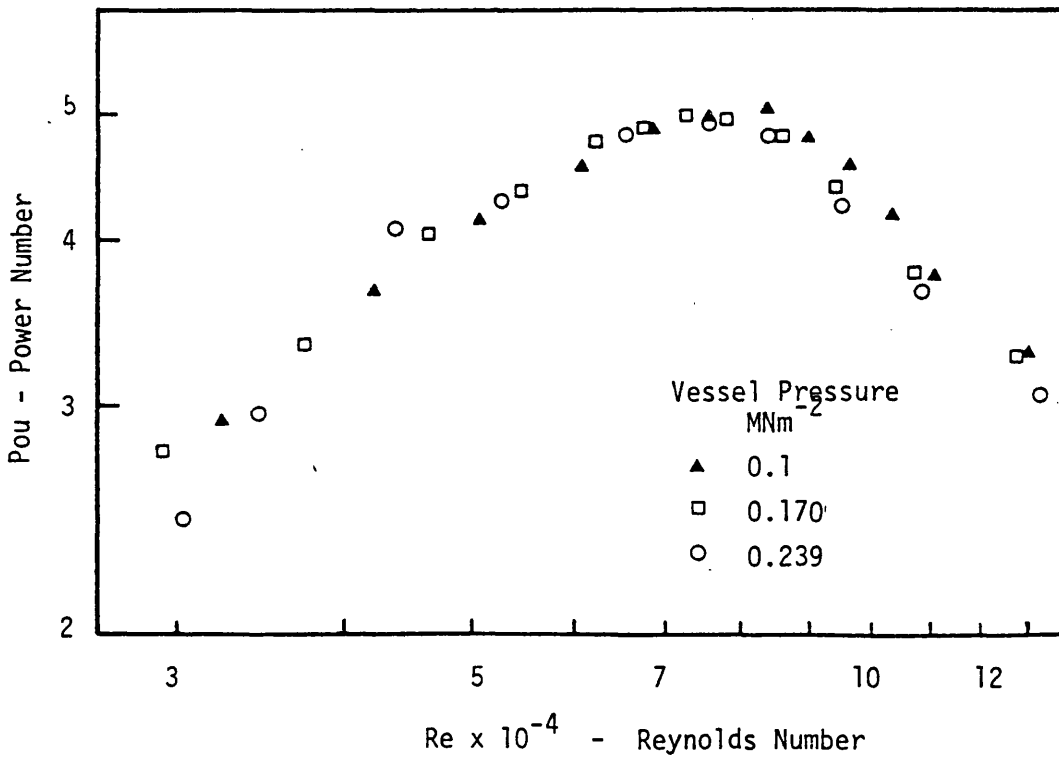Figure 3 Effect of Impeller Diameter on Pou (T = 0.203m,C= H/4)

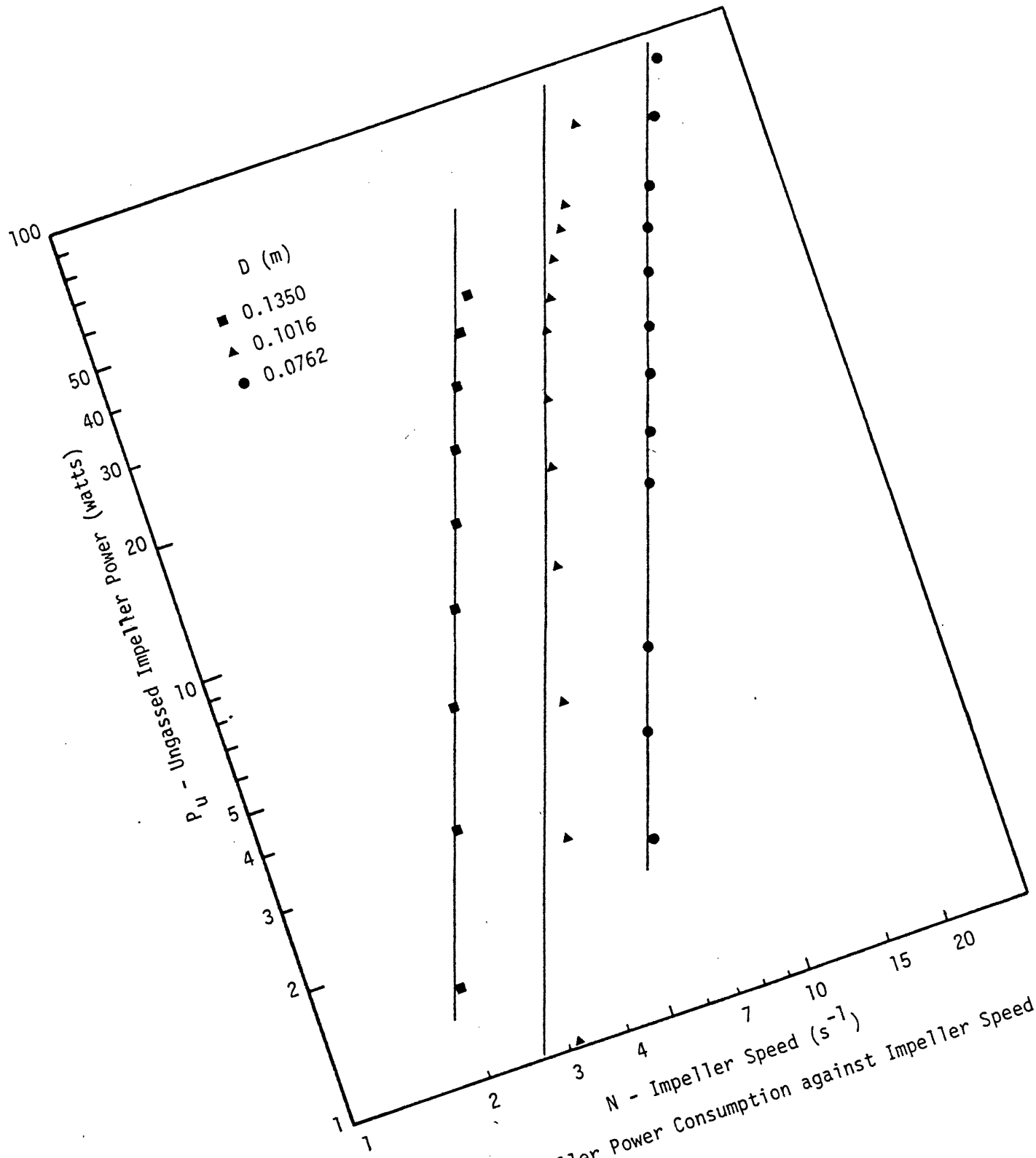Figure 5 Effect of Vessel Pressure on Pou (D = 0.1016m,T = 0.203m)

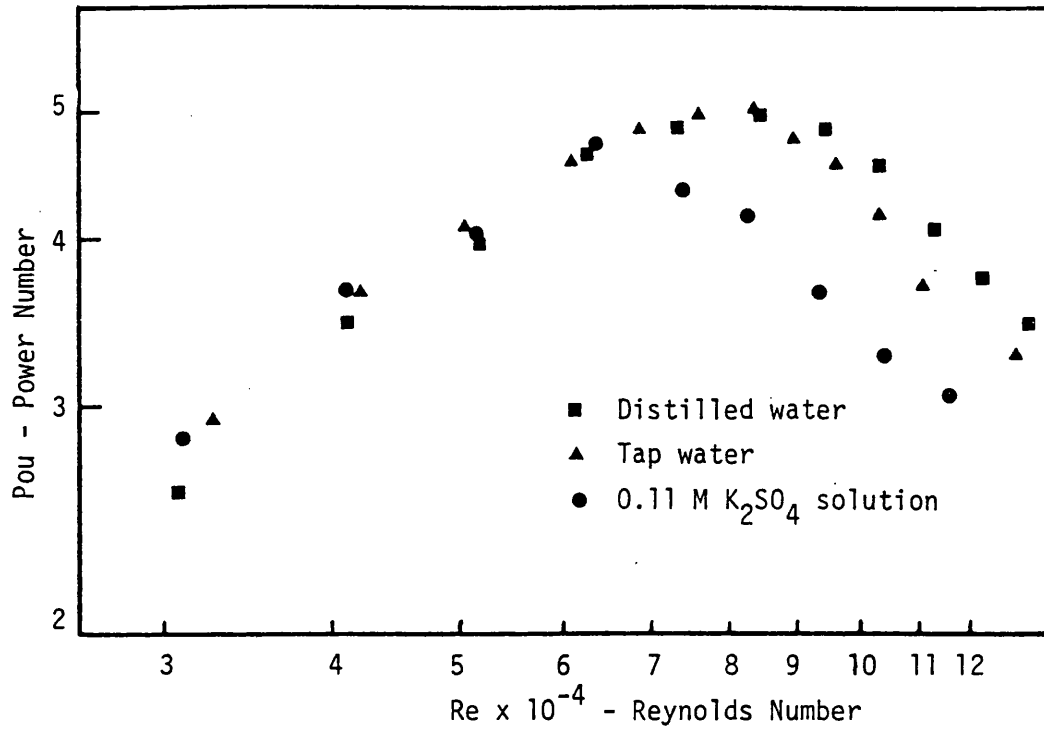Figure 4 Ungassed Impeller Power Consumption against Impeller Speed

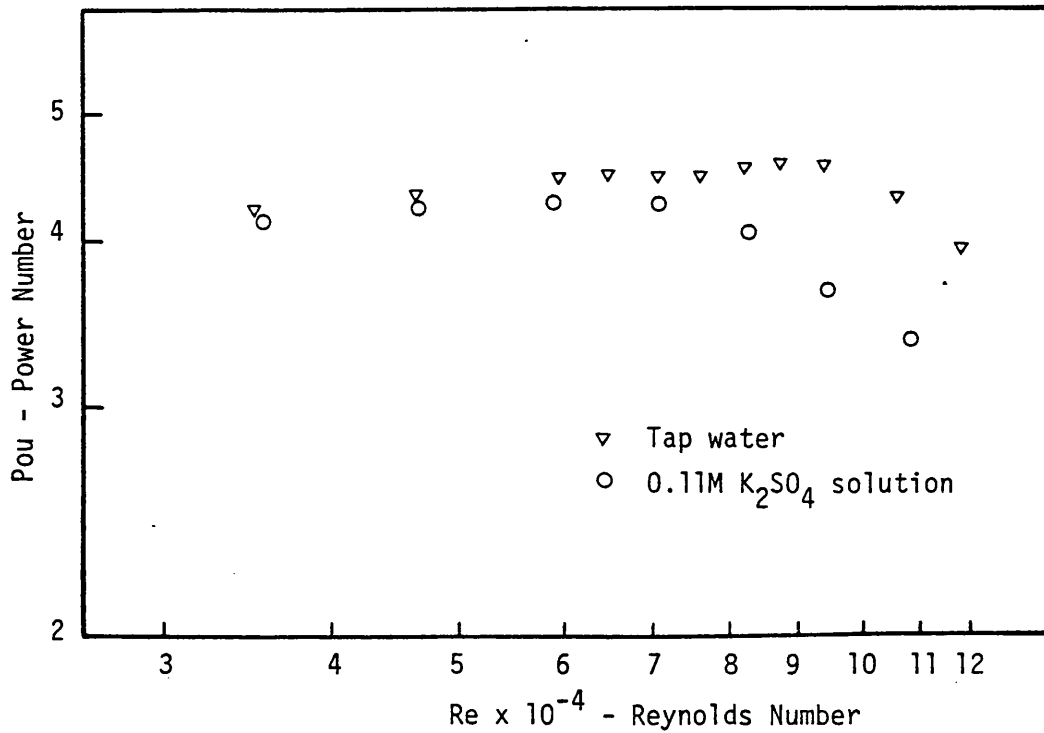Figure 6 Effect of ionic concentration on Pou (D = 0.1016m)

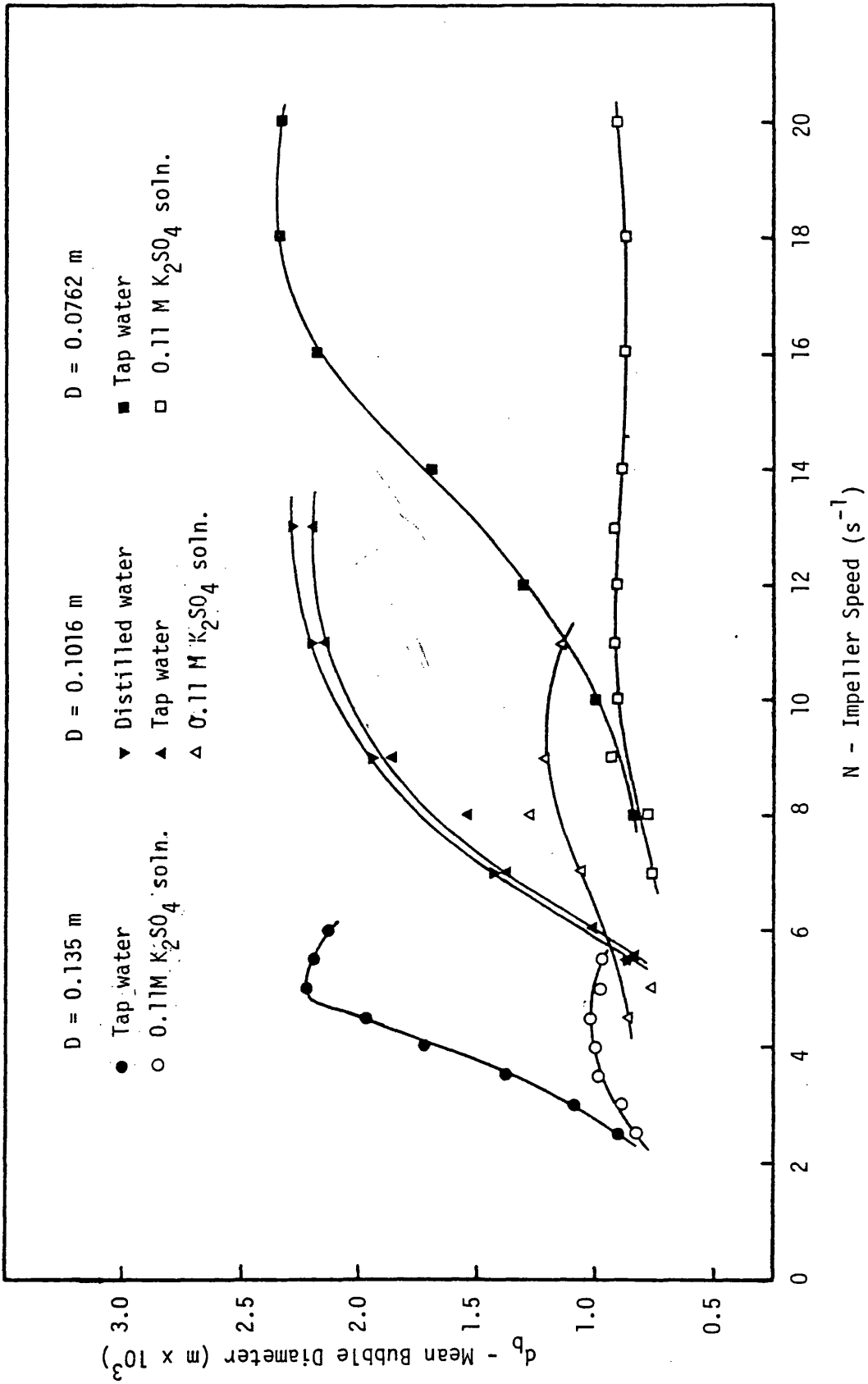Figure 7 Effect of ionic concentration on Pou (D = 0.0762m)

Figure 8 Variation of Bubble Size with Impeller Speed at Sampling Position S (Fig. 10c) in Ungassed Liquid
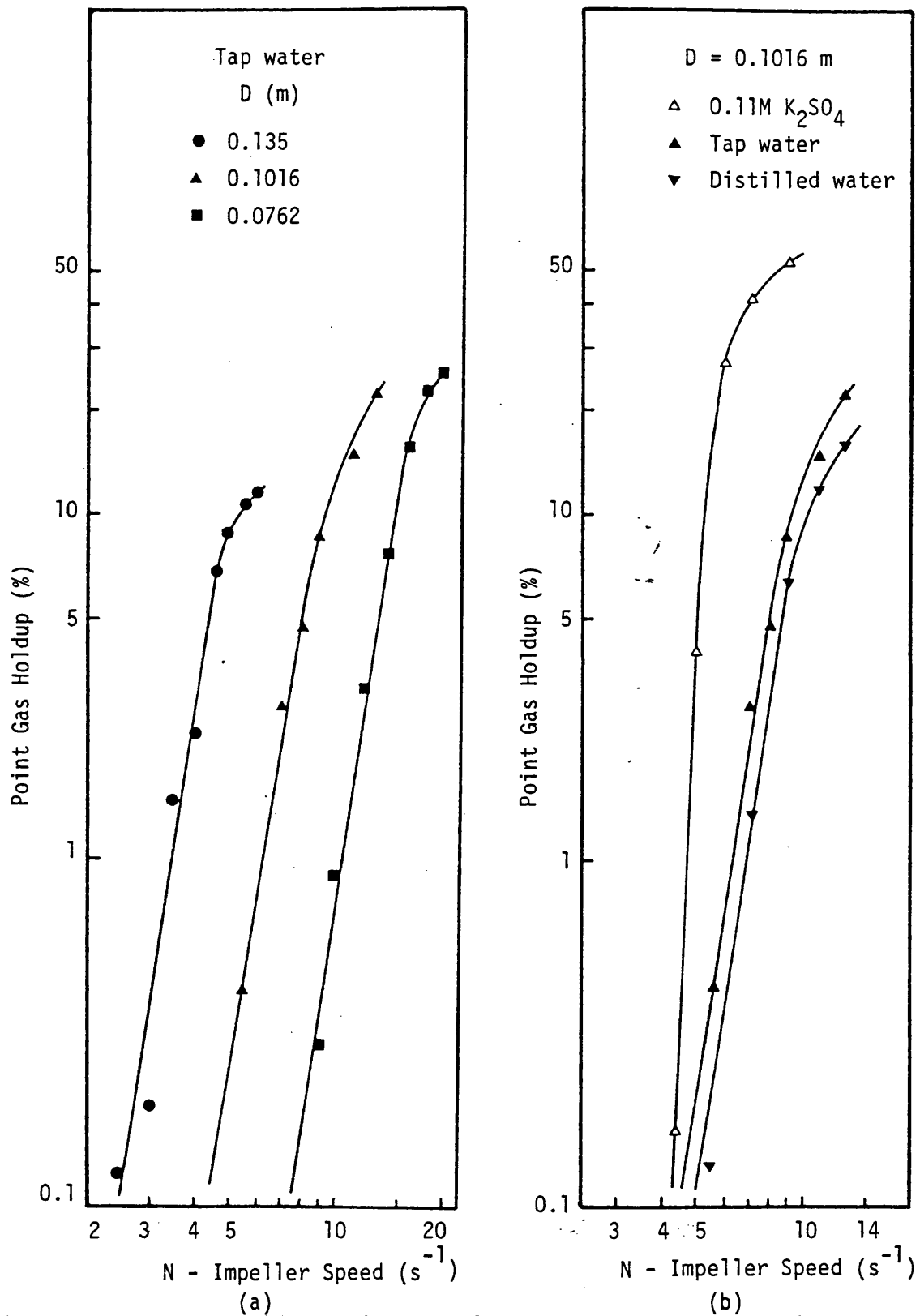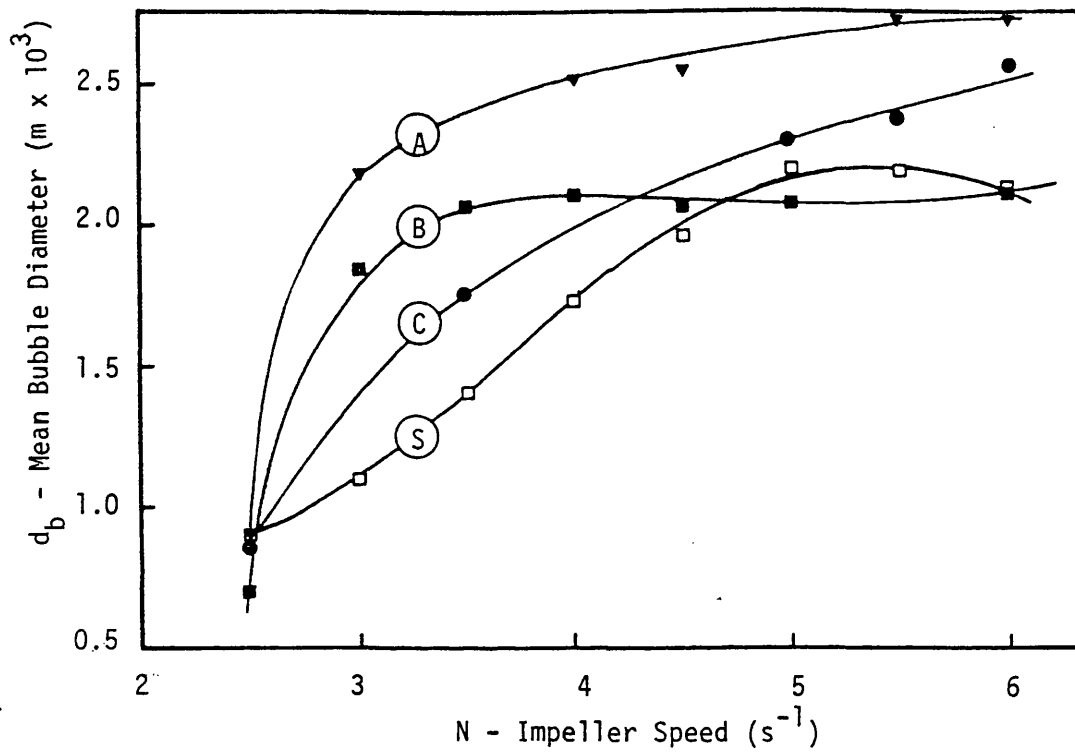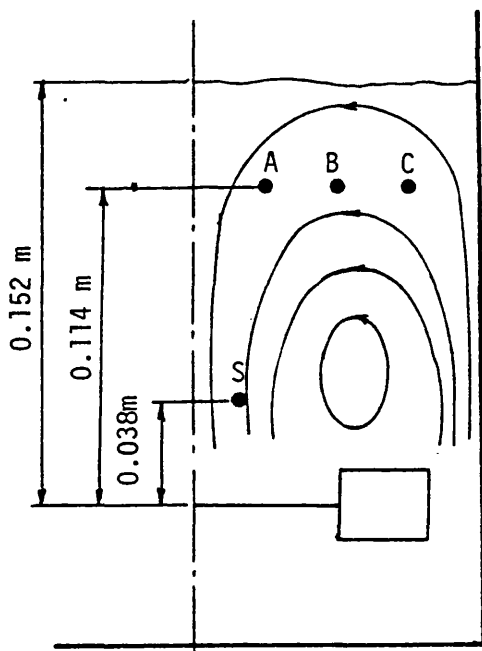
Figure 9 Point Gas Holdup against Impeller Speed at Sampling Position S
(Fig.10c) (a) Effect of Impeller Size,(b) Effect of Ionic Concentration

(a)

(c) Sampling Positions

Figure 10 Variation of Bubble Size and Gas Holdup in the Vessel at Positions A,B,C and S.
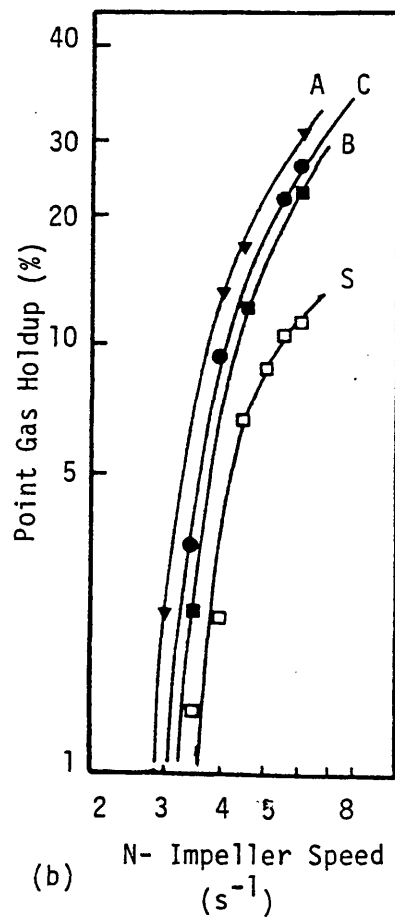
(b)

Figure 11   Schematic Representation of Vortex
Formation at Surface of Liquid in a Baffled
Vessel (8)

(a)

(b)

Figure 12 (a) Primary and (b) Secondary
Flow Circulation in Mixing Vessel (10)

Figure 13 Surface Aeration
Mechanism

Figure 14   Terminal Velocity of Air Bubbles in Tap Water as a
Function of Bubble Size

Figure 15   Correlation of Critical Impeller Speeds for Start of Surface Aeration: Eqns. (9) and (11)

POWER CONSUMPTION AND IMPELLER DISPERSION EFFICIENCY IN GAS-LIQUID MIXING
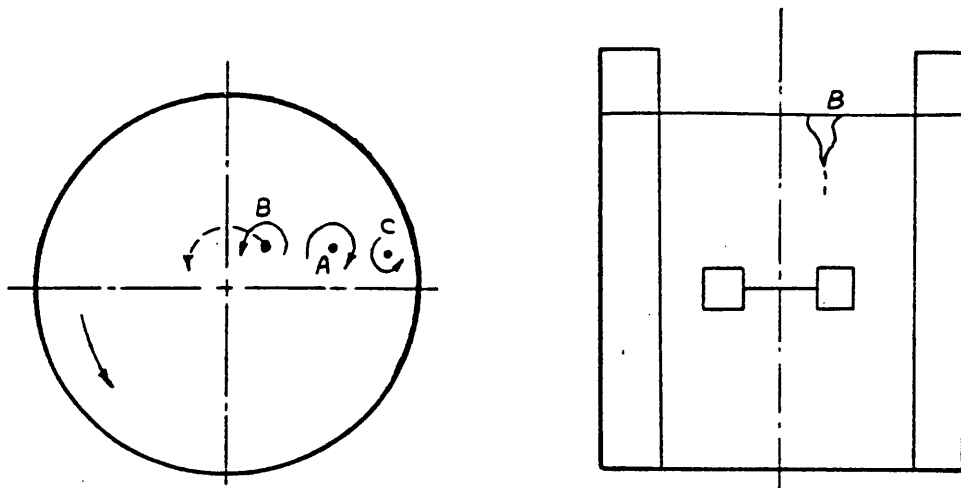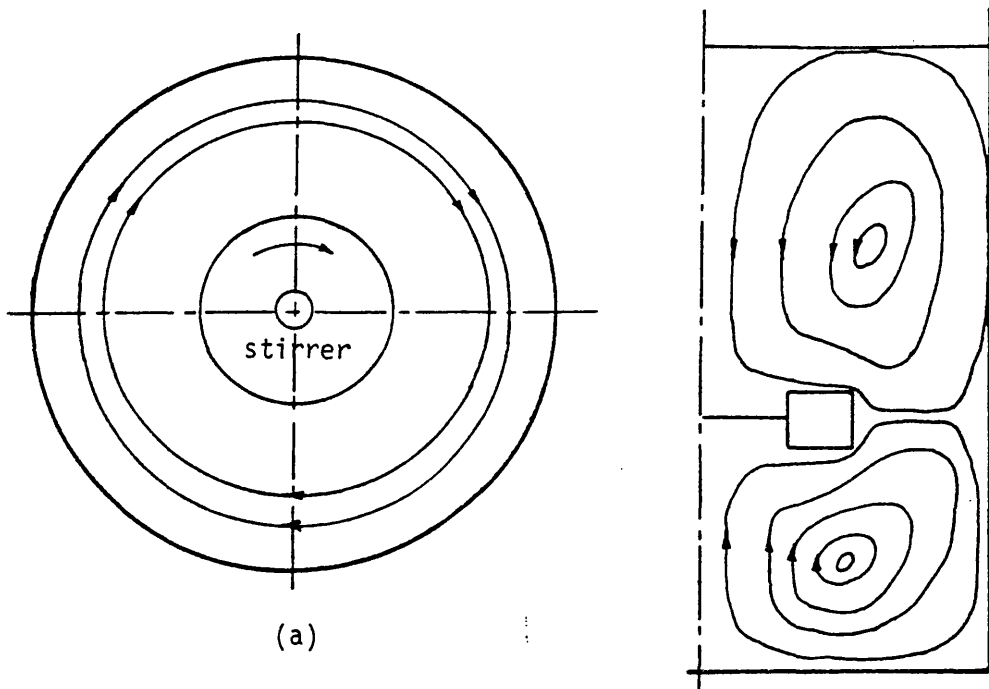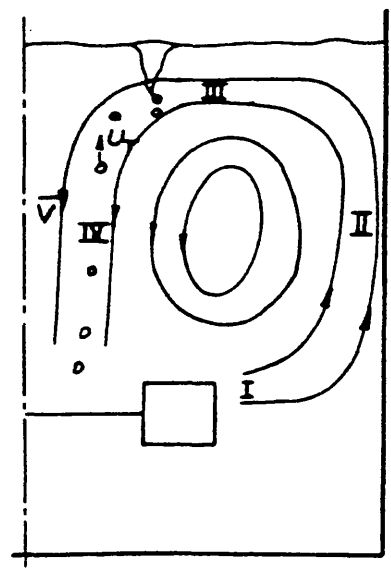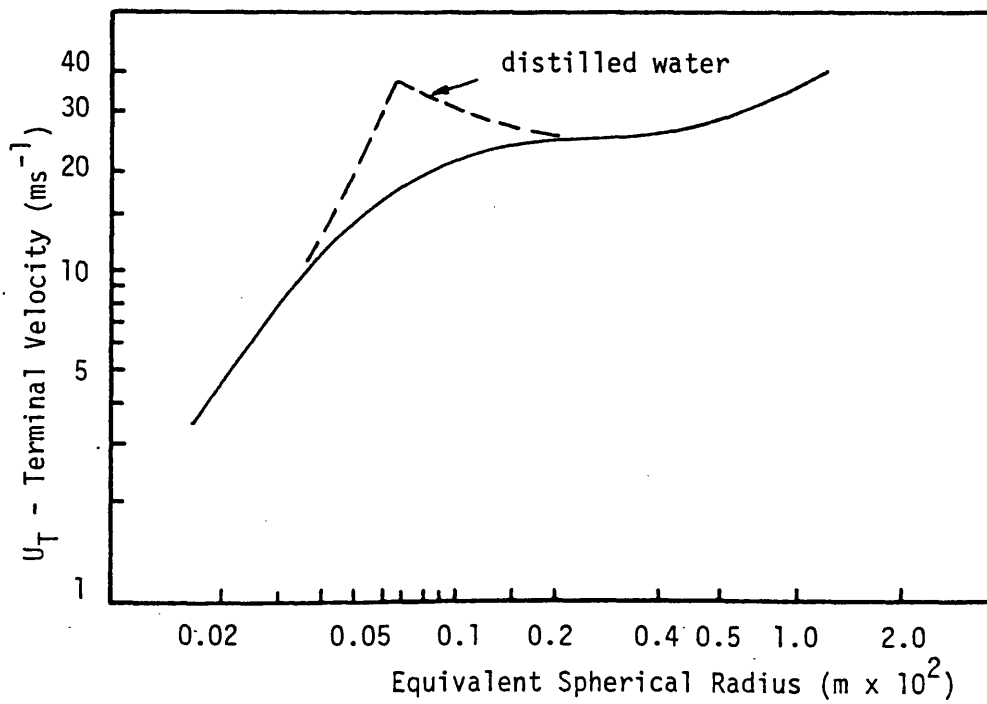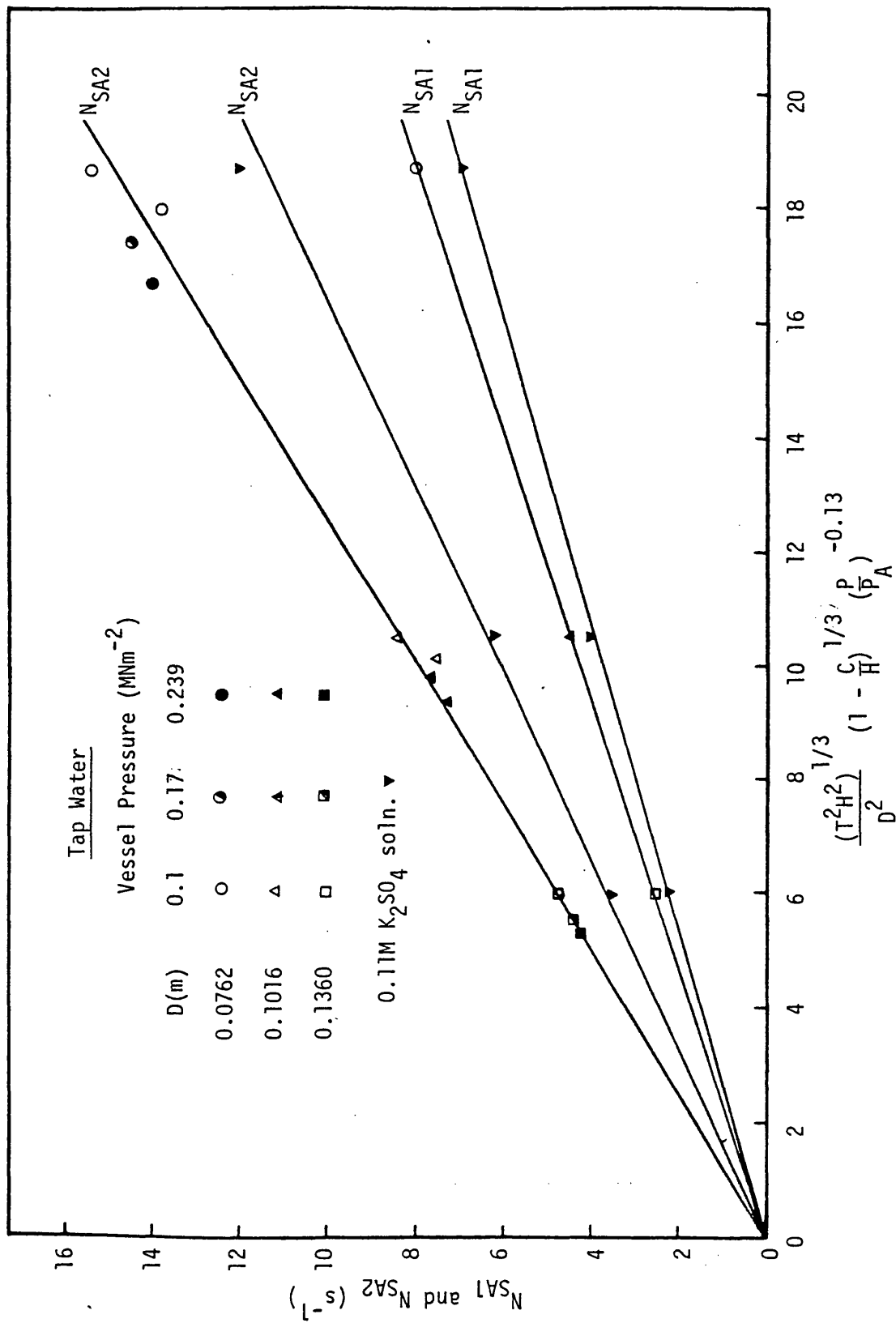
M Greaves* and K A H Kobbacy*

The gassed-power consumption in a turbine agitated vessel has been investigated over a wide range of operating conditions. A measure of impeller dispersion efficiency has been defined which can be used to distinguish the different regions of mixing. It also provides a basis for estimating the degree of flooding or recirculation. Correlations obtained enable prediction of the conditions N_{F1} and N_{R1}, and the gassed power consumption, Pg. In the efficient mixing region, predicted values of Pg are within 10% over a vessel size range of 10:1. This level of accuracy was maintained when the power correlation was generalised to cover any region of mixing.

INTRODUCTION

Disc turbine agitators are widely used to provide the necessary turbulence energy input for gas-liquid reactor vessels. The generation of interfacial mass transfer area in such systems is dependent on the mechanism of energy transfer which takes place from the turbine blades. Nienow et al (1, 6), van't Riet and Smith (2) and Bruijn et al (3), in their extensive studies of the subject, have provided a cornerstone of knowledge regarding the many physical complexities involved. There has to date, however, not been any real improvement in the method for predicting the gassed-power consumption, Pg, over that established some time ago by Michel and Miller (12). Because of its importance for scale-up and design there is a need to determine Pg in a more fundamental manner. In particular, a more precise description of the regions of mixing should be an important factor, since the different processes occurring critically affect the power characteristics.

When a turbine impeller rotates in a liquid in the absence of gas a low pressure liquid filled region, or low pressure separation bubble, forms behind the blades. Once gas is present in the system, these low pressure regions are immediately filled with gas, forming gas cavities. This leads to a rise in pressure behind the blades causing a decreased drag effect and reduction in the impeller power consumption (1,2). For disc-type turbine impellers, rotating at constant speed, three types of gas cavity have been observed (3). At low gassing rates, a vortex cavity is formed, which has no significant effect on the power consumption. At higher gas flow rates a large cavity is formed behind one of the blades. As the gas rate is increased further, the cavity grows in size to cover the blade surface, and the continuation of this process eventually leads to cavities forming behind all of the blades. Associated with the formation of each cavity there is a discontinuity or step-wise drop in impeller power, although this is less distinct in the case of the last two cavities (fifth and sixth).

* School of Chemical Engineering, University of Bath

The mechanism of gas inflow and bubble dispersion from the cavities is very important for understanding mixing and mass transfer, and these effects have been described in detail by Van't Riet (4). Gas bubbles rise to the turbine disc and are carried by the flow and pressure field to the cavity region (the large cavities are the most important from a practical operational standpoint) where coalescence occurs. Dispersion takes place at the rear of the large cavities by a random process, which is controlled by the flow instabilities and turbulence in the wake region behind the cavity.

Another important effect occurs when the impeller speed is high enough so that recirculation of gas bubbles back to the impeller region takes place. Since the total gas inflow to the cavities is now equal to that sparged into the vessel, plus that recirculated from the bulk, there is a further drop in impeller power. Figure 1 illustrates Van't Riet's et al. (5) method of calculating the external distribution coefficient, a , from gassed power curves obtained at constant speed. The alternative method of determining this quantity, which was suggested by Nienow et al. (6), is shown in Figure 2. From their recent investigations of surface aeration using a tracer gas technique, Nienow et al. (7) were also able to show reasonable agreement for values of a calculated from this data with those obtained by the other methods.

As mentioned in the foregoing discussion, there is a fundamental dependency of impeller power consumption on the cavity formation processes. These, in turn, are dependent in some measure on the mixing regime. In the work to be described in this paper the main aim was two-fold: (i) to provide a measure of impeller dispersion efficiency defining regions of recirculation, flooding and efficient mixing, and (ii) on this basis, develop an improved method for predicting impeller power consumption. In addition, a useful comparison was made between the 'coalescing' results for tap water and 'non-coalesing' results for $0.11M K_2SO_4$ solution, although a wider range of liquid properties would inevitably need to be investigated to fully satisfy industrial design requirements.

EXPERIMENTAL

Experiments were carried out in a fully-baffled flat-bottomed tank of 6 litres nominal capacity. It was equipped with a 6 blade disc turbine, and a tubular gas sparger (5 x 1.2 mm holes) was positioned centrally immediately below. For the majority of the experiments filtered mains tap water was used, but the effect of ionic concentration was also investigated in a small number or runs by using $0.11M$ potassium sulphate solution. Filtered air was used throughout. Details of the equipment used and operating conditions are given in Table 1.

On-line measurement and data acquisition was employed with the aid of a Macsym II microcomputer. This approach also permitted a significant amount of data processing to be carried out immediately, or concurrently with data acquisition. The transducers used to measure shaft torque and speed produced typically noisy signals. To improve on this situation, the signals were sampled over a fixed period of time and then averaged. In the case of speed measurement this was 5000 measurements sampled at a rate of 1000 s^{-1}, and for the torque, 4000 measurements sampled at 100 s^{-1}. The input gas rate was sampled at 100 s^{-1} for 10 seconds. The error in speed measurement was less than 0.7%. For the torque measurements, the error was a variable

quantity.   In the worst case, of low speed and small impeller diameter, the
error was about 10%.   For higher speeds, and with Re> 40,000, the error was
usually less than 5%.   The accuracy improved greatly when the larger
impellers were used and was estimated to be well within the 1% order.

TABLE 1 - Equipment and Operating Conditions

Mixing Vessel

Diameter m	0.203
Number of baffles	4
Baffle width m	0.02
Material	316 ss

Impellers	D1	D2	D3
Type	6-blade Rushton turbine		
Diameter m	0.0762	0.1016	0.135
Impeller clearance ratio C/H	1/4	1/4	1/4
Disc thickness m x 10^3	1.59	1.59	1.59
Blade thickness m x 10^3	1.59	1.59	1.00

Operating Conditions	Impeller		
	D1	D2	D3
Impeller speed rpm	300-1200	150-780	120-360
Power per unit mass (max) w/kg	13.12	11.2	5.9
Air flow rate $m^3 s^{-1}$ x 10^4		◄──── 0.8 - 3.8 ────►	
Superficial gas velocity ms^{-1} x 10^2		◄──── 0.26 - 1.231 ────►	

RESULTS AND DISCUSSION

Figure 3 demonstrates how the power number, Pou, varies with increasing
impeller Reynolds number.   Similar changes in Pou have been reported before
by Nienow et al (6) and Wisdom (8).   It is known that the fall-off in Pou
at high Reynolds numbers is caused by surface entrained air reaching the
impeller.   For the impeller clearance ratio of 1/4, these results show an
increase in the slope of the first part of the curve, when the impeller
diameter is increased to 0.1016m (D.2).   However, further increase of the
impeller size to 0.135m (D.3) causes this part of the curve to become flatter.
The point to be made here is, that the largest impeller (D3) had significantly
thinner blades than either D1 or D2.   All three impellers were otherwise
geometrically similar.   This indicates that there is a mechanical symmetry
factor influencing this initial part of the power curve.   If we look at
Figure 4, we can see the effect of increasing the impeller clearance to 1/3.
Pou now becomes almost constant prior to the onset of surface aeration.   A

similar result was also obtained for the smaller impeller (D1).. In the
fully turbulent region, therefore, a reduced value of the ratio C/D causes a
steeper rise in the initial part of the power curve. At higher Reynolds
numbers, the power number reaches its maximum value. There thus appears to
be a short range of Reynolds number over which P_{ou} is relatively constant, at
its maximum. It can be seen that the P_{ou} maximum values are between 4.5 and
5, which is an acceptable range for this type of impeller. The other
observation, concerning the effect of impeller clearance,, as shown in Figure 5,
is· that surface aeration starts at a lower impeller speed when C/H is
increased to 1/3. A similar trend is also apparent in the case of the
smaller tank. In the work that follows, impeller clearance was fixed at H/4,
as recommended by Nienow et al. (6).

Representation of Gassed Power Data

The variation of P_{ou} with Reynolds number, prior to reaching its maximum
value, or before the onset of surface aeration, should be reflected in the
measurement of gassed power consumption. An examination of the measured
power data showed this to be a multiplying effect rather than an additive one.
In other words, ·in order to be able to study the effect of adding gas to the
system, the proper representation of impeller power consumption should be
P_g/P_u, i.e. P_{og}/P_{ou}. Also, there is the problem of surface aeration which
can occur at higher speeds. Nienow et al. (7) have shown that surface
aeration decreases very rapidly with increase in sparged gas rate, even at
low gas loads and high power input. Therefore, it is reasonable to assume
that P_{ou} would have maintained its value at $P_{ou_{max}}$, and that the proper
representation for gassed power consumption at impeller speeds greater than
N_{SA} would be $P_{og}/P_{ou_{max}}$.

To demonstrate these effects, the data for impeller D2 for a constant
gas rate of 3.61×10^{-4} m^3 s^{-1} are used. The most drastic changes in P_{ou}
were observed for this impeller size. In Figure 5, the minimum in the curve
of $P_{og}/P_{ou_{max}}$ is shifted to the right relative to the minimum in the
P_{og}/P_{ou} curve, and this leads to an underestimate of N_{Fl}. This is also clear
in Figure 6 where, at lower gas loads, the flooding point may disappear.
Also in Figure 5, the maximum is not detected in the curve of P_{og}/P_{ou} against
Fl since P_{ou} was falling due to surface aeration. Curve A in Figure 5
demonstrates the presence of both the minimum and maximum when plotted in the
manner indicated, as shown by Nienow et al. (6). When C/H = 1/3 or 1/4
with $D \leqslant T/3$, however, the change in P_{ou} for $N < N_{SA}$ is only small. Under
this condition therefore, a plot of P_{og} against Fl would be a satisfactory
way to represent the gassed power data. In their case, when they used
C/H = 1/2, where the onset of surface aeration was such that $N_{SA} < N_{Fl}$ (first
point of flooding), this represents a false flooding point condition. Thus,
where a smaller condition of C/H and D/T prevails, the onset of surface
aeration will be moved closer to the recirculation region.

Flooding, Efficient Mixing and Recirculation Regime

The power measurements were planned so that the gassed-power could be
obtained for conditions of constant speed and constant gas flow rate,
covering a wide range of these parameters. In addition, the ungassed power
was also determined at each speed condition. These results, for the three
sizes of impeller used, are presented in the form of P_{og}/P_{ou} against aeration
number in Figures 7, 8 and 9.

Selecting a line of constant gas flow rate, as shown, for example, in

in Figure 9, one can see the different regimes of gas mixing which have been described by Nienow et al. (6). The region lying between the minimum and maximum condition on this curve is called the efficient mixing region (zone), where all of the sparged gas passes through the impeller just once (8). To the right of the minimum is the flooding region, and to the left of the maximum the recirculation region. On the other hand, if constant speed curves are examined then, as shown for the small impeller (D1) in Figure 7, the lines connecting the minima and maxima conditions are virtually coincident with a single curve, identified as the efficient mixing line (EML). By comparison, the power curves for the D2 impeller shown in Figure 8 represent an intermediate situation.

In the efficient mixing region (EMZ in Figure 9), the power consumed by the impeller decreases in a smooth continuous fashion as the speed **decreases** at a constant gas flow rate, but in a stepwise manner when the gas rate increases at a constant impeller speed. In principle, the changes in impeller power characteristics in this region are explained by the theories of cavity formation described by Bruijn et al. (3). Thus, the smooth drop in power which is observed in Figure 9 for the large D3 impeller, as the impeller speed decreases, is attributed to enlargement of the gas cavities. However, when the supply of gas to the impeller is increased, another large cavity is formed causing a step change in power. Since the rate of change of power with speed is greatest for the smaller impellers (Figures 7,8) this tends to make the power curves look continuous, obscuring the step change in power which obviously occurs with the formation of large cavities.

The efficient mixing line (EML) depicted in Figures 7, 8 and 9, defines a condition without recirculation (3), and it is constructed by drawing a line through the centre of the efficient mixing zone. This line, for the smallest impeller size (D1 = 0.0762, Figure 7), was found to be almost identical with results obtained using the same size of impeller in a large square tank (3), as shown in Table 2. The lines of constant speed to the left of the efficient mixing zone lie in the recirculation region. When no gas is sparged to the vessel, these curves intersect the ordinate at a value which is less than 1.0. This is due to surface aeration. Curves lying to the right of the efficient mixing region are in the flooded region. A flooded condition can in fact occur with any number of cavities formed on the blades, even with a clinging cavity (e.g. at the lowest gas rate condition in Figure 9).

The mechanism of flooding described by Nienow et al. (6) seems to be suitable, though its possible occurrence under different cavity formation conditions needs further clarification. Evidently the process of gas inflow to the cavities plays an important role. At low impeller speeds only a small fraction of the sparged gas coalesces with the gas cavities and the rest flows past the impeller without being dispersed. With continual increase of impeller speed at constant sparging rate, more of the gas coalesces with the cavities, causing a reduction in the power. The flooding point can therefore be described as the condition when all of the sparged gas coalesces with the cavities. Further increase of the impeller speed will not alter the total rate of gas coalescence with the cavities, which will remain at its maximum, i.e. the sparged gas rate, but because of hydrodynamic changes the size of cavity is reduced, causing the power number to increase. This trend will continue in the efficient mixing zone until further supplies of gas become available. This occurs when the impeller speed is high enough to cause recirculation of gas bubbles back to the impeller and a further reduction then takes place.

. Further increase in the sparging rate, after the gas cavities have been formed, will cause the impeller to flood. This is the special case of flooding referred to by Bruijn et al. (3), and it defines the lower limit of the efficient mixing zone (EMZ). At this condition the EMZ narrows sharply so that it practically coincides with the EML. A similar effect occurs at the upper section of the EMZ. This is due to the sharp change in power associated with the formation of clinging cavities (3); a fact which may also explain the sharp peak marking the onset of gas recirculation at low gas rates (6).

TABLE 2 - Comparison of Pg/Pu_{max} for large and small tank size (D = 0.076m)

$Fl \times 10^2$	Small Tank	Large Tank (3)
0.01	0.87	0.90
0.02	0.675	0.71
0.03	0.52	0.54
0.04	0.47	0.46

Average difference 3%

Speed for Onset of Recirculation N_{R1}

If the average circulation velocity of the liquid in the bulk of the tank becomes high enough to carry gas bubbles back to the impeller region, then this would define a condition for the onset of gas recirculation. Holmes et al. (9) have shown that the average circulation velocity in an ungassed tank, away from the impeller zone, can be estimated from:

$$\bar{V} = C \frac{ND^2}{T} \tag{1}$$

There is, of course, the question as to whether this applies to the gas-liquid case. Examination of our data showed that the ratio of power supplied by the impeller to that supplied by the sparged gas was about 7 for the largest impeller, and at the same highest gas flow rate for the smallest impeller, it had a value of 18. For lower gas rates, the ratio had a much higher value. The liquid flow pattern is consequently mixer-controlled (10), and the addition of gas does not have a significant effect on the liquid flow pattern. Therefore, Eqn (1) still applies.

As a first approximation, to define correlating parameters, a reasonable assumption concerning the necessary condition for the onset of recirculation is:

$$\bar{V} > U_T \tag{2}$$

where U_T is the bubble terminal rise velocity. This assumption is based on the observation that the absolute rise velocity of a bubble in a flowing liquid is equal to the vector sum of the bubble's rise velocity and the local absolute velocity of the liquid (11). Hence, from Equations (1) and (2) we can write that:

$$N_{R1} \propto \frac{T}{D^2} \qquad (3)$$

where the constant of proportionality will be a function of bubble size. Introducing the aeration number to account for the effect of gassing rate, then plotting N_R against (T/D^2) at constant Q and N_R against $Q/N_{R1}D^3$ at constant D in a log-log manner, we find:

$$N_{R1} \propto \left(\frac{T}{D^2}\right)^{1.12} \left(\frac{Q}{N_{R1}D^3}\right)^{0.15} \qquad (4)$$

On rearrangement and correlation with experimental data this gives:

$$N_{R1} = 0.57 \left[\frac{T^{0.97} Q^{0.13}}{D^{2.34}}\right] \qquad (5)$$

The correlation includes the tank dimension, although it was not a variable in our experiments. However, it does show reasonable similarity with the correlation presented by Nienow et al. (6):

$$N_{R1} = 1.5 \left[\frac{T \, Q^{0.2}}{D^2}\right] \qquad (6)$$

which was obtained from measurements on a range of tank diameters. The constant of proportionality in Equation (5) was found to have a lower value for electrolyte solutions, which confirms its dependency on average bubble size.

Impeller Dispersion Efficiency

It was explained previously that an efficient zone of mixing is established when all of the sparged gas coalesces with, and is dispersed from, the cavities behind the impeller blades. When recirculation occurs, more gas is transported from the bulk of the tank to the impeller, and the rate of gas coalescence with the cavities then exceeds the sparging rate. In the flooding region, the gas cavities are only able to capture part of the sparged gas, while the rest flows more or less vertically to the surface without being dispersed. As a measure of the dispersion performance of the impeller in the flooding region, the external distribution coefficient, a , defined by Van't Riet et al. (5), is not sufficient. Instead, an impeller dispersion efficiency, η , is defined such that:

$$\eta = \frac{\text{Rate of gas coalescence with impeller cavities}}{\text{Rate of gas sparging}} \qquad (7)$$

where

$\eta = 1$ in the efficient mixing region

$\eta < 1$ in the flooding region

$\eta > 1$ in the recirculation region

Referring now to Figure 10, if we select a point in the recirculation region (point 2), i.e. lying to the left of the efficient mixing line, the sparged

gas rate is then Q_2. However, because of gas recirculation the power consumption is equivalent to a condition where the rate of coalescence with the cavities is equal to a gas rate Q_1. Hence:

$$\eta_2 = \eta_R = \frac{Q_1}{Q_2} > 1 \qquad (8)$$

where $\quad \eta_R = a + 1$

Similarly, for point 3 in the flooding region, where the sparged gas rate is Q_3, the rate of coalescence with the cavities is only equal to Q_1, and:

$$\eta_3 = \eta_F = \frac{Q_1}{Q_3} < 1 \qquad (9)$$

All of the experimental results in the recirculation region were used to determine a correlation for η_R in terms of D, Q and Fl. The values of η_R calculated from Equation (8), when plotted against Fl on log-log coordinates, gave a parallel series of lines for different Q. From this the impeller efficiency in the recirculation region was found to be:

$$\eta_R = C_1 \left(D^{1.66} Q^{2.2} (Fl)^{2.53} \right) \qquad (10)$$

and on rearrangement:

$$\eta_R = C_1 \left[\frac{N^{2.53} D^{5.93}}{Q^{0.33}} \right] \qquad (11)$$

This equation does not contain the tank dimension. However, from the definition of η_R, $\eta_R \to 1$ when $N \to N_{R1}$. By substituting $\eta_R = 1$ and $N = N_{R1}$ in Equation (11) this gives:

$$N_{R1} = C_2 \left[\frac{Q^{0.13}}{D^{2.34}} \right] \qquad (12)$$

Equations (5) and (12) are similar except for the term $T^{0.97}$. It is important to emphasise, however, that while Equation (5) employed only the data corresponding to the onset of recirculation, Equation (11) is based on all of the data in the recirculation region. To account for the tank dimension in Equation (11) we include T raised to the power (0.97 x 2.53) in the denominator. Thus the correlation for η_R has the general form:

$$\eta_R = 4.13 \left[\frac{N^{2.53} D^{5.93}}{T^{2.45} Q^{0.33}} \right] \qquad (13)$$

Figure 11 shows that the results are well correlated by Equation (13) within $\pm 10\%$. The data of Van't Riet et al. (5) for two different sizes of impeller are also shown in Figure 11, and it can be seen that the trend is the same, except that the graph is displaced upwards by 0.7. It is of interest to note that their results, for the smaller impeller size without recirculation, are identical to ours (see Table 2). In their experiment, however, they measured the power consumption with recirculation using an impeller clearance of T/2 and an increased liquid level to prevent surface entrainment. This suggests that the rate of gas recirculation in the bottom half of the tank may possibly have been increased because of the increased impeller clearance. It is difficult to explain this point which contradicts Nienow's et al (6) finding.

A similar procedure for the flooding region results provided a correlation
for η_F as follows:

$$\eta_F = C_3 \left[\frac{N^{2.53} D^{4.4}}{Q^{0.73}} \right] \qquad (14)$$

Now, since $\eta_F \rightarrow 1$ when $N \rightarrow N_{Fl}$:

$$N_{Fl} = C_4 \left[\frac{Q^{0.29}}{D^{1.74}} \right] \qquad (15)$$

The correlation of this condition given by Nienow et al. (6) is:

$$N_{Fl} = 4 \left[\frac{Q^{0.5} T^{0.2}}{D^2} \right] \qquad (16)$$

There is some measure of similarity between these two equations, and to account
for the effect of tank diameter in Equation (14) we include T raised to the
power (0.2 x 2.53) in the denominator. Thus:

$$\eta_F \propto \frac{N^{2.53} D^{4.4}}{T^{0.5} Q^{0.73}} \qquad (17)$$

In order to simplify treatment of the data in Fig. 12, the data is
represented by two straight lines, such that:

$$\eta_F = 0.4A \qquad \text{for } A \leqslant 1$$

$$\qquad (18)$$

and $\quad \eta_F = 0.25 + 0.26 A \quad$ for $A > 1$

where $\quad A = \dfrac{N^{2.53} D^{4.4}}{T^{0.5} Q^{0.73}}$

For the second condition of Equation (18), by putting $\eta_F = 1$ and $N = N_{Fl}$,
we obtain:

$$N_{Fl} = 1.52 \left[\frac{T^{0.2} Q^{0.29}}{D^{1.74}} \right] \qquad (19)$$

Also shown on Figure 12 are some estimated values of η_F from Nienow's et al.
(6) Pog data for a 0.61m tank, which indicates a reasonable measure of
agreement.

To summarise this aspect on impeller dispersion, then if η_R (Equation 13)
and η_F are calculated for certain points of operation, they will satisfy the
conditions given in Table 3.

Impeller Power Consumption

The previous analysis has shown that the impeller power consumption depends
on the region of mixing. In all previous correlations presented in the
literature, however, there has not been any attempt to discriminate between
these regions. The most popular, and long-standing, correlation of Michel

TABLE 3 - Values of Impeller Dispersion Efficiency defining Regions of Mixing

Impeller Dispersion Efficiency	Mixing Region
$\eta_R > 1$	any point in the recirculation region
$\eta_F < 1$	any point in the flooding region
$\eta_R \leqslant 1$ and $\eta_F \geqslant 1$	any point in the efficient mixing zone (EMZ)

and Miller (12) takes the form:

$$Pg \;=\; C\left(\frac{P_u^2\ ND^3}{Q^{0.56}}\right)^{0.45}$$

where C is 0.83 for non-foaming liquids (13) and 0.812 for both ionic and non-ionic solutions (14). It has never been possible to achieve better than $\pm$ 20% accuracy for this correlation with experimental results (12,13,14). The degree of scatter of the results on this basis is not due to measurement errors, but primarily because the different regions of mixing have been ignored. Moreover, any correlation of this type is also dependent on P_u, which we have shown to be a function of impeller clearance.

In this study we have attempted to correlate the power consumption specifically for the efficient mixing region, since, for this operating condition, it depends solely on the cavity formation. N, D and Q were therefore selected as controlling parameters. The exclusion of T as a correlating parameter implies that any gas which is recirculated for a condition $N < N_{R1}$ is neglected. To attempt to produce a correlation of these parameters on a log-log plot will make the result statistically biased. For example, it is somewhat difficult to find enough experimental points that have exact values of N and Q for different values of D. Instead, multiple regression analysis was used based on the method of least squares. The model is therefore of the general form:

$$Pg \;=\; aN^p D^q Q^r$$

All of the power measurements in the efficient mixing zone for the three sizes of impeller were used. The result obtained is:

$$Pg \;=\; 1007\left[\frac{N^{3.33}\ D^{6.33}}{Q^{0.404}}\right] \tag{20}$$

As shown in Figure 13, Equation (20) provides a good fit of the data, with an accuracy better than $\pm$ 10% over the whole range. The scatter of the results

is due to two main factors.   First, the efficient mixing region is best described by a zone rather than a single line, and secondly, because of measurement error.   Some data of Figureido's (15), which she obtained on 0.38 and 0.91m tanks, is also included in Figure 13.   There is generally excellent agreement with Equation (20), but in the case of her 0.91m tank, the results can be seen to lie above the line at low impeller speeds, and below it at high impeller speeds.   This is to be expected, since these measurements were obtained in the flooding and recirculation regions respectively.

In order to calculate the power requirement in the flooding and recirculation regions it is necessary to make use of the definition of impeller efficiency, in Equation (7).   Thus, the actual rate of coalescence with the gas cavities in these regions is ηQ.   Therefore, by replacing Q in Equation (20) by ηQ, a general equation results which can be applied to any region of mixing:

$$Pg = 1007 \left[\frac{N^{3.33} D^{6.33}}{(\eta Q)^{0.404}} \right] \qquad (21)$$

where the various conditions on η are defined in Table 4 below.

TABLE 4 - Conditions on Impeller Dispersion Efficiency for Calculation of Pg From Equation (21)

Impeller Dispersion Efficiency	Region of Mixing
$\eta = 1$	$N_{F1} \leqslant N \leqslant N_{R1}$
$\eta = \eta_F$	$N < N_{F1}$ defined by Eqn. (18)
$\eta = \eta_R$	$N > N_{R1}$ defined by Eqn. (13)

N_{R1} and N_{F1} are obtained from Eqns. (5) and (19), respectively

The gassed-power measurements shown in Figure 13 cover a range from about 2 watts up to 3000 watts.   A further comparison is made with the results of Pharamond et al. (16), who reached a maximum power of 0.74kw, and Pollard (17), who reached a maximum power of 6.06kw.   Pharamond et al. used a 1.0m tank with D/T = C/H = 1/3.   We have estimated the measured power from their graphs, and the corresponding values of η and Pg calculated by the method described in this paper, are presented in Table 5.   The average error in predicting the power is 4%.   Pollard's detailed power measurements on a 1.81m tank with D/T = C/H = 1/3, are used to compare the observed and predicted values of N_{F1} and N_{R1}, as shown in Table 6.   From inspection of the P_{og}/P_{ou} values in the table

TABLE 5 - Predicted gassed power compared with Pharamond's et al.[16] measured data for 1.0m tank (Q = 8.334 x $10^{-3}m^3s^{-1}$).

N rps	Pg measured watts	η +	Pg* predicted watts	% difference
1.66	50	0.36	51	2.0
2.0	80	0.626	76	4.8
2.5	140	0.912	137.6	1.7
3.0	280	1.0	243	13.2
3.5	425	1.0	406.6	4.3
3.7	505	1.0	489.3	3.1
4.0	630	1.0	634	0.6
4.2	740	1.056	730	1.4

+ Calculated from Eqns. (5), (13), (18), (19)
* Calculated from Eqn. (21)

TABLE 6 - Check on predicted values of N_{F1} and N_{R1} for 1.81m tank

$N\ s^{-1}$ \ $Q m^3 s^{-1}$	Pog/Pou +			
	0.0066	0.0109	0.0183	0.032
0.75	0.95	0.63	0.63	0.685
1.07	0.88	0.77	0.634	0.56
1.34	0.924	0.763	0.59	0.59
1.57	0.92	0.86	0.618	0.574
1.86	0.866	0.88	0.616	0.523
2.15	0.866	0.85	0.684	0.51
2.51	0.88	0.817	0.688	0.508
N_{F1} *	0.96	1.11	1.29	1.52
N_{R1} **	1.72	1.84	1.96	2.113

+ Pollard (17)
* Calculated from Eqn. (19)
** Calculated from Eqn. (5)

it can be seen that there is a fair measure of agreement. It.is not possible
to draw any firm conclusions from this though because of the relatively small;
number of data points available to accurately define the maxima and
minima.   Tables 7, 8 and 9 demonstrate the values of impeller
dispersion efficiency and the accuracy with which the impeller power is
predicted.   Overall, the average error in predicting the power is about 13%.
It can be seen that most of the measured power values are higher than those
predicted.   This may, in part, be attributed to the fact that the sparger
was set some distance below the impeller, causing some .of the gas to escape
capture.   Also, the gas flow rates in Pollard's study were corrected to the
pressure condition prevailing near to the impeller.   These values were used
without adjustment and, if corrected, could improve the accuracy of prediction
to about 10%. The uncorrected values have been employed here though to facili-
tate direct comparison with the original reference source.

Figure 14 shows the results for all regions of mixing correlated by the.
generalised power relationship of Equation (21).   There is generally good
agreement, the dashed lines representing limits of $\pm$ 10 per cent.

TABLE 7 - Comparison of Predicted and Measured Power Consumption for 1.81m
Tank, with $Q = 0.0066 \ m^3s^{-1}$

N s^{-1}	Pg^+ measured watts	η^*	Pg^{**} predicted watts	$\%$ difference
0.4	25	0.123	34	36
0.75	176	0.645	143	18.7
1.07	472	1.0	393.6	16.6
1.34	970	1.0	832.7	14.2
1.57	1550	1.0	1411	8.9
1.86	2430	1.21	2292	5.7
2.15	3840	1.75	3204	16.5
2.51	6060	2.59	4575	24.5

Average error of predicted power = 17.6%

+ Pollard (17)
* Calculated from Eqns. (5), (13), (18), (19)
** Calculated from Eqn. (21)

TABLE 8 - Comparison of Predicted and Measured Power Consumption for 1.81m
tank, with Q = 0.0183 m³s⁻¹

N s⁻¹	Pg⁺ measured watts	η*	Pg** predicted watts	% difference
0.4	30	0.059	30.7	2.4
0.75	116	0.29	130.9	12.8
1.07	339	0.71	298	12.2
1.34	620	1.0	549	11.5
1.57	1044	1.0	930	11.0
1.86	1730	1.0	1637	5.3
2.15	2700	1.25	2420	10.3
2.51	4753	1.83	3473	27.0

Average error of predicted power = 11.6%

TABLE 9 - Comparison of Predicted and Measured Power Consumption for 1.81m
tank, with Q = 0.032 m³s⁻¹

N s⁻¹	Pg⁺ measured watts	η*	Pg** predicted watts	% difference
0.4	30	0.04	28.7	4.5
0.75	126	0.11	123.8	1.7
1.07	3 0	0.556	262	12.7
1.34	625	0.791	481	23
1.57	970	1.0	741	23
1.86	1469	1.0	1303	11.3
2.15	2215	1.04	2077	6.2
2.51	3507	1.54	2969	15.3

Average error of predicted power = 10.7%

+   Pollard (17)
*   Calculated from Eqns. (5), (13), (18), (19)
** Calculated from Eqn. (21)

Ionic Solution Effects

A 0.11 M solution of potassium sulphate was used as a 'non-coalescing' system to investigate the effect on power and gas dispersion. Marucci et al. (18) have shown that a minimum bubble size is produced at this level of concentration and Smith et al. (19) observed no further effect on $K_L a$ with increased concentration. Figure 15 shows the variation of the power ratio against aeration number for the D3 impeller. Comparison with the tap water case of Figure 9 demonstrates that the efficient mixing lines agree fairly closely, indicating that there is no significant change in the power consumption in the efficient mixing zone. This agrees with the findings of Bruijn et al. (3). However, it is observed that the EMZ becomes narrower, so that it is adequately described by a single line (EML). This is due to the fact that there is an increase in N_{Fl}, and corresponding reduction in N_{Rl}, at the same gas rates. At the highest gas rates employed, no minimum or maximum can be distinguished, indicating that N_{Fl} is greater than N_{Rl}. The explanation for the occurrence of this apparently odd situation is that, before the impeller reaches a speed at which all of the sparged gas coalesces with the impeller cavities (N_{Fl} definition), gas bubbles start to recirculate in the upper half of the tank. A similar phenomenom was observed by Nienow et al. (6) for a tank of 1.83m diameter with C/H = 2.8. In their case, however, the drop in N_{Rl}, and increase in N_{Fl}, was due to the increased impeller clearance which, when reduced, caused the minimum to appear again. These remarks simply serve to indicate the importance of selecting the correct impeller clearance and diameter, otherwise an efficient mixing regime may never be achieved. Similar results were achieved for the smaller D1 and D2 impellers, but in these cases, the minima and maxima were observed at all gas flow rates.

The drop in N_{Rl} is not surprising, since the bubble size produced in the sulphate solution is much smaller compared with that of ordinary tap water. On the other hand, the increase in N_{Fl} is probably due to the hinderance, or retardation, of coalescence of the sparged gas with the gas cavities. The correlations of impeller dispersion efficiency obtained for the electrolyte solution are similar to those given previously for tap water. They are:

$$\eta_R = 6.25 \left[\frac{N^{2.53} D^{5.93}}{T^{2.45} Q^{0.33}} \right] \qquad (22)$$

$$\eta_F = 0.4A \qquad \text{for} \quad A \leqslant 1.5 \qquad (23)$$
$$\eta_F = 0.35 + 0.18A \qquad \text{for} \; A > 1.5$$

where $\quad A = \dfrac{N^{2.53} D^{4.4}}{T^{0.5} Q^{0.73}}$

From Equations (22) and (23) (A > 1.5):

$$N_{Rl} = 0.48 \left[\frac{T^{0.97} Q^{0.13}}{D^{2.34}} \right] \qquad (24)$$

and

$$N_{Fl} = 1.66 \left[\frac{T^{0.2} Q^{0.29}}{D^{1.74}} \right] \qquad (25)$$

Comparing Equations (18) and (23) we can see that there is only a small effect on η_F, and therefore the impeller power in the flooding region will not be greatly changed. This is consistent with the observation of Lee and Meyrick (20), who investigated a range of electrolyte concentrations. Equation (22) suggests that a larger drop in power is to be expected in the recirculation region compared to the tap water case. Since the average bubble size is the controlling factor affecting the change of η, a reasonable prediction of power should be obtained by using Equation (21-23) or a 'non-coalescing' system with similar bubble size range. The fit of the results shown in Figure 16 is not as good in this case, but it is nevertheless a very reasonable correlation.

Surface Aeration

As was remarked at the beginning of the paper, the rate of entrainment of gas due to surface aeration increases very rapidly under ungassed conditions, when $N > N_{SA}$. The estimates of the rates of surface aeration in Table 10, which were obtained by the method illustrated in Figure 17, clearly demonstrate the very high dependency that exists on N and D.

TABLE 10 - Rate of Surface Aeration

IMPELLERS					
D1		D2		D3	
N s^{-1}	$Q_{SA} \times 10^4$ $m^3 s^{-1}$	N s^{-1}	$Q_{SA} \times 10^4$ $m^3 s^{-1}$	N s^{-1}	$Q_{SA} \times 10^4$ $m^3 s^{-1}$
18.4	0.45	9.45	1.239	5	0.246
20.5	1.05	10.0	1.783	5.5	0.744
		10.8	2.152	6	1.697
		12.75	3.47		

CONCLUSIONS

The impeller dispersion efficiency, η, (rate of gas coalescence with impeller cavities/rate of gas sparging) has been correlated in terms of the main variables of the system. As well as providing a useful method of identifying the different regions of gas-liquid mixing, it can be used to estimate the degree of flooding or recirculation. On this basis, by making use of all of the experimental data in the flooding and recirculation regions, the conditions N_{R1} and N_{F1} can be more accurately predicted, particularly so in the latter case. In the efficient mixing region, the power consumption over a vessel size range of about 10:1 can be predicted within 10%. Similar relationships have been developed for electrolyte solution, the main difference being the larger drop in power predicted in the recirculation region.

The results serve to indicate that accurate measurements and analysis of

mixing processes on small scale equipment can be successfully applied to larger scale equipment. Indeed, the high sensitivity of Pg and η on impeller speed tends to make it more difficult to obtain precise correlations from measurements obtained on large vessels.

SYMBOLS USED

C = impeller clearance (m)

D = impeller diameter (m)

Fl = flow number, Q/ND^3 (dimensionless)

H = height of clear liquid (m)

N = impeller rotational speed (s^{-1})

P = impeller power (watts)

Po = power number (dimensionless)

Q = sparged gas flow rate $(m^3 s^{-1})$

Re = Reynolds number (dimensionless)

T = vessel diameter (m)

$\bar{v}$ = average liquid circulation velocity (ms^{-1})

u_T = bubble terminal velocity (ms^{-1})

ν = liquid kinematic viscosity $(m^2 s^{-1})$

ρ = liquid density $(kg\ m^{-3})$

η = impeller dispersion efficiency (dimensionless)

α = external distribution coefficient (dimensionless)

Subscripts:

F = flooding region

Fl = flooding point

g = gassed

R = recirculation region

Rl = recirculation point

SA = start of surface aeration

u = ungassed

REFERENCES

1. Nienow, A.W., and Wisdom, D.J., 1974, Chem. Eng. Sci. 29, 1974

2. van't Riet, K., and Smith, J.M., 1973, Chem. Eng. Sci. 28, 1031

3. Bruijn, W., van't Riet, K., and Smith, J.M., 1974, Trans. Instn. Chem. Engrs. 52, 88

4. van't Riet, K., 1975, Ph.D. Thesis, Delft University of Technology.

5. van't Riet, K., Boom, J.M., and Smith, J.M., 1976, Trans. Instn. Chem. Engrs. 54, 124

6. Nienow, A.W., Wisdom, D.J., and Middleton, J.C., "The Effect of Scale and Geometry on Flooding, Recirculation, and Power in Gas Stirred Vessels", 1977, Proc. Second European Conference on Mixing, BHRA, Cranfield, England.

7. Nienow, A.W., Chapman, C.M., and Middleton, J.C., 1979, The Chemical Engineering Journal 17, 111

8. Wisdom, D.J., 1974, Ph.D. Thesis, University of London.

9. Holmes, D.B., Voncken, R.M., and Dekker, J.A., 1964, Chem. Eng. Sci. 19, 201

10. Oldshue, J.Y., 1980, CEP, 64

11. Govier, G.W., and Aziz, K., "The Flow of Complex Mixtures in Pipes", 1972, van Nostrand-Reinhold, 379

12. Michel, B.J., and Miller, S.A., 1962, A.I.Ch.E.J. 8, No. 2, 262

13. Loiseau, B., Midoux, N., and Charpentier, J-C, 1977, A.I.Ch.E.J. 23, No. 6, 931

14. Yung, C.N., Wong, C.W., and Chang, C.L., 1979, Canad. J. Chem. Eng. 57, 672

15. Figuierodo, M., 1978, Ph.D. Thesis, University of Edinburgh.

16. Pharamond, J.C., Roustan, M., and Rogues, H., 1975, Chem. Eng. Sci. 30, 907

17. Pollard, G.J., "Flooding and Aeration Efficiency in Standard Stirred Vessels", 1978, Proceedings of International Conference on Mixing, Mons.

18. Marucci, G., and Nicodomo, L., 1967, Chem. Eng. Sci. 22, 1257

19. Smith, J.M., van't Riet, K., and Middleton, J.C., "Scale-up of Agitated Gas-Liquid Reactors for Mass Transfer", 1977, Proc. Second European Conference on Mixing, BHRA, Cranfield, England.

20. Lee, J.C., and Meyrick, D.L., 1970, Trans. Instn. Chem. Engrs. 48, 737
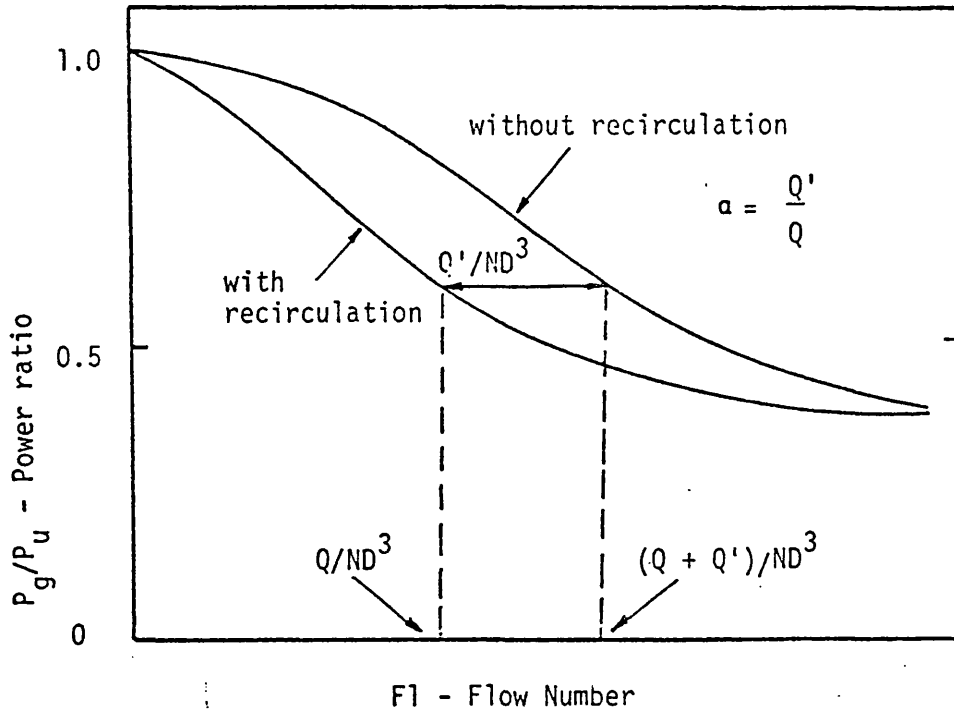
Figure 1   Determination of a from gassed power ratio
curves at constant impeller speed (5)
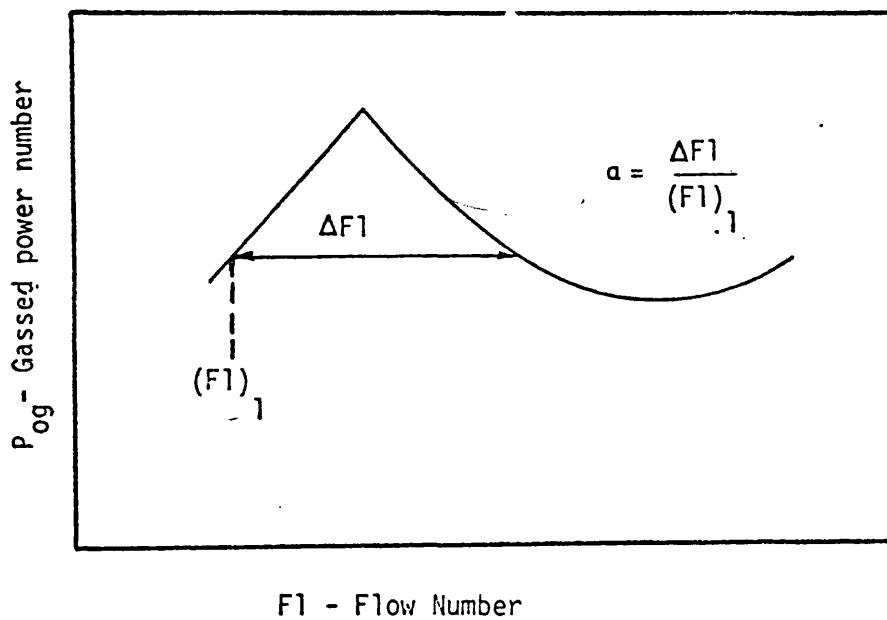
Figure 2   Determination of a from gassed power ratio
curves at constant sparged gas rate (7)
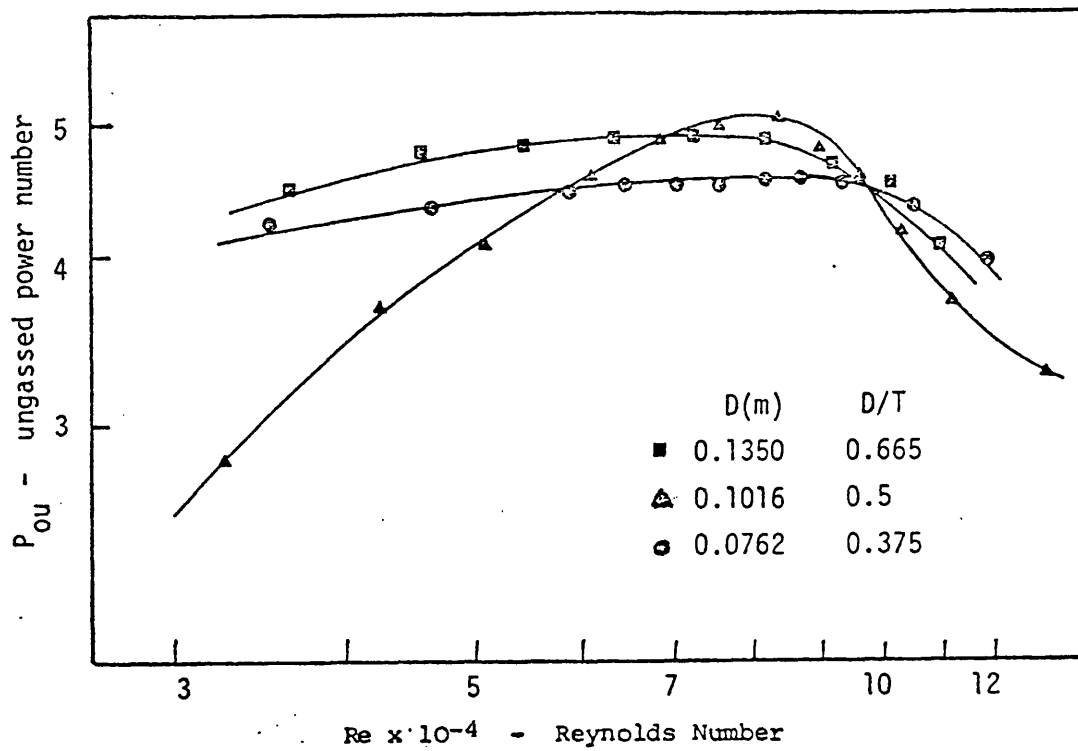
Figure 3   Effect of impeller diameter on ungassed
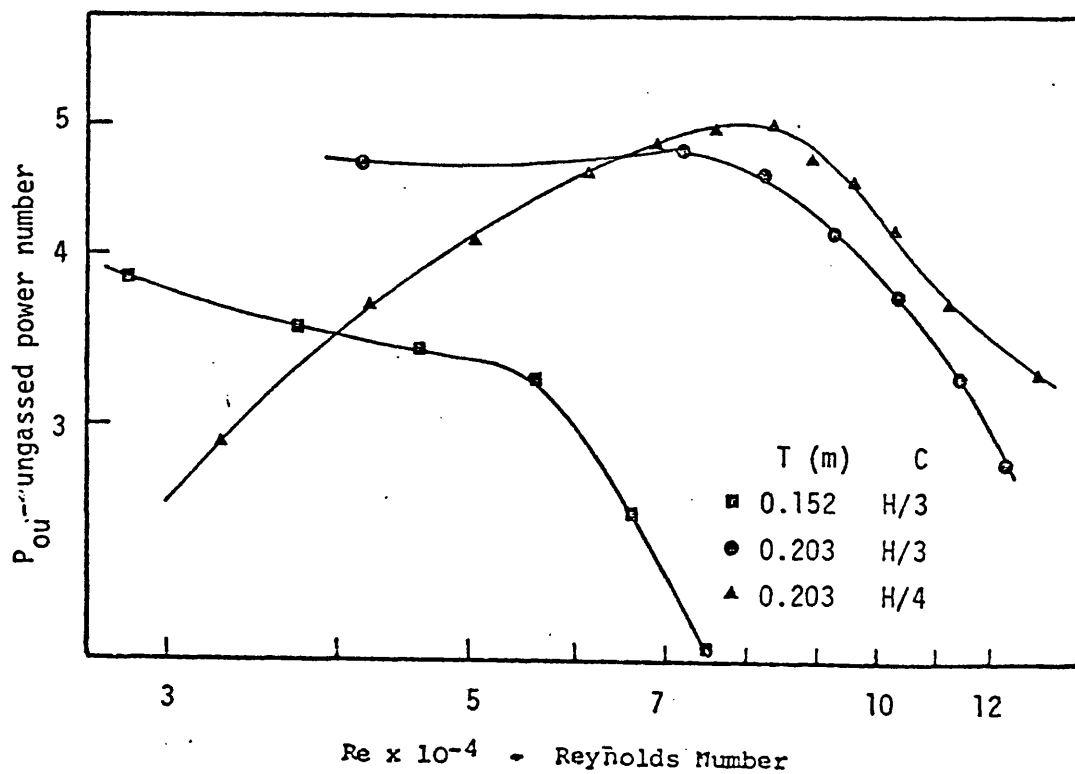power number (T = 0.203 m,C = T/4)

Figure 4   Effect of tank diameter and impeller clearance on
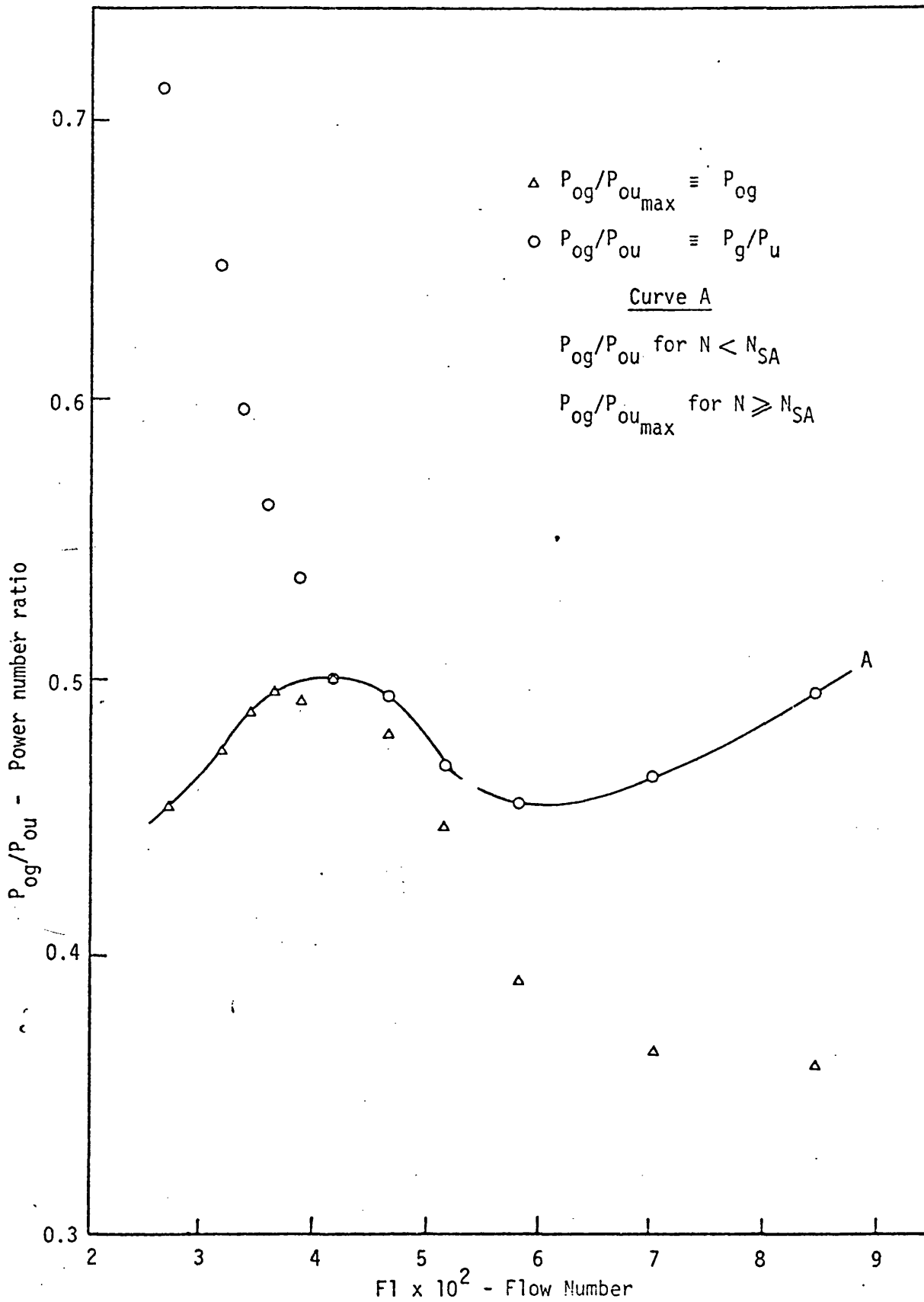ungassed power number (D = 0.1016 m)

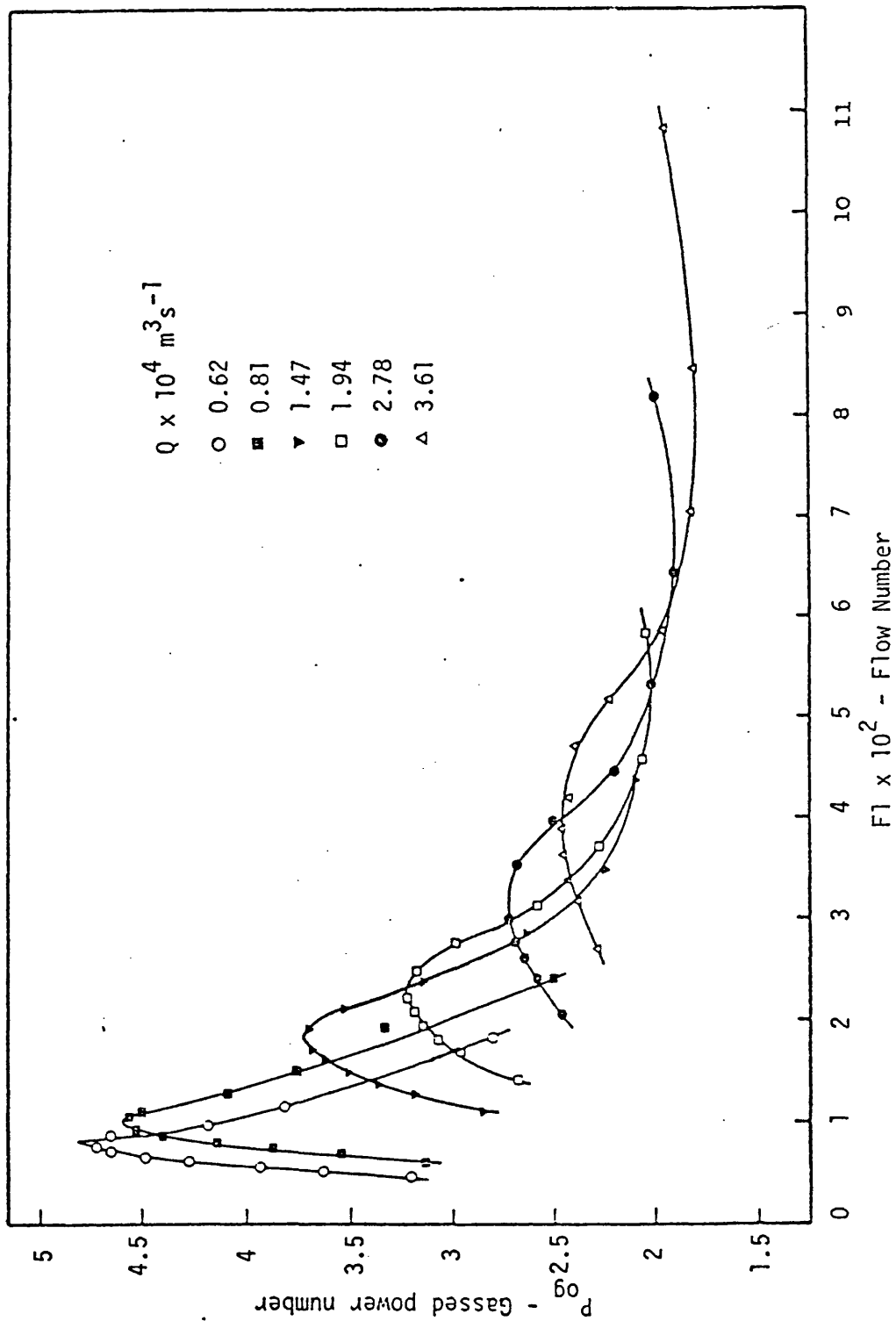Figure 5 Representation of gassed power data ($D = 0.1016$ m, $Q = 3.61 \times 10^{-4}$ m^{3}s^{-1})

Figure 6 Gassed power number against flow number (D = 0.1016 m)
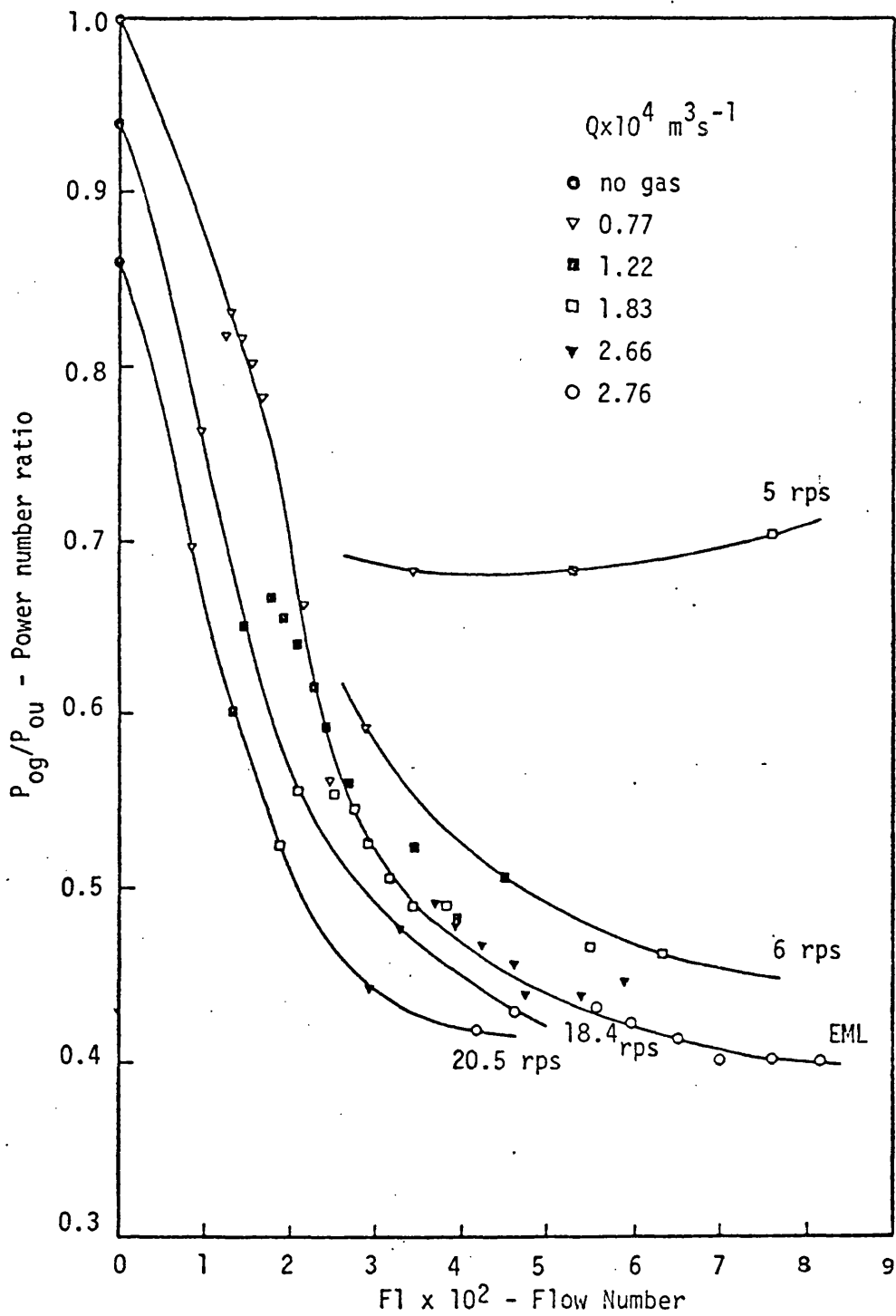
Figure 7 P_{og}/P_{ou} against Flow Number showing efficient mixing line (D = 0.0762 m)
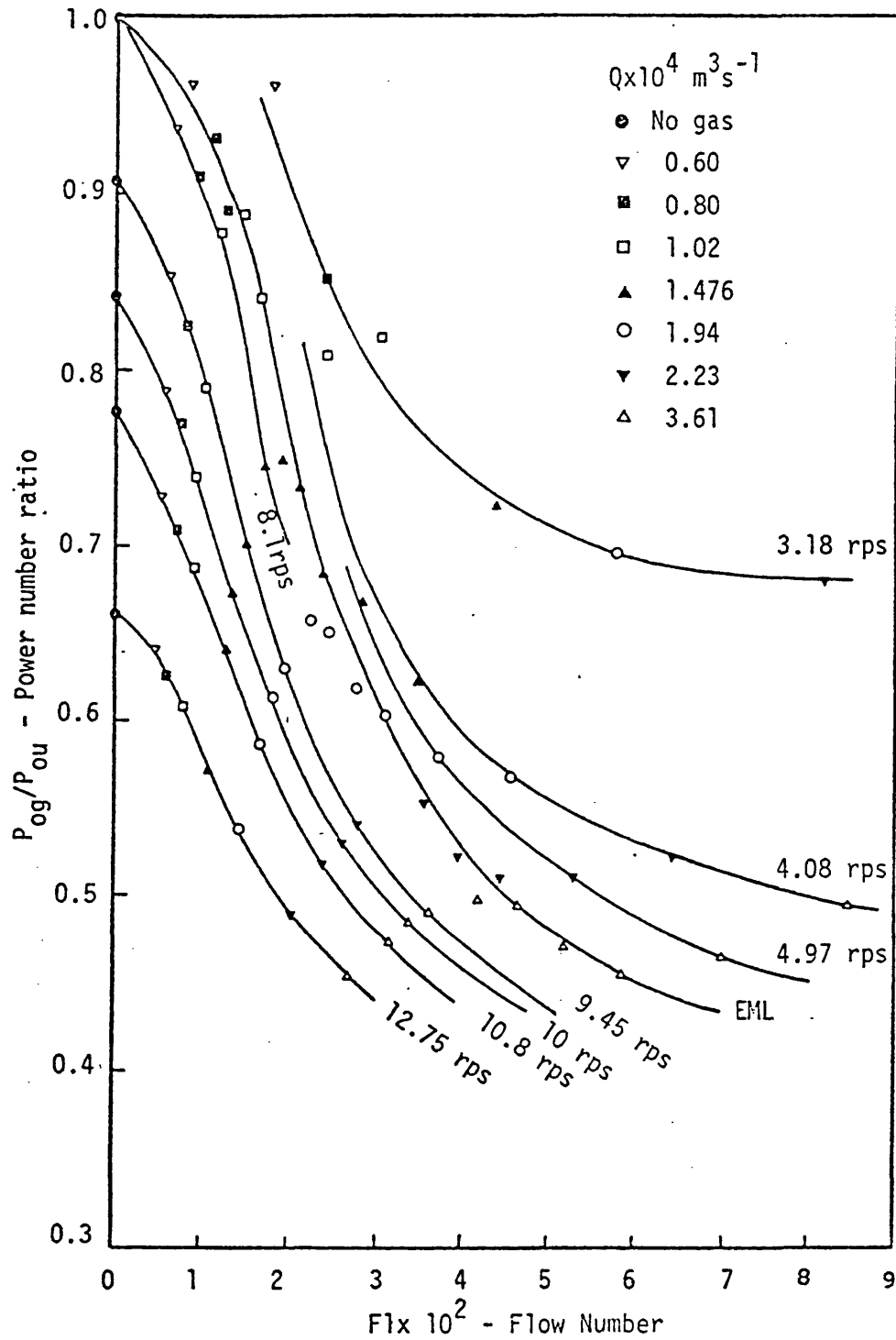
Figure 8 P_{og}/P_{ou} against Flow number showing efficient mixing line (D = 0.1016 m)
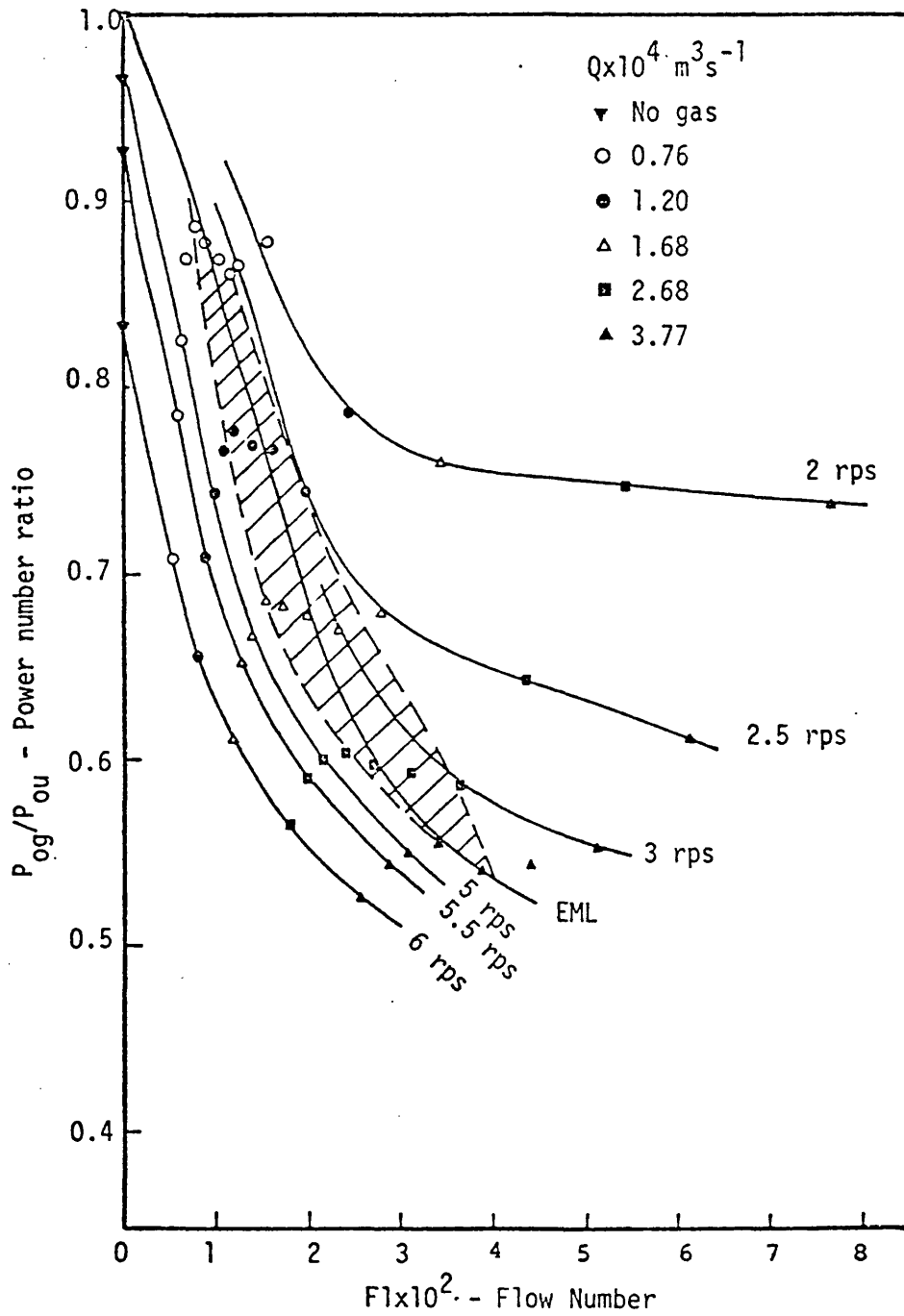
Figure 9 P_{og}/P_{ou} against Flow Number showing efficient mixing zone (////) and efficient mixing line (D = 0.135 m)

$$\eta_2 = \eta_R = \frac{Q_1}{Q_2}$$

$$\eta_3 = \eta_F = \frac{Q_1}{Q_3}$$
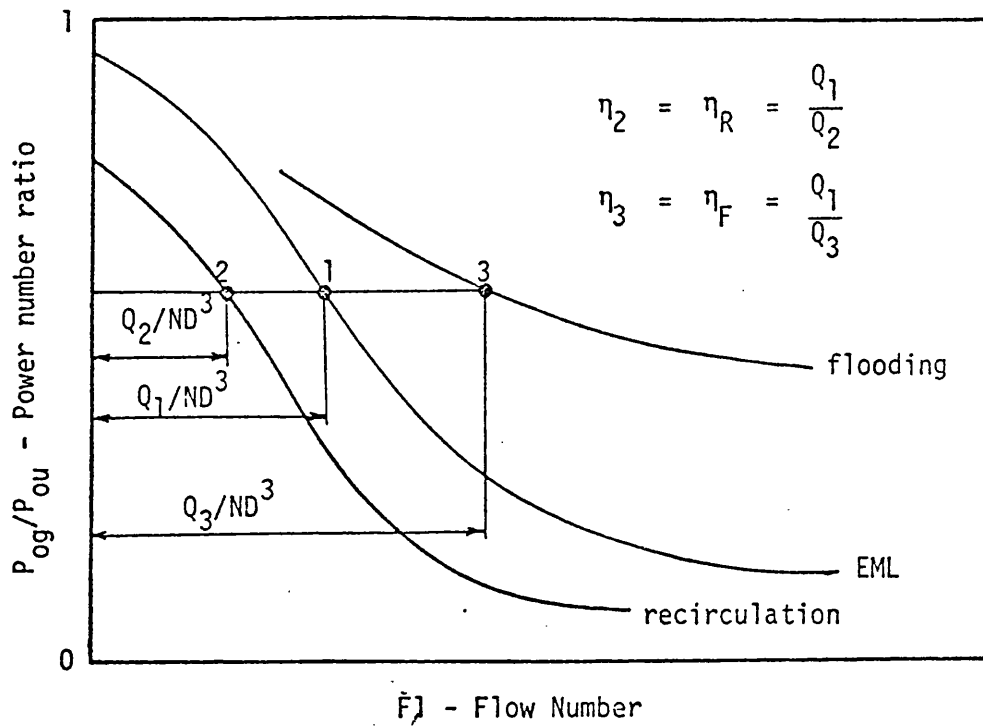
Figure 10   Determination of impeller dispersion efficiency from P_{og}/P_{ou} against Fl
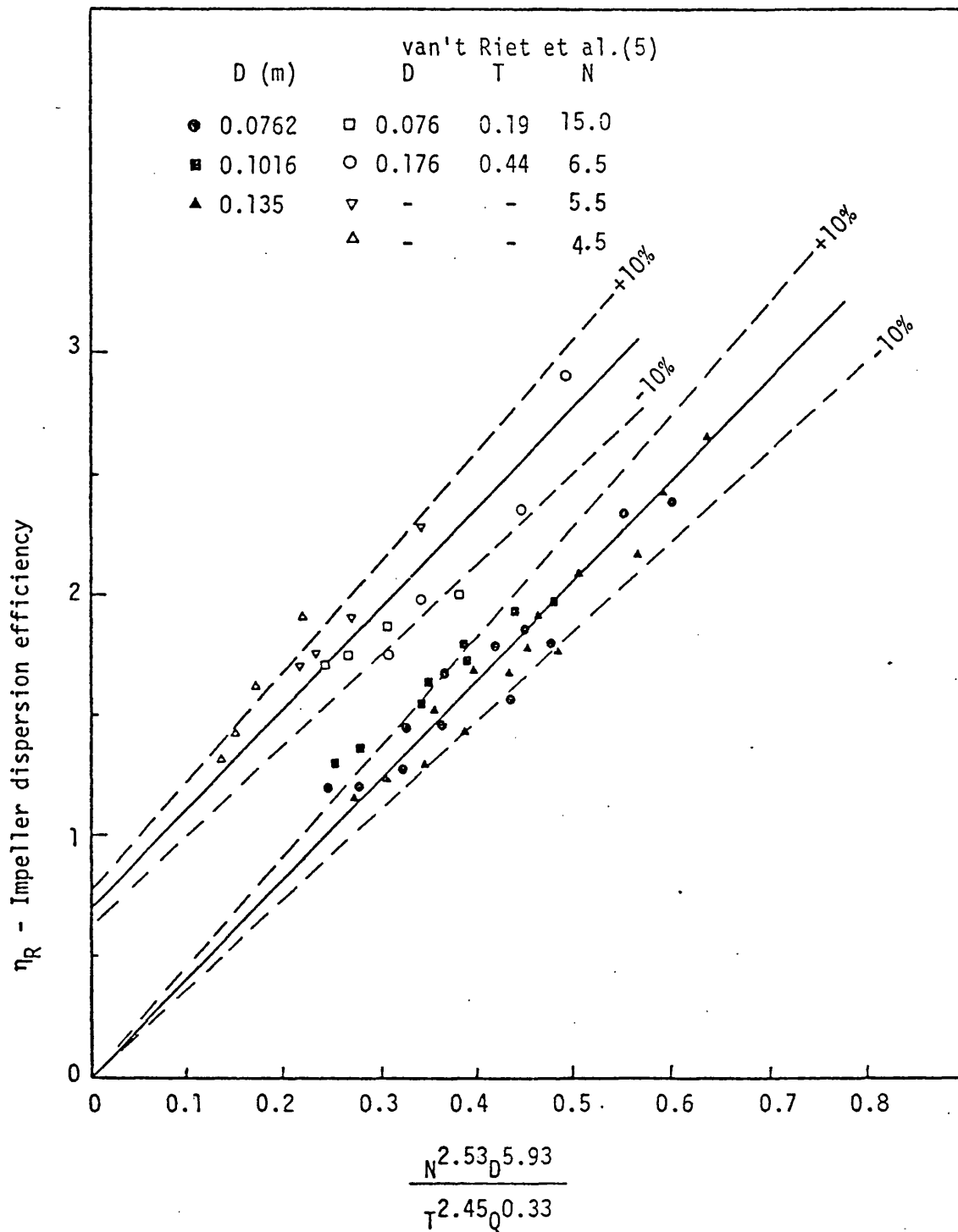
Figure 11   Correlation for impeller dipersion efficiency in recirculation region
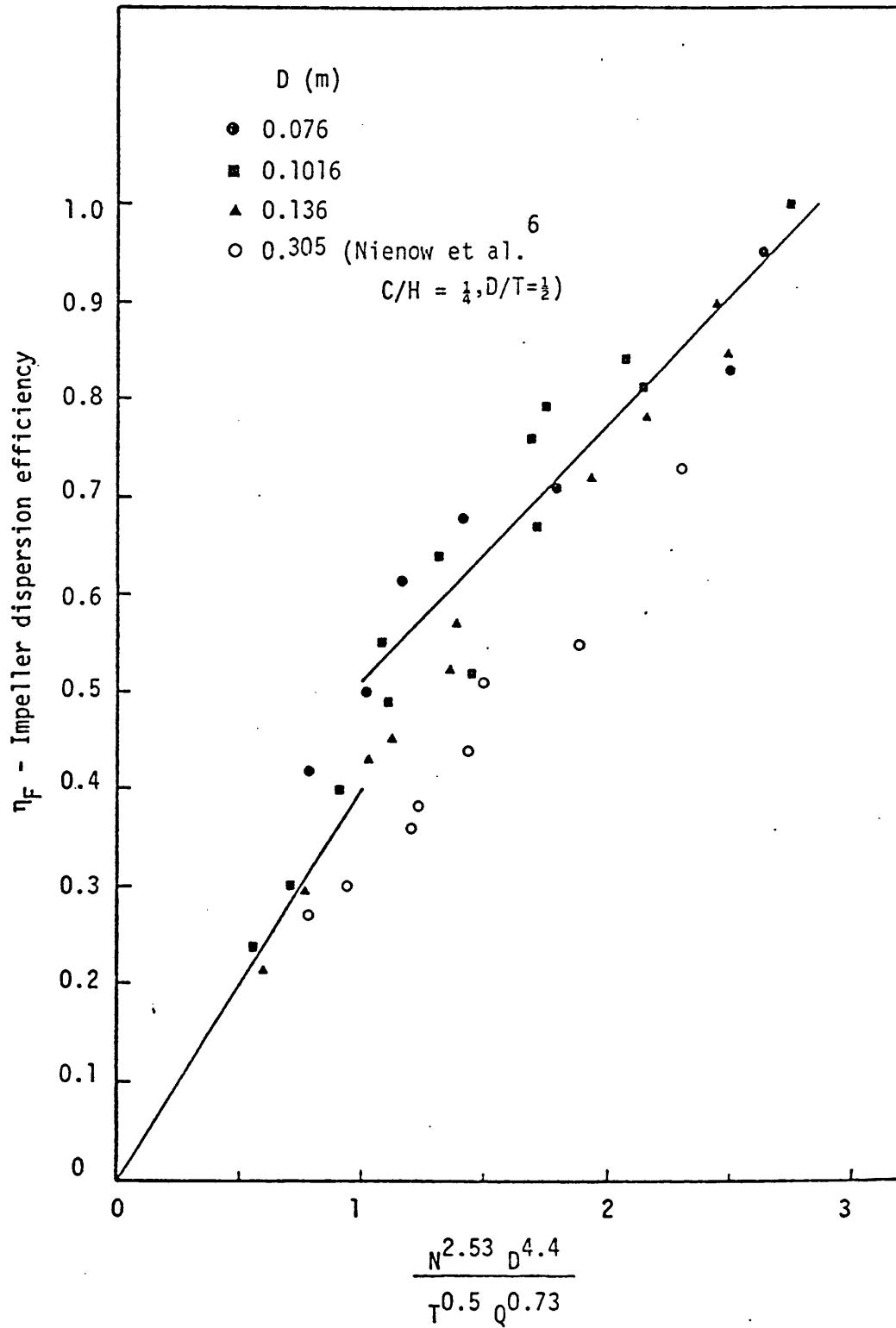
Figure 12 Correlation for impeller dispersion efficiency
in the flooding region
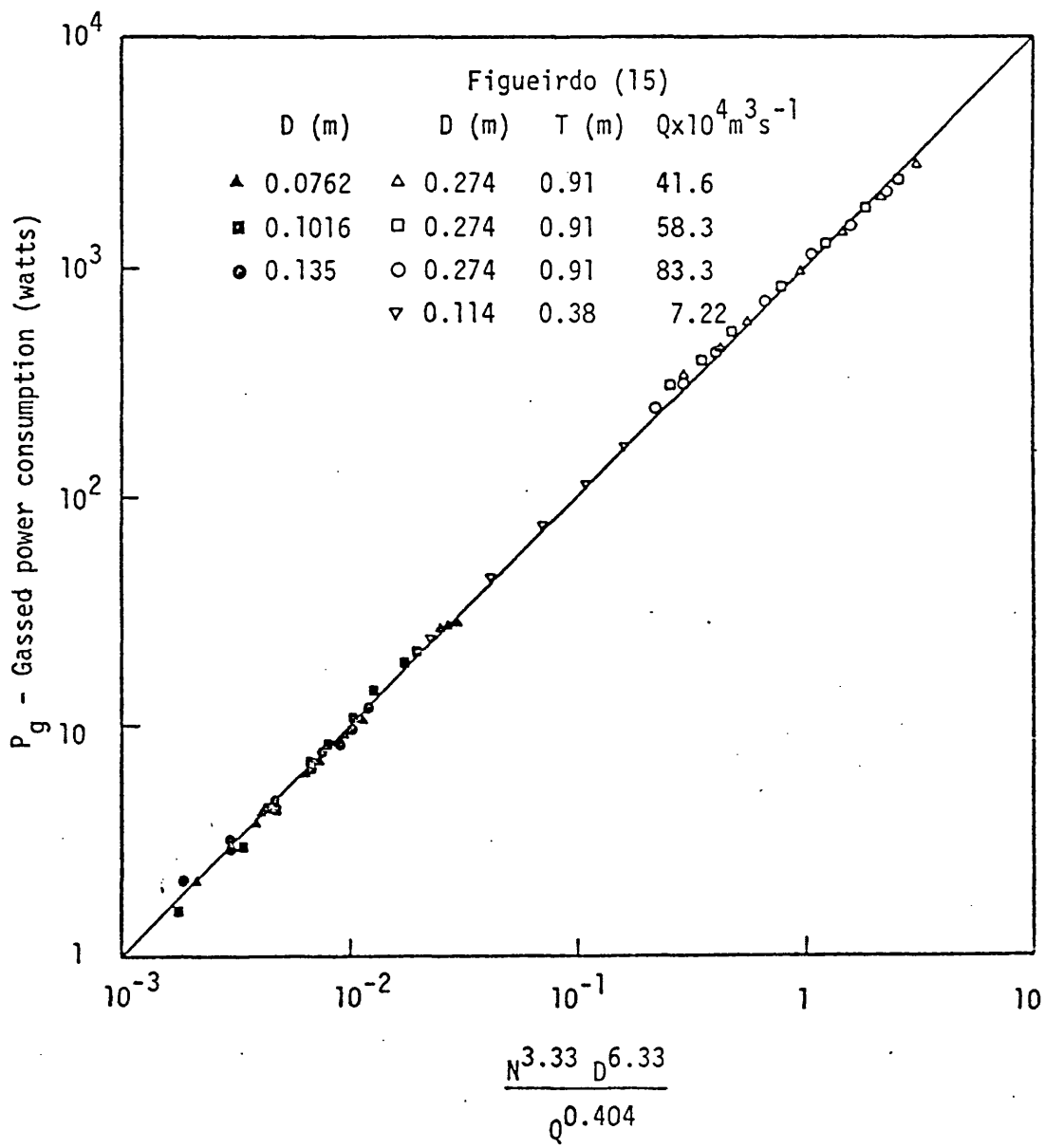
Figure 13   Power consumption in the efficient mixing region
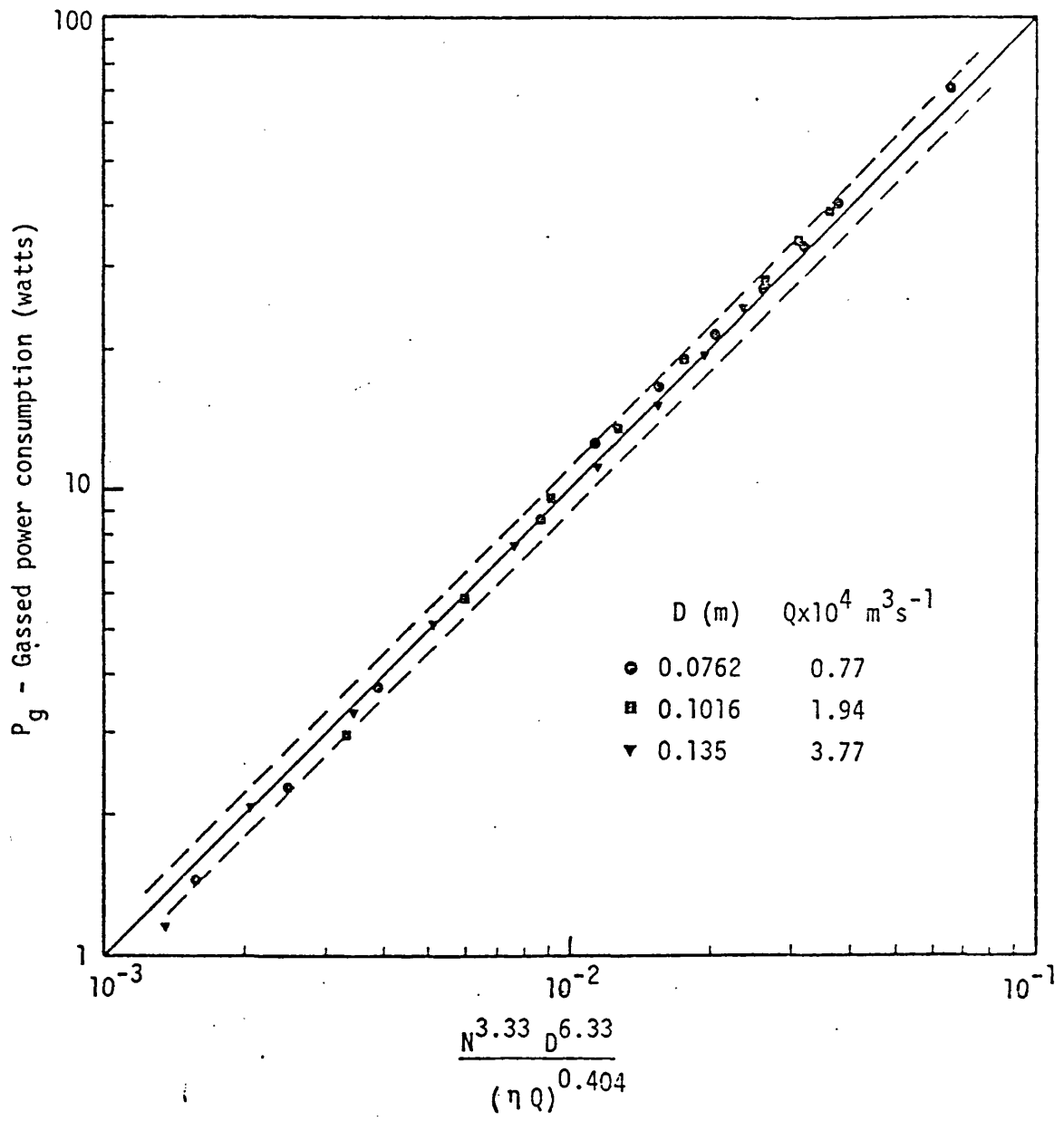
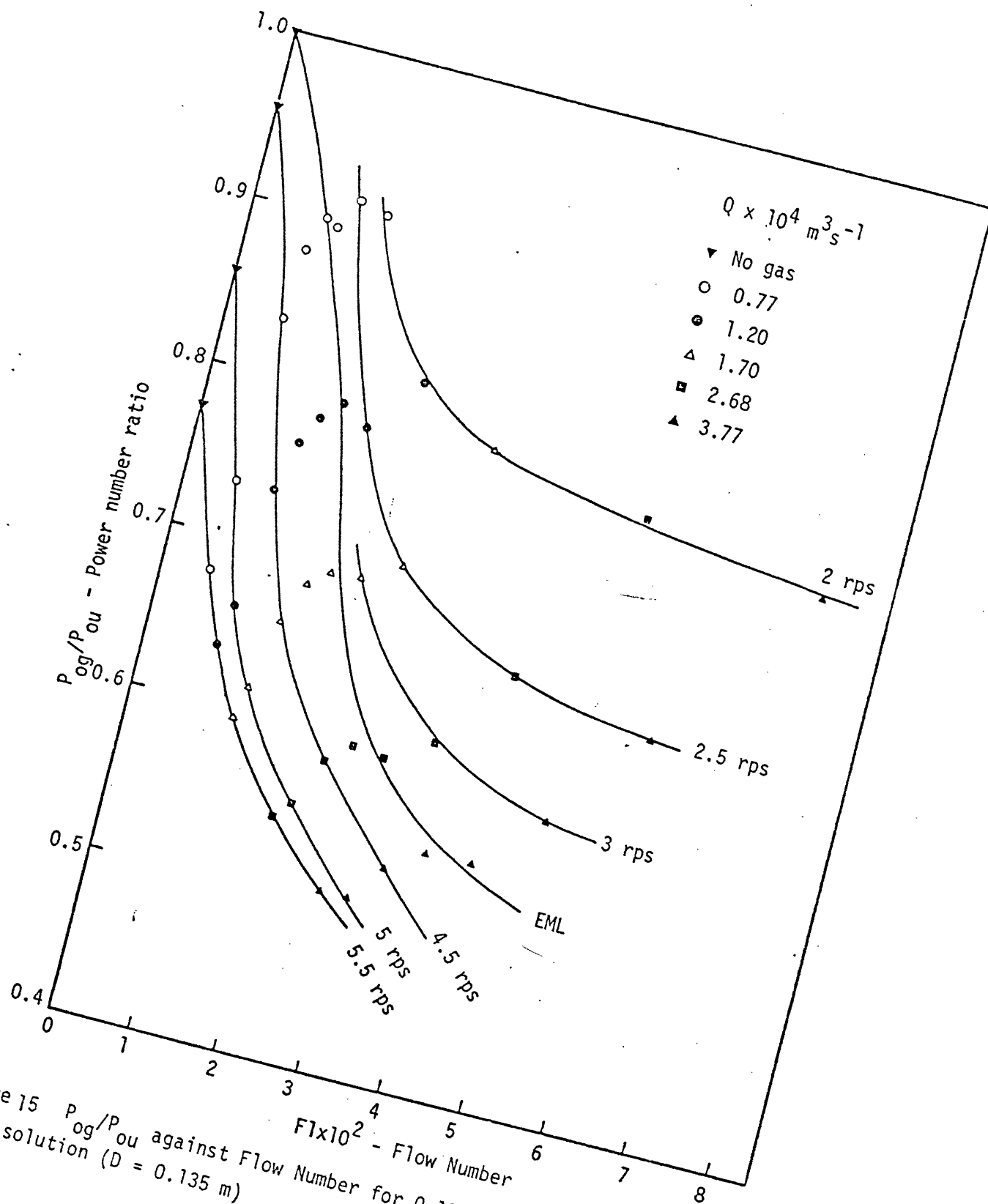Figure 14   Generalised power correlation - Eqn.(21) (Tap water)

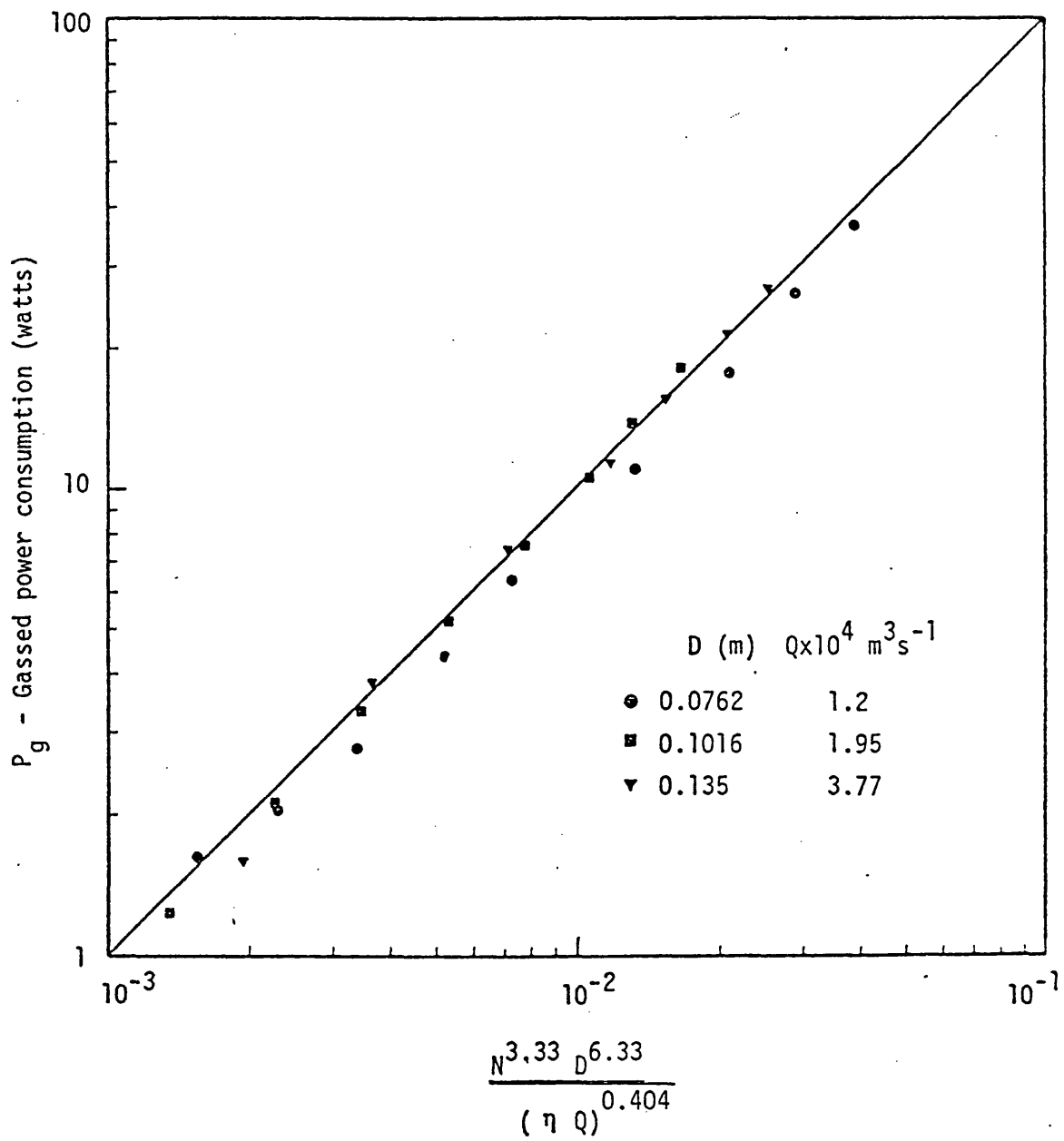Figure 15 P_{og}/P_{ou} against Flow Number for 0.11 M K_2SO_4 solution (D = 0.135 m)

Figure 16 Generalised power correlation - Eqn.(21)
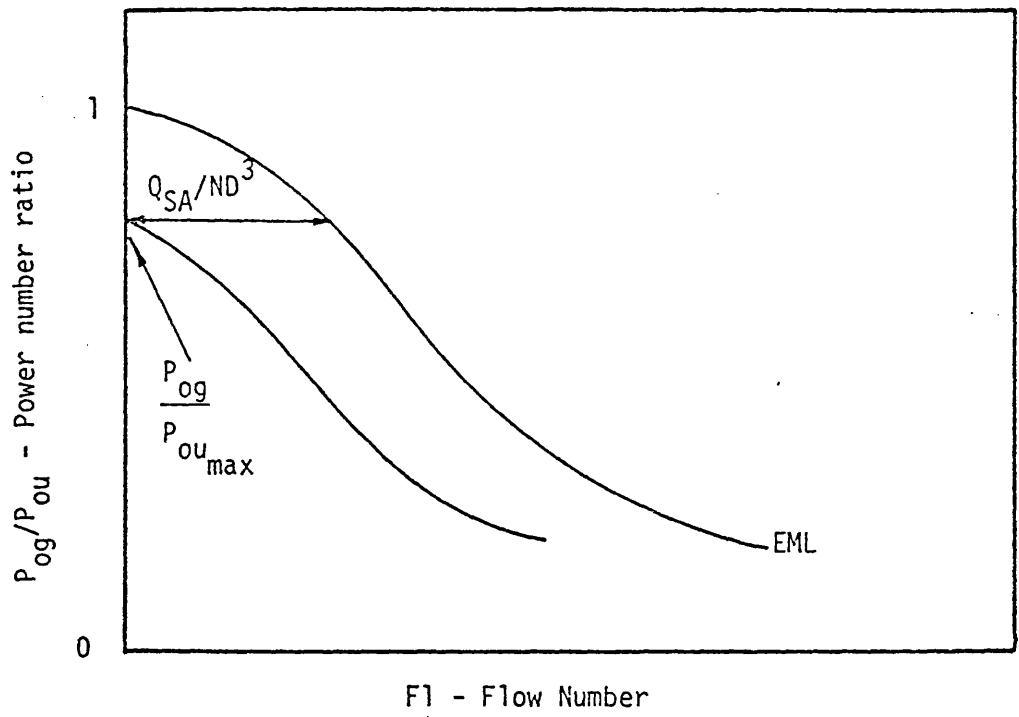
(0.11 M K_2SO_4 solution)

Figure 17 Determination of the rate of surface aeration from a plot of P_{og}/P_{ou} against Fl